Geology and genesis of the Battle Zone VHMS deposits, Myra Falls district, British Columbia, Canada.

Briony Jean

Briony J. Sinclair B.Sc.(Adel.)**Hons**(UTas)

UNIVERSITY OF TASMANIA

Submitted as fulfilment of the requirements
for the degree of
Doctor of Philosophy

School of Earth Sciences
University of Tasmania
January, 2001

This thesis contains no material that has been accepted for the award of any degree or diploma at any university. To the best of the candidate's knowledge this thesis contains no copy or paraphrase of material previously written or published by another person, except where due acknowledgment is made.

Signed: B.J. Sinclair

Date: 30/1/01

Authority of Access

Abstract

The Myra Falls volcanic hosted massive sulfide (VHMS) district, is located on Vancouver Island, British Colombia, Canada. The district has a pre-mining reserve of 40Mt @ 6.2% Zn, 1.8% Cu, 47.5 g/t Ag and 2.1g/t Au. The Battle Mine is the youngest in a series of mines, which have kept the district in continuous production since 1966. The Battle mine was discovered in May 1991 through mine site exploration.

The Battle Mine contains a pre-mining reserve of 7Mt @ 12.5% Zn, 1.8% Cu, 0.7% Pb, 53.2g/t Ag and 1.4g/t Au and is made up of several lenses: Battle, Gopher, South Trough, Upper Zone and Gap. These lenses lie at two stratigraphic levels and represent two distinct styles of VHMS mineralisation.

Host rocks to the Battle Mine lenses are part of the Devonian Sicker Group, which forms the base of the Wrangellia Terrane of the Canadian Cordillera. Footwall to the Battle, Gopher and South Trough lenses is the Price Formation. The Price Formation is a >300m thick sequence of basaltic andesite flows, flow breccias and associated volcaniclastic deposits. The Battle, Gopher, and South Trough lenses are overlain by up to 30m of fine-grained "chert" and then by 30-70m of rhyolitic mass flow deposits with minor intercalated non-volcanic sediments. The rhyolitic mass flow deposits are overlain by 10 to 60m of massive to autoclastic quartz-feldspar-phyric (QFP) rhyolite. The Upper Zone lenses lie at the top of the rhyolitic mass flow deposits along the contact with the QFP, while the Gap lens is hosted within the QFP. The entire sequence is overlain by basaltic-andesite to andesite lavas and related breccias of the Hanging Wall Andesite.

The mine sequence has been subjected to at least two stages of prehnite-pumpellyite to lower greenschist facies metamorphism and at least five stages of post-depositional deformation. Several stages of pre- to syn-mineralisation faulting are also interpreted. Throughout the host sequence there is a strong sub-vertical cleavage with stretching lineation trending NW to NNW. The cleavage is axial planar to folds and the stretching lineation parallels the fold axis. This cleavage is interpreted as pre-Permian and marks the first recognisable post-mineralisation structure in the mine area and is named D2. D3A structures include north striking dextral, west striking sinistral faults and high angle reverse faults with NW strike and are associated with quartz carbonate veins. D3B structures include a variety of south dipping thrust faults range from flat lying to thrusts to high angle structures. Both D3 events show brittle ductile textures (discrete faults surrounded by narrow zones of cleavage development). D3A structures are interpreted as Mid to Late Jurassic in age while D3B structures probably correlate with the a Cretaceous event of England and Calon (1991). The fourth major structural event (D5) is an Eocene thrusting which forms broad zones of anastomosing gouge and brecciation and bounds the ore lenses in NW to NNW orientation. A variety of gougy faults showing normal movement exists through out the Battle Mine and are correlated with D4 and D6 events.

Alteration in the Battle Zone is divisible into several types depending on precursor rocks (Price Formation andesite or HW Rhyolite) and mineralogy and style of alteration. The Price Formation directly underlying the Battle, Gopher and South Trough lenses is intensely altered by texturally destructive sericite-pyrite $\pm$ quartz alteration. Zones of intense Mg-chlorite - pyrite alteration also occur. Approximately 20m below the base of the massive sulfides, alteration changes into less in-

tense sericite-chlorite-quartz alteration, relic textures (eg pillow margins) are visible. The HW Rhyolite is also altered by texturally destructive quartz-sericite alteration, which is heterogeneous creating pseudo-fiamme. Dolomite alteration occurs in the Battle Zone HW Rhyolite away from massive sulfide mineralisation.

Alteration in the Price Formation in the footwall to Battle, Gopher and South Trough lenses is characterised by large gains in S and K for all alteration types and gains Mg and Mn in Mg-chlorite alteration. These gains are due to addition of muscovite and sulfides to the altered rocks and the formation of chlorite in Mg-chlorite alteration. Calcium, Na, Sr, Ni and Cr are depleted in all footwall alteration types while Mg and Mn are lost in the intense sericite-pyrite $\pm$ quartz alteration. Hangingwall alteration is characterised by the addition of S, Cu, Ba, Zn, Ni and As associated with the growth of barite and sulfide minerals. The silicified samples also gain Si, due to the formation of quartz, while sericite-altered samples gain K during muscovite growth. Dolomite-altered samples gain S and metals along with Mg, Ca and Mn resulting in the formation of dolomite. However in all alteration types only the absolute changes in Si significantly affect the change in mass of the rock during alteration.

The Battle, Gopher and South Trough lenses are composed of sphalerite, pyrite, chalcopyrite, galena, tennantite and accessory barite, rutile, and telluride minerals. These lenses show classic VHMS mineralogical zonation from a sphalerite-galena-tennantite-barite-rich top downward through massive sphalerite-pyrite-chalcopyrite, massive pyrite-chalcopyrite and massive pyrite zones towards the base of the lenses. In contrast the Upper Zone and Gap lenses are composed of sphalerite, pyrite, bornite, chalcopyrite, galena, tennantite and barite with accessory colusite, renierite, anilite and electrum. Metamorphism has resulted in the obliteration of most of the primary VHMS ore textures, with the exception of some textures preserved in pyrite.

Zonation of metals correlates with the observed mineralogical zonation within each lens and between lenses. The South Trough lens, which is the stratigraphically lowest lens in the Battle mine, shows the highest Fe and lowest Pb and Ba. In contrast the Gap lens, which is the stratigraphically highest lens, has the greatest Au-Ag-Ba-As-Pb contents. Within each lens sphalerite-galena-tennantite-rich zones are marked by enrichment in Pb-Cu-Ba-Au-Ag-As and Hg. Underlying is a zone of Zn-Cd enrichment followed by a zone of Cu-Fe-Ni+Au toward the base of the lenses. Manganese, Mo and P are elevated in sediments overlying the Battle, Gopher and South Trough lenses, while footwall alteration below the Battle, Gopher and South Trough lenses is enriched in Se and P.

The Gap lens shows a similar zonation in Ba-Pb-As-Zn-Cd and Fe from hangingwall to footwall, although Ba-Pb-As zone is more voluminous due to the enrichment in these elements compared to the underlying lenses. However, metal zoning reveals a strong zone of Cu-Ag and Mo cross cutting the typical VHMS zonation within the Gap lens. This zone of Cu-Ag-Mo corresponds to the distribution of bornite-anilite. Although metamorphism of the Gap lens has destroyed evidence of primary paragenetic relationships textural relationships of bornite and chalcopyrite suggest bornite occurred as a replacement of chalcopyrite. The most likely factor in driving this reaction would be an increase in the fo_2 of the fluid and/or a decrease in temperature.

Detailed mineralogical examination of the Upper Zone and Gap ores has also revealed the presence of stromeyerite (Cu-Ag-S), chalcopyrite, and electrum. This Cu-Ag-Au rich assemblage cross

cuts all other sulfide minerals and forms vermicular intergrowths with bornite and anilite. Delicate textures of this assemblage suggest a late (possibly prograde) metamorphic age for this assemblage, the Cu, Ag and Au being derived from recrystallisation of bornite, anilite and gold during metamorphism.

The Battle, Gopher and South Trough lenses were deposited in the Devonian, on top of the Price Formation on the seafloor with minimal (<10m) of sediment cover until swamped by a massive influx of rhyolitic mass flows. The hydrothermal fluid associated with the deposition of these lenses is interpreted to have had temperatures between 250-350°C, weak acidity (ph = 4-5) and a salinity in the range of 3-8wt%. Sulfur isotope data indicate a reduced seawater sulfate source for the sulfides and a direct seawater source for the sulfates. The swamping of the depositional environment with volcaniclastics did not stop the hydrothermal system. Hydrothermal fluids continued to percolate up through the rhyolitic volcaniclastics until they encountered the QFP. The QFP provided a barrier to the ascending fluids which resulted in the subseafloor deposition of sulfide mineralisation as represented by the Upper Zone and Gap lenses. During percolation of the hydrothermal fluid up through the rhyolitic volcanicaniclastics the fluid cooled and became slightly more oxidised. Toward the end of the hydrothermal system the fo_2 of the hydrothermal fluid increased and the temperature decreased resulting in the formation of bornite from previously formed chalcopyrite. After the hydrothermal system ceased the hangingwall volcaniclastics and associated massive sulfide lenses were covered by the Hanging Wall andesite. The entire sequence was then metamorphosed and deformed. Metamorphism caused the recrystallisation and annealing of all sulfide minerals except pyrite. Metamorphism also resulted in remobilisation of Cu, Ag and Au within the Upper Zone and Gap lenses, with these elements deposited in crosscutting veins during the waning stages of metamorphism.

Acknowledgments

To Dr J.B. Gemmell thank you for choosing me for a project that provided not only an interesting topic but for the opportunity to travel and accomplish many personal goals. Bruce's enthusiasm for the project, the Myra Falls district and massive sulfide research in general and his support throughout the project has made it happen. And to Dr R. Berry for his steadfast support through a frustrating and slow process of working me through the structure of Battle Zone and providing the support to get me there.

This project would not have been possible with out the suggestion by Dr Steve Juras and the support from Westmin Ltd. and Boliden-Westmin Ltd. I'd like to thank Steve Juras for setting up the project and for his support throughout and especially for welcoming me into his family for Thanksgiving. To Albert, Ivor, Rick, Finley, Cliff, Sean, Dean, and Azime for your help and discussions and enthusiasm for the project, which provide a wonderful environment for research. Also to the analytical lab staff Lucia, Rob, Harvey and all the other staff at Myra Falls who contributed to the project. A special thanks to Guy, Nicki, Sam, Louise, Tiffany, Steve, Mat, Sean, Farmer, Andy, Albert, Dan who all helped to enlightened me to the Canadian way and provided a lighter side to the tedium of months in the mining camp.

A big thankyou to the support staff of CODES and the Geology department: June, Peter, Nilar, Di, Christine, Moya, Katie, Lyn, Marylin, and Angela for making the place run and for fixing immumerable hitches, especially June for her constant advice on all things to do with computors.
Phil Robinson, Nilar and Katie for help in the preparation of samples and the execution of XFR analysis. Dave Steele for advice and assistance with microprobe work. Christine Cook and Keith Harris for help with sulfur isotope work.

Gary McArthur for his wonderful thesis which provided inspiration for documentation of sulfide textures and for his help, support and enthusiasm in carrying out the DATAMINE™ modelling.

To my brother in law, Greg, for understanding me and being my big brother through the good times and bad and for sharing the pain and joy throughout the PhD.

To my mum and dad who's support and encouragement through out my life and especially through the ups and downs of this PhD. To my sister Kathy for her love and support through some very difficult times. To the rest of my family: Popa, Jackie, Tim, Leisa, Luke, Bob, Sandy, KJ and Mat for just being there.

To my fellow PhD students past and present, who have provided inspiration and knowledge, and made the day to day grid worth while through their friendship and assistance. Especially Andrew Rae, thanks for all the coffee and for puting up with me for 4 years.

Finally to all the people who have touched my life, the good, the bad and the ugly, their influences have modelled me into the person I am today, and without which I would not have had the strength and determination to complete this work. Thank you all.

Table of Contents

List of Figures Page

List of Tables

List of Plates **Page**

Chapter 1

Introduction

1.1 Introduction

The Battle Zone occurs within the Myra Falls VHMS district, located at the geographic centre of Vancouver Island (Fig. 1) and comprises a multitude of Zn-Cu±Ag-Au rich sulfide lenses on at least two stratigraphic levels (Fig. 2) The upper of these stratigraphic levels was first discovered in the early 1900's (see below) as gossanous outcrop on the slopes of the Myra Valley. Mining commenced in 1966 as the Lynx pit and progressed to underground operations. The lower horizon was discovered in the late 1970's,

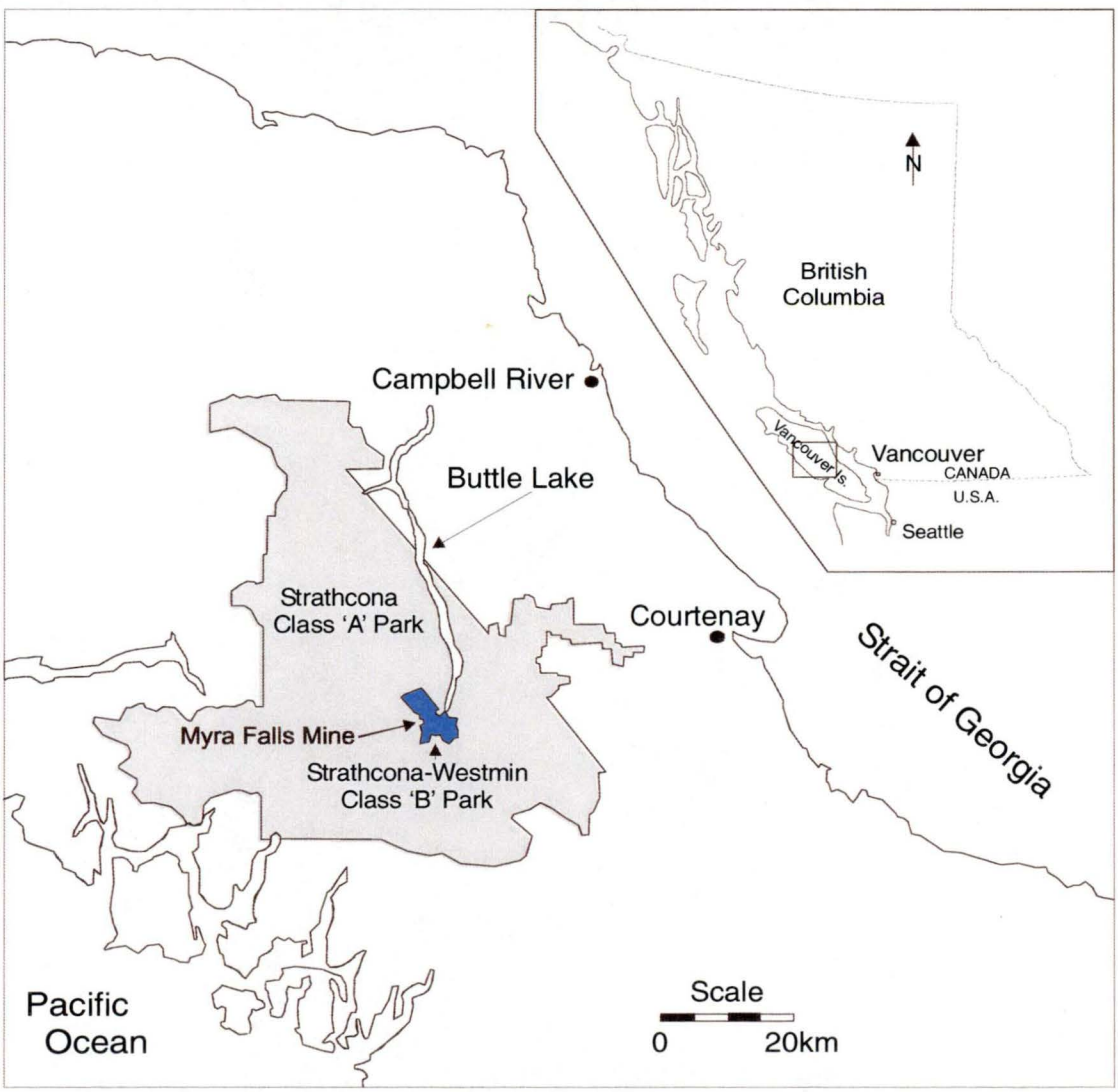

Figure 1. Location of the Myra Falls VHMS District, the Strathcona-Westmin Class "B" Park, and the Strathcona Provincial Park, on Vancouver Island, British Columbia, Canada.

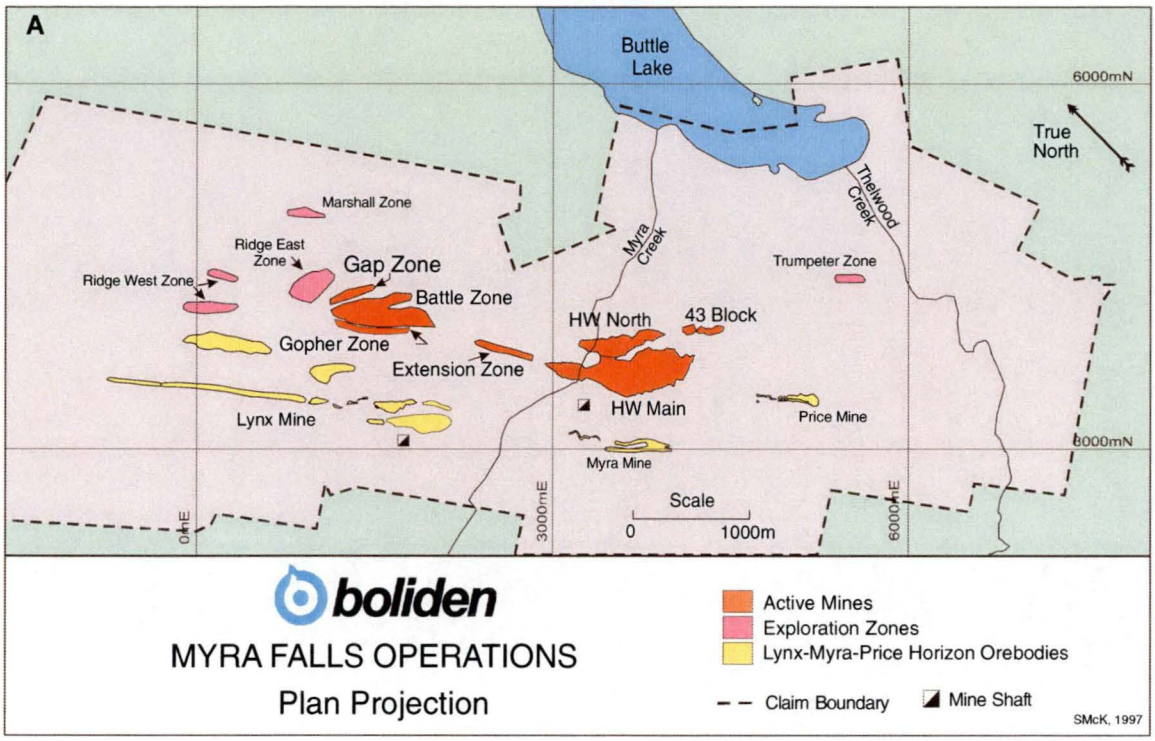

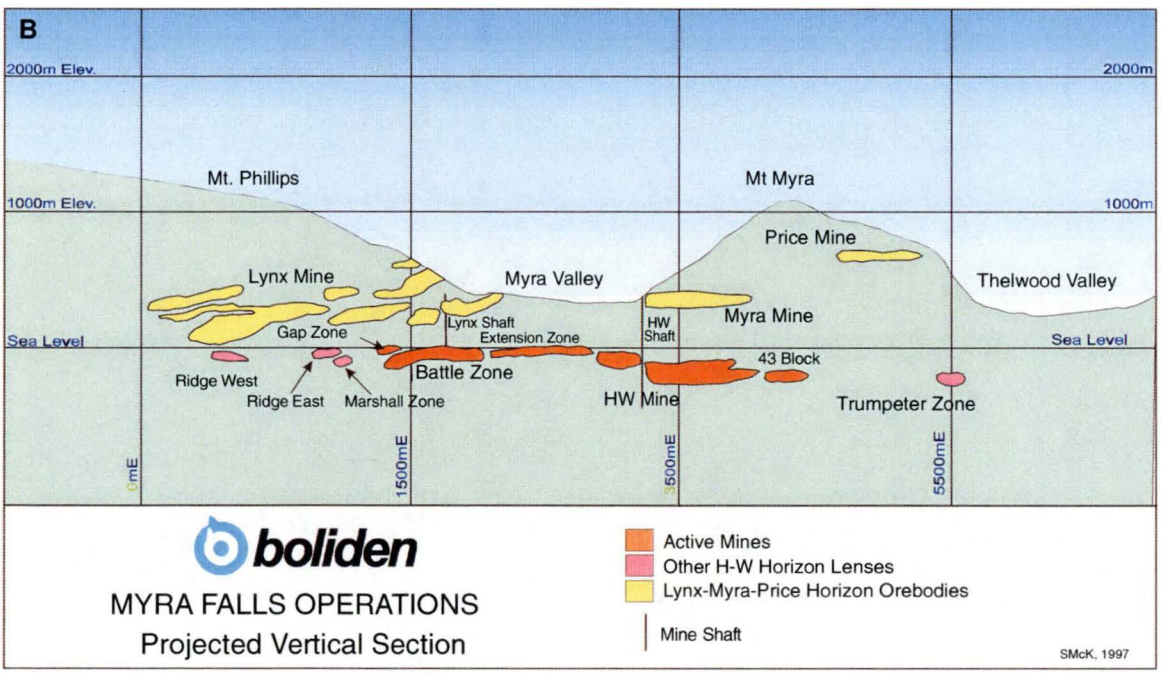

Figure 2. Plan and vertical projections of known ore lenses in the Myra Falls area. A. Plan projection showing the claim block, creeks and lakes. B. Vertical projection showing topography. Both diagrams drawn by McKinley 1997.

350m below the Myra Valley floor, and has been the focus of mining operations since 1985. The district and mining operations are owned and operated by Boliden-Westmin Ltd. The operation consists of two operating underground mines HW and Battle, as well as a 3,500 tonne per day milling facility, producing copper and zinc concentrates.

1.2 Environment

The Myra Falls VHMS district is located within Strathcona Provincial Park, the oldest Provincial Park in British Columbia. The Boliden-Westmin Ltd. claim block is approximately seven kilometers long and two to three kilometers wide, its outline defines the boundary of Strathcona-Westmin Provincial Class 'B' Park. The mining operation is located in the Myra Valley a hanging glacial valley dominated by steep rugged mountainous terrain with up to 1,200 meters of relief. The slopes are covered by cool climate rainforest (fir, hemlock and cedar) which changes to alpine meadows and rocky outcrops above the 4,000 foot level. Black bear and deer are common visitors to the mine, while shyer elk, wolves and cougars have occasionally been sighted near the mining operations.

1.3 History

The claims covering the Lynx and Price orebodies were originally prospected and staked in 1918 by James Cross and Associates of Victoria. The Myra Mine was originally held by the Paramount Mining Company of Toronto. They did some development work between 1919 and 1925 with inconclusive results. In 1959 the claims were acquired and consolidated by the Reynolds Syndicate, who in turn sold them to Western Mines Limited in 1961. Western Mines concentrated their exploration in the Lynx claim group which had the best showings within the camp. By mid-1964, after potential ore zones consisting of 1.5 million tonnes were defined on five levels, a decision was made to begin production.

In 1966, the Lynx Mine started development as an open pit. From 1969 to the end of 1974 the Lynx open pit was gradually phased out in favour of underground ore development. The pit was completed in 1975 with 1.6 million tonnes having been produced. The underground operation continued until 1992 proving the main stay of the Myra Falls operation until 1985 when the HW mine came on line.

Development of the Myra Mine commenced in 1970 with production commencing in 1972. It operated for 13 years and although it was not a large mine, it carried excellent silver and zinc values. Mining was terminated in late 1985 due to depletion of reserves.

The Price orebody, discovered early in the history of the camp. Received serious attention during the period from 1979 to 1981, which resulted in the discovery of the Upper Price zone. However, only a limited amount of development was been carried out and the orebody has not been mined.

In 1976, Brascan Ltd. acquired control of Western Mines Ltd. and merged it with the company's oil interests in Calgary. In 1981, the corporate name was officially changed to Westmin Resources Ltd. Divestiture of their oil and gas holdings in late 1989 resulted in a further name change to Westmin Mines

Ltd. In Febuary 1998 Boliden Limited acquired Westmin and the operating name changed to Boliden-Westmin Ltd.

In early 1979, with the Lynx Mine ore reserve declining, an aggressive exploration program was started. This program located a new massive sulfide deposit, now known as the HW mine (HW, standing for Harold Wright, first president of Western Mines) 350m below the Valley floor. The HW Mine, came on stream in 1985 and was still in operation at the time of writing.

Continuing exploration intersected the Gap lens in May 1991 while following the Ridge trend back toward the HW mine. Step out drilling to trace the Gap lens east resulted in the discovery of the Battle zone ore in October 1991. The Battle Mine began development in 1993 but was disrupted by a labour dispute, finally coming into production in 1995.

Exploration within the camp has also defined several prospective zones: Trumpeter, Ridge and the Marshall (Fig. 2). 30% of the property is as yet unexplored along the trend of the ore zones and good potential exists for further discoveries.

1.4 Ore Reserves

The Myra Falls VHMS District contains 5 major mining zones Lynx, Price, Myra, HW and Battle as well as several exploration zones. Lynx, Myra and Price Mines lie above the Myra Valley Floor and stratigraphically above the HW and Battle Mines (Fig. 2). Pre-mining reserves for these lenses were 5.75, 1 and 0.57 Mt respectively (Table 1). The HW and Battle Mines each encompass multiple lenses or zones of mineralisation (Table 1) and contain pre-mining totals of 22 and 7Mt respectively although the Battle Mine contains significantly higher zinc values than the HW Mine (Table 1). A further 1.9Mt of sulfides are contained within exploration zones throughout the property (Table 1). Current mining reserves are given for the HW and Battle Mines (Table 2) and total 6.8 Mt at 7.7 % zinc, 1.5% copper, 34.9g/t silver and 1.4g/t gold.

Lynx-Myra-Price Horizon (Upper Stratigraphic Horizon)

area	zone	TONNES	Au g/t	Ag g/t	Cu %	Pb %	Zn %	Ba %	Fe %
lynx	lynx 6-level	163,212	1.5	119.7	0.4	1.1	6.6	1.0	10.3
lynx	lynx pit-mined	1,600,000	2.5	90.0	1.6	1.0	7.5	*1.0*	*10.0*
lynx	lynx remaining	316,700	2.7	81.3	1.6	0.9	8.7	1.0	10.0
lynx	lynx underground -mined	3,675,000	2.5	90.0	1.6	1.0	7.5	*1.0*	*10.0*
lynx Total		5,754,912	2.5	90.4	1.6	1.0	7.5	1.0	10.0
myra	myra mine -mined out	1,037,000	3.0	160.0	1.0	1.5	9.5	*3.0*	*10.0*
myra Total		1,037,000	3.0	160.0	1.0	1.5	9.5	*3.0*	*10.0*
price	price	574,243	2.0	76.8	1.3	1.1	8.7	2.7	11.1
price Total		574,243	2.0	76.8	1.3	1.1	8.7	2.7	11.1

Table 1. Pre mining reserves for the Myra Falls VHMS District. Italics indicate estimated grades. Lynx pit, lynx underground and Myra are mined tonnage and grade with estimated dilution removed. Tonnage reported does not indicate economic viability. Compiled by Mr F. Bakker (2000).

HW Horizon (lower stratigraphic horizon)

area	zone	TONNES	Au g/t	Ag g/t	Cu %	Pb %	Zn %	Ba %	Fe %
Battle Mine	battle lower zone	17,626	0.7	20.1	1.9	0.8	9.8	1.8	15.2
Battle Mine	bornite zone	69,666	0.8	128.0	2.0	0.8	7.4	2.2	12.8
Battle Mine	gap zone	902,841	2.8	129.4	1.9	1.3	14.1	13.7	13.1
Battle Mine	gnu zone	383,950	0.7	41.2	1.6	0.9	13.3	0.5	12.5
Battle Mine	gopher zone	1,077,859	1.3	28.6	2.2	0.4	15.3	1.6	17.4
Battle Mine	main zone	2,502,108	1.2	25.0	2.2	0.4	14.6	0.7	14.1
Battle Mine	south trough	777,002	1.2	22.8	2.0	0.3	11.0	0.6	18.7
Battle Mine	U3000-ozone	194,778	1.2	53.7	0.7	0.6	5.3	3.0	7.1
Battle Mine	U3020-ozone	532,973	1.3	77.6	0.8	1.1	5.4	5.6	9.4
Battle Mine	U3030-ozone	650,638	1.4	113.7	0.6	0.9	7.6	4.7	5.3
Battle Mine	upper south trough	8,325	0.6	8.4	0.6	0.1	16.6	0.7	8.3
Battle Mine Total		7,117,766	1.4	53.2	1.8	0.7	12.5	3.3	13.5
extension	extension zone	1,148,066	1.1	32.5	1.4	0.3	4.1	1.8	20.0
extension Total		1,148,066	1.1	32.5	1.4	0.3	4.1	1.8	20.0
HW	HW main zone	14,860,882	2.0	18.7	2.0	0.1	2.2	1.3	32.5
HW	HW north zone	3,341,286	2.7	29.1	2.1	0.2	4.2	3.0	27.7
HW	HW-lower zones	414,040	2.0	37.3	1.5	0.9	8.2	2.9	20.6
HW	main zinc (to south)	1,955,432	2.5	57.6	2.1	0.8	10.8	3.5	18.7
HW	misc upper zones	336,540	2.3	59.2	1.4	1.0	5.8	2.8	12.6
HW	upper zones above main	869,991	2.7	61.5	1.8	1.1	8.6	3.0	12.7
HW	upper zones above north	224,204	2.7	74.4	1.3	0.9	6.7	4.7	14.9
43-block	43-block	933,983	2.6	52.8	1.7	0.5	5.8	3.1	12.8
HW Total		22,936,358	2.1	25.9	1.9	0.3	3.6	1.8	27.9
Exploration Zones									
marshall	marshall-indicated	563,407	1.8	82.4	0.5	0.6	5.5	6.5	5.1
marshall	marshall-inferred	614,767	1.8	81.2	0.5	0.6	5.4	6.5	5.0
marshall Total		1,178,174	1.8	81.8	0.5	0.6	5.5	6.5	5.0
ridge	ridge-east	307,676	1.7	50.2	0.7	0.6	4.2	0.6	6.8
ridge	ridge-west	300,196	0.8	42.6	0.7	0.8	4.9	1.5	12.2
ridge Total		607,872	1.3	46.4	0.7	0.7	4.5	1.1	9.5
trumpeter	trumpeter	210,343	2.5	59.6	3.4	0.3	4.1	2.4	17.2
trumpeter Total		210,343	2.5	59.6	3.4	0.3	4.1	2.4	17.2
Grand Total		40,564,734	2.1	47.5	1.8	0.5	6.2	2.2	21.2

Table 1 continued. Pre mining reserves for the Myra Falls VHMS District. Italics indicate estimated grades. Tonnage reported does not indicate economic viability. Compiled by Mr F. Bakker (2000).

1.5 Previous Work

Work on the geology of the Buttle Lake Uplift started in 1930's with Gunning's (1931) reconnaissance study for the Geological Survey of Canada. Work on the Paleozoic Sicker Group was the focus of Yole (1965, 1969), Jeffery (1970) and Muller (1980) in the Buttle Lake Uplift and work by others in Paleozoic rocks elsewhere on Vancouver Island. Juras (1987) studied the lithologies of the Myra Falls Camp and proposed a revised stratigraphy for the Sicker Group which is now widely accepted and in use at the mine. Gunning (1931), Jeffery (1965), Walker (1980, 1983, 1985), Juras (1987), Reid (1993) and Westmin (internal company reports) have studied the structural setting of the Myra Falls lease.

Most of the available data on Myra Falls occurs as internal company reports and conference presentations by Pearson (1993,1997), Juras & Pearson (1990a, 1990b) and McKinley et al., 1997; Pearson et

MINING RESERVE - PROVEN+PROBABLE									
INCLUDES DILUTION AND EXTRACTION FACTORS									
		TONNES	AU	AG	CU	PB	ZN	BA	FE
HW	PROVEN	1,444,362	1.7	28.4	1.5	0.4	3.6	1.6	21.0
43 BLOCK	PROVEN	808,876	2.1	42.2	1.4	0.4	4.7	2.6	10.4
BATTLE	PROVEN	3,191,888	0.9	30.2	1.4	0.4	10.1	1.1	11.0
GAP	PROVEN	611,141	2.5	109.2	1.6	1.0	11.9	11.4	11.6
HW	PROBABLE	628,777	2.0	17.4	1.1	0.2	1.9	1.1	25.9
43 BLOCK	PROBABLE	99,702	1.5	33.6	1.0	0.4	3.3	1.4	6.7
BATTLE	PROBABLE	303,845	0.9	48.0	1.0	0.6	7.8	1.5	8.8
GAP	PROBABLE	229,425	1.9	96.2	1.6	1.1	10.2	9.8	11.8
EXTENSION	PROBABLE	401,948	0.8	27.5	1.1	0.3	3.7	1.3	14.9
TOTAL	PROVEN	6,056,267	1.4	39.3	1.5	0.5	8.0	2.4	13.4
TOTAL	PROBABLE	1,663,697	1.5	37.3	1.1	0.4	4.6	2.4	17.0
TOTAL		7,719,964	1.4	38.9	1.4	0.5	7.3	2.4	14.2
JANUARY 1999 TOTAL		6,785,826	1.4	34.9	1.5	0.4	7.7	2.0	13.9

Table 2. Proven and probable mining reserves for the Myra Falls VHMS District as of January 2000.

al., 1997; Sinclair et al., 1997. Studies of the mineralisation at Myra Falls have largely been done by company geologists and consultants (internal company reports) with few having been published, Seraphim (1980) excepted.

In the early 1990's MDRU, of the University of British Columbia, studied the lithogeochemistry and alteration of the Myra Falls mines; Robinson (1992), Robinson et al., (1996), Barrett and Sherlock (1996) and internal company reports. Barrett and Sherlock (1996) conducted research on fluid inclusion and oxygen isotopes in HW and a property wide lead isotope study. While Andrew and Godwin (1989) studied lead-isotopes in the HW and Myra Mines.

Creswell (1997) studied the Upper Zone style mineralisation which lies approximately 30m above the Battle deposit. Dishaw (1998) studied the Price Orebody.

1.6 This Study

Detailed mineralogical, metal zoning, and structural studies had not been carried out on the Myra Falls district ore lenses. Such a study was thought useful to the ongoing mining of ore lenses and in providing insights into the formation of the orebodies to aid in future exploration. The Battle Mine was chosen for this study due to the focus of production drilling in this area and the timing of access to underground exposure.

Thus, the aims of this project were to examine underground exposure, drill core and the computer database for the Battle Zone massive sulfide lenses (Battle Main, Gopher, South Trough, Upper Zone and Gap) in order to:

- Update the volcanological nomenclature
- Describe and characterise the alteration mineralogy and geochemistry
- Detail the structural setting of the Battle Zone

- Describe the mineralogy, textues, paragenesis and metal zoning of the mineralisation
- Construct a 3D model of the metal zonation
- Propose an ore genesis model for the deposits

These aims were achieved through field work, carried out over three summers (northern hemisphere) 96, 97, and 98, involving mapping and sampling of underground exposures in the Battle Mine, and logging of production core, as available. Additional logging of the 15+85 exploration section (96) and sampling of 3 holes from the Thelwood Valley (98) was also carried out.

Chapter 2

Regional Geology

2.1 Introduction

The geology of Vancouver Island is divided into two segments; Pre-accretionary Wrangellia Terrane and post accretionary rocks. The Myra Falls polymetallic, volcanic hosted massive sulfide (VHMS) camp lies within felsic volcanic rocks of the Paleozoic Sicker Group. The Sicker Group is the oldest known group of rocks within the Wrangellia Terrane, which together with the Alexander Terrane form the Insular Belt of the Canadian Cordillera. Extensive study of the rocks outside the Battle Mine has not been conducted. However this review provides important information on the regional structural and metamorphic history of Vancouver Island which affects the rocks in the Battle Mine.

2.2 Tectonic Setting of Western Canada

The western margin of Canada, from the base of the continental slope, off the west coast of Vancouver Island and the Queen Charlotte Islands, to the western limit of the undeformed strata underlying the Interior Plains, is known as the Canadian Cordilleran (Yorath and Nasmith, 1995). The Cordillera is divided into five northwesterly-trending subdivision known as terranes, each characterised by a unique lithology, structural style and morphology (Fig. 3). The boundaries between them are faults (Gabrielse et al., 1991). It is known from paleomagnetic and paleontological studies that some terranes originated far from ancestral North America and became accreted to the continent during the Mesozoic and Cenozoic. In other cases their paleogeographic relationships to ancestral North America or to one another are unknown (Gabrielse et al., 1991).

The Insular Belt of the Canadian Cordillera underlies most of Vancouver Island (Juras, 1987). The lower members of this belt, including the Paleozoic Sicker and Buttle Lake Groups, the Triassic Vancouver Group, and the Jurassic Bonanza Groups are considered to be part of an allochthonous terrane named Wrangellia by Jones et al. (1977). The Insular Belt is thought to have collided with the ancestral margin of the North American continent approximately 100 million years ago (Yorath & Nasmith, 1995). It was during this collision that much of the overall structure of Vancouver Island developed. Throughout the succeeding 100 million years, episodes of mountain building, erosion, glaciation and the accretion of additional terranes have moulded Wrangellia into the Vancouver Island that we see today.

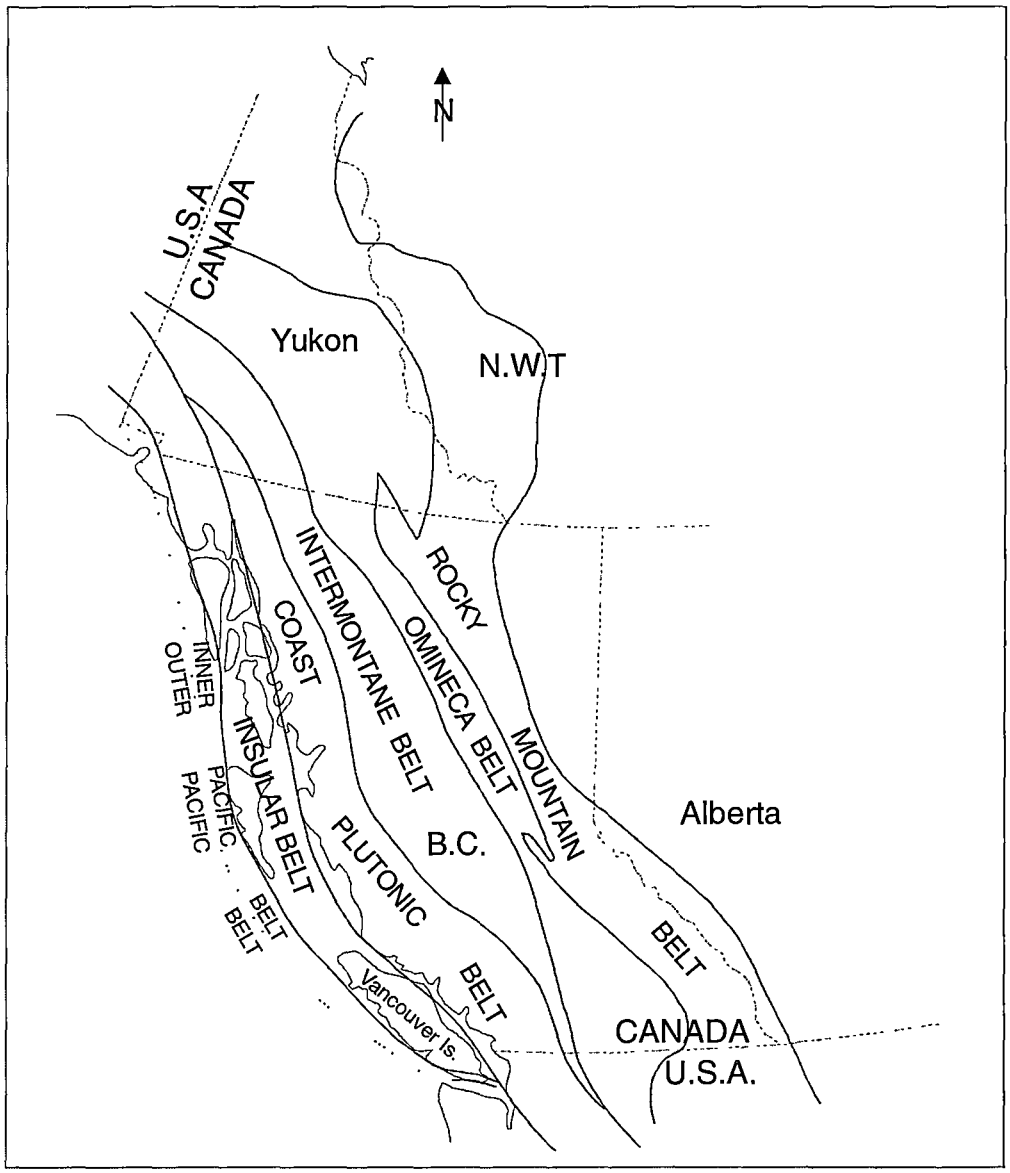

Figure 3. Canadian Cordilleran Belts (modified after Muller, 1977).

2.3 Wrangellia

The Wrangellia Terrane, on Vancouver Island, comprises three thick volcano-sedimentary cycles - the Paleozoic Sicker and Buttle Lake Groups, the Upper Triassic Vancouver Group and the Lower Jurassic Bonanza Group (Fig. 4; Massey, 1992). The formation of Wrangellia began during the Devonian, 380 million years ago, with the evolution of an oceanic island arc system (Juras, 1987) depositing volcanic and volcaniclastic rocks of the Sicker Group. 360 million years ago volcanism ceased and the crinoidal limestones of the Buttle Lake Group were deposited (Yorath and Nasmith, 1995).

Volcanism resumed in the late Triassic when flood basalts covered the surface of Wrangellia forming the Karmutsen Formation[1] of the Vancouver Group. At the end of volcanism limestone was again deposited, while erosion of exposed Sicker Group formed the clastic sediments of the Parsons Bay Formation (Yorath and Nasmith, 1995). 200 Million years ago, at the beginning of the Jurassic, arc volcanism returned to Wrangellia and the volcanic rocks of the Bonanza Group were formed

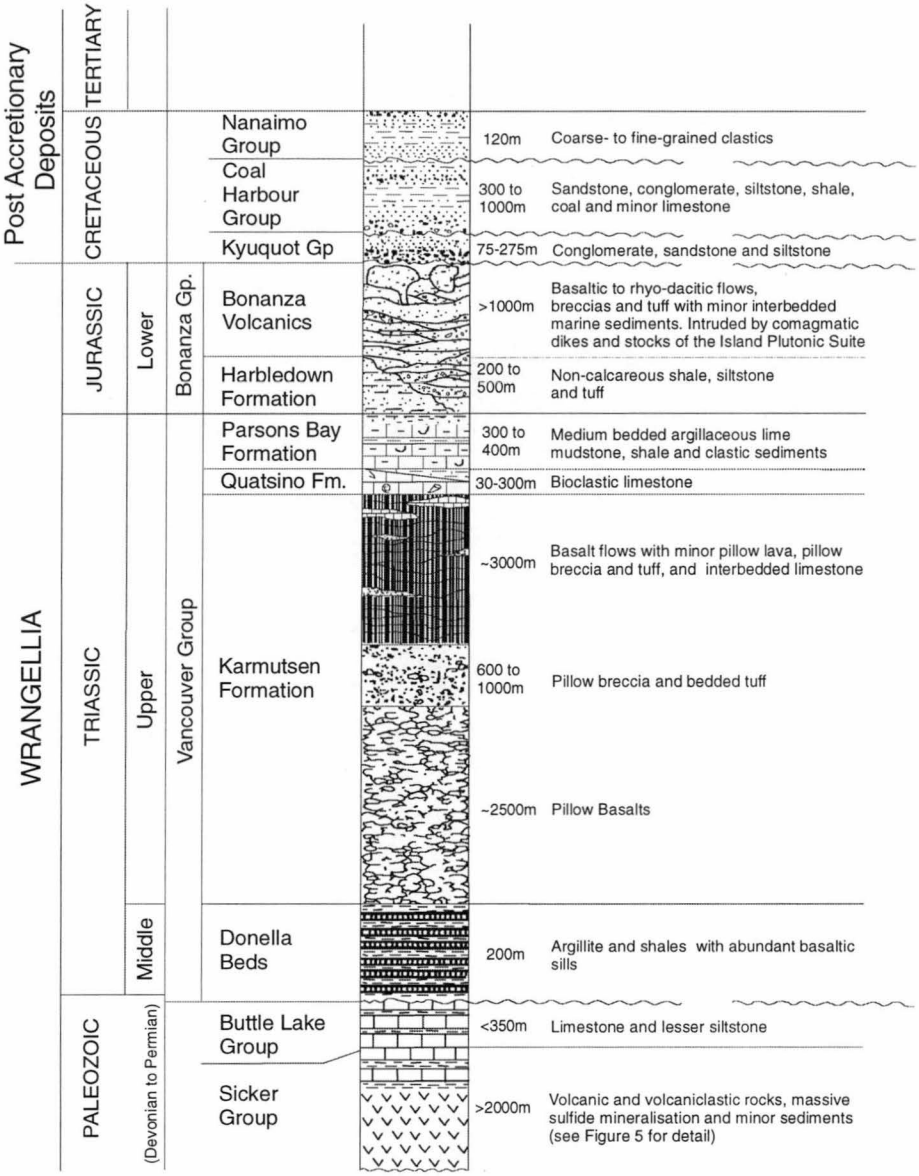

Figure 4. Regional stratigraphy of Vancouver Island. (Modified after Nixon et al., 1992; Muller et al., 1974 & 1981).

(Yorath and Nasmith, 1995). During this time injection of magma into the lower Wrangellian rocks formed the Island Plutonic suite.

Wrangellia is exposed in four major structural uplifts on Vancouver Island - Buttle Lake, Nanoose, Cowichan, & West Coast (Fig. 5). These Uplifts are part of an Early to Middle Jurassic regional scale warping of Vancouver Island (Massey, 1992). This warping is expressed by northwesterly trending anticlinoria which extend throughout much of the islands length (Fig. 5) and are cored by rocks of Paleozoic age (Sicker Group). Several younger parallel and subparallel faults partition these anticlinoria disrupting stratigraphic continuity (Yorath et al., 1999).

[1] Paleomagnetic work by Irving and Yole (1987) suggests that Wrangellia has moved northward a considerable distance relative to the North American craton since the Late Triassic Epoch. Tropical fossils in the limestone near the top of the Karmutsen Formation also suggest the limestone was formed south of its current latitude (Yorath and Nasmith, 1995).

Figure 5. Map of Vancouver Island showing the positions of the four uplifts that expose Wrangellian rocks. After Muller, 1977 & 1980; Yorath et al., 1999.

2.3.1 Paleozoic Rocks on Vancouver Island

Several attempts have been made to formally subdivide the Paleozoic rocks on Vancouver Island. Gunning (1931), Flyles (1955), and Yole (1963, 1964, 1969) were the first to recognise the rocks as Paleozoic in age and named them the Sicker Group. However the first major synthesis of data on the Paleozoic rocks of Vancouver Island did not occur until Muller (1980). This was followed by detailed work in the Buttle Lake Uplift by Juras (1987) and in the Cowichan Uplift by Sutherland Brown et al., (1986), Sutherland Brown and Yorath (1985) and Massey (1992) and has led to a revised stratigraphic subdivision in each of the uplifts (Fig. 6).

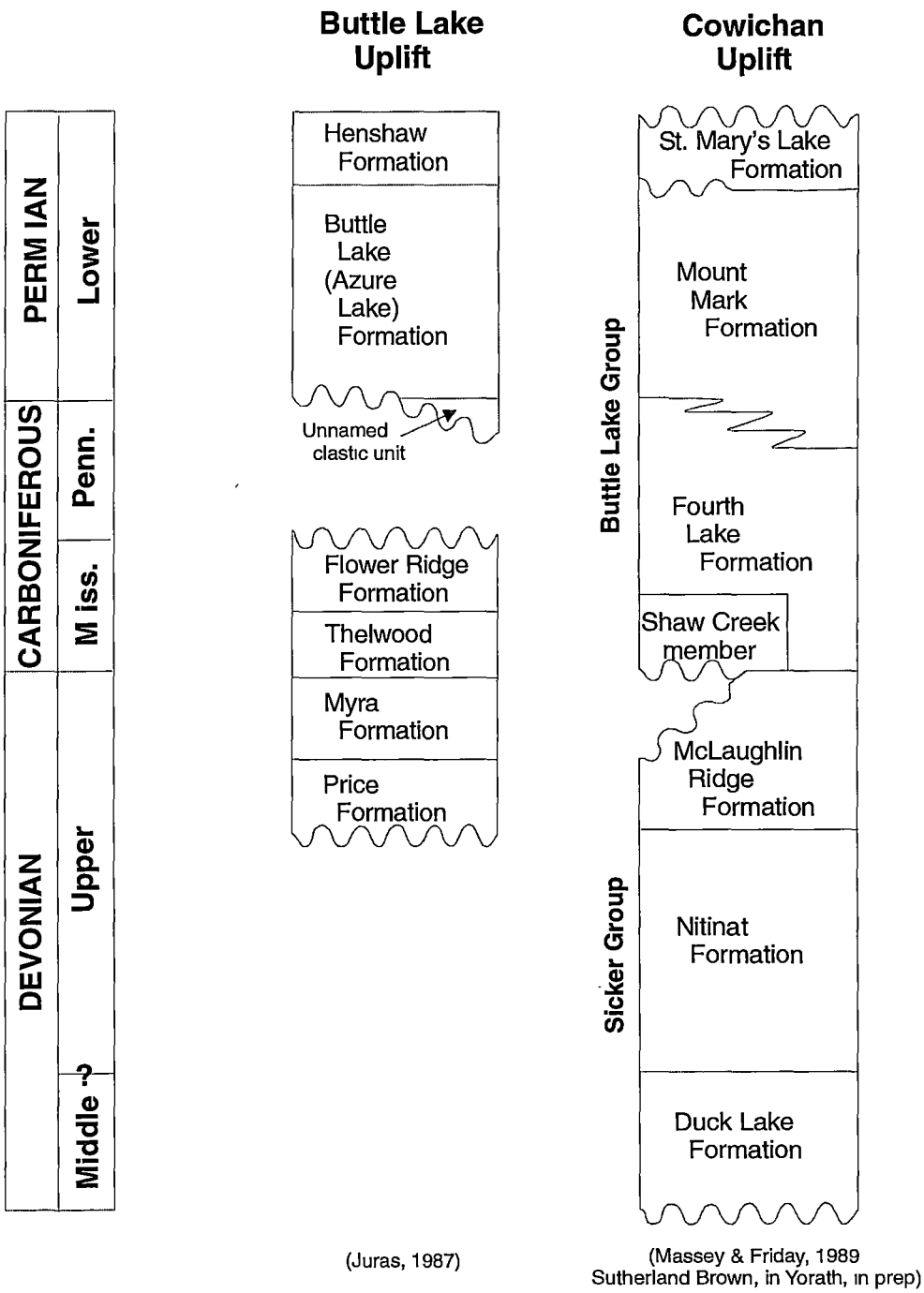

Figure 6. Comparative stratigraphy of the Paleozoic rocks of Vancouver Island. (Adapted from Massey et al., 1992)

The major contribution of these studies has been the formal recognition that the Paleozoic rocks can be separated into a Devonian volcanic-dominated sequence, named the Sicker Group, and a Mississippian to Permian sedimentary sequence renamed the Buttle Lake Group. However, attempts to correlate Sicker Group rocks between the uplifts has encountered problems. Each structural uplift consists of a different volcanic centre with a variety of rock types and rapid facies variations. The spatial relationship between the Buttle Lake and Cowichian Uplifts during the Late Devonian is uncertain, due to later tectonic disruption and different rotation of structural blocks within Vancouver Island (Irving and Yole, 1987; Irving and Wynne, 1990). Due to this difference between uplifts the stratigraphy outlined below is based on the work of Juras (1987) in the Buttle Lake Uplift. Readers are referred to Massey (1992) for detail on the Paleozoic rocks of the Cowichan and Nanoose uplifts.

2.3.1a Sicker Group

The Devonian Sicker Group is a thick (2km+) package of lower greenschist facies, metavolcanic and volcaniclastic rocks that formed in an oceanic island-arc environment (Massey, 1992). Volcanic-hosted massive sulfide deposits are an integral part of the group, occurring mainly in the felsic volcanics and occur in the Buttle Lake area (eg Myra Falls district) and in the Cowichan area (Mount Sicker and Lara deposits) (Massey, 1992; Dawson et al., 1991). In the Buttle Lake Uplift the Sicker Group has been divided into four formations (Fig. 7) - Price, Myra, Thelwood and Flower Ridge, by Juras (1987).

The Price Formation consists of feldspar ± pyroxene porphyritic basaltic andesite flows, flow breccias and coarse volcaniclastic deposits. The unit is moderately to strongly altered to chlorite + epidote + albitic plagioclase ± actinolite assemblages. A conspicuous feature of this formation is the presence of medium to very coarse grained, black to dark green pyroxene phenocrysts invariably pseudomorphed by actinolite. The top of the Price Formation is defined as the lower contact of the first, widespread appearance of rhyolitic volcanic rocks. The thickness of the Price Formation can only be given as >300 meters as the base of the unit is neither exposed in the Buttle Lake area nor in drill core from the Myra Falls operation. The age of the Price Formation is not precisely known except that it is Late Devonian or older because it lies below the Late Devonian (370 Ma) Myra Formation (Juras, 1987). The Price Formation represents the basal unit of the Sicker Group in the Buttle Lake Uplift.

The Myra Formation is a thick (310-440 meters) sequence of complex volcanic-dominated stratigraphy consisting of basaltic to rhyolitic flows and volcaniclastic rocks, lesser epiclastic sediments, argillites, and massive sulfide mineralisation. It lies conformable on the Price Formation and its age is late Devonian (370Ma) as determined by zircon U-Pb dating (Juras, 1987). The Myra Formation has been further divided in into ten litho-stratigraphic units which will be described in chapter 3.

The Thelwood Formation overlies the Myra Formation, in places unconformably, and consists of thinly bedded, fine-grained, siliceous tuffaceous sediments, subaqueous pyroclastic and volcaniclastic deposits, and penecontemporaneous mafic sills. Thickness varies from 270 to 500 meters. No age determinations have been made on this unit in the Buttle Lake Uplift. Microfossil ages from equivalent rocks in the Cowichan Uplift indicate an Early Permian age (Brandon et al., 1986).

The Flower Ridge Formation conformably overlies the Thelwood Formation and consists of mod-

erately to strongly amygdaloidal, feldspar + pyroxene porphyritic basaltic lapilli-tuff and pyroclastic breccia, tuffaceous siltstone and wacke, minor basaltic flows, tuffs and bedded tuffaceous mudstone and argillaceous sediments. A maximum thickness of 650 meters was determined at the Myra Falls mine site by Juras (1987). The age of this formation is not known except that it is bracketed by the late Devonian Myra Formation and the Pennsylvanian Buttle Lake Formation (Juras, 1987).

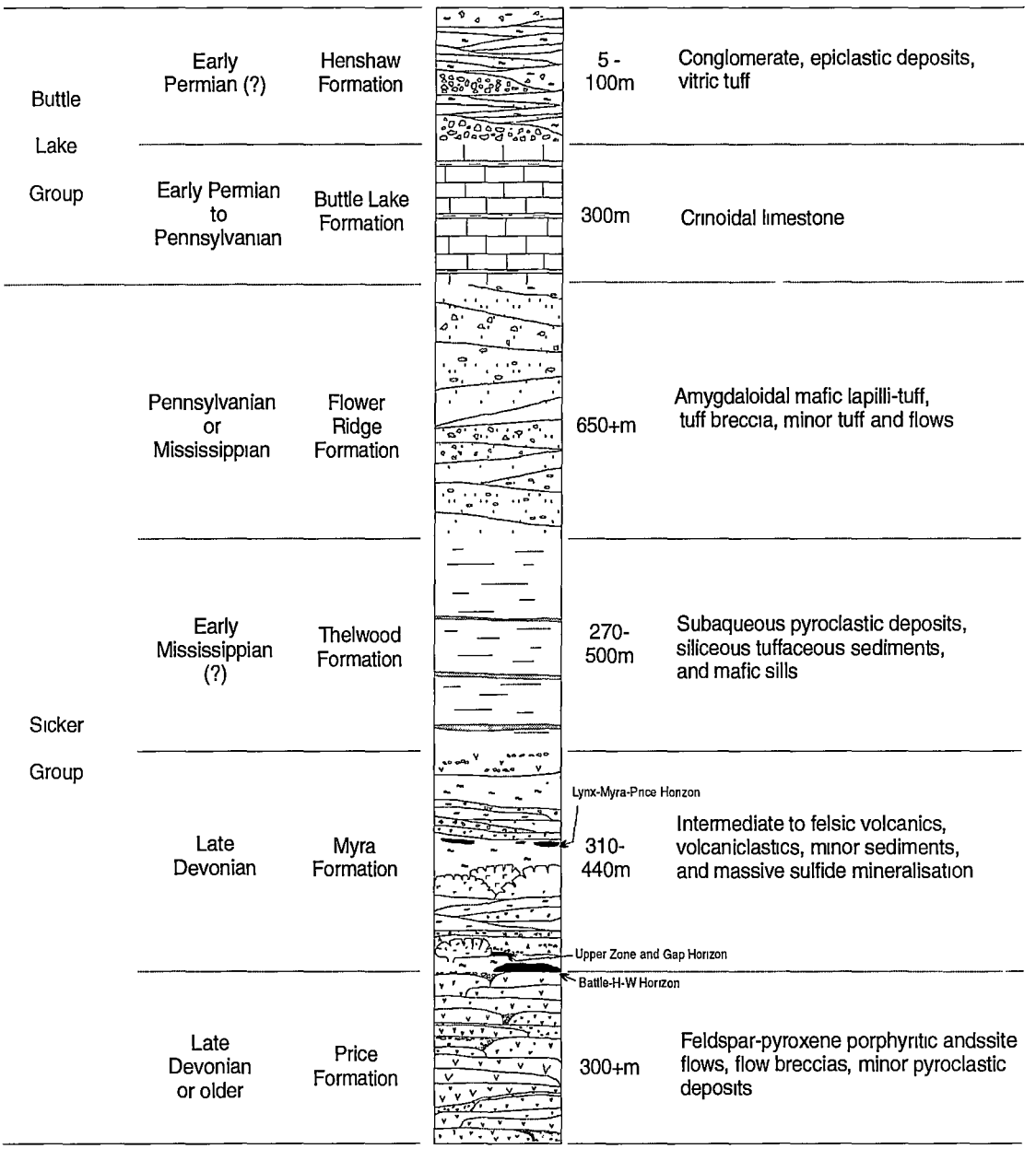

Figure 7. Stratigraphy of the Sicker Group in the Buttle Lake uplift, central Vancouver Island, B.C. (Adapted from Juras, 1987).

2.3.1b Buttle Lake Group

The Buttle Lake Group consists of a dominantly epiclastic and bioclastic limestone sedimentary sequence ranging from Mississippian to Early Permian in age (Yole, 1969; Brandon et al., 1986). In the Buttle Lake uplift it contains of two formations, the Buttle Lake and Henshaw (Fig. 7).

The Buttle Lake Formation (Azure Lake Formation[1]) consists of massive to bedded crinoidal limestone, lesser chert and in places thin interbeds of mudstone and siltstone. It conformably overlies the Flower Ridge Formation (Yole, 1969) and ranges in thickness from 100 to 500 meters. The age of this formation (based on biostratigraphic dating) ranges from Pennsylvanian to Early Permian (Yole, 1969; Brandon et al., 1986).

The Henshaw Formation is a heterogeneous and irregularly distributed group of rocks, consisting of conglomerate, variably purple-coloured epiclastic deposits and purple to grey vitric tuff beds (Jeffery, 1970). It is characterized by the presence of crinodal limestone clasts and boulders, and the variable but ubiquitous purple to red alteration of its volcanic members. Thickness of this unit varies from 5 to 100 meters, and it is overlain by pillowed lavas or thin argillaceous sediments of the Karmutsen Formation of the Triassic Vancouver Group. The Henshaw Formation is thought to be Permian (Jeffery, 1970).

2.3.2 Daonella Beds

The Daonella beds comprise black silicified shale and siltstone (to argillite) intruded by thick diabasic sills (Jones et al., 1977) and were first described by Muller et al. (1974) as the "sediment-sill unit". Their age is mid-Triassic from paleontological studies. This unit overlies the Sicker Group and is overlain by the Karmutsen Formation (Jones et al., 1977; Fig. 4). The sediment-sill complex can be up to 200 meters thick in southern Vancouver Island. However, in northern Vancouver Island Nixon et al. (1994) reports it as 800-1000 meters thick.

2.3.3 Vancouver Group

The early Mesozoic stratigraphy on Vancouver Island is represented by middle Triassic to lower Jurassic volcanic and sedimentary rocks of the Vancouver and Bonanza Groups and lower to middle Jurassic Island Intrusions (England and Calon, 1991). The Vancouver Group is made up of the Karmutsen, Quatsino and Parsons Bay Formations (Fig 4; Nixon et al., 1994).

Karmutsen Formation is an Upper Triassic unit consisting of tholeiitic submarine pillow basalts, breccias and tuffs capped by a subaerial succession of basaltic flows with minor limestone interbeds (Muller, 1977) up to 6000 meters thick.

Quatsino Formation: Overlying the Karmutsen Formation is the Upper Triassic shallow-water or carbonate-platform limestone of the Quatsino Formation. It is described as being thick-bedded and massive and is gradational into sediments of the overlying Parsons Bay Formation.

Parsons Bay Formation consists of clastic-carbonate sediments and is in part overlain by a thin coralline to detrital limestone known as the Sutton Member. The Parsons Bay Formation consists of dark, siliceous and carbonaceous calcareous shale, calcareous arenite and fine grained sandstone up to 300 meters thick (Gordey et al., 1991).

[1] To maintain consistency with the stratigraphic nomenclanture it is proposed by Athol and Juras that the Buttle Lake Formation revert to the Azure Lake Formation originally proposed by Yole (1969), (Massey pers. com., 1998).

Island Intrusions The Sicker and Vancouver Groups are intruded by batholiths and plutons of quartz diorite, granodiorite, and quartz monzonite of the lower to middle Jurassic Island Intrusions. These intrusions are thought to be comagmatic with the overlying Bonanza Group volcanic rocks (Dawson et al., 1991).

2.3.4 Bonanza Group

The Triassic rocks in turn are overlain by a thick (up to 2000 meters) sequence of subaqueous to subaerial, basaltic to rhyo-dacitic flows, breccias, and tuff with minor interbedded marine shale and siltstone of the Lower Jurassic Bonanza Group (Fig. 4). In the northeastern part of the island the Bonanza Group is correlative with non-calcareous, thinly banded shale, siltstone and tuff of the Harbledown Formation. The Harbledown Formation has a thickness of 300 meters (Nixon et al., 1994; Gordey et al., 1991).

2.4 Post Accretionary Rocks on Vancouver Island

Cretaceous and younger rocks on Vancouver Island formed after the collision of Wrangellia with the North American continent and are thus not considered to be part of Wrangellia. Accretionary sedimentary sequences are not important volumetrically but are represented by the Lower Cretaceous Kyuquot Group on Vancouver Island. Post accretionary clastics sequences are represented by the Coal Harbour Group of mid-Cretaceous age, and the Nanaimo Group of Late Cretaceous age (Dawson et al., 1991; Fig. 4).

Kyuquot Group consists of a composite shallow marine clastic wedge which unconformably overlies the Lower Jurassic Bonanza Group (Muller et al., 1980). It occurs in a small area on the west coast of Vancouver Island (Yorath, 1991).

Coal Harbour Group occurs on norther Vancouver Island. It consists of a "coarse arenite unit" (240 to 1650 meters) composed of greywacke, shale, minor limestone, conglomerate and coal, a middle non-marine Blumberg Formation (900+meters) composed dominantly of conglomerate but with minor siltstone, shale and coal and an upper informal "Upper Shale unit" (200+meters) consisting of siltstone, shale and minor conglomerate and limestone (Yorath, 1991).

Nanaimo Group is divided into nine formations consisting of variously alternating sequences of coarse- and fine-grained terrigenous clastics, overall thickness is approximately 2450 meters (Yorath, 1991).

During the Tertiary two more terranes, the Pacific Rim and Cresent Terranes, were accreted to Vancouver Island along the south west coast (England and Calon, 1991; Yorath and Nasmith, 1995).

Pacific Rim Terrane consists of a sequence of Lower Cretaceous melanges which overlie uppermost Triassic fragmental calc-alkaline arc volcanic rocks and subordinate diorite intrusions and

interbedded limestones. The melanges consist of chaotic assemblages of mudstone, sandstone and chert containing slide blocks of the basement volcanic rocks.

Cresent Terrane was emplaced beneath the Pacific Rim Terrane by the end of the Eocene and consists of the Metchosin Igneous Complex and the Cresent Formation. The Metchosin Igneous Complex consist of massive and layered gabbros passing upward into and intruded by a sheeted dyke complex. The sheeted dyke complex is in turn succeeded by subaqueous pillow and sheet flow basalts with minor pyroclastic rocks overlain by possibly subaerial, amygdaloidal flows (Yorath, 1991).

Volcanism and plutonism re-occurred in mid- to late-Paleogene and early Neogene times, resulting in the Catface Intrusions on Vancouver Island (Dawson, 1991). Sedimentary deposit on Vancouver Island are limited in distribution and are not discussed here, readers are referred to Gabrielse and Yorath (1992) for details.

Catface Intrusions are an Eocene suite of small hypabyssal bodies of broadly quartz diorite composition (Muller, 1980; Yorath et al., 1999).

2.5 Alteration and Metamorphism

Two main metamorphic events are recognise on Vancouver Island the first is pre-Triassic in age and is overprinted by a Jurassic event. Post Jurassic rocks on Vancouver Island are essentially unmetamorphosed showing only zeolite-facies assemblages relating to burial (Greenwood 1991; Massey 1992).

The Jurassic event is attributed to the intrusion of the Island Intrusions and varies with age and structural position of the rocks (Massey, 1992). Triassic Karmutsen basalts contain alteration assemblages typical of prehnite-pumpellyite facies (Massey, 1992). While the Paleozoic rocks show mostly lower greenschist metamorphic assemblages, with the exception of rocks along the west coast of Vancouver Island which show amphibolite facies assemblages (Greenwood et al., 1991). This increase in metamorphic grade on the west coast is interpreted to have resulted from deeper level of plutonic emplacement in this region compared with the greeenschist facies rocks elsewhere on Vancouver Island (Isachsen, 1984). Mineral assemblages of the volcanic Price and Myra Formation vary depending on bulk composition of rock (mafic to rhyolite) and are summarised in Table 3. These assemblages indicate lower greenschist grade metamorphism. Mineral assemblages of the Thelwood and Flower Ridge Formations are also summarised in Table 3 and are characterised by prehnite-pumpellyite to lower greenschist facies metamorphism. Conodonts from the Buttle Lake Group have CAI index of 5 to 7 (Brandon et al., 1986) consistent with the prehnite-pumpellyite – greenschist facies transition seen in the underlying rocks.

A prior metamorphic event (pre-Triassic) is also recognised in the Paleozoic rocks. This event is probably related to the formation of the foliation which is seen in all Paleozoic volcanic rocks on Vancouver Island, but does not extend into the Karmutsen Formation or the Jurassic dykes cross cutting the Paleozoic stratigraphy. The Jurassic event has reset K-Ar dates in sericite and masked

many of the features of this earlier metamorphism. However relic metamorphic assemblages of grades higher than lower Greenschist facies are not recorded in any of the published data, thus it is likely the pre-Triassic event was lower-greenschist facies or lower in intensity. It is uncertain if the metamorphic grade of the Buttle Lake Group is due entirely to the Jurassic event, or if the pre-Triassic event affected this unit. Thus the exact age of the earlier event is unknown except that it occurred after the deposition of the Pennsylvanian to Mississippian Flower Ridge Formation and prior to the emplacement of the Triassic Karmutsen Formation.

Formation	Rock type	Mineral Assemblage
Price	basaltic andesite - andesite	chl + ep + ab + q + cc ± act
Myra	high MgO basalt	act + chl + ab + ep
		chl + cc + ser + hem
	basalt	chl + q + ab
		chl + ep + ab + q ± act ± cc
		ep + q + ab + cc ± act
	basaltic andesite - andesite	ep + ab + q ± chl ± cc ± act
		chl + ab + q ± ep ± cc
	feld porphyritic Felsic volcanics	ab + q + ep + ser ± chl ± hem
	qtz – feld porphyritic rhyolite	ser + q + ab ± chl
Thelwood	intermediate tuffs	chl + ep (±clz) + q b+ ab
	mafic sills	chl + ab + ep
Flower Ridge	basalt	chl + ep (± clz) + ab + q + act ± cc ± pp

Table 3. Common metamorphic mineral assemblages for Sicker Group units, from Juras, 1987. Mineral abbreviations: ab = albite, act = actinolite, cc = calcite, chl = chlorite, clz = clinozoisitie, ep = epidote, hem = haematite, pp = pumpellyite, q = quartz, ser = sericite, qtz = quartz, feld = feldspar.

2.6 Metallogeny

Vancouver Island has a wide variety of mostly small mineral deposits and showings reflecting its history of diverse, voluminous, and long-lasting volcanism, related plutonism, intercalated reactive carbonates, and repeated tectonic activity (Dawson et al., 1991). Massey (1992) has grouped the deposits into three metallogenic episodes.

The first major metallogenic episode took place in the Paleozoic during the emplacement of the Sicker Group and is characterised by syngenetic styles of mineralisation. Volcanic-hosted massive sulfide mineralisation occurring in felsic volcanics of the Sicker Group dominate this episode. Known deposits include those of the Myra Falls district in the Buttle Lake Uplift and the Mount Sicker area and the Lara Deposit in the Cowichan Uplift. Iron formations thought to be of exhalative origin are also found in the uppermost Duck Lake Formation (Fig. 6). These are dominantly iron oxide facies although sulphides are present in some areas. Other jasper and oxide-rich cherts occur within the Nitinat and McLaughlin Ridge Formations (Fig. 6) but appear to have negligible economic value (Massey, 1992).

The second major metallogenic episode took place during the early Jurassic, and is characterised by epigenetic mineralisation spatially related to intrusions of the Island Plutonic suite. Skarn deposits commonly occur at or near the contact of the Karmutsen and Quatsino Formations with the Island Intrusions, and less commonly, between plutons that intruded either the Quatsino Formation and Bonanza Group or the Buttle Lake Formation. Most skarns are of the iron-copper-gold (magnetite-chalcopyrite) type and produce only a few million tonnes in short lived mines including Argonaut, Coast Copper, Kennedy Lake, Merry Widow, Nimpkish and Zeballos on Vancouver Island (Dawson et al., 1991). Copper-molybdenum veins and stockworks occur both within intrusions and surrounding volcanic country rocks of either Paleozoic or Mesozoic age.

Porphyry deposits are also associated with plutons of the Jurassic Island Intrusions. The single known economic deposit, the Island Copper Mine, is located at the northern end of Vancouver Island 16km south of Port Hardy. Mineralisation and alteration are related to the intrusion of quartz-feldspar-porphyry dykes into Bonanza Group volcanics (Mathias et al., 1995). Alteration consists of a high sulfidation assemblage containing pyrophyllite, dumortierite and diaspore and cross cuts the copper-molybdenum-gold-rich ore shell (Mathias et al., 1995). The deposit was mined up to 1996 by BHP Minerals Canada.

The third metallogenic phase includes all post-accretionary mineralisation. Many are epigenetic precious-metal accumulations in young fault zones that cut Wrangellian rocks and may involve the redistribution of earlier metals. Also important are porphyry Cu-Mo, Cu-Au-Ag-(Mo) or Au-Ag deposits in the Catface Suite (Dawson et al., 1991).

2.7 Summary

Vancouver Island is underlain by Wrangellia, an allochthonous tectono-stratigraphic terrane, which forms part of the Insular Belt of the Canadian Cordillera. The Insular Belt was accreted onto North America 100 millions years ago.

The Wrangellia Terrane is composed of three known volcano-sedimentary sequences - the Paleozoic Sicker and Buttle Lake Groups, the Upper Triassic Vancouver Group and the Lower Jurassic Bonanza group. Wrangellian rocks show low metamorphic grades with Paleozoic rocks exhibiting greenschist facies while the Mesozoic rocks exhibit prehnite-pumpellyite facies. Wrangellia hosts significant economic mineralisation including the Paleozoic Myra Falls district and the Jurassic Island Copper Mine, as well as smaller volcanic hosted massive sulfide, skarn and vein deposits.

Post accretionary rocks on Vancouver Island are dominated by sedimentary sequences with minor volcanic rocks and plutons. These rocks are generally unmetamorphosed with only diagenetic alteration. Mineral deposits of post accretionary age are mostly epigenetic precious metal accumulations in fault zones that cut Wrangellian rocks. However, porphyry deposits associated with post accretionary intrusions are also important.

Chapter 3

Local Geology

3.1 Introduction

The purpose of this chapter is to outline the host rocks to Myra Falls VHMS deposits (Part A) with particular attention to the Battle Zone (Part B). Part A reviews previous work in the Myra Falls district, nomenclature and facies interpretations are updated by the author to reflect prevailing volcanologic ideas and terminology, however all descriptions are based on the work of Juras (1987). Part B focuses on the Battle Zone host rocks. Results of the current study are presented and then combined with previous work on the Myra Formation to produce updated facies interpretations and a possible depositional setting for the Battle Zone ore bodies. Volcanic terms used in this thesis follow the guide lines and definitions given in McPhie et al. (1993).

Part A:

3A.1 Host Rocks to the Myra Falls Deposits

The Myra Falls massive sulfide lenses (Fig. 7) are hosted by the lowest two formations of the Sicker Group, known as the Price Formation (Footwall Andesite) and the Myra Formation (Mine Sequence). The Price Formation forms the basement sequence onto which the Myra Formation volcanic, volcaniclastic and sedimentary rocks were deposited.

3A.1.1 - Price Formation (Footwall Andesite)

The Price Formation is the lower most unit in the Buttle Lake Camp and in the Buttle Lake Uplift (Fig. 5). It is a thick sequence (>300 m) of massive to pillowed basaltic-andesite lavas and associated fine to coarse volcaniclastic rocks. The base of this formation has not been identified.

The Price Formation can be divided into three facies on the existing data; Feldspar-phyric andesitic lava facies, pyroxene + feldspar porphyritic lava facies and volcaniclastic facies. The feldspar-phyric andesitic lava facies consists of 0.6 to 5 mm plagioclase phenocrysts (15%) and 0.5 to 2.5 mm euhedral clinopyroxene phenocrysts (trace to 0.5%) in a fine grained groundmass. The pyroxene + feldspar porphyritic lava facies contains 1 to 10 mm euhedral clinopyroxene (5%) and 0.8 to 2.5 mm plagioclase phenocrysts (3%). Both lava facies have 0.1-0.3 mm ovoid to elongate amygdales (trace to 7 percent) and occur as alternating, 30-150 m thick lava flows. The third facies consists of fine to coarse, clastic volcanic deposits. The origin of the volcaniclastics is interpreted as autobreccia to resedimented by Juras (1987), however clast shape, size and abundances are not described, in

Juras (1987), making division of this unit impossible.

Within the Buttle Lake Uplift the Price Formation has been regionally altered to epidote, chlorite and carbonate assemblages (Chapter 4). Price Formation rocks underlying massive sulfide accumulations (eg HW and Battle deposits) have intense hydrothermal alteration of sericite-pyrite ± quartz and chlorite assemblages overprinting the regional alteration (Chapter 4).

3A.1.2 - Myra Formation

Previous workers (Juras, 1987) have used a lithology based approach to mapping in the Buttle Lake district, presenting the Myra Formation as a 'layer-cake' stratigraphy (Table 4). Review of this work has shown that units in the Myra Formation need reinterpreting to reflect the complex and interfingering nature of lavas and sediments in volcanic terranes. Thus the Myra Formation is re-described here as a series of facies with some rearrangement of units reflecting the interpretation of units as separate volcanic events from differing source areas (summarised in Table 4). Nomenclature is updated within the following descriptions.

Juras (1987), defined ten informal lithostratigraphic units. From bottom to top these are: HW Horizon, Hanging Wall Andesite[1] Ore Clast Breccia, Lower Mixed Volcaniclastics, Upper Dacite / 5E Andesite / North Dacite, Lynx-Myra-Price Horizon, G-Flow, Upper Mixed Volcaniclastics, Upper Rhyolite, and Upper Mafic. He also recognised and documented lateral facies variations within these lithostratigraphic units. These names are listed in Table 4 as a guide to other workers in the Myra Falls district and the rearrangement of facies types within these units is also given.

Table 4. Subdivisions of the Myra Formation showing units of Juras (1987) in comparison to the facies based units.

<table>
<tr><th>Layer Cake Stratigraphy
(After Juras 1987)</th><th>LithoFacies
(modified -this study)</th><th>Intercalated units</th><th>Intercalated facies</th></tr>
<tr><td>Upper Mafic Unit</td><td>Upper Mafic Unit</td><td></td><td>Argillite Facies</td></tr>
<tr><td>Upper Rhyolite</td><td>Upper Rhyolite</td><td></td><td>Argillite Facies</td></tr>
<tr><td>Upper Mixed Volcaniclastics</td><td>Upper Mixed Volcaniclastics</td><td>Lynx-Myra-Price Horizon</td><td></td></tr>
<tr><td>G-Flow</td><td rowspan="3">Lynx-Myra Price Horizon (including North Dacite)</td><td rowspan="3">Upper Dacite, 5E Andesite, G-Flow</td><td rowspan="3">Argillite Facies & Sulfide Facies</td></tr>
<tr><td>Lynx-Myra-Price Horizon</td></tr>
<tr><td>Upper Dacite/5E Andesite/ North Dacite</td></tr>
<tr><td>Lower Mixed Volcaniclastics</td><td rowspan="2">Lower Mixed Volcaniclastics
Ore Clast Breccia Unit</td><td rowspan="3">Lower Mixed Volcaniclastics</td><td rowspan="3">Mafic lava
Felsic Volcaniclastics</td></tr>
<tr><td>Oreclast Breccia Unit</td></tr>
<tr><td>Hanging Wall Andesite</td><td>Hanging Wall Andesite</td></tr>
<tr><td>HW Horizon</td><td>HW Rhyolite</td><td>H-W Dacite
H-W Mafic Flow Unit,</td><td>Argillite Facies & Sulfide Facies</td></tr>
</table>

[1] Originally named Hanging Wall HW Andesite, the HW has been dropped due to the significance of the unit over both the HW and Battle ore deposits.

Juras (1987) recognised four distinct source areas for the volcanic rocks (Fig. 8):

1. Volcanic arc region, to the northeast outside the basin
2. Arc rift region area to the southwest outside the basin
3. Price Seamount, intra basinal to the southeast
4. West-G Seamount , intrabasinal to the northwest

The exact position of these source areas was not given and Figure 8 is designated as a guide only. The "basin" referred to, into which the volcanic and sedimentary rocks were deposited, is defined by the nothwestern trend of the ore zones. Lateral variations perpendicular to the basin axis are described by designating the area around the ore zones as the central region, while areas to the northeast and southwest are referred to as such. These references are from Juras (1987) and have been retained in the following descriptions.

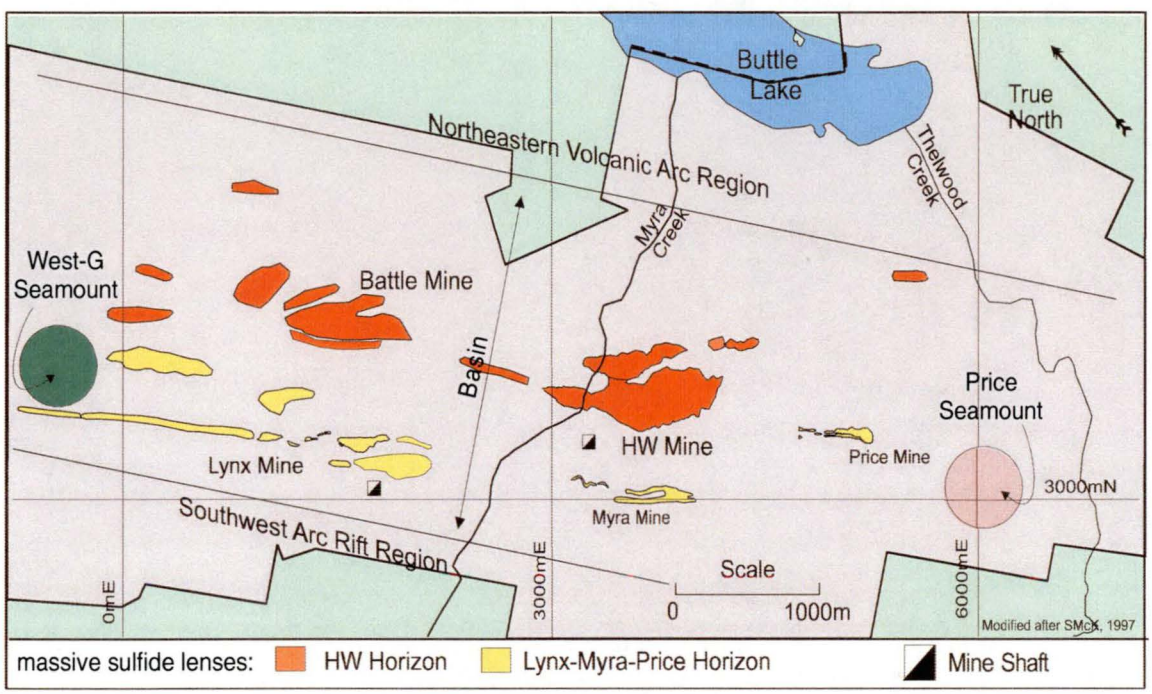

Figure 8. Location Map showing approximate positions of volcanic source areas, relative to known ore lenses. Modified after McKinley (1997).

Rhyolitic Facies

Rhyolitic rocks in the Myra Formation consist of quartz-feldspar-phyric and feldspar-phyric rhyolitic lavas and volcaniclastic rocks. Rhyolite facies are particularly important as they hosts all known massive sulfide mineralisation in the Buttle Lake Camp. The volcaniclastics range from autoclastic breccias, to resedimented syn-eruptive mass flow deposits and rhyolitic mudstones. The rhyolitic volcaniclastics grade from proximal coarse volcaniclastics and lavas in the northeast to volcanic sandstones and intercalated sedimentary deposits toward the southwest (Fig. 9). Juras (1987) interpreted their source to be to the northeast of the depositional basin (Volcanic Arc region). Three felsic units were identified by Juras (1987):

The HW Rhyolite (formerly the HW Horizon) is the lowermost unit of the Myra Formation and consists of three facies: rhyolitic lava flows and domes, volcaniclastic deposits and argillite. The unit occurs throughout the mine area, ranging in thickness from 15 to 200 m and varies

North

East

Figure 9. Fence diagram showing the lateral variations of Myra Formation units in the Mya Falls District

Legend (for figures 9 & 11 to 17)

- Rhyolite
- Dacite
- Andesite
- Altered Andesite
- Ultra-Mafic Flows
- Massive sulfide
- Hematite clasts

- Rhyolite
- Dacite
- Andesite
- Phenocryst-rich andesite
- Andesite lava & breccia
- Angular clasts
- Rounded mixed clasts

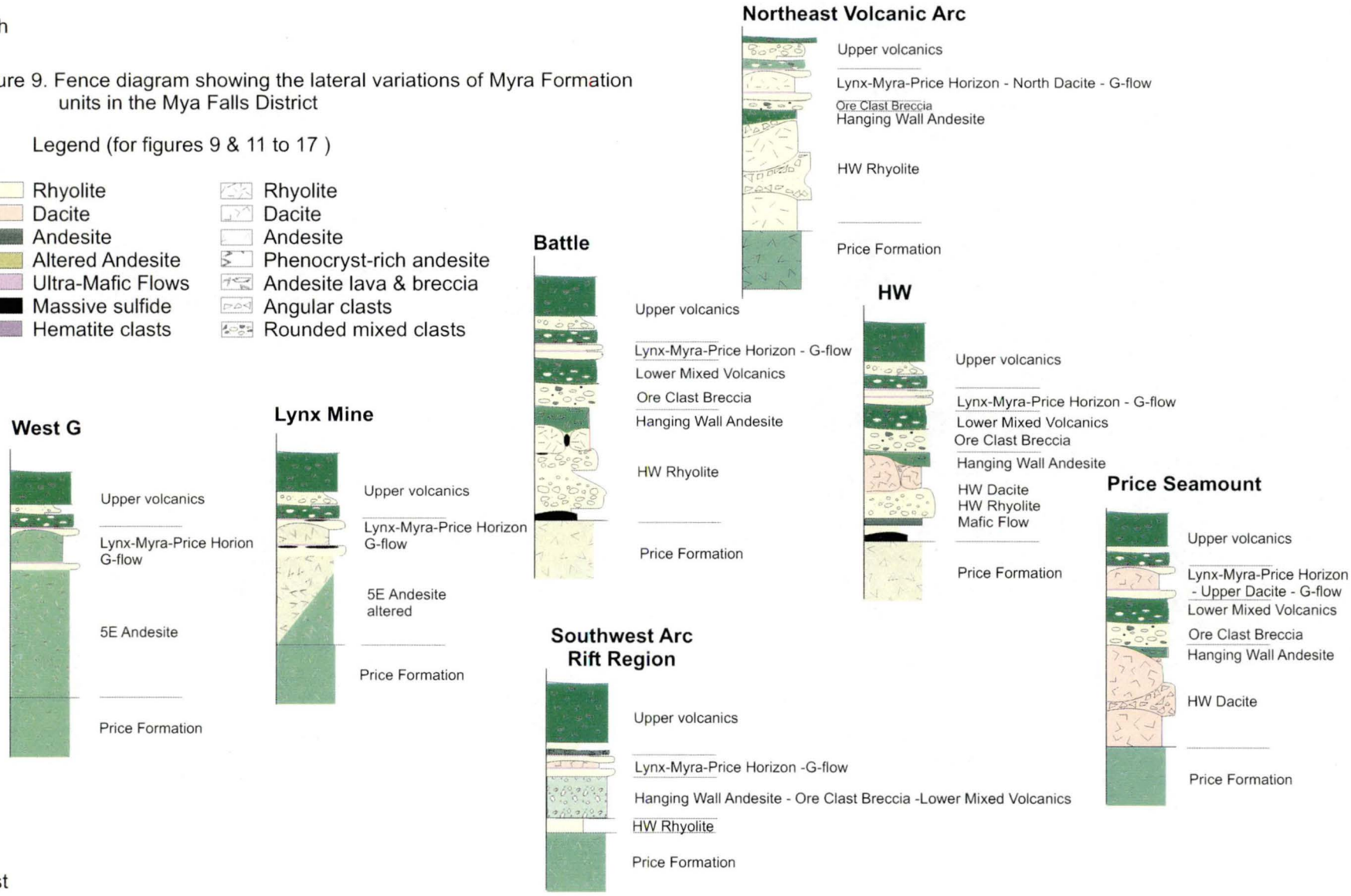

West

South

laterally from northeast to southwest (Fig. 9). The northeast is dominated by coarse volcaniclastics and lavas. While bedded argillite and rhyolitic sandstones dominate toward the southwest (Juras, 1987).

The Lynx-Myra-Price Horizon is the second and central rhyolitic unit within the Myra Formation. It consists of massive to thickly bedded, quartz-feldspar-crystal and vitriclast-bearing rhyolitic volcaniclastic rocks, which range from mudstones to breccias.

The horizon was divided into two spatially distinct units, the G-Zone and the G-Hanging Wall Zone, by Juras (1987). A facies approach makes this division unnecessary, by recognising the intercalated nature of the rhyolitic deposits with deposits from other volcanic centres. Both the G-Zone and the G-Hanging Wall Zone can be traced throughout the mine property, although their lateral extents vary (Fig. 9; Juras, 1987). The units ranges from 10 to 150 m in thickness. Reinterpretation of the volcanic units indicates the North Dacite should also be included in the Lynx-Myra-Price Horizon. The North Dacite is a feldspar-porphyritic, felsic flow unit. It is present only in the northeast of the basin where it is intercalated with volcaniclastic units of the Lynx-Myra-Price Horizon (Fig. 9). Juras (1987), also identified this unit geochemically as originating from the northeastern Volcanic Arc region. Thus it is reinterpreted as a part of the Lynx-Myra-Price Horizon.

The Upper Rhyolite Unit characterised by an association of quartz-feldspar crystal-rich, rhyolite volcaniclastics, argillite, chert and jasper. These units consist of intercalated rhyolitic sandstone to volcaniclastic-breccia and laminated beds of grey to black siliceous argillite, white to pale green chert and minor jasper. In most areas the siliceous argillite - chert facies underlies the volcaniclastic units.

The unit displays distinct lateral facies variation from the northeast to the southwest (Fig. 9). It is thickest (up to 50 m) in the northeast where it consists predominantly of coarse volcaniclastic beds. To the southwest it is finer grained and markedly thinner. The siliceous argillite-chert member ranges in thickness from 1 to 15 m and is largely confined to the central region.

Dacite Facies

Dacite facies rocks consist of feldspar-phyric dacite to rhyolite lavas and are limited in distribution to the south-eastern end of the basin (Fig. 9). This facies is interpreted to have originated from an area named the Price Seamount by Juras (1987; Fig. 8). Two dacite units are recognised.

HW Dacite consists of a feldspar-phyric dacitic lava, which forms massive flows and autobreccia. It is present in the central region and thickens towards the southeast end of the basin (up to 150 m thick). The HW Dacite is intercalated with the HW Rhyolite.

The Upper Dacite is present in the area around the Price orebody (Fig. 8 & 9) and consists of massive to bedded deposits of dacite to rhyolite hyaloclastite, autobreccia and subaqueous volcaniclastic deposits. The extent of this facies is unknown although it is thought to extend to the southwest, it is unknown in the northeast. Two members of dacite were identified by Juras

(1987), only the lower member is referred to here. The upper member is identified by Juras as originating from the West-G seamount making it a separate facies however its distribution has not been differentiated from the Lower member, thus it is omitted here.

Andesite Facies

Andesite facies consists of feldspar + pyroxene porphyritic basaltic-andesite to andesite. The distribution of this facies is limited (see below) and is interpreted as originating from the West-G Seamount area (Fig. 8: Juras, 1987). Two units are recognised:

The Hanging Wall Andesite consists of two facies. Facies 1: basaltic-andesite to andesite lavas and related breccias. Facies 2; andesitic, bedded, feldspar crystal-rich volcaniclastics. The Hanging Wall Andesite is a discontinuous unit which overlies HW Rhyolite north of the 5E Andesite (Fig. 9; Juras pers. com., 1999). Felsic lavas of the HW Rhyolite form paleobarriers which prevented the spread of the Hanging Wall Andesite (Juras, 1987).

5E Andesite is best developed in the West-G area (Fig. 8) and consists of up to 250 m of massive to pillowed, feldspar-porphyritic basaltic to andesite lavas and lesser autoclastic breccia deposits. The 5E Andesite sits directly on Price Formation (Juras pers. com., 1999) and hosts footwall alteration to the Southwall and S-zone Lynx orebodies (Fig. 9). The 5E Andesite is intercalated with the Lynx-Myra-Price Horizon. In some sections (Lynx) it separated the G-Zone and the G-Hanging Wall Zone members of the Lynx-Myra-Price Horizon (Juras, 1987).

Basalt Facies

Basalt rocks consist of clinopyroxene porphyritic komatitic basalt and feldspar + clinopyroxene porphyritic basalt lavas. Abundant volcaniclastic basaltic rocks also occur, however these are interpreted as resedimented products and will be described with the sedimentary facies. Three basaltic units were described by Juras (1987):

HW Horizon Mafic Flow Member consists of a pyroxene-phyric high MgO basalt lava flow and hyaloclastite. Only a single flow unit was recognised by Juras (1987). It occurred in the middle of the HW Rhyolite overlying the HW deposit (Fig. 9) where it forms a >370 m long, ~240 m wide body which is 11 m thick at its centre but thinning to 2 m at its edges.

The G Flow Unit overlies the two members of the Lynx-Myra-Price Horizon and forms the hangingwall to most Lynx ore bodies (Fig. 9). It consists of several, 2 to 15 m-thick mafic lavas and lava breccias, with a total thickness ranging from 5 to 50 m. It is thickest in the Lynx Mine area (Fig. 8). Jasper fragments and lenses are noted in this unit, as are amygdales filled with epidote or calcite.

The Upper Mafic Unit is up to 200 m thick and forms the upper most volcanic unit in the Myra Formation. It contains minor pyroxene + feldspar porphyritic lavas, however the bulk of this unit consists of volcaniclastic deposits containing lava clasts. Subordinate thin-bedded to massive silicified tuffaceous-mudstone, chert and mudstones also occur. The volcaniclastic deposits contain predominantly angular to sub-rounded basaltic lava clasts, however aphyric basaltic clasts (subrounded-rounded), aphyric to weakly feldspar + amphibole porphyritic felsic clasts, and non-volcanic (< 5 %) jasper, chert and mudstone clasts also occur. The volcaniclastics

are interpreted as autoclastic deposits (predominantly angular basaltic lava clasts) and resedimented (subrounded volcanic and non-volcanic clasts) deposits.

The Upper Mafic Unit is present throughout the mine property being thickest (>200 m) to the southwest and thinning to the northeast (5 to 20 m thick). However, the Upper Mafic Unit is missing or notably thinner in some areas (Juras, 1987), this is thought to be due to the upper contact represent an unconformity below the Thelwood Formation (see Chapter 2).

Sedimentary Facies

Sedimentary facies occur throughout the Myra Formation and are generally dominated by rhyolitic or basaltic volcanic clasts, and have occasional interbedded syneruptive volcaniclastic deposits from the dominant arc. Juras (1987), identified three volcano-sedimentary units:

The Ore Clast Breccia Unit contains syn-eruptive rhyolitic volcaniclastics and post-eruptive rhyolite-rich volcanogenic sedimentary deposits and rhyolite-poor volcanogenic sedimentary deposits. It is characterised by subangular massive sulfide clasts. These clasts range in size from 1 cm to 1.5 m but are never abundant enough to form ore (Juras, 1987). The unit is up to 90 m thick and is found throughout the mine area. The Ore Clast Breccia unit overlies the HW Rhyolite and Hanging Wall Andesite Facies.

The Lower Mixed Volcaniclastic Unit is composed of andesitic dominant volcaniclastic deposits, ranging from breccias to mudstones. Rare, thin feldspar porphyritic andesite lavas are also present locally.

The unit occurs throughout the Buttle Lake Camp and is up to 90 m thick. Volcaniclastic breccias are most common in the northeast. It thickens from the Price area to the HW-Myra section before gradually thinning towards the Lynx and West-G sections (Fig. 9). Toward the southwest, the horizon merges with the Hanging Wall Andesite and the Ore Clast Breccia Unit forming an andesite rich volcaniclastic unit with minor dacite and trace rhyolite components (Fig. 9; Juras, 1987). This facies is generally represented as overlying the Ore Clast Breccia Horizon however it is also noted overly the Hanging Wall Andesite in the northeast (Juras, 1987).

The Upper Mixed Volcaniclastics consists of volcaniclastic rocks of mafic to intermediate composition, ranging from bedded mudstone to sandstone and breccia deposits. This unit is up to 50 m thick and occurs throughout the mine property. A lateral compositional variation of clast types is recognised, intermediate and felsic clasts are most abundant in the northeast, with mafic clasts dominant in the southwest. The Upper Mixed Volcaniclastics generally overly the Lynx-Myra-Price Horizon, however in some mine sections undifferentiated volcano-sedimentary rocks are intercalated with the Lynx-Myra-Price Horizon which the author interprets as either Lower or Upper Mixed Volcaniclastic type deposits.

Argillite, chert & jasper facies are found throughout the Myra Formation and are considered to represent non-volcanic input into the basin. Juras noted radiolarian 'ghosts' in cherts of the Upper Rhyolite unit. The origin of these units (in the HW Rhyolite) is the subject of a concurrent PhD study by S. Jones, thus discussion of these units will not be entered into here. However, it is noted

that the argillite facies form interbedded and distal deposits to volcaniclastic deposits in most areas (Juras, 1987). They are intimately associated with the finest grain volcaniclastics thus their description, where relevant, have been included with these deposits in the relevant units above.

3A. 2 Volcanic and Depositional History

The Myra Formation was deposited as a series of volcanic and sedimentary events. An attempt at summarising these events is made below and in Figures 10 - 17. The first volcanic event (Fig. 11), represented by the HW Rhyolite, occurred to the northeast and formed rhyolitic volcaniclastics and lavas. The volcaniclastics formed coarse proximal deposits along the north-eastern edge of the basin with finer grained, more distal rhyolitic sandstones and bedded argillites deposited to the southwest (Fig. 11). Contemporaneous with this rhyolitic volcanism was the deposition of sulfide deposits (HW and Battle lenses), dacite facies from the Price Seamount (HW Dacite) and mafic volcanism (HW Mafic Flow Unit). Deposition of the HW Rhyolite was followed by the eruption and deposition of the Hanging Wall Andesite from the West-G Seamount. The distribution of andesite flows was controlled by the paleotopography created by the underlying rhyolitic and dacitic lava flows and domes (Fig. 12). This cycle of volcanism was followed by a relatively quiescent period in which re-sedimentation of existing rhyolite volcanics from the northeast occured (Fig. 13).

A second phase of volcanism was initiated in several centres around the basin with the eruption

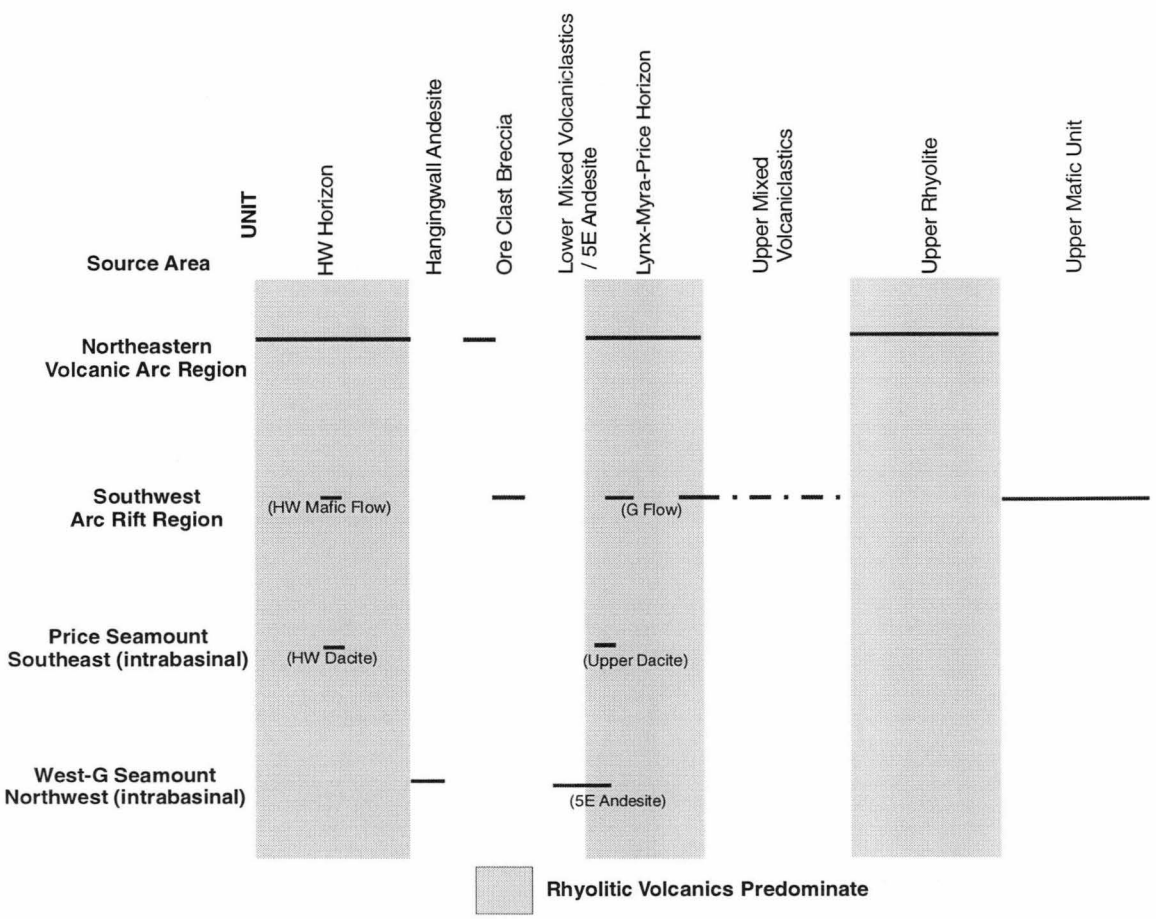

Figure 10. Relative timing of volcanic events which produced volcanic facies of the Myra Formation.

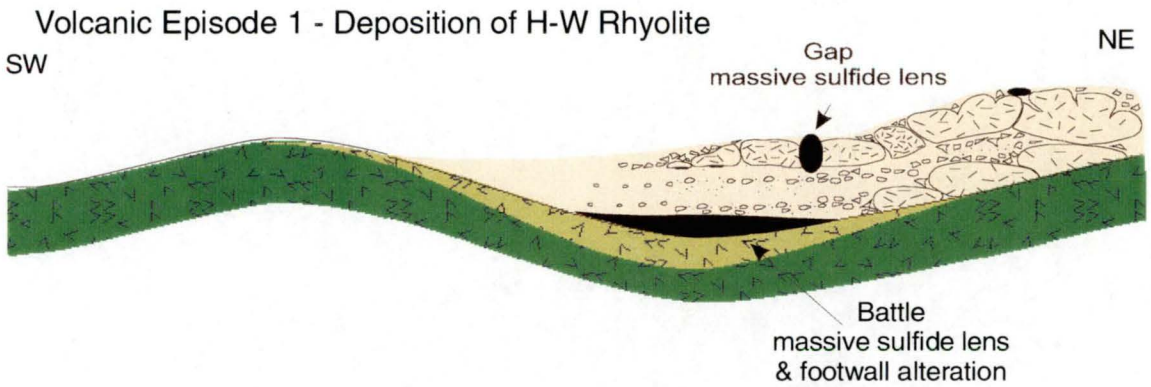

Figure 11. Schematic diagram - Deposition of HW Rhyolite and associated massive sulfide lenses.

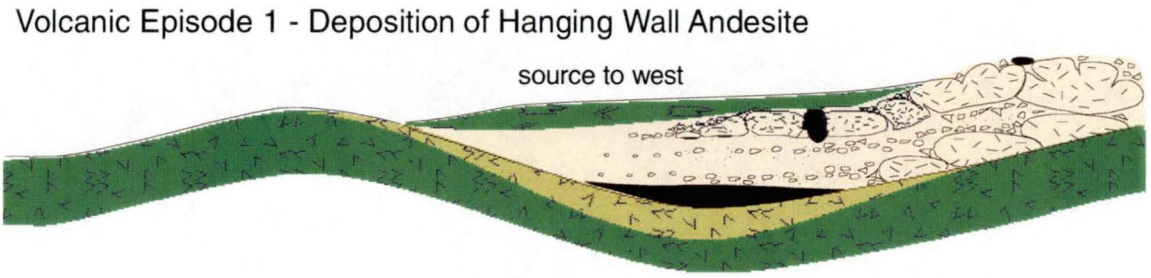

Figure 12. Schematic diagram - Deposition of Hanging Wall Andesite.

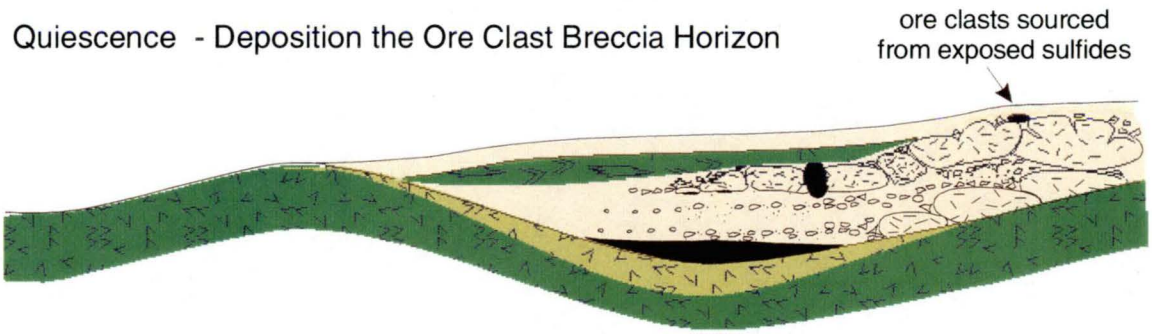

Figure 13. Schematic diagram - Deposition of Ore Clast Breccia Horizon.

of the Upper Dacite from the Price Seamount and the 5E Andesite from the West-G Seamount. Deposition of the predominantly andesitic lower mixed volcaniclastics is probably related to the eruption of the 5E andesite (Fig. 14). Contemporaneous with these events was the reactivation of the northeast volcanic arc which again produced rhyolitic volcanics (Lynx-Myra-Price Horizon) and felsic lavas (North Dacite), massive sulfide mineralisation also re-occurred at this time (Fig. 15). Felsic volcanism was again followed by mafic volcanism, form the G-flow units. G-flow units sourced from the southwestern arc capped the rhyolite units. This cycle may have occurred a number of times, two rhyolite/mafic cycles are identified by Juras (1987) but it is unclear the exact relationship of these units from this work.

Volcanic Episode 2 - Deposition of 5E andesite and Lower Mixed Volcanics

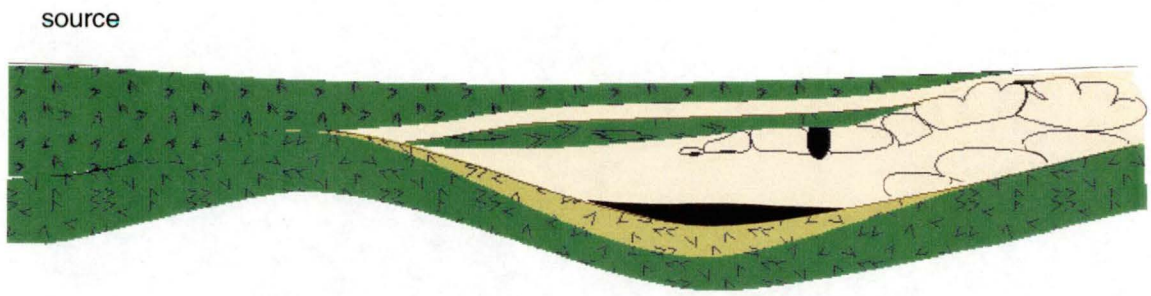

Figure 14. Schematic diagram - Deposition of 5E Andesite and Lower mixed Volcaniclastic Unit.

Volcanic Episode 2 - Deposition of Lynx-Myra-Price Horizon, G-Flow Units and 5E andesite continued.

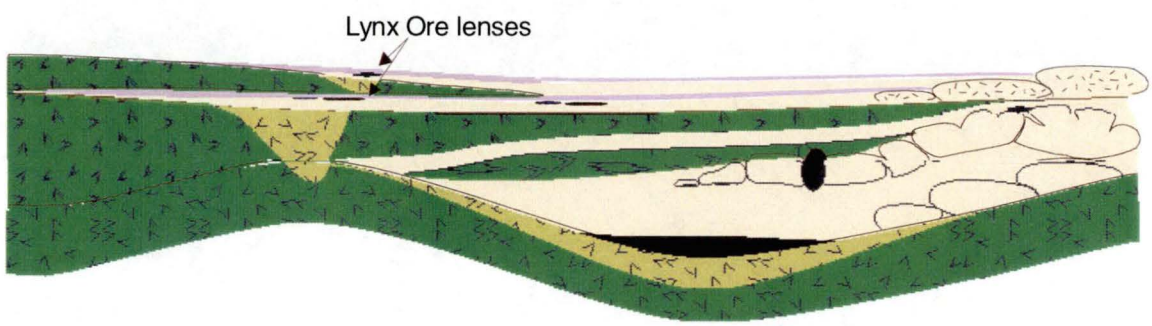

Figure 15. Schematic diagram - Deposition of the Lynx-Myra-Price Horizon and associated massive sulfides, the G-Flow unit and continued eruption of 5E Andesite.

The second volcanic cycle was again followed by a quiescent period in which predominantly mafic to intermediate volcanics were redeposited into the basin (Fig. 16). A third volcanic cycle of rhyolitic (Upper Rhyolite) and mafic volcanism (Upper Mafic Unit) finished the Myra Formation (Fig. 17). Massive sulfide mineralisation is not known in this final cycle.

Quiescence - Deposition the Upper Mixed Volcanics

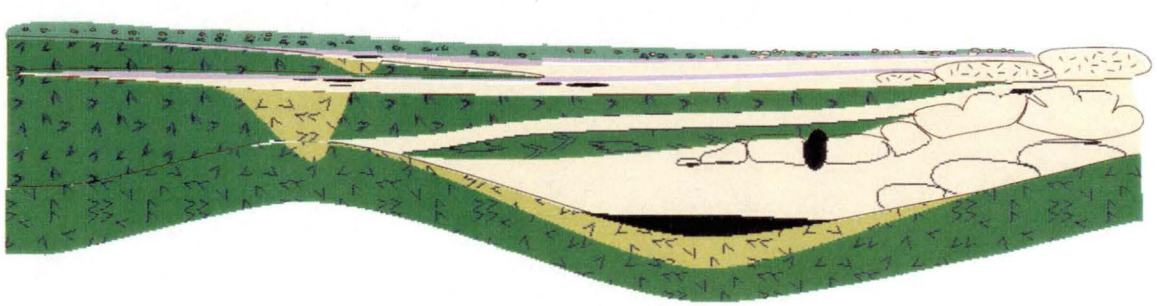

Figure 16. Schematic diagram - Deposition of the Upper Mixed Volcanics.

Volcanic Episode 3 - Deposition the Upper Rhyolite Unit followed by the Upper Mafic Unit

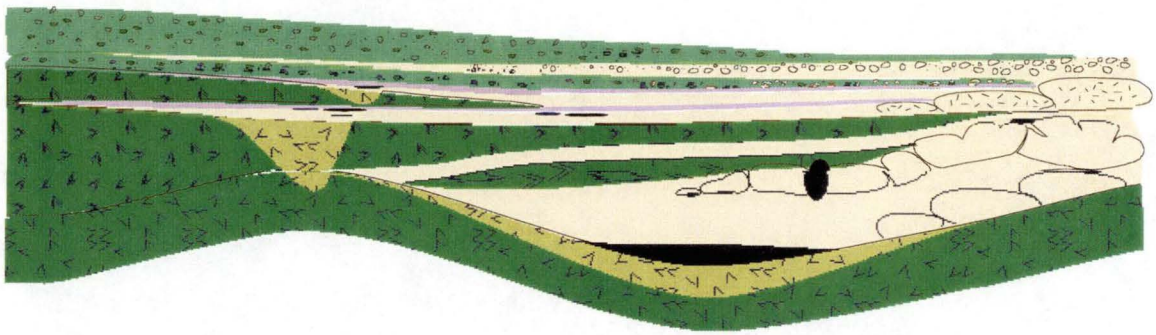

Figure 17. Schematic diagram - Deposition of the Upper Rhyolite Unit followed by the Upper Mafic Unit.

Comments

This review highlights the need for a comprehensive facies based volcanological study of the Buttle Lake Camp. Such a study is needed to improve the understanding of the relation of the volcanic units, i.e. interfingering and timing relationships. A better understanding of volcanic architecture will aid in developing targets for exploration in the Buttle Lake Camp.

Part B:

3B.1 Battle Zone Host Rocks

The Battle Zone includes rocks from the Price Formation and the lower two units of the Myra Formation, the HW Rhyolite and the Hanging Wall Andesite. All the rocks in the Price Formation and the HW Rhyolite in the Battle Zone are moderately to intensely altered by the hydrothermal fluids associated with sulfide mineralisation. The Hanging Wall Andesite is unaffected by the hydrothermal alteration. Facies descriptions below are based on observed alteration mineralogy and textures. Observations were made during the logging of 7 drill sections through the Battle Zone (1780mE, 1750mE, 1600mE, 1540mE, 1450mE, 1420mE, and 1390mE) some of these sections are presented to illustrate the observations. Information, from previous authors, is then presented to ascertain the possible pre-alteration rock types. The author also collected samples from 2 holes in the Thelwood Valley to aid in determining the primary rock types, textures and regional alteration.

3B.1.1 Price Formation

The Price Formation is known to be composed of massive to pillowed basaltic andesite lavas and associated fine to coarse volcaniclastic rocks (Juras, 1987). Only 75 m of the unit has been intersected in exploration drill core in the Battle Zone (Robinson, 1994), less in most definition holes. In all of the drill holes logged for this project the footwall contact was obscured by massive sulfide mineralisation and the rocks intensely hydrothermally altered to sericite-pyrite and lesser chlorite-pyrite assemblages. Most of the intersections are also extensively faulted and foliated.

From the interpreted top of the Price Formation (defined as the base of the economic mineralisation), the unit grades from massive pyrite (± chalcopyrite) in a siliceous to sericitic matrix, through semi-massive pyrite (± chalcopyrite), sericite-pyrite-schists ± chlorite-pyrite-schists, into moderately quartz-sericite-chlorite-(± pyrite) altered andesites (Fig. 18). The gradation from sericite-pyrite-schists to moderately altered andesites occurs approximately 20 m below the ore zone. Occasional quartz ± pyrite ± chlorite ± calcite veinlets occur throughout the sequence. Stringer style veins are uncommon in the Price Formation below the Battle Zone lenses, where they do exist they have sharp margins and are marked by intense sericite-alteration with quartz-pyrite-chalcopyrite ± sphalerite. The intensity of alteration within the Battle Zone makes interpretation of volcanic origins and rock types impossible. The mineral assemblages observed during this study are the products of hydrothermal alteration and subsequent metamorphism. These will be described in Chapter 4.

3B.1.2 - HW Rhyolite

In the Battle Zone, the HW Rhyolite is a 20 - 70 m package of volcaniclastic rocks overlain by a rhyolite flow / dome complex (Fig. 19). All rocks show moderate to intense hydrothermal alteration. The hydrothermal alteration is associated with the fluids that formed massive sulfide mineralisation, the bulk of which lies on the Price Formation - HW Rhyolite contact. Smaller lenses occur throughout the HW Rhyolite, particularly along the underside of the rhyolite flow / dome complex. The hydrothermal alteration is texturally destructive, resulting in the loss of most of the primary volcanic textures.

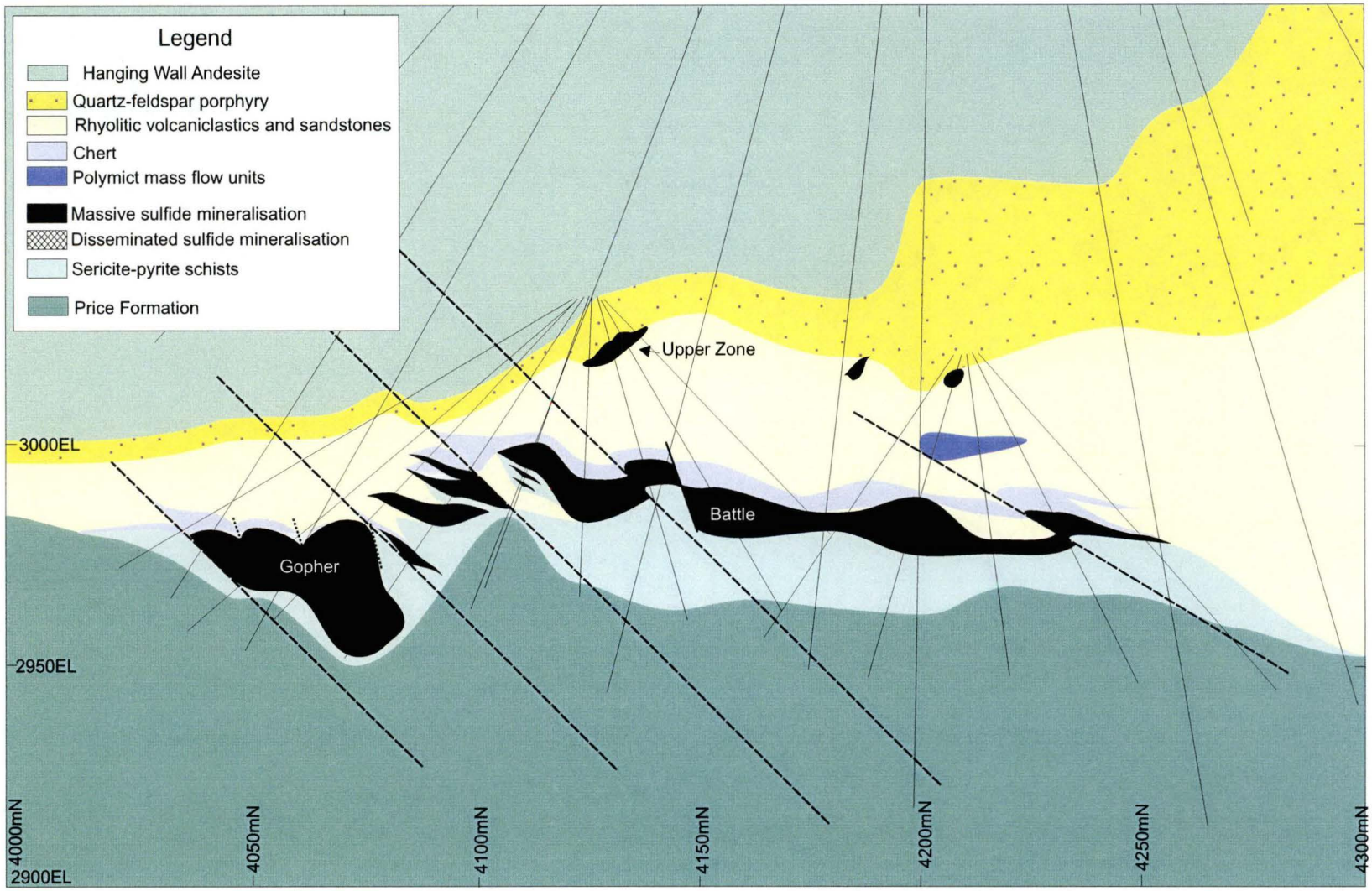

Figure 18. Schematic geology of the 1600mE section through the Upper Zone, Battle and Gopher lenses showing the distribution of the Price Formation, Facies 1 to 4 of the HW Rhyolite and the Hanging Wall Andesite.

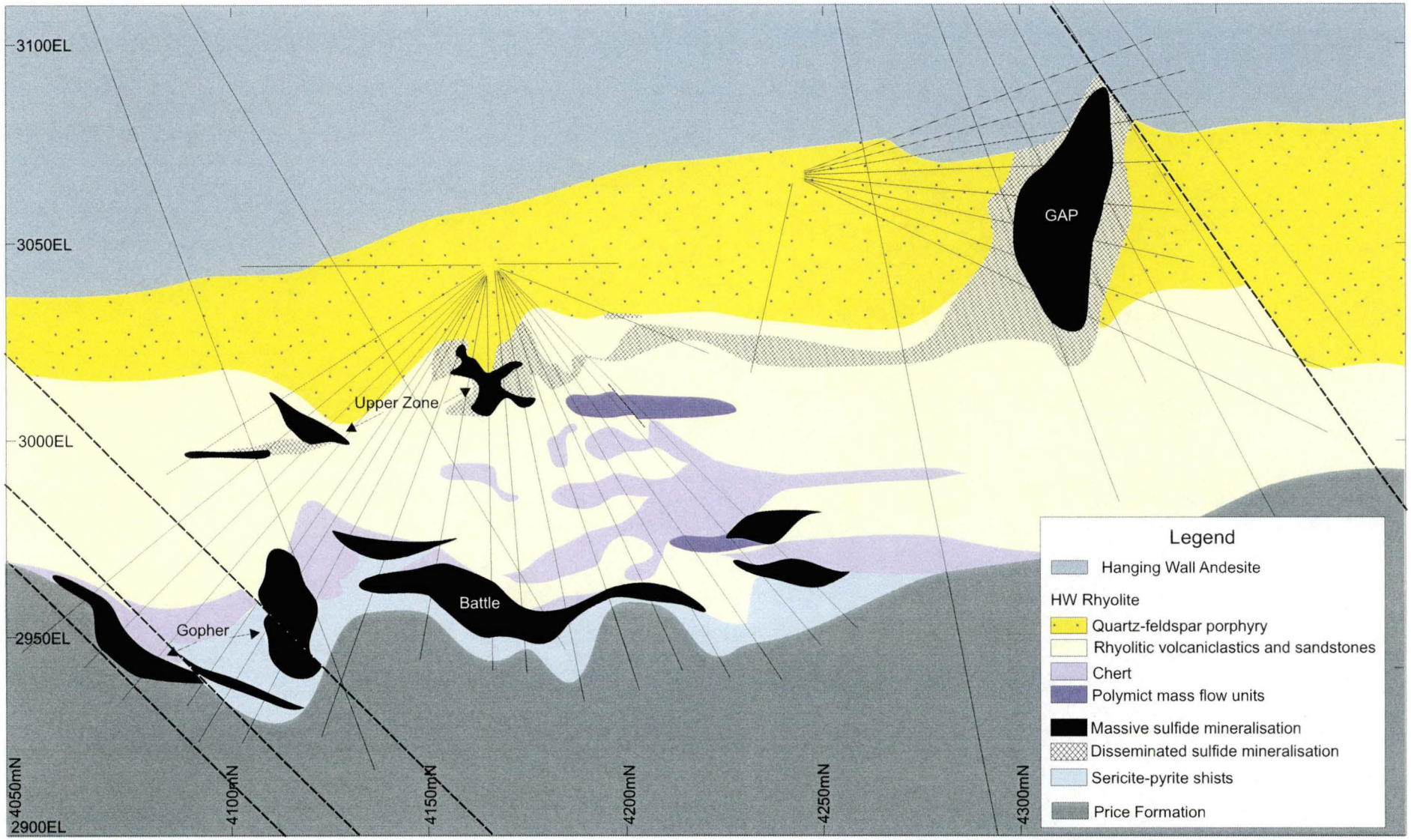

Figure 19. Schematic geology of the 1420mE section through the Gap, Upper Zone, Battle and Gopher lenses showing the distribution of the Price Formation, Facies 1 to 4 of the HW Rhyolite and the Hanging Wall Andesite.

Battle Zone rocks have also been metamorphosed to lower greenschist minerals assemblages, causing recrystallisation of the original phyllosilicate alteration minerals and quartz to sericite-quartz mosaics ± carbonate. The entire Battle Zone has also been affected by at least 4 stages of post-mineralisation deformation (Chapter 6), the most pervasive of which was the regional D2 event, which has produced a foliation that modified some textures and has produced a foliation visible in all samples.

The HW Rhyolite has been divided by previous workers (Juras, 1987; Robinson, 1994) into several lithologies: 1. Massive sulfide lenses, 2. "Cherts" and fine rhyolitic tuffaceous deposits, 3. Mafic sills, 4. Rhyolitic volcaniclastic deposits and 5. Rhyolite flow-dome complex. Revised descriptions of the HW Rhyolite and new data pertinent to its interpretation are presented below. Readers are referred to chapters 6 and 7 for a discussion of the mineralisation. Mafic sills referred to by Juras (1987) and Robinson (1994) were not seen in the Battle Zone during this study and are not included.

Facies 1: Volcaniclastic breccia and sandstone:

This facies is the dominant rock type seen throughout the Battle Zone. The units are moderately to intensely, hydrothermally altered to sericite-quartz-carbonate assemblages. Volcanic textures are rarely preserved, with the exception of quartz phenocrysts. Bed contacts are often hard to distinguish due to alteration and faulting, however sharp basal contacts have been observed. The beds range from ungraded coarse volcaniclastic breccias to normally graded beds. Beds range in thickness from 2 - 15 m.

The beds contain fiamme-like lenses composed of phyllosilicate minerals (see chapter 5) which will be referred to as pseudo-fiamme (Plate 1 A-D). The pseudo-fiamme range in size from 0.2 mm to 3 cm. They are occasionally quartz-phyric, the quartz phenocrysts being 0.5 - 2 mm in size. Some beds also contain moderately to weakly abundant, fine grained quartz-porphyritic (up to 0.5 mm) rhyolite lithic clasts, ranging in size from 0.5 mm to boulders which are commonly rounded (Plate 1A). As well as clasts of sandstone (0.5 mm to boulders; see description below) and quartz crystals. Quartz crystals have resorption embayments consistent with a volcanic origin (Plate 1E & F), are 0.5 to 2 mm in size and commonly have broken surfaces. Clast margins may be sharp (Plate 1E), but many are diffuse and gradational. The indistinct nature of these contacts can in some cases be attributed to hydrothermal alteration. The volcanic sandstone is composed of fine to medium sized, 0.5 - 1.5 cm pseudo-fiamme, 0.5 mm lithic-clasts (of the types seen in breccias) and occasional quartz crystals (Plate 1C & D).

Facies 1 contains broken volcanic quartz crystals, boulders of sandstone and quartz-porphyritic rhyolite lithic clasts with quartz phenocrysts up to 0.5mm in size. Broken volcanic quartz indicates pyroclastic eruption processes, while the boulders of sandstone indicate a reworking of the constituents of this facies. The distribution of lithic clasts, probably from a different eruption phase (quartz-phenocrysts different in size) may indicate they were sourced from around the pyroclastic vent that generated the bulk of Facies 1 (Allen, 1993). The normally graded beds likely have a mass flow origin. While the ungraded coarse volcanic breccias may be mass flow deposits or resedimented

PLATE 1 - HW Rhyolite Facies 1 Volcaniclastics and sandstones

A. Coarse volcaniclastic breccia showing silicified porphyritic clasts and quartz-eyes plus overprinting pseudo-clasts. BG18-886 4.5m

B. Sandstone bed overlain by fine volcaniclastic base, both units contain pseudo-fiamme. BG18-874 20 m

C. Sandstone bed with fine clasts of silicified porphyry and quartz eyes, containing by coarse pseudo-fiamme.BG18-775 83.1 m

D. Rhyolitic sandstone bed containing fine pseudo-fiamme. BG18-775 83.9 m

E. Photomicrograph showing edge of silicified quartz-porphyritic clast in sericite-quartz altered matrix, position of photo shown in A above. BG18- 886 4.5 m

F. Volcanic quartz crystals in sandstone. BG18-799 29.7m

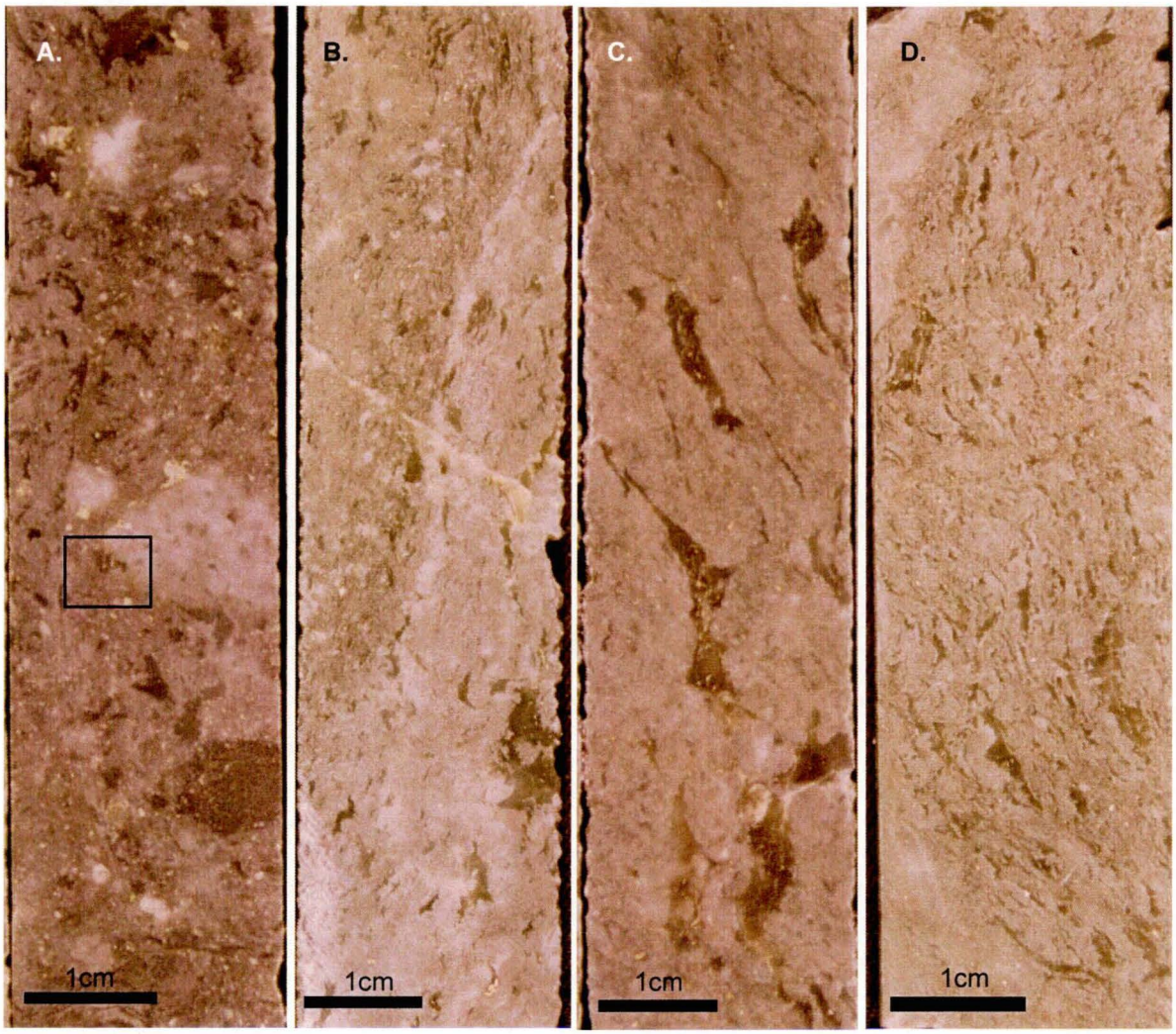
A.
B.
C.
D.
1cm
1cm
1cm
1cm

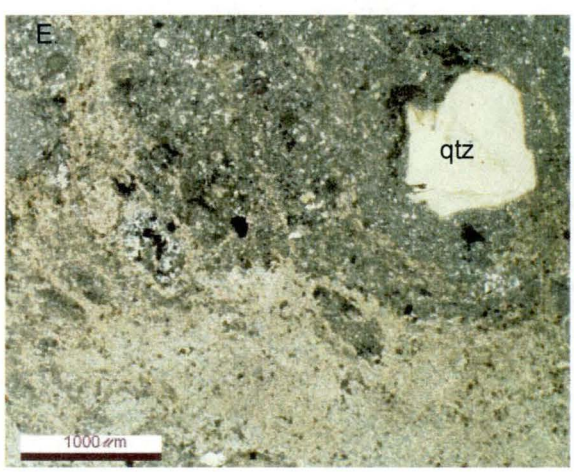
E.
qtz
1000 µm

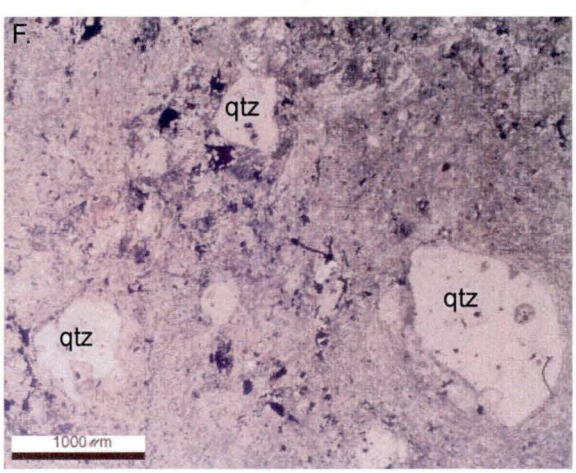
F.
qtz
qtz
qtz
1000 µm

autoclastic breccias.

Facies 2: Siltstones:

Siltstone facies consists of very fine grained, laminated to thinly bedded (<1 to 10 cm) volcanic siltstones (Plate 2). In the Battle Zone the siltstones are moderately to strongly siliceous ranging from rare chert[1] through tuffaceous chert, tuffaceous mudstone to tuffaceous sandstone. Siltstones form units from 0.1 - >20 m in thickness. The units are commonly white to light grey often with dark grey bands, rare green and purple units have also been observed in the Battle Zone (Plate 2C - G). The rocks are commonly pyrite spotted and have pyrite as veins and along laminations (Plate 2J). This facies is commonly brecciated by faulting and has veins of chalcopyrite, pyrite-sphalerite-galena and tennantite (Plate 2E & F). In thin section, quartz phenocrysts (0.02 - 0.1 mm) compose <1% of the rock. The matrix is composed of microcrystalline quartz (minor sericite & carbonate). Sericite-pyrite in silicified samples or abundant quartz crystals (up to 5% in Thelwood Valley samples) define laminations (Plate 2J - L).

The siltstones are rarely seen unsilicified in the Battle Zone (Plate 2H excepted), however, Thelwood Valley holes show only unsilicified finely laminated sediments (Plate 2A & B). In the Thelwood Valley samples the 0.02 - 0.1 mm quartz crystals, are part of a population of feldspar and quartz crystals which make up to 20% of some beds. Feldspar crystals are 0.2 - 0.1mm in size and constitute up to 15% of the rock while quartz crystals constitute up to 5% of the rock. Coarse bands rich in feldspar and quartz crystals have sharp bases and grade up to crystal poor tops (Plate 2J). The feldspars are destroyed by weak sericite alteration thus absent from the Battle Zone (Plate 2K & L). The quartz crystals are only destroyed/obscured by most intense sericite-quartz alteration and can still be seen in some Battle Zone samples (Plate 2J).

Facies 2 siliceous siltstones directly overly sulfide mineralisation on the Price Formation contact forming a >20 m unit (Fig. 18). Siliceous "cherty" beds grade in and out of sandstones and volcaniclastic breccias of Facies 1 throughout their >20 m thickness and eventually give way to Facies 1. However siltstones occur interbedded with Facies 1 throughout the HW Rhyolite, become thinner (0.1 - 2 m) and less common upward.

Facies 2 siltstones occur as laminated to thinly bedded (<1 to 10 cm) deposits with variable feldspar and quartz crystals contents. The graded beds suggest the siltstones were deposited from low density turbidites. The origin of the material that makes up the siltstones is unknown it may be volcanic ash or the fine grained sediment from terrigenous sources. The siltstones may also contain a pelagic and / or exhalative component, however in the Battle Zone they are too altered to confirm or deny this.

[1] Chert is the mine term used to describe these fine grained siliceous rocks, textural evidence described here and chemical evidence in chapter 5, show that these are not true hydrothermal or chemical cherts.

PLATE 2 - HW Rhyolite Facies 2 Siltstones

A. Finely laminated sediments. PR127 93.4 m

B. Coarse siltstone overlain by fine siltstone (cut by quartz-pyrite vein with sericite alteration halo). PR127 93.7m

C. Rare banded sediment from Battle Zone overlying massive dark grey siltstone. BG18-1003 74m

D. Facies1 / 2 contact, coarse grained sandstone overlying and scouring top of fimely laminated siltstone. BG18-1005 84.3m

E. Finely laminated "chert", pyrite is visible along the upper laminations. Laminations are cross cut by a chalcopyrite filled fracture. BG18-797 42.5m

F. Brecciated "chert" infilled by pyrite-chalcopyrite. BG18-798 42 m

G. Weak lamella in chert defined by fine grained pyrite. BG18-977 126 m

H. Graded bedding in siltstone from top of Battle lens (T-174 south wall)

I. Pink and green banded "chert". G.18-163 ramp (near G149DD access)

J. Coarse layer defined by quartz crystals and muscovite overlying finer quartz rich bed. BG18-1006 89.2m

K. Banded sediments bands define by coarser volcanic quartz crystal abundances. PR127 93.4 m

L. Coarse bases grading up to fine tops. BG18-1003 74m

PLATE 2 - HW Rhyolite Facies 2 Siltstones

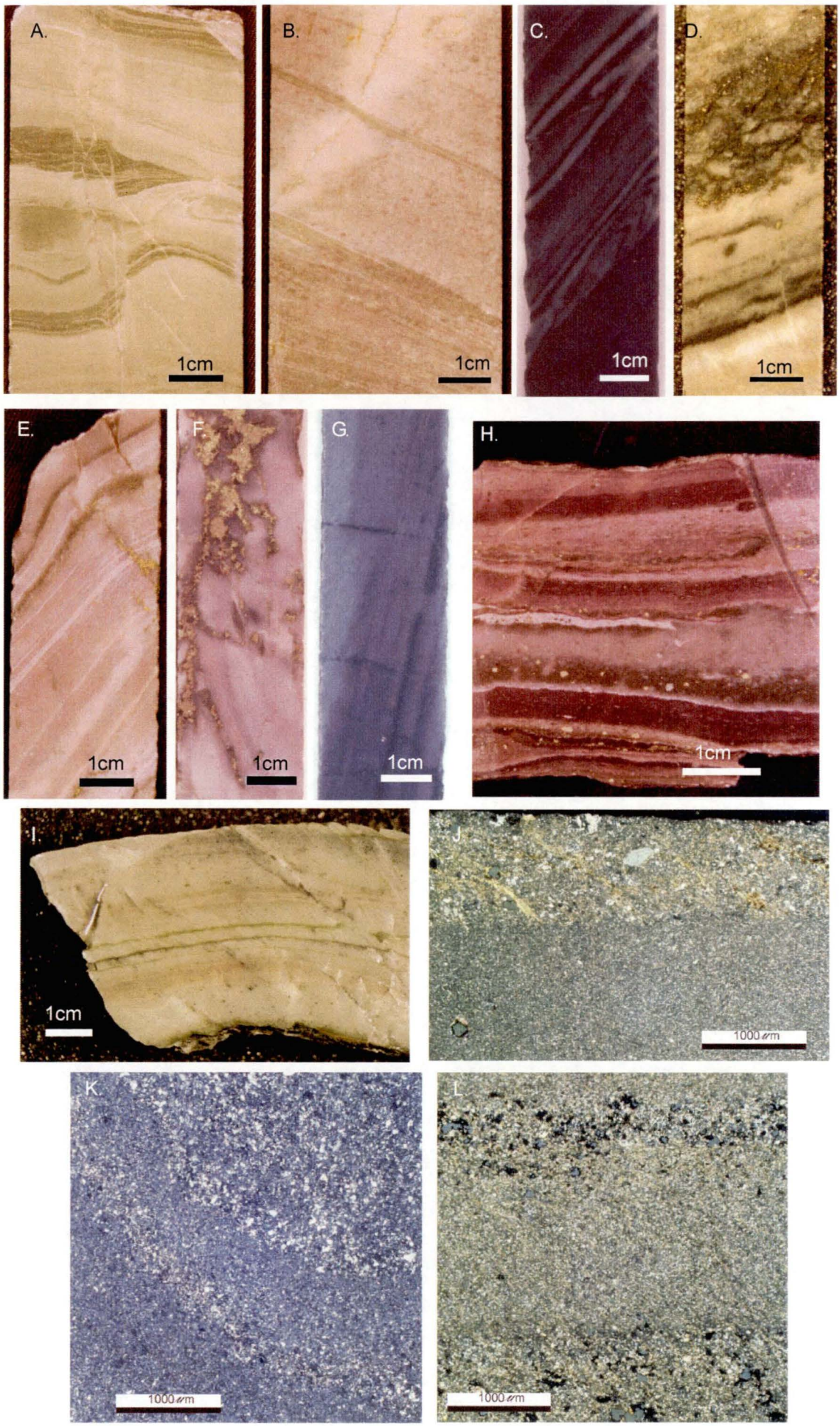

Facies 3: Polymictic, graded, mass flow beds

Facies 3 units are mainly confined to the northern margin of the Battle Zone and become finer eastward (Fig. 19). They occur interbedded with Facies 1 and 2 units. Individual beds are 40 cm to 3.5 m in thickness and occur in packages of two or more, forming units up to 10 m in thickness to the northeast. The units thin and disappear over the Battle lens in the centre of the basin.

The polymictic beds (Plate 3) consist of a volcanic sand matrix (made up of microcrystalline sericite and quartz) with varying proportions of quartz-(feldspar) crystals (up to 40%) and lithic clasts. The lithic clasts include fine grained, quartz-feldspar-porphyritic clasts (rounded, <2 cm), facies 2 cherts and tuffaceous mudstones clasts (0.1 - 5 cm, angular), sub-angular clasts (up to 5 cm) to boulders of facies 1 sandstone, andesite clasts in various alteration states (commonly chlorite-epidote or sericite-pyrite altered, minor fuchsite, sub-rounded, <1 cm), white porphyritic-silicified clasts (rounded, <1 cm, probably quartz-feldspar porphyritic) and rare sericite-altered (sub-angular to irregular, 1 mm to 5 cm) and sulfide clasts (angular, 1 mm to 1.5 cm). The units are strongly graded from coarse (3 - 5 cm clasts) lithic rich bases to fine sandstone tops (Plate 3A).

Facies 3 is characterised by strongly graded beds containing clasts, most of which are rounded and composed of synchronous volcanic units, hydrothermal products, and Price Formation. This material could be reasonably interpreted as the surrounding substrate, suggesting reworking of earlier units by mass flow to produce graded beds. The variety of clast types and their limited distribution suggests they were sourced from an area different from that which produced Facies 1.

Facies 4: Quartz-feldspar porphyritc rhyolite

The quartz-feldspar porphyritic rhyolite (QFP), is a massive to clastic unit of evenly quartz-feldspar-phyric (0.5 - 2 mm) rhyolite. In the Battle Zone, it is weakly (feldspar phenocrysts still visible) to intensely altered and mineralised (Plate 4C - E). Quartz phenocrysts are evenly distributed, 0.5 - 2 mm in size and embayed. Feldspar phenocrysts where visible are mostly 1 mm in size (0.5 - 1 mm; Plate 4G). The phenocrysts are evenly distributed in a ground mass of microcrystalline quartz, sericite and minor carbonate. Alteration in the Battle Zone has destroyed primary volcanic textures, however an example from the Thelwood Valley shows flow-banded clasts (Plate 4A & F).

The QFP forms a dome complex to the northeast (thickness >50 m), and thins to 10 - 20 m, becoming more clastic towards the centre of the basin (Fig. 19). The QFP overlies and truncated facies 1 volcaniclastics, the lower contact commonly consists of 10 - 20 m of clastic QFP grading up to massive QFP. This lower contact is commonly obscured by alteration and mineralisation. The upper contact with the Hanging Wall Andesite is sharp to erosional. Clastic units are non existent to 1.5 m in thickness and pieces of the QFP are incorporated into the base of the Hanging Wall Andesite.

The QFP units have quartz-(feldspar) phenocrysts in the size range 0.5 - 2 mm, consistent with the quartz crystals seen in Facies 1, suggesting they may be related. The unit consists of predominantly massive lavas to the northeast. To the southeast the unit thins, becoming more clastic to-

PLATE 3 - HW Rhyolite Facies 3 Polymictic graded, mass flows

A. Graded polymict mass flow. BG18-762 64.7m

B. Contact between coarse polymict base and fine grained top of flow, contact irregular and erosional, box indicates position of photo micrograph below (F). BG18-1006 49.7m

C. Coarse base of graded polymictic mass flow. AQ core. BG18-1006 48.1m

D. Relic silicified clast in sericite-quartz altered matrix. BG18-763 91 m

E. Various clast types in a quartz-sericite matrix. Pyrite crystal showing quartz pressure shadows. BG18-1006 48.1m

F. Photomicrographs across contact, right - fine grained top of a graded bed sericite-quartz altered, across silicified porphyritic (sericite altered) clast, into coarse base showing a variety of sericite altered and silicified clasts and pyrite crystals. Square in phote B shows postion of photomicrographs. BG18-1006 49.7 m

PLATE 3 - HW Rhyolite Facies 3 Polymictic graded, mass flows

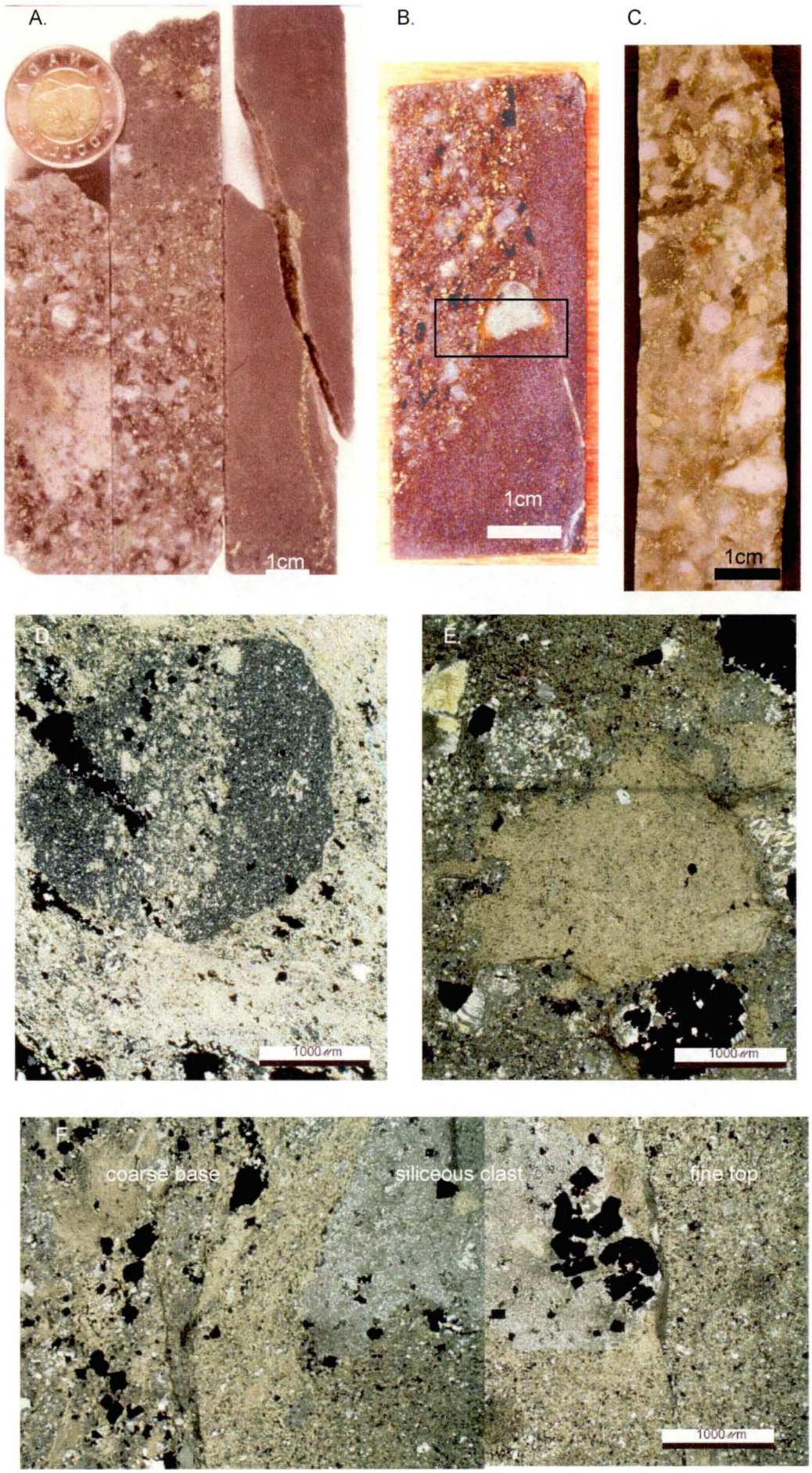

PLATE 4 - HW Rhyolite Facies 4 Quartz-feldspar porphyry

A. Thelwood Valley, QFP breccia, some clasts showing relic flow banding. PR123 100.2 m

B. Thelwood Valley, massive QFP. PR123 128.8 m

C. Least altered QFP sample from Battle Zone. BG18-1080 47.5m

D. Typical silicified and sericite altered Battle Zone QFP, quartz phenocrysts still visible but all trace of feldspar destroyed. BG 18-982 0.6-0.8 m

E. Altered QFP with sphalerite stringer mineralisation, form margin of Upper Zone lenses. H169 P8 (6)

F. Relic flow banded clast (left) and matrix (right), Thelwood Valley sample. PR123 100.2m

G. Feldspar and quartz phenocrysts, feldspar phenocryst weakly altered, twinning still visible (least altered Battle Zone Sample (see chapter 5). BG18-1080 47.5 m

H. QFP showing volcanic quartz crystal. BG18-1008 3.9m

PLATE 4 - HW Rhyolite Facies 4 Quartz-feldspar porhyry

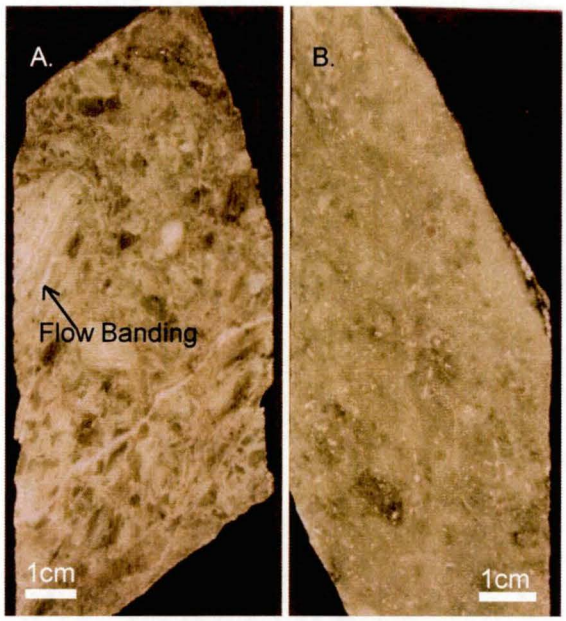

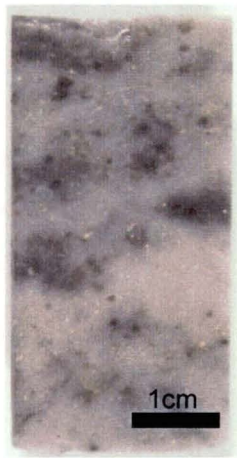

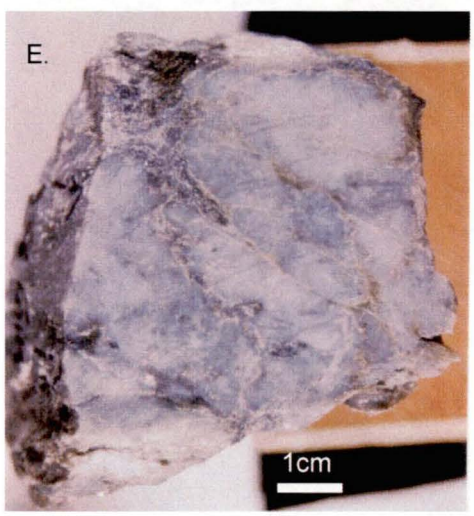

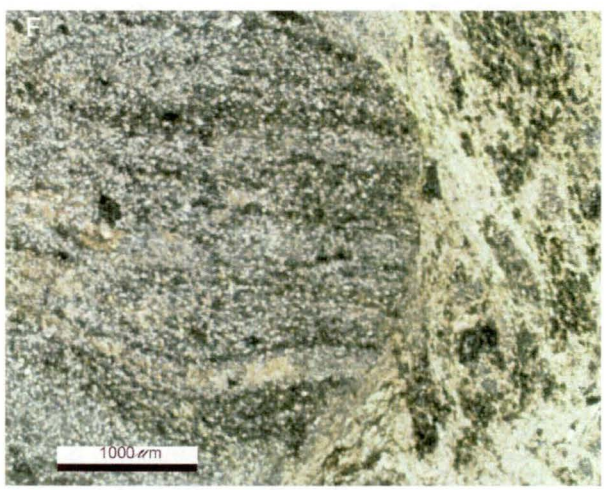

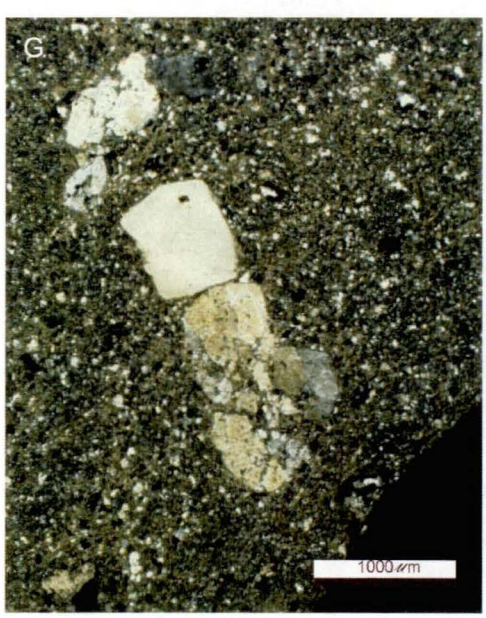

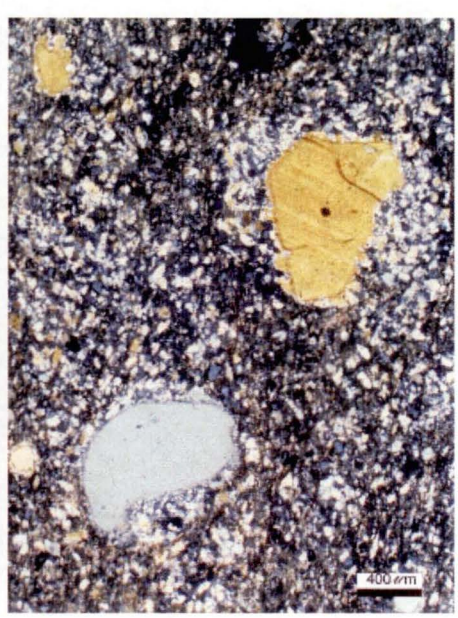

wards the centre of the basin, indicating a source area to the northeast. The clastic beds are monomictic and show little grading, thus they are interpreted as an autoclastic unit, however graded beds with rhyolite and occasional sulfide clasts increase toward the base of the unit and are interpreted as resedimented autoclastic breccias.

3B.1.3 Hanging Wall Andesite

This section is focused on the basal 10 - 15 m of the Hanging Wall Andesite as dictated by drill intersections logged. The basal contact of the Hanging Wall Andesite, is generally sharp but often appears gradational into the underlying rhyolitic units. This is due to the high abundance of rhyolite clasts in the base of the breccia units overlying the HW Rhyolite. The upper contact was not observed.

Near the base of the Hanging Wall Andesite, the most common facies is andesitic volcaniclastic deposits with varying proportions of andesite and lithic clasts. Andesitic lavas are less common. The volcaniclastic deposit range from moderately to well sorted, normally graded beds, to poorly sorted, crudely graded units (Juras, 1987). The width of units was undeterminable from the limited core seen, however units of 2 m to >20 m are suggested from Thelwood drilling.

The andesite volcaniclastics (Plate 5) contain three types of andesite clasts. The most abundant are medium to dark green, fine grained, non- to weakly-porphyritic (plagioclase, 0.1 - 1 mm), pervasively chlorite-altered, ragged to angular andesite clasts. These clasts range in size from 0.1 to 10 cm but are commonly around 3 cm and make up about 60% of the rock (Plate 5A & C). The second most abundant clast type are light green, strongly porphyritic (plagioclase, 0.1 - 2 mm), epidote-altered, andesite clasts (commonly sub-angular to sub-rounded and ranging in size from 0.5 cm to 4 cm with occasional boulders). They usually constitute 1 - 2% of the rock, however, they are much more abundant in places (Plate 5B). Occasional clasts of light-dark green, subangular, 1 - 10 cm, silicified porphyritic (plagioclase 0.5 - 1 mm) andesite clasts also occur (Plate 5D).

The lithic component of these breccias is made up, rhyolite clasts, scattered quartz crystals (0.01 - 1.5 mm, Plate 5E) and occasional sulfide clasts. Rhyolite clasts are light grey to white, fine grained, quartz-porphyritic and are commonly 0.5 - 5 cm in size, although boulders also occur. The rhyolite component commonly makes up around 2% of the breccia clasts although the abundance of rhyolite clasts increases rapidly toward the base of the Hanging Wall Andesite. Sulfide clasts to disseminated sulfides (Plate 5D), consisting of pyrite ($\pm$ chalcopyrite $\pm$ pyrrhotite) are often associated with rhyolite clasts, and constitute <1% of the rock and range in size from 0.1 mm to 2 cm individual clasts to 2 - 5 cm fragmented clasts. Jasper and mudstone clasts also occur in the breccias (Juras 1987), however, they were not seen in the logged sections for this project.

All these clasts are hosted in a fine grained matrix. The matrix is predominantly andesitic in composition, however the rhyolitic component of the matrix increases toward the base of the unit. Fine (1 - 2 mm wide) calcite $\pm$ quartz veinlets occur throughout (Plate 5H & I). Plagioclase crystals also occur throughout the matrix, ranging in size from 0.1 - 2 mm. Crystals show zoning and alteration consistent with that observed in the clasts, although some are broken. Thus they are considered to be liberated from the andesite.

Andesitic lavas are dark green in colour, plagioclase-phyric and vesicular (quartz-chlorite filled).

PLATE 5 - Hanging Wall Andesites

A -D Variations in basal Hanging Wall Andesite, Battle Zone. All AQ core Scale bar on D for all samples. A.BG18-486, 4.2m, B. BG18-486 19.9m, C. BG18-486 22.3m, D. BG18-1048 49.5m

E. Andesite clast (bottom left) and andesite-rhyolite mixed matrix with quartz crystals (top right). BG18-486 22.3m

F. Andesitic clast, strongly feldspar phyric with chlorite-epidote-carbonbate alteration. Note cross cutting carbonate vein. BG18-1048 49.5m

G. Close up showing alteration with feldspars weakly chlorite altered around margin, chlorite altered patch hosting epidote crystals and relic feldspars. BG18-1048 49.5m

H. A carbonate vein cross cutting andesite clast and mixed andesite-rhyolite matrix, plain polarisd light, box shows area of I. BG18-1048 49.5m

I. Close up of clacite vein under cathodluminescence. BG18-1048 49.5m

PLATE 5 - Hanging Wall Andesites

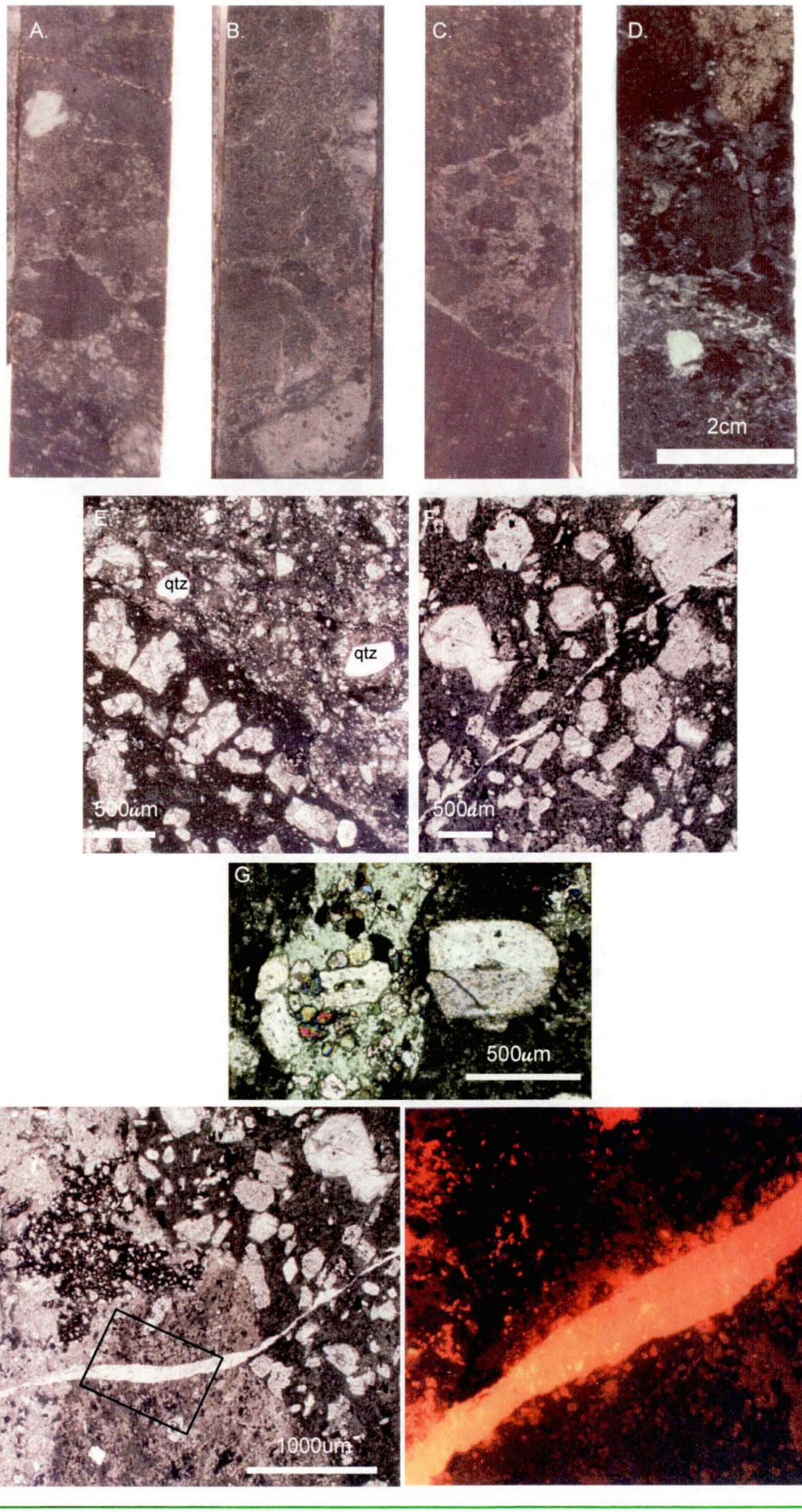

The plagioclase phenocrysts range from 0.1 - 1 mm euhedral (to zoned) phenocrysts, to 1 - 2 mm glomerocrysts and constitute 20 - 35% of the rock (Plate 5F). The lavas occur as individual flow units 2 - 5 m wide (Robinson, 1994) with brecciated irregular margins, which are monolithic, matrix poor and show jigsaw fit textures (Robinson, 1994).

Hanging Wall Andesite clastic facies range from well sorted, normally graded beds, to poorly sorted, crudely graded units. The basal beds contain clasts of altered rhyolite and massive sulphide. These are interpreted as clasts scoured from underlying units during transport and emplacement of the andesite. The well sorted, normally graded beds are probably deposited by mass-flow, while the poorly sorted, crudely graded deposits are more characteristic of resedimented autoclastic deposits.

3B.1.4 Mafic Dykes

All facies of the HW Rhyolite as well as the underlying Price Formation are intruded by mafic dykes-sills which are generally porphyritic, have chilled margins and intrude ore as well as host rocks. Dykes are generally 10-30cm wide, although widths of up to 10 m are known from drilling in the South Trough area (see chapter 6). All dykes in the Battle Zone are moderately to strongly altered to chlorite-carbonate assemblages. Mafic dykes were not observed in the limited Hanging Wall Andesite. The age and affinity of these dykes has not been tested, however their intrusive relations indicate they post-date deposition of HW Rhyolite and mineralisation. Dykes are folded and foliated by D2 event (see chapter 8) indicating a pre-Permian age.

3B.2 Interpretation of Battle Zone Facies

This section aims to provide interpretation of the Battle Zone facies, including their overall timing and depositional setting and proximity to source. Several key observations by Allen (1993) are introduced in this section to help with this interpretation.

Price Formation

The Price Formation consists of three facies; feldspar-phyric andesitic lava facies, pyroxene + feldspar porphyritic lava facies and a volcaniclastic facies. The volcaniclastics were interpreted by Juras (1987) as autobreccia to resedimented. Allen (1993) noted well preserved hyaloclastite at the top of the Price Formation, with the directly overlying felsic mass flow breccias incorporating (scouring up) andesite hyaloclastite clasts presumably from this underlying andesite. The pillowed nature of the lavas (Juras, 1987) is characteristic of sub-aqueous deposition.

The Price Formation is interpreted as a massive pile, >300 m thick, of basaltic-andesite lavas, associated autoclastic deposits. The andesites are extrusive and were implaced into a sub-aqueous setting. The andesites pre-date massive sulfide deposition and the deposition of the HW Rhyolite.

HW Rhyolite

The HW Rhyolite is composed of four volcano-sedimentary facies and two sulfide associations. Sulfide association A. (sphalerite-pyrite-chalcopyrite) is the lower most unit of the HW Rhyolite. While sulfide association B (sphalerite-pyrite-tennantite-galena-bornite-chalcopyrite) occurs around the Facies 1 - 4 contact.

The Volcaniclastic breccias and sandstones of Facies 1 are the predominant facies throughout the Battle Zone forming a 70m thick package. The normally graded beds likely have a mass flow origin. While the ungraded coarse volcanic breccias may be mass flow deposits or resedimented auto clastic breccias. They are interbedded with Facies 2 siltstone deposits which were likely deposited as low density turbidites. The siltstones are most predominant at the base of the HW Rhyolite overlying sulfide association A suggesting the represent an quiescent period between the eruption of andesitic lavas and the emplacement of large volumes of rhyolitic debris. Also interbedded within the HW Rhyolite are Facies 3 polymict, graded mass flow beds. The polymict, graded mass flow beds are post-eruptive, deposits from a separate source.

Facies 1 to 3 are overlain by quartz-feldspar porphyritic units which are thickest and most massive toward the north, thinning and becoming more clastic toward the south. This distribution indicates a source area toward the north. The composition of Facies 1 and 4 units is very similar (see chapter 5) suggesting they may be related. The presence of rhyolitic lavas suggest the source volcano for the Facies 1 and 4 units was resonaly proximal to the Battle Zone.

Broken volcanic quartz crystals and the presence of "excellent relic tube pumice" textures noted by Allen (1993) suggest the Facies 1 material was generated by pyroclastic eruptions. The material was then reworked and deposited in the basin by mass flow. The Facies 4 QFP may represent degassed magma from the same eruption phase as Facies 1. However the possibility of two magma chambers producing very similar magmas can not be ruled out at this stage.

Hanging Wall Andesite

The Hanging Wall Andesite consists of two facies: Facies 1: basaltic andesite to andesite lavas and related breccias. Facies 2 andesitic, bedded, feldspar crystal-rich volcaniclastics. The basal volcaniclastics contain clasts of altered rhyolite and even semi-massive sulphide. They are interpreted as reworked, syn-eruptive, mass-flow deposits. Neither these basal mass flows or andesitic lavas are altered by hydrothermal fluids indicating the hydrothermal system which formed Battle Zone mineralisation had shut down by the time the Hanging Wall Andesite was emplaced.

Timing of the deposition of Battle Gopher and South Trough lenses appears to be before the bulk of Facies 1 material was deposited, and probably represents a period of quissence between the cesation of the eruption of andesitic volcanics and the start of initially violent pyroclastic eruption of rhyolites. As the rhyolitic magama degassed the eruption of rhyolite became more effusive and lavas covered the reworked volcanic products. Burial of the hydrothermal system by rhyolitic volcanics caused a shift in the depositional environment of the sulfides. The deposition of sulfide mineralisation shifted from the top of the Price Foirmation to the Facies 1 / 4 contact and into the Facies 4 QFP where hydrothermal fluids could penetrate. Allen (1993) noted a rhyolitic sediment-matrix hyaloclastite

breccia at the base of the Hanging Wall Andesite indicating the andesite lavas intruded wet unconsolidated sediments. Thus The Facies 1 sedimets were wet an unconsolidated throughout deposition of the Upper Zone and Gap lenses. However, the hydrothermal system had ceased by the time the Hanging Wall Andesite was emplaced.

3B.3 Summary

The Battle Zone of the Myra Falls VHMS district is hosted by the HW Rhyolite of the Myra Formation with footwall alteration extending into the underlying Price Formation. The Hanging Wall Andesite overlies the HW Rhyolite. All three formations are part of the Sicker Group.

The Price Formation is a sub-aqueous, extrusive sequence of andesite lavas and related breccias. The Battle Zone is dominated by a sequence of syn-eruptive, resedimented rhyolite deposits characterised by evidence of rapid emplacement by mass-flow processes. The syn-eruptive units are interbedded with post-eruptive turbidites and fine grained low density turbidites. The post-eruptive units display textural and compositional evidence of reworking prior to final deposition, including rounded clasts and a polymict composition. Overlying these sedimentary units is a rhyolitic lava sequence, this rhyolitic lava is compositionally related to the syn-eruptive rhyolitic facies. The Hanging Wall Andesite is a sequence of andesitic lavas, hyaloclastic breccias and re-sedimented mass-flows.

Chapter 4

Alteration Mineralogy and Distribution

4.1.1 Introduction

The Myra Falls district has evolved through a complex geological history of mineralisation, diagenesis, metamorphism and deformation. The resultant alteration mineral assemblages are influenced by primary volcanic composition and texture as well as the intensity and composition of alteration fluids. Regional alteration assemblages seen throughout the Myra Falls district are controlled by the original composition and texture of the volcanics; i.e. composition: andesite or rhyolite, and texture : glassy, crystalline, clastic or massive. In proximity to massive sulfide mineralisation (such as the Battle Zone lenses) the rocks have been subject to hydrothermal alteration involving high temperatures (250-400°C) and high fluid/rock ratios, resulting in the alteration of the rocks to assemblages independent of the primary rock compositions, although the distribution of the alteration appears to be controlled by the porosity of the primary volcanics. In the Jurassic, the intrusion of the Island Intrusions (see chapter 2, not seen during logging in the Battle Zone) caused regional greenschist facies metamorphism.

The aims of this chapter are to describe the mineralogy and distribution of alteration types found in the Battle Zone. Background alteration styles seen in equivalent rocks outside the Battle Zone and away from other mineralised zones, are reviewed, with examples from the Thelwood Valley. Description of alteration types is divided into units (andesite and rhyolite) to highlight the importance of initial rock composition to some alteration styles. The origin of the alteration styles is discussed. Chapter 5, continues the alteration study by quantifying the geochemical changes that occur in the rocks with alteration.

4.1.2 Methods

Regional alteration mineralogy has been determined by examining samples collected from regional exploration drilling in the Thelwood Valley and by comparison with Juras (1987). Battle Zone alteration was determined by the author through detailed logging, thin section examination, and analysis of PIMA spectra, additional information on carbonate mineralogy was obtained through microprobe studies and cathodoluminecence (CL). Microprobe analysis of selected chlorites from the footwall alteration was also carried out to determine Mg number (Mg#: the atomic ratio 100*Mg/[Mg+Fe]). Core logging was done on site at Myra Falls during the three field work seasons. Thin

section work, PIMA analysis, microprobe and CL work were all carried out on samples collected during logging, using facilities at the University of Tasmania.

PIMA analysis was used to determine the composition of the fine grained phyllosilicate minerals. Phyllosilicate compositions are difficult to quantify by mesoscopic inspection, however their composition may provide important information on the composition of the fluids responsible for creating the alteration (Pontual et al., 1977; Huston, 1999; Denniss et al., 1999; Herrmann et al., 1999). Pima analysis were conducted at the University of Tasmania, under the guidance of Mr W. Herrmann. Analysis were done on dry, flat (sawn surfaces) of drill core samples using a PIMA-II spectrometer and PIMAView 3.1 software. The resultant spectra were then imported into The Spectral Geologist 1.0 software for interpretation. Determination of minerals and measurement of wavelengths was done by The Spectral Geologist software using The Spectral Assistant (TSA) on hull quotient spectra. Each spectra was also checked manually by the author, this was necessary, particularly for muscovite rich samples, as TSA has problems differentiating muscovite and illite due to limitation in the reference library (pers. com. Pontual, 1999). All spectra (except those for dolomite rich samples) are presented as reflectance spectra. The slope of reflectance spectrum (otherwise known as raw spectra) between 1300nm and 1600nm provides information which allows iron-bearing minerals to be distinguished from non-iron-bearing equivalents due to a Fe^{2+} absorption feature outside the PIMA spectral range. This is significant for chlorites and chlorite-muscovite mixtures in the Myra Falls area. Applying the hull quotient correction eliminates this feature, and has only been used to present dolomite-rich samples as dolomite features are clearer in hull quotient corrected spectra.

Particular attention has been paid to carbonate alteration (calcite and dolomite) during this study as these minerals have been largely ignored by previous investigations. Recent studies on carbonate alteration around VHMS deposits (Orth & Hill, 1994; Allen et al., 1998; Herrmann and Hill, 1999 in prep) have shown that carbonates can provide important indications as to the environment of deposition of VHMS ore bodies (see discussion), and provide vectors to ore bodies (Allen et al., 1998).

Sericite alteration is widespread in the Myra Falls Area. In this and other alteration styles the fine grained white mica has been identified as muscovite. Thus in subsequent discussion "sericite" is used as a descriptor for alteration style while where the mineralogy is discussed the mineral is listed as "muscovite".

4.2 Regional alteration styles, Myra Falls District

4.2.1 Price Formation

4.2.1a chlorite-epidote-albite-carbonate

Chlorite-epidote-carbonate alteration (Plate 6A - B) effects samples of the Price Formation collected from the Thelwood Valley and was noted by Juras (1987) as characterising the Price Formation throughout the Myra Falls district. In hand specimen samples are characterised by a medium to dark green colour with patchy light green epidote as disseminated grains and clusters. This mineral assemblage is non destructive with volcanic textures; feldspar phenocrysts, pillows, flow margins

PLATE 6 Price Formation - Thelwood Valley & Footwall Alteration

A. Price Formation - regional chlorite-epidote-carbonate-alteration. Sample shows pervasive chlorite alteration, heterogeneous epidote and calcite veins. PR127 - 112.7m

B. Photo micrograph showing feldspar phenocrysts - albitized and replaced by epidote, calcite and chlorite. PR127 - 112.7m

C. Price Formation - hydrothermal alteration associated with massive sulfide mineralisation (weak). Quartz-sericite alteration heterogeneous creating pseudo-clastic texture. PR123 - 206.3m

D. Photomicrograph of feldspar destruction by weak quartz-sericite alteration. PR123 - 206.3m

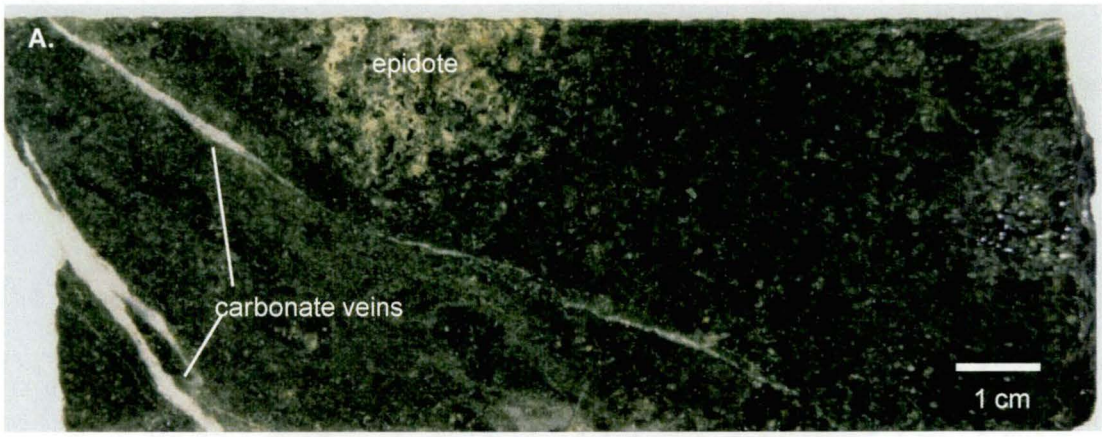
A.
epidote
carbonate veins
1 cm

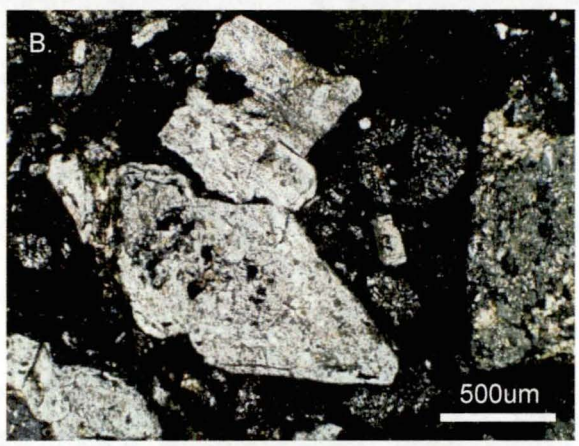
B.
500um


C.
pseudo-
clast
1 cm

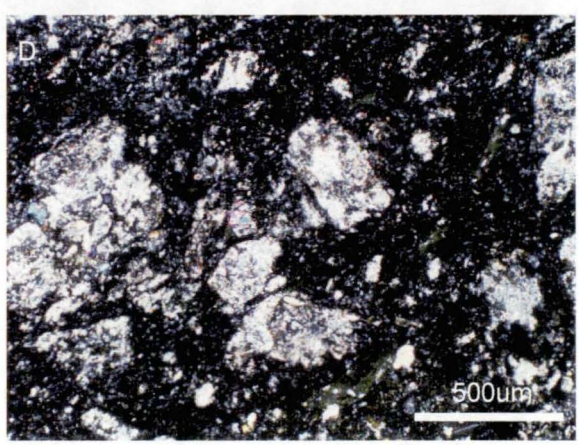
D.
500um

and clasts margins, preserved. Calcite veinlets occur throughout the formation.

In thin section feldspar phenocrysts are albitised and weakly to strongly replaced by epidote, calcite and chlorite (Plate 6B). Pyroxene phenocrysts are pseudomorphed by actinolite-chlorite-epidote and calcite. Disseminations and clots of leucoxene occur throughout the groundmass. While the quartz-feldspar groundmass is pervasively altered to chlorite-epidote-calcite-albite (Juras, 1987).

PIMA analysis indicate chlorites in the Thelwood Valley, Price Formation, samples to be composed of intermediate-chlorite (Fig. 20, Table 5). Microprobe analysis of chlorites form this regional alteration confirm intermediate chlorite Mg# = 0.55 (Appendix 2). Calcite(known from thin section work) was not picked up in the PIMA analysis. Epidote, observed in thin section work is not detected by PIMA analysis.

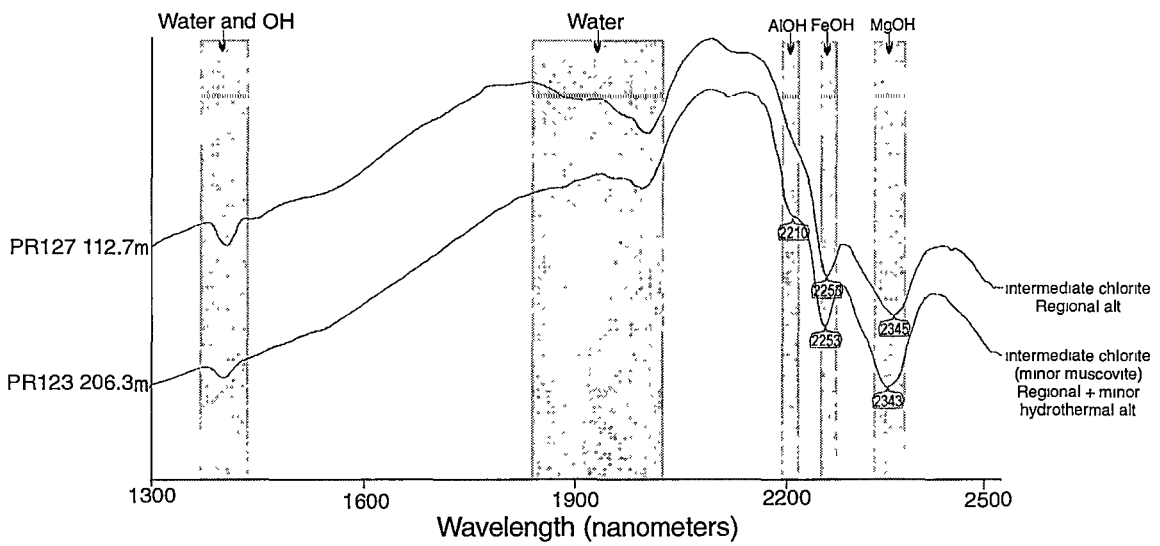

Figure 20 Pima spectra for Price Formation, Thelwood Valley samples, showing intermediate-chlorite and intermediate chlorite-muscovite spectra corresponding to regional chlorite-epidote-carbonate-alteration and hydrothermal alteration respectively. Note slope of the spectra at low wavelengths (<1800nm) indicating Fe-rich chlorites.

4.2.1b weak sericite-quartz alteration

Weak sericite-quartz alteration is also seen in some of the Thelwood Valley, Price Andesite samples. This alteration consists of heterogeneous, texturally destructive, quartz-sericite alteration . The quartz-sericite alteration causes destruction of the feldspar phenocrysts and forms a pseudo clastic texture in the rock, with chlorite-epidote altered pseudo clasts in pseudo matrix of quartz-sericite alteration (Plate 6C & D). Composition of the phyllosilicate phases were determined as intermediate chlorite and muscovite (Fig. 20, Table 5), although the muscovite is masked by the chlorite due to the low abundance of sericite.

The weak sericite-quartz alteration is interpreted to be related to the hydrothermal alteration system due to its texturally destructive nature. However its distribution throughout the property has not been mapped.

Table 5 Price Formation PIMA results, Thelwood Valley and Battle Zone samples

Hole No	Depth	Alteration	Mineral 1	Mineral 2	AlOH wavelength	FeOH wavelength	MgOH wavelength
Thelwood Valley samples - Least Altered							
PR127	112.7-112.8	ep-chl-carb	IntChlorite	-	-	2253	2345
PR123	206.3-206.45	ep-chl-carb + wk ser-qtz	IntChlorite	Muscovite	2210	2253	2343
Battle Zone Samples							
Sericite-pyrite-quartz altered							
BG18-481	65.4-65.7	ser-py-qtz	Muscovite	-	2200	2246	2345
BG18-481	67.1-67.3	ser-py-qtz	Muscovite	-	2200	2244	2352*
BG18-796	188.8-189.0	ser-py-qtz	Muscovite	-	2201	-	2350
BG18-797	63.1-63.25	ser-py-qtz	Muscovite	-	2201	2244	2346
BG18-1003	112.0-112.1	ser-py-qtz	Muscovite	-	2202	-	2349
BG18-1006	120.4-120.6	ser-py-qtz	Muscovite	-	2199	2246	2342
Mg-chlorite-pyrite altered							
BG18-1003	105.1-105.3	chl-py	MgChlorite	-	-	2249	2341
BG18-1006	124.8-125.0	chl-py	MgChlorite	-	2215	2246	2344
Sericite-chlorite-pyrite altered							
BG18-978	141.6-141.8	ser-chl	Muscovite	IntChlorite	2200	2249	2341
BG18-981	122.3-122.5	ser-chl	IntChlorite	Muscovite	2200	2249	2342

*picked visually, not picked up by Spectral geologist

4.2.2 HW Rhyolite

sericite-quartz-albite ± chlorite alteration

HW Rhyolite samples from the Thelwood Valley and a Battle Zone sample (BG18-1080 47.5m) have sericite-quartz-albite ± chlorite mineral assemblages. This alteration type obscures volcanic textures but has not completely destroyed them. Some samples show relic volcanic textures; quartz and feldspar phenocrysts/crystals, flow banding and clast boundaries (Plate 4). In thin section, feldspar phenocrysts are moderately to strongly altered to sericite. The groundmass consists of quartz-muscovite-albite-pyrite-calcite ± chlorite ± epidote assemblages. PIMA analysis on these samples show both normal muscovite (AlOH wavelength = 2196-2199nm) and muscovite that tends toward phengitic compositions (AlOH wavelength = 2212-2215, Table 6) and intermediate-chlorite (Fig. 21).

The Battle Zone samples with this alteration lie away from massive sulfide mineralisation. This alteration assemblage is attributed to devitrification, hydration and diagenesis of rhyolitic volcanic and volcaniclastics and subsequent metamorphism and is considered the "background" alteration to the hydrothermal alteration styles.

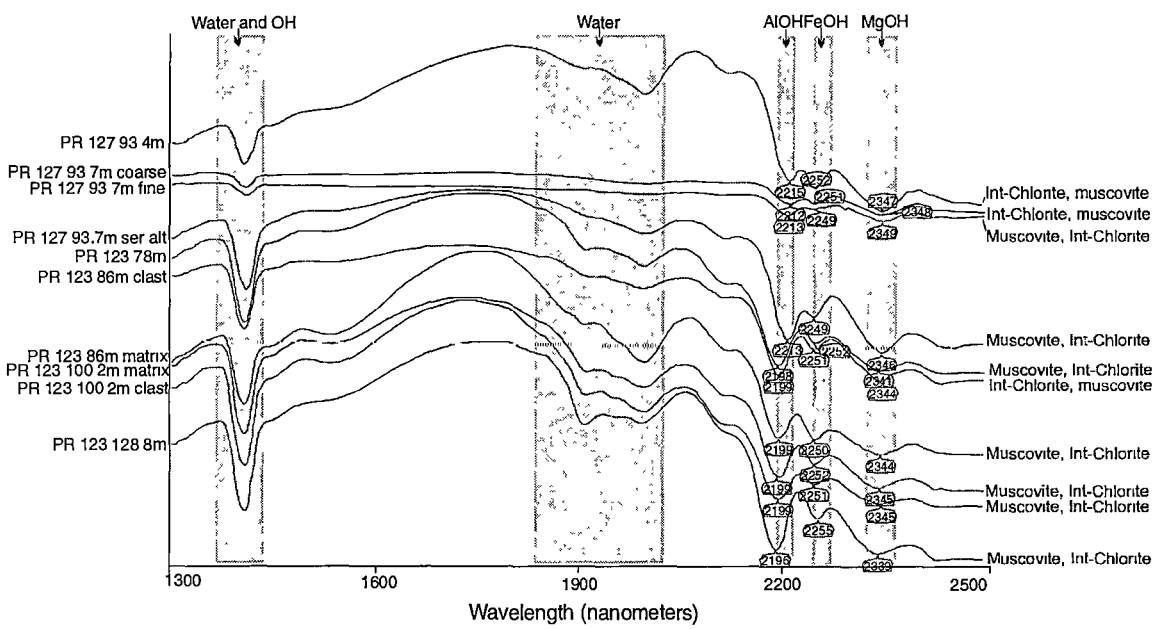

Figure 21 Stacked reflectance spectra for HW Rhyolite, Thelwood Valley Samples, showing intermediate chlorite and muscovite

4.2.3 Hanging Wall Andesite

chlorite-epidote-albite-carbonate ± sericite-quartz-alteration

Hanging Wall Andesite lavas are pervasively chlorite-quartz-epidote altered (Juras, 1987) resulting in plagioclase being replaced by albite-epidote-calcite, chlorite pseudomorphs after pyroxene and leucoxene and hematite after opaque oxides (Juras, 1987). The basal reworked volcaniclastics are made up of andesitic clasts showing a variation in alteration types (Chapter 3). Most clasts show moderate chlorite-epidote-calcite alteration however some clasts are completely altered to epidote and quartz (Plate 5A-D). The matrix contains feldspar crystals which are commonly broken but are no more altered than those in adjacent andesite clasts. The matrix may also contain volcanic quartz crystals, clasts of Facies 4 QFP and rare massive sulfide clasts. The matrix is altered to chlorite-

Table 6 HW Rhyolite PIMA results, Thelwood Valley samples.

Hole No	Depth	Unit / Alteration	Mineral 1	Mineral 2	AlOH wavelength	FeOH wavelength	MgOH wavelength
PR127	93.35-93.45	Rhy Sed	IntChlorite	Muscovite	2215	2252	2347
PR127	93.6-93.9	coares sed	IntChlorite	Muscovite	2212	2251	2348
PR127	93.6-93.9	fine sed	Muscovite	IntChlorite	2213	2249	2349
PR127	93.6-93.9	ser alt	Muscovite	IntChlorite	2213	2249	2346
PR123	78.0-78.2	4 - QFP	Muscovite	IntChlorite	2198	2252	2341
PR123	86.0-86.3	Rhy Vc clast	IntChlorite	Muscovite	2199	2251	2344
PR123	86.0-86.3	Rhy Vc matrix	Muscovite	IntChlorite	2199	2250	2344
PR123	100.1-100.25	Flow banded Rhy	Muscovite	IntChlorite	2199	2252	2345
PR123	100.1-100.25	Flow banded Rhy-clast	Muscovite	IntChlorite	2199	2251	2345
PR123	128.75-128.85	4 - QFP	Muscovite	IntChlorite	2196	2255	2339

Table 7 PIMA results for Hanging Wall Andesite samples

Hole No	Depth	Mineral 1	Mineral 2	AlOH wavelength	FeOH wavelength	MgOH wavelength
BG18-1048	49.4-49.7	IntChlorite	-	2207.388	2251.983	2342.12
BG18-1048	93.9-94.1	IntChlorite	-	-	2253.58	2340.991
BG18-486	20.9-21.1	IntChlorite	FeChlorite	-	2254.476	2343.689
BG18-486	22.3-22.5	IntChlorite	Muscovite	2203.991	2253.405	2345.62
BG18-486	22.3-22.5	IntChlorite	FeChlorite	-	2254.105	2345.54
BG18-486	4.2-4.4	IntChlorite	FeChlorite	2204.018	2253.96	2347.738
PR123	44.5-44.7	Illite	IntChlorite	2198.35	2252.33	2341.216
PR127	24.2-24.4	IntChlorite	-	-	2253.554	2344.137

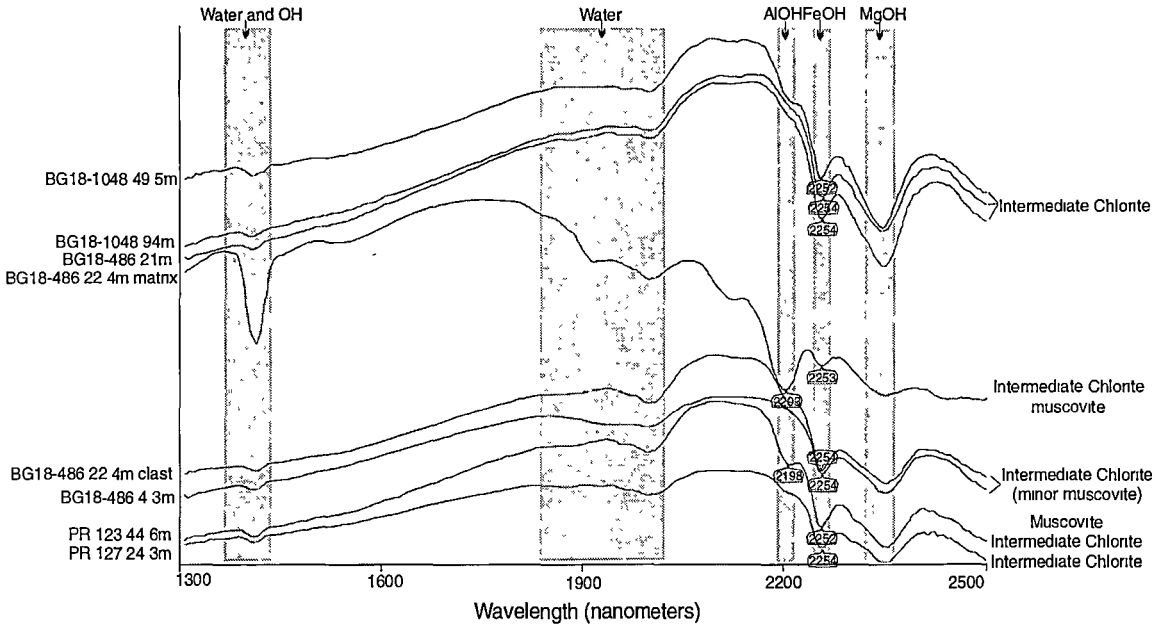

Figure 22 PIMA spectra, reflectance, for Hanging Wall Andesite samples, showing intermediate chlorite (note slope toward lower wavelengths indicating Fe^{2+} absorbtion feature), and minor muscovite.

epidote muscovite and quartz. The abundance of muscovite and quartz in the alteration is directly related to the occurrence of quartz crystals, clasts of Facies 4 QFP clasts and massive sulfide clasts. The sericite-quartz alteration affects only the matrix (andesite clasts are not visibly affected) and it is non-texturally destructive. It occurs only in the basal portion of the Hanging Wall Andesite and is associated with resedimented, predominantly andesitic volcaniclastic deposits. PIMA spectra for Hanging Wall Andesites are shown in Figure 22 and Table 7. Composition of phyllosilicate minerals in Hanging Wall Andesite varies from Intermediate to Fe-rich chlorites and muscovite.

The weak sericite-quartz-alteration, in the Hanging Wall Andesites, is interpreted as a result of diagenesis and metamorphism. The alteration mineralogy interpreted as being the direct result of primary rock composition (i.e. mixture of rhyolite and andesite). The alteration of andesitic clasts is consistent with the chlorite-epidote-carbonate alteration noted in the overlying lavas by Juras (1987). Variation of clasts within the andesitic breccias suggests it occurred on the seafloor prior to incorporation and redeposition of the andesitic clasts within the andesitic breccias.

4.3 Hydrothermal alteration - Battle Zone

4.3.1 Introduction

Hydrothermal alteration is characterised by its texturally destructive nature and composition unrelated to primary rock compositions (Allen et al., 1998). This type of alteration dominates the Battle Zone and consists of muscovite-quartz-pyrite and rutile, with minor chlorite in the footwall, and dolomite in the hangingwall. The hydrothermal alteration affects the Price Andesite and the HW Rhyolite, but does not extend into the Hanging Wall Andesite. Thus the Hanging Wall Andesite will not be discussed in this section.

4.3.2 Footwall alteration - Price Formation

4.3.2a intense sericite-pyrite + quartz alteration

Intense sericite-pyrite alteration is represented by schists which range in colour from light to dark grey, or brown-grey (occasionally orange-brown; Plate 7A - C). The colour being dependent on the amount of pyrite and quartz associated with the muscovite. Intense sericite-pyrite alteration is pervasive and texturally destructive forming a mosaic of fine grained muscovite commonly intergrown with fine grained quartz. Calcite occurs in this zone as irregular dissemination in quartz-muscovite matrix or more commonly as veins with quartz and pyrite. No primary textures are recognisable in this alteration type. Metamorphism and deformation have caused some coarsening of the muscovite and quartz especially along fractures and as pressure shadows around pyrite crystals. This alteration can be polyphase, often forming domains of quartz-rich alteration versus quartz-poor alteration on mm to cm scale giving the rocks a pseudo-clastic texture (Plate 7B). Quartz occasionally dominates over muscovite forming a quartz-pyrite rock (Plate 7E & F). This quartz-pyrite alteration was commonly noted in the stringer zone directly underlying the massive pyrite-chalcopyrite ore, however it was not restricted to this area. Disseminated grains and laths of rutile also occur throughout this alteration type. PIMA analysis on these rocks show they contain muscovite as the only phyllosilicate mineral (Fig. 23, and Table 5).

This style of alteration is found directly underlying the Battle Zone massive sulfide lenses (Fig. 24 & 25). It commonly has a gradational contact with semi-massive to massive pyritic sulfides above and the sericite-chlorite-pyrite alteration below. The intense sericite-pyrite alteration appears to form a massive blanket of strata-bound muscovite-quartz-pyrite. This "blanket" is approximately 20m thick, but its lateral extent is unknown.

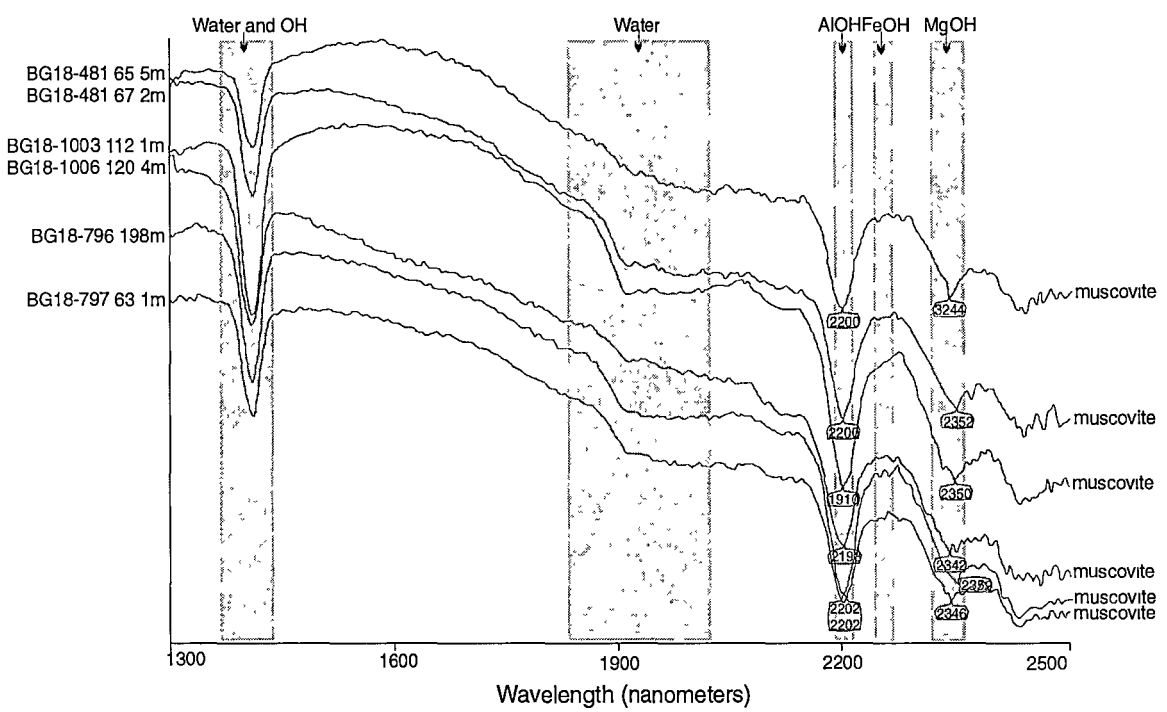

Figure 23 PIMA spectra for Battle Zone footwall intense sericite-pyrite ± quartz alteration.

PLATE 7 - Footwall Alteration - Battle Zone

A. Intense sericite alteration with semi-massive pyrite. BG18-905 38.8m

B. Heterogeneous sericite-quartz alteration. BG18-796 189m

C. Strong sericite alteration plus pyrite, with siliceous overprint. BG18-1006 120.6m

D. Heterogeneous sericite-quartz alteration with overprinting quartz-pyrite veining. BG18-797 63.25m

E. Dominantly siliceous alteration post sericite alteration, no textural preservation. BG18-481 45.7m

F. Quartz-sericite heterogeneous alteration. BG18-1003 112m

G. Mg-chlorite - pyrite alteration. BG18-1003 105.2m

H. Mg-chlorite - pyrite alteration. BG18-1006 124.9m

I. Sericite-chlorite-pyrite altered Price Andesite. BG18-981 122.3m

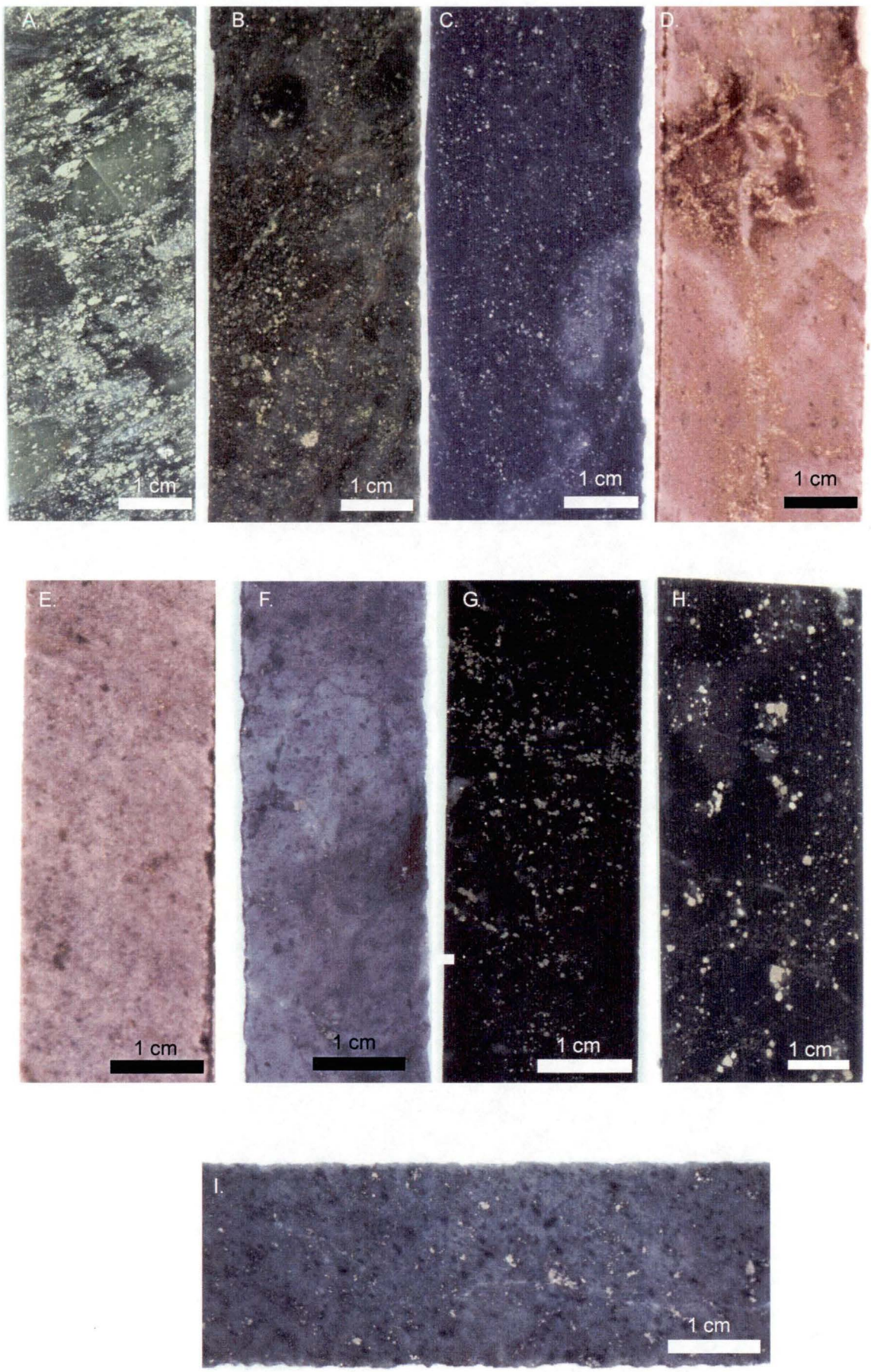
A.
1 cm
B.
1 cm
C.
1 cm
D.
1 cm
E.
1 cm
F.
1 cm
G.
1 cm
H.
1 cm
I.
1 cm

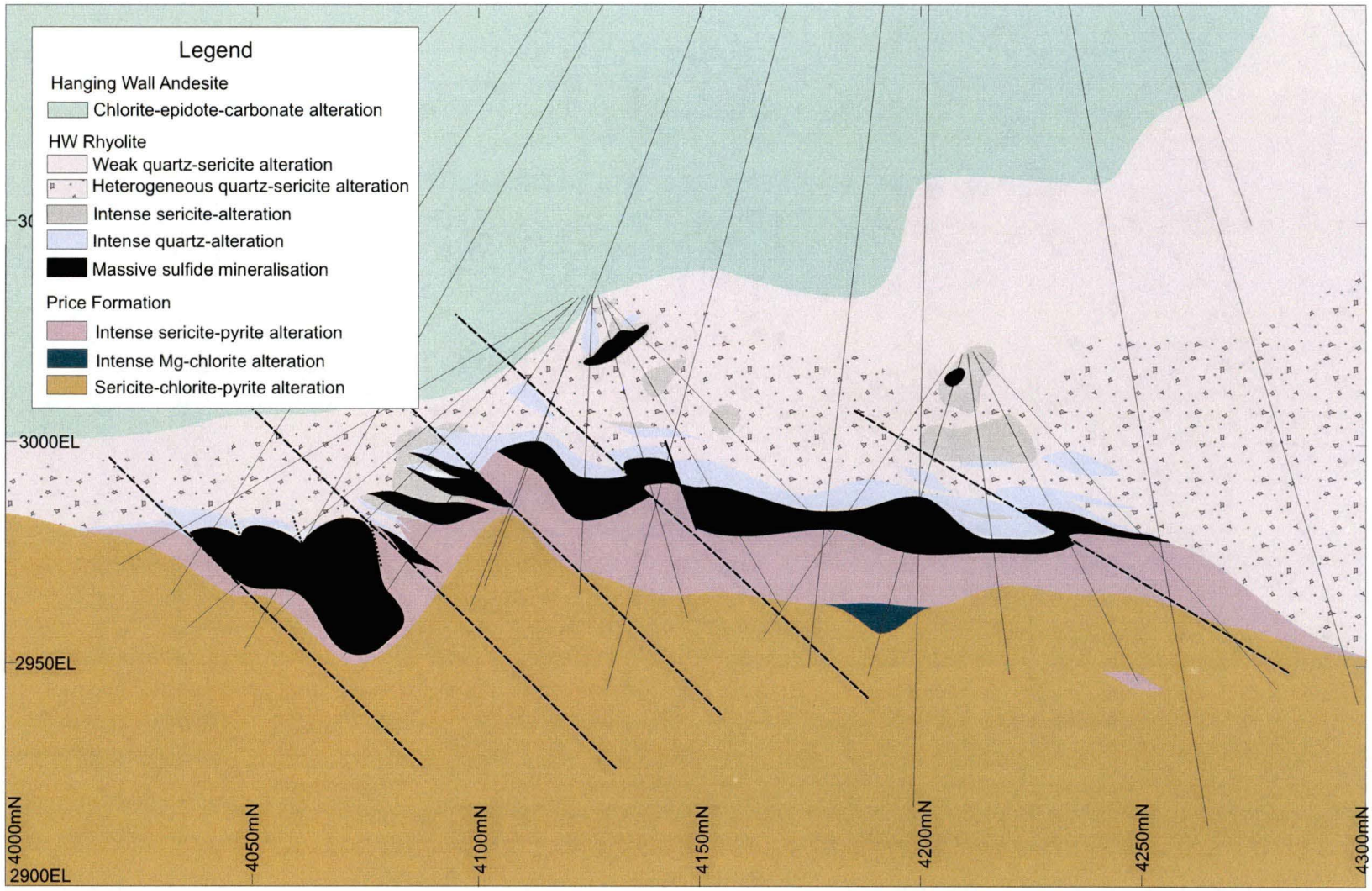

Figure 24. 1600mE section through the Battle Zone showing the distribution of alteration types within the Battle Zone

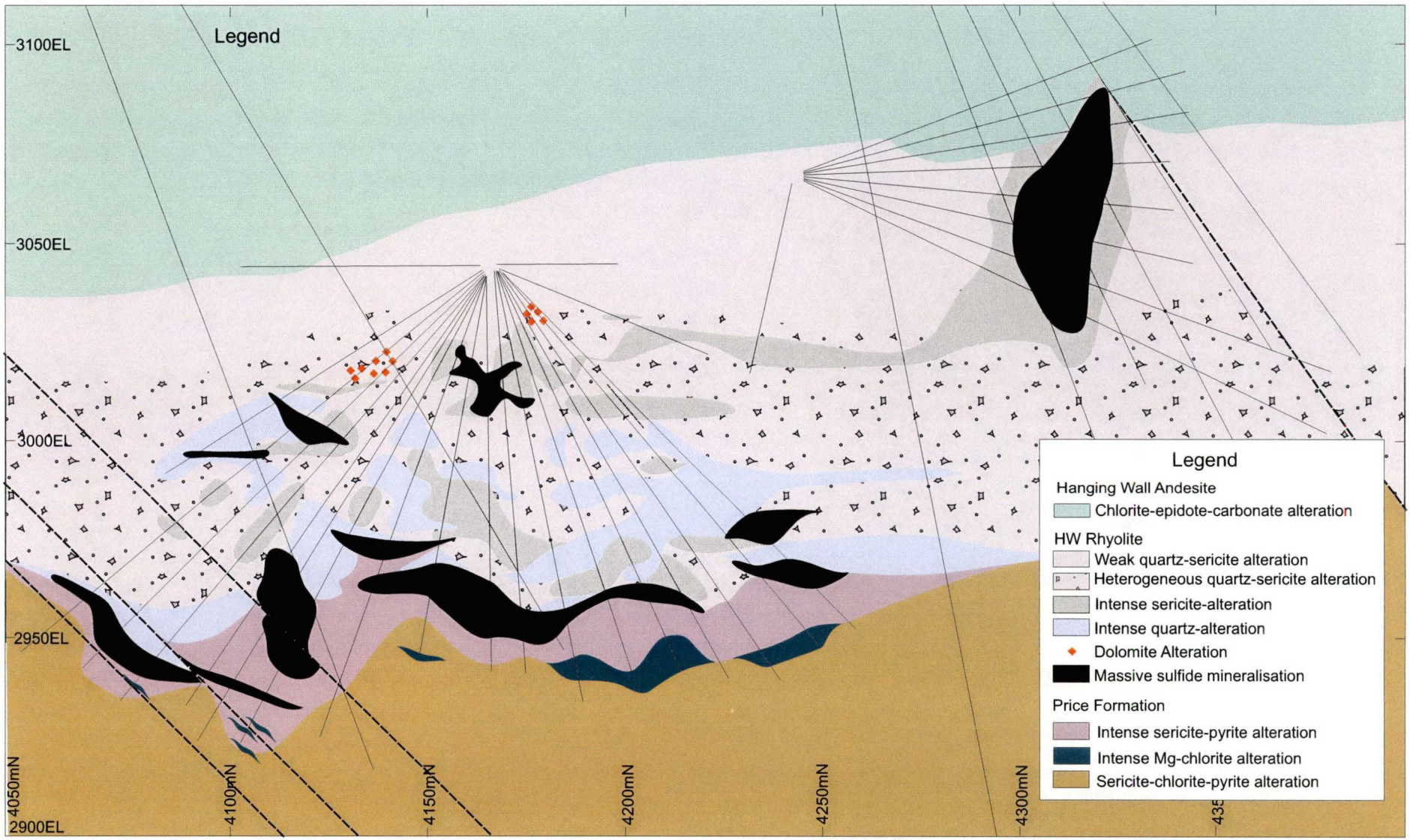

Figure 25. 1420mE section through the Battle Zone showing the distribution of alteration types within the Battle Zone

4.3.2b intense Mg-chlorite alteration

Intense chlorite alteration produces the precursor composition to chloritic schists which are dark green in colour and are composed of fine grained chlorite with variable amounts of muscovite (10-20%) and pyrite (Plate 7G & H). Quartz and calcite commonly occur as cross cutting veins. Intense chlorite alteration was noted throughout the footwall mainly as small domains within the sericite-pyrite alteration. Occasionally these zones can be followed between drill holes. On section 1420mE (Fig. 25) they form a sub-horizontal band 4-10 m wide about 10 m below the base of the ore zone. However they are much less common and thinner (10-20cm) in the other sections logged (Fig. 24). No lithological control was established for the chlorite-pyrite alteration during this study.

These chlorite altered samples produce poor PIMA spectra, as the rocks are quite dark. However results show the chlorite to be strongly Mg-rich (Fig. 26 and Table 5). Mg-rich nature of chlorite was confirmed by microprobe ananlyis of chlorite from this alteration type (Mg# = 0.82, Appendix). Mg-rich chlorite is significantly different from the intermediate-chlorite found in the regional alteration of the Myra Falls district.

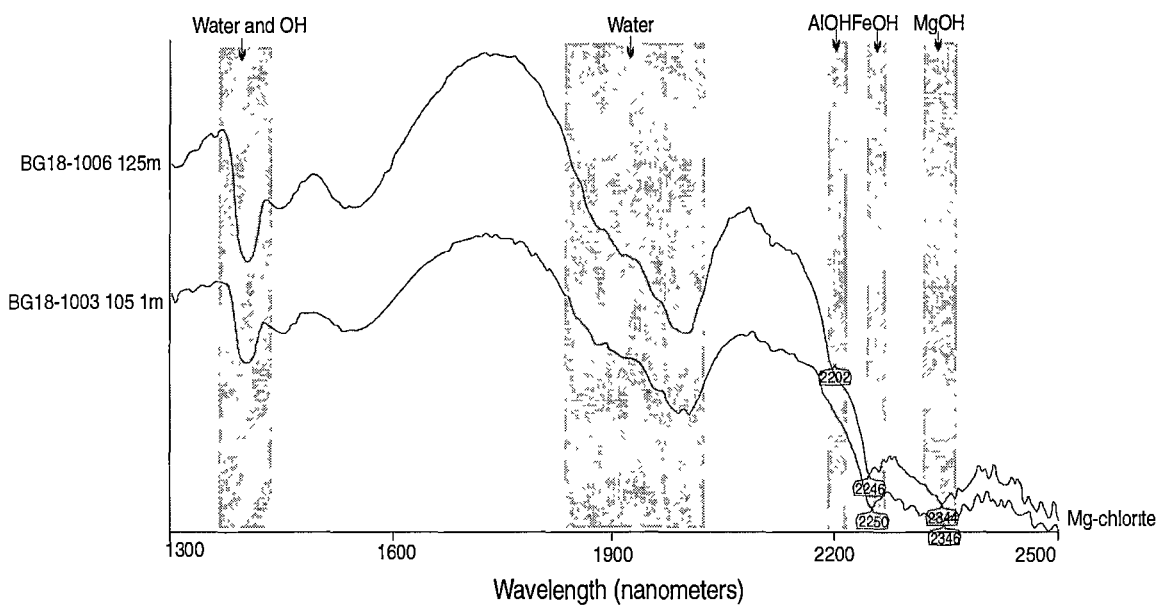

Figure 26. PIMA spectra for Battle Footwall intense chlorite-pyrite alteration. Note spectra Mg-rich chlorite lacks Fe^{2+} slope shown by Thelwood Valley samples (Fig. 20)

4.3.2.c sericite-chlorite-pyrite alteration

Sericite-chlorite-pyrite alteration is characterised by a relict textures such as flow margins and amygdales which are visible in hand specimen. Thin section work, shows the rocks to be composed of muscovite, chlorite, quartz and calcite. Fine grained disseminated pyrite and occasional disseminations or veinlets of chalcopyrite and sphalerite also occur in this alteration. This alteration type affects Price Formation andesites and underlies the intense sericite-pyrite $\pm$ quartz alteration, the boundary between these alteration types is gradational although commonly faulted and occurs approximately 20 metres below the ore zone (Fig. 24 & 25; except where disrupted by faulting).The extent of this alteration below the deposit is unknown.

PIMA analysis shows the phyllosilicate assemblage to be composed of muscovite and intermediate chlorite (Fig. 27, Table 5). However, microprobe analysis of the chlorites reveal very high Mg number (Mg# = 0.93; Appendix 2) indicating a problem with the PIMA identification of chlorite compositions in this alteration type. Herrmann et al. (in press) also noted that PIMA anaysis was unreliable in identifying chlorite compositions in white mica-rich rocks.

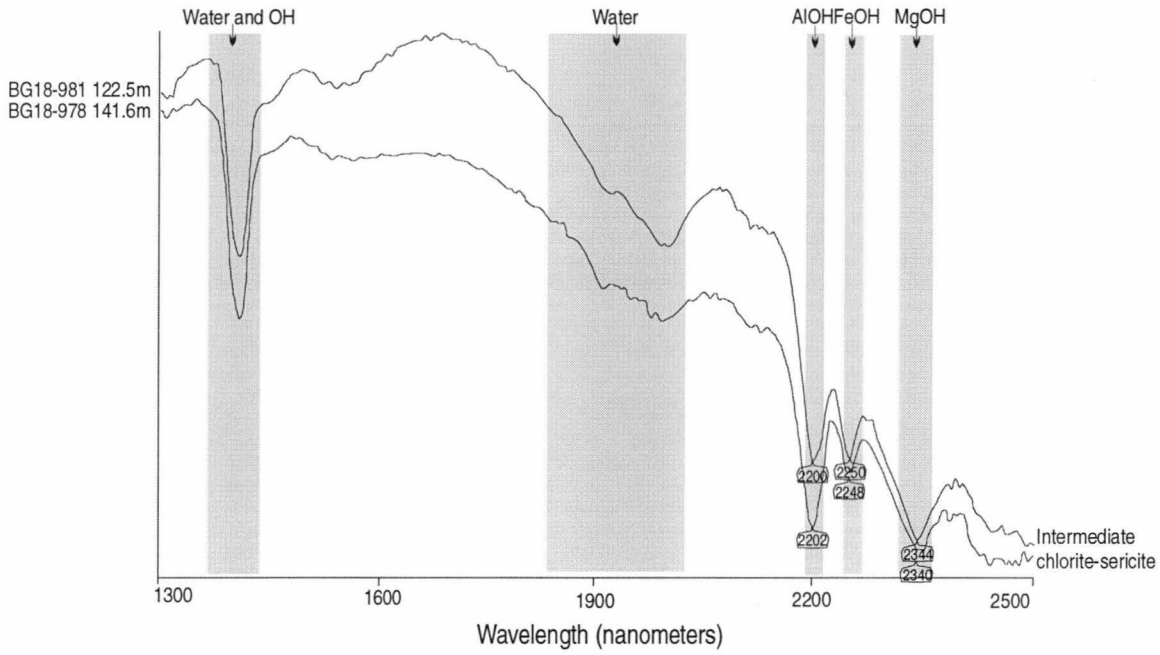

Figure 27 PIMA spectra for Battle Zone footwall sericite-chlorite-pyrite alteration zone.

4.3.2.d footwall alteration summary

Intense sericite-quartz alteration and intense Mg-chlorite alteration found in the Price Formation, Battle Zone samples are both pervasive and texturally destructive styles of alteration and both are found closely associated with massive sulfide mineralisation. Their composition show little relation to primary mineralogy. These characteristics suggest the alteration styles are due to hydrothermal alteration and subsequent metamorphism. In contrast the sericite-chlorite-pyrite alteration is less intense, some volcanic textures are still visible (pillow margins). However the composition of chlorite is simmilar to that found in the intense Mg-Chlorite alteration that chlorites in the regional alteration.

Footwall alteration observed in the Battle Zone appears, from current drilling (Fig. 24 & 25), to be semi-conformable or stratabound in distribution. No evidence for pipe shaped alteration zones (similar to that seen at Hellyer, Gemmell and Large, 1992) were observed during this study.

4.3.3 Hangingwall alteration - HW Rhyolite

4.3.3a sericite-quartz-pyrite

The relationships between sericite, quartz and pyrite in the HW Rhyolite are complex and overprinting, their effects can be described separately, however their distributions are overlapping with diffuse to gradational boundaries (Fig. 24 & 25). Rutile (composition confirmed by microprobe analysis) occurs as an accessory mineral through out the hangingwall rocks as fine grained (<10μm) clusters or disseminations and occasionally defining relic diamond shapes.

sericite alteration

Sericite forms a pervasive, texturally destructive alteration throughout the Battle Zone. It imparts a grey-brown colour to most rocks where associated with pyrite or a light green colour where no pyrite is present. Within the sericite alteration feldspar phenocrysts and most of the primary volcanic features are destroyed. Primary volcanic features such as clast margins and types can be distinguished by close inspection, in rocks with moderate sericite alteration. In rocks with strong to intense sericite alteration primary volcanic features (with the exception of quartz crystals) cannot be distinguished unless preserved by quartz alteration prior to sericite alteration (Plate 8A - D). PIMA analysis shows the composition of the sericite to be normal muscovite (AlOH wavelength = 2198-2202nm; Fig. 28 & 29, Table 8). The presence of muscovite tending toward phengitic compositions (AlOH wavelength = 2212-2215) in the regional alteration indicates a change in composition between the regional alteration and the hydrothermal alteration.

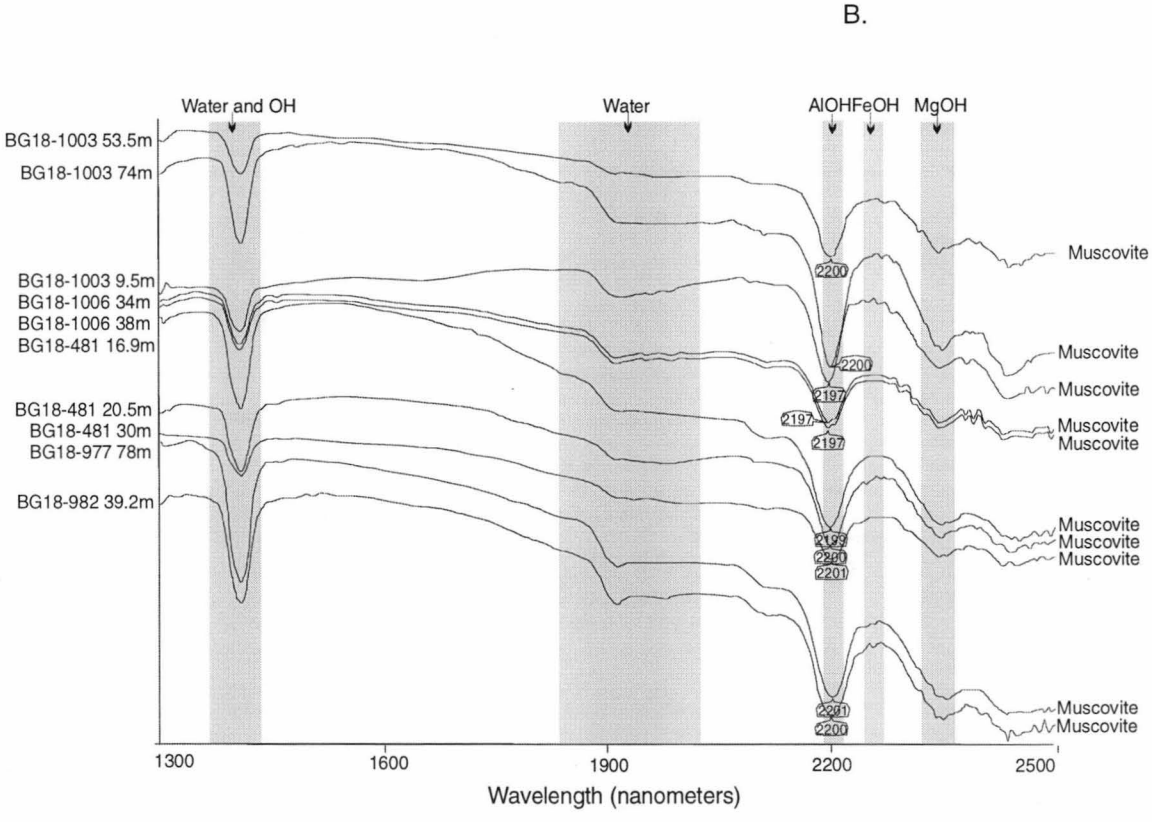

Figure 28. PIMA spectra for Facies1volcaniclastics - sericite alteration

Table 8 HW Rhyolite PIMA results, Battle Zone samples. Cherts and dolomite alteration excepted.

Hole No	Depth	Unit / Alteration	Hydrothermal Alteration	Mineral 1	Mineral 2	AlOH wavelength	FeOH wavelength	MgOH wavelength
BG18-1054	36.9-37.2	4 - QFP	quartz - sericite	Muscovite	-	2198	-	2343
BG18-1080	47.5-47.7	4 - QFP	quartz > sericite	Muscovite	-	2200	-	2348
BG18-481	1.4-1.55	4 - QFP	sericite	Muscovite	-	2200	-	2341
BG18-481	1.55-1.65	4 - QFP	quartz - sericite	Muscovite	-	2200	-	2345
BG18-982	0.6-0.8	4 - QFP	quartz > sericite	Muscovite	-	2198	-	2342
BG18-1003	53.4-53.6	1 - Volcaniclastic	sericite > quartz	Muscovite	-	2200	-	2344
BG18-1003	73.9-74.0	1 - Volcaniclastic	quartz - sericite	Muscovite	-	2200	-	2347
BG18-1003	9.3-9.5	1 - Volcaniclastic	quartz > sericite	Muscovite	-	2197	-	2343
BG18-1006	33.9-34.1	1 - Volcaniclastic	quartz > sericite	Muscovite	-	2197	-	2344
BG18-1006	38.0-38.2	1 - Volcaniclastic	sericite > quartz	Muscovite	-	2197	-	2344
BG18-977	78.0-78.2	1 - Volcaniclastic	quartz - sericite	Muscovite	-	2201	-	2343
BG18-481	16.7-16.9	1 - Volcaniclastic	sericite > quartz	Muscovite	-	2199	-	2345
BG18-481	20.45-20.6	1 - Volcaniclastic	sericite > quartz	Muscovite	-	2200	-	2346
BG18-481	29.8-30.1	1 - Volcaniclastic	sericite > quartz	Muscovite	-	2201	-	2344
BG18-982	39.2-39.3	1 - Volcaniclastic	sericite-dolomite	Muscovite		2200	-	2346
BG18-1006	49.6-49.8	3 - Mixed	sericite	Muscovite		2201	-	2345
BG18-1006	49.6-49.8	3 - Mixed	sericite	Muscovite		2201	-	2344
BG18-799	29.65-29.85	3 - Mixed	sericite	Muscovite		2199	-	2348
BG18-798	51.9-52.15	3 - Mixed	quartz - sericite	Muscovite	-	2200	-	2341
BG18-798	51.9-52.15	3 - Mixed	quartz - sericite	Muscovite	-	2201	-	2347

PLATE 8 - HW Rhyolite Alteration

A. Heterogeneously altered Facies 1 coarse clastic showing silicified quartz-feldspar phyric clasts, quartz crystals and pseudo-clasts. BG18-886 4.5 m

B. Silicified and weakly sericite altered Facies 1, relic feldspar crystal shapes visible suggesting silicification occured prior to sericite alteration. BG18-776 58.8 m

C. Strongly sericite altered and mineralised Facies 1 or 4. BG18-778 54.1 m

D. Strongly sericite altered Facies 4 or 1. G158 D2 Sample No. 8

E. & F. Strongly sericite altered and quartz-tennantite-calcite veined QFP, quartz phenocrysts still visible (margin of Gap ore body). BG18-891 22m

G Heterogeneously altered QFP showing pseudo-clastic texture, note quartz-phenocrysts evenly distributed through both pseudo matrix and pseudo-clasts. G158 B2 (3)

H. Volcanic quartz crystals in intensely altered (muscovite) matrix. BG18-886 4.5m

I. Volcanic quartz crystal overgrown by quartz in silicifed quartz > sericite matrix. BG18-982 0.6m

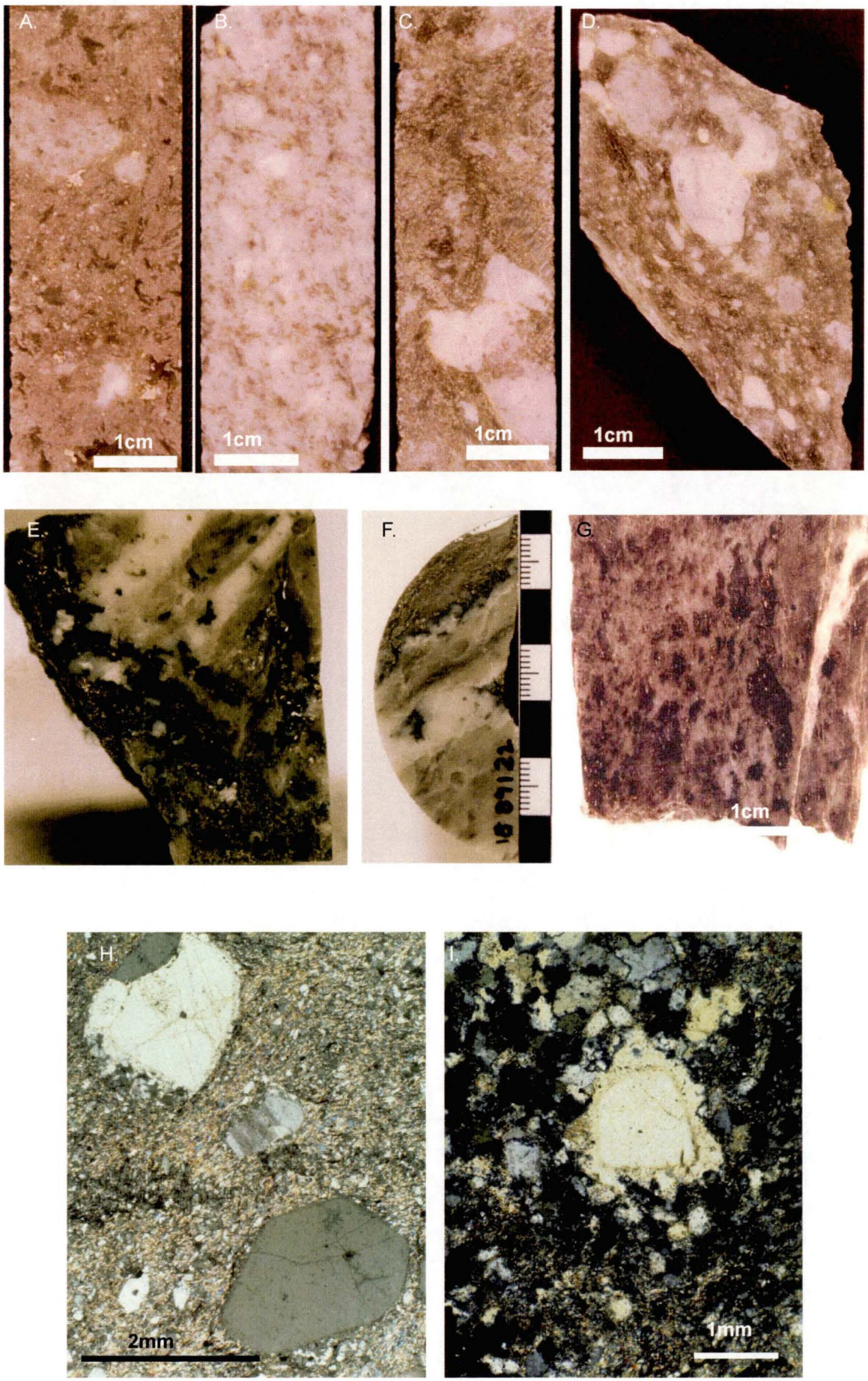
A.
1cm
B.
1cm
C.
1cm
D.
1cm
E.
F.
G.
1cm
H.
2mm
I.
1mm

quartz alteration

Quartz alteration imparts a light grey to white colour to the rocks (Plate 8B). In weak to moderately silicified rocks quartz alteration is heterogeneous, however, as it increases in intensity it becomes more homogeneous. In thin section, it occurs as a mosaic of microcrystalline quartz. Strong quartz alteration is indicated by overgrowths of quartz on volcanic quartz crystals (Plate 8I). Quartz alteration usually post dates the sericite alteration, however where quartz alteration predates sericite alteration or sericite alteration is absent the quartz alteration preserves volcanic features.

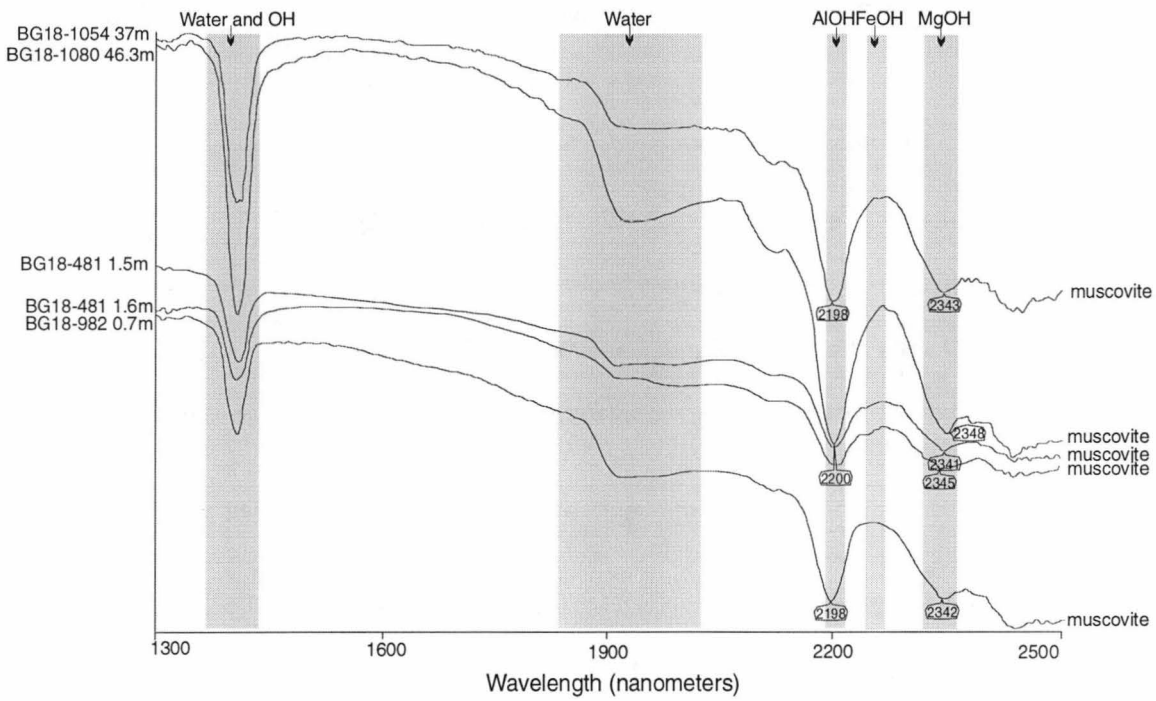

Figure 29 PIMA spectra for Facies 4: quartz-porphyritic rhyolites - sericite alteration

pyrite + other sulfides

Pyrite is ubiquitous through out the Battle Zone alteration. It occurs as fine grained 10 -100μm euhedral to anhedral grains, disseminated through altered rocks. As alteration intensifies and other minerals are introduced the pyrite grains coarsen to >100μm, often becoming more euhedral. Sphalerite, chalcopyrite, galena and tennantite occur as fine anhedral disseminations throughout the rocks and can become major components of the alteration around ore lenses. Barite is also a major component of the alteration zones around the ore lenses, particularly for Upper Zone and Gap mineralisation and at the top of the Battle lens (see chapter 6).

4.3.3b blebby-dolomite alteration

Dolomite as spheroids or "blebs" form a minor but distinctive alteration within the Battle Zone (Fig. 25). Spheroids range from <1mm to 3cm and occur as isolated spheroids to coalesced masses (Plate 9A - E) and overgrow rhyolite facies. Spheroids show little internal texture, occasionally quartz accumulations can be seen within the dolomite spheroids but they are not considered to be cores. Some spheroids show relic rhombohedral shapes usually overgrown by the spheroid (Plate 9G). In

PLATE 9 - Dolomite Alteration

A. Dolomite alteration (blebs) in banded sediments. BG18-1006 17.7m,

B. Dolomite alteration in banded sediments. BG18-1006 18.95 m

C. Dolomite alteration in banded sediments. BG18-1006 22.3 m

D. Dolomite rhombs overgrown by further dolomite in heterogeneously altered Facies 1 rhyolite. BG18-775 75.2 m

E. Dolomite blebs and pseudo-fiamme in altered Facies 1 sediment. G158 B2 sample 3

F. Anhedral masses of dolomite (red) with minor calcite (yellow) alteration occasionally picking out fractures and rare zonation, Cathodoluminescent photo, field of view ~0.75cm. BG18-1006 17.7 m

G. Dolomite blebs showing no internal texture, possible relic rhomb shapes, catholuminescent photo, field of view ~1cm. G158 B2 sample 3

H. Plain light photo showing zoned dolomite rhombs, zoning defined by variations in dolomite-sericite content . BG 18-343 58m

I. Cathodeluminescence photo showing zoned dolomite crystals overgrown by yellow calcite. Same view as for G. BG 18-343 58m

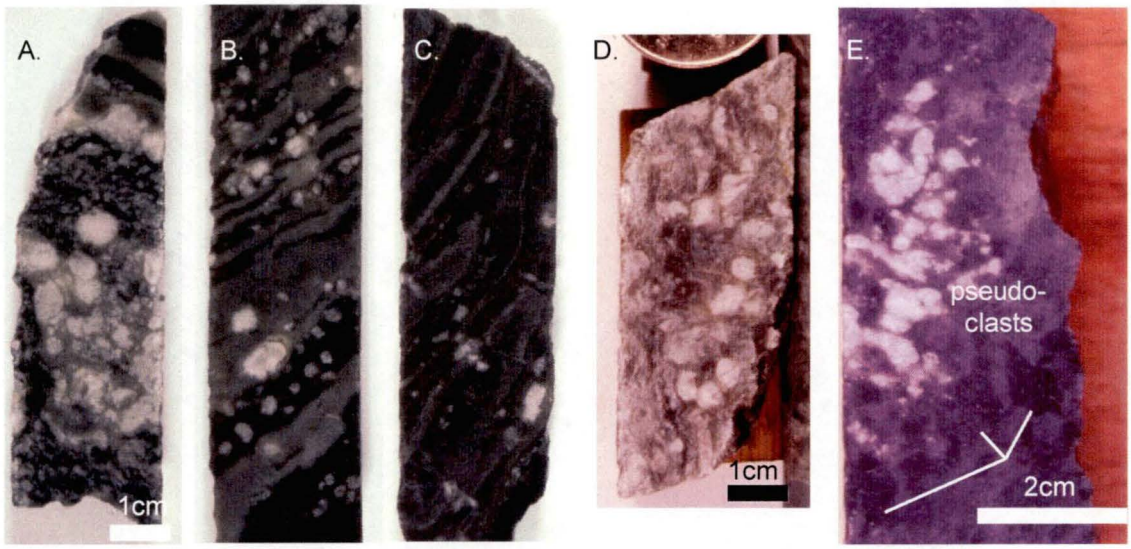
A.
1cm
B.
C.
D.
1cm
E.
pseudo-
clasts
2cm

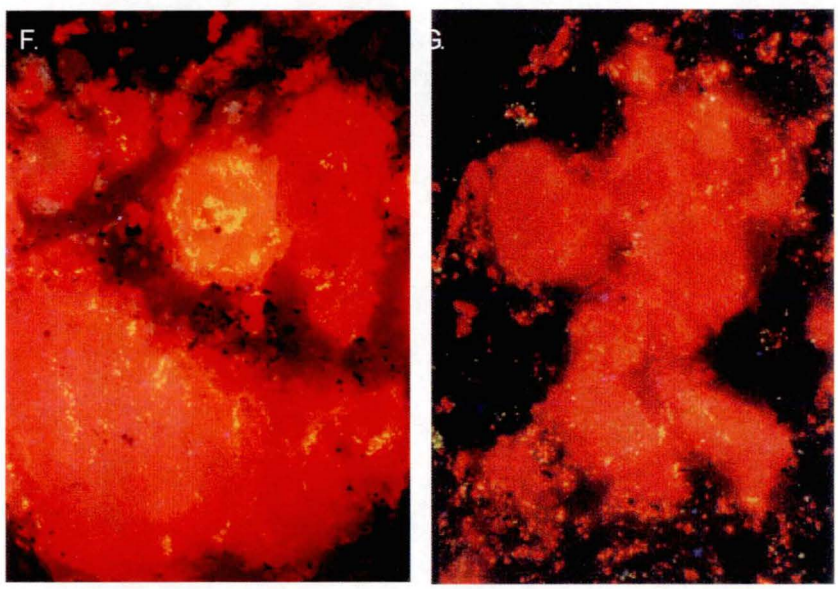
F.
G.

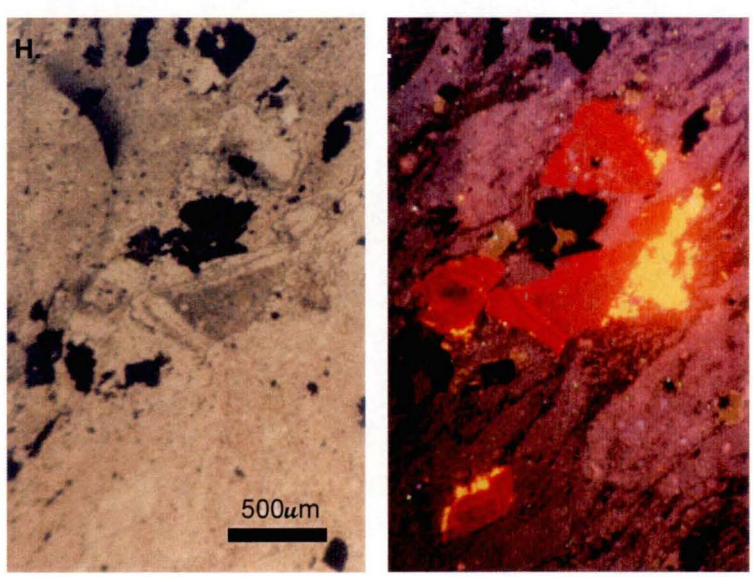
H.
500um

thin section most spheroids show alteration by sericite, quartz and calcite the extent of this alteration varies between samples. Cathodoluminescence (CL) photos fail to display any zonation in the "blebs" (Plate 9F & G). However zonation in the dolomite rhombs is highlighted under CL (Plate 9I).

Dolomite alteration occurs as discrete zones, most commonly seen at the top of the hydrothermal system near the Facies 1 - 4 boundary peripheral to the Upper Zone ore bodies (Fig. 25). The zones are usually traceable between definition holes for short distances, and show similar levels of alteration and overprinting. Dolomite spheroids overprint, and are overprinted, by sericite-quartz alteration.

Dolomite is picked up by the PIMA only when in high concentrations (>20%; Herrmann, 1998). It was found that the PIMA only detected dolomite when a spheroid was placed directly over the 2x10mm aperture of the spectrometer. Figure 30 demonstrates this, two analysis were done on each sample - spectra A was measured directly on a spheroids, while spectra B was measured between the dolomite spheroids. These results are summarised in Table 9. This example also highlights the advantage of using drill core over powders, where the grain size or heterogeneity of the samples is greater than the aperture area of the PIMA.

4.2.2.c discussion of false pyroclastic textures

The combination of sericite and heterogeneous quartz alteration often leads to a distinctive pseudoclastic or false pyroclastic texture (Fig. 24, 25 & Plate 8A & G). The presence of false pyroclastic textures in the host rocks of VHMS deposits has been documented in a number of deposits in Skellefte district, Sweden (Allen et al., 1997) and in some Australian deposits (Allen, 1988). The false pyroclastic textures resemble compacted pumice leading to incorrect interpretation of the rocks as clastic pumice breccias or welded ignimbrites.

Of interest to the Myra Falls district is the occurrence of apparent fiamme. The apparent fiamme are the result of heterogeneous alteration which leads to phyllosilicate-rich domains (pseudo clasts) in a less phyllosilicate-rich, siliceous domain or pseudo matrix (Allen, 1988). True pumice breccias or welded pyroclastic flows have phyllosilicate altered and flattened pumice clasts which define a pre-tectonic bedding parallel foliation. The flattened pumice have smooth outlines which may accommodate more rigid clasts or phenocrysts and have sharp to feathery ends (Fig. 31A). Pumice textures may also still be visible in less altered patches between the flattened pumices.

In contrast pseudo-fiamme are characterised by sharp angular and either broadly concave to delicately cuspate margins defined by alteration fronts (Fig. 31B; McPhie et al., 1993). They also lack preserved internal textures consistent with pumice compaction. However they are consistent with alteration, especially two-phase heterogeneous alteration involving phyllosilicate alteration phase and an incomplete siliceous alteration. Thus they are interpreted as the products of heterogeneous hydrothermal alteration, rather than a primary volcanic component.

4.3.3d effect of variations in quartz-sericite alteration on different facies

Facies 1 Volcaniclastics and sandstones: are dominated by false pyroclastic textures created by heterogeneous quartz-sericite alteration. Alteration destroys primary volcanic textures - feldspar phe-

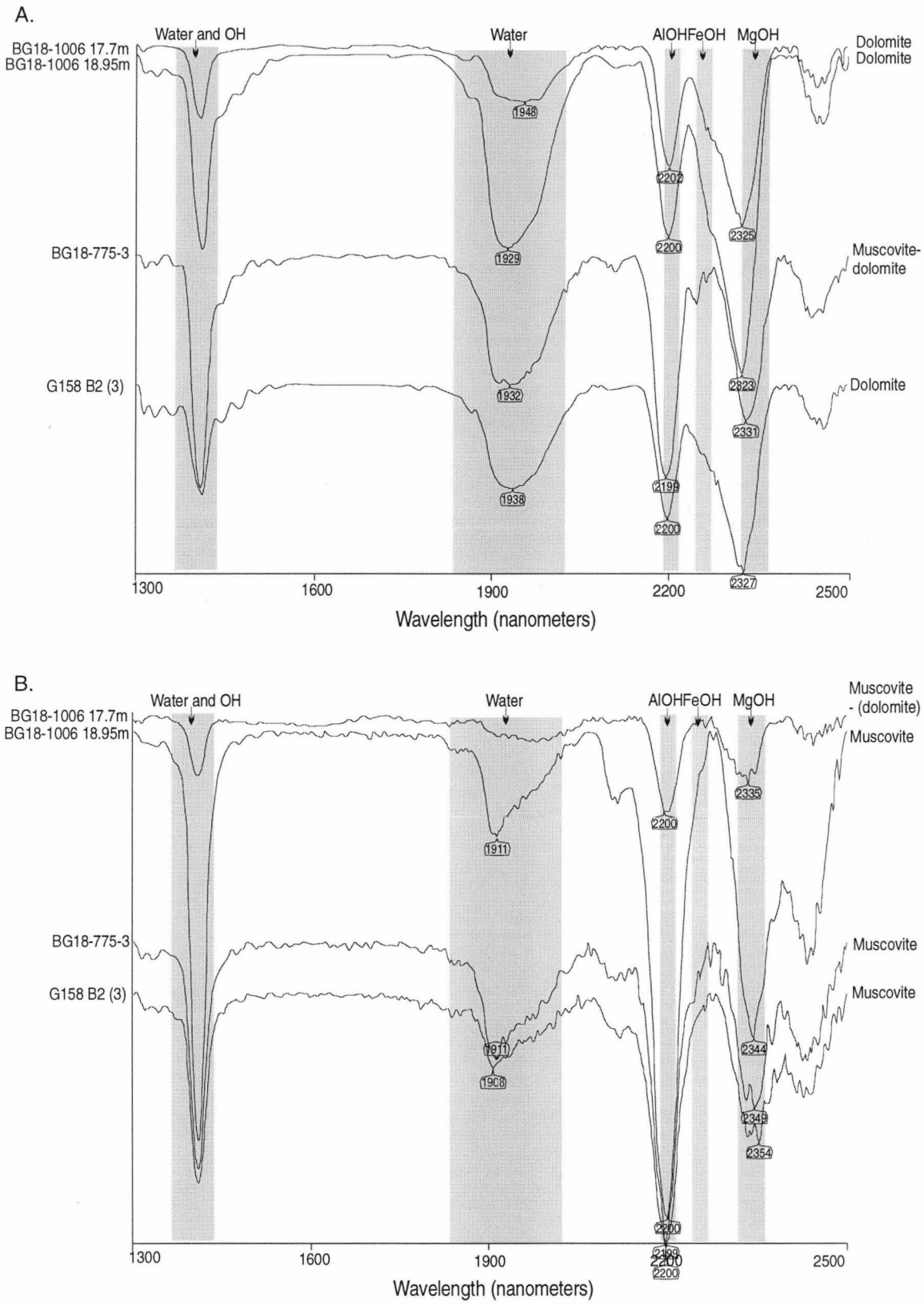

Figure 30. Hull quotient spectra for dolomite-alteration, spectra on graph A . taken with dolomite bleb directly over apature and gives good dolomite spectra. Spectra on graph B. tacken between dolomite blebs and show muscovite (dolomite not detected).

Table 9 HW Rhyolite PIMA results, dolomite alteration, Battle Zone samples.

Sample	Depth	Dolomite Bled or Background	Mineral 1	Mineral 2	Water feature (~1910)	AlOH wavelength	FeOH wavelength	MgOH wavelength
BG18-1006	17.7	Background	muscovite	Dolomite	-	2200	-	2335
BG18-1006	17.7	Dolomite bleb	Dolomite	muscovite	1948.579	2202	-	2325
BG18-1006	18.95	Dolomite bleb	Dolomite	muscovite	1929.85	2200	-	2323
BG18-1006	18.95	Background	muscovite	-	1911.185	2200	-	2344
BG18-775	75.2	Dolomite bleb	muscovite	Dolomite	1932.968	2199	-	2331
BG18-775	75.2	Background	muscovite	-	1911.144	2199	-	2349
G158 B2	20.4	Dolomite bleb	Dolomite	muscovite	1938.073	2200	-	2327
G158 B2	20.4	Background	muscovite	-	1908.024	2200	-	2354

*G158 B2 backfill hole (breather hole) drilled from 18-179DW Remuck Bay ~1575E, 4150N to G158stope

Table 10 HW Rhyolite PIMA results, Cherts, Battle Zone samples.

Hole No	Depth	Unit / Alteration	Hydrothermal Alteration	Mineral 1	Mineral 2	AlOH wavelength	FeOH wavelength	MgOH wavelength
BG18-1003	83.9-84.0	2 - Chert	quartz > sericite	IntChlorite	muscovite	2200	2250	2340
BG18-1006	89.2-89.4	2 - Chert	quartz > sericite	Muscovite	-	2200	-	2344
BG18-798	41.9-42.1	2 - Chert	quartz > sericite	Muscovite	-	2199	-	2346
BG18-977	125.9-126.1	2 - Chert	quartz > sericite	Muscovite	-	2202	-	2348

A. Pumice Breccia with compacted pumice

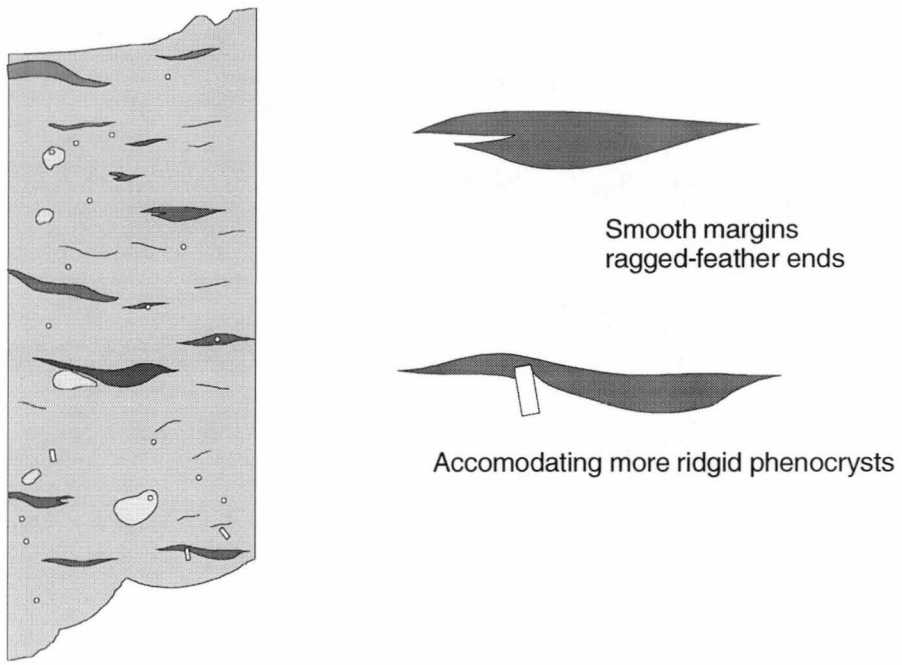

B. False pyroclastic texture in volcanic facies

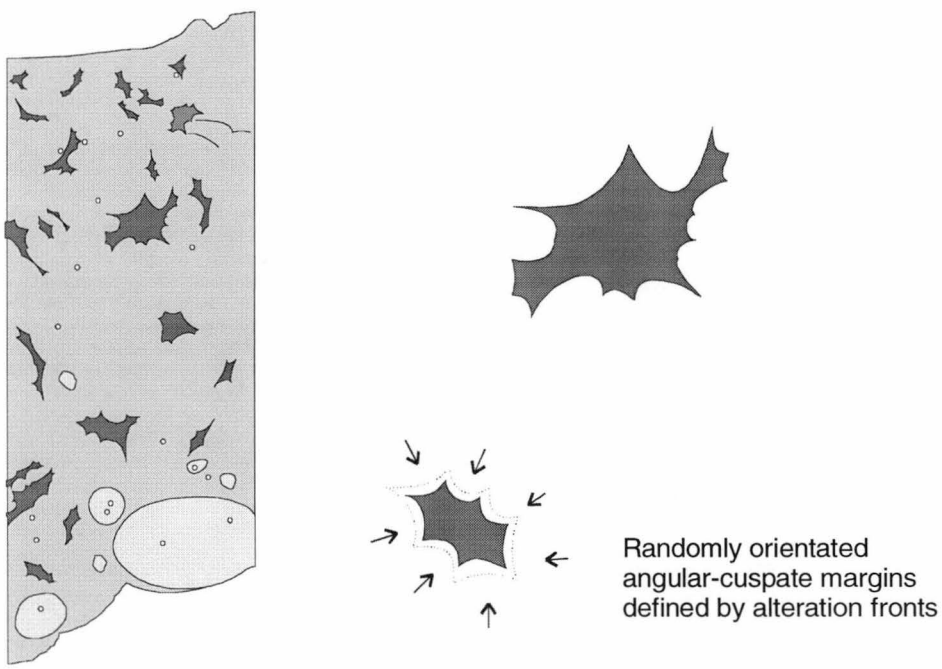

Figure 31. Comparison of genuine fiamme, and phyllosilicate altered pseudo-fiamme in drill core. A. Pumice breccia with compacted pumice or genuine fiamme (adapted from McPhie et al., 1993). B. False pyroclastic texture in a Battle Zone sample (based on BG18-886 4.5m)

nocrysts, pumice, and obscures clast margins within the volcaniclastics. Alteration also overprints contacts between units making bedding hard to distinguish.

Facies 2 Cherts: are the most silicified rocks found in the Battle Zone with up to 96% SiO_2, however they also show sericite alteration. Battle Zone cherts are mostly medium grey with darker grey bands/lammellae defined by increased pyrite content (observed in thin section) and occasional coarser quartz crystals and sericite. The cherts give flat PIMA spectra due to their high silica content, but contain muscovite (Table 10). One sample also contains chlorite, which is unusual for Battle Zone, HW Rhyolite, however it is consistent with sediments found in the Thelwood Valley. This chlorite may have been preserved by early silicification prior to sericite alteration.

Facies 3: Polymict, graded beds: As the unit becomes intensely altered by sericite ± quartz, all unsilicified clasts are destroyed along with any feldspar phenocrysts and primary volcanic textures. The resulting rock contains silicified fine grained porphyritic clasts and quartz crystals in a variable quartz-sericite altered matrix. Thus it becomes impossible to differentiate altered facies 3 units from facies 1 coarse volcaniclastics which may also contain silicified porphyritic clasts and quartz crystals.

Facies 4: Quartz-feldspar porphyritic rhyolite, Heterogeneous quartz-sericite alteration, gives the QFP units a clastic appearance defined by moderately altered quartz-phyric clasts (0.5 - 30 cm, feldspar phenocrysts not visible due to alteration), in a moderately to strongly sericite-altered and mineralised matrix. Pseudo-fiamme described in facies 1 can also be seen in this unit (Plate 8G). This alteration obscures primary volcanic features - feldspar phenocrysts, flow banding, clast margins, making interpretation of volcanic facies difficult. QFP units are identified by their evenly distributed quartz phenocrysts where all other volcanic feature are destroyed. Battle Zone QFP may also contain considerable mineralisation (sphalerite-chalcopyrite-galena-tennantite-barite).

4.3.3.e Summary

Hangingwall alteration in VHMS systems is often weak, and can be obscured by metamorphism (Large, 1992). The Battle Zone, provides an exception with an extensive hangingwall alteration zone. The presence of Upper Zone mineralisation is associated with the large "hangingwall" alteration zone as the alteration is largely footwall to the Upper Zones (Fig. 24 & 25).

Sericite-quartz alteration dominates the Battle Zone hangingwall and affects all volcanic facies types in the HW Rhyolite. The sericite and quartz are accompanied by ubiquitous rutile and pyrite. Dolomite, barite, and the sulfides (sphalerite, chalcopyrite, galena and tennantite) complete the alteration assemblages. Sericite and quartz alteration in the Battle Zone rhyolites probably occurred synchronously and repeatedly within the alteration halo as shown by their complex overprinting relations, with the resultant alteration a product of both processes in varying proportions. In contrast, dolomite alteration has a restricted distribution and is interpreted as marking the edges of the hydrothermal system.

4.4 Origin of alteration styles

4.4.1 Origin of epidote-chlorite-carbonate alteration.

Epidote-chlorite-carbonate alteration seen in the Price Formation and Hanging Wall Andesite samples is characteristic of "sea-floor" metamorphism or diagenesis (Dimroth and Lichtblau, 1979). Alt (1995) provides a review of studies on modern seafloor systems. Seafloor metamorphism comprises the partial or complete devitrification of volcanic glass, its replacement by palagonite, clay minerals, zeolites, silica and carbonate, its oxidation by reaction with oxygen-rich sea water, and the filling of primary porosity - amygdales, vesicles, and inter-particle porosity of volcaniclastic rocks (Dimroth and Lichtblau, 1979). This may occur via passive circulation of seawater at low temperature (2-150°C) or in "active" systems via convective heat flow, where temperatures may be higher. However, Alt (1995) also found that the initial stages of recharge that occur in active systems are inseparable from the passive low-temperature alteration.

The Price Formation is a sequence of andesite lavas and related breccias that can be equivalent to Alt's (1995) permeable volcanics which lie at the top of oceanic crust and range in thickness from several hundred meters to 1km thick. The presence of VHMS style mineralisation on the Price Formation - HW Rhyolite contact suggest alteration in the Price Formation may be related to or driven by a geothermal gradient, with epidote-chlorite-carbonate alteration occurring as part of a diffuse recharge zone, while the hydrothermal alteration produced by focused higher temperature discharge fluid that formed the massive sulfide mineralisation (Alt, 1995).

However epidote-chlorite-carbonate assemblages may also form directly through greenschist facies metamorphism of andesitic rocks. No well defined boundary exists between sea-floor metamorphism (or diagenesis) and a metamorphism of low grade (Dimroth and Lichtblau, 1979). Several studies (Dimroth and Lichtblau, 1979; Gifkins 1999, in prep) suggest evidence for the formation of zeolites may be preserved (as fibrous-radiating textures in filled amygdales and vesicle) by quartz pseudomorphs. However this is limited to areas where dynamo-thermal metamorphism is minimal (Dimroth and Lichtblau, 1979). No such structures were observed in the Price Formation samples collected during this study.

Alteration in the Hanging Wall Andesite is much more likely to occur as the result of passive seafloor oxidation after the hydrothermal system had ceased. The occurrence of clasts in various states of alteration in reworked breccias, at the base of the Hanging Wall Andesite also suggests this alteration occurred prior to the incorporation of these clasts within the predominantly andesitic breccias, possible as part of the volcanism that produce the Hanging Wall Andesite.

4.4.2 Origin of Mg-rich footwall chlorite alteration.

Chlorite altered zones are considered a common result of intense fluid flow zones in hydrother-

mal systems. Semi-conformable chlorite alteration is known to occur within the copper-rich stringer mineralisation of strata-bound footwall alteration system - Mount Chalmers, West lode, Scuddles and Woodlawn, Australia (Large, 1992). Thus the chlorite-schists seen in the Battle Zone footwall may represent zones of intense fluid flow, and may be important for recognising source regions or upflow zones. The discontinuous nature of most Mg-chlorite rich zones at Myra Falls is probably due to post emplacement faulting.

4.4.3 Origin of Dolomite

Carbonates have been studies at a number of VHMS deposits, Renstrom, Sweden (Duckworth, 1991), Rosebery, Tasmania, Australia, (Orth & Hill, 1994) and Hellyer, Tasmania, Australia (Gemmell and Large, 1992; Bradly, 1997), Mt Chalmers, Eastern-Australia (Hunns et al., 1994), the Hokuroko district, Japan (Shikazonon et al., 1998) and Middle Valley on the northern Juan de Fuca Ridge (Goodfellow et al., 1993). The dolomites at Myra Falls show many similarities to the carbonates described although differ in their association with muscovite. In most of the studies carbonates are associated with chloritic assemblages.

The distribution of the dolomite zones in the Battle Zone, suggests an association with the edge of the hydrothermal system where hydrothermal fluids may have mixed with seawater. Thin section and cathodoluminescence work illustrates variations in the dolomite spheroids and rhombs with respect to sericite-alteration. Variation in overprinting between dolomites at various levels within the hydrothermal system may represent periodic changes in the growth and evolution of the hydrothermal system with time. The Mg-rich nature of these horizons may also indicate the influence of seawater in the formation of carbonates (Duckworth, 1991). No cross cutting relations between sulfides and dolomite rhombs or blebs were observed. The processes of carbonate deposition will be discussed in Chapter 11.

4.5 Summary

The Battle Zone is the site of massive sulfide mineralisation and the surrounding host rocks have been altered by the fluids associated with the mineralisation. The alteration assemblages described in this chapter are the result of metamorpism of the original alteration mineralogy to greenschist facies. Rocks out side the Battle Zone (eg Thelwood Valley), have undergone processes of devitrification, diagenesis and seafloor alteration. Minerals formed during devitrification and diagenesis were then subsequently metamorphosed to the current mineral assemblages. Mineral assemblages in the regional alteration are strongly dependant on the primary rock type. Hydrothermal footwall alteration is confined to the Price Formation (Juras, 1987) and hangingwall alteration is confined to the HW Rhyolite. The Hanging Wall Andesite is not affected by the hydrothermal system which produced the mineralisation. However basal mass flows in the Hanging Wall Andesite contain altered rhyolitic sediments. Table 11 summarises the alteration types found in the Battle Zone and the expected regional / background alteration types found in rocks away from sulfide mineralisation.

Table 11 Summary of alteration types in Battle Zone and regional alteration types form Thelwood Valley

Alteration Type	Rock Unit(s)	Distribution	Nature, Destructive/ Non-Destructive	Phyllosilicate mineralogy
chlorite-epidote-albite-carbonate	Price and Hanging Wall Andesites	regional	non-destructive	intermediate-chlorite
weak sericite-quartz	Hanging Wall Andesite	base of the Hanging Wall Andesite	non-destructive	intermediate-chlorite + muscovite
sericite-quartz-albite	HW Horizon	regional	pervasive, relic textures visible	muscovite to phengitic muscovites
sericite	HW Horizon	local	destructive, pervasive	muscovite
quartz	HW Horizon	local	heterogeneous, non-destructive	
dolomite	HW Horizon	local	overprinting	dolomite
weak sericite-quartz	Price Formation	unknown	heterogeneous, destructve	intermediate-chlorite + muscovite
intense sericite-pyrite ± quartz	Price Formation	local	pervasive, destructive	muscovite
intense chlorite	Price Formation	local	pervasive, destructive	Mg-chlorite
sericite-chlorite-pyrite	Price Formation	local	pervasive, relic textures visible	muscovite + intermediate-chlorite

Chapter 5

Alteration Geochemistry

5.1 Introduction

This chapter details the geochemistry of the hydrothermal alteration that effects the Battle Zone, with the aim of providing a geochemical characterisation of the alteration types and the elemental changes that occurred in the rocks during hydrothermal alteration. A number of lithogeochemical data treatment methods have been devised to quantify mass changes occurring in rocks during alteration (Gresens, 1967; Pearce, 1968; MacLean and Kranidiotis, 1987). All the lithogeochemical approaches assume that the rocks under investigation are related, and most (Pearce element ratio's excepted) require the designation of a parent rock. Thus relations between rocks will first be established, then immobile elements tested. Alteration is described qualitatively, then quantitatively.

Juras (1987), Robinson (1994), Robinson et al. (1996), and Barrett and Sherlock (1994, 1995 & 1996) have carried out previous geochemical studies of the Myra Falls district. Juras (1987) used whole rock, trace element and rare earth element data to characterise five volcanic series in the Myra Falls district and showed that the volcanic units are the result of at least three distinct but contemporaneous magmatic lineages. Juras (1987) data will be used in this chapter to represent least altered rocks along with samples collected by the author. Robinson et al. (1996) used Pearce element ratios to evaluate alteration in the Battle Zone. Barrett and Sherlock (1996) used the methods of MacLean and Kranidiotis (1987) and Barrett and MacLean (1991) to characterise the volcanic rocks and alteration around the HW deposit. A review of the results of the previous studies and this study will be presented at the end of the chapter.

5.2 Samples and Methods

Samples of underground definition drill core (AQ, 10-30cm long) were collected during logging as representative samples of the rock and alteration types observed in the Battle Zone. Samples were also collected from a surface drill program in the Thelwood Valley to act as least altered samples (Battle Zone samples have moderate to intense alteration). Fifty samples were chosen on two sections (1420mE and 1600mE) to represent the major rock units and alteration types found in the Battle Zone. Samples were crushed, pulverised (tungsten-carbide mill) and made into press powder pills and discs, by the author. They were then analysed for major and trace elements by XRF at the University of Tasmania. XRF analyses were conducted by Phil Robinson on the Phillips, PW1480, X-ray florescence spectrometer. Analytical conditions and analytical results for standards are summarised

in Appendix 2.

Hangingwall and footwall alteration in the Battle Zone affects two distinct units; the Price Formation and the HW Rhyolite. These units are treated separately throughout this chapter. The Hanging Wall Andesite overlies the HW Rhyolite but is not affected by hydrothermal alteration and thus will not be discussed in this chapter. Footwall alteration has been plotted according to the three alteration types identified in chapter 4: sericite-pyrite alteration, Mg-chlorite alteration and sericite-chlorite-pyrite alteration. Hangingwall alteration samples are divided by facies types identified in Chapter 3 and then further subdivided by alteration type identified in Chapter 4. The subdivisions are Facies 1 - volcaniclastics and sandstones, Facies 2 - cherts, Facies 3 - polymictic sediments and Facies 4 - quartz-feldspar porphyry (QFP), and alteration styles; 1. sericite > silica alteration, 2. silica > sericite alteration and 3. dolomite alteration. All data is presented in Appendix 2.

5.3 Geochemical characterisation of rock units and least altered samples

Massive sulfide districts, such as the Myra Falls district, commonly contain volcanic sequences of different magmatic affinity (Barrett and MacLean, 1994). Identification of units of differing magmatic affinity is important not only in understanding the geological environment for exploration purposes, but also forms the basis of mass balance calculations where one of the assumptions is that the rocks under investigation are related to a common homogeneous parent (Stanley and Madeisky, 1994).

The different affinities in a VHMS district are best-established using the fresh or least altered samples. Juras (1987) grouped the volcanic rocks at Myra Falls into five volcanic series, which resulted from at least three distinct, but contemporaneous magmatic lineages. These series are described in Chapter 3. Of interest to the Battle Zone are the Price Formation and the HW Rhyolite. The HW Rhyolite is divided into 4 facies - Facies 1 - volcaniclastic-breccias and -sandstones, Facies 2 - siltstones, Facies 3 - polymict graded beds and Facies 4 - quartz-feldspar porphyritic rhyolite. Intercalated with these units in the Price area (Fig. 3.1) is the HW Dacite (Chapter 3).

Al, Ti, Zr, Y, Nb and REE are considered immobile during seafloor alteration and low grade metamorphism (up to greenschist facies; Cann, 1970; Pearce and Cann 1973; Floyd and Winchester, 1975). These elements are used to discriminate volcanic rocks of differing magmatic affinity. Plots of TiO_2 versus Zr are shown for andesite and rhyolitic series mentioned above (Fig. 32 & 33). If rock compositions plot along a line that passes through the origin, within measurement error, then the rocks are considered related (Stanley and Madeisky, 1994). Ti/Zr ratios are calculated as a measure of each volcanic series, and plots of Zr/TiO_2 versus Nb/Y, from Floyd and Winchester (1975), are used to discriminate magma types.

Price Formation

The Thelwood Valley samples of Price Formation and samples from Juras (1987) form two suites (Fig. 32A). Suite 1 is characterised by Ti/Zr ratio of 52, while suite 2 has higher Ti/Zr ratio of 71. This indicates there is a variation in composition of the Price Formation throughout the Myra Falls property. Juras (1987) identified two flow types within the Price Andesite (chapter 3), these two flow types were not identified geochemically but their distribution may account of some of the variation in Ti/Zr ratios of Price Formation.

Despite the variartion in Ti/Zr ratio the Price Formation is characterised by SiO_2 contents between 48-58 wt%, MgO 4-8 wt%, CaO 4-10 wt%, Na_2O 3-6 wt%, low K_2O (0.05-0.8 wt%), Ba (50-400 ppm) and metal (Pb, Cu, Ni, and As) values less than 100 ppm, and high Sr contents (200-800 ppm). Figure 32B, shows the Price Andesite to be dominantly dacite in composition.

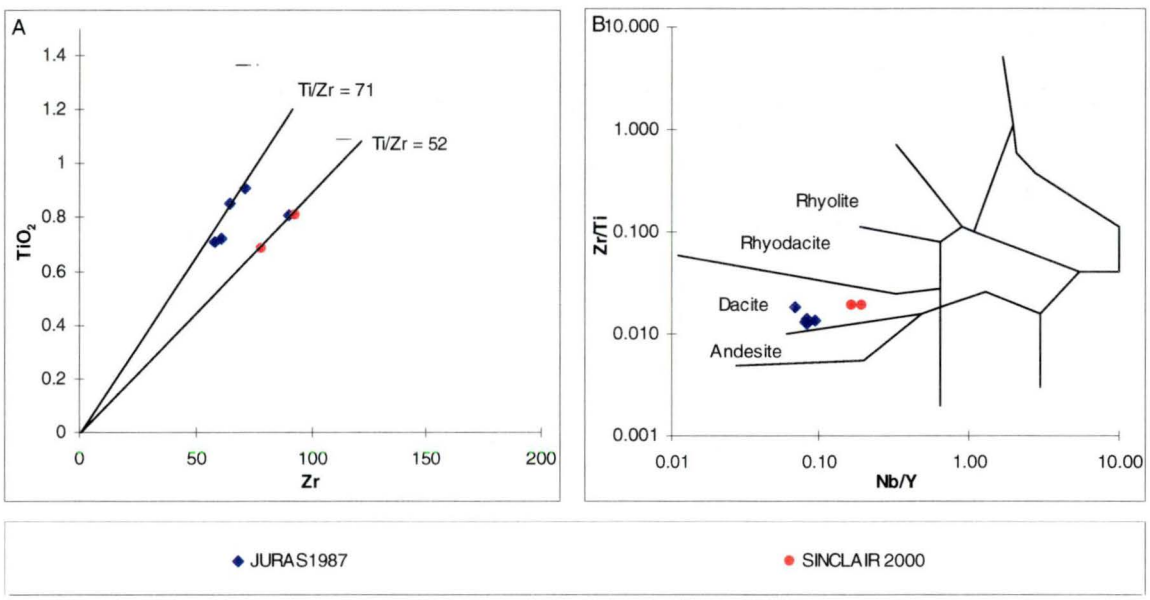

Figure 32 A. Plot of TiO_2 versus Zr for Price Andesite least altered samples. B. Zr/TiO_2 versus Nb/Y plot with the fields of Floyd and Winchester (1975), for least altered Price Andesite samples.

HW Rhyolite

Least altered samples of HW Rhyolite taken from the Thelwood Valley were visually divided into two series, series 1 made up of quartz-feldspar porphyritic (QFP) units and the second series made up of fine grained sediments. The two series are plotted on TiO_2 versus Zr scatter plot (Fig. 33A). The QFP series has a Ti/Zr ratio of 10-11 and lie along a line through the origin. The Thelwood Valley sediments, however, show a much higher Ti/Zr ration of 51 and do not form a related set. Thus the QFP and sediments from the Thelwood Valley are unrelated. Included in Figure 5.2A are two samples of HW Dacite from the Thelwood Valley and HW Rhyolite samples of Juras (1987). HW Dacite samples have a Ti/Zr ratio of 30 and are clearly unrelated to the QFP samples from the Thelwood Valley. Juras's (1987) HW Rhyolite samples have a Ti/Zr ratio of 10 and lie along the same trend as the QFP samples from the Thelwood Valley. The slight variation between Juras (1987) samples and

those from the Thelwood Valley is probably related to the variation in calibration at different laboratories (inter-laboratory analytical variations). QFP samples from the Thelwood Valley have SiO_2 contents 64-70 wt%, Fe_2O_3 2.5-3 wt%, MgO 1-2.5 wt%, CaO 1-5 wt%, Na_2O 0.4-1.5 wt%, Sr 100-200ppm, Zn <100 ppm, Cu <20 ppm. Sulfur and the metals (Pb, Ni, As) are close to or below detection.

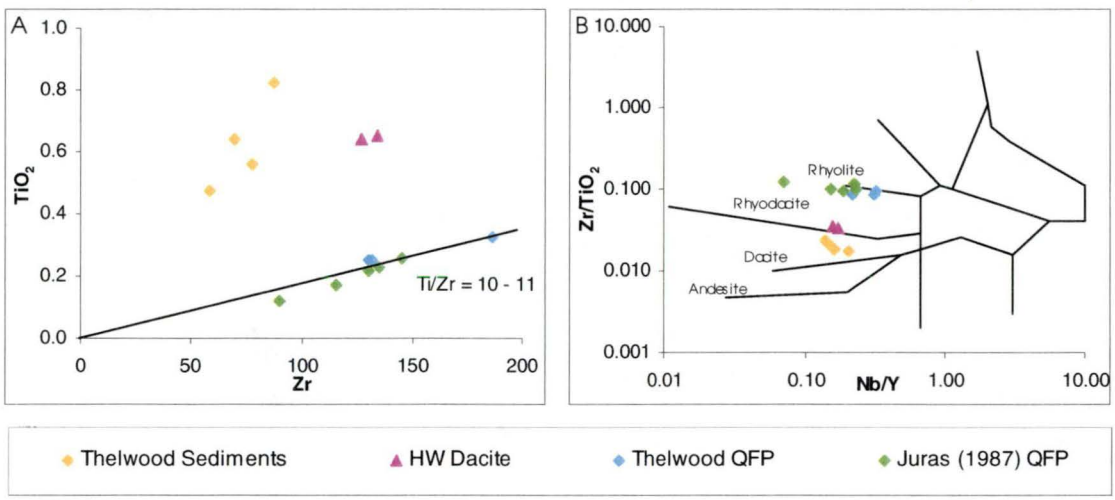

Figure 33 A. Plot of TiO_2 versus Zr for Thelwood Valley sediments, Thelwood Valley QFP HW Dacite and Juras (1987) QFP samples. B. Zr/TiO_2 versus Nb/Y plot with the fields of Floyd and Winchester (1975).

5.4 Immobile Elements

In altered rocks, such as those found in the Battle Zone, magmatic affinity can only be established using lithogeochemical techniques (Barrett and MacLean, 1994). However, elements such as Al, Ti, Zr, Y, Nb and REE are considered immobile during seafloor alteration and low-grade metamorphism (Cann, 1970; Pearce and Cann, 1973; and Floyd and Winchester, 1975). Under intense hydrothermal alteration or higher grade metamorphism, such as those seen in ancient VHMS districts, these elements may become mobile (Finlow-Bates and Stumpfl, 1981; Rubin et al., 1993; Barrett and Sherlock, 1996; Pascual, 1997). Thus the identification of elements which remain immobile during hydrothermal alteration and metamorphism is important for the identification of volcanic rock types (basalt, andesite, rhyolite) and in the quantification of mass changes that occur within the rock during alteration.

Immobility is tested by plotting suspected immobile element pairs on x-y scatter plots (Fig. 34). If elements are immobile they form a highly correlated linear trend, which ideally pass through the origin (MacLean and Barrett, 1993; Herrmann, 1998). Mass gains and losses of the mobile components causes changes in the concentration of immobile elements, but the inter-element ratios of immobile elements will be not vary (Herrmann 1998). This causes a spread of data along the linear trend, net mass gains move the rocks toward the origin, whereas net mass loss moved data in the opposite direction (Fig. 34; MacDonald et al., 1996).

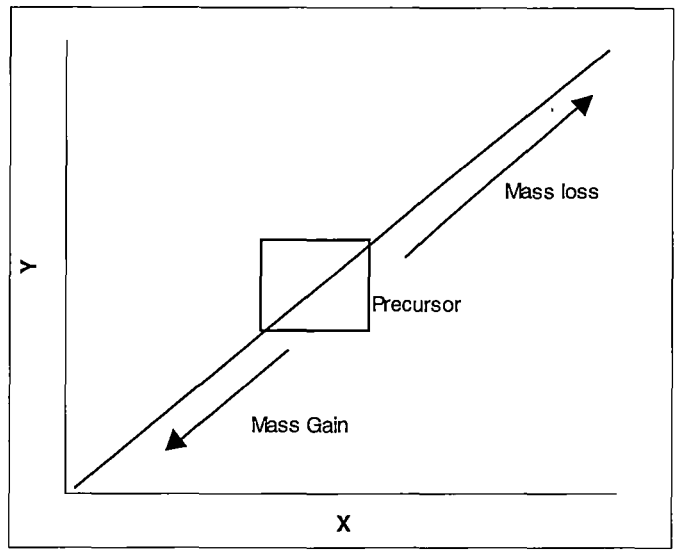

Figure 34. X-Y scatter plot. Precursor rock represented by box. Affect of mass gain and mass loss from precursor rock show by arrows. Adapted from Herrmann (1998).

Price Formation

Figure 35 shows the Battle samples (this study) plotted with the Thelwood Valley samples (this study) and includes data from Juras (1987) and Robinson (1994). On Figure 35A the samples conform to the two volcanic series found in the least altered samples, indicating that these sample represent the range of primary variability found in the Price Formation. Due to this primary variability in andesite composition determination of immobile elements in each alteration types will be made from the isocon diagrams. However, samples from Juras (1987) and Robinson (1992) show significant variations Nb. Nb is close to detection (2ppm) in both studies, thus these samples will not be used in the following calculations.

HW Rhyolite

Figure 36A & B shows TiO_2, Zr and Al_2O_3 scatter plots for altered Facies 1 and 4 rocks. These elements form strong linear trends that pass through the origin, thus TiO_2, Al_2O_3 and Zr can be considered immobile elements in the HW Rhyolite Facies 1 & 4. Nb also shows a reasonably linear trend when plotted against Al_2O_3 (Fig. 36C). However Y shows a fair scatter when plotted against Nb (Fig. 36D) and is thus considered to be mobile in the Battle Zone hangingwall hydrothermal alteration. The Facies 2 cherts lie close to the origin on all diagrams, due to their high SiO_2 content (>90%), thus they appear to lie on the trend defined by Facies 1 and 4. Close inspection, however, shows that these samples do deviate from this trend. Figures 36A, B, and C clearly illustrate that the Facies 3 polymictic sediments do not conform to the trend shown by the Facies 1 and 4 rocks, and don't form separate trend of their own.

Ti/Zr ratio for all hangingwall samples are listed in Table 12. Thelwood QFP, Facies 1 – Volcaniclastics, Facies 4 - QFP and dolomite altered sample all have similar Ti/Zr values and form a strong linear trend on immobile element plots (Fig. 36), indicating they are related. However, cherts

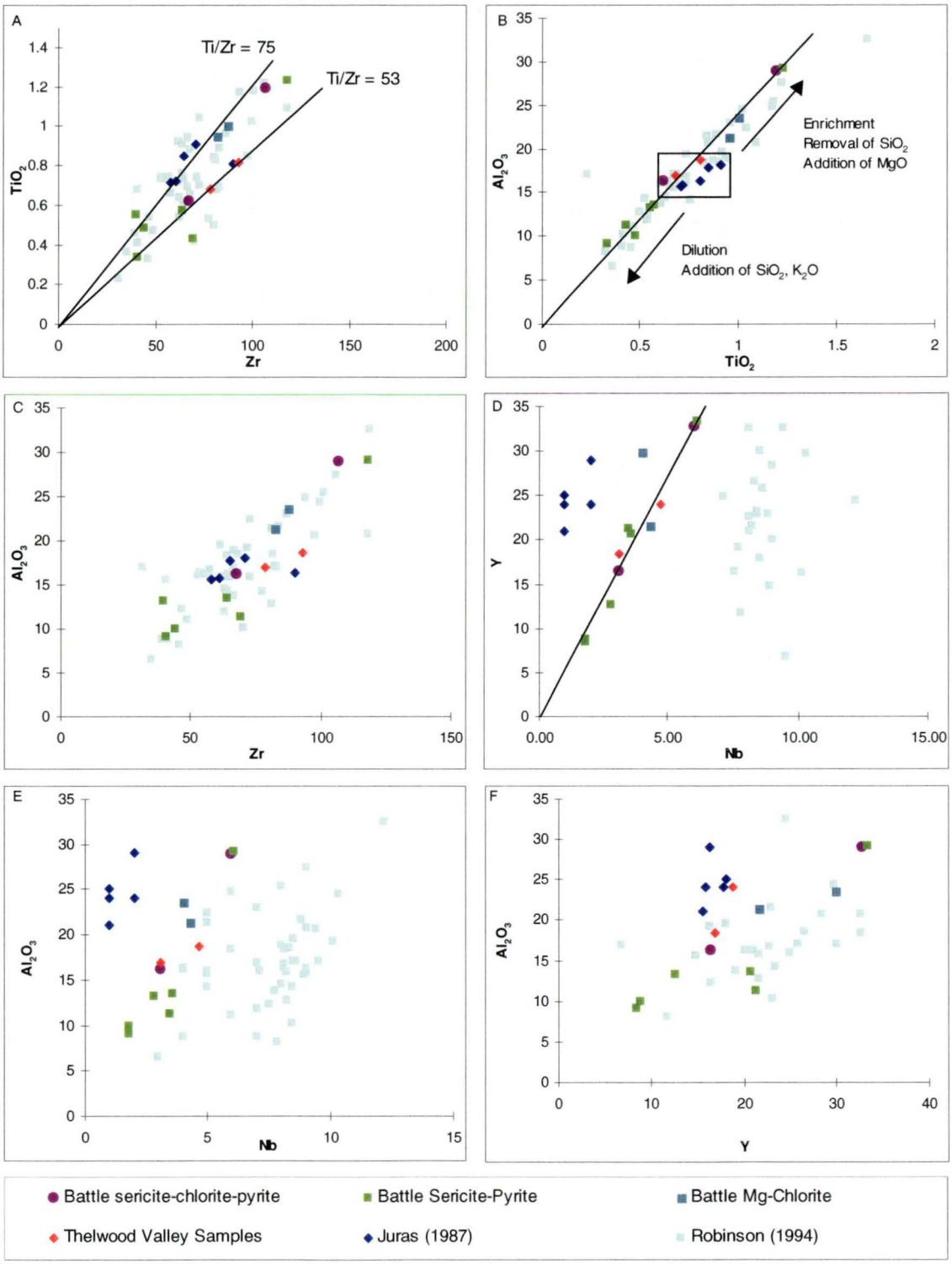

Figure 35. X-Y scatter plots of possible immobile element pairs for Price Formation footwall alteration.

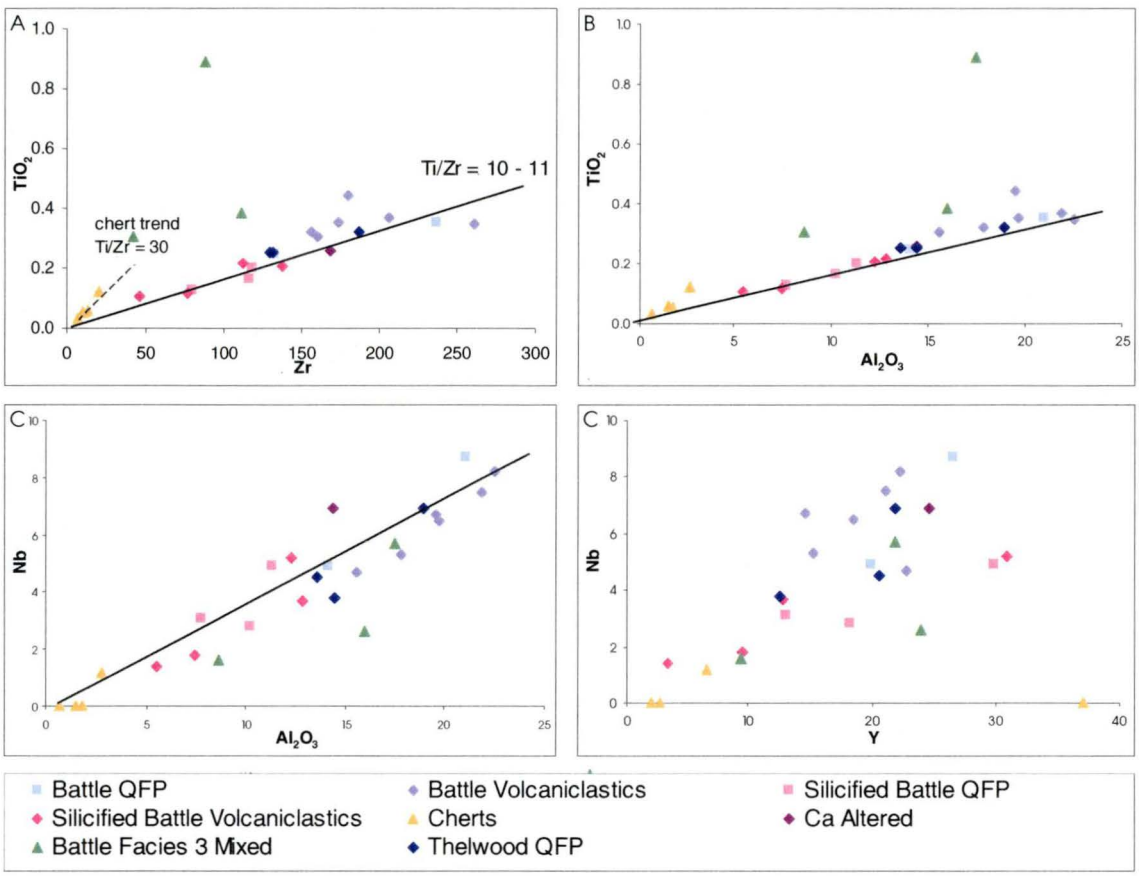

Figure 36. Immobile element ratio diagrams for HW Rhyolite, Battle Zone Samples.

(Ti/Zr = 26 - 35) and polymict sediments (Ti/Zr = 21 - 61) have very different Ti/Zr ratios suggesting that these rocks are unrelated to Thelwood Valley QFP or Battle Zone Facies 1 and 4 rocks. Thus cherts and polymict sediments will not be considered in the following alteration analysis.

Unit	Ti/Zr	Average
Thelwood QFP	10 - 11	11
Facies1 - Volcaniclastics	8 - 15	11
Facies 4 - QFP	8 - 11	10
Facies 2 - Chert	26 - 35	30
Facies 3 - Polymict sediments	21 - 61	42
Dolomite-alteration	9	-

Table 12. Ti/Zr ratio for HW Rhyolite facies rocks from Battle Zone and Thelwood Valley.

5.5 Alteration - Chemistry of alteration types

Alteration mineral assemblages observed in The Battle Zone are the result of metamorphism of the original hydrothermal alteration assemblages. Some authors (Jolley, 1978) believe that minerals formed on seafloor during hydrothermal alteration are also the stable phases in the surrounding regional greenschist facies rocks. Regardless of this and for the purpose of this study, it is assumed that chemical analysis will reflect the changes in the rocks caused by hydrothermal alteration without significant modification from latter processes (e.g. metamorphism).

Footwall Alteration – Price Formation

Footwall alteration occurs in the Price Formation as a stratiform blanket directly underlying the Battle lenses (Fig. 24 & 25). Alteration mineralogy grades from intense sericite-pyrite alteration directly below the massive sulfide mineralisation into less intense sericite-chlorite-pyrite alteration approximately 20m below the base of the massive sulfide. Intense Mg-chlorite alteration cross cuts the intense sericite-pyrite alteration. Table 13 summarises the chemical changes that occur in the three alteration types relative to the least altered Price Formation value (average of 2 samples). All alteration types show relative gains in K_2O, S and Ba and losses of Na_2O, CaO and Sr. While MgO and MnO show a gain in the Mg-chlorite alteration and a loss for sericite alteration but little change for the sericite-chlorite-pyrite altered samples. SiO_2 is gained in the intense sericite-pyrite alteration, lost from the Mg-chlorite alteration, but shows little change in the sericite-chlorite-pyrite alteration. Fe_2O_3 is gained in the sericite-pyrite and Mg-chlorite alteration and shows little change in sericite-chlorite-pyrite alteration.

These results fit with the observed mineralogy of the alteration types (see section 4.3.2). Sericite-pyrite alteration shows gains in SiO_2 due to the addition quartz, the gains in Fe_2O_3 and S reflect the addition of pyrite, while K_2O and Ba are accommodated in muscovite. Mg-chlorite alteration also shows pyrite addition (Fe_2O_3 and S), the gain in K_2O and Ba reflect the moderate sericite content of this alteration type, while MgO and MnO are accommodated in chlorite. In contrast the sericite-chlorite-pyrite alteration zone show only addition of K_2O and Ba due to muscovite and addition of S to form pyrite apparently from existing Fe as no Fe_2O_3 addition was found.

Alteration Type	SiO_2	Fe_2O_3	MnO	MgO	CaO	Na_2O	K_2O	S	Sr	Ba
Sericite-pyrite	+	+	-	-	-	-	+	+	-	+
Mg-chlorite	-	+	+	+	-	-	+	+	-	+
Sericite-chlorite-pyrite	/	/	/	/	-	-	+	+	-	+

Table 13. Summary of relative changes in geochemistry of altered rocks in comparison to the least altered protolith. Symbols + minor gain, + major gain, - minor loss, / no change.

Hangingwall alteration - QFP and related sediments

Three alteration types effect the QFP (Facies 4) and their related sediments (Facies 1 – volcaniclastics): Silicification, sericite alteration and dolomite alteration. Table 14 summarises the chemical changes that occur in the samples during alteration. The silicified samples have increases in SiO_2 and S and losses of MgO, CaO and Sr relative to unaltered QFP. Sericite altered samples have losses of Na_2O and gains in K_2O, S, Cr and Ba. Dolomite alteration has massive increases in MgO, CaO, lesser increases in S, Cr and Ba and a loss of SiO_2. The distribution of metals (Fe, Zn, Cu, Pb, and As) is erratic and probably the result of variations in disseminated sulfide concentrations.

These results reflect the observed mineralogy well, in silicified samples quartz is gained leading to an increase in SiO_2. In sericite altered samples the addition of K_2O and Ba (in volcaniclastics) reflects the addition of muscovite. Chromium addition in the volcaniclastic rocks is highly variable and probably reflects trace mafic component in the origiunal rocks rather than an alteration feature. In contrast the dolomite altered sample shows addition of MgO and CaO reflecting the formation of dolomite. The addition of Ba in the dolomite alteration probably reflects the addition of barite. Addition of S to all hangingwall alteration types reflects the presence of sulfide minerals.

Alteration Type	Facies	SiO_2	Fe_2O_3	MgO	CaO	Na_2O	K_2O	S	Sr	Cr	Ba
Silicification	QFP	+	/	-	-	-	/	+	**-**	/	/
	Vc	+	/	-	-	/	/	+	**-**	/	/
Sericite alteration	QFP	/	/	/	-	-	**+**	+	-	/	/
	Vc	/	+	/	/	-	+	+	-	+	+
Dolomite alteration	Vc	**-**	/	**+**	**+**	/	/	+	/	/	+

Table 14. Summary of relative changes in geochemistry of altered rocks in comparison to least altered protolith, Facies: QFP: quartz-feldspar porphyry, Vc: volcaniclastic. Symbols + minor gain, **+** major gain, - minor loss, **-** major loss, / no change.

5.6 Alteration indexes

A number of alteration indices have been developed to characterise alteration styles and intensity related to VHMS systems. Two such indices are used here to characterise the alteration around the Battle Zone:

Ishikawa alteration index -

$$AI = 100*(K_2O + MgO) / (K_2O + MgO + Na_2O + CaO)$$

Chlorite/carbonate/pyrite index -

$$CCPI = 100*(MgO + FeO) / (MgO + FeO + Na_2O + K_2O)$$

The Ishikawa alteration index (AI) was originally developed by Ishikawa et al. (1976) to delineate alteration halos around the Kuroko deposits. It operates on the principal that hydrothermal alteration begins as a zone of feldspar destruction accompanied by sodium and calcium depletion, which cause an increase in the AI ratio. Subsequent alteration to sericite and chlorite assemblages further increase this index providing a method of quantifying the intensity of alteration around VHMS deposits (Large et al., in press).

The chlorite/carbonate/pyrite index (CCPI) was designed to measure the increase in MgO an FeO associated with Mg-Fe chlorite alteration toward the centre of VHMS related hydrothermal systems (Large et al., in press). In addition this index is also positively affected by Mg-Fe bearing carbonates (dolomite, ankerite and siderite) found in some hydrothermal systems and by pyrite. The CCPI provides an additional means of quantifying hydrothermal alteration.

Regional alteration

Price Formation andesites effected by regional alteration show low AI (28-44) and moderate to high CCPI (52-82). Their CCPI index is due to high initial Mg-Fe contents and are characteristic of andestes. In the HW Rhyolite alteration indices are fairly low for regionally chlorite-carbonate-epidote-altered samples, (AI = 30-50 and CCPI = 51-53) although one sample showed an AI of 79. This sample is a clastic QFP and may be contaminated with non-QFP related material.

Footwall alteration

Footwall alteration in the Battle Zone is characterised by extreme AI indices with sericite-pyrite alteration (AI = 86-98), Mg-chlorite alteration (AI = 96), and sericite-chlorite-pyrite alteration (AI = 91-93). Indices for each sample are listed in Table 4, Appendix 2 and summarised in Table 15. CCPI

provides a better discriminator in the footwall with sericite-pyrite alteration having relatively low values except where pyrite is abundant (CCPI = 48-82). Mg-chlorite alteration has an extreme CCPI index of 90-93 reflecting the predominance of chlorite in this zone. The sericite-chlorite-pyrite alteration has a moderately high CCPI of 69-80 caused by chlorite and pyrite.

Alteration Type	AI	CCPI
Sericite-pyrite	+	-
Mg-chlorite	+	+
Sericite-chlorite-pyrite	+	/

Table 15. Summary of change in alteration indices due to different styles of footwall alteration, changes are relative to least altered protolith. Symbols + minor gain, **+** major gain, - minor loss, **-** major loss, / little change.

Hangingwall alteration

Alteration indices for each sample are listed in Table 4, Appendix 2 and summarised in Table 16. The Battle Zone QFP and related volcaniclastics show a variation in AI, with sericite altered QFP having AI of 67-71 similar to that of the silicified QFP samples (AI = 63-78) but lower than the sericite altered volcaniclastics (AI = 85-95). The silicified volcaniclastics have the lowest AI of this group (AI = 37-66). The dolomite altered sample has an AI of 50.

The CCPI index for QFP and related volcaniclastics in the Battle Zone is low for both sericite altered and silicified samples (CCPI = 25–66), reflecting the predominance of sericite alteration in the hangingwall to the Battle Zone. The dolomite altered sample has a higher CCPI index of 71 reflecting the Mg-rich nature of the dolomite.

Alteration Type	Facies	AI	CCPI
Silicification	QFP	+	-
	Volcaniclastic	+	-
Sericite alteration	QFP	+	-
	Volcaniclastic	+	-
Dolomite alteration	Volcaniclastic	/	+

Table 16. Summary of change in alteration index due to different styles of hangingwall alteration, changes are relative to least altered protolith. Symbols + minor gain, **+** major gain, - minor loss, **-** major loss, / little change.

Alteration Box Plot

The alteration box plot combines the power of the Ishikawa alteration index (AI) and the chlorite/carbonate/pyrite index (CCPI), and allows the characterisation of different alteration trends and intensities related to massive sulfide ores (Large et al., in press). Figure 37 shows the alteration trends distinguishable by the alteration box plot. Unaltered volcanics plot in a box toward the central left of the diagram, while altered volcanics plot toward the edges of the diagram depending on alteration type and intensity (Fig. 37).

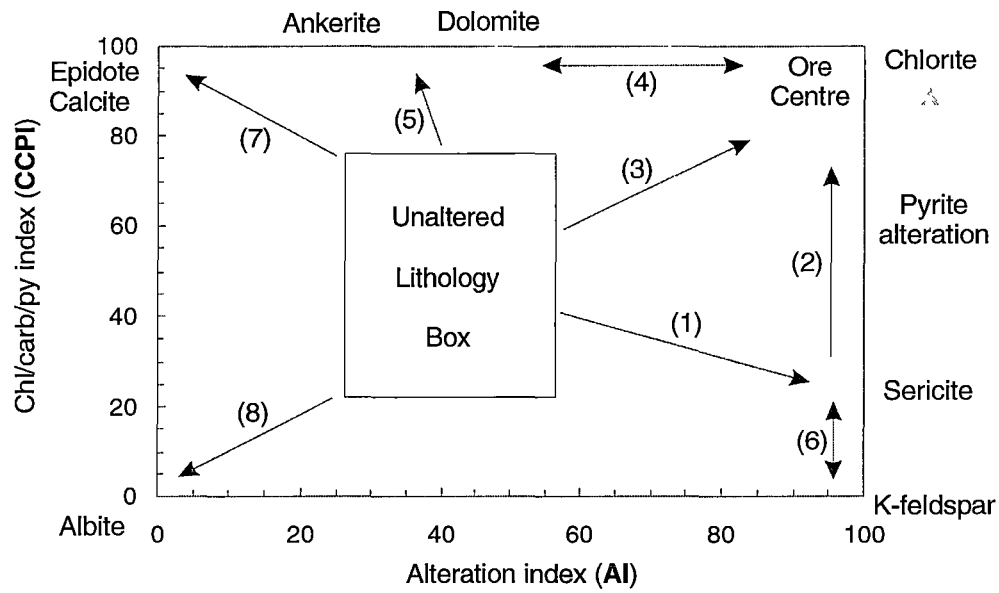

Figure 37 Alteration box plot showing hydrothermal alteration trends: (1) sericite alteration, (2) sericite-chlorite + pyrite, (3) chlorite + sericite + pyrite, (4) chlorite-carbonate, (5) Fe-Mn carbonate, (6) K-feldspar-quartz, (7) epidote + calcite alteration, (8) albite alteration. Modified from Large (1998).

The S/Na_2O has also been developed by CODES as an indicator of alteration surrounding VHMS deposits. It measures Na depletion, caused by the destruction of feldspar, and S content of altered rocks due to pyrite and other sulfide mineralisation (Large et al., in press). This provides an indication of the alteration state of rocks in VHMS related alteration system.

Figure 38A shows that the footwall alteration, least altered samples from Thelwood Valley and Juras (1987) data plot in a least altered box toward the centre of the diagram while altered samples from the Battle Zone plot toward the right hand side of the diagram. Sericite-pyrite altered samples plot towards sericite with samples having higher pyrite-content plotting towards chlorite. Sericite-chlorite-pyrite samples plot towards chlorite while Mg-chlorite altered samples plot in the top right hand corner due to their chlorite-rich nature.

Figure 38B shows S/Na_2O for footwall alteration and Price Formation samples. Least altered samples from the Thelwood Valley have high Na_2O contents (>3wt%) and low sulfur (0.01wt%). In contrast, Battle Zone samples have low Na_2O contents (<1.0wt%) and sulfur content (>1.5wt%). Thus the S/Na_2O ratio provides an excellent regional discriminator in the Myra Falls area.

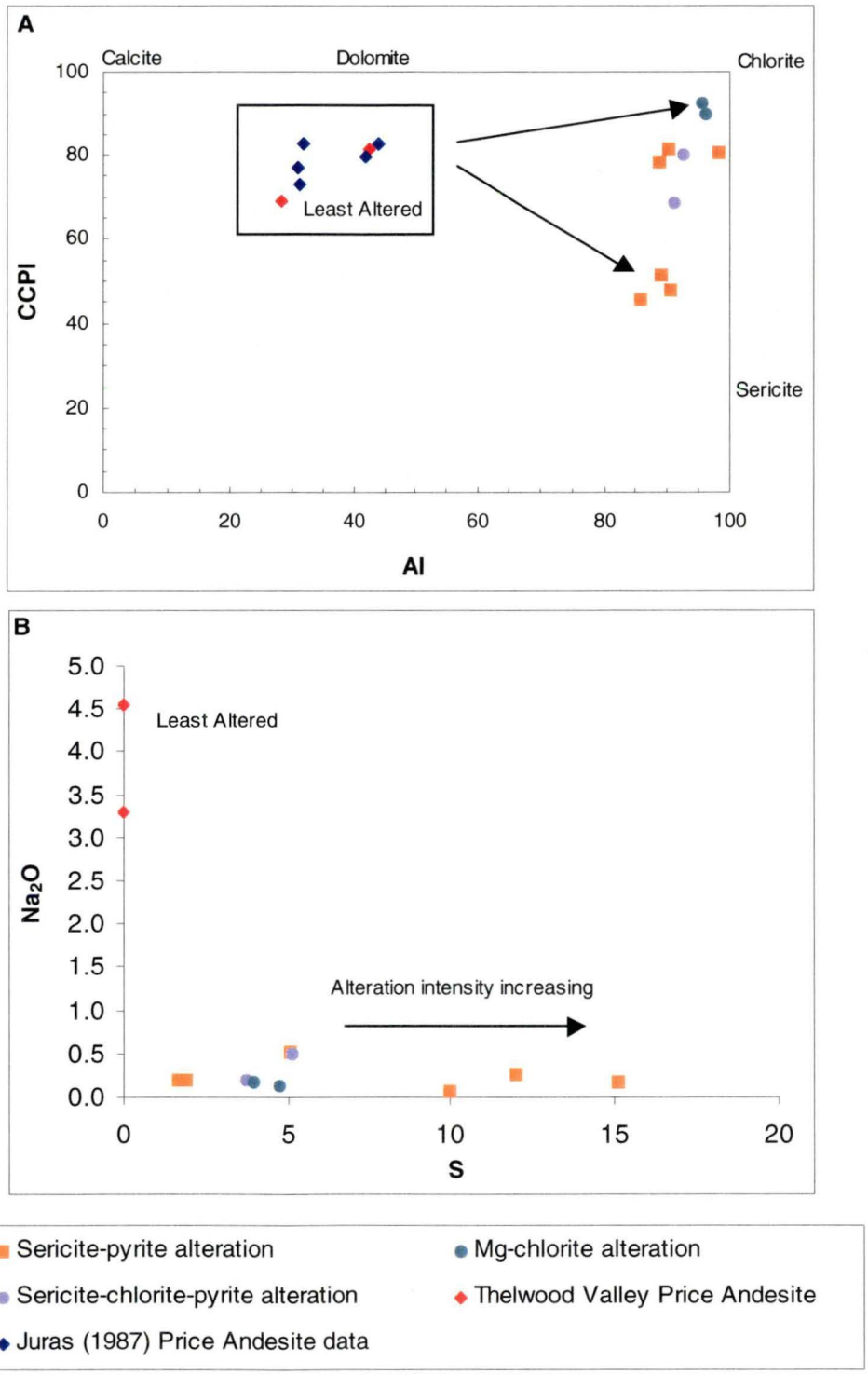

Figure 38 A. Alteration box plot for footwall alteration. B. S/Na_2O plot for Price Formation. S was not measured in Juras (1987) samples thus they are not plotted on S/Na_2O plot.

Figure 39A shows hangingwall alteration with all Battle Zone samples, except the dolomite altered sample, plotting towards sericite. Only two of the Thelwood Valley QFP samples plot in the least altered field, which is important for determining precursor rocks in section 5.6. The S/Na_2O index (Fig. 39B) for hangingwall alteration is less effective than in the footwall Price Formation due to the low Na_2O content of rhyolites. However as a proximal vector to ore it may prove useful.

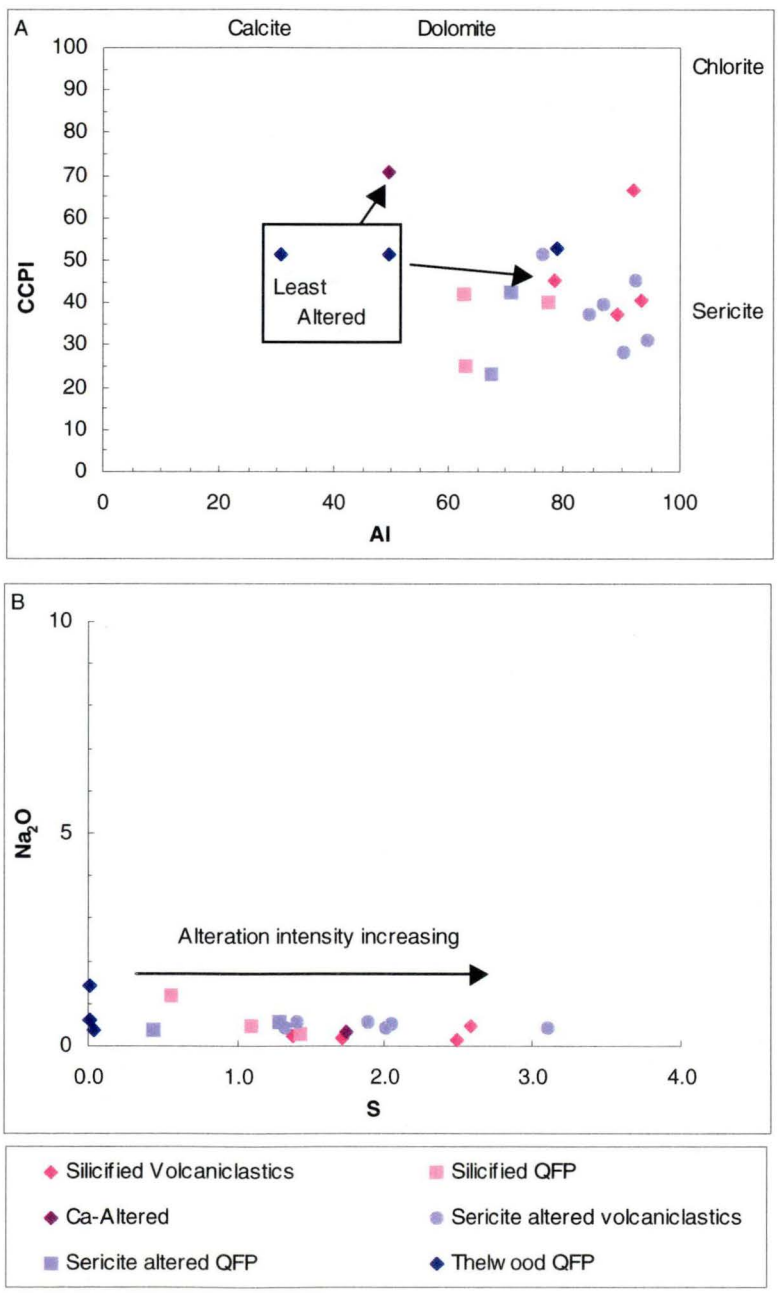

Figure 39A. Alteration Box plot for altered HW Rhyolite. B. S/Na_2O plot for altered HW Rhyolite.

5.7 Down hole plots

A composite down hole plot from the 1420mE section is provided as a visual guide to the chemical changes occurring between alteration types and in proximity to ore (Fig. 40). In the footwall SiO_2 is generally low reflecting the original andesite compositions although highs occur in the sericite-pyrite alteration zone associated with localised silicification. In the hangingwall SiO_2 shows a general decrease from >90% in cherts overlying massive sulfide mineralisation, up through the hangingwall alteration to the lowest values in the dolomite altered sediments. This SiO_2 trend is disrupted when Upper Zone mineralisation is present, as SiO_2 contents are high around these lenses. MgO shows moderate values in the sericite-chlorite-pyrite altered footwall, low values in the intense sericite-pyrite altered sediments, with sharp increases in Mg-chlorite altered zones. MgO is also low in the hangingwall except where dolomite alteration occurs. CaO is low in all alteration types except in the dolomite altered hangingwall. In the footwall K_2O is sporadic in the sericite-pyrite-altered zone and strongly depleted in the Mg-chlorite alteration. In the hangingwall K_2O is low around ore zones (e.g. in cherts and around Upper zone ore lenses) but moderate through the rest of the hangingwall. Cr shows peaks in cherts and mixed sediments but is low elsewhere. Fe_2O_3 shows moderate values in the footwall with a general increase toward the base of the massive sulfide lenses, and is low in the hangingwall. Barium decreases toward the base off the massive sulfides in the footwall but is enriched in the hangingwall above the zone of strong SiO_2 enrichment. The metals Cu, Pb and Zn are generally low in the footwall, but show sporadic enrichments in the hangingwall. Cu shows a small increase directly below the massive sulfide ores while Zn is elevated directly above ore lenses. The alteration index (AI) decreases around ore lenses in both the footwall and hangingwall, while CCPI alteration index is more sporadic. In the footwall the CCPI is higher associated with the Mg-chlorite alteration. In the hangingwall the CCPI is very sporadic, showing lows around ore lenses (Battle and Upper zone), with highs in the cherts, mixed sediments and dolomite alteration.

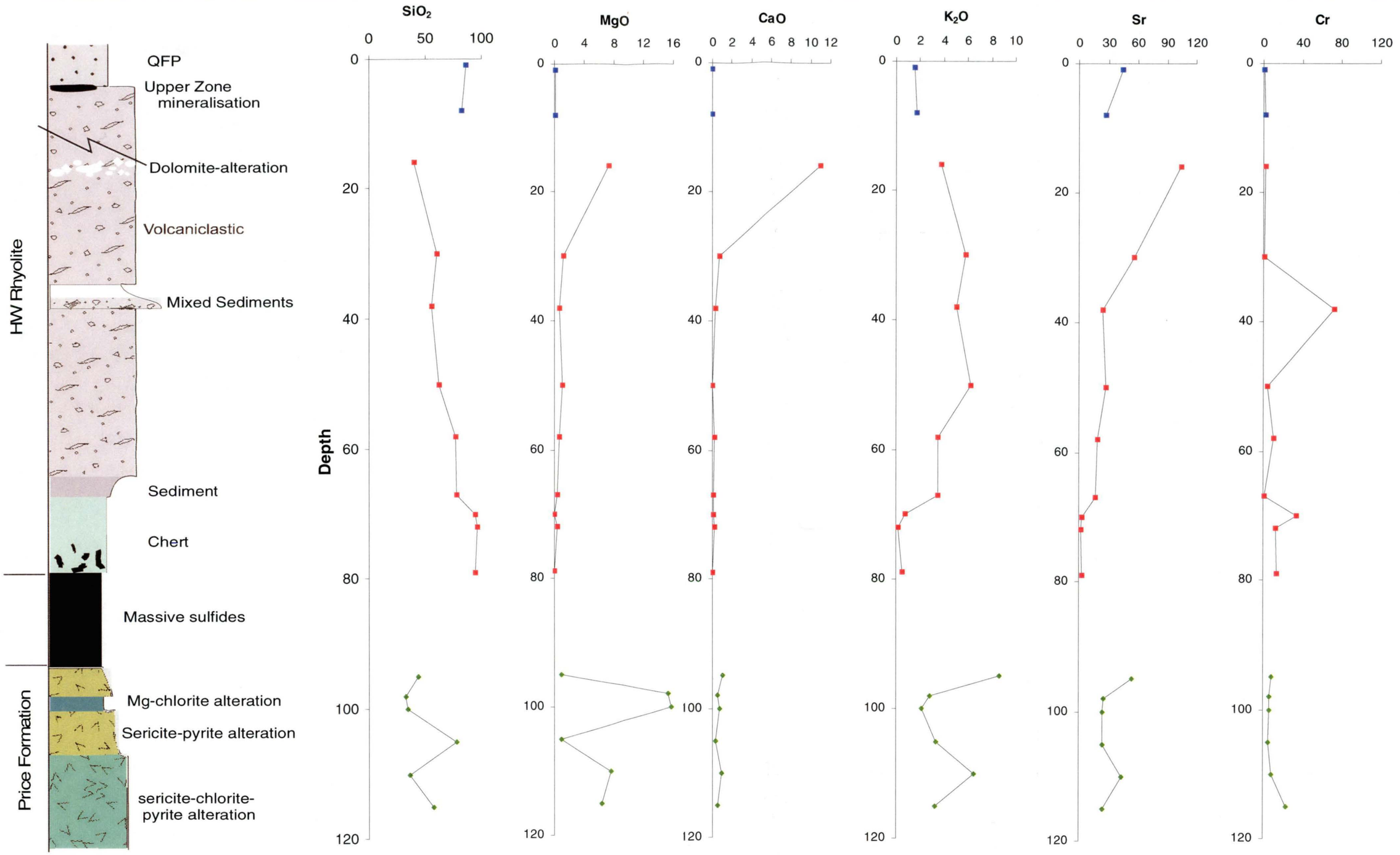

Figure 40 Composite Down hole plot from 1420mE section showing changes in chemistry with alteration type.

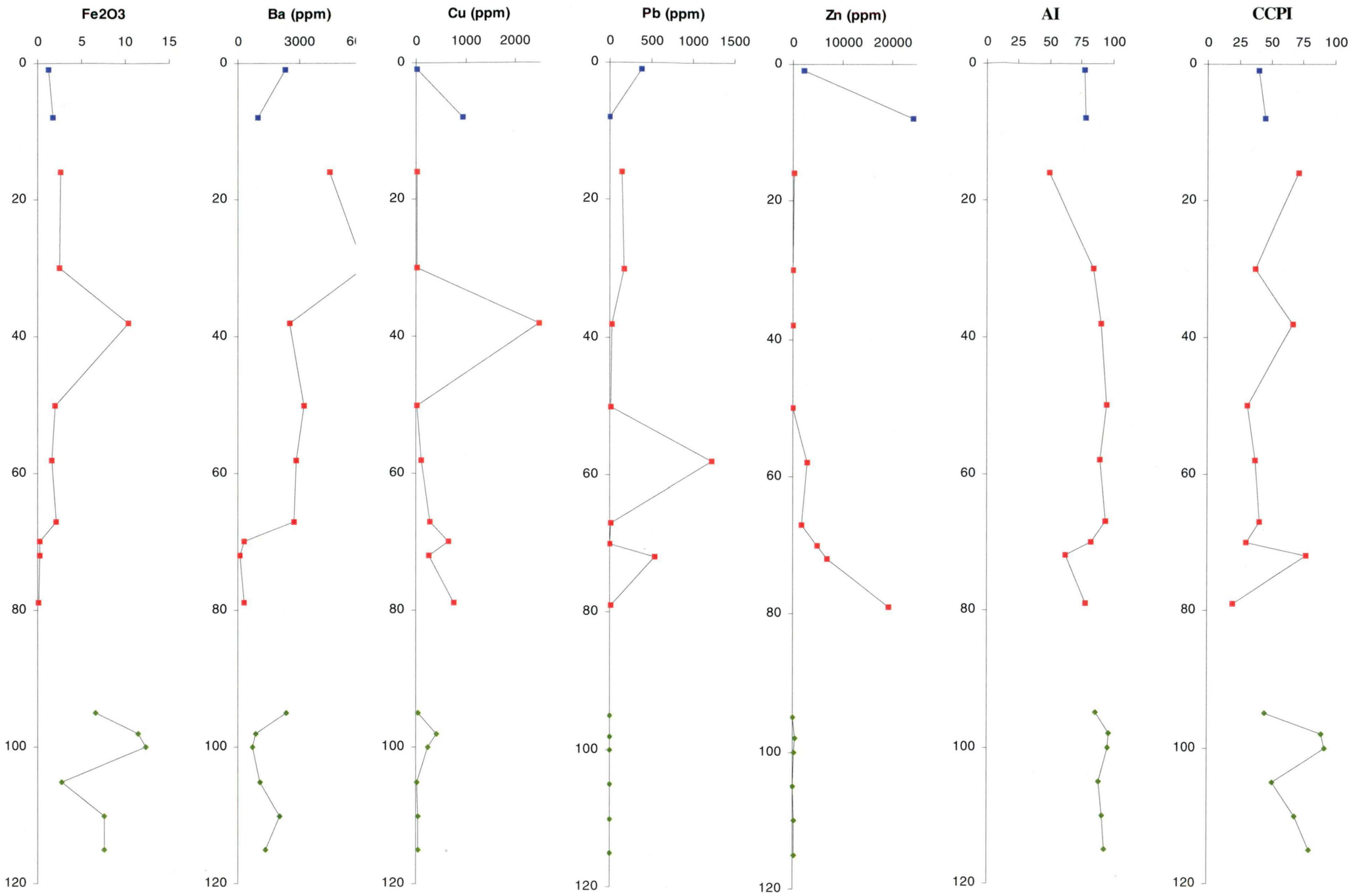

Figure 40continued. Composite Down hole plot from 1420mE section showing changes in chemistry with alteration type.

5.8 Mass balance analysis to determine chemical changes

5.8.1 Introduction

A number of lithogeochemical data procedures have been devised to quantify mass changes occurring in rocks during alteration. These techniques are summarised in Lentz (1994) and form three major groups: Gresens Analysis - based on work of Gresens (1967); Pearce Element Analysis - based on the work of Pearce (1968); and a method developed by MacLean and Kranidiotis (1987), MacLean (1990), and MacLean and Barrett (1993). Robinson (1994 & 1996) used Pearce Element ratios to evaluate the alteration in the Battle Zone, while Barrett and Sherlock (1996) used the methods of MacLean and Kranidiotis (1987) to calculate the mass changes for the alteration surrounding the HW deposit. This study uses Gresens analysis, as modified by Huston (1987), to quantify the mass changes in alteration around the Battle Zone and compares the results with previous studies in the Myra Falls district to further the understanding the geochemical changes produced by hydrothermal alteration.

5.8.2 Treatment of Data

Gresen (1967) derived a set of equations, using the chemical analyses of unaltered and altered rocks and specific gravity that allowed the calculation of changes of elements during hydrothermal alteration. These equations were used by Grant (1986) to provide a graphical method, the isocon diagram, for determining gains and losses during alteration. Huston (1987) refined the graphical method of Grant (1986) to produce the equations and diagrams used in this study. A number of authors (Gemmell and Large, 1992; Huston, 1987& 1993), have used this method to quantify alteration around VHMS orebodies.

The isocon diagram plots scaled chemical analyses from altered against unaltered rocks as an indication of changes in composition. The isocon is defined by immobile elements which plot along a straight line, that passes through the origin (Grant, 1986). The slope is dependant on the addition (or subtraction) of net mass without gain or loss of the immobile elements and is used to define the isocons. The isocon are determined by plotting scaled concentrations of elements (CiS) using the formula (Huston 1993):

$$CiS = ni\ [Ci / CiO] \qquad (1)$$

where ni = an integer, each element is assigned an integer depending on their order on the diagram (eg 1, 2, 3,...), Ci = the concentration of element (i) in the sample and CiO = the concentration of element (i) in the least-altered equivalent, both Ci and CiO are in wt%. The isocon slope (m) can be estimated by inspection, fitting a line through the immobile elements. However a more rigorous approach is to take the mean and standard deviation of:

$$m = CiA,im / CiO,im \qquad (2)$$

where CiA,im = the concentration of immobile element (i) in the altered sample and CiO,im = the concentration of immobile element (i) in the least-altered equivalent.

Once the isocon is determined the net gain or loss of mass during alteration can be determined. If no net mass change occurred during alteration, the isocon slope is one. If a change has occurred the net mass change (MA) relative to the least-altered equivalent can be estimated using the equation (Huston 1993):

$$MA(\%) = [100/m]-100 \quad (3)$$

The isocon diagram can also be used to estimate the relative gains and losses for particular oxides and elements. Elements that gained mass during alteration will plot above the isocon and elements that lost mass will plot below the isocon. Relative mass changes (CiA) can be quantified using:

$$CiA(\%) = 100*((m*(CiA / CiO))-1) \quad (4)$$

Absolute Mass changes may also be calculated using the equation (Grant, 1986):

$$CiA(g/100g) = [CiA(\%)/100] * CiO \quad (5)$$

The calculated relative and absolute mass changes are then plotted on histograms for interpretation.

This method of calculating mass changes has several limitations: (1) mass changes are calibrated against a least-altered equivalent, which may or may not be the protolith to the altered rock, (2) the least-altered equivalent may have internal variations in composition independent of alteration. The choice of a least-altered sample should be combined with detailed field mapping, petrographic and immobile element studies to minimise the risk of choosing an unrelated rock. Internal variations in the least-altered sample can be minimised by using the means and standard deviations of several analyses of the least-altered equivalent where available. Huston (1987) also recommended that small (< 5g/100g) apparent gains or losses calculated from the isocon should not be interpreted as the result of alteration as altered rocks also have internal variation in composition due to the variation in intensity of alteration. This should also be minimised by using the average of multiple altered samples.

5.8.3 Precursor rocks

Price Formation (Footwall) – Figure 38 shows the Thelwood Valley samples (this study) along with Juras (1987) Price Formation samples. All these samples lie within the least altered box. However, Juras's (1987) data is not used due to the discrepancy in the Nb values between these samples and the current data. Thus the least altered precursor used for the Gresens analysis is the average of the Thelwood Valley samples from the present study only. The author acknowledges that these samples may not represent the exact initial compositions of the Price Formation in the Battle Zone, thus small gains and losses (<10%) in the following results may not be significant. Both the Thelwood Valley samples show weak regional chlorite-epidote-carbonate assemblages (see chapter 4). Thus the Gresens analysis below defines only the hydrothermal component of alteration and not the regional alteration. However, as all samples away from sulfide mineralisation are assumed to have undergone regional alteration (Juras 1987), this comparison is considered valid.

HW Rhyolite (Hangingwall) - Figure 39 shows that only two of the Thelwood Valley QFP samples lie within the precursor box, thus only these samples will be used as precursor rocks for the HW Rhyolite in the Battle Zone. Mass balance calculations have not been carried out for the cherts and mixed sediments because of a lack of a reliable precursor composition.

5.8.4 Relative Mass Change

Footwall alteration - Price Formation

Sericite-pyrite alteration - An average six analyses of samples from the sericite-pyrite alteration zone are to represent the variation in this alteration style (Table 2A and 3A, Appendix 2). On the isocon diagram (Fig. 41A) Zr, Ti, Al, Nb and Y all lie along the a line passing through the origin. Thus all were used to calculate the isocon (m = 0.802). Isocon analysis shows a large gains in S, Cu, Ba, Rb, K, Pb and As. With moderate gains in Si, P and Fe. Manganese, Mg, Ca, Na, Ni, Cr and Sr all show loses.

The gain in K, Rb, Ba and Si and loss of Sr, Ca, Na, Mg and Mn reflect the destruction of feldspar, chlorite, epidote and carbonate and replacement by muscovite and quartz. Gains of S, Cu, Pb, Fe, and As result from sulfide minerals (particularly pyrite, chalcopyrite and galena) in the alteration.

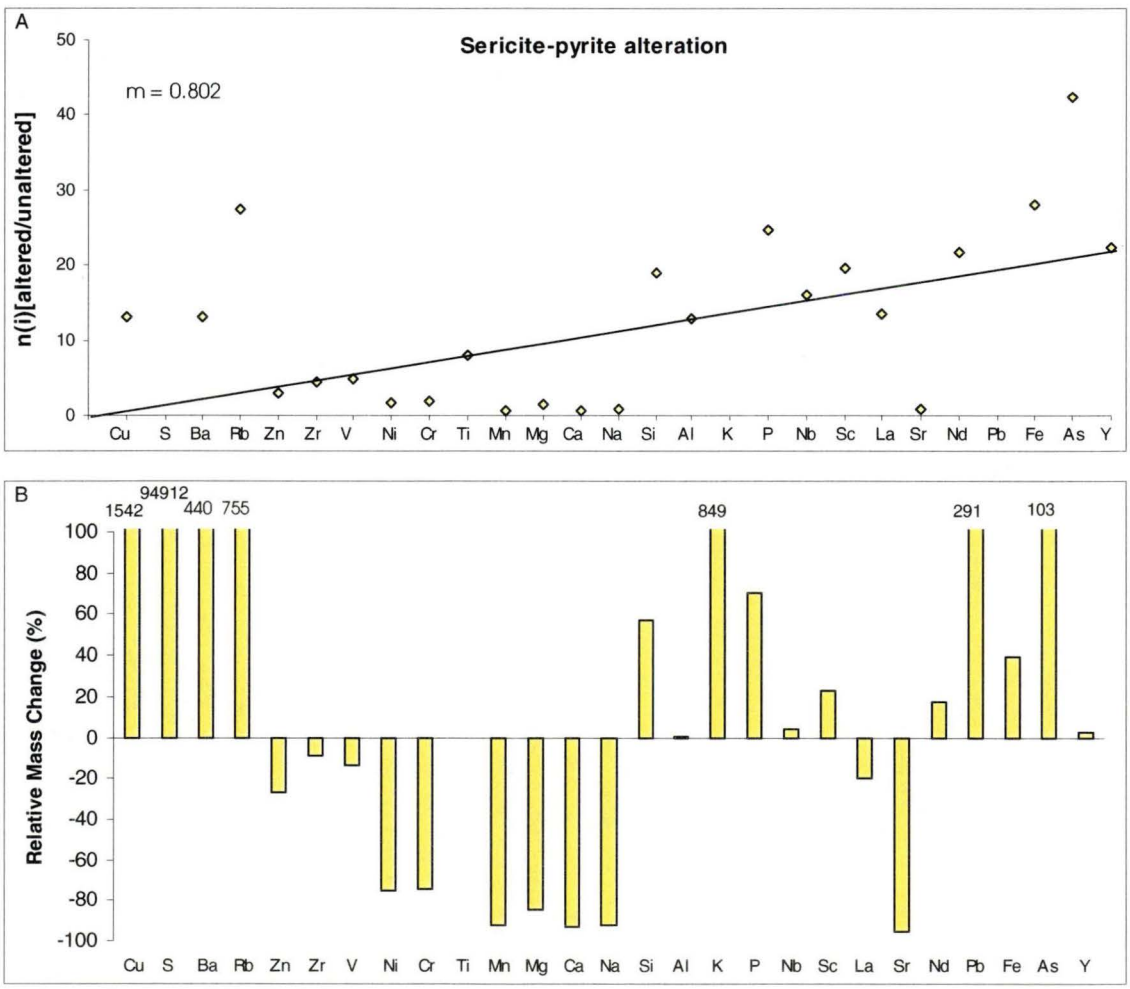

Figure 41. A. Isocon diagram for sericite-pyrite altered Price Andesite underlying the Battle Zone Deposits. B. Relative mass change for footwall sericite-pyrite altered Price Andesite.

Mg-chlorite alteration - This alteration style shows less variation than the sericite-pyrite alteration and is less abundant thus the average of two samples were used to characterise the Mg-Chlorite alteration in the Battle Zone (table 2A and 3A, Appendix 2). Figure 42A shows Zr, Ti, Al and Y all lying on a line through the origin, thus these four elements are used for the calculation of isocon. The isocon slope was calculated at m = 1.188 indicating a decrease in the mass of rock during alteration. The isocon has large gains in S, Cu, Ba, Rb, Zn, Mg, Mn, and K. Nickel, Cr, Ca, Na, Sr, and As all show moderate losses. While Si and Pb show small losses.

Gain in Mg and Mn reflects the formation of Mg-rich chlorites in the alteration type. Gains of K, Rb and Ba are due to the presence of muscovite in the Mg-chlorite alteration. Calcium, Na and Sr are lost through the destruction feldspar. Gain in S, Cu, and Zn indicate the presence of sulfides in the Mg-chlorite alteration.

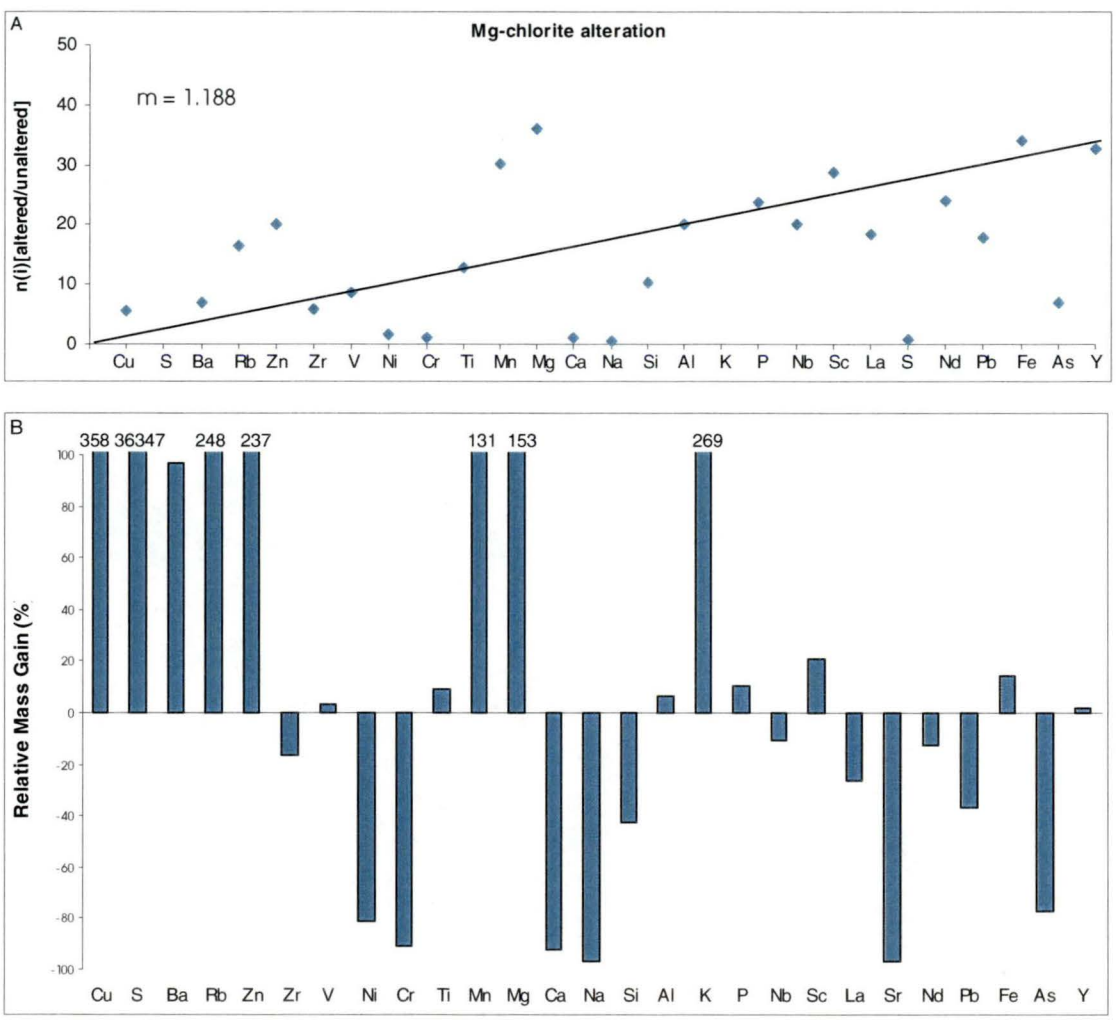

Figure 42. A. Isocon diagram for Mg-chlorite altered Price Andesite underlying the Battle Zone lenses. B. Relative mass change for footwall Mg-chlorite alteration of Price Andesite.

Sericite-chlorite-pyrite alteration is represented by the average of two analyses in the Battle Zone(table 2A and 3A, Appendix 2). Zirconium, Ti, Al, Nb and Y all lie along a line that passes through the origin (Fig. 43), thus all are used to calculate the isocon. The isocon has a slope of 1.166 indicating a decrease in the mass of the rock during sericite-chlorite-pyrite alteration. Sulfur, Ba, Rb, K, Pb, P and Zn all show gains in the sericite-chlorite-pyrite alteration. Copper, Zn, Ni, Cr, Ca, Na, Sr, Fe and As all show losses.

Sericite-chlorite-pyrite alteration is the weakest alteration type in the Battle Zone footwall. Feldspar is destroyed (loss of Ca, Na and Sr) and muscovite added (increase in K, Rb and Ba). Chlorites are converted from intermediate compositions (Mg# = 0.52) to Mg-rich (Mg# = 0.93) retaining Mg while Fe is lost. Sulfur is added along with Pb and Zn indicating the addition of ore forming minerals.

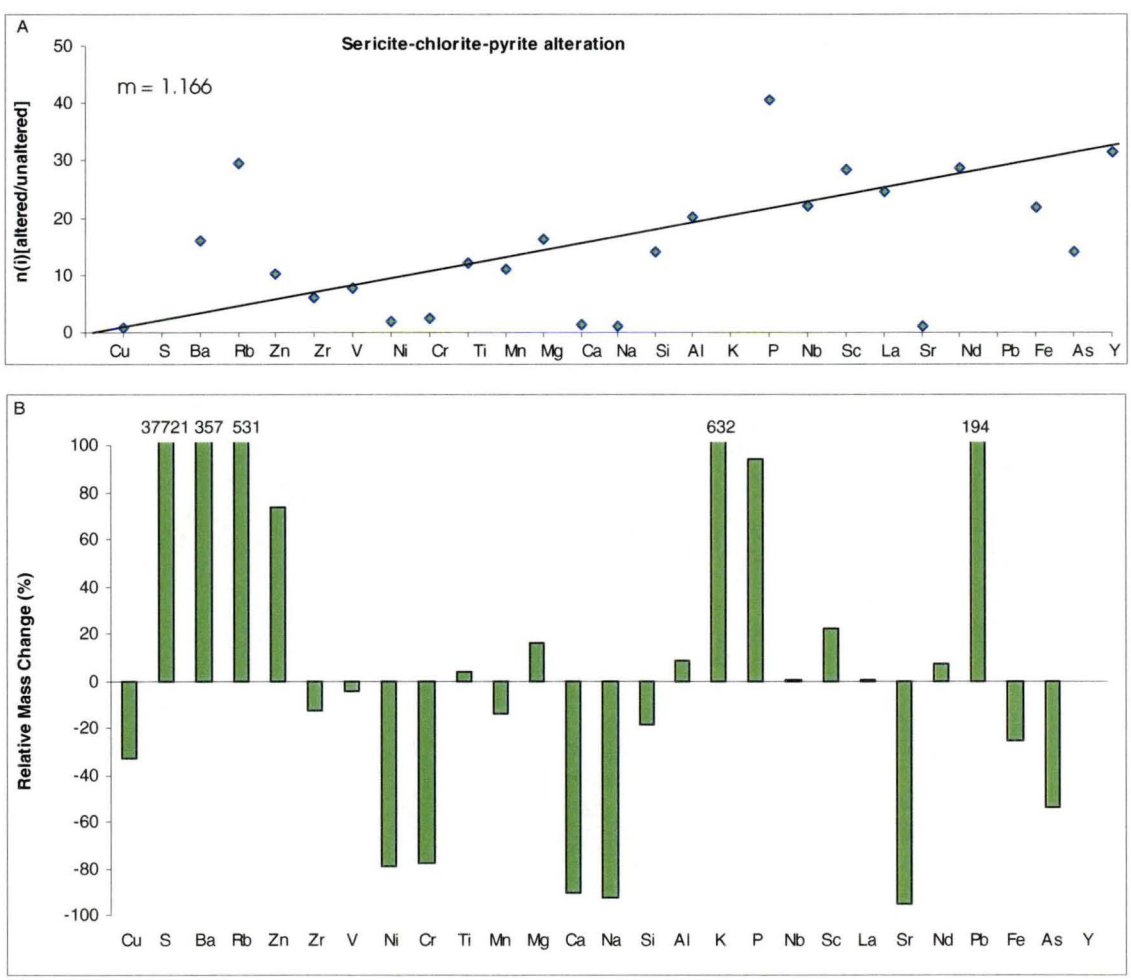

Figure 43. A. Isocon diagram for sericite-chlorite-pyrite altered Price Andesite, underlying Battle Zone lenses. B. Relative mass change for footwall sericite-chlorite-pyrite alteration.

Summary of the relative changes during alteration of Price Formation

All footwall alteration types show relative mass gains in Ba, Rb and K. The Mg-chlorite alteration shows a gain in Mg and Mn, while the sericite-pyrite alteration loses Mg and Mn and the sericite-chlorite–pyrite alteration has a weak gain in Mg and a weak loss of Mn. All alteration types show relative losses of Sr, Cr, Ni, Ca and Na. Phosphorous is gained in the sericite-pyrite and sericite-chlorite-pyrite alteration types. In the Mg-chlorite alteration P is highly variable resulting in little overall change. Silica is gained in sericite-pyrite alteration and lost from the Mg-chlorite and sericite-chlorite–pyrite alteration zones.

The metals (Cu, Zn, Pb, Fe and As) show a great deal of variation. Copper shows a massive relative gain in the sericite-pyrite and Mg-chlorite alteration but is lost in the sericite-chlorite–pyrite alteration. Zinc is gained in the Mg-chlorite alteration but shows small to moderate losses in the sericite-pyrite and sericite-chlorite-pyrite alteration types. Lead shows gains in the sericite-pyrite alteration and sericite-chlorite–pyrite alteration and a loss in the Mg-chlorite alteration. Arsenic shows a strong gain in the sericite-pyrite alteration, but is lost from the Mg-chlorite and sericite-chlorite–pyrite alteration. Iron is gained in the sericite-pyrite and Mg-chlorite alteration zones and is lost in the sericite-chlorite-pyrite alteration. Sulfur has massive relative gains in all footwall alteration types.

Hangingwall alteration - HW Rhyolite

Silicification – In silicified rocks Zr, Ti and Al all fall on a line passing through the origin for both facies (Fig. 44 A & C) therefore all three elements are considered immobile and were used to calculate the isocon slope. The isocon slopes for silicified Facies 1: Volcaniclastics, and Facies 4: QFP, are 0.68 and 0.78 respectively. Both facies show strong gains in S, Cu, Zn, Ni, Cr, Nd, Pb and As, with lesser gains in Ba, Si, K, and La. Both Facies also show relative losses of Ca, Mg, V, P and Na. The Facies 1 volcaniclastics also lose Na and Sr. While the Facies 4: QFP loses Fe and gains Sr. These changes reflect the addition of quartz, barite and sulfide minerals (sphalerite, galena, chalcopyrite and tennantite) along with the destruction of feldspar (loss of Ca & Na in the volcaniclastics).

Sericite alteration – Zr, Ti and Al all lie on a line that passes through the origin for both facies (Fig. 44 E & G). Isocon slopes for Facies 1 Volcaniclastics (1.415) and Facies 4: QFP (1.57) indicate a decrease in the mass of these rocks during alteration. Facies 1 sericite-alteration (Fig. 44 E & F) has gains in S, Cu, Ba, Zn, Pb, Ni, As, Nd, La and K. Losses of Ca, P, Sr, Na, V, Mg, and Si are recorded in the Facies 1 sericite-altered rocks. In contrast the sericite-altered QFP shows strong gains in S, Ba, Ni, La, Nd, and Pb along with lesser gains in Nb, K and Zn. Sericite altered Facies 4 (QFP) has losses of Ca, Na, Sr, V, Cr, Si, P, Fe and As.

The difference in relative changes between the facies reflects the variation in intensity of alteration between the highly permeable volcaniclastics which directly overlie the ore and host Upper Zone lenses, and the less porous QFP which occurs further away from ore lenses. Feldspar destruction (loss of Ca and Na) and the addition of sericite (gain of K, Rb, Ba) and barite (Ba) is recorded in both

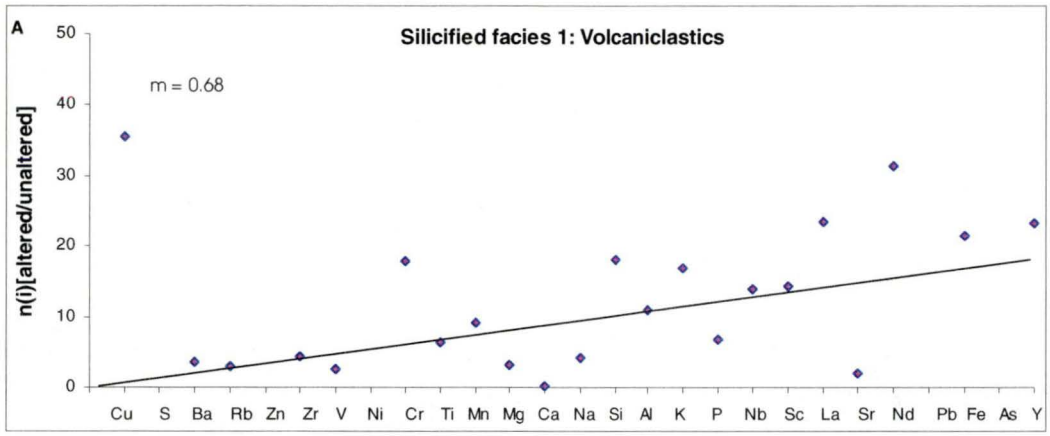

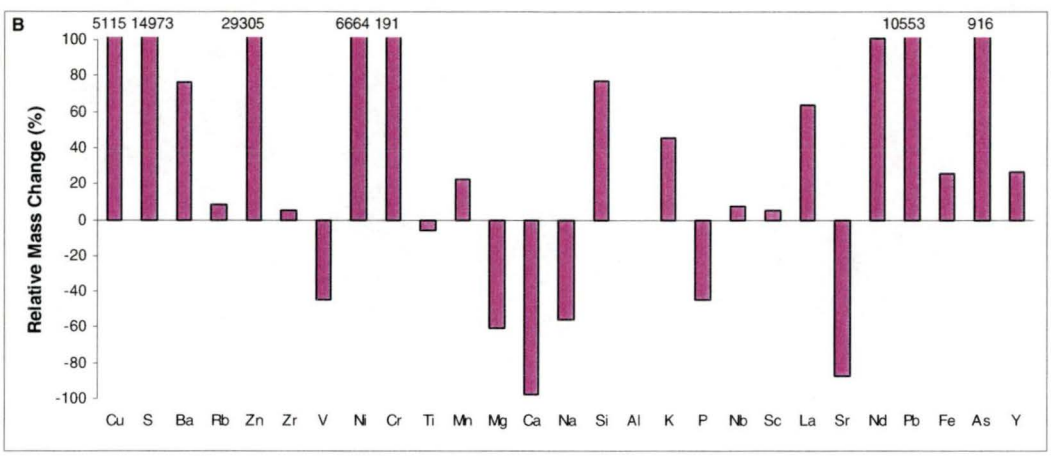

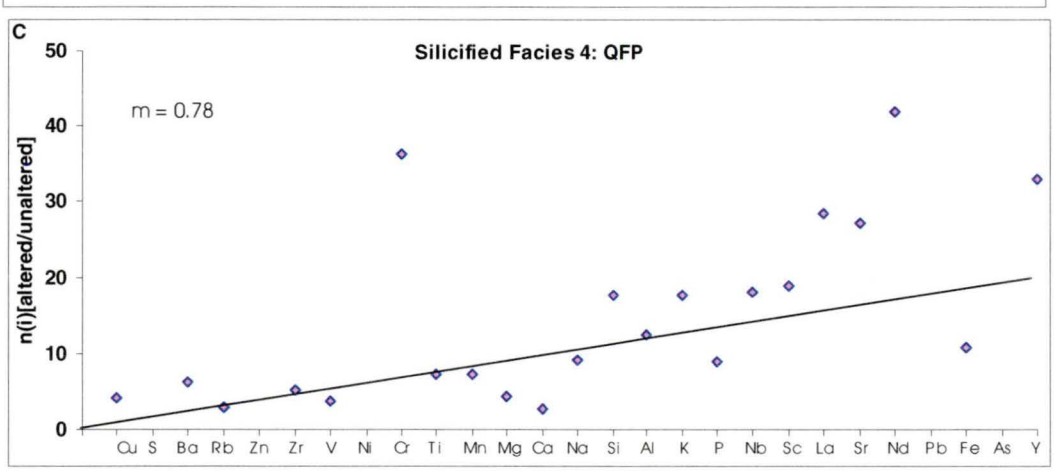

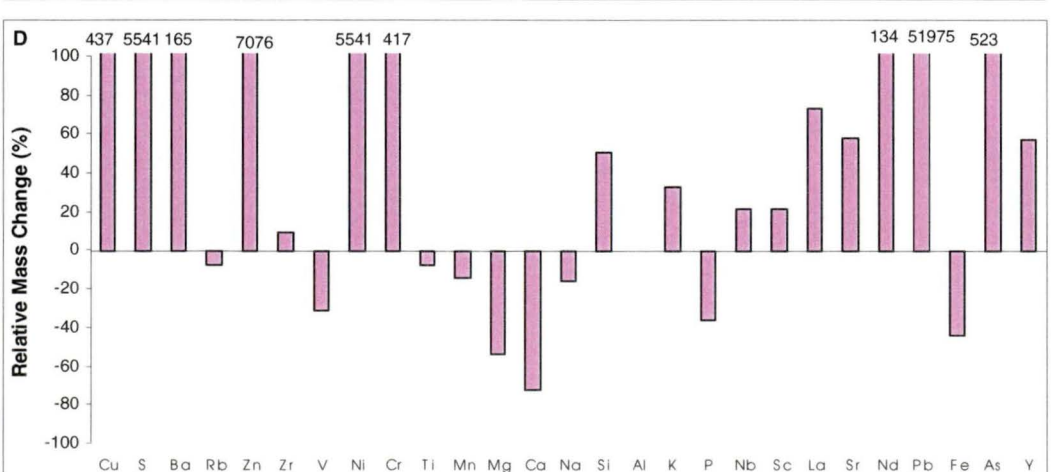

Figure 44 A - D. Isocon diagrams and relative mass change plots for silicified Facies 1 (A & B) and silicified Facies 4 (C & D).

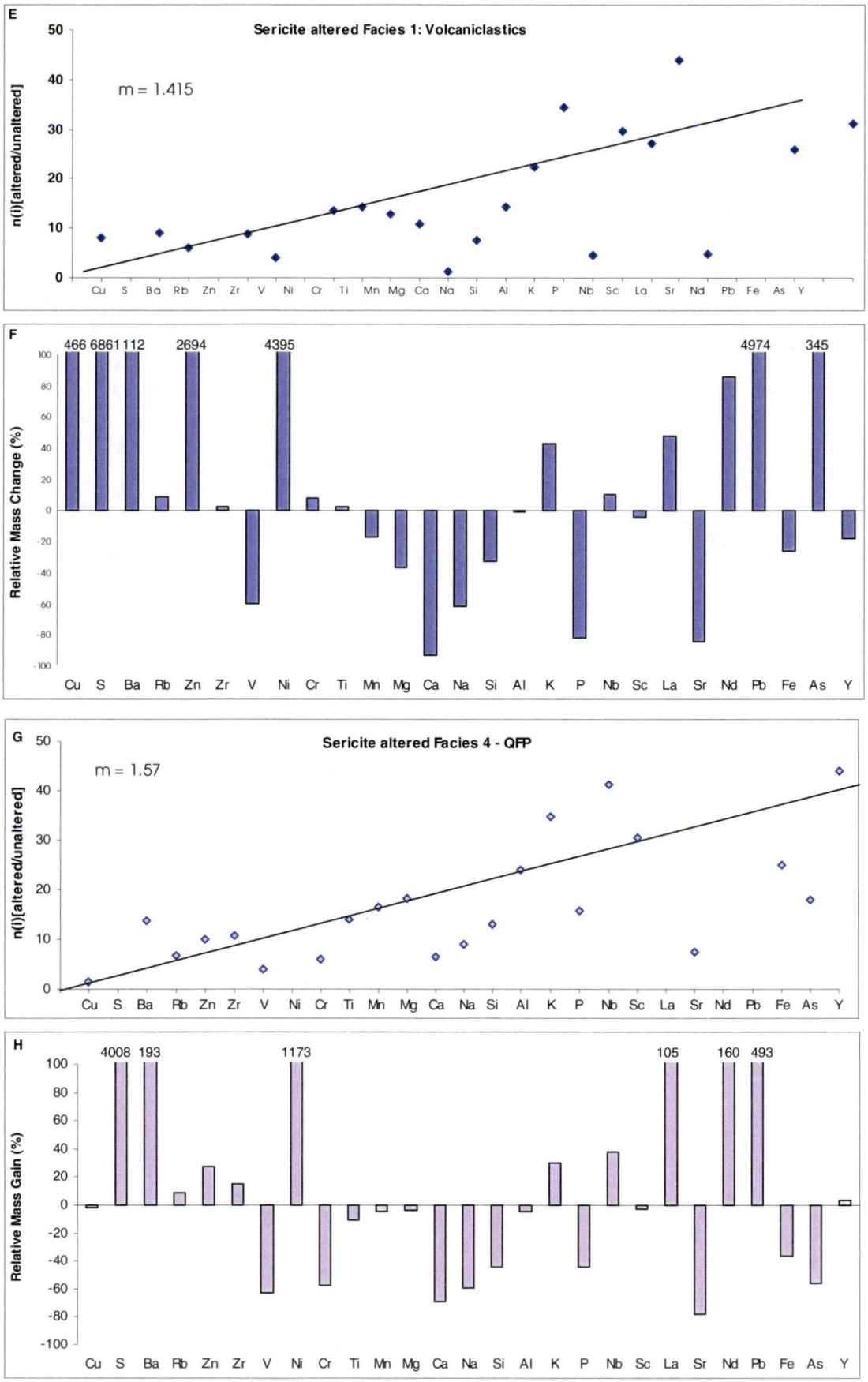

Figure 44 continued E - H. Isocon diagrams and relative mass change plots for sericite altered Facies 1 (E & F) and sericite altered Facies 4 (G & H).

facies. Greater relative gains and losses show the intensity of alteration in the Facies 1 volcaniclastics.Enrichment of rare earth elements La and Nd due to primary La/Zr and Nd/Zr ratios being lower in the precursor rocks than in the Battle Zone samples (Fig. 45).

Both alteration types gain S, Zn, Pb and Ni indicating the addition of sulfide minerals. However, the Facies 1 rocks gain larger amounts than the Facies 4 rocks, Facies 1 rocks also gain Cu. Loss of V may indicate leaching of this element by the hydrothermal fluid, which fits with the mineralogy of Upper Zone and Gap lenses (Chapter 7).

Dolomite alteration the isocon (Fig. 44I) is defined by Zr, Ti and Al and has a slope of 1.12 indicating a loss in mass of the rock during alteration. Large relative gains in S, Ba, Zn, Ni, Mn, Mg, Ca, La, Nd, Pb and are observed while lesser gains in Cu, K, Nb, Sc and Y are also observed. Vanadium, Na, P, Sr, and Si all show losses.

The relative changes reflect the destruction of feldspar (loss of Na and Sr) and the removal of Si. Along with the addition of Mg, Mn and Ca in the form of dolomite and the addition of sulfide minerals (S, sphalerite (Zn), galena (Pb), tennantite(As)) and barite (Ba). Muscovite alteration (addition of K) also occurs in the carbonate alteration rocks.

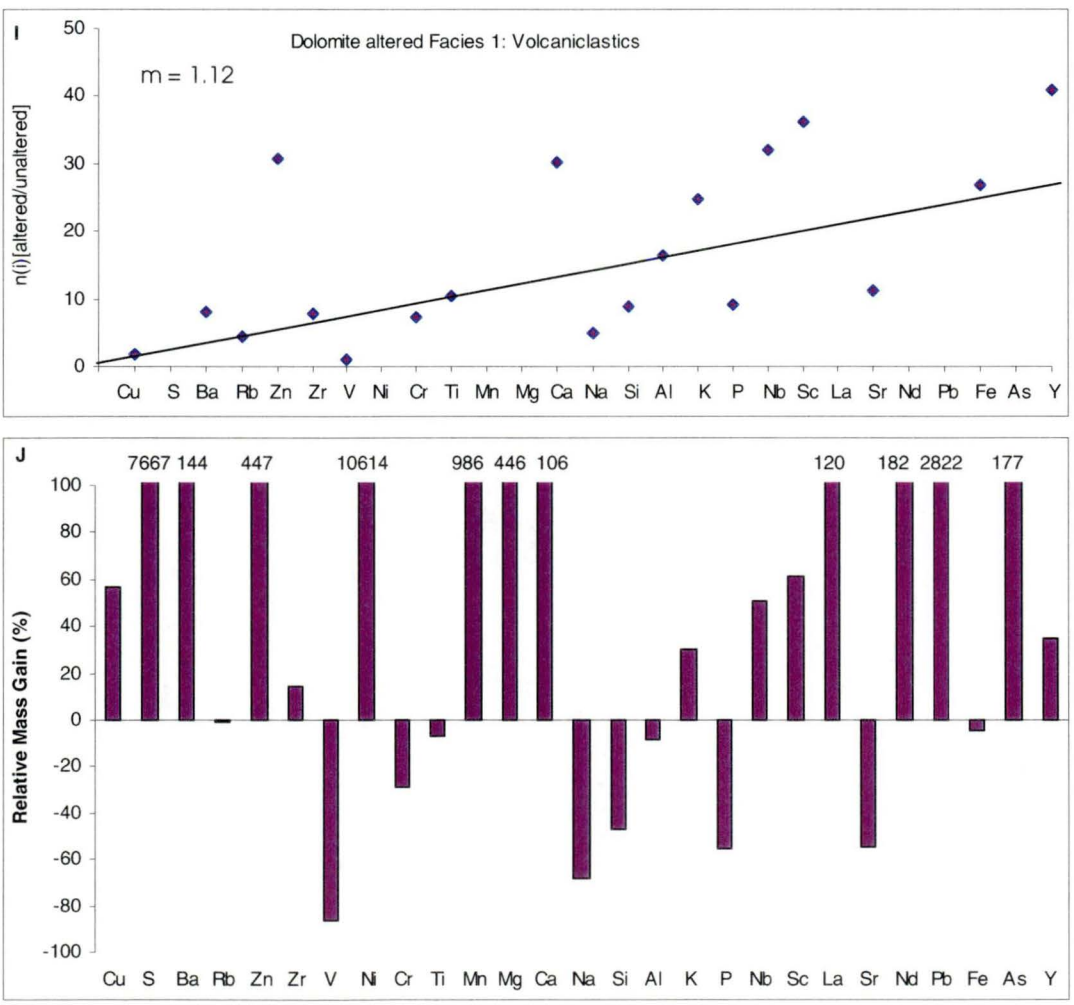

Figure 44 continued I-J. Isocon diagrams and relative mass change plots for dolomite altered Facies 1.

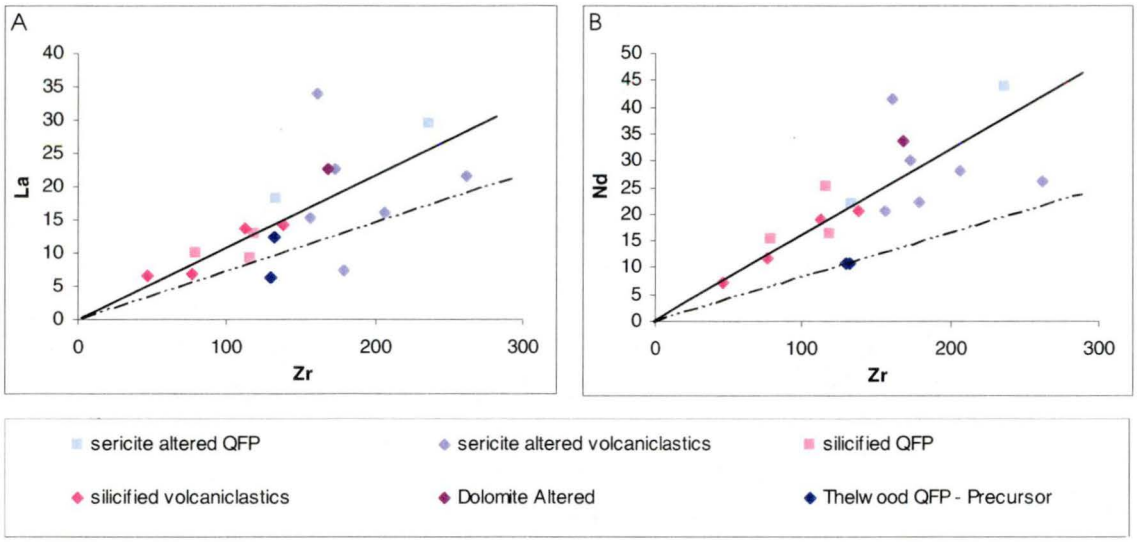

Figure 45 La-Zr and Nd-Zr plots for HW Rhyolite alteration facies.

Summary of the relative changes during alteration of HW Rhyolite

In all hangingwall alteration types K and Ba are gained due to the formation of muscovite. Silicified and sericite altered rocks show losses of Mg, Ca and Na due to the destruction of feldspar, while Si is gained in the silicified facies (addition of quartz) and depleted in sericite altered facies (removal of quartz). Dolomite alteration shows a loss of Sr, Na and Si due to the destruction of feldspar and removal of quartz. However, dolomite alteration gains in Mg and Ca, due to the formation of dolomite. Phosphorus and V is lost in all alteration types. Strontium is also lost in all alteration types except the silicified QFP.

Sulfur, Ni, and Pb show large relative increase in all alteration types, while Cu and Zn are gained in all alteration types except the sericite altered QFP. These changes represent the addition of sulfide minerals (galena, chalcopyrite and sphalerite) to all alteration types except the sericite altered QFP which gains only galena. Iron shows weaker changes in the hangingwall alteration than the other metals with increases in the silicified volcaniclastics and dolomite alteration due to the formation of pyrite and decreases in the silicified QFP and sericite alteration (both facies). Arsenic is also gained in all alteration types except the sericite altered QFP due to the formation of tennantite.

5.8.5 Absolute Mass Change

Footwall alteration

Absolute mass change for footwall rocks is summarised in Figure 46 and Table 17. All footwall alteration types loose Ca and Na due to the destruction of feldspar and gain K through the formation of sericite. However the absolute loss or gain of Si is the major contributor to the gain or loss of mass in the rock during alteration. Sericite-pyrite alteration shows a mass gain of 24.7g/100g of rock due to an absolute mass gain of Si (28.1g/100g), S (9.5g/100g), Fe (3.5g/100g) and K (4.8g/100g) and a loss of CaO (-6.3g/100g), MgO (-4.4g/100g) and Na (-3.6g/100g). The Mg-chlorite alteration has an absolute mass loss of -15.8g/100g of rock due to a loss of Si (-20.9g/100g), Ca (-6.3g/100g) and Na (-3.8g/100g), however the chloritic nature of the alteration is effected by mass gain of 7.9g/100g of Mg and pyrite is added Fe (1.3g/100g) and S (3.6g/100g). The sericite-chlorite-pyrite alteration has a mass loss of -14.2g/100g made up of loss in Si (-9.3g/100g), Fe (-2.2g/100g), Ca (-6.1g/100g) and Na (-3.6g/100g) and a gain in K (3.6g/100g) and S (3.8g/100g). All other elements show absolute mass changes of less than 1g/100g (Tables 6-8, Appendix 2).

	Sericite-pyrite	Mg-chlorite	Sericite-chlorite-pyrite
Change in mass	24.7	-15.8	-14.2
SiO_2	28.1	-20.9	-9.3
Fe_2O_3	3.5	1.3	-2.2
MgO	-4.4	7.9	0.8
CaO	-6.3	-6.3	-6.1
Na_2O	-3.6	-3.8	-3.6
K_2O	4.8	1.5	3.6
S	9.5	3.6	3.8

Table 17 Summary of the absolute changes (g/100g) in rock in the different styles of footwall alteration. Changes are relative to the least altered Price Andesite.

Hangingwall alteration

Absolute mass change for hangingwall rocks is summarised in Figure 47 and Table 18. Silicified Facies 1 Volcaniclastics show mass gains of Si (51.8g/100g) and Zn (11.0g/100g) along with minor gains in S and K and minor losses in Ca, resulting in a mass gain of 47.1g/100g. Silicified QFP show a similar, but lower gain and loss of elements with a resultant mass gain of 28.2g/100g due largely to the addition of quartz. In contrast the sericite altered rocks loose Si (-22.1 and -30.0g/100g respectively) and Ca (-4.4 and -3.2g/100g respectively) for a net mass loss of -29.3g/100g for sericite altered volcaniclaisitics and -36.3g/100g for sericite altered QFP. The dolomite altered sample also looses Si (-31.8g/100g) but gains Mg (5.4g/100g) and Ca (5.0g/100g) along with minor gains of K and S for a -10.7g/100g overall mass loss.

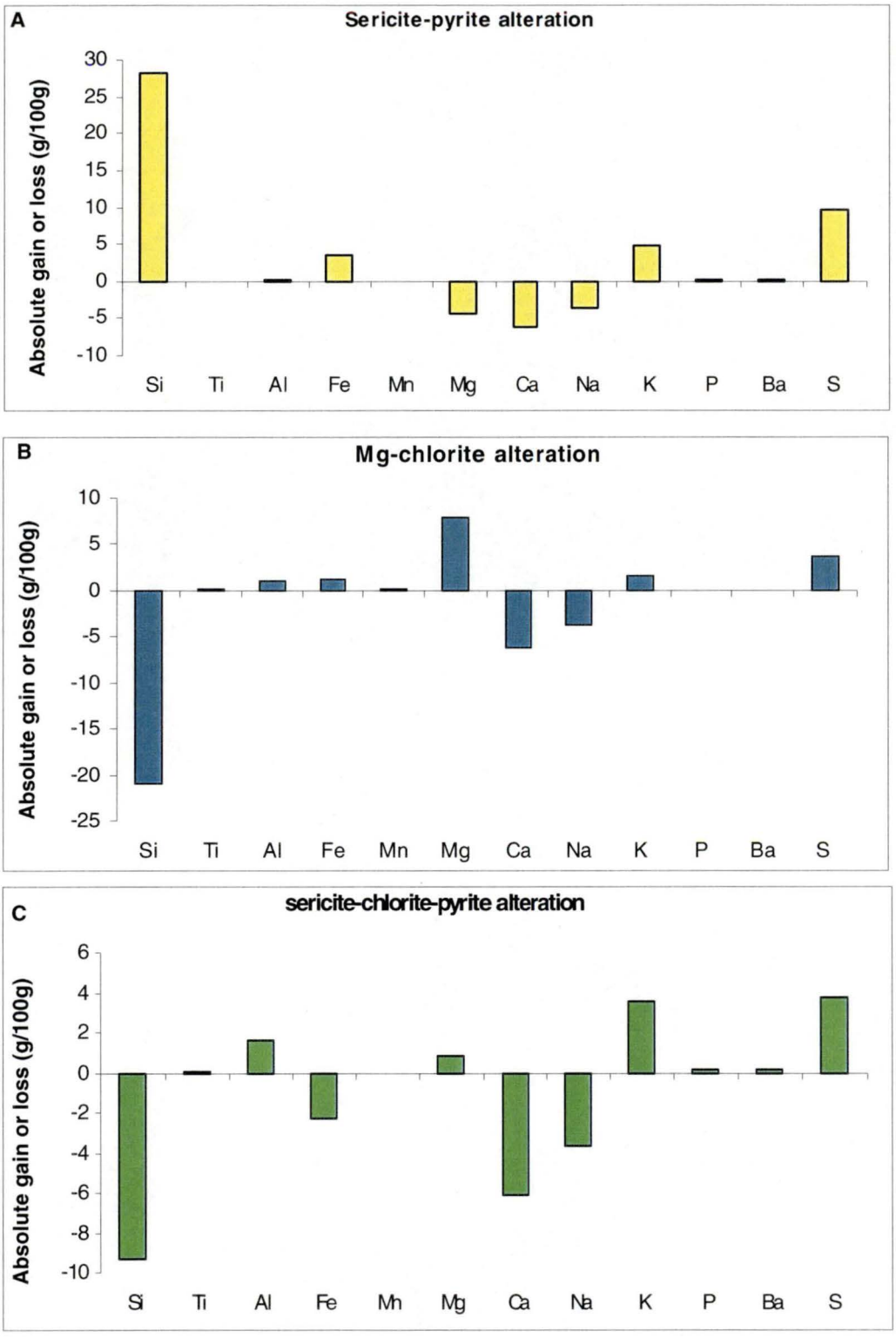

Figure 46. Absolute mass change in the different styles of footwall alteration. Changes are relative to least altered Price Andesite.

	Silicified Volcaniclastics	Silicified QFP	Sericite-altered Volcaniclastics	Sericite-altered QFP	Dolomite-altered Volcaniclastic
Change in mass	47.1	28.2	-29.3	-36.3	-10.7
SiO_2	51.8	34.0	-22.1	-30.0	-31.8
Fe_2O_3	0.6	-1.1	-0.7	-0.9	-0.1
MgO	-0.7	-0.7	-0.4	0.0	5.4
CaO	-4.6	-3.4	-4.4	-3.2	5.0
Na_2O	-0.5	-0.1	-0.6	-0.6	-0.6
K_2O	1.2	0.9	1.1	0.8	0.8
S	3.0	1.1	1.4	0.8	1.5
Pb	0.5	2.3	0.2	0.0	0.1
Zn	11.0	2.6	1.0	0.0	0.2

Table 18 Summary of the absolute changes (g/100g) in rocks due to hangingwall alteration of the HW Rhyolite. Changes are relative to least altered QFP.

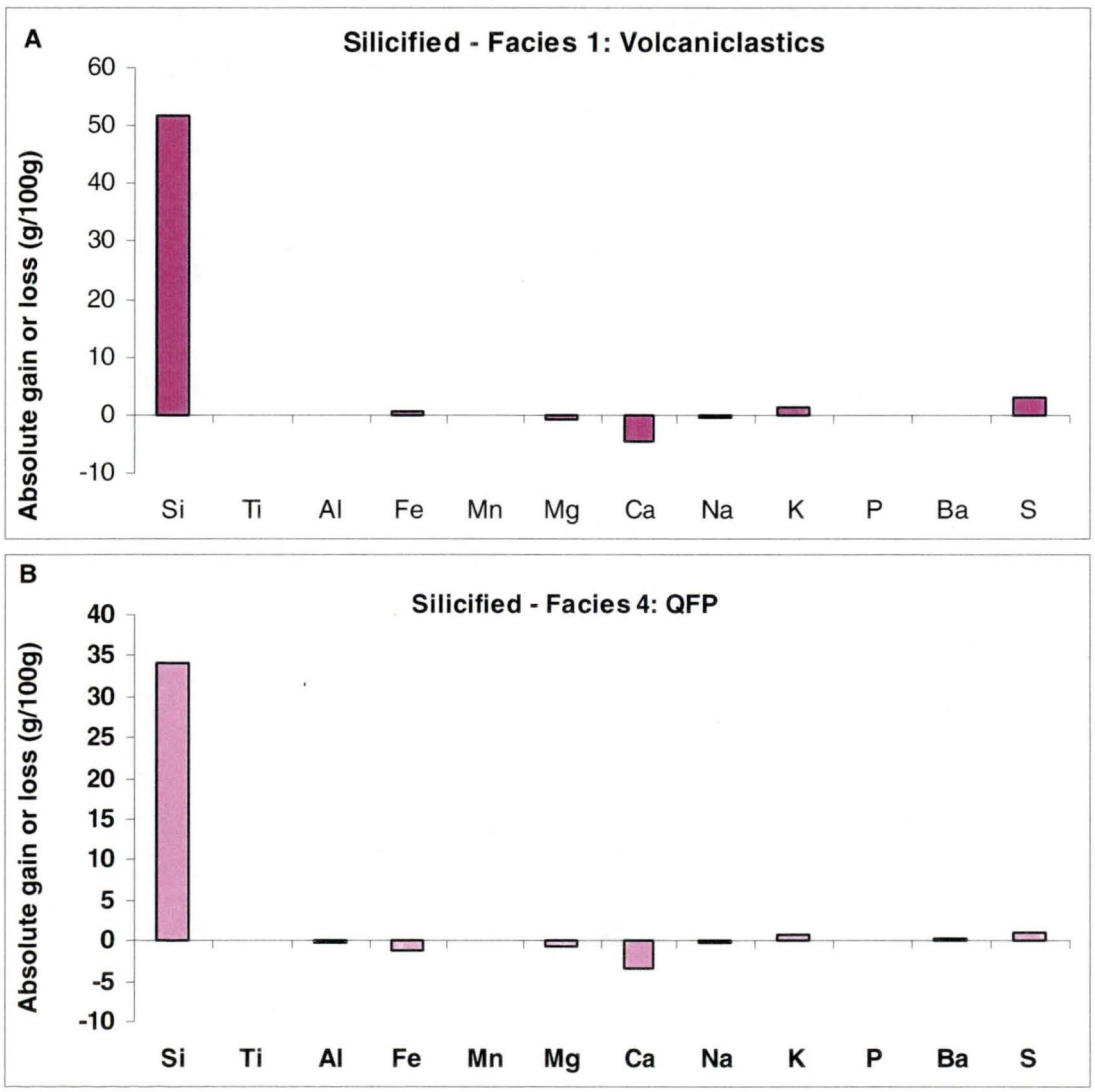

Figure 47 Absolute mass change for major elements due to hangingwall alteration of the HW Rhyolite. Changes are relative to least altered QFP.

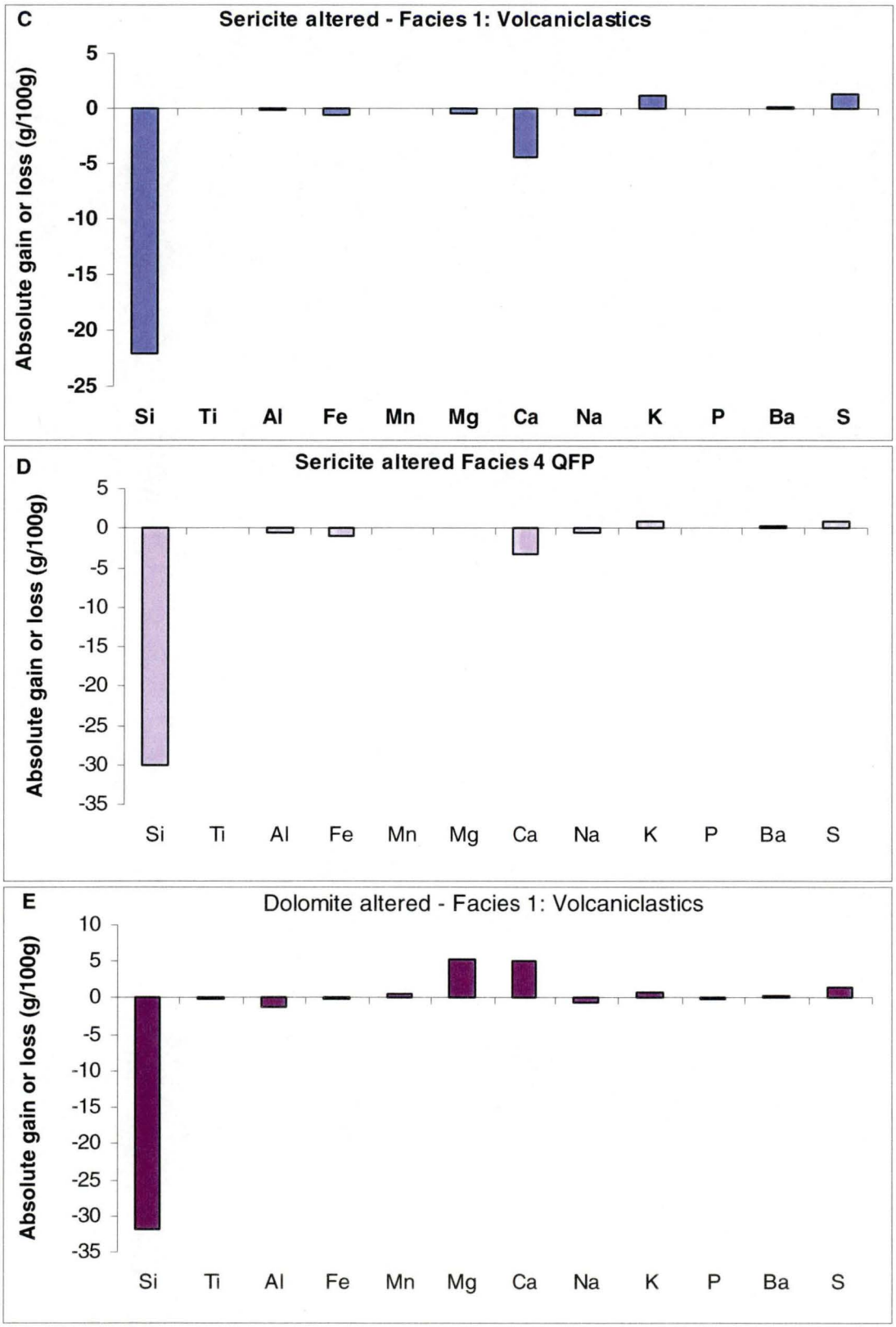

Figure 47 continued. Absolute mass change for major elements due to hangingwall alteration of the HW Rhyolite. Changes are relative to least altered QFP.

5.9 Comparison with previous studies

Previous studies in the geochemistry of the alteration at Myra Falls were conducted as part of a research project in to massive sulfide deposits of the Canadian Cordillera by MDRU (Barrett and Shelock, 1996; Robinson et al., 1996). These studies focused on the MacLean and Kranidiotis (1987) and Pearce element ratio methods to characterise the alteration and are summarised in Table 19A & 19B. Robinson et al. (1996) noted losses of Ca and Na and a gain of K in both footwall and hangingwall alteration. Ba and Rb were found to have the same trends as K. Robinson et al. (1996) also noted Mg was lost in most footwall alteration samples, however a few samples showed Mg addition. Mg addition in the footwall was interpreted as occurring in confined envelopes (where chlorite occurs) close to feeder faults in the footwall. Less than half the footwall alteration samples studied by Robinson et al. (1996) had silica added to them. Hangingwall alteration samples studied by Robinson et al. (1996) showed a loss of Si and Mg, except at the top of the volcanic pile where Mg addition was noted. Mg addition in the hangingwall was interpreted as due to the formation of Mg-bearing illite (Robinson et al., 1996). Barrett and Sherlock (1996) used method of MacLean and Kranidiotis (1987) and found very similar results Table 19B.

The current study, summarised in Table 19C, provides a more detailed analysis of changes during alteration in both the footwall and hangingwall by differentiating alteration types prior to chemical analysis and investigates a broader range of elements. This approach allows chemical trends such as the addition of Mg to be interpreted in relation to the observed mineralogical changes (Mg-chlorite in footwall and dolomite alteration in hangingwall) and also provides absolute changes during alteration. Pearce element analysis and the method of MacLean and Kranidiotis (1987) only present relative changes during alteration.

5.10 Conclusions

Hydrothermal alteration associated with the Battle Zone ore lenses affects two units the Price Formation and the HW Rhyolite. Regional samples and previous reports show that the Price Formation away from the hydrothermal alteration zones is altered to chlorite-epidote-carbonate-albite assemblages. The Price Formation has a variaties in composition throughout the Myra Falls property with Ti/Zr ratios between 52 and 71. In the Thelwood Vally the Price Foramtion is characterised by SiO_2 contents between 48-58 wt%, MgO 4-8 wt%, CaO 4-10 wt%, Na_2O 3-6 wt%, low K_2O (0.05-0.8 wt%), Ba (50-400 ppm) and metal values (Pb, Cu, Ni, and As) less than 100 ppm, and high Sr contents (200-800 ppm).

The HW Rhyolite is composed of QFP and related sediments (Facies 1 and 4) and unrelated, intercalated polymict sediments and chert. The QFP series has a Ti/Zr ratio of 10 - 11 with 64-70 wt% SiO_2, 2.5-3 wt% Fe_2O_3, 1-2.5 wt% MgO, 1-5 wt% CaO, 0.4-1.5 wt% Na_2O, 100-200ppm Sr, <100 ppm Zn, and <20 ppm Cu while S and the metals (Pb, Ni & As) are close to or below detection. The HW Rhyolite has regionally undergone a weak sericite-quartz-albite alteration.

Table 19. Summary of results of geochemical analysis of alteration in Myra Falls District. A. Uses Pearce element analysis by Robinson et al (1996). B. Uses method of MacLean and Kranidiotis (1987) by Barrett and Sherlock (1996). C. Uses Gresens analysis, this study.

Table 19A. Robinson et al. (1996) - Method: Pearce element ratios

footwall alteration Price Andesite	gain	K, Rb, Ba	(Fe, Mg)
	loss	Ca, Na, Mg,	
hangingwall alteration HW Rhyolite	gain	K, Rb, Ba, Fe	(Mg)
	loss	Ca, Na, Si*	

(Mg) - element occasionally added
Si* gained in cherts only

Table 19B. Barrett and Sherlock (1996) - Method: MacLean and Kranidiotis (1987)

footwall alteration Price Andesite	gain	K	(Si)
	loss	Si, Ca, Na, Mg,	
hangingwall alteration HW Rhyolite	gain	K	
	loss	Ca, Na, Si	

(Si) - element occasionally added

Table 19C. This study - Sinclair (2000) - Method: Gresens (1967) - Relative changes

footwall alteration Price Andesite	***Sericite-pyrite***	gain	**S, K**, Ba, Rb, **Si**, P, Cu, Pb, As, **Fe**
		loss	**Mg**, Mn, **Ca, Na**, Sr, Ni, Cr, Zn
	Mg-chlorite	gain	**S, Mg**, Mn, **K**, Ba, Rb, Cu, Zn
		loss	**Ca, Na**, Sr, Cr, Ni, As, **Si**, Pb
	Sericite-chlorite-pyrite	gain	**S, K**, Ba, Rb, Pb, P, Mg, Zn
		loss	**Ca, Na**, Sr, Ni, Cr, As, Cu, **Fe, Si**, Sr
hangingwall alteration HW Rhyolite	***Silica > sericite***	gain	**S, Si, K**, Ba, Ni, Cr, Zn, Cu, As, Pb
		loss	**Ca**, Na, Mg, P
	Sericite > silica	gain	**S, K**, Ba, Rb, Ni, Cu, Zn, Pb, P, Mg
		loss	**Si, Ca**, Na, P, Sr, Fe
	dolomite	gain	**S, Mg, Ca**, Mn, K, Ba, Ni, Cu, Zn, Pb, As
		loss	Na, **Si**, P, Sr

Si - element also a significant absolute mass change

Alteration indices provide useful vectors to ore in the footwall Price Formation with low background alteration index (AI) of 26-42 in regional epidote-chlorite altered andesites. The AI index increases rapidly during hydrothermal alteration with AI values >86 in the Battle Zone. Andesites have a high background CCPI alteration index values due to their Fe and Mg bearing mineralogy and the CCPI values decreases as rocks become progressively sericite altered (CCPI = 69-80) for sericite-chlorite-pyrite altered samples and as low as 48 in sericite-pyrite alteration, depending on pyrite content of rock. Mg-chlorite alteration has a very high CCPI value of 90-93. When the CCPI index is used in conjunction with AI they provide a useful discriminator of footwall alteration types (Fig. 38A). The S/Na_2O ratio also provides an excellent regional discriminator for alteration in Price Formation.

Alteration indices are less effective in hangingwall HW Rhyolite. Sericite alteration increases the AI index, however, the silicified samples have a wide range of AI indices and overlap with both the regional samples and the sericite altered samples. The lack of chlorite in HW Rhyolite limits the use of CCPI. However dolomite alteration does cause an increase in the CCPI due to the magnesium rich nature of the dolomite.

Footwall alteration

Footwall alteration in the Battle Zone affects the Price Formation andesite and consists of three distinct styles:

- **Sericite-pyrite ± quartz alteration** which shows large relative gains in S, K, Rb, Ba and lesser gains in Si, P, Sc and Nd and losses of Ca, Na, Mg, Mn, Sr, Ni and Cr reflecting the destruction of feldspar and the formation of muscovite-quartz and sulfide mineralisation. Relative gains in ore forming elements Cu, Pb, Fe in the sericite-pyrite alteration reflecting the presence of pyrite-chalcopyrite and galena. However only the absolute changes in Si, Ca, Mg, Na, K and Fe effect the mass change in rock during alteration.
- The less intense **sericite-chlorite–pyrite alteration** shows relative mass gains in S, K, Ba, Rb and P and losses in of Ca, Na, Sr, Ni and Cr. The ore forming elements Zn and Cu and Fe all have relative losses, while Pb has a relative gain. Only the absolute mass gain in K and S and losses of Si, Fe, Ca and Na affect the mass change during alteration.
- **Mg-Chlorite alteration** shows relative gains of S, Ba, K, Rb, MgO and Mn and the ore forming elements Cu, Zn and Fe. With relative losses of Ca, Na, Sr, Ni, Cr and Si, and the ore forming elements, As and Pb. Absolute mass changes, including the gain of MgO and S and losses of Si, Ca and Na, reflect the bulk change in composition of the rock from intermediate-chlorite-epidote-carbonate to nearly pure Mg-chlorite.

Hangingwall alteration

Hangingwall alteration in the Battle Zone affects the HW Rhyolite and also consists of three styles:

- **Silicification** in the Battle Zone shows large relative gains in S, Cu, Ba, Zn, Ni, Cr, Pb and As along with smaller relative gains in Si, and K and relative losses in Ca, Mg, and P. However only absolute gains of Si, and S and loss of Ca effect the mass gain in rock during alteration.
- In contrast **sericite alteration** is dependent on rock type and proximity to ore lenses. Facies 1 Volcaniclastics show relative mass gains in S, Cu, Ba, Zn, Pb, Ni, As and K, and relative losses of Ca, P, Sr, Na, V, Mg, Si, Mn and Fe. While sericite altered Facies 4 QFP shows relative gains in S, Ba, Ni, Pb, K, Zn and Rb and losses of Sr, Ca, Na, V, Cr, Si, P, As and Fe. Net mass change in both rock types is dominated by the loss of SiO_2 and Ca, with small gains in K and S.
- **Dolomite alteration** shows relative gains of S, Cu, Ba, Zn, Ni, Mn, Mg, Ca, Pb and As along with relative losses in V, Na, P, Sr, Si and Cr. However only the absolute changes in concentration of Si, Ca, Mg and S effect the mass change in the rock during alteration.

Chapter 6

Ore Deposit Geometry and Mineralogy.

6.1 Introduction

The deposits in the Myra Falls district consist of many individual massive sulfide lenses grouped into several major zones. The Battle Zone is one such group and is the focus of this study. The Battle Zone lies approximately 400 meters below the floor of the Myra Valley (Pearson, 1993) and 1.5 kilometres from the HW shaft (Fig. 2). The Battle Zone consists of the Battle, Gopher, South Trough, Upper Zone and Gap lenses. Additional lenses (Gnu, Bornite Zone and the Extension Zone) were not studied during this project due to the timing of definition drilling. This chapter describes the position, morphology, mineralogy and mineralogical zonation of the Battle Zone lenses. All orientations and maps in this chapter are given in mine grid.

Battle Zone deposits are mined via a single access drift from the 18 level of the HW shaft and the mining operation is known as the Battle Mine. Pre-mining reserves for the Battle Mine are given in Table 1 and consist of 7MT @ 1.4 g/t gold, 53.2 g/t silver, 1.8 % copper, and 12.5 % zinc. Proven and probable mining reserves for the Battle Mine (as of January 2000) are given in Table 20:

MINING RESERVE- SUBSET OF GEOLOGICAL INVENTORY - PROVEN+PROBABLE								
INCLUDES DILUTION AND EXTRACTION FACTORS								
		TONNES	Au g/t	Ag g/t	Cu%	Pb%	Zn%	Ba%	Fe%
BATTLE	PROVEN	3,191,888	0.9	30.2	1.4	0.4	10.1	1.1	11.0
GAP	PROVEN	611,141	2.5	109.2	1.6	1.0	11.9	11.4	11.6
BATTLE	PROBABLE	303,845	0.9	48.0	1.0	0.6	7.8	1.5	8.8
GAP	PROBABLE	229,425	1.9	96.2	1.6	1.1	10.2	9.8	11.8
TOTAL	PROVEN	3,803,029	1.2	42.9	1.5	0.5	10.4	2.7	11.1
TOTAL	PROBABLE	533,270	0.8	41.4	0.7	0.5	4.4	4.2	5.1
TOTAL		4,336,299	1.1	42.7	1.4	0.5	9.6	2.9	10.3

Table 20. Ore reserve summary for the Battle Mine as of January 2000, complied by Mr F. Bakker. Battle includes Battle, Gopher , South Trough and Upper Zone lenses.

6.2 Methods

Mineralogy and mineral zonation were examined during detailed core logging and underground mapping. This was followed by examination of polished thin sections of representative samples taken during logging and mapping. Unknown minerals and mineral compositions were identified using electron microprobe analysis at the University of Tasmania.

To aid in understanding the spatial distribution of the lenses, the lenses have been modelled using Datamine software under the guidance of Dr. Gary McArthur. Ore lens outlines were defined using a zinc equivalent:

$$Zn_{(eq)} = Zn + 1.53*Cu$$

(with a cut off grade of 5% $Zn_{(eq)}$) on a drill hole data base provided by the geological team at Myra Falls as of February 1999 (special thanks to Mr F. Bakker and Mr A. Chong). DATAMINE™ software was kindly made available, for the purpose of this research, by Datamine Australia Inc.

6.3 Lens - position, morphology, mineralogy and mineralogical zonation

6.3.1 Introduction

The Battle, Gopher and South Trough lenses all lie at the contact of the HW Rhyolite and the underlying Price Formation. Gap and Upper Zone lenses lie stratigraphically above the other lenses toward the top of the HW Rhyolite (see Fig. 19). Figure 47 shows the distribution of the Battle Mine ore lenses, as defined by the >5% $Zn_{(eq)}$. Lenses are modelled between 1385mE and 1800mE, mineralisation continues east and west of these boundaries, however the study area of this project is

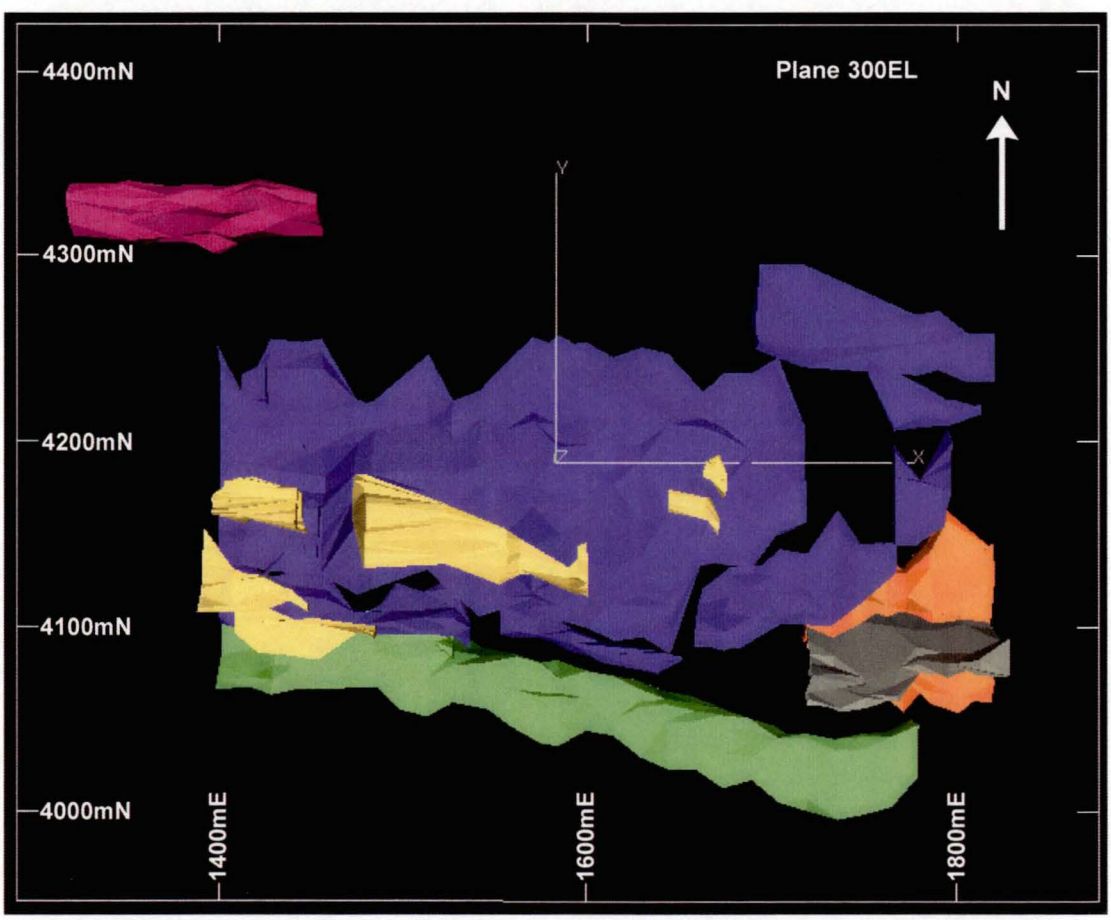

Figure 47. A Plan view of Battle Zone lenses, Battle (blue), Gopher (bright green) South Trough (orange, with mafic dyke - dull green), Upper Zones (yellow) and Gap (pink).

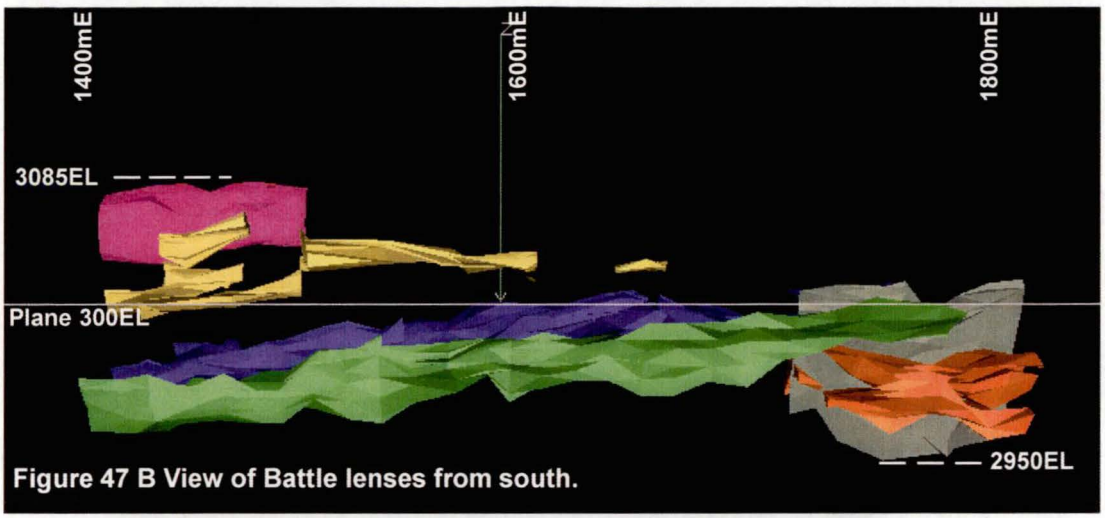

Figure 47 B View of Battle lenses from south.

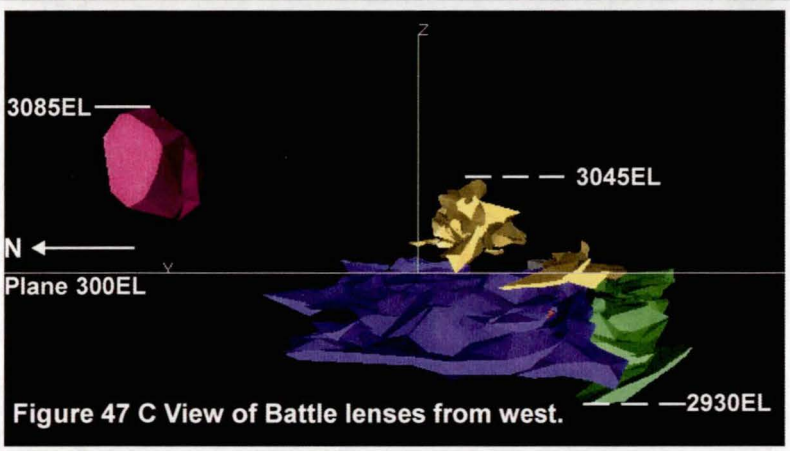

Figure 47 C View of Battle lenses from west.

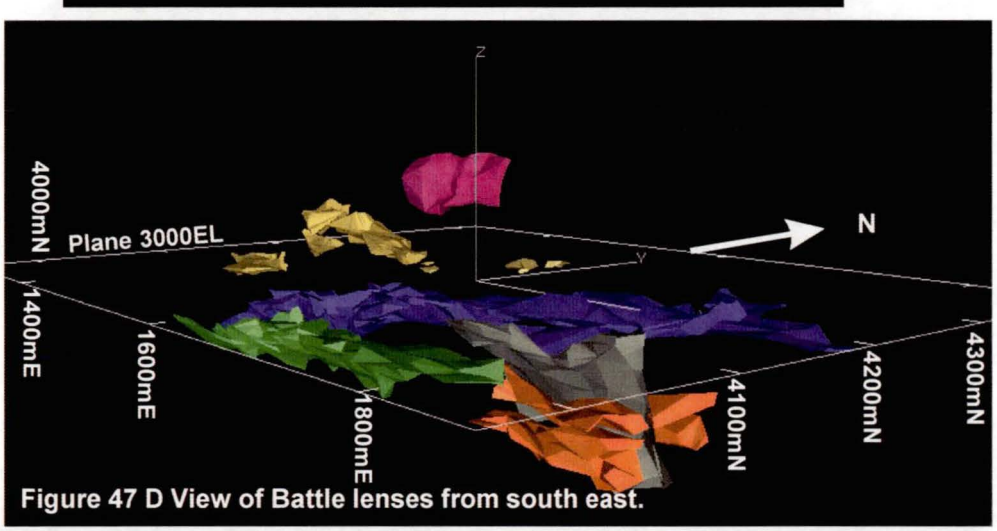

Figure 47 D View of Battle lenses from south east.

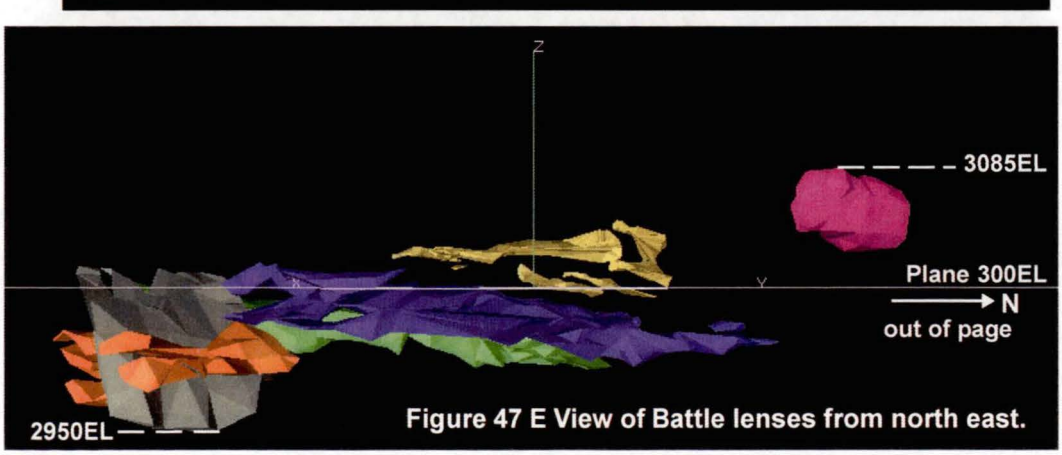

Figure 47 E View of Battle lenses from north east.

Lens Colours: Battle (blue), Gopher (bright green), south Trough (orange; mafic dyke - dull green), Upper Zone (yellow), Gap (pink).

confined to this region due to the timing of definition drilling and underground development. This model may be viewed in 3D using the CD provided.

6.3.2 Battle lens

The Battle lens has a sheet-like morphology ranging in thickness from 3 to 25 meters. It starts around 1720mE and is open to the west. However, this project was concerned only with the active portion of the mine (during the period June 96 to September 98) which consisted of the portion between 1400mE and 1720mE. The Battle lens is up to 200 meters wide (Pearson et al., 1997), although widths of 100 to 150 meters are more common. The sheet dips gently to the west ranging in elevation from 3000EL[1] in the east to 2950EL in the west (Fig. 48).

The Battle lens consists of sphalerite, pyrite and chalcopyrite, with minor galena and tennantite occurring toward the top of the lens. Accessory rutile, and the tellurides; altaite (PbTe), pilsenite (Bi_2Te_3) and hessite (Ag_2Te_3), have also been identified (see chapter 7).

The Battle lens sulfides shows a strong zonation of ore types from top to bottom (Fig. 49). Over-

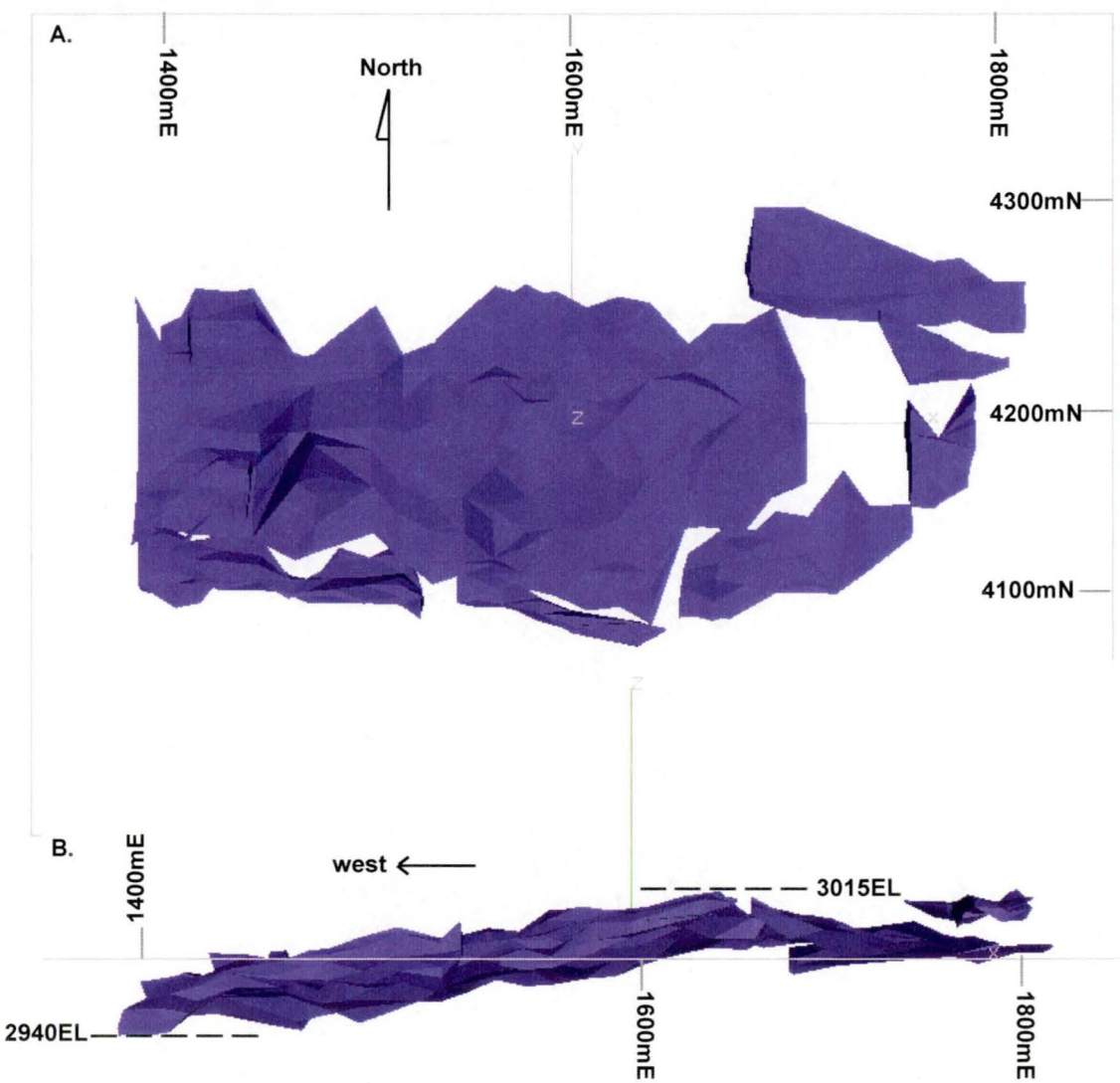

Figure 48. View of Battle lens, showing broad sheet like morphology and gentle eastward dip. (A) Plan view, (B) Section.

[1] EL is the mine terminology for elevation, 3048EL is sea level.

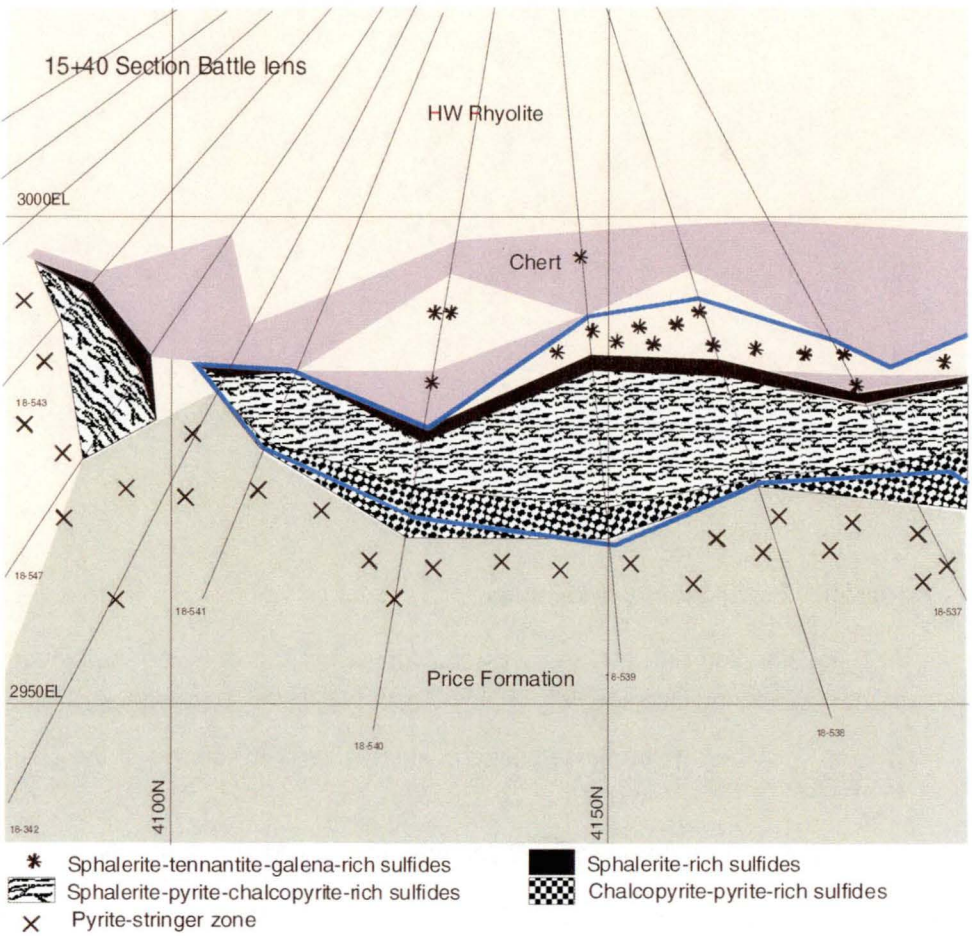

Figure 49. Mineralogical zonation in Battle lens. Blue line shows DATAMINE™ modelled ore outline.

lying the Battle lens is a siliceous horizon made up of chert and silicified fine grained Facies 1 volcaniclastic sediments (see chapter 3). This horizon contains frequent quartz-carbonate veins, coarse pyrite, chalcopyrite, tennantite, sphalerite and barite (Plate 10A and Fig. 50A). The distribution of these sulfides is random. The massive sulfides occur below this "cherty" horizon and consists of honey yellow (Plate 10B) to black (Fig. 50B) sphalerite, the black sphalerite commonly containing aboundant sphalerite-tennatite-galena giving the ore a silvery appearence. Abundant inclusions of siliceous rhyolite occur within the sulfides at the top of the massive sulfide lens. The upper contact of the ore is commonly faulted due to competency contrasts between the massive sulfides and the silicified sediments. However, the contact appears intercalated with areas of honey yellow sphalerite extending up into the silicified rocks (Plate 10A).

The honey-sphalerite and silvery, sphalerite-galena-tennantite-rich sulfides grades downward into a thin (1-2m) zone of massive sphalerite with very few other sulfides (Fig. 49 & Fig. 50C) and then into a broad zone of massive sphalerite-pyrite-chalcopyrite-rich sulfides (Fig. 49, Plate 10C, D & E & Fig. 50D, E & F). The sphalerite-pyrite-chalcopyrite-rich sulfides may show strong banding, defined by sphalerite-rich versus pyrite-chalcopyrite-rich layering. This layering is locally overprinted by D2 and/or D3 structural events (see chapter 8). Sphalerite-pyrite-rich sulfides grade downward through massive pyrite-chalcopyrite ore (Fig. 49, Plate 10F & Fig. 50G) and into massive pyrite at the base of the lens (Fig. 49 & Plate 10G). Underlying the Battle lens is a zone of semi-massive pyrite within strongly sericite-quartz altered Price Formation. This zone is commonly referred to as the

Plate 10 Battle Main ore samples

A. Silica flooding and coarse pyrite-chalcopyrite at top of Battle lens, overprinting sphalerite-tennantite-galena. M159 corner with 18-168DW

B. Honey coloured sphalerite plus tennantite-galena at the top of the Battle lens. M159DD2 sample No.2

C. Massive sphalerite with minor pyrite-chalcopyrite. M159 sample No.3

D. Pyrite and chalcopyrite content of ore increases forming bands alternating with sphalerite-rich sulfides. M159 EX4

E. Weakly banded chalcopyrite-rich, sphalerite-pyrite ore. M154DD corner with 18-168DW

F. Massive pyrite-chalcopyrite with minor sphalerite. M167 Panel 2 sample No.2

G. Semi-massive pyrite in strongly sericite altered stringer mineralisation. M167 Panel 2 sample No.6

H. Silicification preserves clasts of host rocks (white) in intense sericite-pyrite alteration. M167 Panel 2 sample No. 4

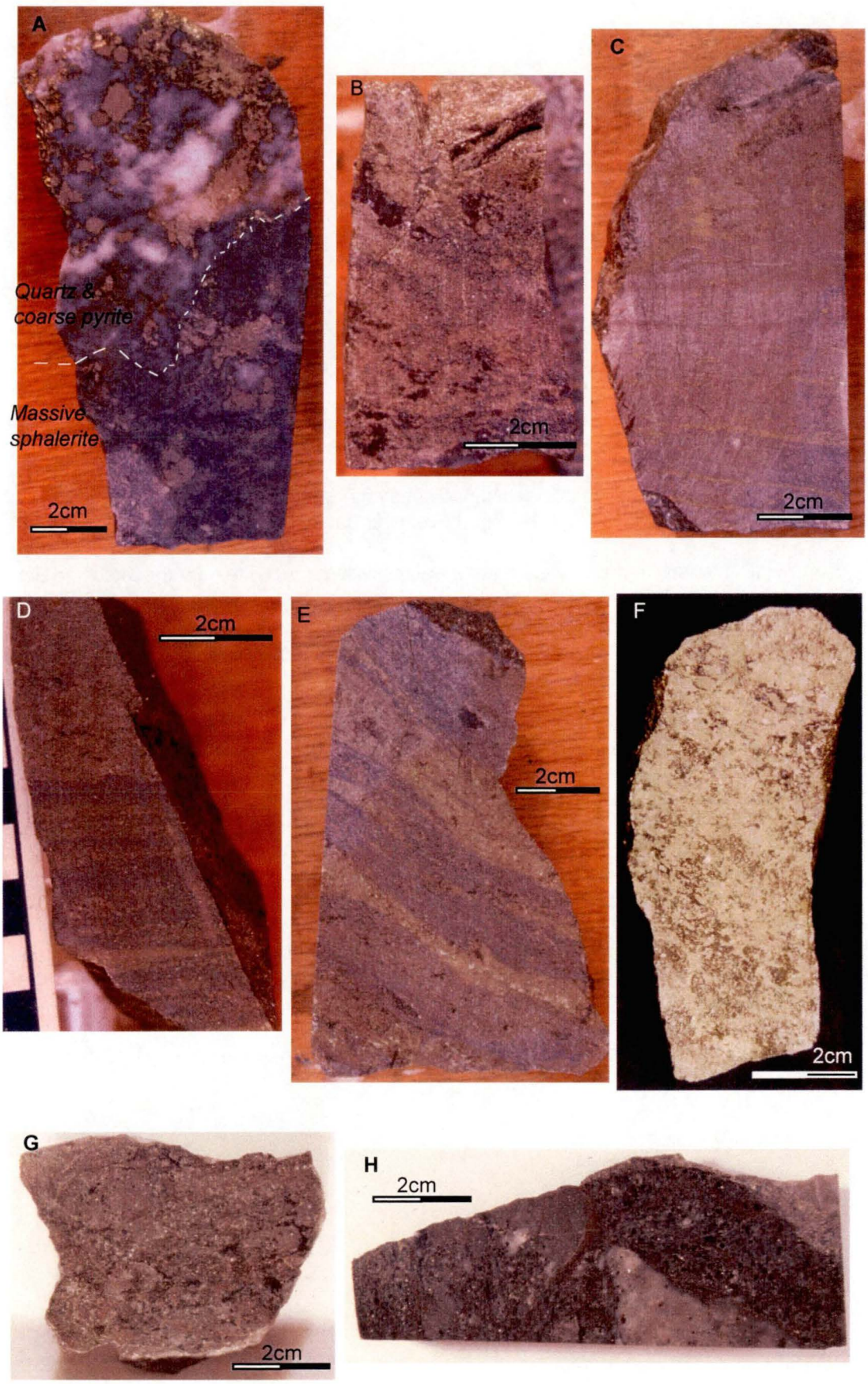
A
Quartz &
coarse pyrite
Massive
sphalerite
2cm
B
2cm
C
2cm
D
2cm
E
2cm
F
2cm
G
2cm
H
2cm

Figure 50 - Drill log through the Battle lens

A. Semi-massive to disseminated sphalerite-tennantite-galena-rich and silicious alteration of HW Rhyolite - chert overlying Battle lens.BG18-539 49.2m

B. Massive sphalerite-galena-tennantite with minor pyrite near the top of the Battle Lens. BG18-539 57.1m

C. Massive sphalerite with very minor pyrite-chalcopyrite-galena-tennantite. BG18-539 63.2m.

D. Massive sphalerite-pyrite-chalcopyrite showing weak banding which consists of sphalerite versus pyrite-chalcopyrite-rich layers. BG18-539 64.7m

E. Sphalerite-galena with minor pyrite-chalcopyrite, the blebby alteration is sericite. BG18-539 67.7m.

F. Sphalerite-chalcopyrite illustrating annealed texture of chalopyrite grains distributed between sphalerite grains (see chapter 8). BG 18-539 71m

G. Massive sphalerite-pyrite-chalcopyrite showing banding of sphalerite versus pyrite-chalcopyrite-rich layers. Note pyrite-chalcopyrite content increases toward base of Battle lens (compare with D). BG18-539 76.2m

H. Pyrite stringer in quartz-sericite altered Price Formation underlying Battle lens. BG18-539 84.3m

sph = sphalerite, ten = tennantite, py = pyrite, gal = galena, cpy = chalcopyrite

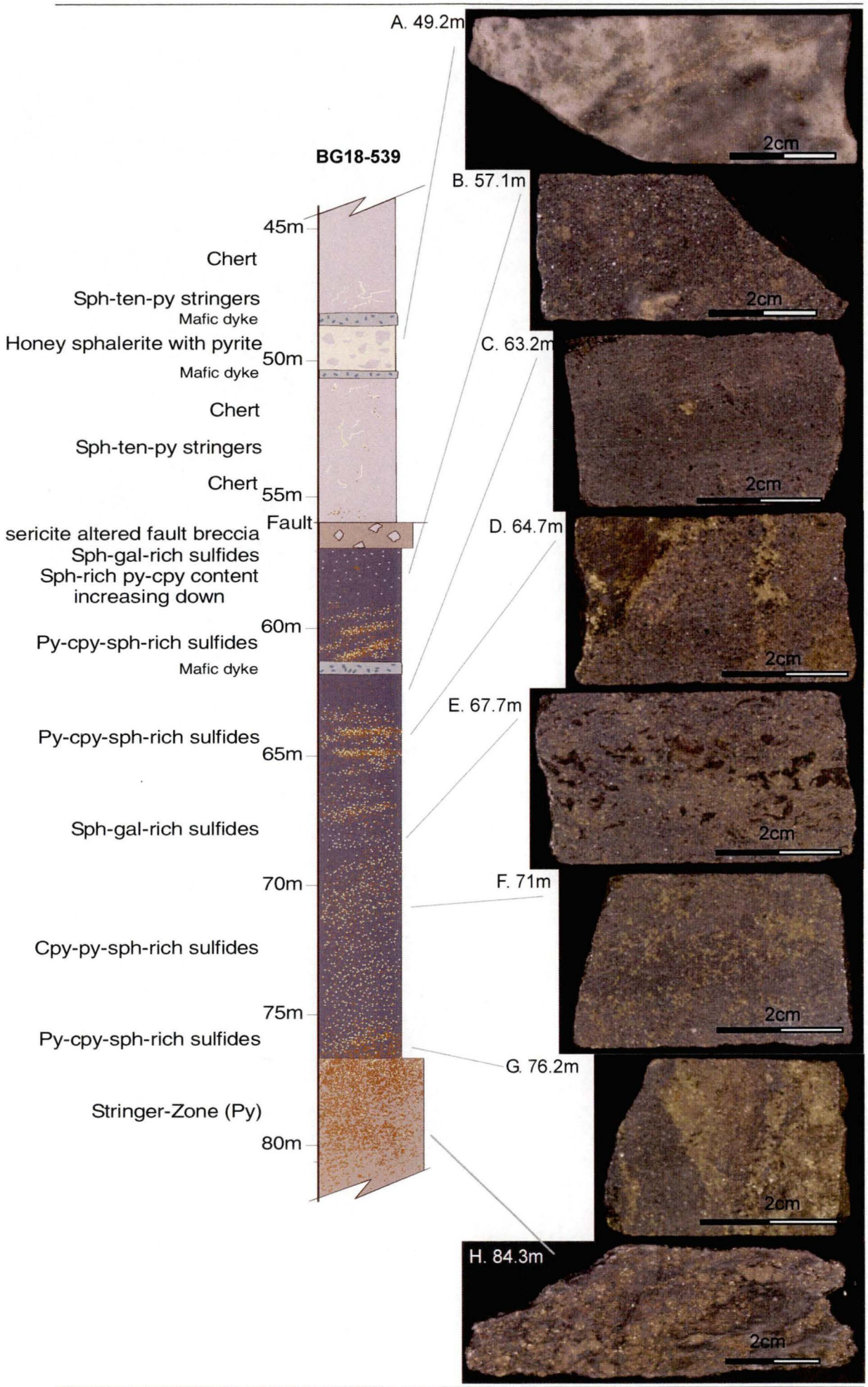

Sinclair 2000

stringer zone (Fig. 49, Plate 10H & Fig. 50H).

6.3.3 Gopher lens

The Gopher lens lies south of the Battle lens (Fig. 47A) and forms the southern boundary of the economic deposits in the Battle Mine. The Gopher lens differs significantly in shape from the Battle lens by having a strongly asymmetric - wedge shaped cross section to the east (Fig. 51A). To the west the shape of the Gopher lens becomes more complex as faulting disrupts the sulfides (Fig. 51B). The Gopher lens sits slightly lower than the Battle lens with top at 2990EL to the east and base around 2935EL. It is approximately 50 m wide by 700 m long (Pearson et al., 1997) strikes north-west to west northwesterly and dips gently to the west (Fig. 52) .

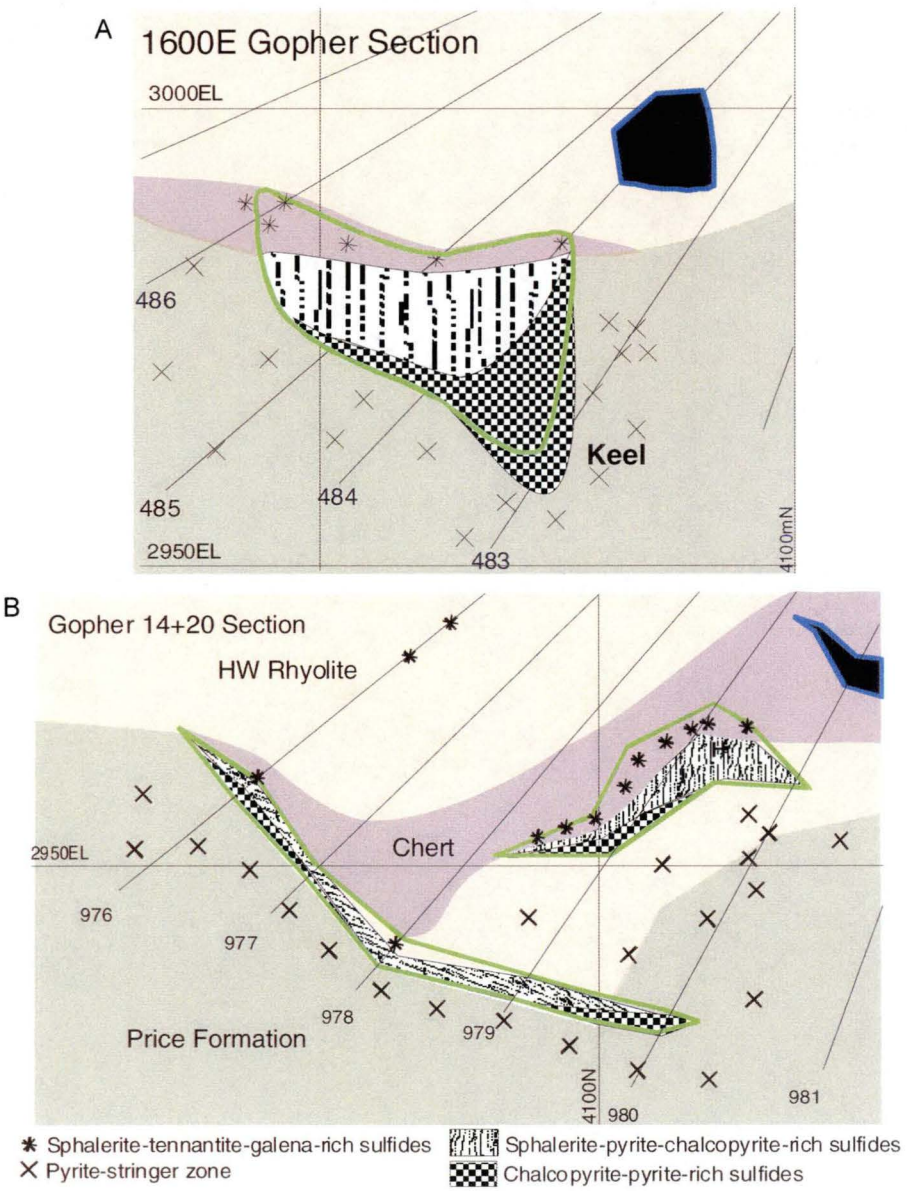

Figure 51. cross sections through the Gopher lens A. Strongly asymmetric - wedge shaped cross section of the eastern Gopher lens (1600mE). B. Gopher lens disrupted by faulting giving a more complex shape (1420mE). Green outline Gopher lens, Blue Battle lens.

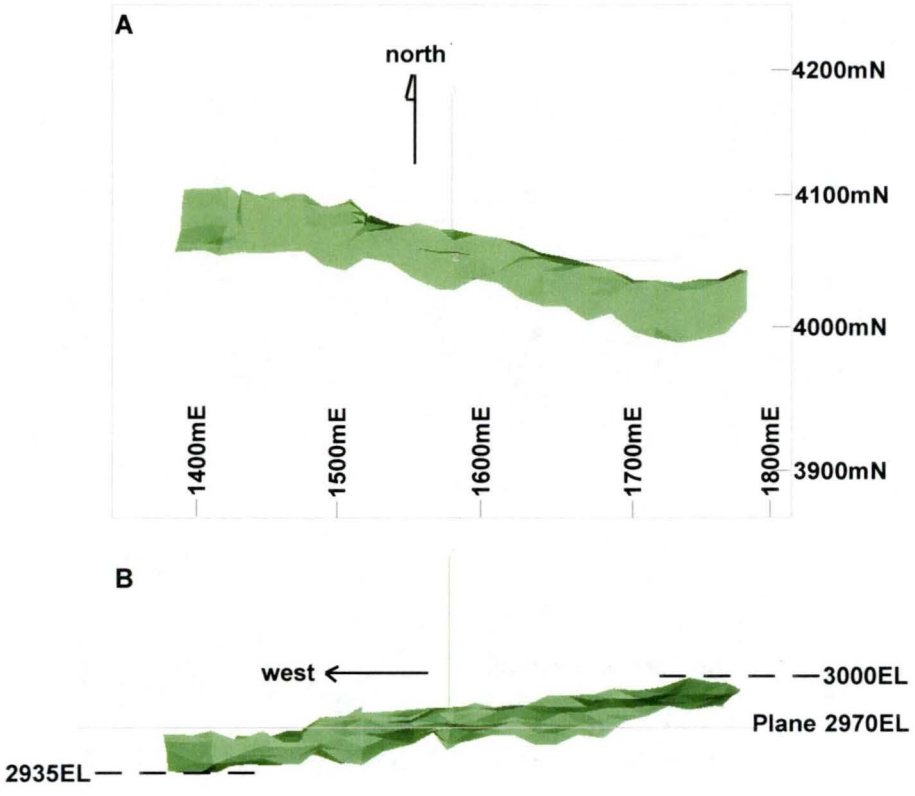

Figure 52 Views of the Gopher lens (A) in plan view and (B) from the south. Showing north-west to west northwesterly strike and gently west dip.

Mineralogically the Gopher lens is very similar to the Battle lens with sphalerite, pyrite, chalcopyrite and moderately higher galena and tennantite contents. There is a similar mineralogical zonation from hangingwall to footwall throughout the Gopher lens as the Battle lens. This zonation is slightly asymmetric due to the shape of the Gopher lens (Fig. 51A). Chert and silicified Facies 1 rhyolite overly the Gopher lens and in places sulfide mineralisation can be seen replacing these siliceous rocks (Plate 11A). Disseminated honey-sphalerite, tennantite and galena occur within the silicified rocks and at the top of the Gopher lens (Plate 11A & Fig. 53A). Sphalerite, galena and tennantite rapidly grade into massive sphalerite-pyrite-chalcopyrite which commonly show a strong foliation parallel to banding (see chapter 8 for discussion; Plate 11B & C, Fig. 53B-E). Toward the base of the Gopher lens (or the keel region; Fig. 51A), the sphalerite content decreases and massive chalcopyrite-pyrite becomes dominant (Plate 11D & Fig. 53F & G). The massive chalcopyrite-pyrite grades into massive coarse grained pyrite at the base of the Gopher lens (Plate 11E & Fig. 53H & I). The footwall is strongly altered by sericite-pyrite (Plate 11G) and rare pyrite veins (Plate 11F). The stringer zone is strongly foliated forming sericite-pyrite schists due to the presence of the Flat Fault underlying the Gopher lens (see chapter 8; Plate 11I).

Plate 11 Gopher lens ore samples

A. Massive sphalerite-tennantite-galena and banded chert. G156 DD sample No.1

B. Massive sphalerite-pyrite-chalcopyrite ore. G158 DD sample No. 2

C. Strongly banded sphalerite-pyrite-chalcopyrite ore. G158 DD sample No. 1

D Massive pyrite-chalcopyrite enclosing a rare chert band. G149 DD sample No.2

E. Massive coarse grained pyrite. G168EX sample No. 1A

F. Rare pyrite-quartz vein in the footwall to the Gopher lens. G149 DD sample No. 4

G. Semi-massive pyrite in strongly sericite altered footwall - stringer mineralisation. G158DD sample No5

H. Strongly sheared pyrite-sericite stringer zone. G168EX sample No.3

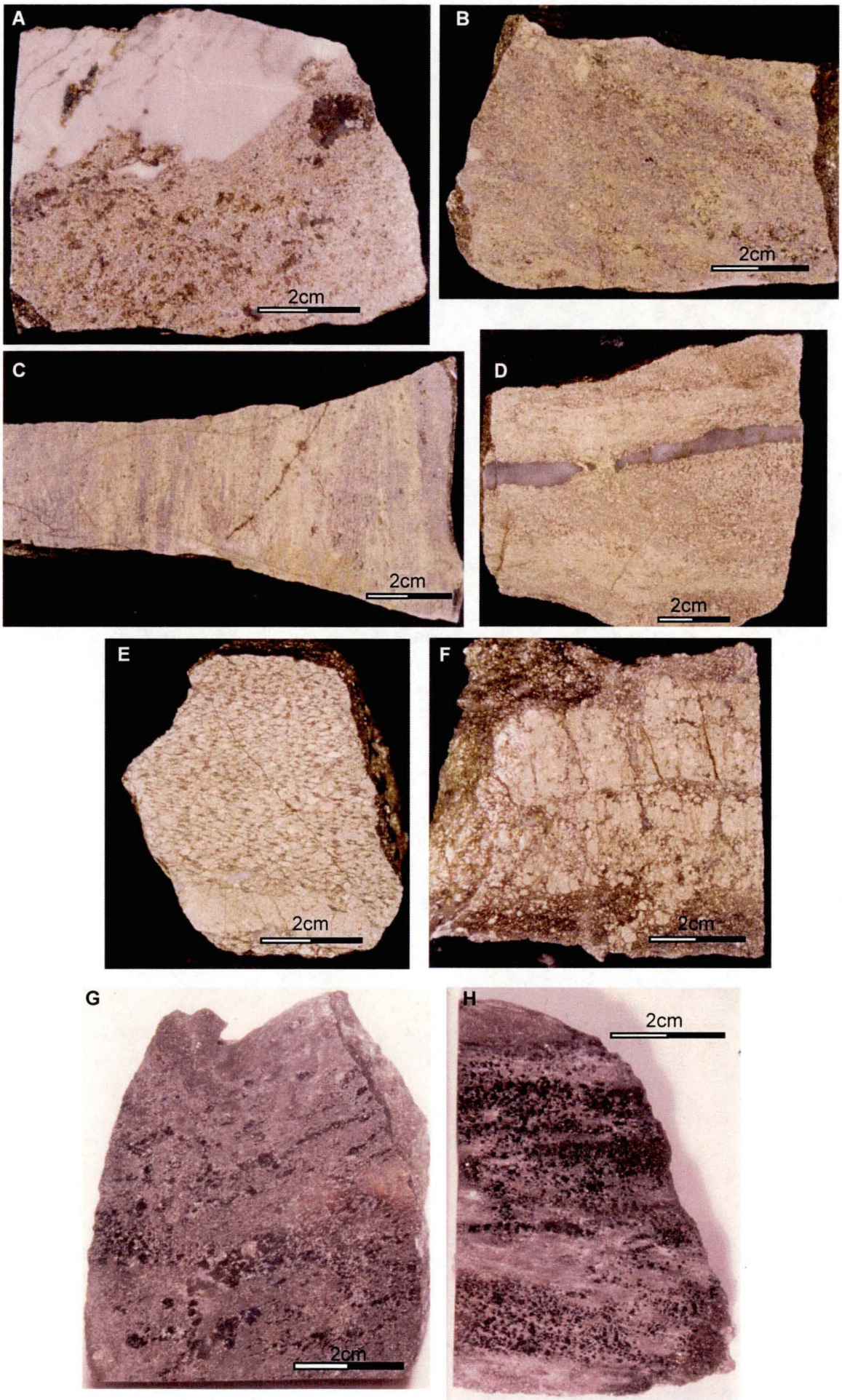
A
2cm
B
2cm
C
2cm
D
2cm
E
2cm
F
2cm
G
2cm
H
2cm

Figure 53 Drill log through the Gopher lens

A. Semi-massive sphalerite-tennantite-galena in HW Rhyolite volcaniclastic sediments that overly the Gopher lens. BG18-485 76.2m

B. Semi-massive sphalerite-pyrite in HW Rhyolite volcaniclastic sedments that overly the Gopher lens. BG18-485 81.1m

C. Massive pyrite-sphalerite-galena-tennantite from the top of the Gopher lens. BG18-485 86.95

D. Massive pyrite-sphalerite-galena-tennantite from the top of the Gopher lens. BG18-485 88.5

E. Pyrite-sphalerite from the middle of the Gopher lens. BG18-485 91.2m

F. Sphalerite-chalcopyrite-pyrite with banding parallel to the strong foliation. Sulfide banding is off set by late brittle fault (arrow). BG18-485 94.1m

G. Pyrite-chalcopyrite. Sphalerite content decreasing toward the base of the Gopher lens. BG18-485 95.4m

H. Massive coarse pyrite in silicified Price Formation at the base of the Gopher lens. BG18-485 97.3m

I. Disseminated chalcopyrite-pyrite with strong foliation, from the stringer zone underlying the Gopher lens. BG18-485 99.6m

sph = sphalerite, ten = tennantite, py = pyrite, gal = galena, cpy = chalcopyrite

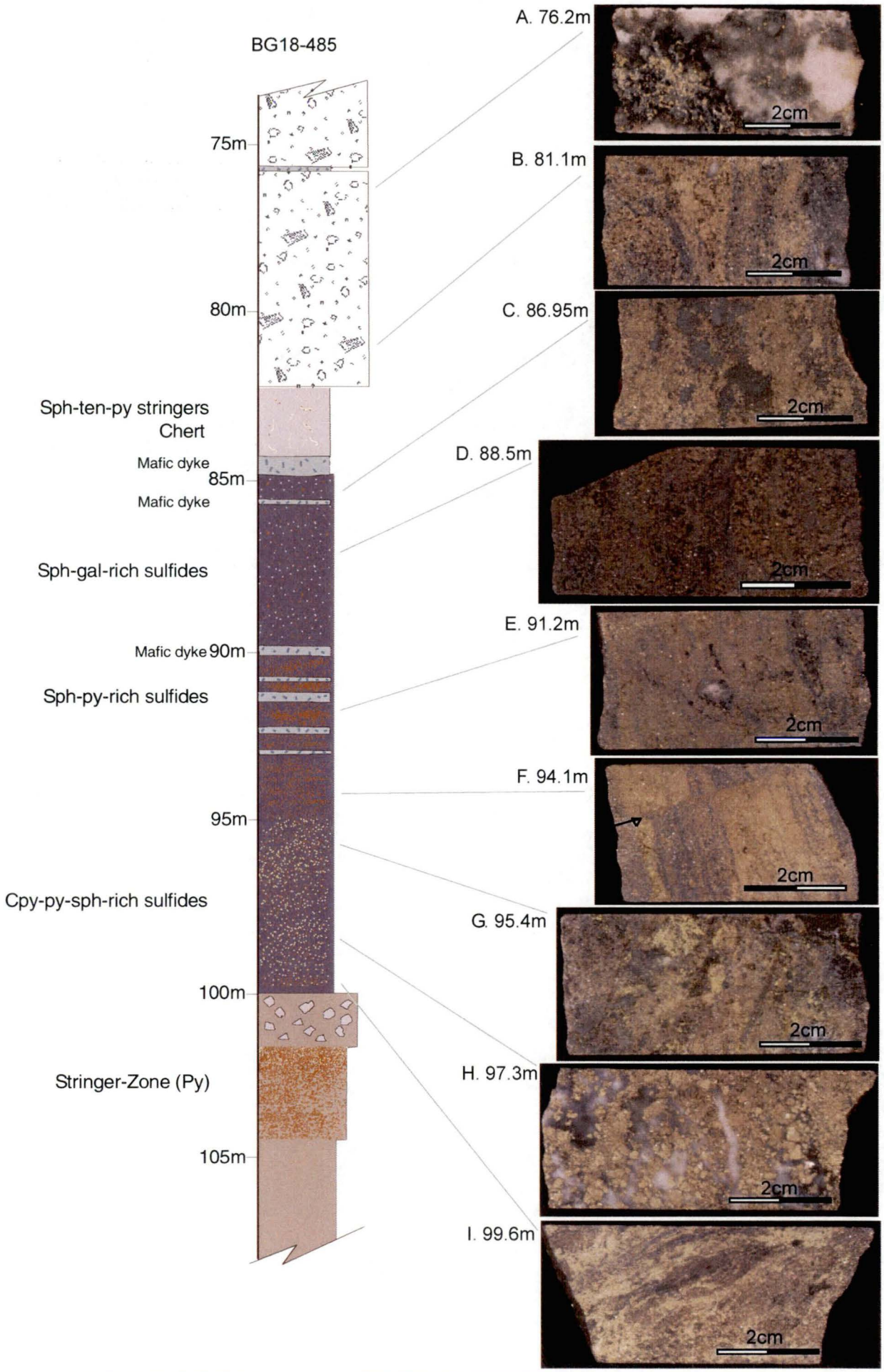

Sinclair 2000

6.3.4 South Trough lens

The South Trough lens lies at the eastern end of the Battle Mine within a topographic depression (2970-2940EL), 20 to 30 meters below the Battle and Gopher lenses (Fig. 47 & 54). The South Trough lens starts around 1700mE and continues eastward into the area known as the "Extension Zone". Only the portion of the South Trough between 1700mE and 1800mE has been considered in this study. The South Trough lens extends from 4125mN to 4050mN and consists of a body of sulfides 40m thick and 100m wide.

The sulfide body contains higher grade zones (sub-lenses). These sub-lenses are modelled using the >5% Zneq cut off (Fig. 55). The high grade sub-lenses are 3-7m thick. A large mafic dyke cuts through the area. It is strongly chlorite-carbonate-(pyrite) altered, and pyrite porphyroblasts are common within the surrounding sulfides.

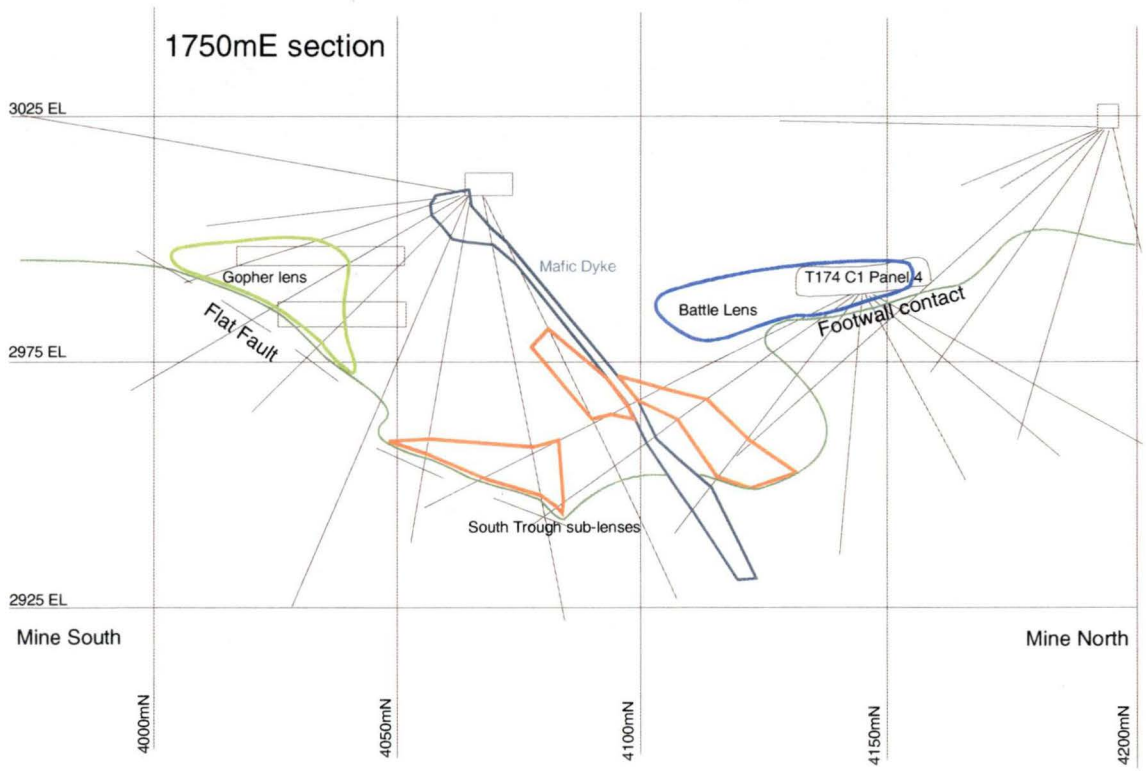

Figure 54 Eastern end of Battle lens (known as T-zone) showing the spatial relationship to South Trough and Gopher lens. 1750mE section.

Above the South Trough lens, disseminated sulfides are observed in a clastic unit containing fragments of silicified rhyolite and quartz crystals (Fig. 56A, B & C; Plate 12A & B). The sulfides range from clasts of sphalerite-pyrite-chalcopyrite to massive pyrite, similar to those in the underlying South Trough lens. Accessory galena, tennantite and rutile also occur in the South Trough area. The South Trough sub-lenses grade laterally and vertically from massive pyrite above the footwall contact toward the northern end (Fig. 56 & Plate 12C & D, Fig. 57G & H), to massive sphalerite-chalcopyrite toward the hangingwall contact and at the southern end (Plate 12E - G, & Fig. 57E & F). The only deviation from this trend is a general increase in tennantite content toward the footwall at the southern end of the lens within sphalerite-pyrite-(chalcopyrite)-rich massive sulfides (Plate 12F).

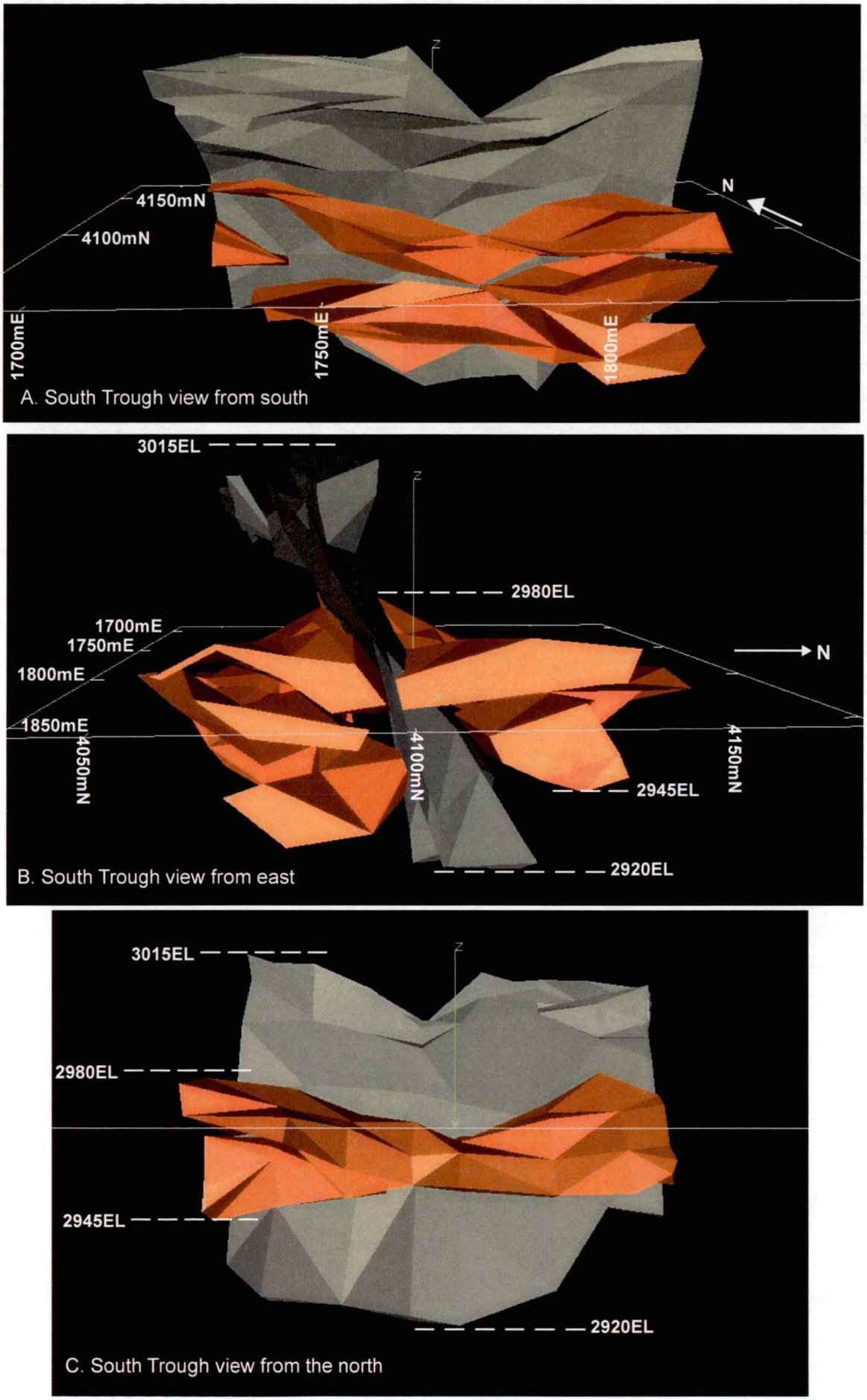

Figure 55. South Trough sublenses defined by Zn(eq) = 5% cutoff shown in orange, mafic dyke in green.

Semi-massive sulfides occur between the sub-lenses and show a zonation from pyrite-dominated to the north (Plate 14H) to sphalerite-tennantite-(galena-barite)-rich to the south (Plate 12I). The South Trough lens is underlain by a stringer zone of sericite-pyritic altered Price Formation (Fig. 56).

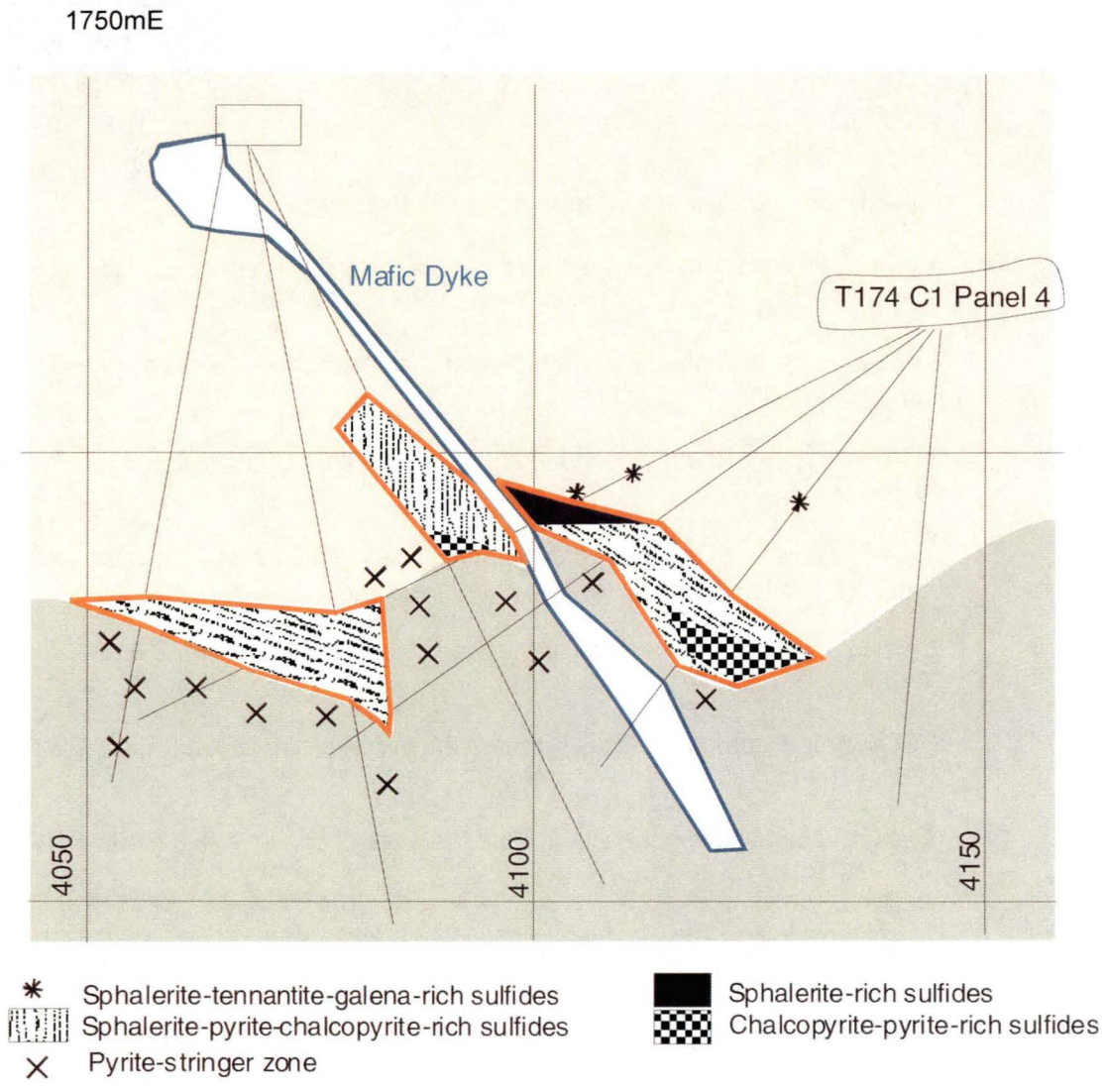

Figure 56. 1750mE South Trough section showing the postion of ore samples in Plate 12.

Plate 12 Ore types and zonation in the South Trough lens

A. Semi massive honey-sphalerite, tennantite, galena with strongly silicified clasts of rhyolite showing relic volcaniclastic textures.BG18-906 21.9 - 22.7m.

B. Massive pyrite-chalcopyrite in intense sericite alteration. Pyrite shows pseudoclastic texture.BG18 906 42.9 - 43.0m

C. Massive pyrite-chalocpyrite at the base of sub-lens (Fig 6.10). BG18-906 46.4 - 46.6m

D. Semi-massive to massive pyrite in intense sericite alteration, underlying sub-lens (Fig 6.10). BG18-906 49.2 - 49.3m

E. Sphalerite-galena-tennantite at the top of sub-lens (Fig 6.10). BG18-904 68.9 - 69.0m

F. Sphalerite-pyrite-galena-chalcopyrite in the middle of sub-lens (Fig 6.10) BG18-904 71.6 - 71.7m

G. Massive sphalerite-chalcopyrite from the base of sub-lens (Fig 6.10). BG18-905 76.0 - 76.1m

H. Semi-massive pyrite, in intense sericite alteration with strong foliation from between the sub-lenses . BG18-904 54.7-54.8m

I. Massive pyrite, from between the sub-lenses. BG18-904 61.2 - 61.3m

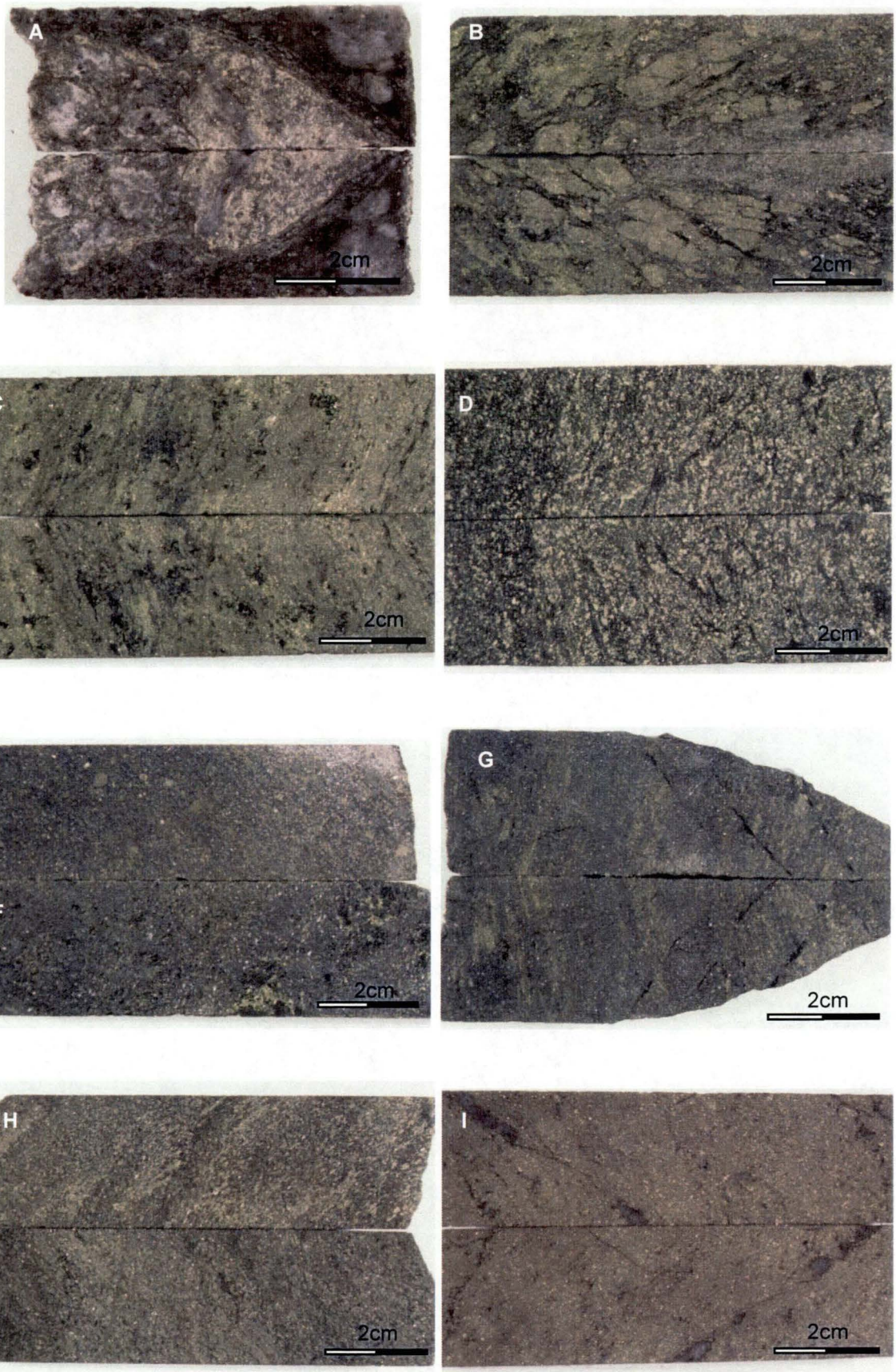
A
2cm
B
2cm
C
2cm
D
2cm
E
F
2cm
G
2cm
H
2cm
I
2cm

Figure 57 Schematic log through South Trough Lens

A. Semi-massive sphalerite-galena-pyrite with fragments of silicified rhyolite in quartz-sericite gangue. BG18-342 29.2 - 33.4m

B. Coarse pyrite crystals rimmed with chalcopyrite plus sphalerite. BG18-342 36.8 -37.3m

C. Massive sphalerite with occasional pyrite crystals. BG18-342 37.3 - 38.5m

D. Finely banded chert, hangingwall to South Trough lens. BG18-342 46.8m

E. Massive pyrite-sphalerite-chalcopyrite in sericite gangue. BG18-342 48.7 - 49.8m

F. Massive sphalerite-pyrite-chalcopyrite. Pyrite and chalcopyrite form bands within sphalerite. BG18-342 54.3 -56.0m

G. Semi-massive to massive pyrite in sericite gangue, between South Trough sub-lenses. BG18-342 56.0-59.3.

H. Massive-pyrite with minor chalcopyrite. Basal sub-lens within South Trough lens. BG18-342 59.3 - 61.2m

sph = sphalerite, ten = tennantite, py = pyrite, gal = galena, cpy = chalcopyrite

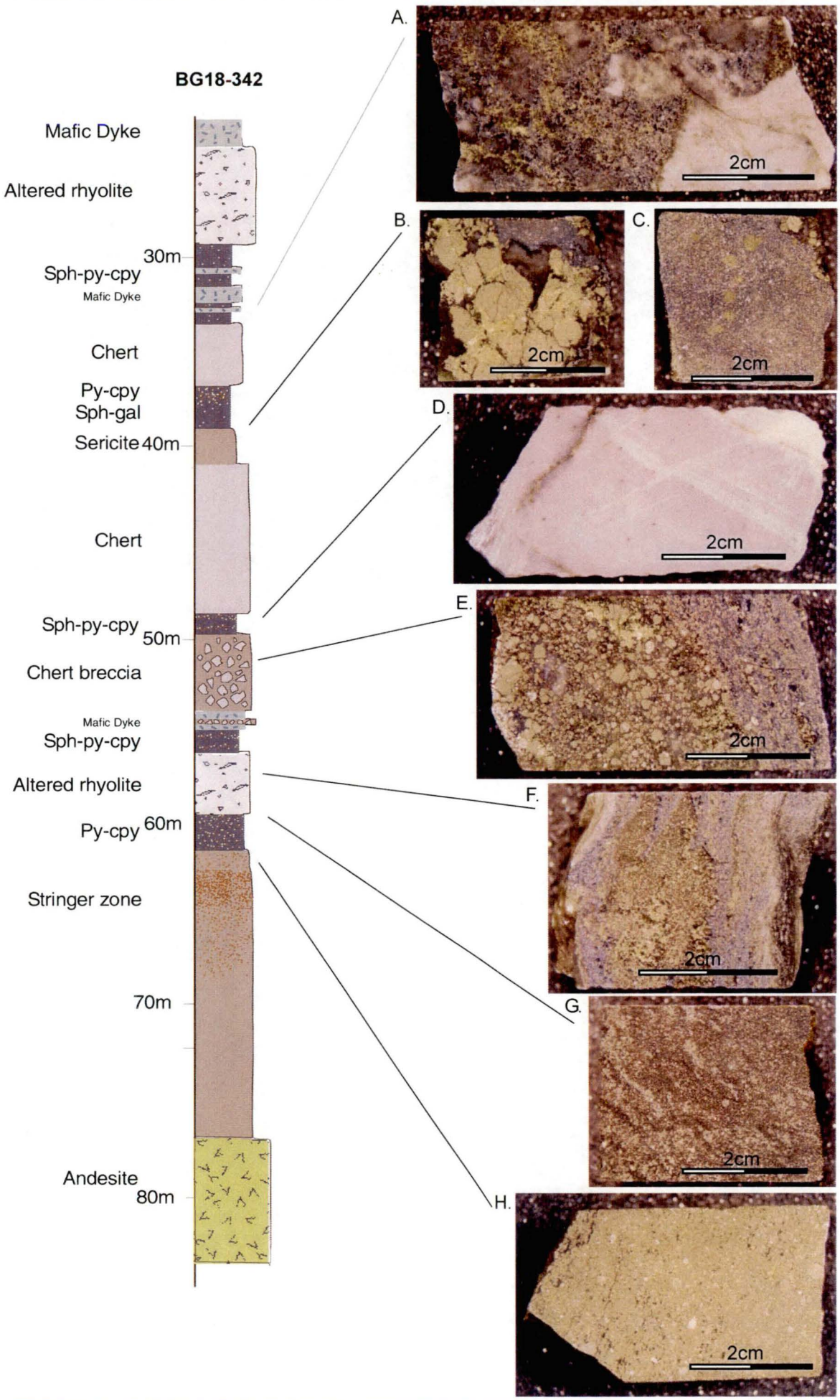

Sinclair 2000

6.3.5 Gap lens

The Gap lens is situated to the north of the Battle lens and sits at the top of the HW Rhyolite 30 - 50 meters stratigraphically above the Battle lens (3020 - 3090EL; Fig. 47). It has an estimated (from exploration drilling) strike length of 250 meters (Pearson, 1993). However, only 60 meters (1390mE to 1450mE) of definition drilling was available during this project. In cross section (Fig. 58B & C) the Gap lens is a pipe shaped body approximately 40-50 meters high, 20-25 meters wide (Fig. 58B), thinning to 10 meters wide eastward (Fig. 58C). It is hosted within the Facies 4: quartz-feldspar-porphyritic rhyolite body (QFP) that overlies the Facies 1 rhyolitic sediments. Sericite alteration, minor silicification and mineralised veins associated with the lens extend into the QFP. The pipe shape of the Gap lens is attributed to its replacive nature within the QFP (Sinclair, 1998).

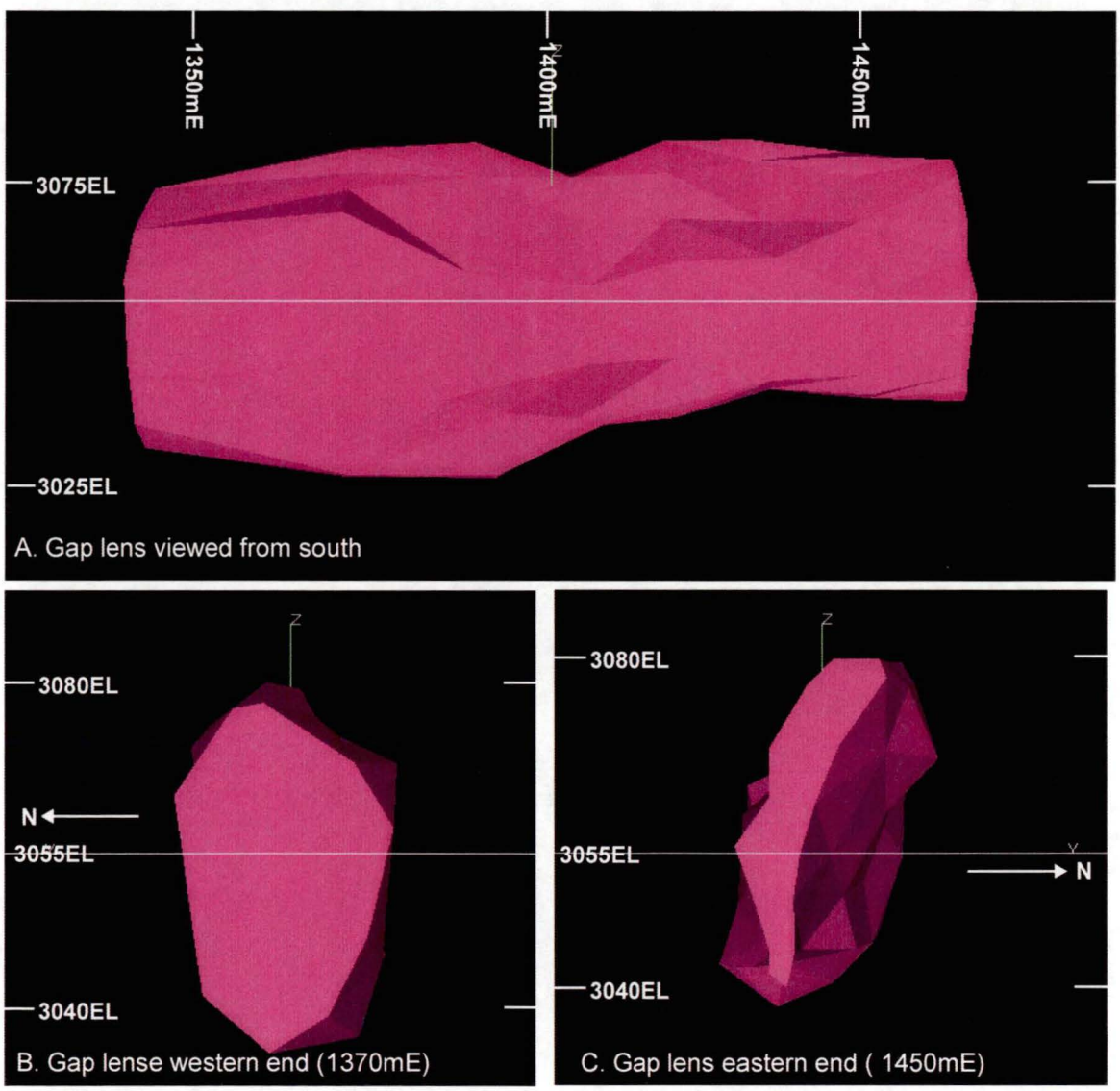

Figure 58. DATAMINE views of Gap lens showing pipe shaped cross section.

Mineralogically the Gap lens is more complicated than the Battle, Gopher and South Trough lenses. The main sulfides consist of sphalerite, pyrite, chalcopyrite, bornite, galena, and tennantite as well as minor to accessory colusite, renierite, rutile, anilite, stromeyerite and electrum.

The top of the Gap lens (Fig. 59A) is dominated by semi-massive sphalerite-galena-colusite

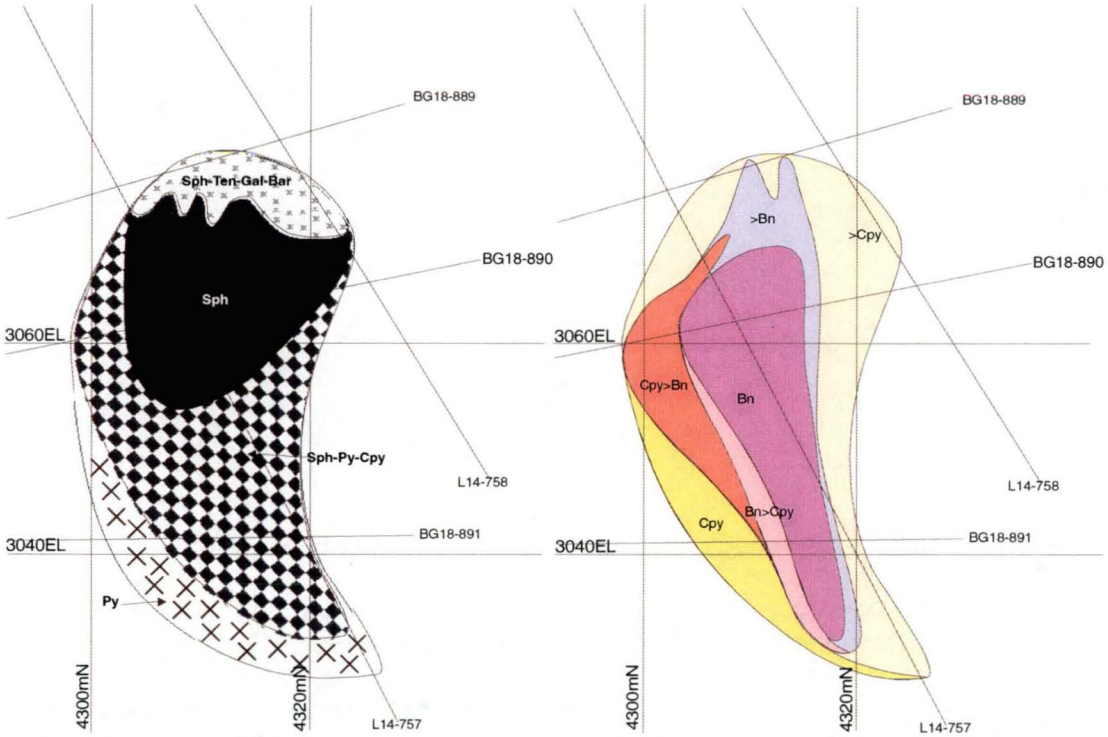

Figure 59. Cross section and mineralogy of Gap lens A. Barite-sphalerite-galena- tennantite-pyrite distribution showing a classic VHMS mineral zonation. B. Bornite-chalcopyrite-distribution (showing bornite cutting through the middle of the Gap lens). Sph = sphalerite, Ten = tennantite, Gal = galena, Bar = barite, Py - pyrite, Cpy = chalcopyrite, Bn = bornite.

within a baritic matrix. Barite crystals up to 2 centimetres (Plate 13A) occur within this zone. The sulfides become more massive as the barite content decreases downward through the lens (Fig. 59A) forming massive sphalerite-galena with barite inclusions (Plate 13B-C & Fig. 60A). These sulfides have a silvery appearance due to the high galena content. Further down the lens the barite and galena contents decrease and the sulfides become sphalerite-pyrite-rich (Fig. 59A, Plate 13D & Fig. 60B). Pyrite and chalcopyrite contents then begin to increase and the pyrite becomes coarser (Plate 13E & F, and Fig. 60D). These sulfides grade into massive pyrite (Plate 13G - J, & Fig 60E). At the base of the Gap lens, the interstitial material between pyrite grains varies widely from sphalerite (Plate 13G) and or chalcopyrite (Plate 13H) to quartz (Plate 13I), quartz-sericite or sericite (Plate 13J). Pyrite-chalcopyrite-rich sulfide also occurs at the base of the lens but is not common in the drill holes logged (this may be a reflection of drilling rather than actual occurrence; confirmed by underground exposure pers. com. Mr A. Chong, 2000). Underlying the Gap lens is a zone of pyrite-sericite schists occcur in altered Facies 1 rhyolitic sediments (Fig. 60F).

Bornite overprints the sphalerite-pyrite throughout the Gap lens (Fig. 59B). In the barite-rich area at the top of the lens, bornite occurs as massive, anhedral patches of bornite (± anilite and gold) in barite-rich gangue (Plate 14A & B). In the sphalerite-rich zone bornite occurs within the sphalerite and as a matrix within pyrite bands (Plate 14C & D). In the pyrite-rich sulfides at the base of the Gap lens bornite becomes forms a matrix to the pyrite grains (Plate 14E).

Plate 13 Mineralogy and mineralogical zonation of Gap lens

A. Barite crystals at top margin of Gap lens: the sediments are strongly barite altered with minor pyrite, sphalerite and galena. BG18-889 155m

B. Sphalerite-galena in a barite-rich gangue (including barite crystals) and minor pyrite. Note sulfides have a silvery appearence due to high galena and barite contents. BG18-1050 73.7m

C. Sphalerite-galena-pyrite in a barite rich gangue. Baritic matrix decreasing and pyrite content increasing. BG18-889 152.9m

D. Banded sphalerite-pyrite, minor galena and minor barite. BG18-890 157.7m

E. Massive pyrite-sphalerite-chalcopyrite. Banding within sample defined by variations in sphalerite versus pyrite-chalcopyrite content. BG18-891 143.9m

F. Massive pyrite-sphalerite-chalcopyrite. Weak banding within sample defined by variations in sphalerite versus pyrite-chalcopyrite content. BG18-891 145.5m

G. Massive coarse pyrite with chalcopyrite matrix and sphalerite bands. BG18-891 136.6m

H. Massive pyrite, minor chalcopyrite matrix and sericite-quartz gangue, note coarse nature of pyrite (up to 2mm). BG18-891 135.7m

I. Massive coarse pyrite with minor chalcopyrite, quartz gangue. BG18-891 138.7m

J. Massive pyrite in strongly sericite altered gangue, note grain size of pyrite fine to medium due to shearing. Contrast with pyrite grain size in unsheared pyrite in G. BG18-891 139.6m

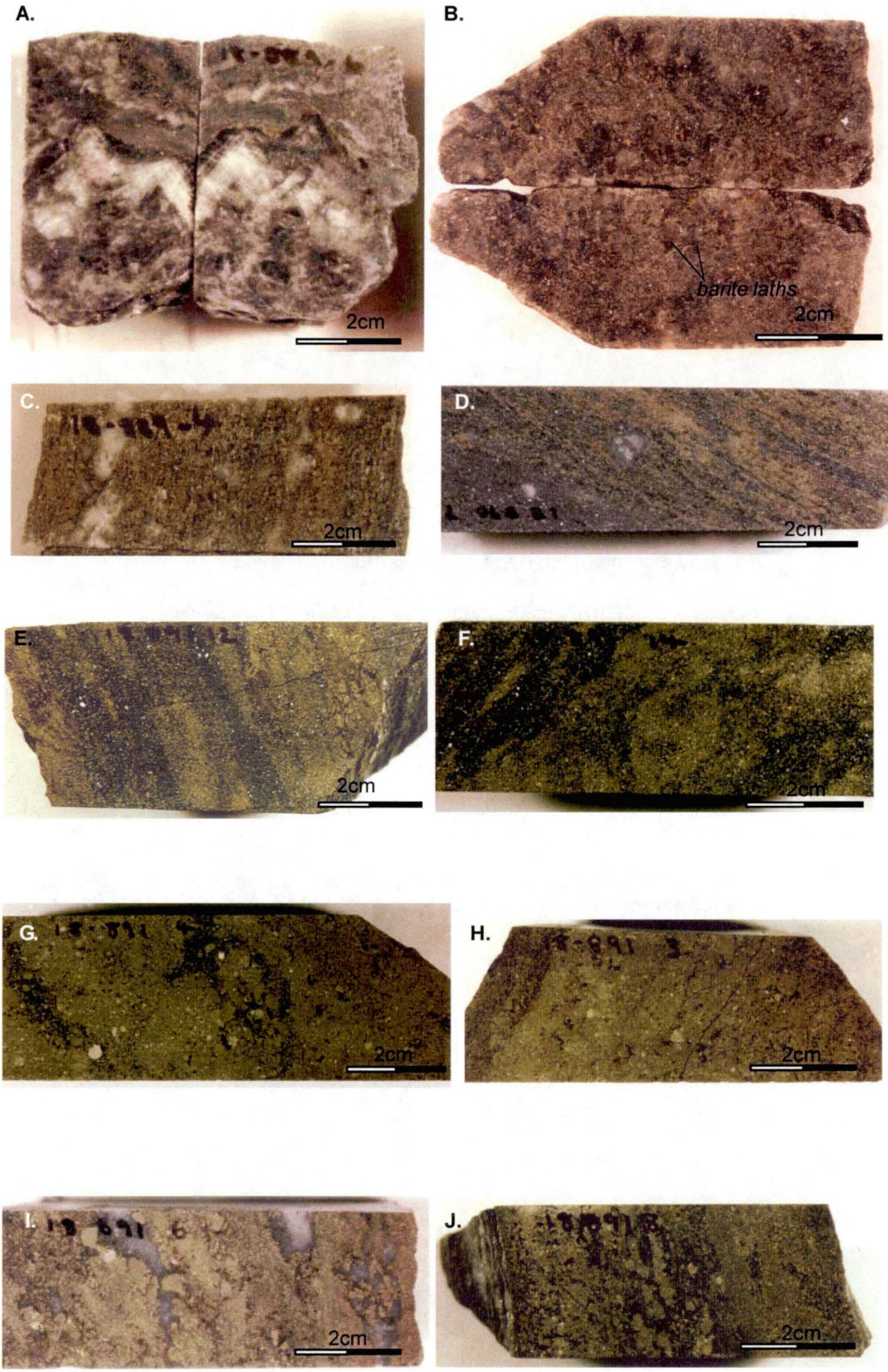
A.
2cm
B.
barite laths
2cm
C.
2cm
D.
2cm
E.
2cm
F.
2cm
G.
2cm
H.
2cm
I.
2cm
J.
2cm

Plate 14 Bornite in the Gap lens Zn-Fe-Pb-rich sulfides

A. Bornite in sphalerite-galena-tennantite-rich sulfides in barite-rich gangue at the top of the Gap lens. BG18-889 153.6m

B. Chalcopyrite and barite. BG18-890 495-505ft NQ core.

C. Bornite in coarse-pyrite within pyrite-sphalerite-rich massive sulfides. BG18-891 151.5m

D. Bornite with minor chalcopyrite in sphalerite-pyrite-rich massive sulfides. BG18-761 29.7m

E. Bornite in pyrite-sphalerite massive sulfides. Bornite preferentially replacing chalcopyrite-rich matrix to the pyrite grains, rather than sphalerite. BG18-1053 58.8m

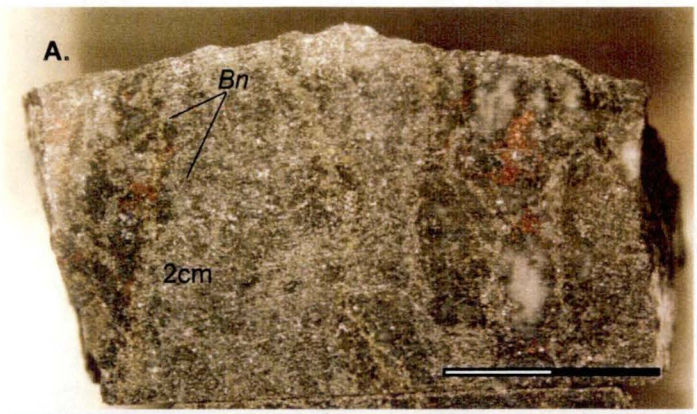
A.
Bn
2cm

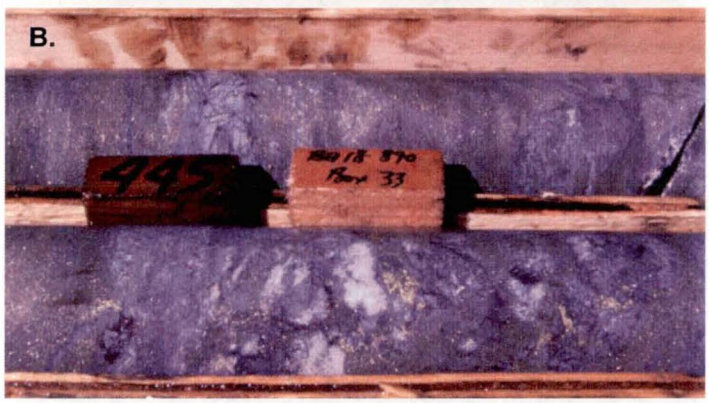
B.
495


C.
GSA
CM
IN
mm

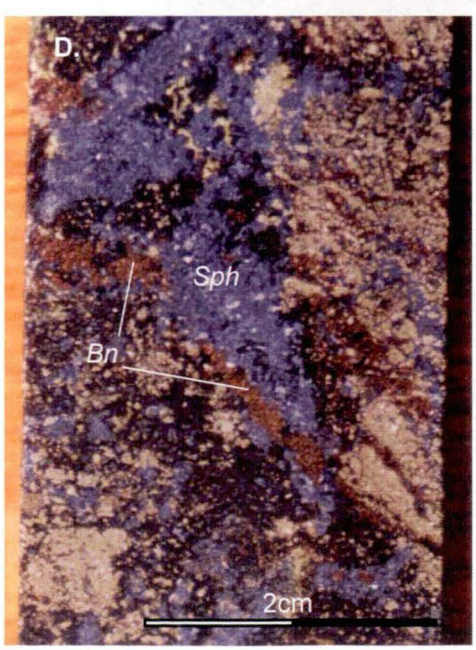
D.
Sph
Bn
2cm

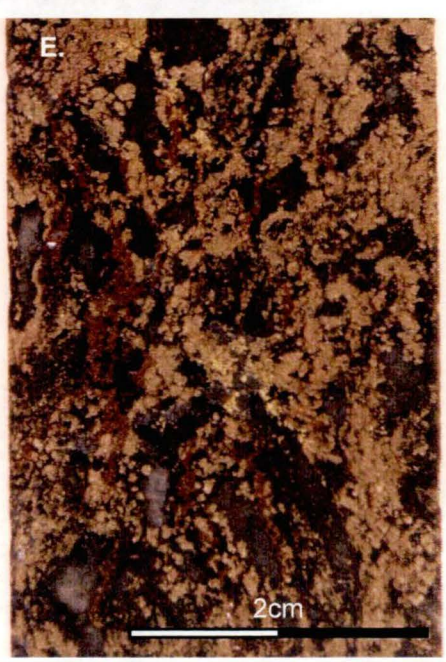
E.
2cm

Figure 60 Schematic log through Gap lens

A. Semi-massive sphalerite-galena-chalcopyrite in barite. Top of the Gap lens. L14-757 197.6m

B. Massive sphalerite-pyrite within barite. Toward the top of the Gap lens. L14-757 210.0m

C. Massive sphalerite-pyrite with minor chalcopyrite. Gangue quartz-sericite. Middle of Gap lens. L14-757 215.9m

D. Massive pyrite-sphalerite with minor chalcopyrite and bornite. Gangue quartz-sericite, toward the base of the Gap lens. L14-757 229m

E. Massive pyrite, gangue quartz. Base of Gap lens . L14-757 238.1m

F. Intense sericite alteration cross cut by quartz-pyrite alteration. Footwall to Gap lens. L14-757 258.3m

G. Sericite-(pyrite) altered HW Rhyolitic fine grained, volcanic sediments. Underlying the Gap lens. L14-757 322m

sph = sphalerite, ten = tennantite, py = pyrite, gal = galena, cpy = chalcopyrite, bar = barite, bn = bornite

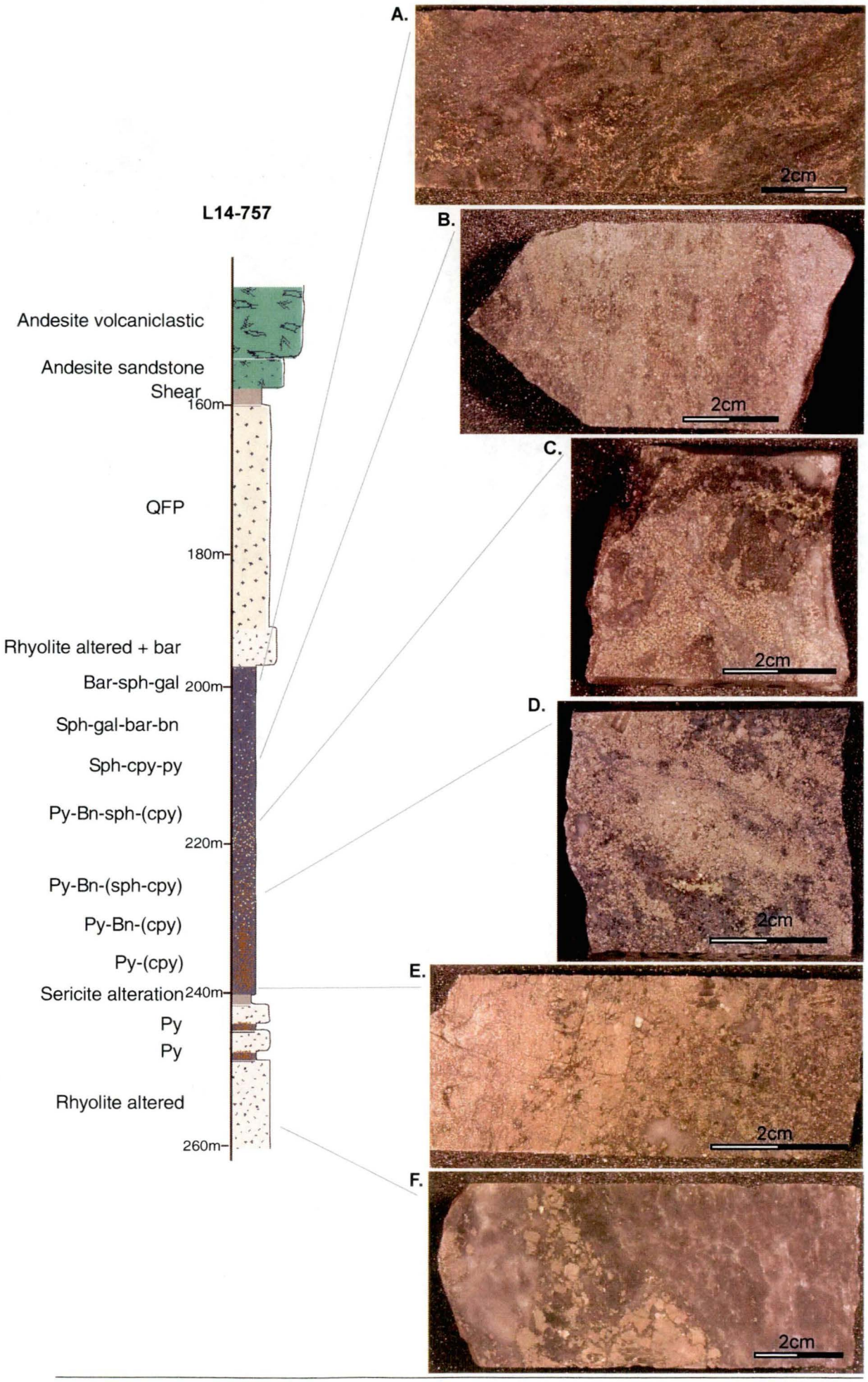

Sinclair 2000

6.3.6 Upper Zones lenses

Upper Zone lenses occur ten to thirty meters above the Battle lens, on the boundary between Facies 1 volcaniclastics and Facies 4 QFP (Fig. 18 & 19). Upper Zone mineralisation has been intersected near the top of drill fans planned to delineate Battle and Gopher lenses. Mining of the Upper Zone lenses has been restricted by the placement of the definition drill drifts. However, Upper Zone mineralisation has been mined between 1500mE and 1690mE, and 4100mN and 4210mN (as of August 1998). Figure 47 shows the modelled Upper Zone mineralisation above the Battle and Gopher lenses. The true extent of this style of mineralisation has not been explored in the Battle Zone due to the focus of definition drilling on the underlying Battle and Gopher lenses. The modelled lenses are provided as a guide only to the position of this mineralisation relative to other lenses, as structural complexity within the Upper Zone and lack of extensive drilling make true modelling impossible from current data.

Mineralogically the Upper Zone lenses are similar to the Gap lens, although they contain lesser amounts of colusite and renierite. A number of types of massive sulfides are discernible from drilling and underground mapping (Plate 15): barite-sphalerite-rich ore, sphalerite-pyrite ± chalcopyrite ore, massive pyritic sulfides, and honey yellow sphalerite with dark bands. These sulfides have been variably overprinted by chalcopyrite and bornite in two separate events. The relationship of these ores to one another and hence the ore zonation in the Upper Zones is difficult to access due to faulting. However, Upper Zone lenses are underlain by a zone of disseminated pyrite (± sphalerite), and zones which are barite-rich with stringer veinlets of sphalerite ± pyrite, galena, bornite, chalcopyrite, and stromeyerite. These are interpreted to be hosted in altered HW Rhyolite mass flows.

Barite-sphalerite-rich sulfides vary from massive barite with disseminated sphalerite and minor chalcopyrite-pyrite-bornite to massive sphalerite-galena-barite-rich sulfides (Plate 17A). Sphalerite is commonly black, although minor yellow sphalerite occurs in some areas. The sulfides commonly have a silvery appearance due to the high galena contents (Plate 15B) . The sphalerite-galena-barite grades downward into sphalerite-pyrite (Plate 15C & D).

The sphalerite-pyrite generally occurs as bands of coarse grained sphalerite (up to 2mm) and bands of coarse pyrite or coarse pyrite and chalcopyrite. Sulfides are commonly medium to coarse grained. However, where sericite gangue is abundant the sulfide grain size is smaller and a strong foliation is defined by the sericite (Plate 15E).

Massive pyrite forms coarse (1-2mm) grains in a matrix of sphalerite, chalcopyrite or gangue. This style of massive sulfide occurs as pods enclosed by shearing, suggesting they form coherent blocks which are not easily deformed (Plate 15G, H & I).

Honey yellow sphalerite with dark bands is a very distinctive ore type (Plate 15J). It occurs as massive, fine to medium grained, honey coloured sphalerite which is cross cut by regular black sphalerite bands. This type of ore shows few other sulfides in hand specimen, although accessory pyrite, chalcopyrite, galena and tennantite are seen in thin section (Chapter 7). The honey sphalerite generally occurs as blocks (see in underground mapping) and is observed throughout the Upper Zone lenses.

Chalcopyrite forms massive, irregularly shaped patches which cross cut the original sulfide features. Chalcopyrite also occurs on fracture planes as thin coatings with carbonate, and in quartz-carbonate veins. However, it is not seen associated with bornite.

Bornite also occurs in the Upper Zones, in underground exposure the bornite imparts a strong blue hue to the sulphides. On weathered surfaces leaching and oxidation of copper from the bornite results in a greeny-blue stain on the faces. In the sphalerite-rich ores, bornite appears to be concentrated around siliceous clast margins (Plate 15K), however, it can occurs throughout the sphalerite. In the more pyritic ores, bornite appears as a matrix to the pyrite grains giving the rock a coarse, granular appearance (Plate 15L).

Host rocks vary from moderately to strongly quartz-sericite altered, quartz phenocrysts are commonly visible despite the rock being veined or impregnated with sulphides (Plate 15M). Veinlets of sphalerite-tennantite-galena-pyrite (Plate 15M, O & P) as well as rare bornite veins (Plate 15N) occur throughout the surrounding rock. Disseminated to massive pyrite mineralisation also occurs in the surrounding host rocks. This pyrite is characteristically fine grained and is locally accompanied by minor sphalerite, tennantite and/or chalcopyrite, and is hosted in intense sericite alteration.

A schematic drill log through the Upper Zone lens is presented in Figure 61. Above the Upper Zone lenses moderately altered (quartz-sericite) , Facies 4 QFP is variably mineralised with sphalerite, tennantite, galena, pyrite and chalcopyrite veinlets (Figure 61A & C). Quartz phenocrysts are still clearly visible in Fig. 61 A & C, while Fig. 61B shows fine pseudo-fiamme due to incomplete silicic alteration. Within the Upper Zone lens massive sulfides of varying types (as described above) are faulted together with "swirly" patches of sericite altered matrix indicative of strong deformation (Fig. 61D - F shows just a few of the ore types seen within the Upper Zone lenses).

Plate 15. Upper Zone lens mineralogy (underground samples)

A. Massive barite, with disseminated sphalerite and galena. H169, Panel 10, Sample 1

B. Massive sphalerite-galena-barite with minor yellow sphalerite. Galena gives the sample a glittering silvery appearence. H152, EX2, Sample 1.

C. Massive sphalerite with barite-galena and pyrite - transitional ore type. H169, Panel 8, Sample 10.

D. Pyrite-sphalerite ore, gangue of quartz and sericite. H169, Panel 8, Sample 1

E. Strongly foliated fine grained sphalerite-pyrite in sericite alteration. H169 D2 P9 Sample 3

F. Massive sphalerite-pyrite with minor chalcopyrite. H169 P7 Sample 2

G. Massive, medium to coarse pyrite with sphalerite-bornite matrix. H169 P10 Sample 2

H. Fine to medium grained, massive pyrite with chalcopyrite matrix. H169 P10 sample 3

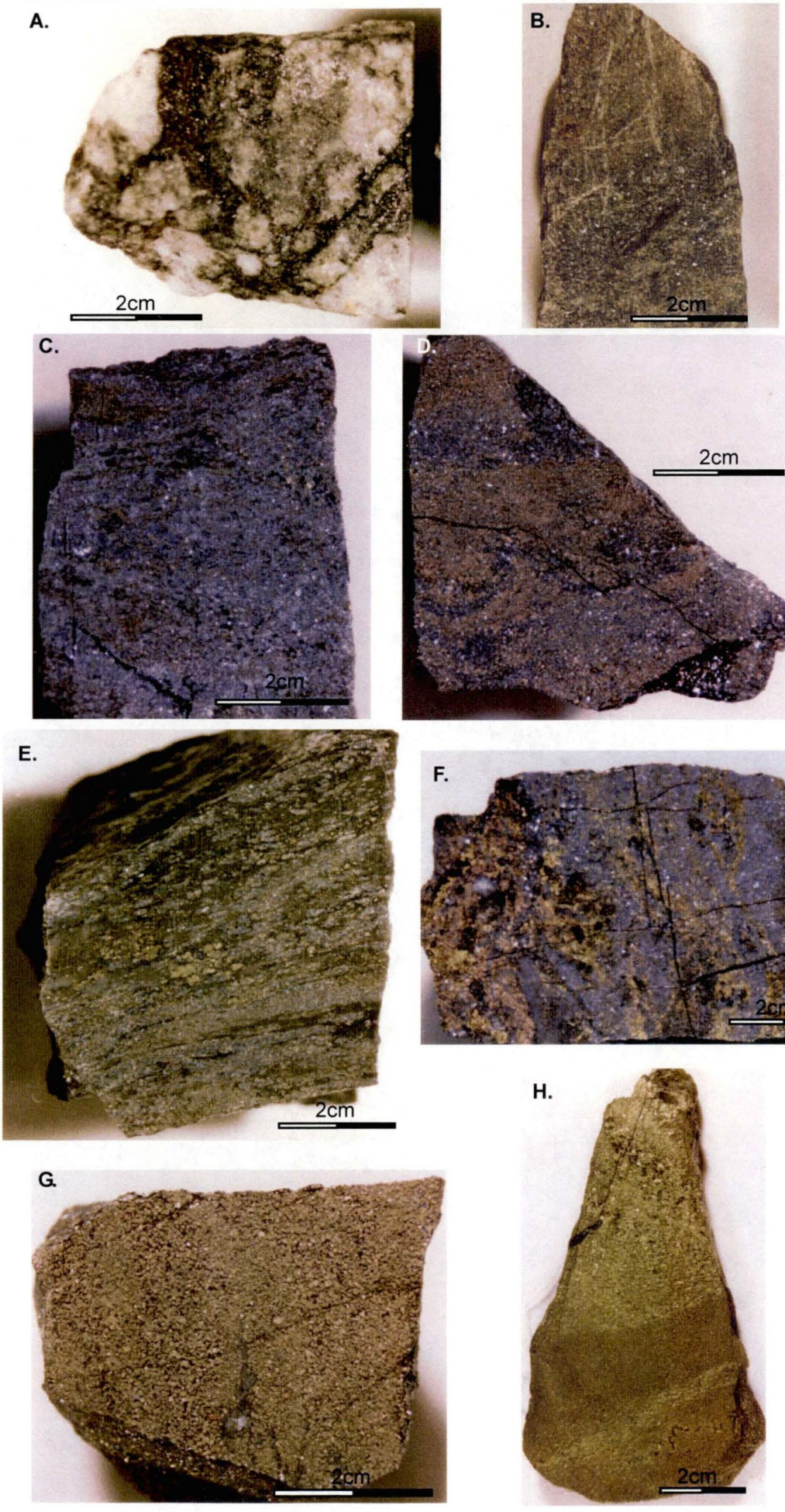
A.
2cm
B.
2cm
C.
2cm
D.
2cm
E.
2cm
F.
2cm
G.
2cm
H.
2cm

Plate 15 continued

I. Massive, coarse grained pyrite in siliceous matrix. H169 P8 Sample 4.

J. Honey-yellow sphalerite with dark sphalerite bands (or veinlets). H169 P7 sample 1

K. Bornite in pyrite-sphalerite-rich sulfides. Bornite appears to be concentrated around silicious inclusion. However, thin section observations indicate bornite is disseminated throughout the whole sample. H169 P8 sample 8

L. Bornite, chalcopyrite and sphalerite forming a matrix to coarse pyrite crystal. H152EX2 sample 1A.

M. Sphalerite-rich veinlets in moderately altered (QFP). This sample faulted against ore at end panel 8. H169 P8 sample 6

N. Bornite vein in strongly sericite altered host rock. 18-168DW

O. Coarse quartz-chalcopyrite-pyrite vein (D2 associated) bounding massive sphalerite-pyrite. H169 D1 sample 3.

P. Massive pyrite-chalcopyrite-galena-(quartz) vein within weakly altered host rock (OFP). H169 P8 sample 3

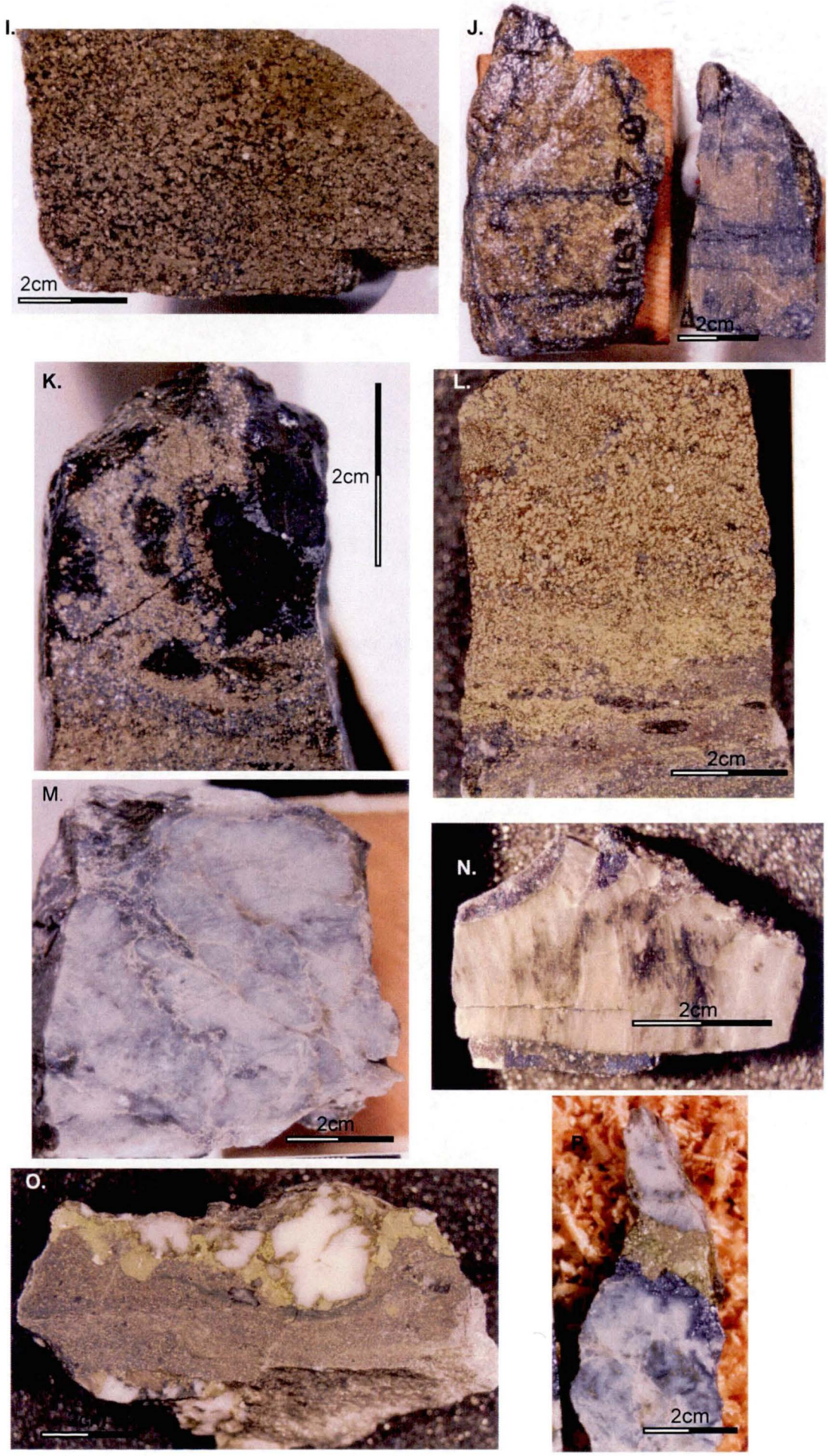
I.
2cm
J.
2cm
K.
2cm
L.
2cm
M.
2cm
N.
2cm
O.
P.
2cm

Figure 61 Drill log through an Upper Zone lens

A. Disseminated sphalerite-stringers in weakly altered QFP. BG18-1000 0.5m

B. Disseminated sphalerite-tennatite-galena-pyrite in moderately altered (sericite-quartz) QFP. BG18-1000 6.4m.

C. Sphalerite-galena-tennantite-pyrite stringer mineralisation in QFP, note quartz phenocrysts are still visible between stringer mineralisation. BG18-1000 13.5m

D. Massive sphalerite-galena-tennantite-pyrite with sericite altered matrix.BG18-1000 30.5m

E. Massive pyrite-sphalerite-chalcopyrite-bornite-tennantite-galena. BG 18-1000 33.0m.

F. Massive pyrite-chalcopyrite with minor sphalerite in silicified matrix. BG18-1000 34.1m

sph = sphalerite, ten = tennantite, py = pyrite, gal = galena, cpy = chalcopyrite

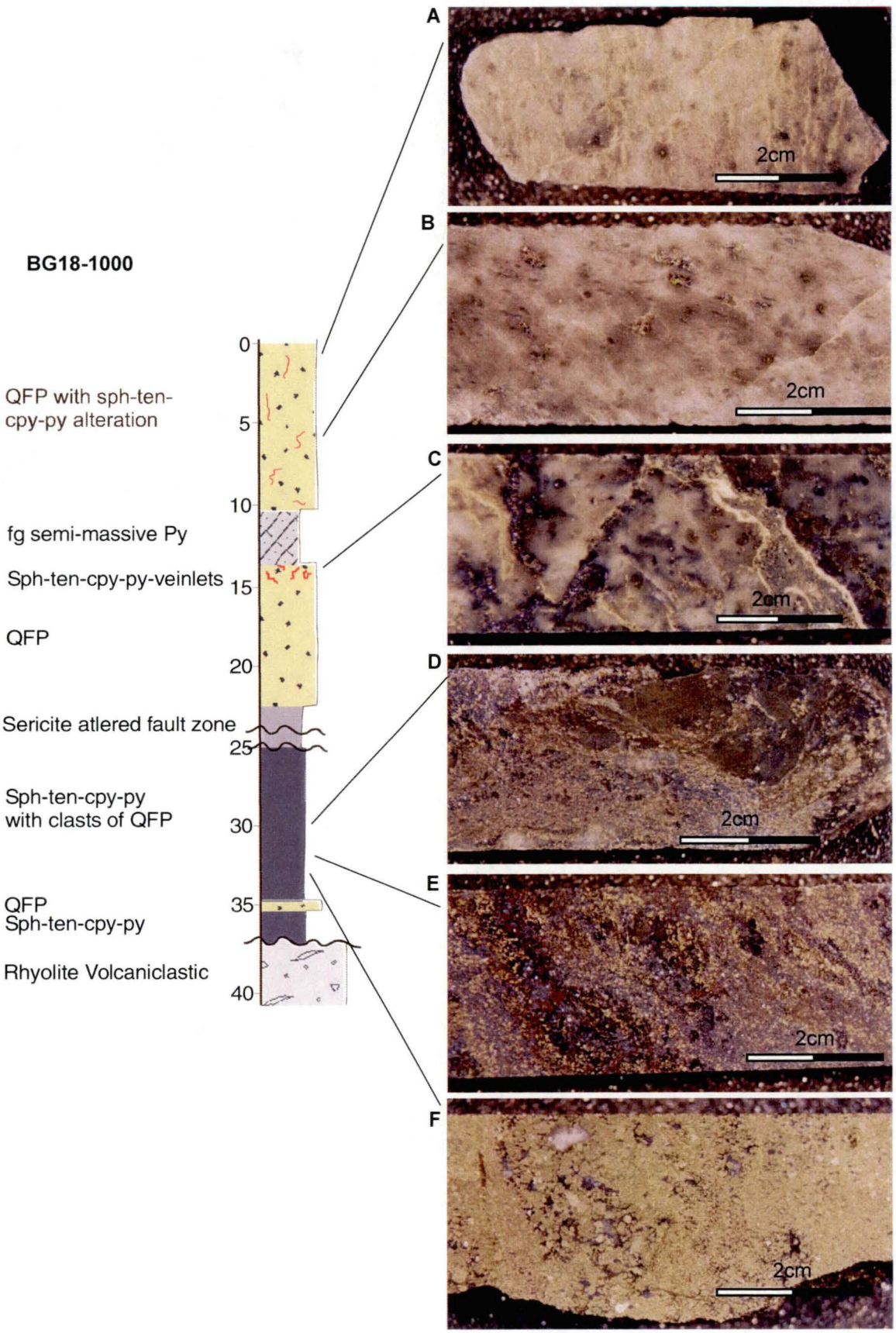
BG18-1000
QFP with sph-ten-cpy-py alteration
fg semi-massive Py
Sph-ten-cpy-py-veinlets
QFP
Sericite atlered fault zone
Sph-ten-cpy-py with clasts of QFP
QFP
Sph-ten-cpy-py
Rhyolite Volcaniclastic
0
5
10
15
20
25
30
35
40
A
B
C
D
E
F
2cm

6.4 Summary

The Battle Mine is a zone of individual massive sulfide lenses (Battle, Gopher, South Trough, Upper Zone and Gap). These lenses fall into two groups. The Battle, Gopher and South Trough all lie at the base of the HW Rhyolite with footwall alteration extending into the Price Formation. They are characterised by simple sphalerite-pyrite-chalcopyrite mineralogy with minor galena and tennantite, and accessory rutile and altaite. In contrast the Upper Zone and Gap lenses sit within and toward the top of the Facies 1 rhyolite, either at or near the base of QFP (Upper Zone) or within the QFP (Gap). These lenses are characterised by a more complicated mineralogy including sphalerite-pyrite-bornite-chalcopyrite-tennantite-colusite-renierite-anilite and electrum.

The shape of the Battle Zone lenses varies considerable from a sheet like morphology for the Battle lens (and possibly the Upper Zone lenses); asymmetric for the Gopher lens; and pipe shaped for the Gap lens. However, all lenses show typical VHMS mineralogical zonation (Franklin, 1993). Additionally the Gap and Upper Zone lenses have mineralogy enhanced by bornite, anilite and electrum.

Chapter 7

Ore Mineralogy, Textures and Mineral Chemistry

7.1 Introduction

Ore mineralogy at Myra Falls has been previously described by Chryssoulis (1989), Robinson (1992), Cresswell (1997) and internal company reports. All ore lenses in the Battle Zone have sphalerite-pyrite-tennantite-galena and chalcopyrite with accessory altaite and rutile. The Gap and Upper Zone lenses also contain bornite, anilite, coulsite, renierite, stromeyerite and electrum. This chapter describes the textures of each mineral, their relationship to other mineral phases and the mineral chemistry of each phase. These descriptions follow the ore types described in Chapter 6, and highlight the changes in sulfide mineralogy and texture in the lenses (from hangingwall to footwall). Mineral descriptions are divided into three assemblages to reflect the observed paragenetic sequence and the minerals associated with each mineralising event.

The Battle Zone sulfides have undergone metamorphism to lower greenschist facies and structural deformation, both of which have modified mineral textures. Thus the interpretation of sulfide textures in the Battle Zone must consider primitive textures due deposition, reworking by hydrothermal fluids during sulfide deposition and the formation of secondary sulfide textures resulting from metamorphism and deformation. Different chemical conditions apply during formation of VHMS ores and metamorphism, thus chemistry will also be used where applicable to differentiate mineralogical processes.

Primary mineral textures in VHMS deposits are well understood from the study of both modern seafloor black smoker systems (summaries in Rona and Scott, 1993) and undeformed ancient deposits (Sato, 1972; Ishihara et al., 1974; Ohomoto and Skinner, 1983; Eldridge et al., 1983; Lianxing and McClay, 1992; Larocque and Hodson; 1993). The criteria used to distinguish primary mineral textures are documented in Eldridge et al. (1983) and Larocque and Hodgson (1995), these descriptions are used in the following interpretations to provide a basis for comparison with facies resulting from metamorphism and deformation.

The effects of metamorphism and deformation on massive sulfide deposits have been described by many authors (Vokes 1969; Mookherjee 1976; McClay 1991; Craig and Vokes 1992, 1993; Vokes and Craig 1993; Spry et al., 2000). In particular greenschist facies metamorphism was found, by Craig and Vokes (1992), to have little effect in altering the mineralogy of ores. However, greenschist metamorphism had a significant effect on ore textures and the distribution of minor elements among co-existing minerals (Larocque and Hodgson, 1995). The interpretation of metamorphic mineral textures in the Battle Zone draws on the descriptions of metamorphosed ores and on experimental

work into the deformation of polymetallic ores (references will be given where appropriate).

7.2 Methods

Samples were taken during logging of core and under ground mapping as representative of the ore types logged (Chapter 6). Samples were chosen from this collection to represent the main ore types and their variation from hangingwall to footwall within each lens as well as their lateral distributions and variations between lenses. The chosen samples were made into polished thin sections at the University of Tasmania. A total of 400 polished thin sections were examined under reflected and transmitted light to determine ore and gangue mineralogy, with textures of each ore mineral being recorded by digital camera. Representative slides were chosen and probed using the Cameca microprobe under the guidance of Dr D. Steele at the CLS laboratories, University of Tasmania. Analytical conditions for each element are summarised in Table 1, Appendix 3. Microprobe results are listed in Appendix 3.

7.3 Cu-Pb-Zn-Fe-rich mineral assemblage

7.3.1 Sphalerite

Sphalerite occurs as anhedral masses (Plate 16A - E) with no internal features in transmitted light. Overlying the massive sulfide lenses disseminated sphalerite occurs in barite or interstitial to barite laths (Gap, Upper Zone) or disseminated in strongly silicified sediments (or "cherts") above the Battle and Gopher lenses (Plate 16A & B). At the top of the massive sulfide lenses, sphalerite occurs as a massive anhedral matrix which hosts irregular shaped disseminations of galena, chalcopyrite, and lesser amounts of tennantite and pyrite (Plate 16C & D) and in the Gap and Upper Zones - colusite (Plate 16E & F). Where galena is the dominant sulfide, sphalerite forms rounded grains enclosed by massive galena (Plate 16G). Otherwise sphalerite grains are polygonal with by fine-grained (<20 μm) inclusions of galena, chalcopyrite and tennantite along the grain boundaries (Plate 16H). Sphalerite grains average ~200μm in size and have triple points approaching 120° (Plate 16H). In the banded ores, sphalerite forms bands of anhedral grains, which show chalcopyrite 'disease' (refer to discussion on chalcopyrite disease 7.5.2) and granoblastic textures with chalcopyrite (Plate 17A - D). As the sphalerite content of the ores decreases into the pyrite-chalcopyrite-rich sulfides sphalerite becomes increasingly rounded against chalcopyrite (Plate 17D - F). Sphalerite masses are more intensely chalcopyrite-diseased in the Battle, Gopher and South Trough lenses (Plate 17G & H). One zoned sphalerite crystal was observed in a Battle lens sample (Plate 18A & B).

Sphalerite in the Battle Zone lenses at the base of the HW Rhyolite contain abundant (< 20 μm) rounded and irregularly arranged chalcopyrite blebs, and rarer "flecks" aligned along cleavage plains of the sphalerite (Plate 17G & H). These blebs are referred to as chalcopyrite "disease". Upper Zone lenses also show chalcopyrite "disease" but in much lower intensity that the underlying lenses while

Plate 16 Photomicrographs of Battle Zone ore

A Upper Zone sphalerite-galena-barite-rich ore. Barite gangue hosting disseminated, irregularly shaped grains of sphalerite, galena and tennantite. BG18-542 13.7m

B Sphalerite-galena disseminated in quartz rich gangue. BG18-479 20.7m

C Upper Zone sphalerite-galena-barite-rich sulfides. Anhedral to equant sphalerite outlined by galena and hosting equant tennantite grains with minor anhedral chalcopyrite. BG18-542 13.7m

D Massive sphalerite with cuspate galena and equant tennantite blebs outlined sphalerite grains. BG18-1050 76.7

E Colusite grains in sphalerite. BG18-889 153.6m

F Colusite grain with bornite and chalcopyrite in sphalerite BG18-890 152.35m

G Polygonal sphalerite plus galena showing annealed texture. L14-733 317.95m

H Sphalerite grains outlined by <20um chalcopyrite and pyrite trapped along grain boundaries. Note 120° junctions. BG18-780 93.85

sph = sphalerite, py = pyrite, ten = tennantite, gal = galena, cpy = chlacopyrite, col = colusite, bn = bornite, r = rutile, alt = altaite, anil = anilite, ren = renierite, bar = barite, qtz-quartz, carb = calcite, ser = sericite

Plate 16

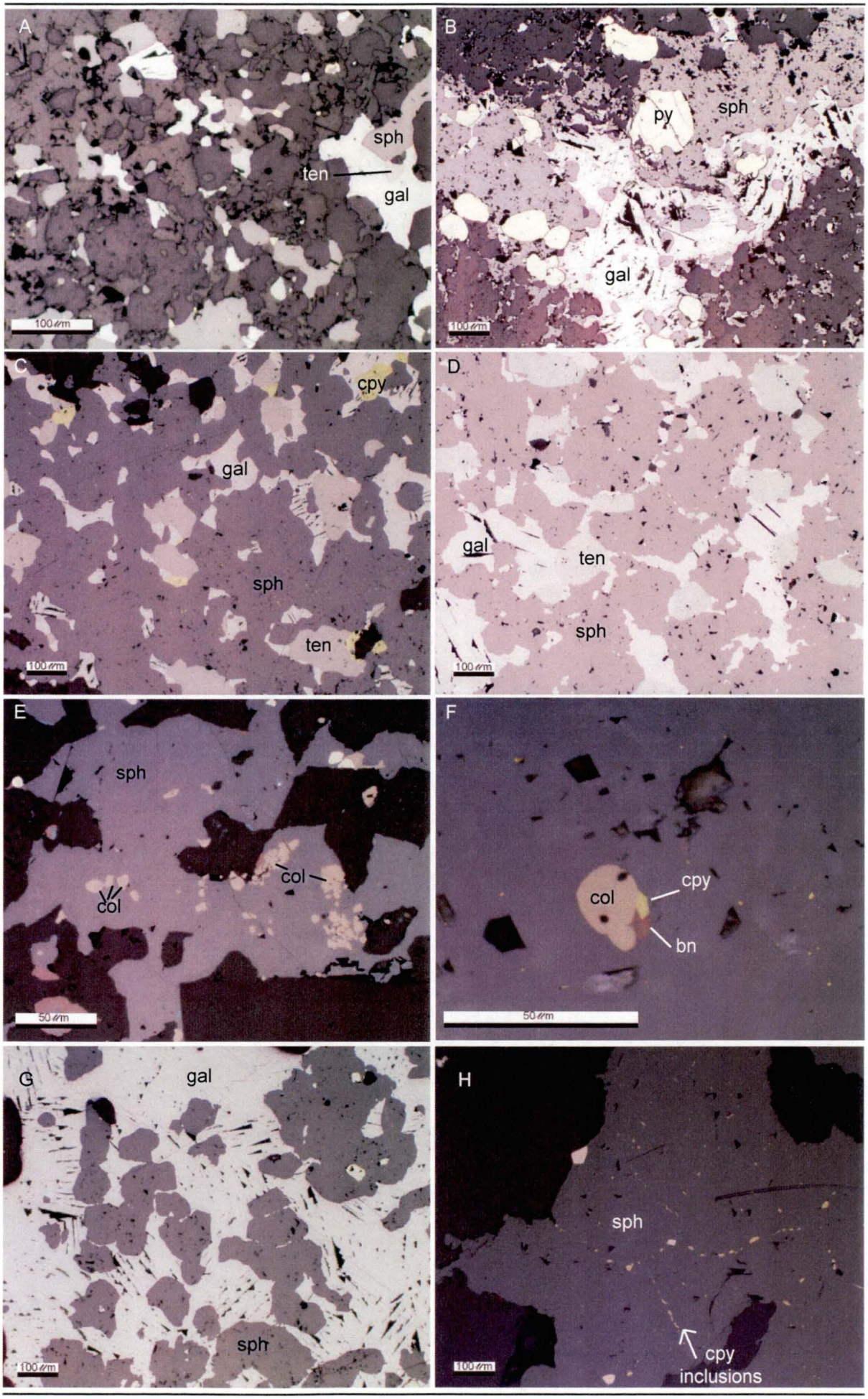
A
sph
ten
gal
100 µm
B
py
sph
gal
100 µm
C
cpy
gal
sph
ten
100 µm
D
gal
ten
sph
100 µm
E
sph
col
col
50 µm
F
col
cpy
bn
50 µm
G
gal
sph
100 µm
H
sph
cpy
inclusions
100 µm

Plate 17 Photomicrographs of Battle Zone ore

A. Massive sphalerite-pyrite ore. Annhedral to embayed coarse (50-300um) pyrite grains and equant tennantite grains in massive anhedral sphalerite. BG18-890 151.3m.

B. Granoblastic textured sphalerite, galena and chalcopyrite indicating near textural equilibrium. BG18-343 57.1-59.2m

C. Close up of granoblastic sphalerite, galena and chalcopyrite from B. Central sphalerite grain shows strong chalcopyrite disease. BG18-343 57.1-59.2m

D. Granoblastic sphalerite-chalcopyrite with minor anhedral pyrite and minor tennantite. BG18-485 81.15m

E. Strongly resorbed recrystallised pyrite grains in chalcopyrite. BG18-891 146.3m

F. Granoblastic sphalerite-pyritre-chalcopyrite texture. BG18-479 10.8m

G. Intense chalcopyrite disease in sphalerite. BG18-343 57.1-59.2m

H. Chalcopyrite along cleavage planes in sphalerite. BG18-481 18.25m

sph = sphalerite, py = pyrite, ten = tennantite, gal = galena, cpy = chlacopyrite, col = colusite, bn = bornite, r = rutile, alt = altaite, anil = anilite, ren = renierite, bar = barite, qtz-quartz, carb = calcite, ser = sericite

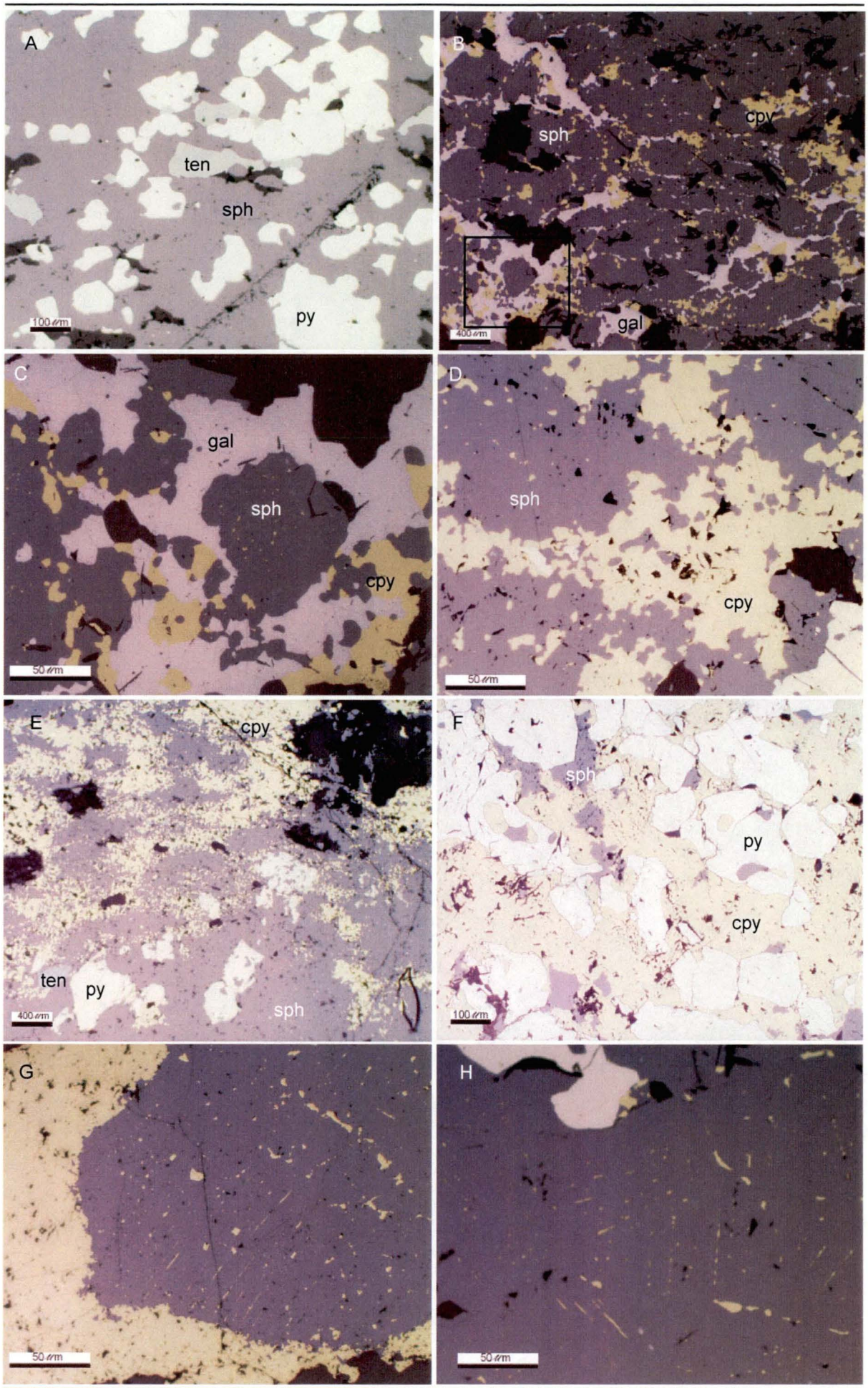
A
ten
sph
py
100 µm
B
sph
cpy
gal
400 µm
C
gal
sph
cpy
50 µm
D
sph
cpy
50 µm
E
cpy
ten
py
sph
400 µm
F
sph
py
cpy
100 µm
G
50 µm
H
50 µm

the Gap lens sphalerite is almost entirely free of chalcopyrite "disease".

The honey yellow sphalerite with dark bands (described in Chapter 6) is characteristic of Upper Zones (also seen in minor amounts in the Battle and Gopher lenses). The dark bands that give this ore its distinctive appearance are not visible in reflected light but can be seen in plain polarised transmitted light (Plate 18C & D). The bands are darker at centre with diffuse margins and often enclose thin bands of gangue consisting of minor sericite and recrystallised quartz.

The textures of sphalerite described above, with the exception of the one crystal showing zoning, are entirely consistent with the textures of sphalerite from metamorphosed ore deposits (Stanton, 1964; Craig and Vokes, 1993). Metamorphism causes the coarsening of sphalerite grains, the formation of 120° triple junctions and the migration of other phases to grain boundaries and triple point junctions. However the association of sphalerite with chalcopyrite, galena and barite toward the top of the lenses and the decrease in sphalerite content and increase in chalcopyrite disease of the sphalerite toward the base of lenses is consistent with Eldridge et al., (1983) zone refining model for VHMS lenses. Thus the metamorphism of Battle Zone ores has destroyed primary sphalerite textures, but mineral associations are apparently retained.

Mineral Chemistry

Microprobe analyses of sphalerite form the Battle Zone are listed in Table 2, Appendix 3 and summarised in Table 21. Cadmium and Fe were detected in sphalerite from all lenses and are plotted along with Zn on Figure 62. Iron content of Battle Zone sphalerite varies considerable between lenses. The South Trough has two populations of sphalerite based on Fe, to the north in pyrite-chalcopyrite-rich sulfides Fe contents of 4500-5500ppm are common with Cd >1500ppm. In contrast sphalerite at the southern end of the South Trough lens within sphalerite-pyrite-chalcopyrite rich sulfides have lower Fe (1000-2000ppm) and Cd (<1500ppm) contents. The Battle and Gopher lens sphalerite has a wide range of Fe contents (up to 6300ppm) and Cd contents mostly between 2500-3500ppm (Fig. 62). Upper Zone sphalerite shows a similar range of Cd contents to the under-

Lens	No points	Mineral	Formula	major elements
Upper Zone	23	Sphalerite	ZnS	Cd 0 – 5000ppm Fe 0–2600ppm Cu 0ppm
Battle Main	19	Sphalerite	ZnS	Cd 0 - 4600ppm Fe 1500 – 6300ppm Cu 0 – 3300ppm
South Trough	12	Sphalerite	ZnS	Cd 2700-3400ppm Fe 1400ppm-1.4wt% Cu 0 – 2400ppm
Gap	15	Sphalerite	ZnS	Cd 2600 – 3700ppm Fe 0 - 7200ppm Cu 0 - 5300ppm

Table 21. Summary of sphalerite mineral chemistry. 0 - used where analyses are below detection. Detection limits Cd = 1000ppm, Fe = 1000ppm and Cu = 1000ppm.

Plate 18 Photomicrographs of Battle Zone ore

A & B Zoned sphalerite crystals. A) transmitted light, B) reflected light. BG18-482 37.0-38.1m

C & D Honey yellow sphalerite from Upper Zone, dark bands not visible in reflected light (C), but clearly visible in transmitted light. H169 P7 Sample No.1

E. Pyrite framboid infilled with bornite in quartz gangue. BG18-1053 58.8m

F. Pyrite framboids in quartz gangue. BG18-1051 71.1m

G. Pyrite framboid infilled with anilite and minor bornite, hosted in quartz gangue along with coarse pyrite subhedra. BG18-1051 71.1m

H. Pyrite framboids in quartz gangue. BG18-1051 71.1m

sph = sphalerite, py = pyrite, ten = tennantite, gal = galena, cpy = chlacopyrite, col = colusite, bn = bornite, r = rutile, alt = altaite, anil = anilite, ren = renierite, bar = barite, qtz-quartz, carb = calcite, ser = sericite

Plate 18

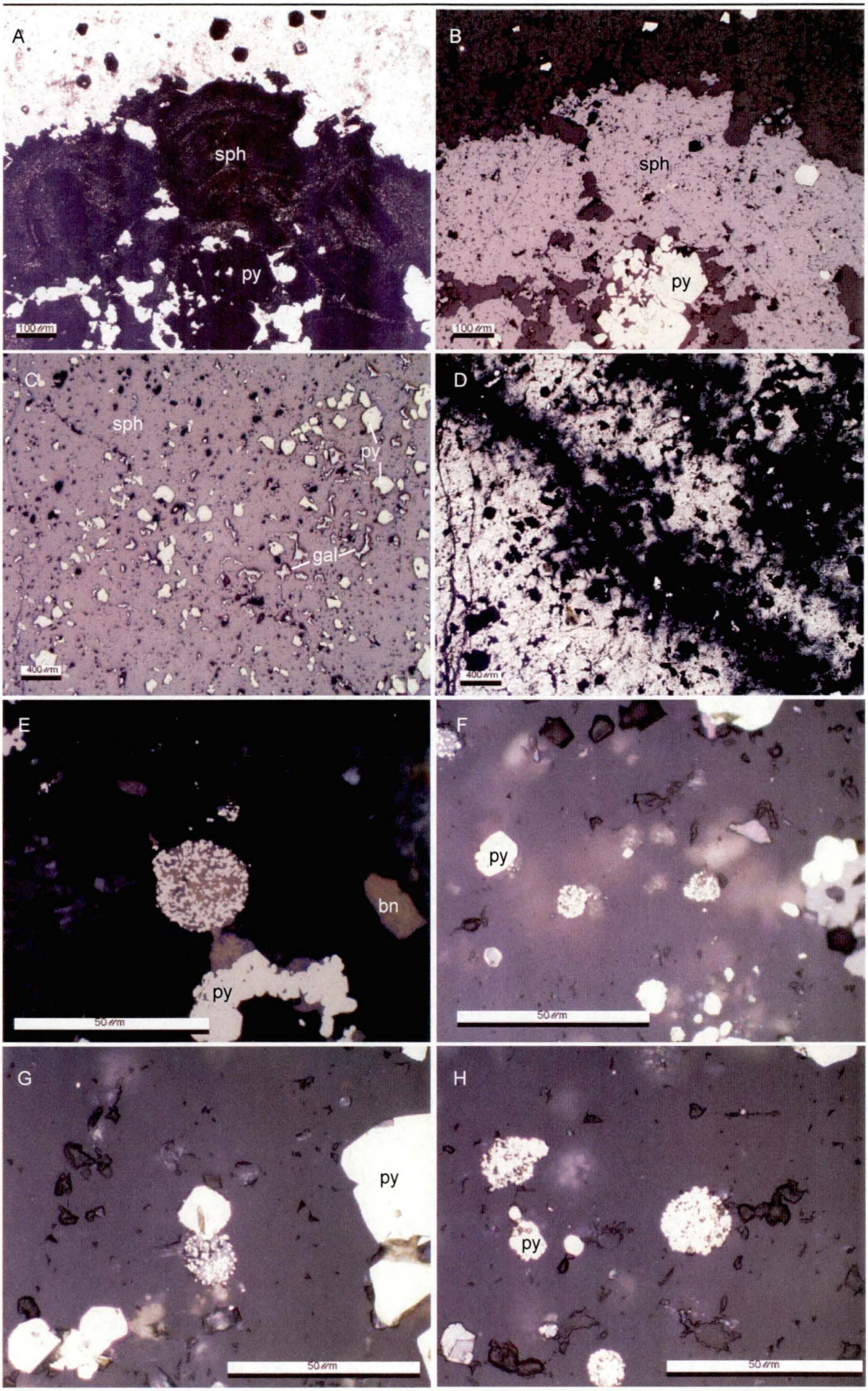
A
sph
py
100 µm
B
sph
py
100 µm
C
sph
py
gal
400 µm
D
400 µm
E
bn
py
50 µm
F
py
50 µm
G
py
50 µm
H
py
50 µm

lying lenses, but lower Fe contents than seen in underlying Battle and Gopher lenses. Gap lens sphalerite show similar Fe contents to the Upper Zone sphalerite, with the exception of one analysis that showed 7200ppm Fe. This 7200ppm Fe may be due to the presence of finely disseminated pyrite within the sphalerite. Copper in sphalerite was recorded in all lenses except the Upper Zone lens (Table 21). The presence of copper is sphalerite was assumed to be due to the presence of finely disseminated chalcopyrite within the sphalerite.

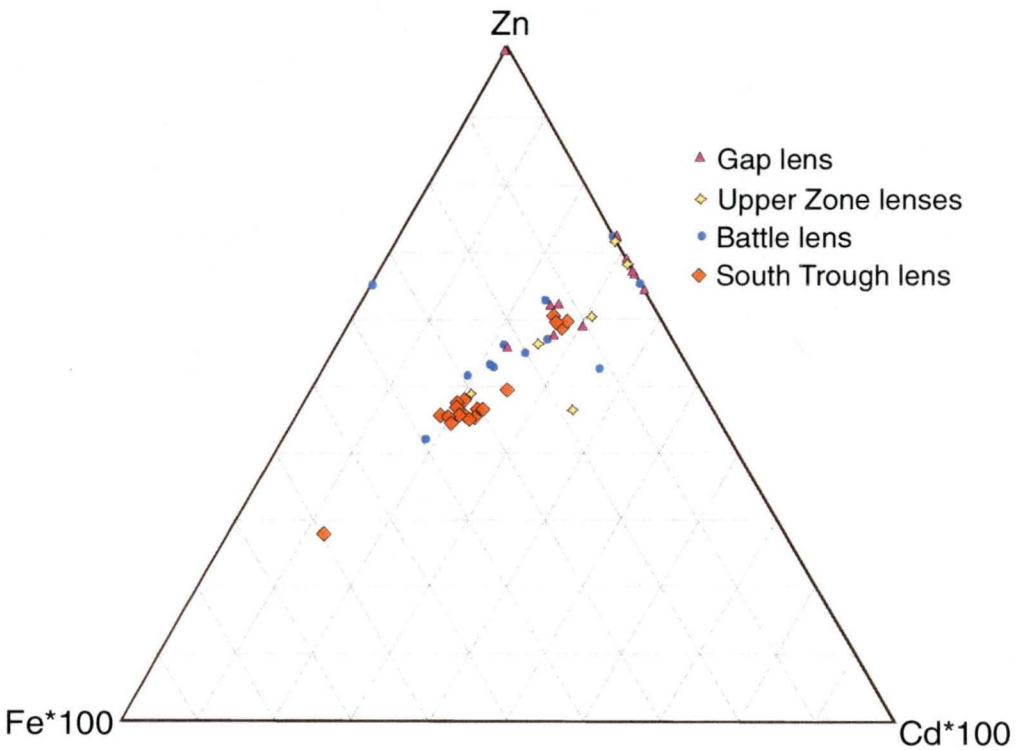

Figure 62. Zn-Fe-Cd ternary diagram showing variation in sphalerite mineral chemistry between the Battle Zone lenses.

A traverse across a sample of honey yellow sphalerite with dark bands was conducted to determine the composition of these bands. Result are listed in Table 3 in Appendix 3 and summarised in Figure 63. The microprobe traverse shows iron content in dark bands to be erratic but overall greater than in the light bands. Thus the dark band represent more iron rich sphalerite than the surrounding honey yellow sphalerite.

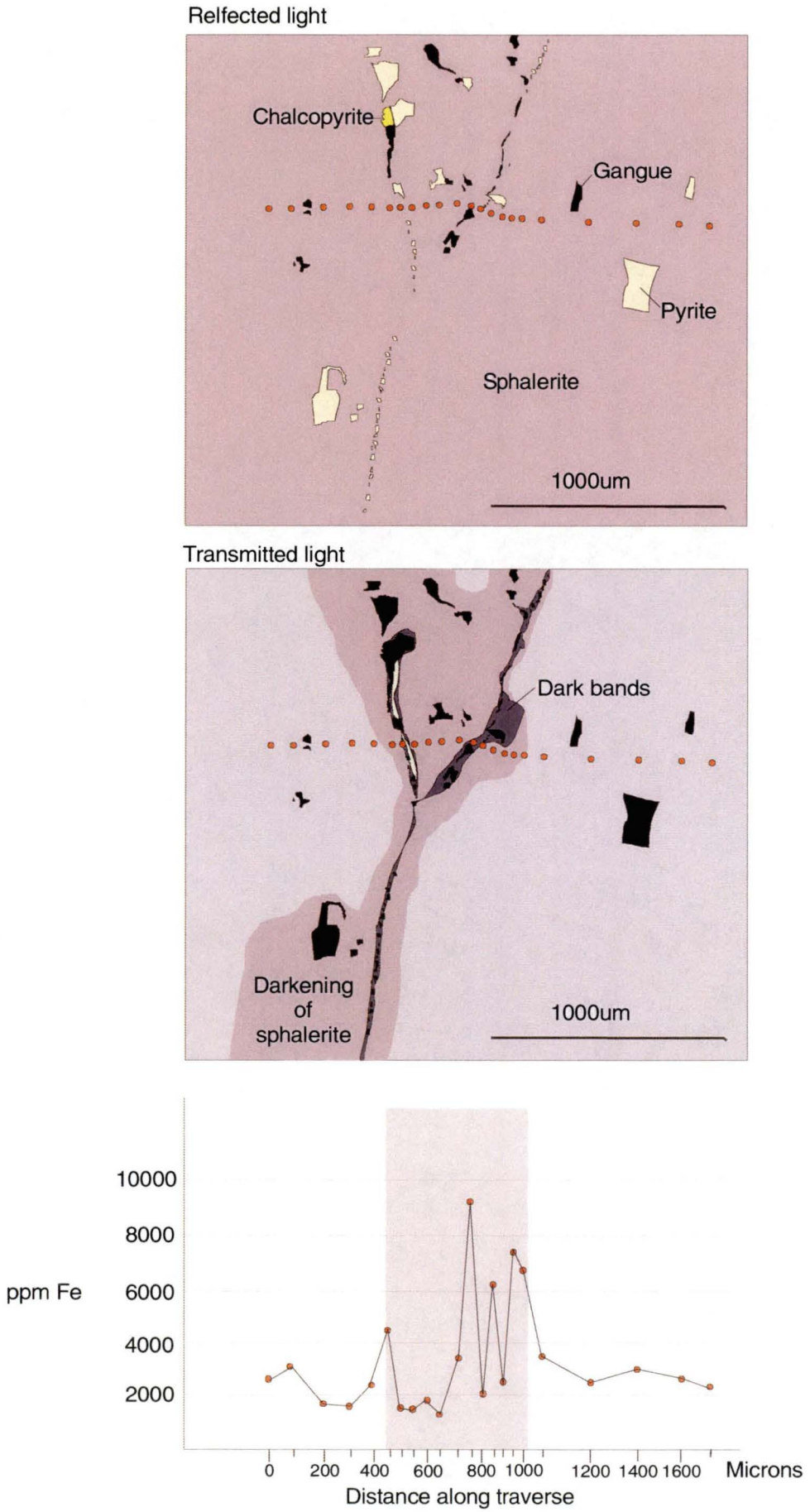

Figure 63. Microprobe traverse across honey yellow sphalerite with dark bands.

7.3.2 Pyrite

Pyrite shows a wide variety of textures in the Battle Zone. Textures range from fine grained framboids, fine grained disseminated euhedra and rings of radiating crystals, to coarser anhedral to euhedra pyrites, as well as porphyroblasts.

Framboids and delicate framboidal textures are observed in all ore types, except the strongly baritic ores at the top of the Gap (and equivalent ores in Upper Zones). Framboids are composed of individual <1μm pyrite grains and form circular clusters up to 50μm (Plate 18E - H). They are preserved in strongly quartz-altered (silicified) host rocks. Also associated with gangue are fine grained (5-20μm) euhedral pyrites that occur disseminated through the quartz-sericite alteration and surrounding sediments. Circular structures of radiating fine grained, pyrites are rare but occur in quartz gangue associated with the ores (Plate 19A - C). These structures may be filled with sphalerite, chalcopyrite or gangue. Fine grained masses of pyrite also occur, these masses are distinguished by their spongy texture (Plate 19D). This spongy texture is due to fine grained sulphides (chalcopyrite, galena and sphalerite) or gangue (quartz and/or sericite) between the pyrite grains.

Coarse pyrite ranges in size from 100 to 700 μm (most 200-400μm; Plate 19E – H & Plate 20A - E). Many coarse pyrite grains have abundant 20μm inclusions of chalcopyrite, tennantite and galena toward the centres of the grains (Plate 19G & H & Plate 20C). These inclusion rich centres are overgrown by inclusion free pyrite or pyrite that contains large (upto 100μm) inclusions of sphalerite, tennantite and chalcopyrite (Plate 19G & Plate 20A & B), and galena (up to 50μm; Plate 20D & E). In the Gap lens and Upper Zone lenses, the coarse pyrite may also contain inclusions of colusite up to 50μm (Plate 20F).

Coarse pyrite grains are euhedral at the top of the Gap lens (Plate 19F & Plate 20F), however at the top of all other lenses they show subhedral to weakly embayed outlines (Plate 16D). Coarse pyrite increases in abundance downward in all ore lenses. Rounding and embayment of the coarse pyrites also increases downward. In the sphalerite-rich ores, coarse pyrites form pyrite-rich bands with chalcopyrite. Downwards the pyrite-chalcopyrite bands increase in size and abundance. Pyrites in these bands are slightly smaller (100-300 μm) than pyrites in the surrounding sphalerite. Where pyrite is abundant, it occurs as polycrystalline aggregates of polygonal grains (Plate 20G & H). Chalcopyrite-pyrite-rich ores grade down into massive polycrystalline pyrite (Plate 21A) and eventually into disseminated, coarse euhedral to anhedral grains and fine-grained euhedra of pyrite in sericite-quartz gangue (Plate 21B).

Pyrite also occurs as porphyroblasts ranging in size from 500μm to 5mm. Porphyroblasts are subhedral to round in outline and increase in size and abundance downward through the ore types (Plate 21C – F). Porphyroblasts from the Gap lens (Plate 21D) are notably smaller than those from the underlying lenses (Plate 21C, E & F). Pyrite porphyroblasts are inclusion rich with inclusions of quartz, muscovite, sphalerite, chalcopyrite, galena and tennantite depending on the surrounding mineralogy. Inclusion may define circular to subhedral outlines within the porphyroblasts.

Fine grained pyrite such as the pyrite framboids, ring structures and fine grained masses of spongy pyrite are interpreted as primitive textures formed during VHMS mineral deposition. How-

Plate 19 Photomicrographs of Battle Zone ore

A & B Pyrite ring structures. B) Close up showing each ring made of pyrite euhedra. L14-733 314.55m

C. Pyrite framboid overgrown by recrystallised pyrite and infilled with chalcopyrite and sphalerite. BG18-485 76.2m

D. Fine grained pyrite. BG18-1053 58.8m

E. Massive pyrite-sphalerite ore. Anhedral, sub-hedral and embayed pyrite crystals in sphalerite plus minor fine grained spongy pyrite on sphalerite/quartz margin. BG 18-890 151.3

F. Euhedral pyrite crystals. BG18-1002 77.7m

G. Pyrite subhedral to euhedral pyrite crystals with chalcopyrite-galena and bornite inclusions. Central pyrite crystal showing a nice zonation of inclusions around core. BG18-1000 33m

H. Sphalerite and chalcopyrite inclusions concentrated in and around inclusion-rich core. Core overgrown by clear recrystalised pyrite. H169 P10 Sample No 2

sph = sphalerite, py = pyrite, ten = tennantite, gal = galena, cpy = chlacopyrite, col = colusite, bn = bornite, r = rutile, alt = altaite, anil = anillite, ren = renierite, bar = barite, qtz-quartz, carb = calcite, ser = sericite

Plate 19

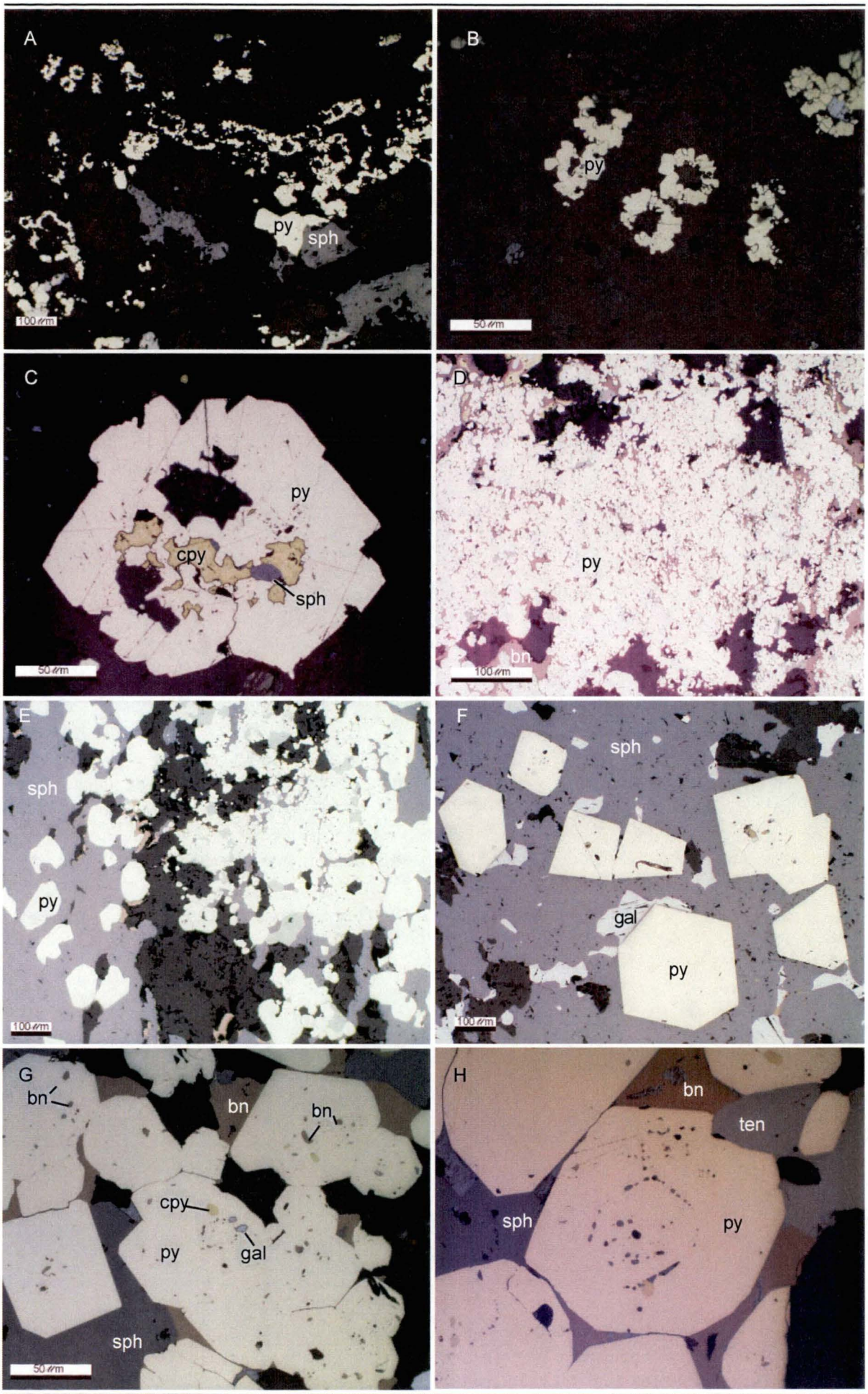
A
py
sph
100 µm
B
py
50 µm
C
py
cpy
sph
50 µm
D
py
bn
100 µm
E
sph
py
100 µm
F
sph
gal
py
100 µm
G
bn
bn
bn
cpy
py
gal
sph
50 µm
H
bn
ten
sph
py

Plate 20 Photomicrographs of Battle Zone ore

A. Sphalerite and chalcopyrite inclusion rich coarse pyrites in sphalerite. BG18-479 10.8m

B. Strongly embayed pyrite in sphalerite matrix BG18-484 54.0-54.9m

C. Sphalerite and chalcopyrite inclusion rich coarse pyrite grains in chalcopyrite. BG18-484 54.0-54.9m

D. Poikiloblastic pyrite grains with galena and sphalerite inclusions, hosted in sphalerite and chalcopyrite. BG18-542 15.8m

E. Poikiloblastic pyrite grain with large galena and tennantite inclusions, hosted in sphalerite and chalcopyrite. BG18-542 15.8m

F. Massive sphalerite-pyrite ore with abundant colusite grains in coarse euhedral pyrite crystals and in sphalerite matrix. Large tennantite grains also occur in sphalerite. BG18-889 153.6m

G. Polygonal pyrites separated by chalcopyrite, BG18-1000 96.2m

H. Massive pyrite-chalcopyrite ore, pyrite junctions 120° indicative of annealing. Pyrite grains have sphalerite inclusions, chalcopyrite preferentially occupies grain boundaries of pyrite. BG18-891 146.3m

sph = sphalerite, py = pyrite, ten = tennantite, gal = galena, cpy = chlacopyrite, col = colusite, bn = bornite, r = rutile, alt = altaite, anil = anilite, ren = renierite, bar = barite, qtz-quartz, carb = calcite, ser = sericite

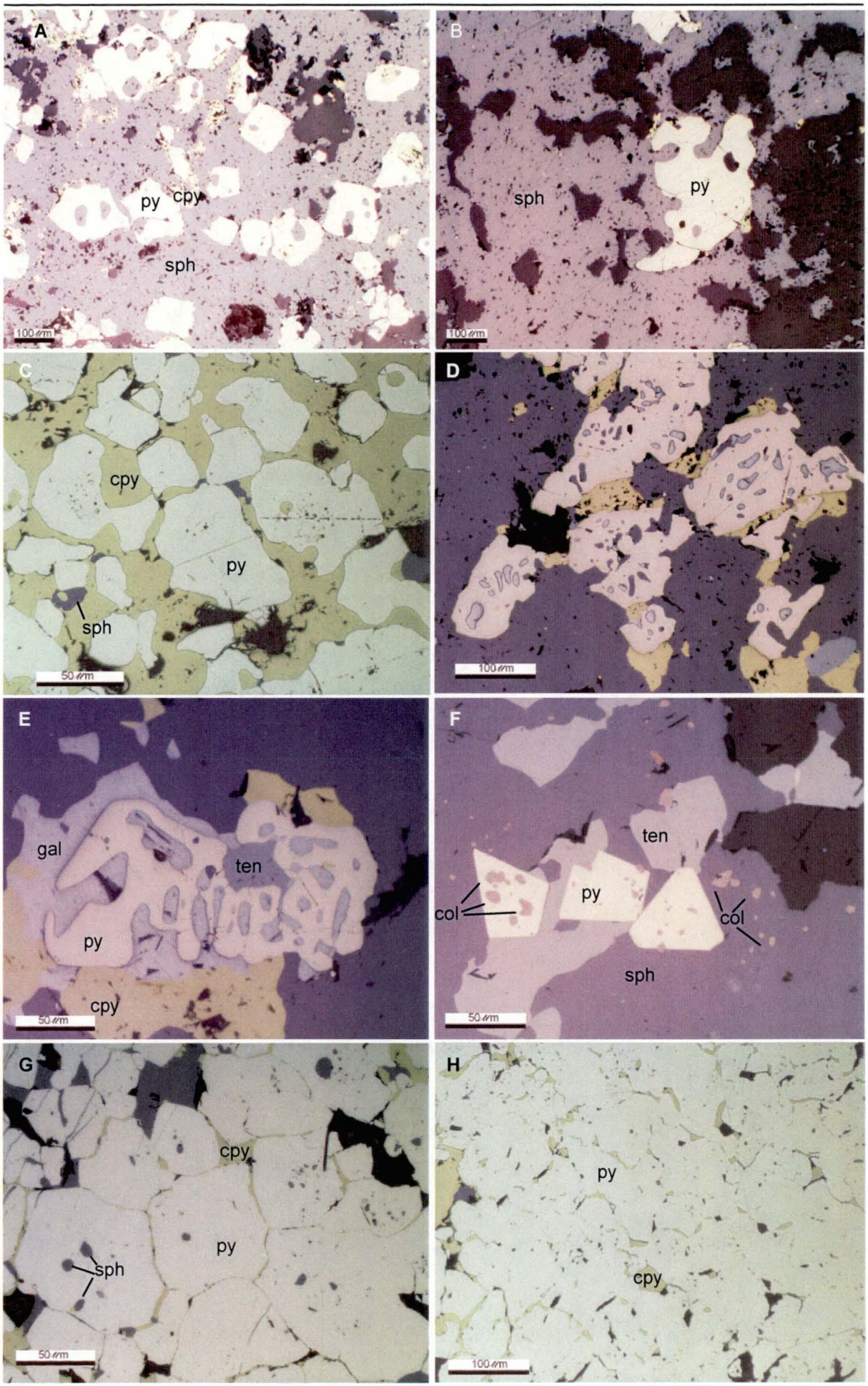
A
py
cpy
sph
100 µm
B
sph
py
100 µm
C
cpy
py
sph
50 µm
D
100 µm
E
gal
ten
py
cpy
50 µm
F
ten
py
col
col
sph
50 µm
G
cpy
py
sph
50 µm
H
py
cpy
100 µm

Plate 21 Photomicrographs of Battle Zone ore

A. Massive annealed pyrite. BG18-539 19.9m

B. Ragged pyrite crystals and minor rutile in sericite-quartz alteration. BG18-539 14.5m

C. Rounded, inclusion-rich pyrite porphyroblasts in a mixture of sphalerite, galena and tennantite. Inclusions in the porphyroblasts consist of quartz and sphalerite with minor sericite, galena and tennantite. BG18-904 35.3m.

D. Pyrite porphyroblast, hosted in sphalerite and chalcopyrite. Bornite rim between pyrite and chalcopyrite. L14-757 220.8m

E. Pyrite porphyroblast hosted in a mixture of chalcopyrite and pyrite. BG18-904 68.1m.

F. Pyrite porphyroblasts in quartz-sericite alteration. BG 18-904 48.1m

G. Galena in barite with straight cleavages and 120° triple junctions. Other sulfides are bornite and tenantite. BG18-889 153.6m

H. Galena and chalcopyrite inclusions trapped along tennantite grain boundaries. BG18-542 15.8m

sph = sphalerite, py = pyrite, ten = tennantite, gal = galena, cpy = chlacopyrite, col = colusite, bn = bornite, r = rutile, alt = altaite, anil = anilite, ren = renierite, bar = barite, qtz-quartz, carb = calcite, ser = sericite

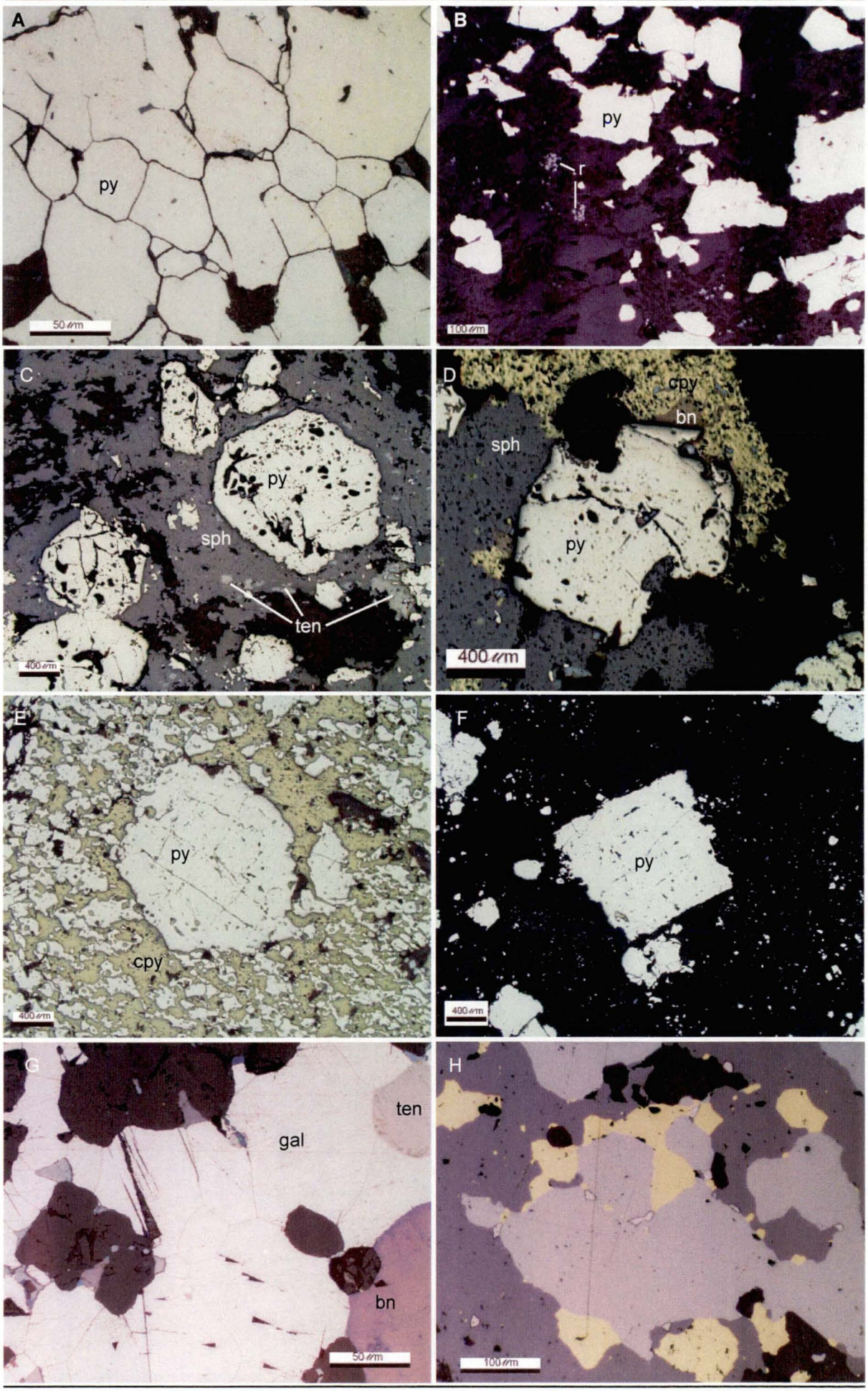
A
py
50 µm
B
py
r
100 µm
C
py
sph
ten
400 µm
D
cpy
bn
sph
py
400 µm
E
py
cpy
400 µm
F
py
400 µm
G
ten
gal
bn
50 µm
H
100 µm

ever the interpretation of coarse pyrite grains is more complex. Both primary VHMS zone refining and metamorphic growth may account of pyrites in the size range 100μm to 1mm. The fine grained cores of coarse pyrite grains are probably primary in origin. However the overgrowths of inclusion free pyrite to pyrite containing large inclusions of sphalerite, galena and chalcopyrite and tennantite may have formed by zone refining or metamorphic recrystallisation. Pyrite porphyroblasts may also be due to VHMS zone refining as their size and abundance increase toward the pyrite –rich zones at the base of the massive sulfide lenses, however some porphyroblasts especially those found in the hangingwall are due to metamorphism. Polycrystalline aggregates of pyrites are typical of primary VHMS ores especially toward the base of the mound. The effect of metamorphic recrystallisation on these zones of pyrite is unknown due to the similarity of pre-metamorphic and metamorphic textures.

Mineral Chemistry

Microprobe analyses of pyrites from the Battle Zone lenses are given in Table 4, Appendix 3 and summarised in Table 22. Impurities (Zn, Cd, Cu) are due to chalcopyrite and sphalerite inclusions in the pyrite.

Pyrite shows a zonation in Ni content with the highest values occurring in polymetallic ores in the middle of ore lenses, with Ni depleted toward the hangingwall and footwall. Figure 64 shows the distribution of Ni in the South Trough lens with highest values occurring in pyrite-chalcopyrite-sphalerite ores. In the massive pyrite to the north and sphalerite-galena-tennantite-rich ores above the lens Ni was below the detection limit.

Arsenic was only measured in South Trough and Gap lenses, both lenses show consistent As values between 600 and 700ppm. With the exception of one sample from above the South Trough lens which showed a value of 1600ppm, and one sample from the Gap lens which showed values of 600ppm, 3200ppm and 6700 ppm (average 3500ppm).

Lens	Number of points	Mineral	Formula	Minor elements	inclusions
Gap		Pyrite	FeS_2	Ni 0-1100ppm As 600–6700ppm	Zn, Cd
Upper Zone	21	Pyrite	FeS_2		Cu, Zn, Pb
Battle Main	24	Pyrite	FeS_2	Ni	Cu, Zn, As, Mn
South Trough	26	Pyrite	FeS_2	Ni 0-1500ppm As 550-1500ppm	Zn

Table22 Pyrite mineral chemistry. 0 used where analyses are below detection. Detection limits Ni = 1000ppm, As = 500ppm.

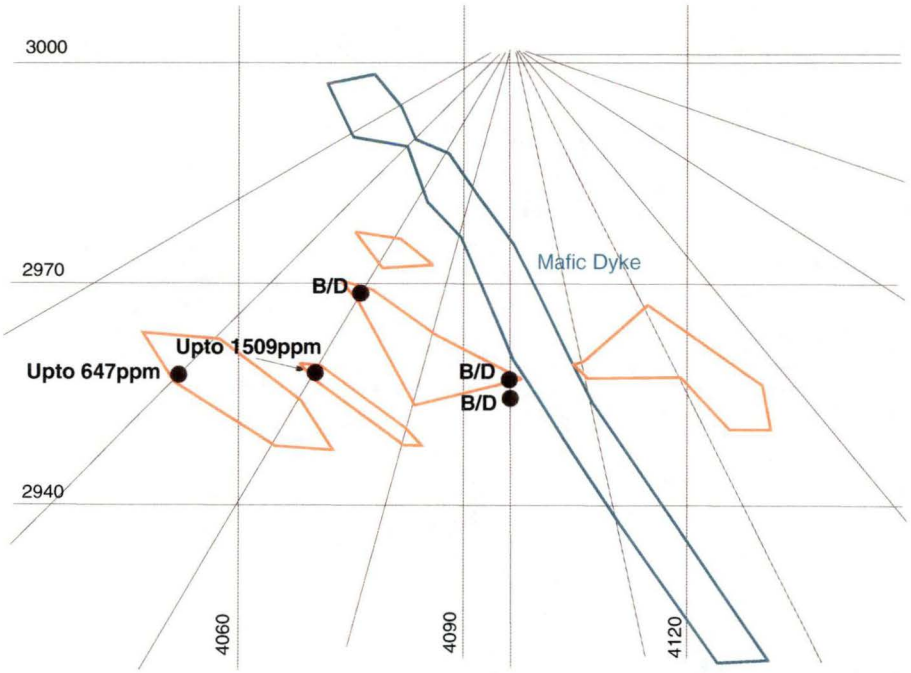

Figure 64 Distribution of nickel in pyrites within the South Trough lens. det = detection limit.

7.3.3 Galena

Galena in all lenses occurs as irregularly shaped masses. These masses show several directions of cleavage traces, indicating that several individual crystals combined to form each galena mass. In tarnished thin sections perfect 120° triple junctions of grain boundaries within the galena masses (Plate 21E) are commonly visible. At the top of the lenses, galena occurs as irregularly shaped masses disseminated in barite or interstitial to barite laths, or disseminated in strongly silicified sediments (Plate 16C & D). Where galena is abundant, at the top of the ore lenses, it encloses rounded grains of sphalerite (Plate 16G). Elsewhere galena shows cuspate margins against sphalerite and occurs as fine grained (< 20 μm) inclusions along sphalerite grain boundaries (Plate 16D & F, & Plate 17B & C). Galena also occurs as inclusions (up to 50 μm) in coarse pyrites grains (Plate 19G & Plate 20D & E). Galena is most abundant at the top of the lenses and decreases in abundance rapidly downwards through the sphalerite-rich ore. Within the banded ores galena is primarily an accessory mineral and in pyrite-chalcopyrite-rich ores is found only as inclusions in pyrite.

Galena in the Battle Zone has been completely recrystallised by the effect of metamorphism, the straight cleavage and 120° triple point textures indicate annealing occurred after deformation.

Mineral Chemistry

Galena analysis are shown in Table 5, Appendix 3 and summarised in Table 23. Microprobe analyses indicates galena contains significant Se and Te. Selenium and Te commonly substitutes for S. Tellurium may also occur as tiny inclusions of PbTe (altaite) or other telluride minerals within the galena (see trace elements for details on telluride minerals). Silver was below the detection limit (3000ppm) in galena.

Lens	No points	Mineral	Formula	major elements	minor substitutions - impurities
Gap	13	Galena	PbS	Te 1500ppm	Zn
Upper Zone	12	Galena	PbS	Se 0 - 6000ppm	Zn, Fe
Battle Main	12	Galena	PbS	Te 1800-2700ppm Se 1300-7400ppm	Zn, Fe
South Trough	12	Galena	PbS	Se 1400-3700ppm Te 1100-2200ppm	Cu, Zn

Table 23 Galena mineral chemistry. 0 used where analyses are below detection. Detection limits Te = 5000ppm, Se = 2000ppm.

7.3.4 Tennantite

Two types of tennantite were found in the Battle Zone. The most common type occurs as inclusion-free, equant grains in sphalerite and is often associated with galena and chalcopyrite (Plate 21H, Plate 22A & B, Plate 16C & D, & Plate 17A). A second less common population of tennantite contains abundant inclusions (1-5μm) of chalcopyrite, galena and altaite (Plate 22C & D), and is associated with galena-rich ores.

Tennantite (population 1) in the Battle Zone occurs as rounded, equant to weakly elongate grains in sphalerite, chalcopyrite and galena. Tennantite grains range in size from 100-300μm equant grains up to 700μm long and 300μm for the elongate grains. In one sample these large tennantite masses were seen to be composed of coalesced grains (Plate 22A). Grain boundaries are rounded against galena and chalcopyrite and rounded to irregular against sphalerite. Tennantite also occurs as inclusions (up to 100 μm) in recrystallised pyrite grains.

Tennantite occurs in all ore types mainly as an accessory phase, although it may constitute a significant mineral in the massive-black ores where it may be more abundant than galena. Tennantite grains often exhibit a blood red colour in transmitted light, a characteristic property of the Cu-As-end member of the tetrahedrite-tennantite series (Ramdohr, 1980). Galena trapped along grain boundaries was observed in a few cases (Plate 21H & Plate 22B). Tennantite also occurs as remobilised, anhedral masses in veins, especially along the sheared margins of ore (see Chapter 8).

The equant shapes of tennantite grains and occasional trapping of galena and chalcopyrite along grain boundaries in consistent with metamorphic recrystallisation (Craig and Vokes, 1993). However the distribution of tennantite (toward the top of lenses) is consistent with VHMS zone refining model.

Mineral chemistry

Microprobe analysis of tennantite grains (inclusion free) are shown in Table 6, Appendix 3 and summarised in Table 24. Due to the dominance of As over Sb this mineral is tennantite, the As rich end member of the fahlor group (Ramdohr, 1979). The trace element chemistry of tennantite varies significantly between the ore lenses. The Fe content of tennantite decreases from a maximum of 3.5wt% in the South Trough lens, to below detection in the Gap lens (Table 24). Se is also detected

Plate 22 Photomicrographs of Battle Zone ore

A. Coalesced tennantite grains, surrounded by galena and bornite in sphalerite. BG18-1000 33.0m

B. Tennantite grains with galena trapped along grain boundary. Lens like shape of the trapped galena is a typical annealing texture (Craig and Vokes, 1993). BG18-779 3.8m

C. Chalcopyrite and altaite inclusions in tennantite. L14-733 324.1-324.2m

D. Chalcopyrite and altaite inclusions in tennantite grain which is surrounded by galena, altaite, chalcopyrite and sphalerite. BG18-537-18

E. Masses of rutile grains pseudomorphing pre-existing Fe-Ti oxides. BG18-539 11.4m

F. Rutile grains intergrown with sphalerite. BG18-780 96.7-96.85m

G. Rutile grains intergrown with pyrite and chalcopyrite in quartz-sericite alteration. BG18-484 47.1-47.3m

H. Rutile. BG18-537 77.5m

sph = sphalerite, py = pyrite, ten = tennantite, gal = galena, cpy = chlacopyrite, col = colusite, bn = bornite, r = rutile, alt = altaite, anil = anilite, ren = renierite, bar = barite, qtz-quartz, carb = calcite, ser = sericite

Plate 22

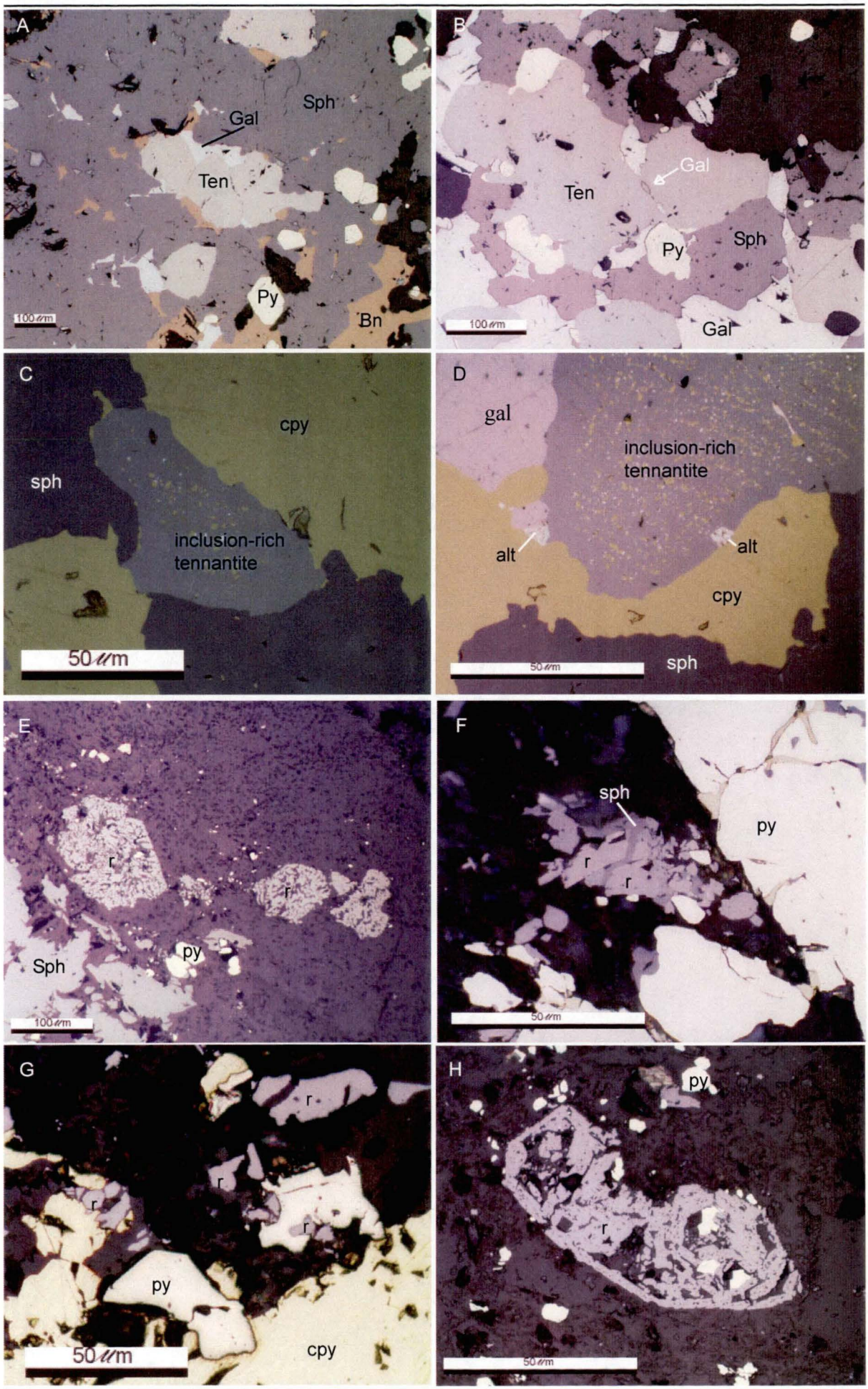
A
Sph
Gal
Ten
Py
Bn
100 µm
B
Gal
Ten
Py
Sph
100 µm
Gal
C
cpy
sph
inclusion-rich
tennantite
50 µm
D
gal
inclusion-rich
tennantite
alt
alt
cpy
50 µm
sph
E
r
r
Sph
py
100 µm
F
sph
py
r
r
50 µm
G
r
r
r
r
py
50 µm
cpy
H
py
r
50 µm

in tennantite from the South Trough, Upper Zone and Gap lenses. However only in the South Trough lens is Se of sufficient abundance to be included in the mineral formula where it substitutes for S. Ag was detected in tennantite from the South Trough, Battle, Upper Zone and in one sample from the Gap lens. However it is most consistent in the South Trough lens and highest in the Upper Zone lenses.

Lens	No points	Mineral	Formula	major elements
Gap	12	Tennantite	$(Cu_{10}Ag_{0.01})(Zn_{1.9}Fe_{0.03})(As_{3.54}Sb_{0.37})S_{13.1}$	Fe 0 - 2900ppm Se 0 - 900ppm Ag 0 - 2000ppm
Upper Zone	12	Tennantite	$(Cu_{9.96}Ag_{0.07})(Zn_{1.9}Fe_{0.46})(As_{3.3}Sb_{0.7})S_{12.9}$	Fe 1000 - 9900ppm Se 0 - 900ppm Ag 0 - 7300ppm
Battle Main	10	Tennantite	$(Cu_{9.5}Ag_{0.01})(Zn_{2.8}Fe_{0.5})(As_{3.14}Sb_{0.43})S_{12.6}$	Fe 9500ppm –3wt% Se 0 Ag 0 – 1800ppm
South Trough	9	Tennantite	$(Cu_{10}Ag_{0.03})(Zn_{1.3}Fe_{0.7})(As_{3.64}Sb_{0.23})S_{13}Se_{0.07}$	Fe 1.8 - 3.5wt% Se 0 - 1100ppm Ag 1600-2800ppm

Table 24 Group 1 tennantite compositions. 0 used where analyses are below detection. Detection limits Fe = 1000ppm, Se = 600ppm, Ag = 800ppm.

7.3.5 Chalcopyrite

Chalcopyrite in the Battle Zone occurs as anhedral irregular masses, commonly associated with galena, tennantite and sphalerite (Plate 16C & Plate 17B - F). It also occurs as disseminated fine grained (< 20 μm) blebs in sphalerite (as described in chalcopyrite disease above), along sphalerite grain boundaries (Plate 16H) and as flecks along sphalerite cleavage plains (Plate 17G & H). Chalcopyrite increases in abundance from < 0.5 % at the top the ore lenses to up to 40% of ores toward the base. In the banded ores chalcopyrite forms irregular bands subparallel to sphalerite bands, or as rounded inclusions within sphalerite, or as inclusions in sphalerite as described above (Plate 17F). Chalcopyrite forms bands with pyrite, hosting equant, rounded sphalerite and tennantite grains (Plate 17F). Chalcopyrite is interstitial to pyrite at the base of massive sulfide lenses (Plate 20B, G, & H). Chalcopyrite is also seen in veins in chert and peripheral to Upper Zone lenses (see Chapter 8).

Chalcopyrite occurs as anhedral masses to equant grains in sphalerite and as inclusions along sphalerite grain boundaries, as granoblastic intergrowths with sphalerite and galena or as a massive anhedral matrix to pyrite. These textures are typical of annealed ore due to metamorphic recrystallisation (Stanton, 1969).

Mineral Chemistry

Analysis of chalcopyrite from the Battle Zone lenses are shown in Table 7, Appendix 3 and summarised in Table 25. Chalcopyrite in the Battle Zone is relatively pure. Ag was below detection in all samples measured, while three samples contained minor zinc, probably due to contamination by tiny inclusions of sphalerite. The only other major contaminant detected was Ba, which was found in

the Gap and South Trough lenses.

Lens	No points	Mineral	Formula	Impurities
Gap	8	Chalcopyrite	Cu FeS_2	Ba
Upper Zone	16	Chalcopyrite	$CuFeS_2$	Zn
Battle Main	22	Chalcopyrite	$CuFeS_2$	Zn, Ba
South Trough	20	Chalcopyrite	$CuFeS_2$	Zn, Ba

Table 25. Chalcopyrite mineral chemistry

7.3.6 Trace Minerals

Rutile

Rutile occurs as fine grained ~20μm needles to 100μm pseudomorphs of oxide minerals (Plate 22E). Rutile has also been observed within sphalerite (Plate 22F) and pyrite (Plate 22G). Rutile also occur as clusters in gangue (quartz-muscovite; Plate 22H). Rutile is most abundant in the altered Price Formation andesite at the base of the massive sulphide lenses, but occurs in minor amounts in all ore types and throughout the HW Rhyolite except where the alteration consists of massive barite.

Mineral Chemistry

Rutile analysis are shown in Table 8, Appendix 3 and summarised in Table 26. Rutile in the Battle Zone contains up to 6200ppm Fe. Silica and Al were detected but probably come from neighbouring muscovite as the rutile grains are very small.

No points	Mineral	Formula	minor substitutions - impurities
15	Rutile	TiO_2	Si, Al, Fe

Table 26. Rutile mineral chemistry

Tellurides

Telluride minerals occur as inclusions (associated with chalcopyrite) in tennantite (Plate 22C & D). They also commonly occur with galena but have been seen as irregular inclusions in chalcopyrite and sphalerite (Plate 23A & B). Telluride grains are anhedral and vary in size from 10μm to 70μm.

Plate 23 Photomicrographs of Battle Zone ore

A. Grains of altaite in sphalerite. BG18-53775.4m

B. Altaite associated with galena, surrounded chalcopyrite and sphalerite. BG18-547 80.3m

C. Colusite grains in sphalerite. BG18-890 135.6-135.8m

D. Large accumulation of colusite grains in gangue and on the edges of galena. BG18-889 155m

E. Bornite hosting two masses of anilite. Anilite masses are linked by a vermicular intergrowth of anilite and galena. Box shows the position of close up in Plate 7.10F. BG18-890 151.3-151.5m

F. Bornite within sphalerite hosting anilite and galena. Chalcopyrite needles or "flames" occur on the boundary between anilite and bornite. BG18-889 155m

G. Bornite containing grains of colusite and renierite in barite. BG18-1052 69.3m

H. Anhedral bornite intergrown with sphalerite. Bornite contains grains of colusite and renierite. BG18-1052 69.3m

sph = sphalerite, py = pyrite, ten = tennantite, gal = galena, cpy = chlacopyrite, col = colusite, bn = bornite, r = rutile, alt = altaite, anil = anilite, ren = renierite, bar = barite, qtz-quartz, carb = calcite, ser = sericite

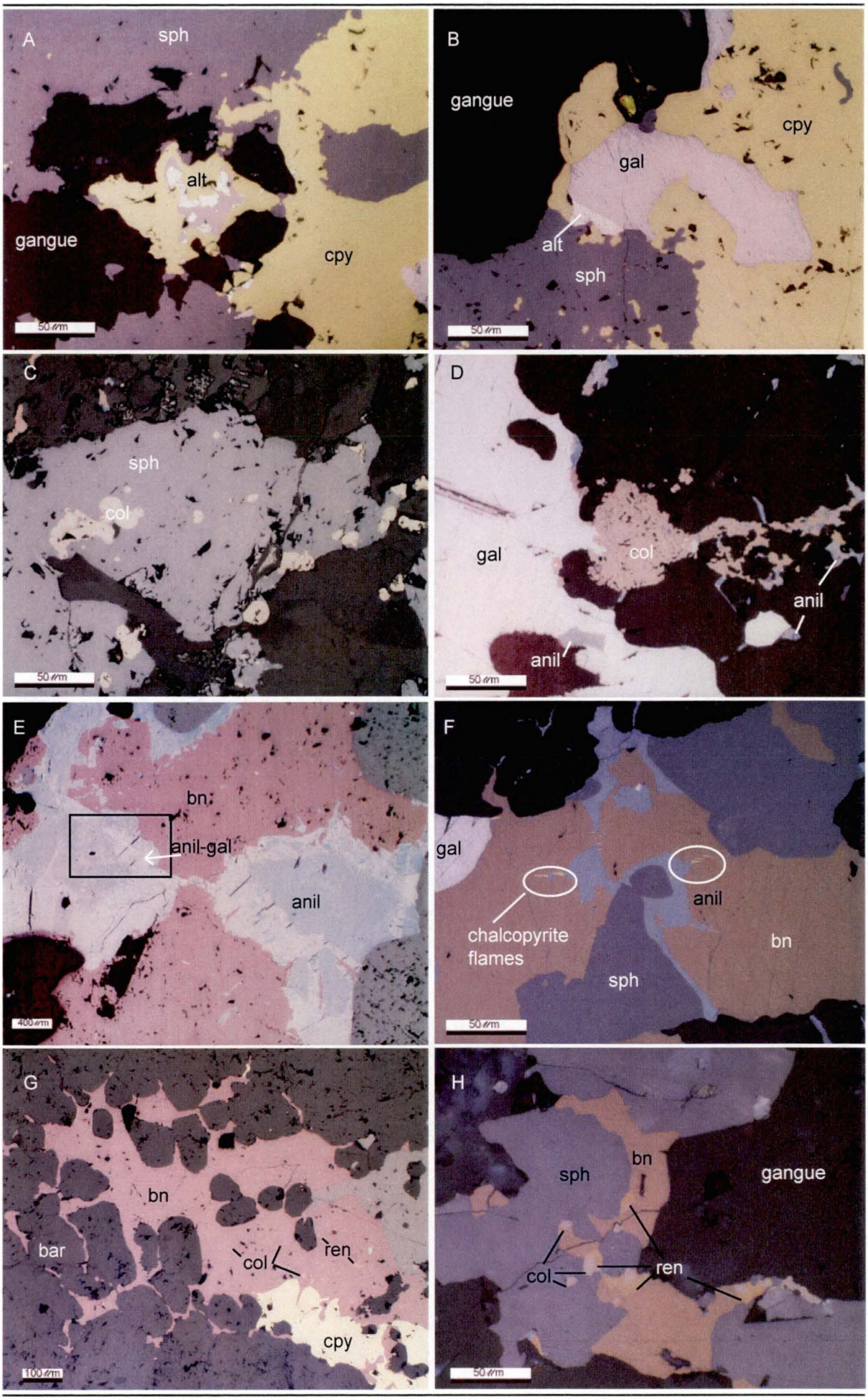
A
sph
alt
gangue
cpy
50 µm
B
gangue
cpy
gal
alt
sph
50 µm
C
sph
col
50 µm
D
gal
col
anil
anil
50 µm
E
bn
anil-gal
anil
400 µm
F
gal
anil
chalcopyrite
flames
bn
sph
50 µm
G
bn
bar
col
ren
cpy
100 µm
H
sph
bn
gangue
col
ren
50 µm

Mineral Chemistry

Microprobe results for telluride minerals are listed in Table 9, Appendix 3. Three minerals were identified, the most abundant was altaite (PbTe) which was identified in three samples. Hessite (Ag_2Te_3) formed a minor component of the telluride mineral mixture in two of the three samples. One of these samples also contained a second phase that consisted of a mixture of pilsenite (Bi_2Te_3) and hessite.

Colusite

Colusite occurs exclusively in the Gap and Upper Zone ores. It is most abundant in the Gap ore body constituting up to 1% of the ore. It occurs in much lower amounts (<<1%) in the Upper Zones and has not been observed in Battle, Gopher or South Trough lenses. In the Gap ore body it is most abundant at the top, occurring as rounded blebs in sphalerite, pyrite, bornite (Plate 20F & Plate 23C & D). Most grains are 2.5 to 15μm in size, although grains up to 50μm have been observed.

Mineral Chemistry

Microprobe data for colusite is listed in Table 10, Appendix 3, and summarised in Table 27. Colusite in the Battle lens contains Ge but no Sn (below detection in all analyses). Fe and Zn were detected but contamination by Zn, Cu and S from host minerals (sphalerite, pyrite) makes it impossible to establish the exact Fe and Zn content of the colusite.

Mineral	Formula	Major substitutions	Impurities
Colusite	$Cu_3(AsGeV)S_4$	Ba 0 - 7500ppm Sb 0 - 5000ppm	Ag, Mo, Zn, Fe

Table 27. Colusite mineral chemistry. 0 used where analyses are below detection. Detection limits Ba = 1000ppm, Sb = 1000ppm.

7.4 Cu-rich assemblage

7.4.1 Bornite (& Renierite)

Bornite occurs throughout the Gap lens from the semi-massive, siliceous, pyritic sulfides at the base of the lens through the chalcopyrite-pyrite rich ores, the sphalerite-pyrite ores and up into the barite-galena-sphalerite-rich top. Bornite forms anhedral masses, and commonly hosts anilite, colusite, renierite, and chalcopyrite "flames" (Plate 23E – H).

In barite-rich material at the top of the Gap (and equivalent Upper Zone ores) bornite occurs as irregular inclusions in an equigranular barite matrix, interstitial to barite laths (Plate 24A), or in association with other sulfides as described below. Within the massive sulfides bornite occurs with chalcopyrite, sphalerite and pyrite (Plate 24B – H, & Plate 25A & D). Bornite commonly surrounds chalcopyrite grains (Plate 24B - D). Bornite also preferentially surrounds pyrite grains isolating them from sphalerite and chalcopyrite (Plate 24G & H, & Plate 25A & D). In sphalerite-rich ores bornite is concentrated along sphalerite grain boundaries (Plate 24E & F). In the chalcopyrite-pyrite-rich ores bornite forms a matrix to pyrite. Delicate grate-like textures of pyrite around the margin of the pyrite crystals are also associated with bornite (Plate 24G & H). Bornite also occurs along fractures and as inclusions within pyrite crystals (Plate 25C & D). Chalcopyrite "flames" (5-10μm needle to flame shaped inclusions of chalcopyrite) occur within bornite and always extend from bornite grain boundaries into the middle of grains (Plate 23F & Plate 25E).

Renierite, also known as orange bornite, ((Cu, Fe, Ge, Zn)S , Plate 23H & Plate 25F, G & H) has very similar properties to bornite except for its distinct orange colour and its greater resistance to tarnishing than bornite (Ramdohr, 1979). Renierite occurs as rounded grains in bornite, or in sphalerite where bornite is abundant, and is often seen rimming or associated with colusite grains (Plate 25H). Renierite grains vary in size from 20μm by 20μm equant grains to elongate grains 120μm by 70μm.

Bornite has a low thermal stability, thus shows a strong tendency to re-equilibrate at metamorphic temperatures (Hannington et al., 1999b). In the Kidd Creek bornite zone Thorpe et al. (1976) and Hannington et al. (1999b) noted the development of post metamorphic intergrowth, exsolution and reaction textures due to prograde metamorphism. Hannington et al. (1999b) also noted that minor elements (Ag and Se) were expelled from the bornite during metamorphism forming complex assemblage of Ag-selenides minerals.

In the Battle Zone bornite is massive and non-descript typical of metamorphosed bornite ores (Hannington pers. com., 2000). The presence of renierite associated with bornite may represent exsolution of Ge and As from the bornite during metamorphism. Renierite rimming colusite grains may represent metamorphic reaction rims. Hannington et al. (1999b) also interpreted the chalcopyrite flames in the Bornite ores at Kidd Creek to represent a metamorphic exsolution feature. Ramdohr (1979) described the occurrence of chalcopyrite flames, and considered them as disintegration products of unstable bornite to form chalcopyrite. Metamorphism would aid in this process.

Plate 24 Photomicrographs of Battle Zone ore

A. Barite laths with interstitial sphalerite-pyrite and bornite-chalcocite assemblages. BG18-1051 70.1m

B. Bornite preferentially replacing chalcopyrite which was originally associated with tennantite and galena in sphalerite. Relic chalcopyrite occurs as isolated islands within the bornite while tennantite and galena are unaffected by bornite. BG18-761 21.7m

C. Characteristic association of bornite replacing chalcopyrite. Fine grained pyrite is also surrounded by bornite. BG18-1053 58.8m

D. Bornite altering the chalcopyrite matrix of a pyrite-chalcopyrite-rich ore, while tennantite grain is not affected. BG18-1054 68.5m

E. Bornite surrounding sphalerite. BG18-890 151.3-151.5m

F. Bornite intergrown with sphalerite along grain boundaries. L14-757 220.8m

G. Bornite preferentially replacing chalcopyrite along pyrite grain boundaries. The replacement of chalcopyrite by bornite causes pyrite to form grate texture around grain margins of pre-existing pyrite grains. Bornite also alters pyrite along fractures (arrow) possible replacing intergranular chalcopyrite. BG18-1054 68.5m

H. Bornite preferentially replacing chalcopyrite along grain boundaries with pyrite, forming grate texture around pre-existing pyrite crystal margins. L14-757 220.8m

sph = sphalerite, py = pyrite, ten = tennantite, gal = galena, cpy = chlacopyrite, col = colusite, bn = bornite, r = rutile, alt = altaite, anil = anilite, ren = renierite, bar = barite, qtz-quartz, carb = calcite, ser = sericite

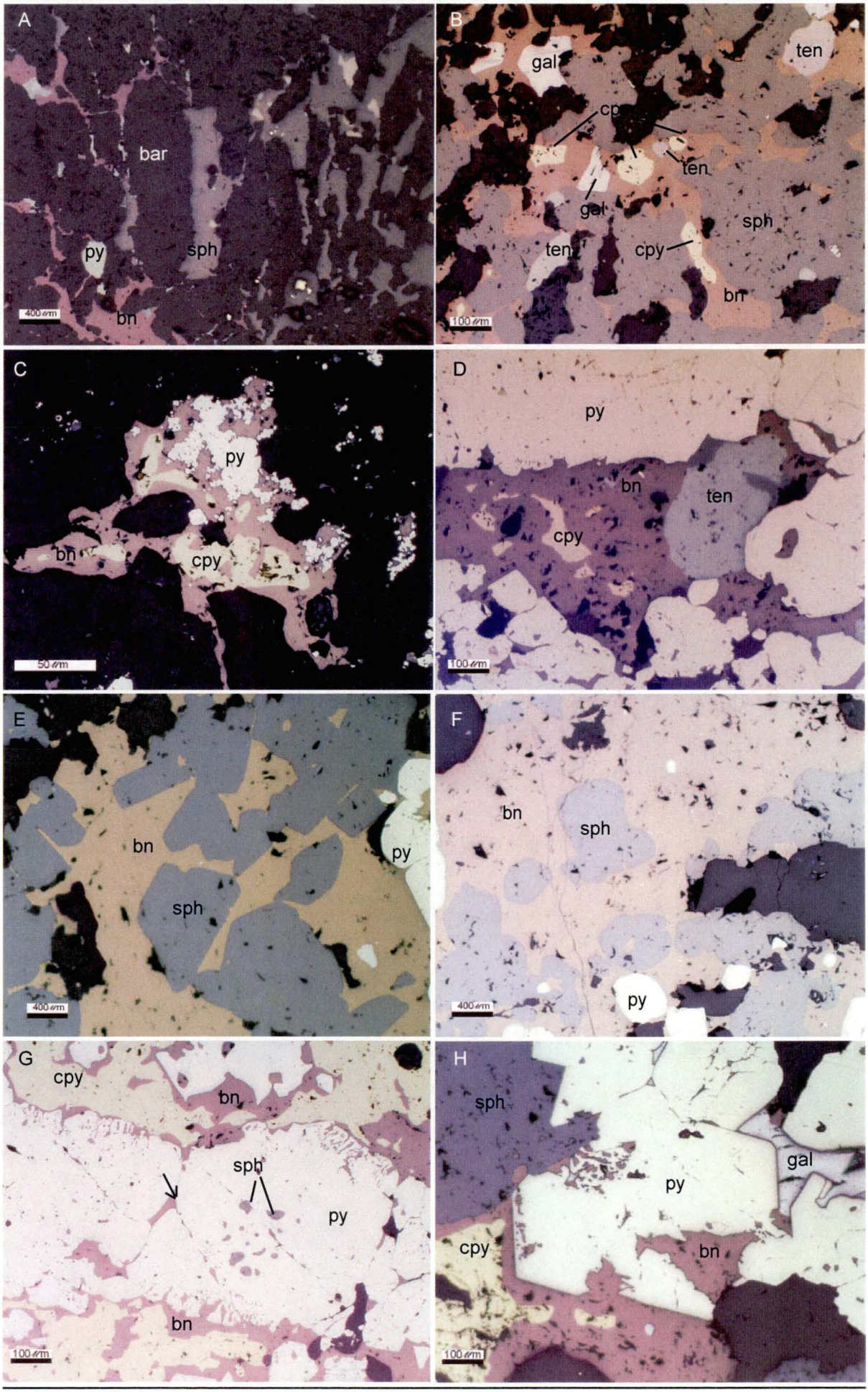
A
bar
py
sph
bn
400 µm
B
gal
ten
cp
ten
gal
sph
ten
cpy
bn
100 µm
C
py
bn
cpy
50 µm
D
py
bn
ten
cpy
100 µm
E
bn
py
sph
400 µm
F
bn
sph
py
400 µm
G
cpy
bn
sph
py
bn
100 µm
H
sph
gal
py
cpy
bn
100 µm

Plate 25 Photomicrographs of Battle Zone ore

A. Bornite replacing chalcopyrite, leaving relic anhedral chalcopyrite within bornite, galena has lobate grain boundaries. Pyrite forms complex grain boundaries. BG18-1051 71.1m

B. Bornite replacing chalcopyrite matrix. Pyrite grows during the replacement reaction forming complex textures. BG18-1051 71.1m

C. Bornite altering chalcopyrite. Chalcopyrite was intergrown with galena and tennantite in sphalerite matrix. Galena, tennantite and sphalerite unaffected by bornite alteration. Bornite also alters chalcopyrite within pyrite crystal (arrows). BG18-761 21.7m

D. Bornite replacing matrix sulfides (probably originally chalcopyrite) except minor sphalerite. Pyrite grain show overgrowth structures due to the formation of pyrite during the bornite replacement. BG18-1051 71.1m

E. Chalcopyrite needles forming from bornite grain boundary into bornite. L14-757 220.8m

F. Renierite sphalerite associated with bornite and galena. BG18-890 151.3-151.5m

G. Renierite in sphalerite, plus smaller renierite grain associated with bornite and anilite on margin of sphalerite. BG18-890 148.8-148.9m

H. Colour variations in anilite. Colusite with a reaction rim of renierite. BG18-890 151.3-151.5m

sph = sphalerite, py = pyrite, ten = tennantite, gal = galena, cpy = chlacopyrite, col = colusite, bn = bornite, r = rutile, alt = altaite, anil = anilite, ren = renierite, bar = barite, qtz-quartz, carb = calcite, ser = sericite

Plate 25

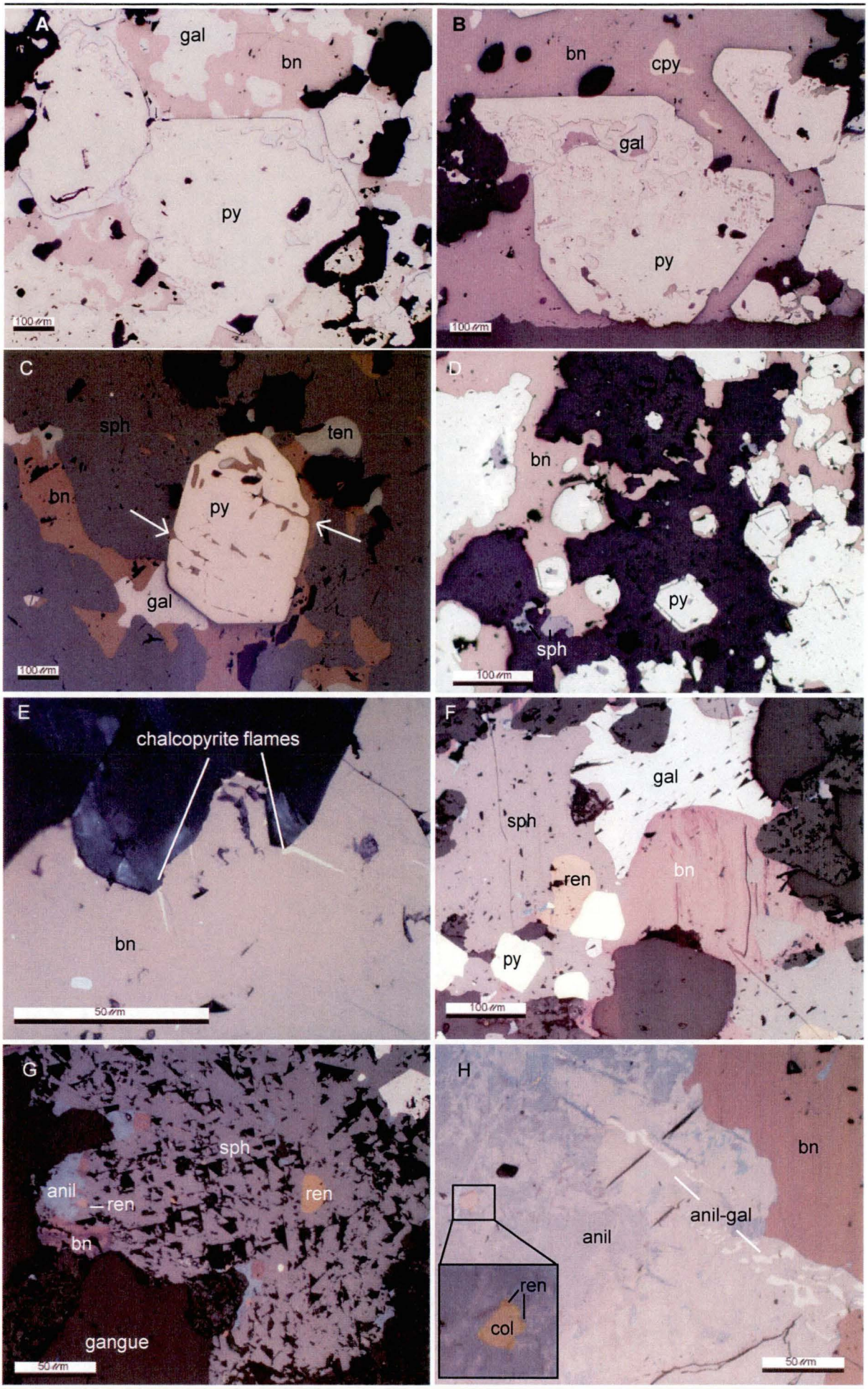
A
gal
bn
py
100 µm
B
bn
cpy
gal
py
100 µm
C
sph
ten
bn
py
gal
100 µm
D
bn
py
sph
100 µm
E
chalcopyrite flames
bn
50 µm
F
gal
sph
ren
bn
py
100 µm
G
sph
anil
ren
ren
bn
gangue
50 µm
H
bn
anil-gal
anil
ren
col
50 µm

The texture of bornite commonly enclosing chalcopyrite suggests bornite may be replacing chalcopyrite. While the presence of abundant pyrite within the bornite indicates pyrite was stable during bornite alteration. There are two possibilities for this replacement:

(a) It could be due to metamorphic re-equilibration by a reaction such as

$$5CuFeS_2 < — > Cu_5FeS_4 + 2FeS_2 + 2FeS$$

chalcopyrite bornite pyrite Fe in sphalerite

However this reaction implies a dramatic increase in the Fe content of sphalerite in the near vicinity of bornite and no such zonation or enrichment was detected.

(b) It may be a result of the zone refining process with open system behaviour such as

(i) $4Cu^+ + CuFeS_2 + 2ZnS \text{ —> } Cu_5FeS_4 + 2Zn^{2+}$

(ii) $O_2 + 2H_2S + 5CuFeS_2 \text{ —> } Cu_5FeS_4 + 4FeS_2 + 2H_2O$

(iii) $2Cu^+ + 3CuFeS_2 \text{ —> } Cu_5FeS_4 + Fe^{2+} + FeS_2$

The first reaction represents the reaction of a Cu-rich fluid with chalcopyrite and sphalerite to produce bornite and a Zn enriched fluid. This matches the textural evidence for extensive bornite formation along chalcopyrite-sphalerite grain boundaries and is probably an important process. The second reaction is widely quoted for the conversion of chalcopyrite to bornite and pyrite and occurs as the fo_2 increases. This process may be important, but based on the molar volumed it would produce equal volumes of pyrite and bornite which is not consistent with the textures. Equation (iii), reflects the reaction of a Cu-rich fluid with chalcopyrite without oxidation and is more consistent with the molar proportions of products suggested by the textures. The bulk of the bornite textures observed support a zone refining process involving reactions like (i) and (iii) above and are not consistent with closed system reequilibration during metamorphism,

Mineral Chemistry

Microprobe results for bornite from the Gap and Upper Zone lenses are shown in Table 11, Appendix 3, and summarised in Table 28. Bornites from both lenses contain Ag and Ba. Barium content of bornite between the lenses is fairly consistent. However Ag contents show a marked variation with Upper Zone bornite having higher Ag contents than the Gap lens bornite.

Mineral	Formula	major elements	impurities
Bornite (Gap)	$Cu_{(4.54-5.39)}Fe_{1.00}S_{(3.90-4.55)}$	Ag 0 – 3300ppm Ba 0 – 2700ppm	Zn, Cd
Bornite (Upper Zone)	$Cu_{(4.75-5.1)}Fe_{1.00}S_{(3.90-4.23)}$	Ag 2500 – 7500ppm Ba 0 – 2900ppm	Zn
Renierite	$(Cu_{0.66}Fe_{0.22}Ge_{0.10}Zn_{0.06}As_{0.03})S_{1.01}$	V 0 – 4500ppm Sb 1200 – 2600ppm Ba* 1100 - 1400ppm	

Table 28. Bornite and renierite minerals chemistry. 0 used where analyses are below detection limit. Detection limits Ag = 2000ppm, Ba = 2000ppm, V = 1000ppm, Sb = 1000ppm, Ba* = 1000ppm.

Microprobe results for renerite from the Gap lens are shown in Table 12, Appendix 3, and summarised in Table 28. Renierite from the Gap lens contains significant As and trace V, Sb and Ba. Tin and Ag were below detection (500ppm).

7.4.2 Anilite

Anilite occurs as anhedral masses within bornite or around the margins of bornite and along grain boundaries and fractures in sphalerite (Plate 23E & F, Plate 25G – H, & Plate 26A). Two samples showed bornite and anilite as vermicular intergrowths, but this texture is rare (Plate 25D & E). Anilite is occasionally observed as vermicular intergrowths with galena (Plate 26E & F). More commonly anilite and stromeyerite form vermicular intergrowths (Plate 25G).

The mineral referred to here as anilite is made up of two, or more, distinct phases in thin section. These phases show varying shades of white and blue and appear complexly intergrown within the anilite masses (Plate 23E & Plate 25H).

Anilite has a very low thermal stability, thus will quickly re-arrange at metamorphic temperatures. Anilite textures in the Battle Zone are typical of metamorphosed ores (anilite occurring as irregular masses toward the margin of bornite grains). Thus metamorphism has destroyed textural evidence of anilite formation in the Battle Zone, the origin of anilite is unknown.

Anilite may form via supergene oxidation of bornite ore, via hypogene alteration of bornite or via the exsolution from bornite during metamorphism (Hannington et al., 1999b). Supergene formation is not favoured due to the distribution of anilite throughout the Gap lens similar to the distribution of bornite. Anilite formation via hypogene fluids either during the bornite alteration or at the end of the bornite alteration as the fluids cooled and receded seems the most likely origin. The abundance of anilite in some areas suggests it could not have formed via the exsolution from bornite during metamorphism. Thus a hypogene origin for the anilite is favoured in the Upper Zone and Gap lenses.

Mineral chemistry

Microprobe analyses for anilite are shown in Table 13, Appendix 2 and summarised in Table 29. The mineral phase analysed has the average formula $Cu_{1.74}Ag_{0.01}S_1$ thus it is named anilite. Anilite shows elevated Ag and Ba contents. Silver contents range from 2600ppm to 20700ppm, while Ba contents up to 3600ppm were measured, with all anilite grains measured showing barium levels above detection i.e. >2000ppm. Probing did not revealed significant differences between the various shades of anilite seen in the Gap and Upper Zone ores. Thus the variations in colour are interpreted as polishing irregularities or in one case (Plate 26B) the presence of crystal twins within the recrystallised anilite.

Plate 26 Photomicrographs of Battle Zone ore

A. Massive anhedral anilite around the edges of bornite. Light and dark blue colours within anilite likely due to polishing irregularities. BG18-1051 70.1m

B. Irregular shaped mass of anilite within bornite. Stripes are possible twins. BG18-981 17m

C. Anilite intergrown with bornite forming a matrix to pyrite crystals. BG18-105171.1m

D. Bornite intergrown with anilite and colusite. BG18-890 152.3m

E. Anilite-bornite and anilite-galena vermicular intergrowths. BG18-889 153.6m

F. Vermicular intergrowth between galena and anilite in bornite. BG18-889 153.6m

G. Vermicular intergrowth of anilite and stromeyerite within bornite. Electrum riming pyrite. Stromeyerite is distinguished from chalcocite by its relatively poor polish. H169 Panel 10 sample No.2

H. Irregular intergrowths of stromeyerite and anilite within a bornite matrix. H169 Panel 10 Sample No 2

sph = sphalerite, py = pyrite, ten = tennantite, gal = galena, cpy = chlacopyrite, col = colusite, bn = bornite, r = rutile, alt = altaite, anil = anilite, ren = renierite, bar = barite, qtz-quartz, carb = calcite, ser = sericite

Plate 26

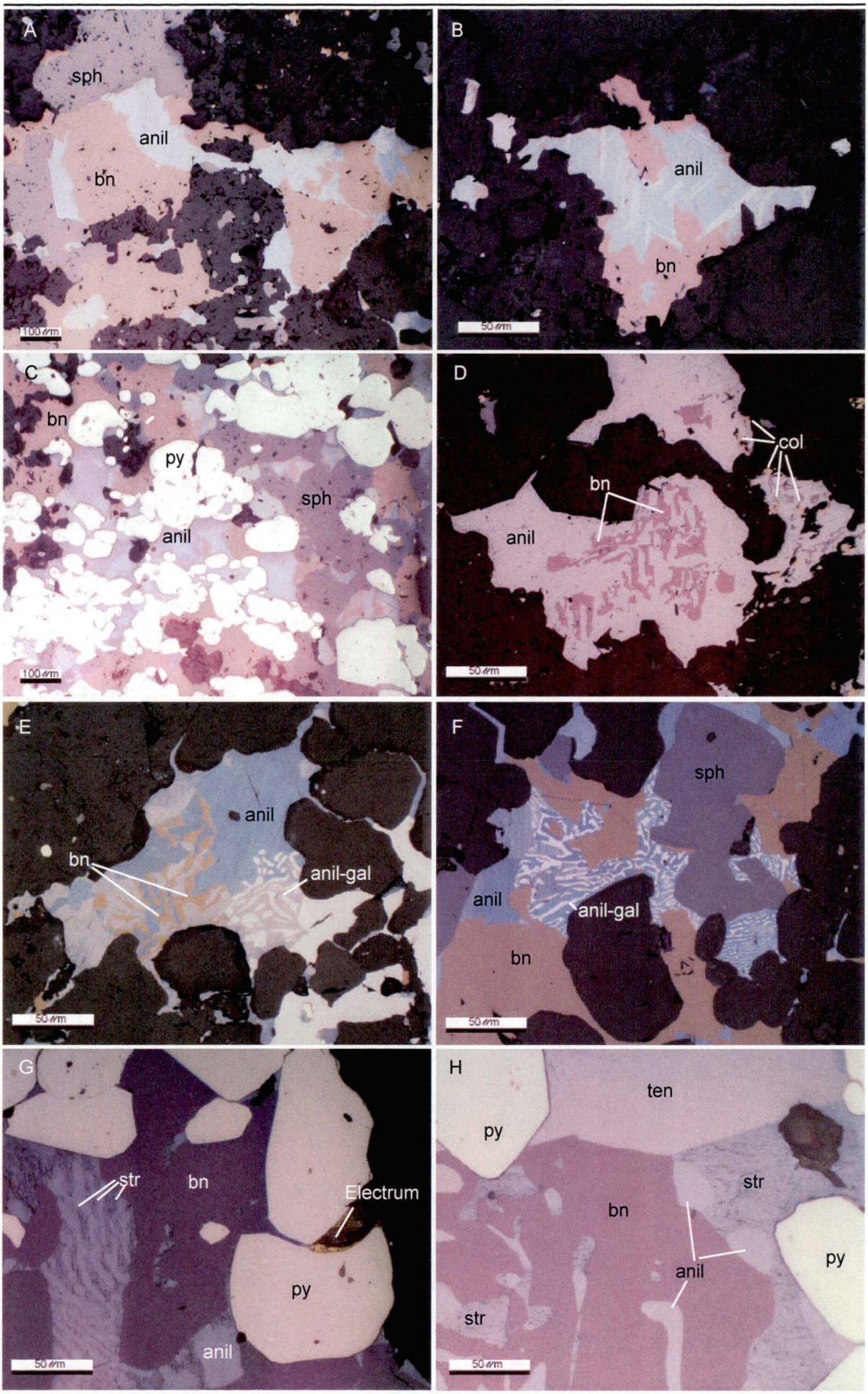
A
sph
anil
bn
100 µm
B
anil
bn
50 µm
C
bn
py
sph
anil
100 µm
D
col
bn
anil
50 µm
E
anil
bn
anil-gal
50 µm
F
sph
anil
anil-gal
bn
50 µm
G
str
bn
Electrum
py
anil
50 µm
H
ten
py
str
bn
anil
py
str
50 µm

Sample	Number of points	Lens	Formula	Trace elements
BG18-889 153.6m	34	Gap	$Cu_{1.76}Ag_{0.01}S_1$	Ag 1.7wt% - 3500ppm Ba 4600 – 2100ppm
BG18-890 148.8m	11	Gap	$Cu_{1.73}Ag_{0.01}S_1$	Ag 7700 – 2700ppm Ba 3000 – 2300ppm
BG18-890 152.3m	6	Gap	$Cu_{1.70}S_1$	Ag 4600 – 2600ppm Ba 2600 – 2300ppm
H169 Panel 10 No.2	6	UZ	$Cu_{1.82}Ag_{0.02}S_1$	Ag 2.07wt% - 5800ppm
BG18-1052 74.4m	6	UZ	$Cu_{1.66}S_1$	Ag 3500 – 5000ppm Ba 6300 – 4000ppm

Table 29 Summary of microprobe analyses for anilite. UZ = Upper Zone. Detection limits for trace elements Ag = 2000ppm, Ba = 2000ppm.

7.5 Late Ag-Au-rich assemblage

7.5.1 Stromeyerite

The mineral stromeyerite[1] (CuAgS) was also identified during this study. Its optical properties are nearly identical to that of chalcocite group minerals. However, in all sections where it has been identified, it has a rougher polish than anilite due to fine scratches on the surface of the mineral. Stromeyerite occurs as vermicular to irregular intergrowths with anilite (Plate 26G & H), as irregular intergrowths in bornite (Plate 27B), and as rims and fracture fill of sphalerite grains (Plate 27B). Stromeyerite is commonly associated with electrum.

An unusually delicate texture consisting of vermicular intergrowths of stromeyerite and chalcopyrite was observed along fractures in bornite (Plate 27C - F). The same fractures were observed cutting chalcopyrite and pyrite, but do not contain the intergrowth of stromeyerite and chalcopyrite.

Metamorphism can have a significant effect on the distribution of minor elements (Larocque and Hodgson, 1995). Stromeyerite shows delicate textures and is not highly abundant leading to the conclusion that stromeyerite and the related chalcopyrite may be the result of the exsolution of Ag and Cu from pre-existing mineralogy during metamorphism resulting in the deposition of stromeyerite and chalcopyrite. Vermicular intergrowths of bornite and anilite with stromeyerite support the exsolution of Ag-Cu from bornite and anilite during metamorphism. The delicate textures suggest deposition of stromeyerite-chalcopyrite and electrum occurred late possible during pro-grade metamorphism after the main metamorphic event.

[1] Stromeyerite has previously been reported in "Chryssoulis S.L., 1989. Determination of invisible gold in flotation products and four ore types from the HW Mine, British Columbia" unpublished company report.

Plate 27 Photomicrographs of Battle Zone ore

A. Irregular intergrowths of stromeyerite in bornite. BG18-539 14.5m

B. Stromeyerite rimming sphalerite, pyrite and bornite grains. BG18-539 14.5m

C. Stromeyerite-chalcopyrite vein cross cutting chalcopyrite, pyrite and bornite. BG18-1000 34.1m

D. Stromeyerite-chalcocite mineralogy is best developed where fracture cuts bornite. BG18-1000 34.1m

E. Stromeyerite vein in bornite. Vein also contains delicate vermicular intergrowths between stromeyerite and chalcopyrite and minor covellite. BG18-1000 33.0m

F. Close ups of the delicate intergrowth between stromeyerite and chalcopyrite. BG18-1000 34.1m

G. Electrum grain in bornite, from Gap lens. BG18-891 149.3m

H. Grains of electrum in chalcopyrite (Upper Zone). H167 Panel 7 Sample No.2

sph = sphalerite, py = pyrite, ten = tennantite, gal = galena, cpy = chlacopyrite, col = colusite, bn = bornite, r = rutile, alt = altaite, anil = anilite, ren = renierite, bar = barite, qtz-quartz, carb = calcite, ser = sericite

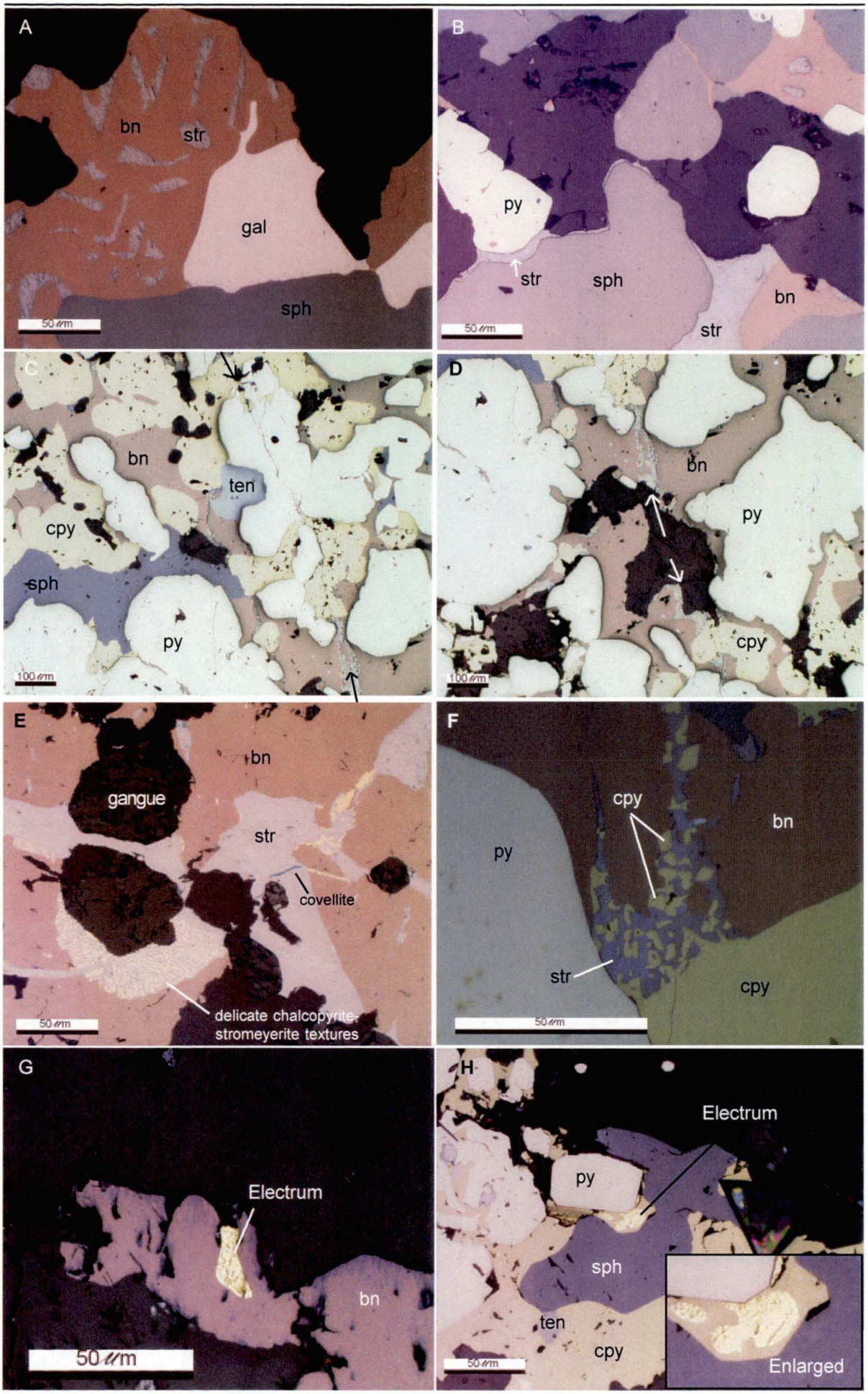
A
bn
str
gal
sph
50 µm
B
py
str
sph
bn
str
50 µm
C
bn
ten
cpy
sph
py
100 µm
D
bn
py
cpy
100 µm
E
bn
gangue
str
covellite
delicate chalcopyrite-stromeyerite textures
50 µm
F
cpy
bn
py
str
cpy
50 µm
G
Electrum
bn
50 µm
H
Electrum
py
sph
ten
cpy
50 µm
Enlarged

Mineral Chemistry

Microprobe analyses for stromeyerite are shown in Table 13, Appendix 3, and summarised in Table 30. Stromeyerite grains have a slight but consistent excess of Cu ($Cu_{1.01}AgS$).

Two chalcopyrite grains that form vermicular intergrowths with stromeyerite were analysed and showed a lower iron content (~250ppm lower) than "normal" chalcopyrite found throughout the Battle Zone, and higher Ag values of upto 16000ppm (c.f Table 25).

Mineral	Number of Points	Formula	Trace elements
Stromeyerite	31	$Cu_{1.01}AgS$	Fe 0 – 3700ppm
Chalcopyrite	2	$Cu_{1.00}Fe_{0.95}S_{20.3}$	Ag up to 16000ppm

Table 30 Summary of microprobe analyses of stromeyerite and related fine grained chalcopyrite. 0 used where analyses are below detection limit. Detection limit Fe = 2000ppm, Ag = 800ppm.

7.5.2 Electrum

Electrum was observed in five samples, one from the Gap lens and the rest from the Upper Zone. In the Gap lens, visible gold was commonly seen associated with the bornite in hand specimen. In a polished thin section of this material electrum is observed as a grain (40 by 20μm in size) hosted in bornite (Plate 27G). Of the Upper Zone samples all but one electrum grain occured within stromeyerite-filled fractures or intergrown with stromeyerite grains in a bornite or sphalerite matrix (Plate 28A – F). The one electrum grain not associated with stromeyerite was hosted in chalcopyrite (Plate 27H).

In addition to textural changes resulting from metamorphism, chemical changes also occur during metamorphism and deformation. In the Mobrun deposit metamorphic recrystallisation of pyrite resulted in the release of invisible gold and its subsequent deposition in electrum (Larocque and Hodgson, 1995). In the Battle Zone the presence of stromeyerite indicated Ag and Cu were expelled from pre-existing mineralogy during metamorphism. It is highly likely that Au was also released, and combined with Ag to form electrum during metamorphism, the variety of electrum textures and host sulfides suggests the formation of electrum occurred over a wider period of time than stromeyerite deposition.

Mineral chemistry

Microprobe analyses of electrum grains are shown in Table 14, Appendix 3 and summarised in Table 31. Electrum from the Gap lens has low Ag contents (high fineness). In contrast electrum in Upper Zone lenses shows higher Ag contents (lower fineness).

Plate 28 Photomicrographs of Battle Zone ore

A Grains of electrum associated with bornite and tennantite in sphalerite. BG18-761 21.7m

B Electrum within a stromeyerite filled fracture in sphalerite. BG18-539 14.5m

C Electrum with stromeyerite in fractured sphalerite. BG18-761 29.7m

D Anilite intergrown with stromeyerite and electrum. Stromeyerite is distinguished from chalcocite by relatively poor polish. H169 Panel 10 sample No.2

E Electrum in stromeyerite inclusions within bornite. H169 Panel 10 Sample No.2

F Electrum in stromeyerite on pyrite grain boundary within sphalerite. H169 Panel 10 Sample No.2

sph = sphalerite, py = pyrite, ten = tennantite, gal = galena, cpy = chlacopyrite, col = colusite, bn = bornite, r = rutile, alt = altaite, anil = anilite, ren = renierite, bar = barite, qtz-quartz, carb = calcite, ser = sericite

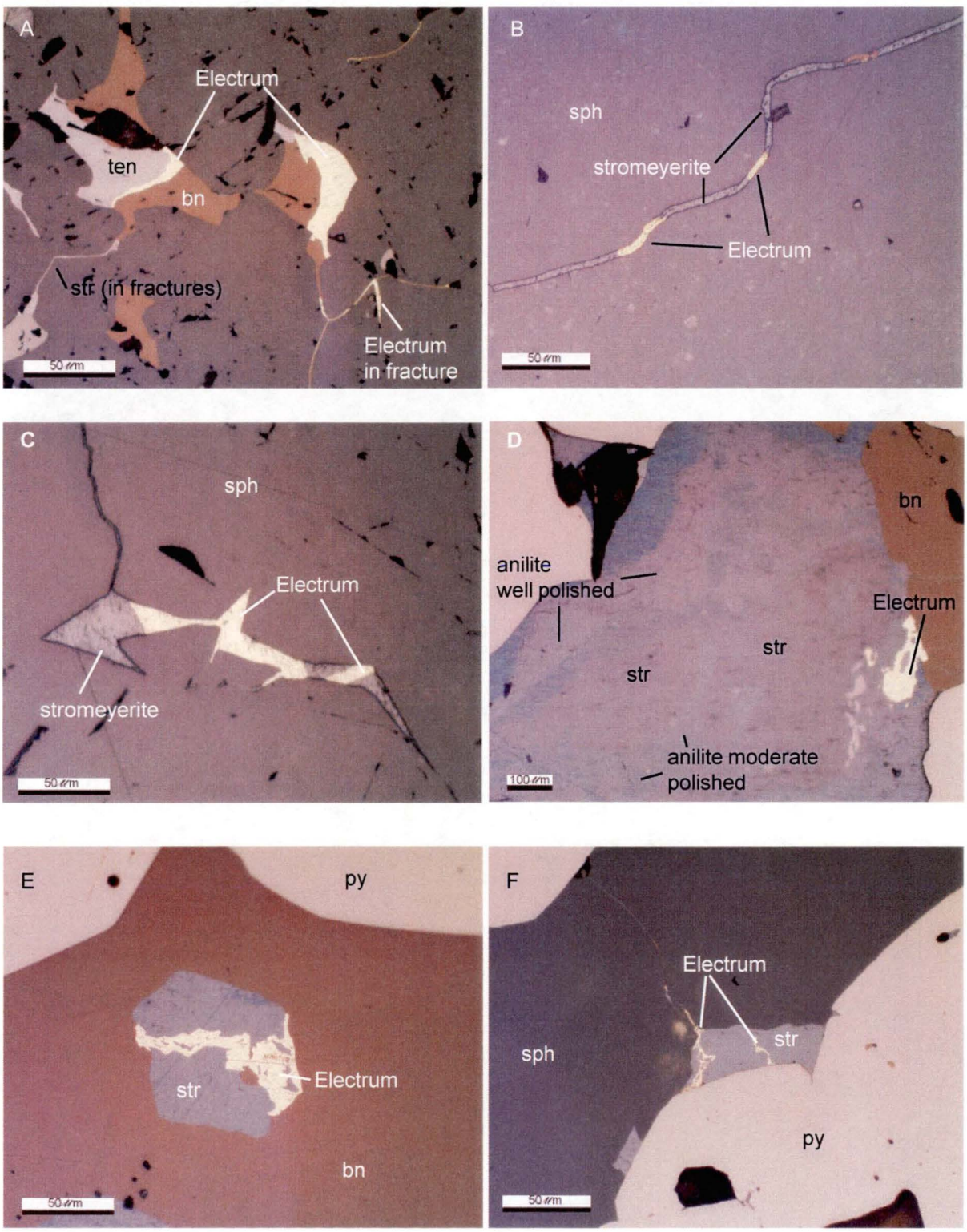
A
Electrum
ten
bn
str (in fractures)
Electrum
in fracture
50 µm
B
sph
stromeyerite
Electrum
50 µm
C
sph
Electrum
stromeyerite
50 µm
D
bn
anilite
well polished
Electrum
str
str
anilite moderate
polished
100 µm
E
py
str
Electrum
bn
50 µm
F
Electrum
str
sph
py
50 µm

Sample	Lens	Host minerals	Formula	Fineness	Grain size
BG18-891 149.3m	Gap	Bornite	$Au_{71.5}Ag_{28.5}$	715	40-20μm
			$Au_{73.3}Ag_{26.7}$	733	
H169 Panel 7 sample 2	UZ	Chalcopyrite	$Au_{49.4}Ag_{50.6}$	494	50-15μm
		Chalcopyrite	$Au_{49.8}Ag_{50.2}$	498	
BG18-761 21.7m	UZ	Stromeyerite vein in sphalerite	$Au_{55.9}Ag_{44.1}$	559	50-10μm
			$Au_{55.6}Ag_{44.4}$	556	
H169 Panel 10 sample 2	UZ	Stromeyerite/Chalcocite	$Au_{66.8}Ag_{33.2}$	668	50-20μm
H169 Panel 10 sample 2		Pyrite grain boundary	$Au_{63.4}Ag_{36.6}$	634	50-10μm
BG18-539 14.5m	UZ	Stromeyerite* vein in sphalerite	$Au_{55.9}Ag_{44.1}$	559	70-10μm
			$Au_{56.3}Ag_{43.7}$	563	
			$Au_{55.1}Ag_{44.9}$	551	

Table 31. Analytical results for electrum grains form Gap and Upper Zone lenses. All probed electrum grains shown in Plates 27 and 28.

7.6 Gangue mineralogy and textures

Gangue minerals in the Battle Zone are barite, quartz, muscovite, and calcite. Dolomite and chlorite also occur in the alteration assemblages associated with the ore lenses but were not observed in contact with ore minerals (Chapter 4). All ore lenses show a zonation from barite-rich gangue at the top of the lenses to quartz-muscovite-rich gangue at the base.

Barite

Barite is most common at the top of the ore lenses. In the Gap lens it constitutes up to 90% of the rock and occurs as large laths up to 2cm and clusters of radiating crystals (Plate 24A & Plate 29A) as well as masses interlocking equant crystals (100-200μm, Plate 29B). Sulfides occur as disseminated, irregular masses within the baritic matrix (Plate 29A) and interstitial to barite laths (Plate 24A). Barite abundance decreases rapidly downwards through the sphalerite-rich ore as the abundance of quartz and muscovite increase, and is virtually absent in banded and pyrite-chalcopyrite-rich ores. Barite is less abundant in the Battle, Gopher and South Trough lenses, but follows the same zonation as in the Gap lens. Upper Zone lenses have massive baritic-rich rocks with disseminated sulfides and massive sphalerite with barite-rich gangue.

Quartz

Quartz shows a wide variety of forms, from fine grained (Plate 29C & D), to fluid inclusion-rich coarsely crystalline masses (Plate 29C - E) that occasionally appear to be pseudomorphing barite laths (Plate 29F), and clear massive quartz. Quartz occurs as anhedral intergrowths with all sulfides (Plate 30A), and occasionally filling vughs in massive sphalerite and pyrite, These vughs are commonly rimmed by euhedral pyrite crystals. Quartz in veins, which cross cut ores and gangue, occurs

Plate 29 Photomicrographs of Battle Zone ore

A. Coarse bladed barite fans with interstitial sphalerite, pyrite, tennantite, bornite and anilite. BG18-1051 70.1m

B. Equigranular barite with disseminated sphalerite-tennantite-anilite and bornite. BG18-890 151.3-151.5m.

C. Fine grained quartz-muscovite with minor pyrite. BG18-340 45.5-46.8m

D. Two varieties of quartz, fine-grained quartz (1) cross cut by a vein containing coarsely crystalline, fluid inclusion-rich quartz (2). BG18-342 45.3-56.0m

E. Coarse quartz and muscovite in a pyrite pressure shadow. BG18-340 45.5-46.8m

F. Inclusion-rich, coarsely crystalline quartz interpreted as pseudomorph after barite crystals. Sphalerite occurs between quartz crystals. BG18-889 153.6m

sph = sphalerite, py = pyrite, ten = tennantite, gal = galena, cpy = chlacopyrite, col = colusite, bn = bornite, r = rutile, alt = altaite, anil = anilite, ren = renierite, bar = barite, qtz-quartz, carb = calcite, ser = sericite

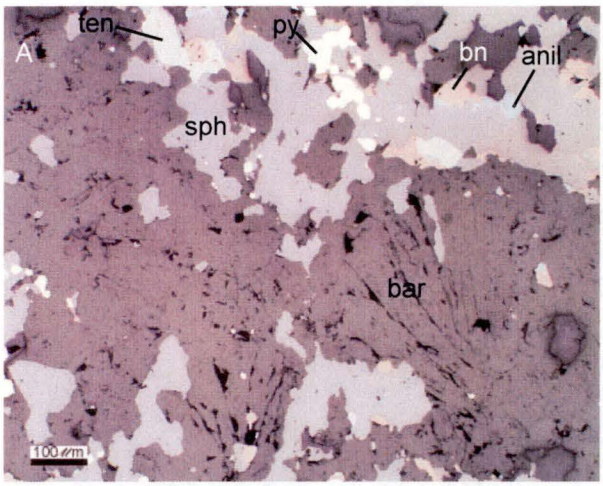
A
ten
py
bn
anil
sph
bar
100 µm

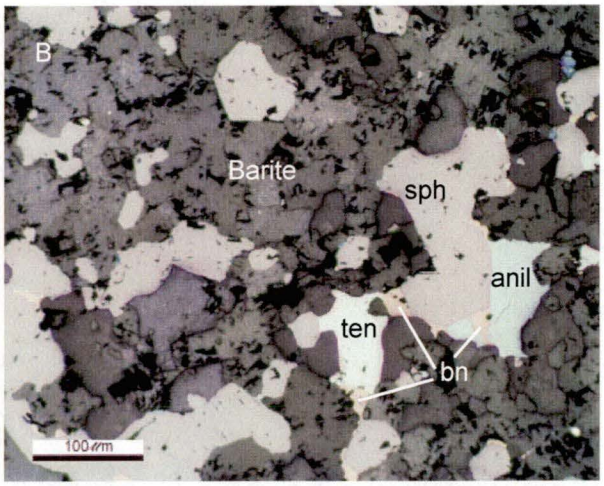
B
Barite
sph
anil
ten
bn
100 µm

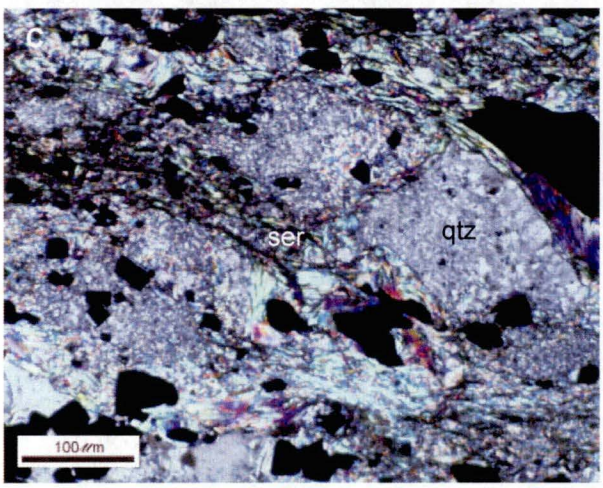
C
ser
qtz
100 µm

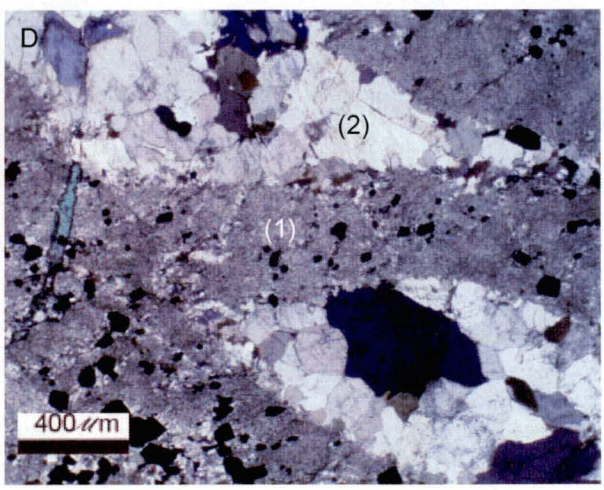
D
(2)
(1)
400 µm

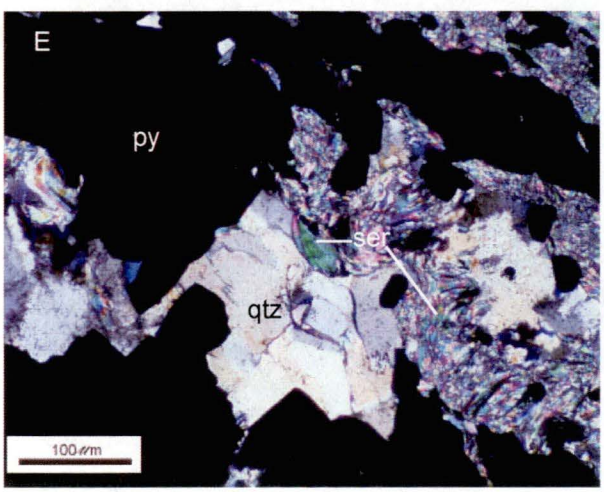
E
py
ser
qtz
100 µm

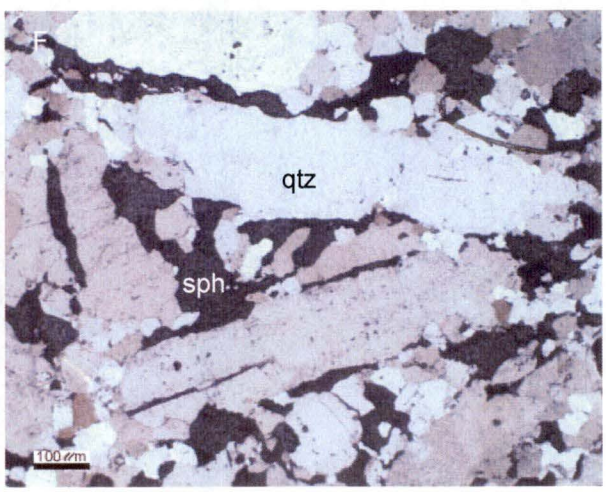
F
qtz
sph
100 µm

as euhedral grains (Plate 30B) and also occurs as massive anhedral grains. Relic volcanic quartz crystals (Plate 30C) can also be seen associated with some semi-massive ores (particularly in Upper and Gap lenses) and are often overgrown by later quartz.

Muscovite

Muscovite occurs as fine grained masses (after sericite) with or without fine grained quartz (Plate 29C & Plate 30C) and as coarser crystals (up to 100μm) intergrown with coarse anhedral quartz and sulfides (Plate 29E). Coarse 100μm crystals of muscovite intergrown with sphalerite and pyrite (Plate 30D) are attributed to metamorphic recrystallisation.

Calcite

Calcite occurs as anhedral masses and veins throughout the Battle Zone (Plate 30B & C). Calcite also occurs intergrown with chalcopyrite (Plate 30E). Calcite is not abundant, constituting < 1% of the rock but is ubiquitous throughout the ore zones. The common occurrence as veins suggests the presence of calcite is due to metamorphism.

7.7 Discussion

7.7.1 VHMS mineralogy

Primary sulfide textures due to the formation of VHMS deposits and to zone refining by hydrothermal fluids within the developing sulfide mound have been documented by many authors (Sato, 1972; Eldridge et al., 1983; Lianxing and McClay, 1992,). Eldridge et al., (1983) provided a comprehensive review of these mineral textures in the Kuroko VHMS deposits. The formation of textures was divided into a four-stage evolution, all of which may have taken place nearly contemporaneously but at different sites within the accumulating sulfide deposit and are summarised below:

Stage 1; precipitation of primitive or facies 1 sulfides, characterised by fine grain size (< 50 μm) and morphology; euhedral crystals, framboids, botryoidal and colloform growths as well as anhedral to subhedral blebs and bands and irregular shaped patches. Facies 1 sulphides are typically tightly inter-grown - sphalerite, galena, pyrite, tetrahedrite, barite and minor chalcopyrite.

Stage 2; hotter hydrothermal fluids dissolve facies 1 minerals and repricipitate the elements resulting in the formation of coarser grained facies 2 minerals. Sphalerite forms sub-hedral to euhedral crystals, clusters or semi-linear bands exhibiting well-developed growth banding. Facies 2 pyrite is coarse grained (100μm to 1mm) and typically subhedral to euhedral. Facies 2 galena occurs as large irregularly shaped patches intergrown with sphalerite and pyrite.

Stage 3; hotter, Cu-rich hydrothermal solutions are introduced into the ore pile. This results in the replacement of facies 2 sulfides by facies 3 chalcopyrite in the lower parts of the orebody

Stage 4; introduction of hotter (and undersaturated with Cu) fluids into the ore pile, resulting in the dissolution of chalcopyrite and the formation of pyritic sulfides in the lower most part of the ore

Plate 30 Photomicrographs of Battle Zone ore

A. Anhedral to sub-hedral quartz infill in sphalerite-chalcopyrite-pyrite. G158DD Sample No. 5

B. Quartz-calcite vein cross cutting pyrite-chalcopyrite. BG18-340 44.2-45.5m

C. Calcite and quartz crystals in intense sericite-quartz alteration, close to sphalerite-pyrite mineralisation with recrystallised quartz matrix. BG18-479 9.4m

D. Muscovite flakes in sphalerite-galena-chalcopyite mixture. BG18-342 54.3-56.0m

E. Chalcopyrite-calcite intergrowth. H169 P7 sample No. 3

sph = sphalerite, py = pyrite, ten = tennantite, gal = galena, cpy = chlacopyrite, col = colusite, bn = bornite, r = rutile, alt = altaite, anil = anilite, ren = renierite, bar = barite, qtz-quartz, carb = calcite, ser = sericite

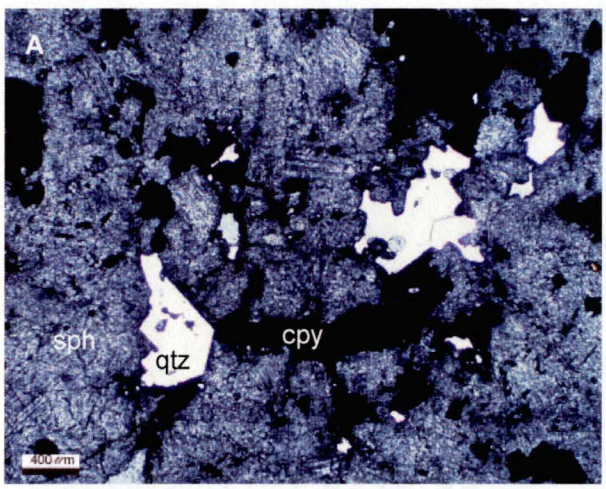
A
sph
qtz
cpy
400 µm

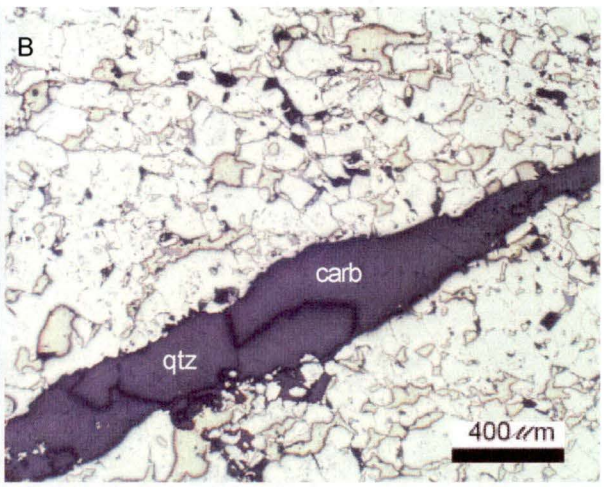
B
carb
qtz
400 µm

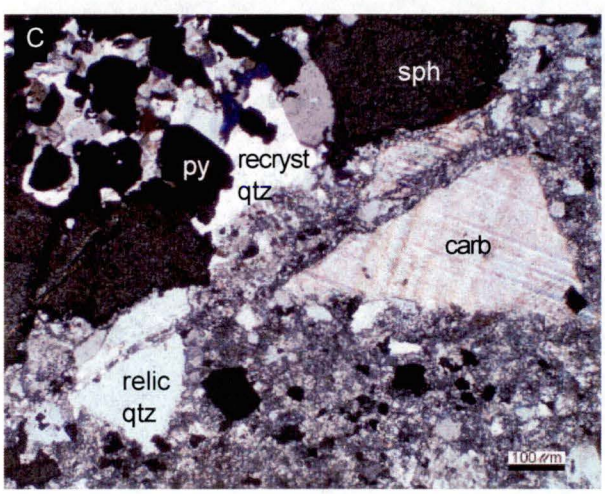
C
sph
py
recryst
qtz
carb
relic
qtz
100 µm

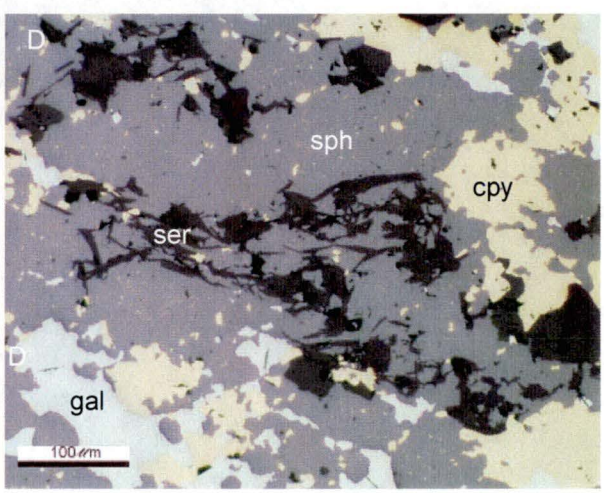
D
sph
cpy
ser
gal
100 µm

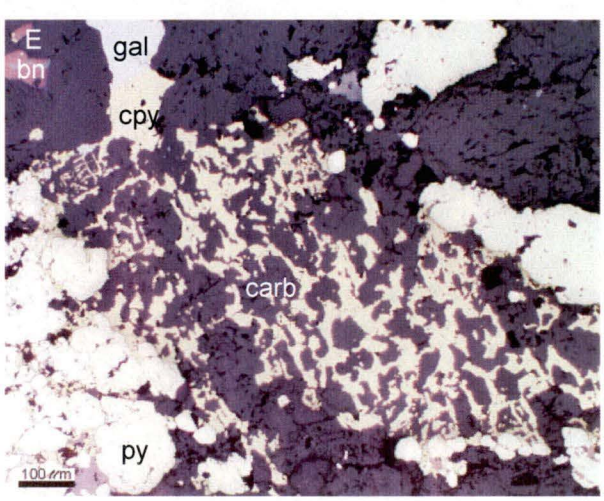
E
bn
gal
cpy
carb
py
100 µm

pile.

These textures are greatly modified by subsequent deformation and metamorphism. Pyrite is the most resistant of the sulfides and commonly shows these textures in moderately deformed and metamorphosed ores. The textures for pyrite are summarised in Table 32.

Stage:	Pyrite textures
Facies 1	Colloform, botryoidal, or framboidal, or as aggregates and semilinear to curved bands up to a millimetre or so in length, small ~20μm anhedral or subhedral blebs, and rare euhedral cubic and pyritohedral (~20μm) crystals
Facies 2	Coarse grained (100μm to 1mm) subhedral to euhedral, cubes, pyritohedrons and / or aggregates of cubes. Crystals commonly contain inclusions of sphalerite and galena.
Facies 3	Rounding, corrosion and atoll textures

Table 32. Pyrite ore textures in undeformed Kuroko-deposits, from Eldridge et al. (1983).

The Battle Zone sulfides, sphalerite, galena and chalcopyrite are recrystallised partially destroying and/or modifying mineral textures. Pyrite, however, show a range of textures consistent with Eldridge et al. (1983) facies model for VHMS development as well as textures due to metamorphic recrystallisation.

7.7.2 Origin of framboids and ring structures

England and Ostwald (1993) provide a review of the origin of the early formed pyrite (primitive structures or facies 1 of Eldridge et al., 1993) including framboids, fine grained euhedral pyrites and ring structures of radiating pyrite crystals, that occur in VHMS deposits. Framboids and fine grained euhedra are considered to be products of diagenesis, with framboids generally considered to form early in the burial history of the sediments, from bacterial sulfate reduction or by non-biogenic means (England and Ostwald, 1993), while the euhedra are considered as recrystallisation products during later diagenesis. England and Ostwald (1993) suggest that ring structures are derived from original framboids through recrystallisation. They also propose that the rings may form intermediate products between framboids and the recrystallised euhedra.

The Battle Zone has pyrite framboids and ring structures (Plate 18E - H & Plate 19A - C) contained in quartz. These mineral textures suggest pyrite deposition in the Battle Zone occurred (at least partly) as a product of diagenesis within the sediments. These diagenetic pyrites were then recrystallised to form ring structures and pyrite euhedra. The occurrence of pyrite framboids and ring structures in quartz relates to their preservation, the quartz isolated the pyrite framboids and rings from surrounding sulfides limiting their growth and preserving the intermediate structures.

7.7.3 Chalcopyrite disease in sphalerite

Chalcopyrite disease was first named and described by Barton (1978) and has been described by Barton (1978, 1987), Ramdohr (1979) and Scott (1983) as well as many others. It occurs as a fine "dusting" of < 1 μm-sized chalcopyrite inclusions in sphalerite to vermicular intergrowths of chalcopyrite (2 to 20 μm) in sphalerite.

The origin of chalcopyrite disease has been the subject of much discussion and experimental work (Eldridge et al., 1983, 1988; Scott, 1983; Stanton, 1972; Craig and Vaughan, 1994; Barton and Bethke, 1987). It is now widely considered that chalcopyrite disease in VHMS deposits is the result of a reaction between sphalerite and Cu-Fe-bearing solutions produced by the evolving mound. This mechanism of formation is supported by experimental data of Hutchison and Scott (1981). Chalcopyrite disease has earlier been attributed to the exsolution of chalcopyrite from sphalerite on cooling of the ores. However, it is now widely recognised that chalcopyrite will not dissolve in sphalerite in significant amounts unless temperatures are above 500°C (Wiggins and Craig, 1980; Hutchinson and Scott, 1981). The temperature of formation from modern black smokers (200 to 350°C; Eldridge et al., 1983) indicates that the solubility of copper in sphalerite is too low to account for the chalcopyrite disease observed in VHMS deposits (Eldridge, 1983). Metamorphism complicates the interpretation of chalcopyrite disease by coarsening the sulfides and destroying the original textures.

The chalcopyrite "disease" seen in Battle Zone sphalerite differs from the disease described by Barton (1978) in its grain size and the shape of the inclusions (mainly rounded 20μm blebs). The difference between Battle Zone chalcopyrite "disease" and the disease described by Barton (1978) may be due to metamorphism of chalcopyrite diseased sphalerite. However, similar textures to those seen in the Battle Zone could also be produced by metamorphism of co-precipitated sphalerite and chalcopyrite (Barton and Bethke, 1987). Thus the reaction of sphalerite with Cu-Fe-bearing solutions or the co-precipitation of sphalerite and chalcopyrite may form the chalcopyrite "disease" seen in the Battle Zone ores. For Myra Falls the author favours the reaction of sphalerite with Cu-Fe-bearing solutions due to the distribution of chalcopyrite disease (most abundant toward the footwall), but co-precipitation cannot be rule out.

7.7.4 The effect of metamorphism on sulfide textures

The Battle Zone ore has been subjected to at least two metamorphic events of prehnite-pumpellyite to lower greenschist facies (Chapter 2). Metamorphism results in a general coarsening of grain size and the annealing in polymetallic ores (Clark & Kelly, 1973; Craig and Vaughan, 1994). At the temperature of prehnite-pumpellyite to lower greenschist facies metamorphism (250-400°C) chalcopyrite and galena are recrystallised and sphalerite acts in a ductile manner, while pyrite remains brittle. Chalcopyrite recrystallisation occurs at temperatures as low as 200°C (Kelly and Clark, 1975).

The effect of metamorphism on sphalerite has been to increase the grain size and homogenise any zonation or banding within the sphalerite crystals. Metamorphism increases the grain size of sphalerite through recrystallisation and the annealing of sphalerite with chalcopyrite and galena (Stanton, 1972). During recrystallisation inclusions of other minerals are expelled from the growing

grains and into areas where less interfacial energy is required i.e. along grain boundaries and to triple junctions (Stanton, 1972).

Sphalerite grains have also been homogenised. Eldridge et al. (1983) described the zonation of facies 2 sphalerite crystals in the Kuroko ores (similar to that seen in Plate 16A). Scott (1983), explained this zonation as due to slight variations in the activity of sulfur and temperature conditions during the deposition of sphalerite. However buffering of the compositional variation occurs during metamorphism creating homogeneous grains. The one sample that shows zoned sphalerite crystals (Plate 16A) occurs within millimetres of sphalerite showing completely annealled textures. The annealed sphalerite shows no internal features when viewed under transmitted light. The author suggests that this occurrence of zoned sphalerite represents a late (post metamorphic) deposition of sphalerite in a cavity rather than a primary depositional feature.

Metamorphism has caused the annealing of galena, producing perfect 120° triple junctions (Plate 21E). Chalcopyrite, like galena is strongly annealed in the Battle Zone lenses. However, it lacks the cleavage of galena so little textural clues remain as to its origin. Annealing has also occurred between galena-chalcopyrite and sphalerite (Plate 16D – F, & Plate 17A, B, D-G) resulting in equant rounded sphalerite grains with chalcopyrite and galena remobilised to grain boundaries where they show cuspate margins against sphalerite.

Under greenschist-facies metamorphic conditions, pyrite deforms by cataclasis (Atkinson 1975; Cox et al., 1981). Deformation of pyrite by cataclasis is confined to fault zones in the Battle Zone sulfide lenses (see chapter 8). In the Battle Zone sulfides metamorphism more commonly causes the recrystallisation of pyrite. Metamorphism results in the development of granular and massive metablastic mineralisation. Granular and metablastic mineralisation consists of coarse-grained, commonly idioblastic, pyrite megacrysts (Craig and Vokes, 1993; Vokes and Craig, 1993). Metamorphic pyrites are generally free of inclusions and may show Caries-like growth embayments indicative of metablastic growth (Vokes and Craig, 1993; hook texture of Robinson, 1994).

Within the pyrite and pyrite-chalcopyrite rich ore zones at the base of the massive sulfide lenses the interpretation of pyrite textures becomes complicated. Massive pyrite shows the typical "foam" texture of Stanton (1964) with triple junctions indicative of recrystallisation. However this recrystallisation may occur by hydrothermal reworking (zone refining) during mound formation or by metamorphic recrystallisation. Pyrite porphyroblasts may also form during mound growth, the distribution of pyrite porphyroblasts in the Battle Zone (increasing in size and abundance toward the base of the massive sulfide lenses) suggests this is the case. However some pyrite porphyroblasts in the hangingwall may have formed during metamorphic recrystallisation.

The bornite-anilite mineral assemblage also shows evidence of metamorphism and annealing with bornite being massive and anilite being remobilised to the margins of bornite grains and into large anhedral masses. The chalcocite group, of which anilite is a member is extremely mobile under metamorphism and will quickly rearrange itself into large masses commonly at the edges of bornite grains. This rearrangement destroys any primary texture and disguises the origin of the bornite-anilite mineralogy.

The origin of bornite and anilite may be due to hypogene or supergene processes. The distribu-

tion of the bornie-anilite mineralogy (as a pipe like feature cross cutting all mineralogical zonation in the Gap lens (Chapter 6) is suggestive of a hypogene origin. Supergene alteration tends to occur as blanket like alteration toward the top of sulfide deposits (Ney et al., 1976).

In contrast stromeyerite, which is also extremely mobile under metamorphic conditions (Bergstol and Vokes, 1974), and the associated electrum and fine grained chalcopyrite, shows delicate complex intergrowth textures. These textures suggest a late metamorphic (retrograde) timing for this mineral assemblage.

7.7.5 Paragenesis

Metamorphism of the Battle Zone ores has destroyed primary textures such as those seen by Eldridge et al. (1983) in sphalerite, galena and chalcopyrite. Pyrite, however shows a range of textures from the primitive textures of Eldridge et al. (1993) through to metamorphic porphyroblasts. Thus the textures seen in pyrite and the relation of pyrite textures to other minerals are the basis for a paragenetic sequence in the Battle Zone (Fig. 65). Primary pyrite textures have survived later deformation processes due to pyrites high textural stability (McClay and Ellis, 1983).

In the Battle Zone pyrite shows evidence of framboidal formation and fine grained intergrowths similar to that seen in the undeformed Kuroko-deposits, as discussed by Eldridge et al (1983). The observation of textures in the Battle Zone suggest that the precipitation of sulfides started as the deposition of fine grained (<50μm) intergrown pyrite, sphalerite, galena, tennantite, chalcopyrite. Bornite may also have been part of this early stage of mineralisation, as the cores of some pyrite crystals contain fine inclusions of bornite in Battle, Gopher and South Trough lenses.

Sulfide textures in the Battle Zone were then most likely coarsened similar to the Eldridge et al. (1983) model. This phase includes the formation of euhedral pyrite grains (1-100μm in size). Zonation of minerals from Pb-Zn-rich at the top of the ore lenses to Cu-Fe-rich at the base indicates that the Battle Zone lenses continued to evolve with the introduction of chalcopyrite as chalcopyrite disease of the sphalerite and as massive chalcopyrite as per the Eldridge et al. (1983) model. The final stage in the formation of Cu-Pb-Zn-Fe-assemblage was most likely the removal of chalcopyrite at the base of the mound leaving massive pyrite.

In the Upper Zone and Gap lenses this process of mound evolution was followed by an alteration of chalcopyrite to bornite (Fig. 65) and deposition of pyrite. Anilite deposition was synchronous with this alteration or during the waning stages of alteration. Formation of the bornite and anilite was followed by metamorphism, which destroyed most of the primary sulfide textures resulting from the formation of the Cu-Pb-Zn-Fe-assemblage and bornite alteration. Pyrite is the only sulfide from the first two mineralogical associations whose textures were not destroyed by metamorphism. Pyrite porphyroblasts may have also formed during metamorphism.

The third and final mineralogical association (Fig. 65) resulted from the expulsion of excess Ag and Cu from bornite and anilite and the remobilisation of Au during metamorphism. The Au-Ag and Cu were deposited during the retrograde stage of metamorphism along grain boundaries and as alterations of anilite and bornite.

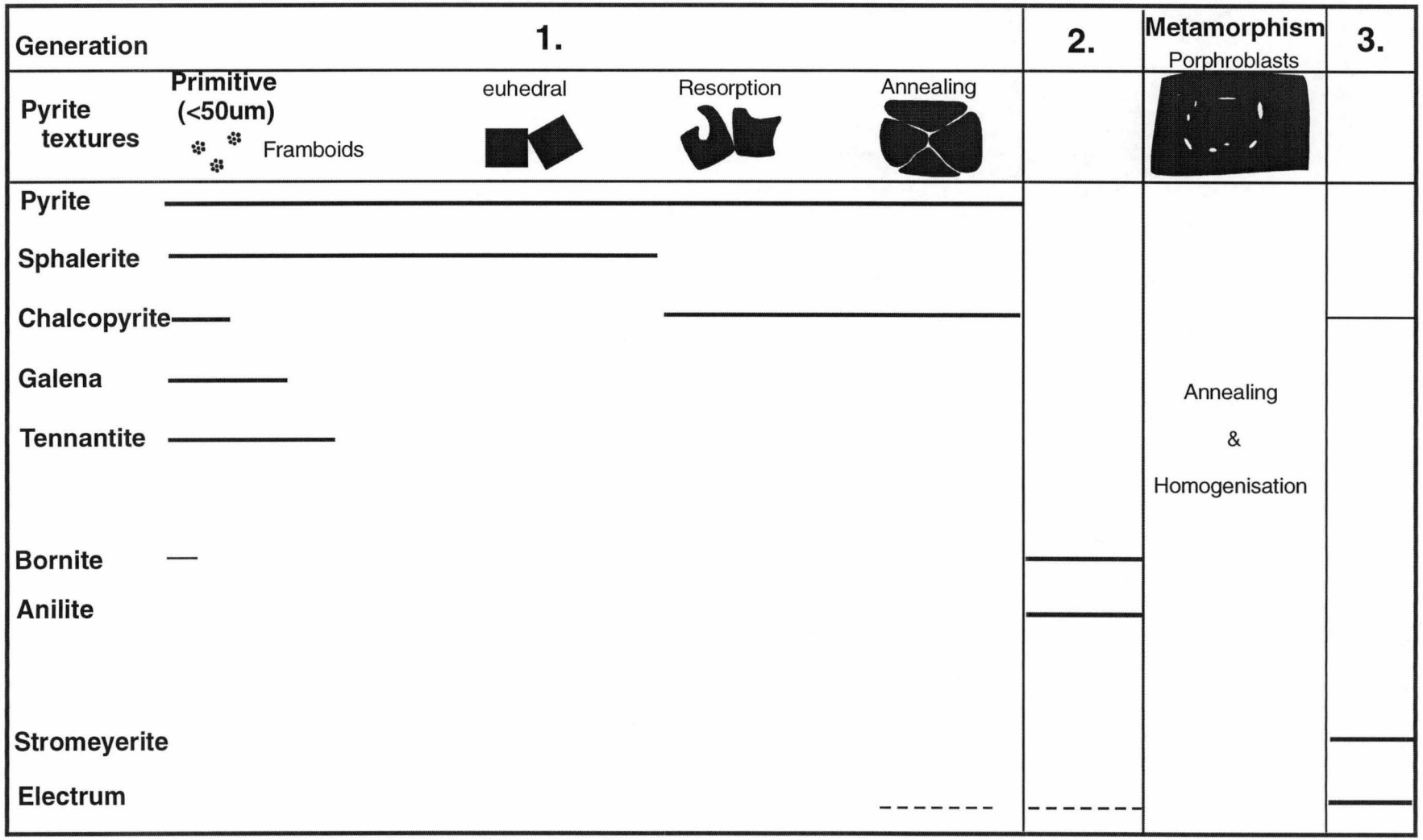

Figure 65. Paragenesis for Battle Zone lenses (Battle, Gopher, South Trough, Upper Zone and Gap).

7.8 Summary

Battle Zone massive sulfide lenses have undergone at least two metamorphic events resulting in a metamorphic grade of lower greenschist facies. Thus sulfide textures are modified. Three assemblages of sulfide mineralisation have been identified in the Battle Zone:

Assemblage 1: Cu-Pb-Zn-Fe-rich mineralogy consisting of sphalerite-pyrite-chalcopyrite-galena and tennantite with accessory rutile, tellurides and colusite. Within this generation only pyrite shows evidence of primitive textures with framboids and delicate ring structures preserved in siliceous alteration. Sphalerite has been homogenised destroying any compositional banding formed during deposition and partially annealed causing the migration of inclusions (chalcopyrite, galena and pyrite) to grain boundaries and the formation of 120° triple points on grain boundaries. Galena and chalcopyrite are completely annealed. Pyrite also shows annealing due to primary mound formation and resorption of pyrite euhedra to for pyrite porphyroblasts during metamorphism.

Assemblage 2: Cu-rich mineralogy consisting of bornite-anilite with accessory renierite and electrum. This generation is confined to Upper Zone and Gap lenses and causes replacement of assemblage 1 chalcopyrite. However the bornite-anilite mineralogy has been annealed destroying evidence of its primary textures.

Assemblage 3: Au-Ag-rich mineralogy consisting of stromeyerite-electrum and minor chalcopyrite. This stage of mineralisation cross cuts assemblage 1 and 2 sulfides forming delicate, intricate intergrowths. This third generation of is also confined to the Upper Zone and Gap lenses and is interpreted to be the result of metamorphic remobilisation.

Chapter 8

Structural Geology

8.1 Introduction

Structural studies in the Myra Falls area (Walker, 1985; Juras, 1987; Reid, 1993; & internal company reports) had shown the mine area to have a complex structural history. The rocks are deformed and metamorphosed to lower greenschist facies with folding and tectonic fabrics variably developed. Schistose and lineated rocks are common. The predominant schistosity strikes northwesterly with considerable variations in dip (Walker, 1985). Small scale folding and post-metamorphic, brittle deformation have also been noted and in some cases documented.

The aim of this study was to define the structural style of the Battle Mine. This was conducted in conjunction with a wider study of the structure in the Myra Falls camp by Berry (1995, 1996, 1998 & 2000). In the following discussion all structures are referred to by regional orientation (mine grid orientations are in brackets).

8.2 Previous Work

8.2A Regional Structure

The post-Jurassic structure on Vancouver Island has been discussed in a number of papers by Muller (1977; 1980), Campbell et al. (1992), England and Calon (1991), Nixon et al. (1994) and Yorath et al. (1999). Nixon et al. (1994) provided a detailed statement of the Jurassic to Tertiary structural history of northern Vancouver Island (Fig. 66). They proposed the following history:

Phase 1 Mid- to late-Jurassic northeast-directed compressional event which produced northwesterly trending folds and northwesterly striking thrust faults.

Phase 2 Late-Cretaceous northerly directed compression producing dominantly northwesterly striking strike-slip faults and lesser thrusting (e.g. oblique dextral faults).

Phase 3 Tertiary - northwesterly to north-northwesterly directed extension producing minor northeasterly to east-northeasterly striking normal faults in Upper Cretaceous and older strata, as well as weak reactivation of pre-existing strike-slip faults.

In contrast the structural history of southern Vancouver Island (Fig. 66) is dominated by the effects of contractional events in the Cretaceous and Eocene. The following summary is from Massey (1992):

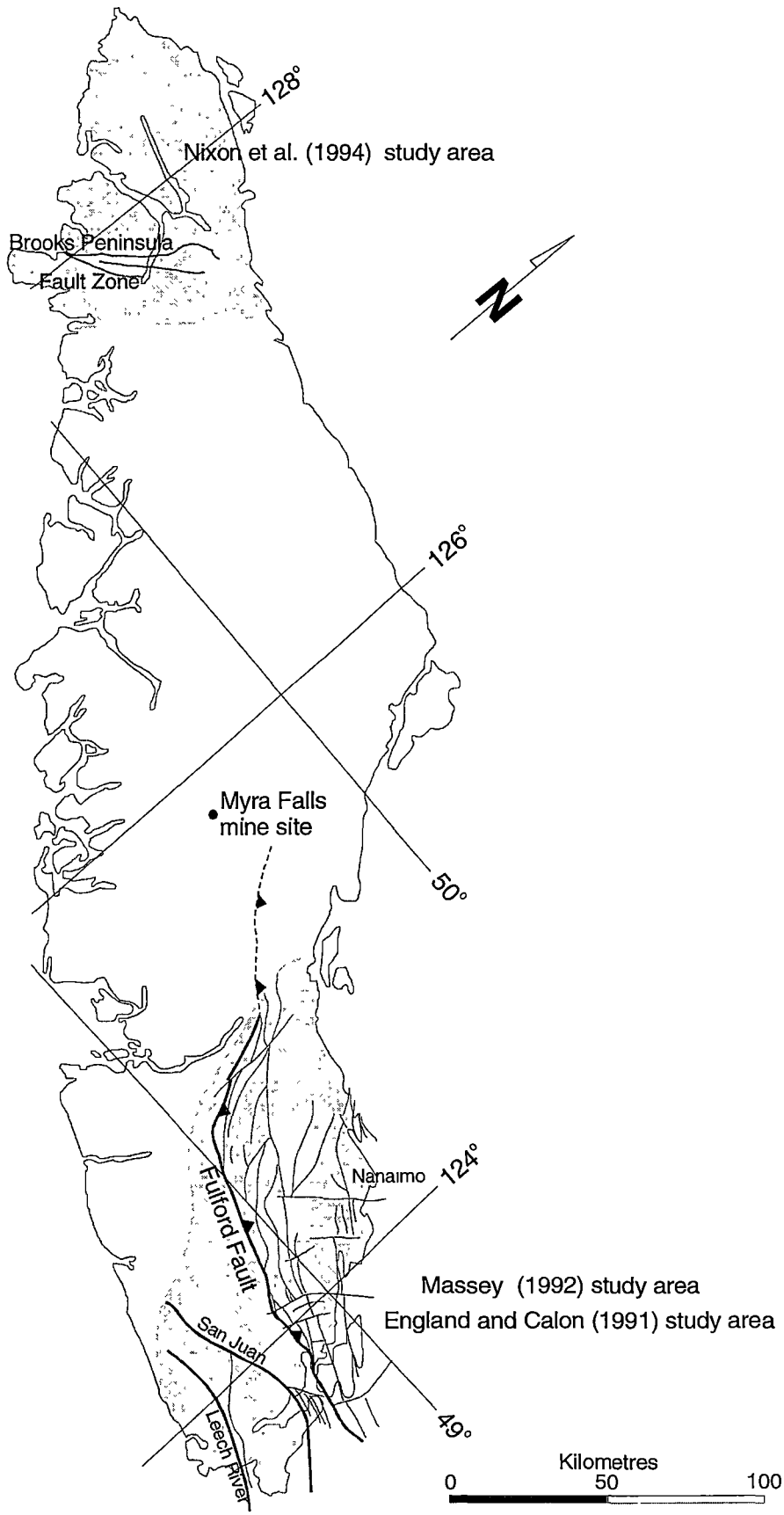

Figure 66. Map of Vancouver Island showing the areas mapped by various authors and major faults. Details from Nixon et al. (1994), England and Calon (1991), and Massey (1992).

Phase 1 Late-Devonian to earliest Mississippian deformation producing large-scale open folds in the Sicker Group Volcanics.

Phase 2 Mid-Permian to pre mid-Triassic deformation producing west-northwest trending, southwest verging, asymmetric folds, with associated axial planar penetrative fabric dipping moderately to steeply northeast.

Phase 3 Late-Triassic - extensive crustal dilation accompanying the evolution of the Karmutsen Formation (see chapter 2 for Karmutsen Formation). Structures associated with this event were not documented.

Phase 4 Early to Middle Jurassic regional-scale warping of Vancouver Island, thought to produce the three major geanticlinal uplifts cored by Sicker Group rocks (see chapter 2).

Phase 5 Eocene - contraction producing west-northwesterly trending faults of the Cowican fold and thrust system (England and Calon, 1991). High angle reverse faults dipping 45° to 90° to the north-northeast, parallel the earlier axial foliation in Paleozoic rocks.

England and Calon (1991) also note a mid to late-Cretaceous contractional event which produced a northwest verging nappe pile, resulting from the collision of the Wrangellia Terrane with North America. The mid-Jurassic events, Phase 1 Nixon et al. (1994) and Phase 4 Massey et al. (1992), appear to effect the whole of Vancouver Island, as does the Cretaceous event (Phase 2, Nixon et al., 1994: and England and Calon, 1991). Although the effects of the Cretaceous event may be overprinted by the latter Eocene contraction south of the Fulford Fault (Fig. 66; England and Calon, 1991).

8.2B Mine Scale structure

The structural setting of the Myra Falls lease area has been studied by Gunning (1931), Jeffery (1965), Walker (1980, 1983, 1985), Juras (1987), Reid (1993) and Westmin Resources Ltd. (internal company reports). Work prior to Reid focussed on the Lynx, Myra, and Price massive sulfide bodies and their immediate host lithologies (see chapter 3). Work by mine geologists (Walker, 1983 & 1985; internal company reports) recognised a subhorizontal, northwest trending asymmetric anticline with steeply dipping southwestern limb and a gentle dipping northeast limb (Fig. 67). The fold has a northwest striking, near-vertical to steeply northeast-dipping, axial planar foliation. In places a second, less prominent foliation was observed having similar strike but moderately steep southwest dipping surfaces. Linear elements in these regions have variable bearings and plunges from shallow northwest to shallow southeast.

Reid (1993) produced the first structural study of the Myra Falls mines outside the northwest trending asymmetric anticline which dominated the Lynx, Myra and Price mines. A summary of Reid's structural history is listed below (Reid, in Berry, 1995):

1. Horizontal upright open northwesterly (W) trending folds.
2. Anastomosing subvertical zones of strong cleavage with stretching lineation trending northwesterly to north-northwesterly (W to WNW). These zones were at least partly dextral.
3. Northwesterly (W) striking faults partly related to cleavage have early sinistral and late dextral movement.
4. North (NW) striking dextral and west (SW) striking sinistral faults.
5. High angle reverse faults with northwesterly (W) strike.

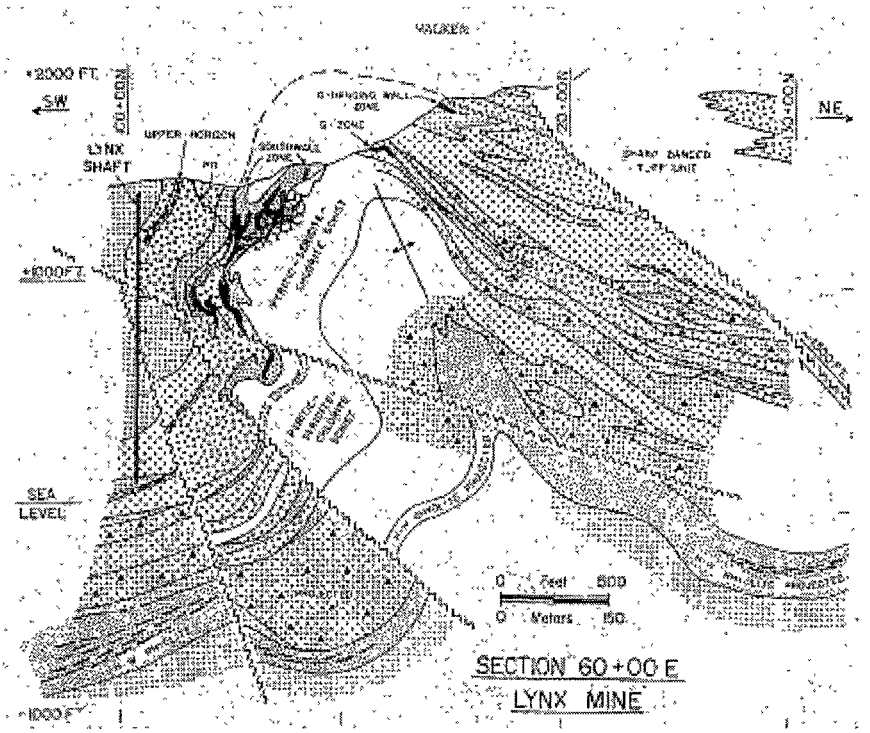

Figure 67. Section showing Lynx anticline. From Walker 1995.

6. Normal movement on northwest (W) striking, northeasterly (N) dipping, faults which contain clay gouge.

This structural history correlates well with the regional structure of Nixon et al. (1994). Events 4 and 5 as described by Reid are consistent with the late Jurassic event. While the normal faults (6) correlate with Nixon's Tertiary extension. However, Nixon et al. (1994) indicates that the southern boundary of this extensional regime appears to be marked by the Brooks Peninsula fault zone (Fig. 66), the mine is ~200km south of this fault zone making this unlikely. A major difference seen at the mine is that the Cretaceous dextral movement on northwesterly striking faults recognised in northern Vancouver Island are only recognised as reactivation of earlier faults in the mine area (late stage of 3 and possibly 2). Reid's (2) and (3) structures are the only major mine structures which have no known analogues in the Mesozoic stratigraphy of northern Vancouver Island. Juras (1987) observed that these structures predate the Island granitoids of mid-Jurassic age. While Massey's phase 2 - northwesterly trending folds with axial planar penetrative fabric, fit well with Reid's event 2.

8.3 Structure of the Myra Falls Area

Berry (1995, 1996, 1998, 2000) simplified the multi-stage structural history of the Myra Falls area in to a six stage evolution. The aim of this system is to provide a useable set of criteria to aid fault recognition in sections and include kinematic aspects of faulting which can support a more predictive model for ore lens geometry. It also has the advantage that the structures are recognisable from textures and orientation in core. Berry's structure is summarised below and in Figure 68.

Devonian basement and growth structures - D1

This stage includes any pre mineralisation faults that effect the basin geometry and syn-depositional growth structures, both of which may have controlled the distribution of the volcano-sedimentary and mineralising sequences. These structures are obscured by alteration and overprinted by later deformation events making them difficult to recognise in core and outcrop. The growth structures are generally recognised by detailed stratigraphic assessment by the mine geologists (McKinley et al. 1997; Pearson et al., 1997). These structures are named D1. However it is noted that D1 may represent several generations of structural evolution.

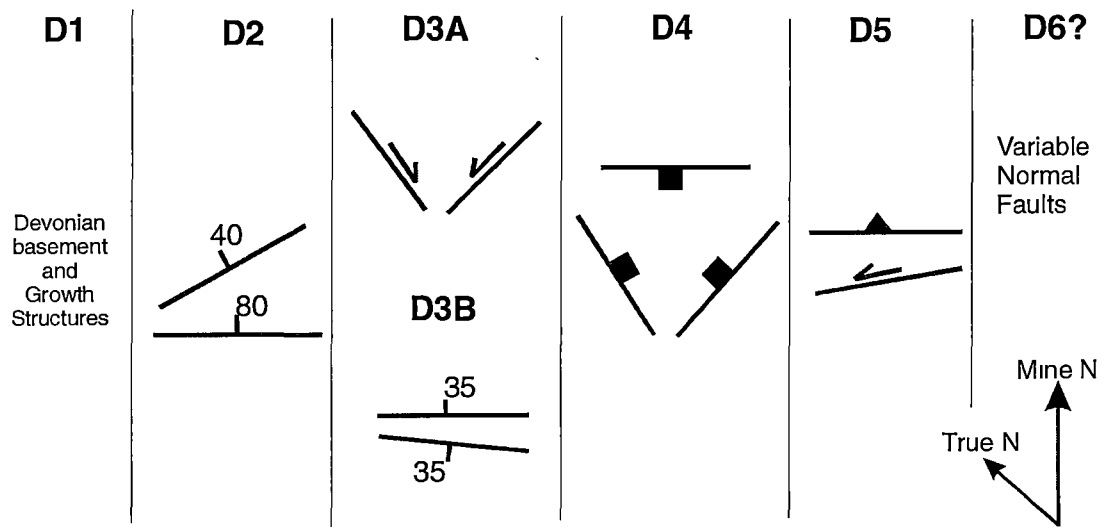

Figure 68. Summary of structural patterns in Mine grid orientation (after Berry, 2000)

Pre-Permian - D2

The second generation tectonic structures are the first major post-depositional deformation recognised in the Myra Falls area. Two structures are recognised as belonging to this event. The first occur as sub-vertical zones of strong cleavage with stretching lineation trending northwesterly to north-northwesterly (W to WNW). The second set of structures occur as moderately northeast (N) dipping intense cleavage zones. These intense cleavage zones also trend northwesterly to north-northwesterly (W to WNW) and are characterised by a northwest-southeast (E-W) mineral stretching lineation. No overprinting evidence was seen and the stretching lineation is parallel to the intersection of the two planes. These structures are the first penetrative structures recognised in the Myra Falls area. However, considerable pre-deformational faulting is known to have occured in the area, thus these structures are named D2.

Late Mesozoic - D3

The third major deformation event is characterised by northeast-southwest (N-S) directed compression and has been split into two events D3A, and D3B in line with the work of Nixon et al. (1994). D3A includes north (NW) striking dextral and west (SW) striking sinistral faults, while stage D3B is characterised by reverse faults with NW (W) strike and associated with quartz carbonate veins. All

faults of this generation have brittle ductile textures (discrete faults surrounded by narrow zones of cleavage development.

D4

The fourth major structural event is characterised by normal movement on northwest (W) striking, northeast (N) dipping, faults which contain clay gouge. A down dip lineation is observable on some fault planes, however it is not always present. Veins were commonly found spatially associated with this gouge, but are not always present. Faults of this generation are discrete structures with upto 1cm of gouge, with no apparent cleavage or brecciation in the surrounding rocks.

D5

The fifth major structural event is characterised by gouge and fault breccia, with minor quartz vening. These structures strike southeast (E) to east (NE) and show a sinistral sense of movement. These structures are interpreted to have resulted from an east-west compression. Commonly reactivate D2 and D3A structures and form structures of their own. D5 zones of intense cataclastic deformation are common in the Battle Mine.

D6

A sixth deformation event has been postulated by Berry (2000) and contains N dipping, gougy, normal faults with no associated veining. Berry (2000) correlated this stage of faulting with the formation of the Queen Charlotte basin (Miocene).

8.4 Battle Zone Structure

The aim of this section is to define the structural style of the Battle Mine. The structure presented below, is the result of underground mapping during the three field seasons (see chapter 1). Structures have been grouped by structural style and orientation and are presented in the order considered most likely to represent the sequence of events from available evidence. The relationship between fault types were not always observable in mine drifts thus the order is only very approximately the temporal order of the structures. Areas mapped are show in Figure 69, mapping was restricted by availability of drifts at the time of field work. Conventions used here are those obtained from mine survey. All measurements were made in magnetic north, and are converted to mine grid (+25°) and true north (-20°), All data summarised in Appendix 2.

Foliation - D2

The first deformation event recognisable in the Battle Zone is a pervasive foliation. These structures are equivalent to the D2 - pre-Permian structures identified by Berry (1995, 1996, 1998), and thus are named D2 here. The intensity of this foliation varies from zones of weak foliation, where the foliation is barely recognisable, to intense foliation zones or shear zones. Zones of moderate to intense foliation vary

A. Battle Zone map - Upper Zone level

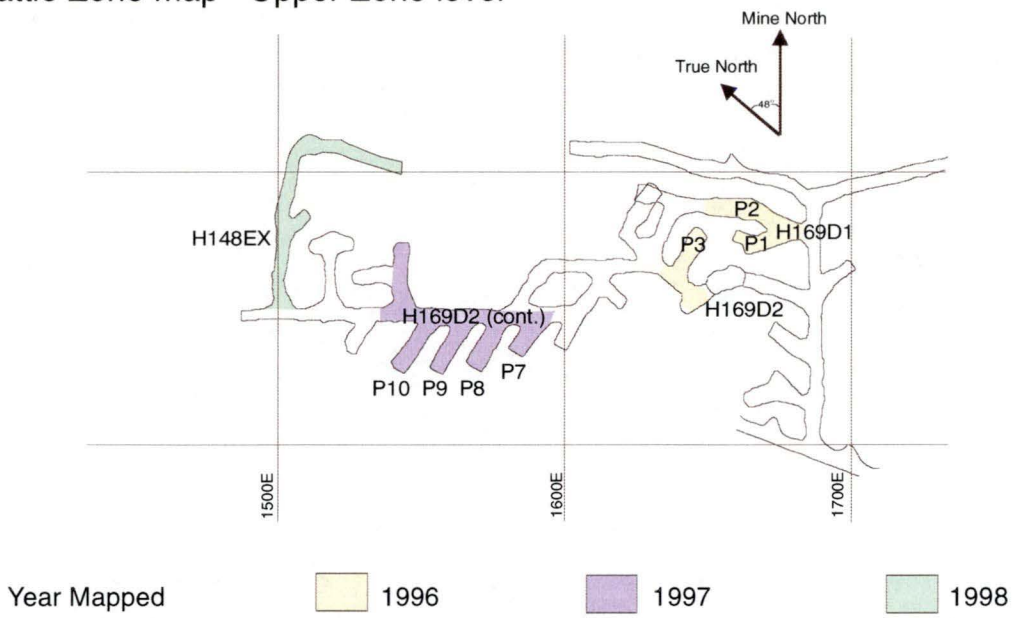

Figure 69A. Level maps for the Upper Zone level of the Battle Mine showing the drifts mapped, colour coded by year. All maps in mine grid, (continued over page).

B. Battle Zone map - Main level

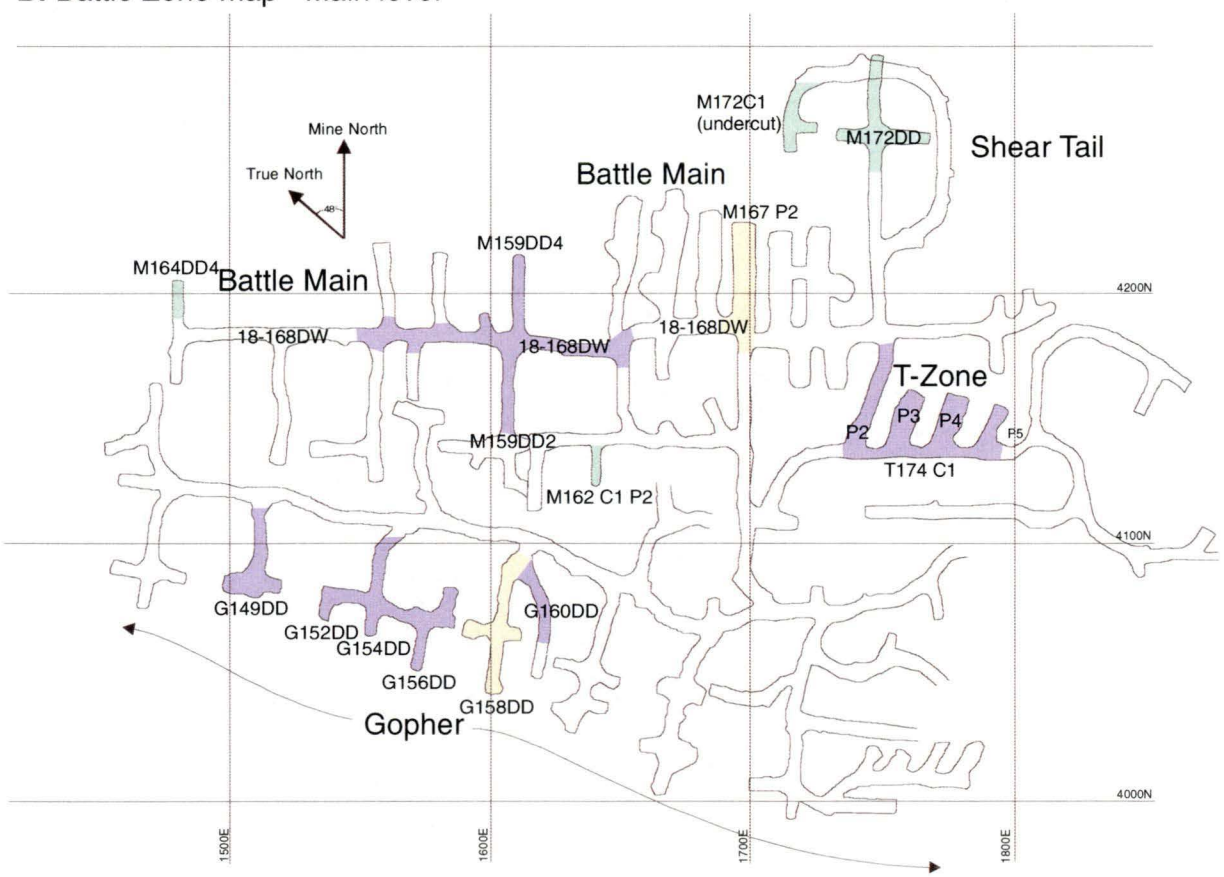

Figure 69B. Level maps for the Battle Mine main level showing the drifts mapped, colour coded by year. All maps in mine grid, (continued over page).

C. Battle Zone map - Undercut level

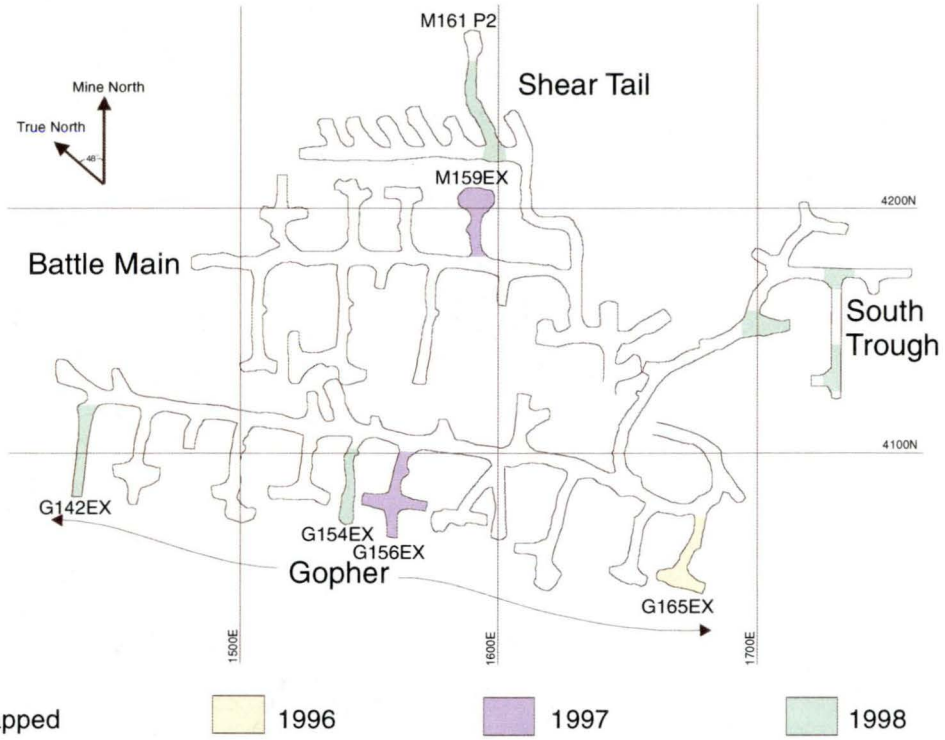

Figure 69C. Level mapsfor the Undercut level of the Battle Mine showing drifts mapped, colour coded by year.

from half a metre to ten metres in width and form two sets distinguishable by their dip. Steeply dipping, strong foliation zones range in dip from 60°N to 80°S (ninety percent dip between 60°N and 80°N, Fig. 70) and have strikes of 130° (085°) to 155° (110°), Figure 70. In contrast moderately dipping, strongly foliated zones (flat faults of Berry, 1995) are characterised by dips of 30° to 45°N and have strikes of 110° to 150° (065-105°) Figure 70. The most common movement on these structures observed during this study was strike slip (wrench), defined by the elongation of pyrite. However many of the surfaces also show dip slip

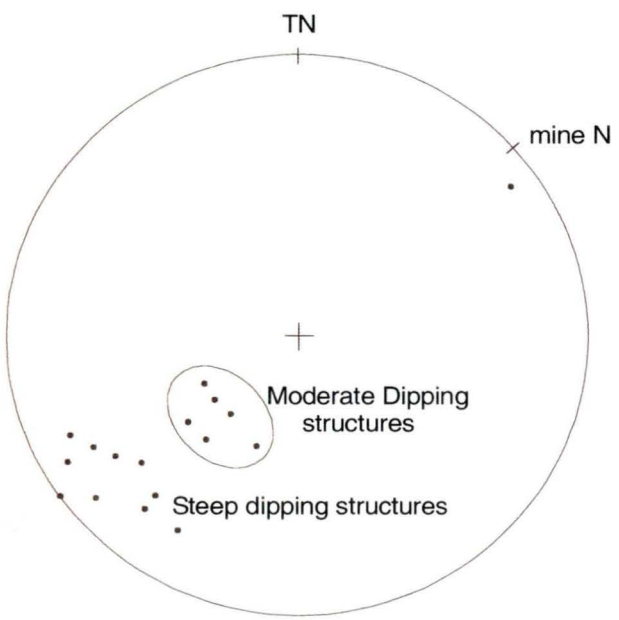

Figure 70. Lower hemisphere equal area projection of structural data from the Battle Zone. D2 - moderately dipping, strong foliation zones (circled), and D2 steep dipping, strong foliation zones. Poles to foliation plotted.

lineation (moderate dipping structures) defined by ridges of phyllosilicate minerals.

The foliation is most commonly observed in sericite altered host rocks, where it is defined by the alignment of muscovite and elongation of pyrite (Plate 31A & B) . Foliation is not well developed in cherty and strongly quartz-altered host rocks. The sulfides react in a variety of ways to the D2 foliation. Sphalerite rarely shows elongation in the massive ores but may be elongated in semi-massive to disseminated sulfides (Plate 31C). In contrast chalcopyrite and galena both show elongation parallel to S2 in both massive and semi-massive ores. Chalcopyrite inclusions in sphalerite are a good indication of the D2 foliation as they are nearly always elongate parallel to S2 (Plate 31D). Galena inclusions in sphalerite are sometimes elongate parallel to the foliation, but more commonly form elongate masses perpendicular to the foliation (Plate 31E) or infilling extension cracks in pyrite crystals perpendicular to S2 (Plate 31F).

Pyrite varies in its reaction depending on its surrounds, massive ore versus gangue (Plate 31A), and on the intensity of the foliation. In massive sulfides pyrite shows no indication of D2 deformation in low strain zones, but a pronounced elongation parallel to the S2 foliation is seen in zones of moderate to strong foliation (Plate 31A, G &H). In zones of intense foliation, pyrites may also be pulled apart perpendicular to the foliation creating zones of low pressure which are filled by the more ductile sulfides: chalcopyrite, sphalerite and galena (Plate 31E & F). In sericite-pyrite altered rocks pyrite crystals are commonly aligned parallel to the S2 foliation (Plate 31G). In these sericite-altered rocks other sulfides (chalcopyrite and sphalerite) and clear quartz infill low pressure areas around pyrite crystals (Plate 31H).

The foliation shows no consistency in relation to banding of the ore, it may be parallel (Plate 32A), oblique (Plate 32B & C), or at right angles. Where foliation occurs at right angles to ore banding the bands are transposed into tight folds with the foliation axial planar (Plate 32D & E). Thus ore banding is considered pre-D2 (see chapter 6). In zones of intense foliation ore banding and mafic dykes are transposed

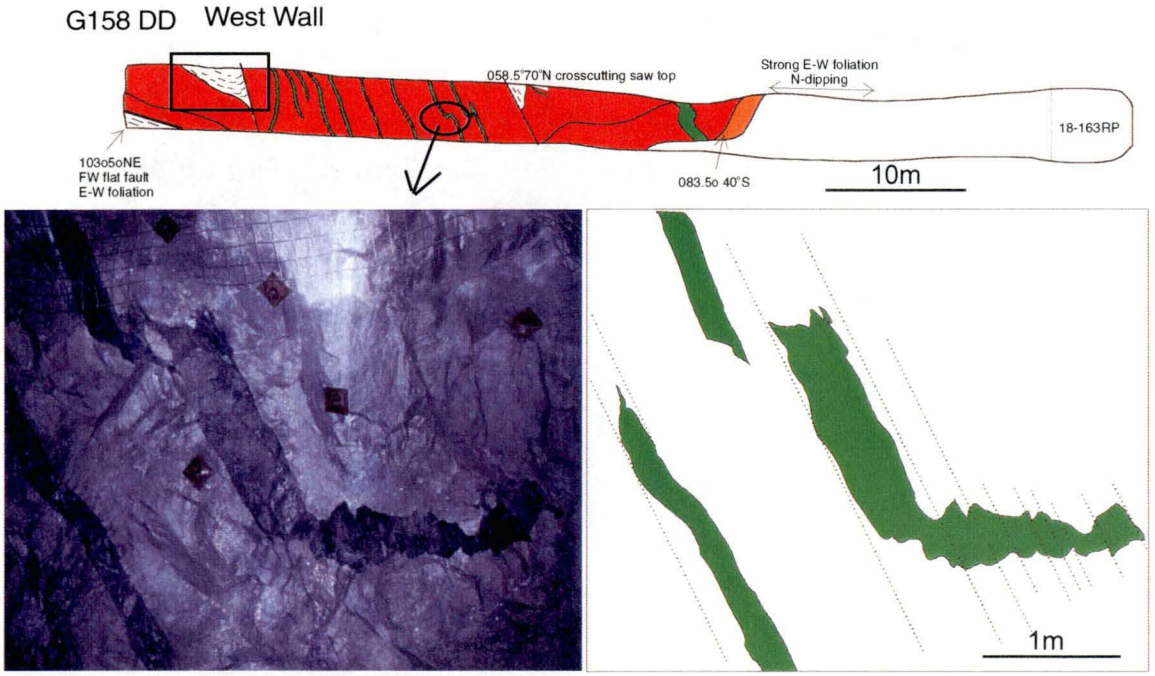

Figure 71. G158DD west wall showing the "flat fault" (D2 moderately dipping intense foliation zone) which undercuts and defines the base of the Gopher lens. D2 steeply dipping intense foliation also effects the ore causing dismembered and rotated mafic dykes and structurally induced ore banding parallel to D2. Sphalerite-rich ore is annealed masking the foliation. Box shows position of photo.

Plate 31 Sulfide microtextures due to D2

A Contrast between pyrite in sericite-alteration - elongated parallel to S2 and pyrite within sphalerite, unaffected by D2. BG18-547 115.4m

B Strongly foliated sphalerite-chalcopyrite ore. S2 foliation defined by the alignment of muscovite and chalcopyrite inclusions in sphalerite. Cross cut by a chalcopyrite filled veinlet . BG18-546 134.6m

C Sphalerite elongate parallel to S2 in semi-massive ore

D Chalcopyrite elongate parallel to S2 in sphalerite-rich band, note banding of ore defined by pyrite versus sphalerite-rich layers is oblique to S2.

E Galena elongate perpendicular to S2 in sphalerite-rich ore. In pyrite-rich ore, chalcopyrite infilling extension cracks in pyrite masses perpendicular to S2.

F Pyrite pulled apart perpendicular to S2 in sphalerite ore. Chalcopyrite, galena and sphalerite filling cracks in pyrite, perpendicular to S2. BG18-539 67.7m.

G Pyrite and minor sphalerite elongate parallel to S2 in strongly foliated sericite alteration.

H Strongly foliated zone, pyrite crystals are elongated parallel to S2 and quartz is confined to boudinage necks and pressure shadows. G158DD 5A

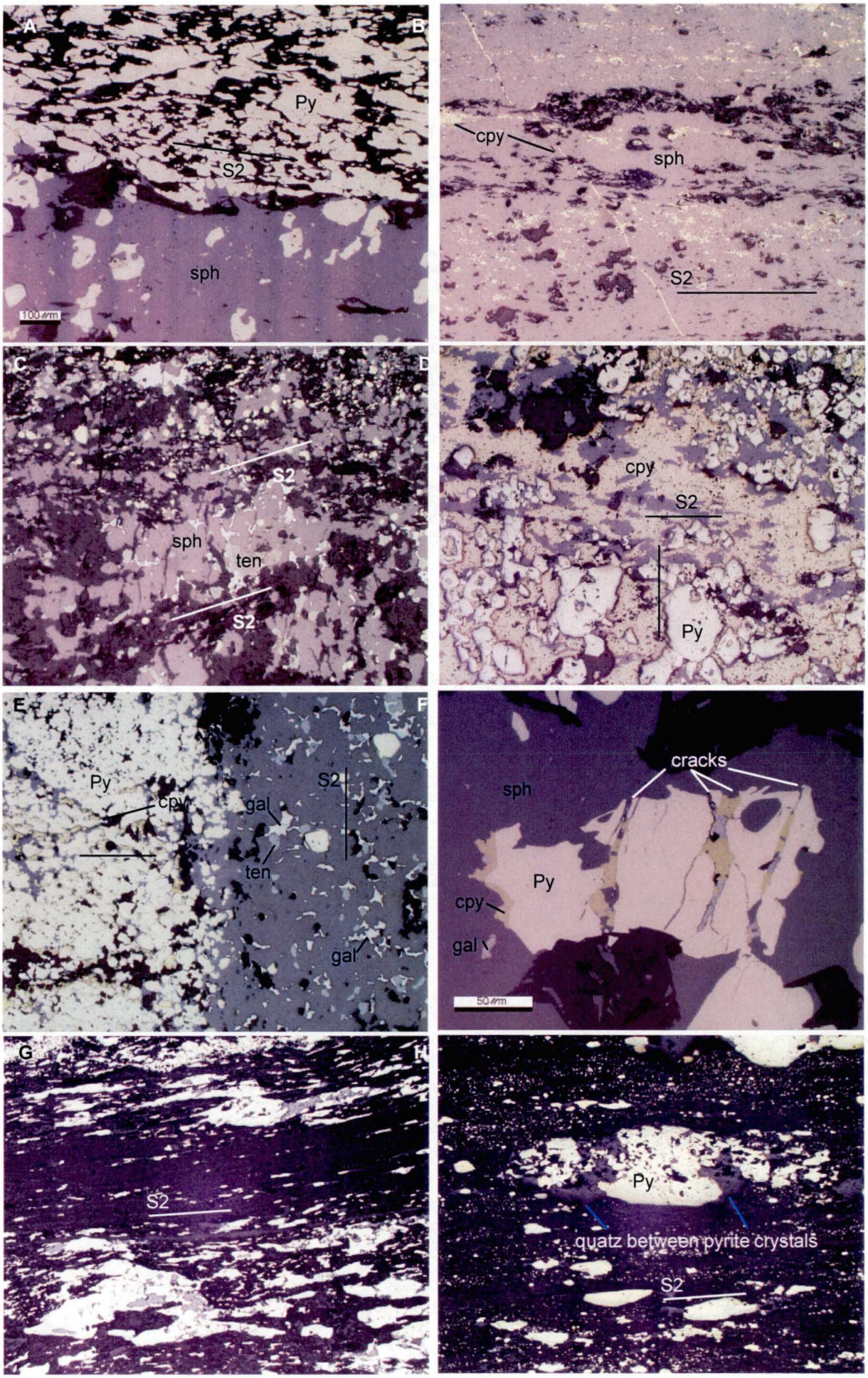

Sinclair 2000

Plate 32. Sulfide microtextures due to D2

A D2 foliation, defined by elongation of muscovite (parallel to banding of ore) BG18-979 125.4m

B Sphalerite elongate defining foliation in chalcopyrite-pyrite ore, note foliation is oblique to banding of sulfides defined by varaiation in pyrite and sphalerite content. L14-733 317.95 - 318m

C Banding of ore defines an open fold, one limb of this fold is parallel to S2. L14--733 325.0 - 325.05m.

D Folding in bedding with axial planar foliation. BG18-547 111.2m

E Photomicrograph of D. showing foliation axial planar to folding defined by sphalerite versus chalcopyrite-pyrite-rich layering. Chalcopyrite in sphalerite-rich layer elongate parallel to S2. BG18-547 111.2m

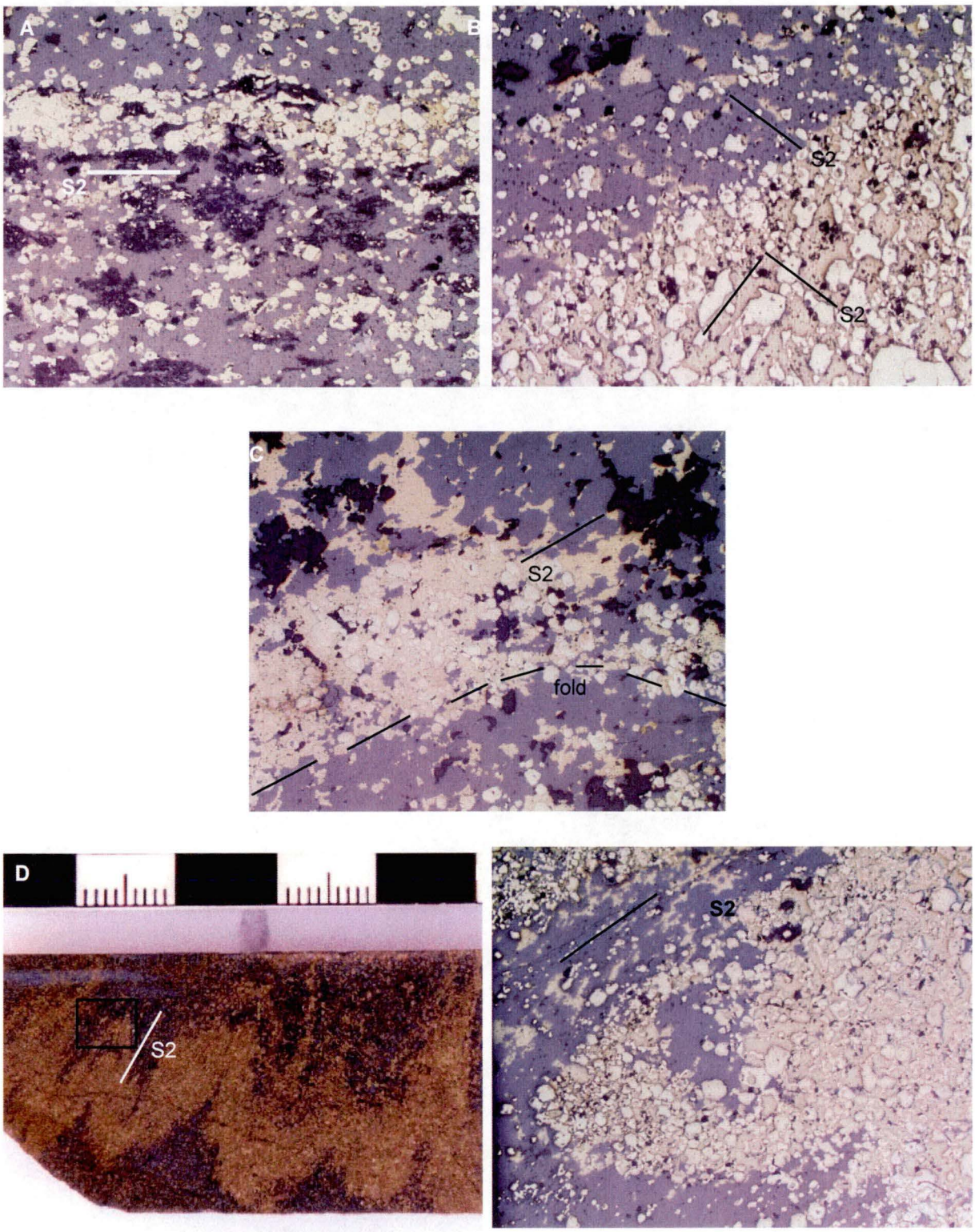
A
S2
B
S2
S2
C
S2
fold
D
S2
S2

G154EX - Plan View

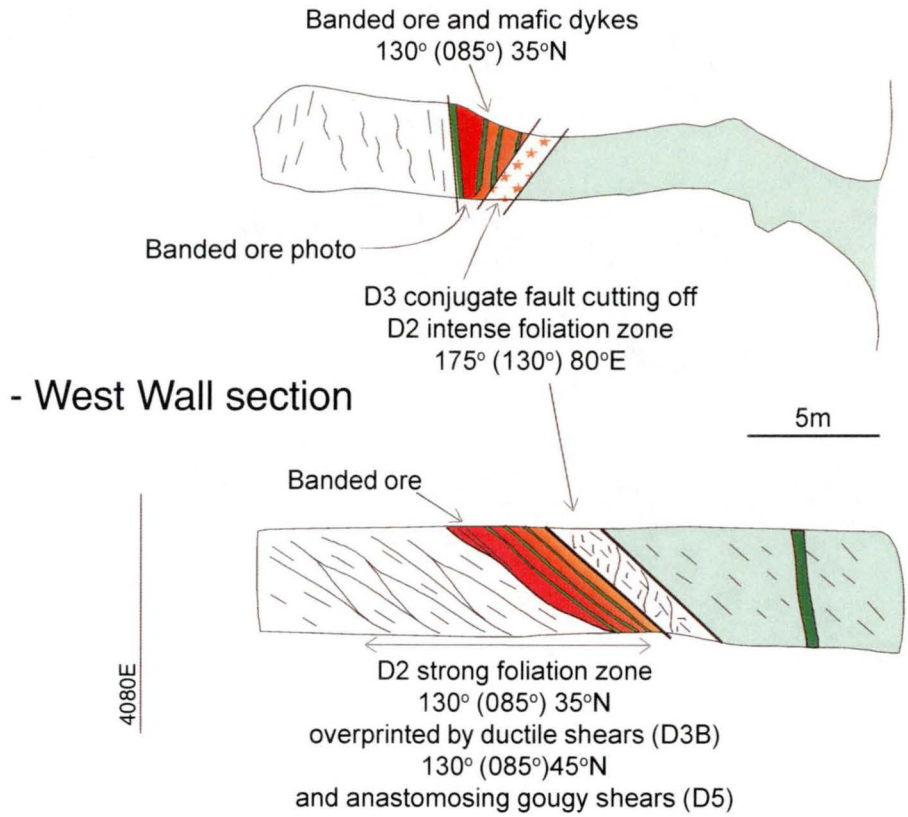

Figure 72. D2 moderately dipping intense foliation Zone, cut off by a conjugate fault. Plan view and west wall section. Gopher lens - Undercut level G154EX.

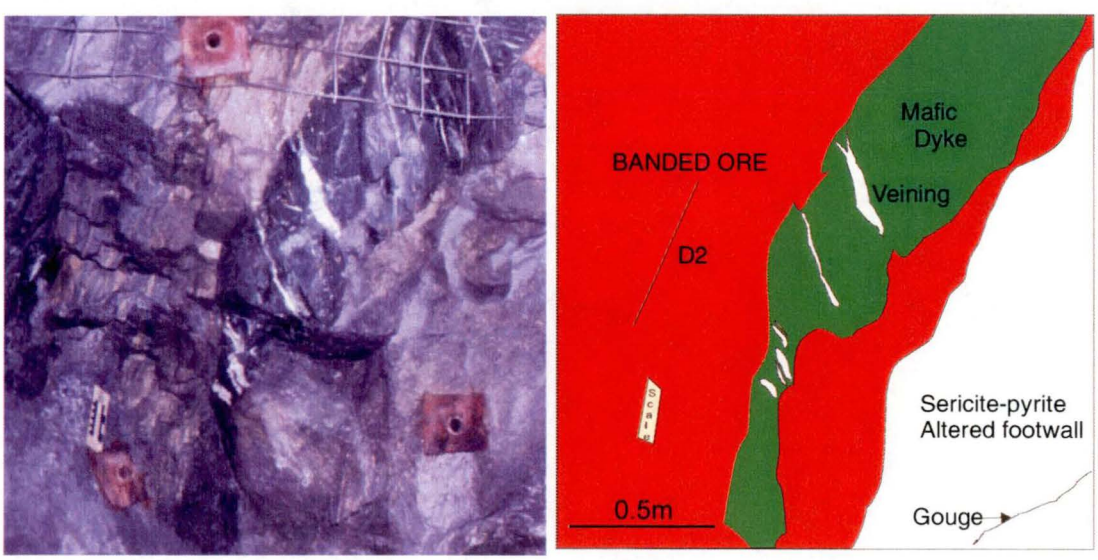

Figure 73. Photo and accompanying sketch show banding on east wall, field of view 1.5m.

Congugate faults - D3A

Two sets of faults thought to form a conjugate set are seen through out the mine area and show a spatial association with quartz-carbonate-(+chalcopyrite, galena, tennantite, bornite) veining. This set of structures fit with D3A structures of Berry (1995, 1996, 1998) thus the D3A terminology is continued here. They cut D2 strong foliation zones and the discrete faults seen in M159DD2 (Fig. 74). Fault surfaces show an E-W lineation defined by the elongation of pyrite grains (although the grains are broadly aligned in an EW plane their orientations are quite variable). Where they intersect sericite altered host rock a weak foliation is developed. In sericite altered host rocks they form 1-2 metre zones of intense foliation and gouge showing dextral movement . The fault may be marked by quartz-chalcopyrite-tennantite veining indicating fluid movement and remobilisation of some sulfides occured during this deformation event .

The first set strikes 090-095° (045-050°) and dips 70-80°N (Fig. 74). Examples of this set are shown in Figures 75 and 76. In Figure 75 the congugate fault cuts of D2 strong foliation zone underlying the Gopher lens, the fault occurs as a zone of intense foliation that bounds semimassive sulfides to the east. Figure 76 shows a fault cutting off ore at the northern margin of the Battle lens, this fault shows quartz-carbonate-tennantite-chalcopyrite veining along the hangingwall side of the fault against massive sphalerite-pyrite-chalcopyrite (Plate 33B), on the footwall side of the fault pyrite crystals defined an east-west lineation along the fault plane with in a narrow zone of foliation (10cm) in sericite-pyrite altered host rock.

The second set strike 175° to 185° (130-140°) and dip 30-40°E (Fig. 74). Figure 73 shows this structure cutting off D2 strong foliation zones and bounding ore at the base of the Gopher lens. In cherty host rocks, above the ore, these faults are less well developed but cause offset of chert layers in the form of drag folds (Fig. 77 & 78)

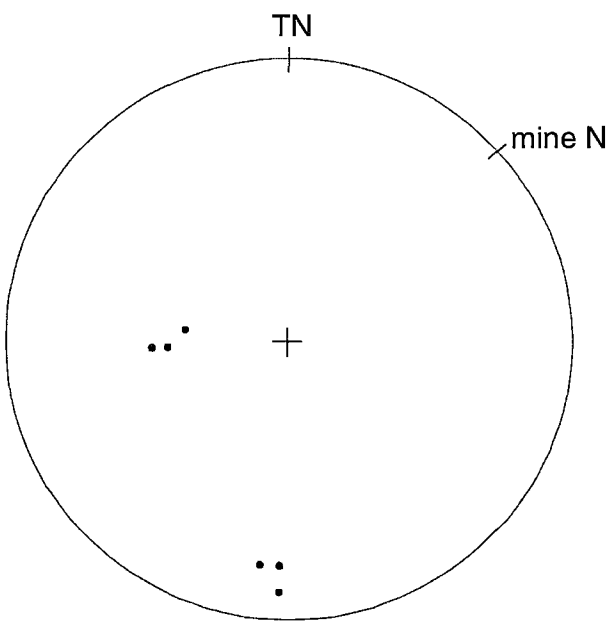

Figure 74. Lower hemisphere equal area projection of structural data from the Battle Zone - Conjugate set (D3A). Poles to faults plotted.

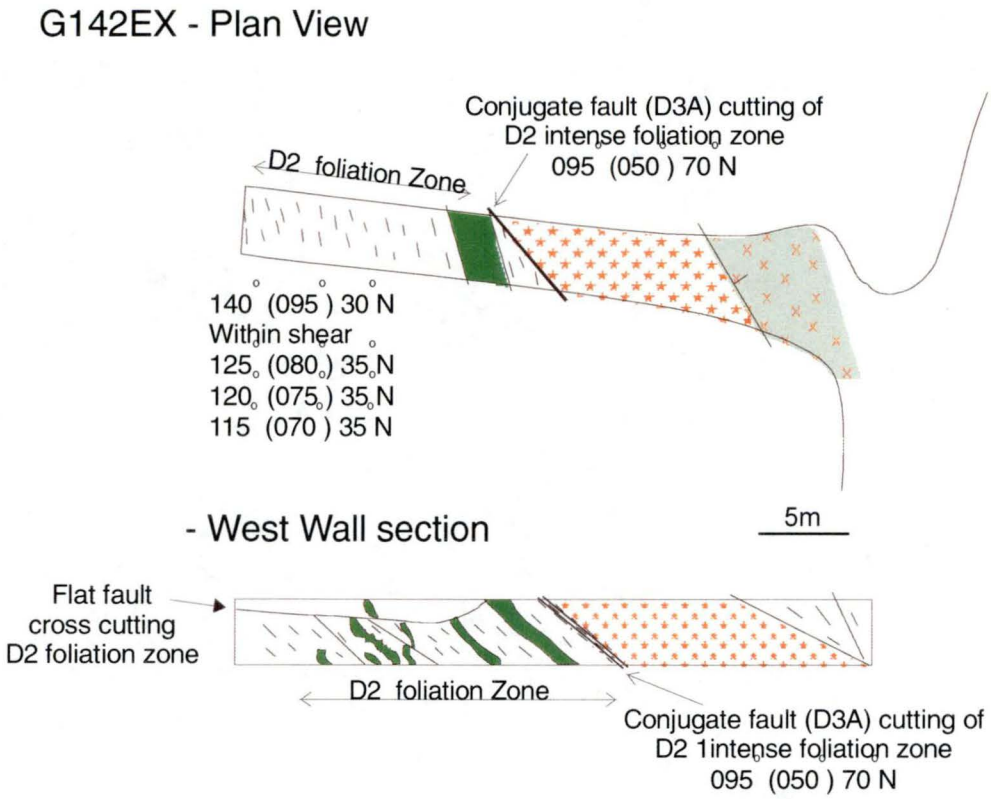

Figure 75. Conjugate fault (D3A) cutting of D2 intense foliation zone and bounding ore in the Gopher lens. A flat lying thrust fault also cross cuts the D2 intense foliation zone. G142EX see fig. 6.3 C for position.

In thin section the fabric in these faults occurs as discrete spaced foliation zones (identified here as D3A) defined by elongation of sericite and/or the elongation of sphalerite, chalcopyrite, galena, tennantite and pyrite, Plate 33C-F & Plate 34 A - C). In most cases they can be seen crenulating the D2 foliation and showing a strong reverse sense of movement (Plate 34 B & D). Where intense this deformation creates lenticular shaped sericite lenses within massive and semi-massive sulfides (Plate 34D). In the Battle lens (M167 drift 2) the D3A foliation can also be seen disrupting ore banding, creating the impression of disharmonic folding (Plate 34 E & F). The D3A structures are distinguished from the D2 foliation by their spaced nature (D2 pervasive foliation) and by the fact that they are often seen crenulating the D2 foliation.

M172 C1 - Shear Tail undercut

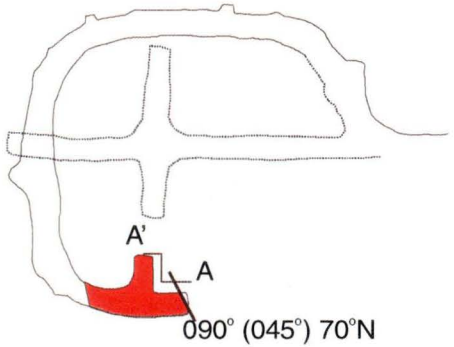

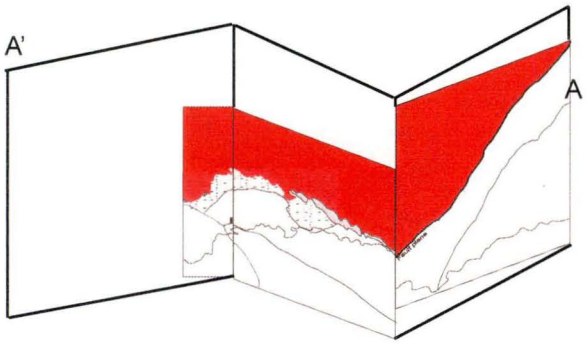

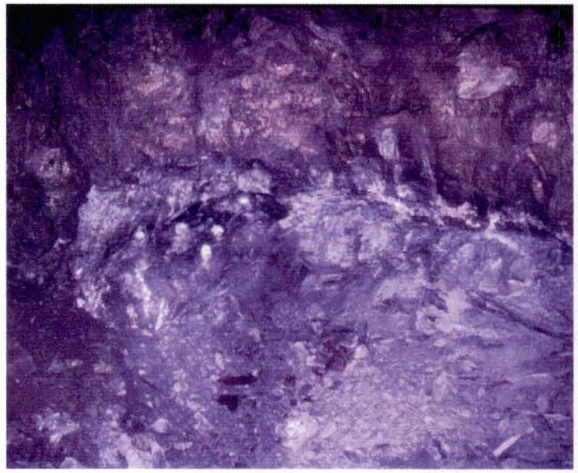

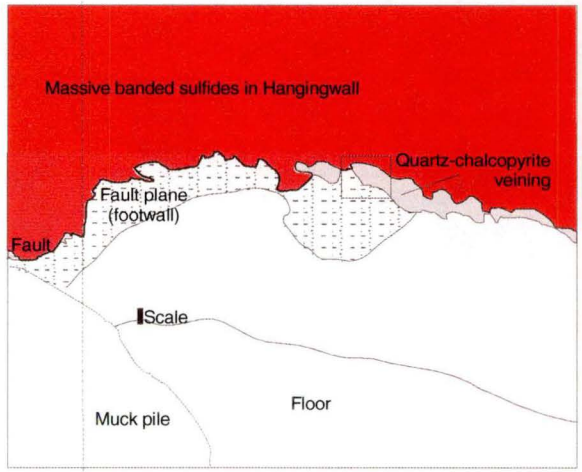

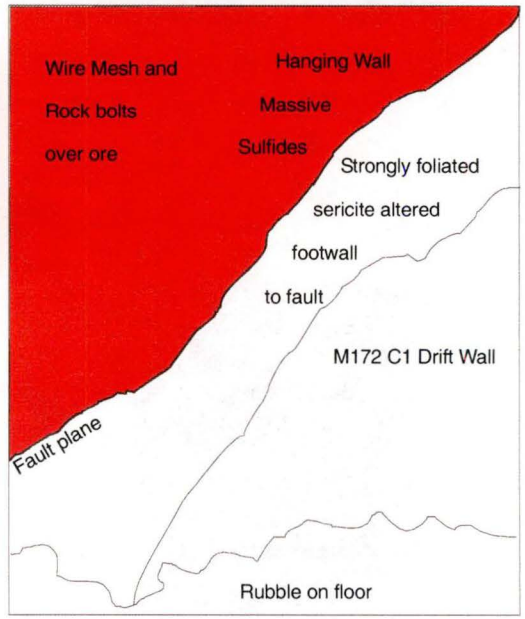

Figure 76 Conjugate fault bounding ore in Battle lens, 090 (045) 70°N. Fault plane (not seen here) shows broad E-W lineation defined by the elongation of pyrite crystals, however this lineation is not as defined as that seen in D2 foliation zones. Strongly foliated sericite occurs on the footwall side of the fault, while the hanging wall side of the fault is marked by quartz-chalcopyrite veining (square shows the position of close up (Plate 7.6 B). Sketches show relative position of two photographs underground.

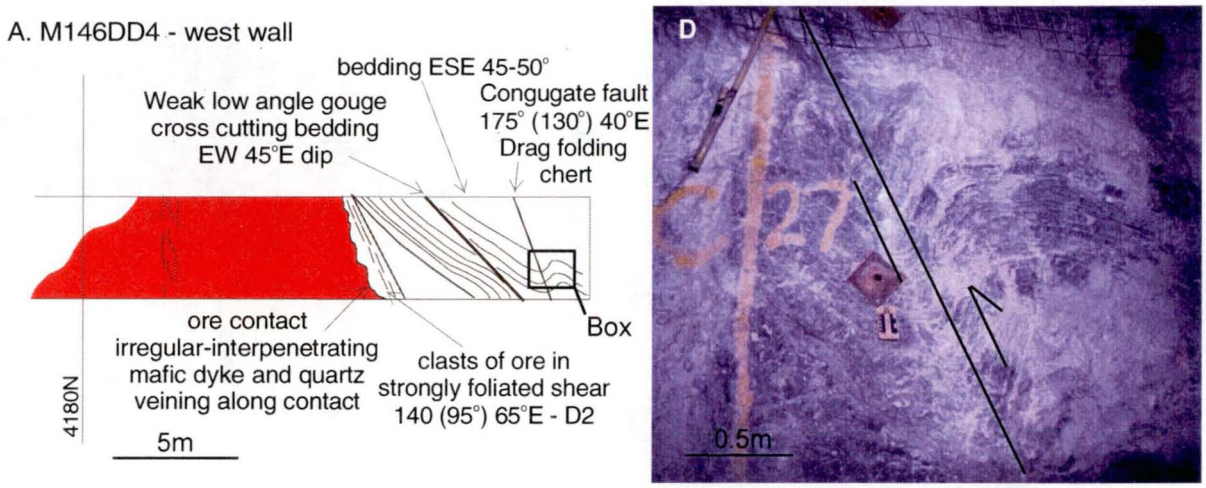

Figure 77. Battle lens drill drift M146 west wall section showing a conjugate fault drag folding chert layers to the north, to the south D2 intense foliation zone forms the boundary between ore ond chert. Box shows position of photo B. B. Conjugate fault 175° (130°) 40°E forming a drag fold in chert above the Battle lens, M146DD4. See C this plate for wall map.

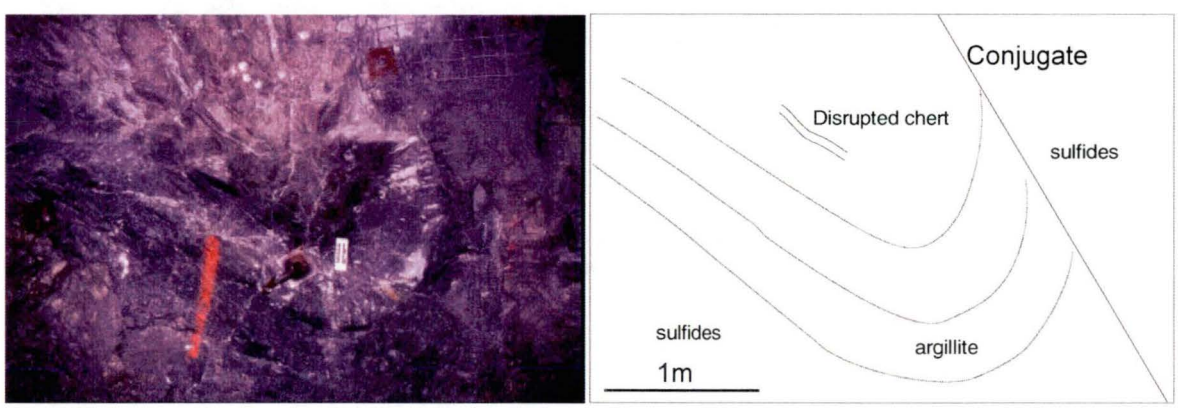

Figure 78. Conjugate fault (unmeasured) causing folding of argillite layers at top of Gopher lens (G158DD) see Figure 8.8 for position of photo. Photo courtesy Dr. B. Gemmell.

Plate 33 Sulfide microtextures due to D3A

A Fault striation visible on hangingwall side of a conjugate fault, striations indicate dextral movement of ore, footwall side of the fault consists of sericite altered H-W rhyolite with a weak foliation due to this fault event. H169 Drift 2 Panel 10 Upper Zone lens.

B Quartz-chalcopyrite vein along fault contact between ore and footwall alteration. Fault 090° (045°) 70°N conjugate fault. M172 C1 Drift 2 Battle lens.

C D2 foliation defined by sericite and elongation of pyrite crystals, cross cut by D3A. D3A foliation deforms D2 and has remobilised chalcopyrite along it. L14-733 325.0-325.05m

D D2 foliation truncated by D3A, sulfides (sphalerite, chlacopyrite, galena and tennantite) recrystallised into masses elongate parallel to D3A while muscovite is deformed into swirls or clots by the D3A foliation.H167 P8 (1)

E Drill core sample (AQ) showing quartz-chalcopyrite-calcite vein associated with conjugate faulting (represented by D3A foliation). BG18-778 128.1-128.3m

F Photomicrograph of square shown in G. Photomicrograph shows S2 defined by the elongation of chalcopyrite inclusions in sphalerite. S3A crenulates S2, and is partially defined by quartz-chalcopyrite-carbonate vein. Quartz veinlets within the massive sulfide are parallel and perpendicular to D3A. BG18-778 128.1-128.3m

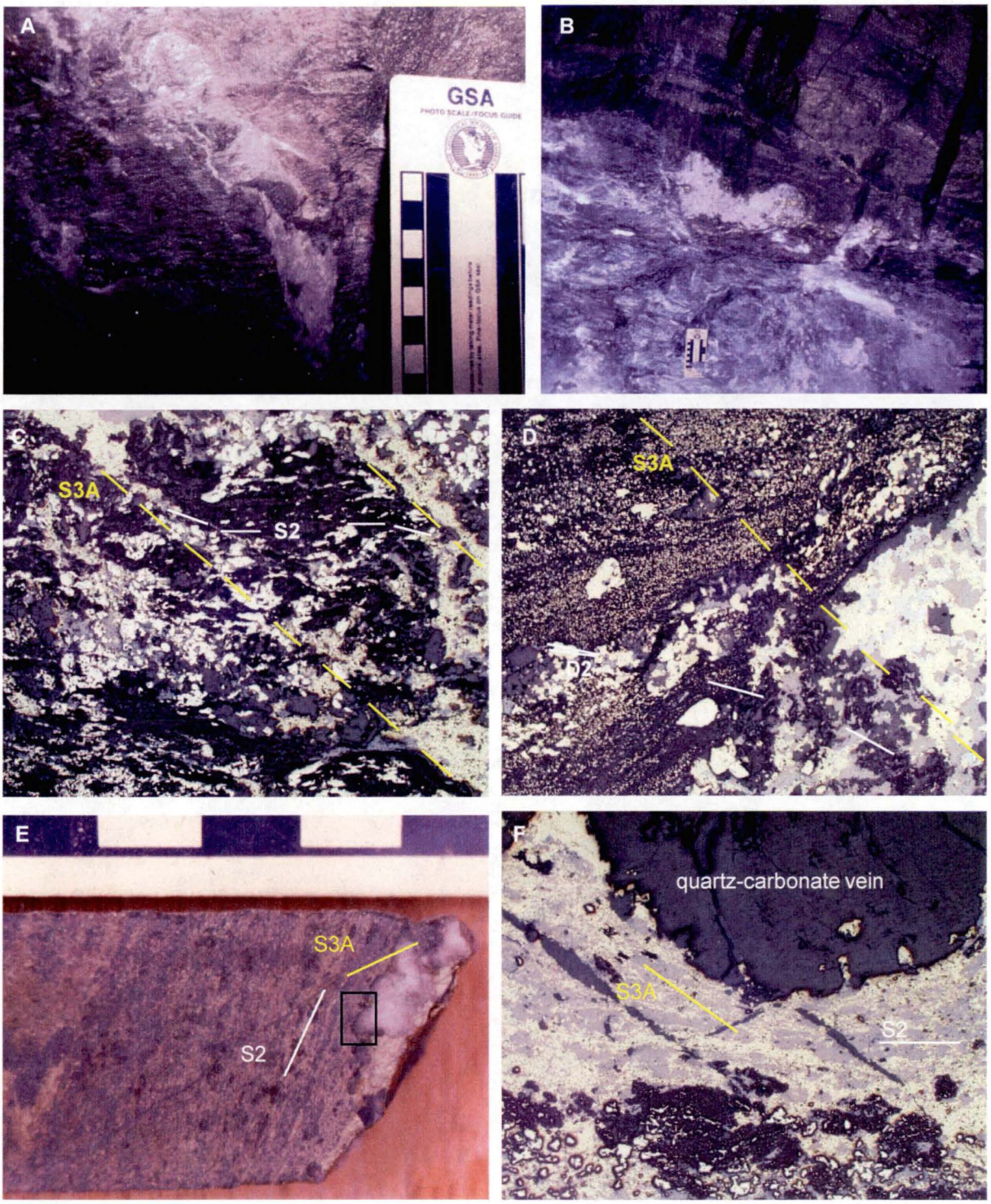
A
GSA
B
C
S3A
S2
D
S3A
S2
E
S3A
S2
F
quartz-carbonate vein
S3A
S2

Plate 34 contined. Sulfide microtextures due to D3A

A Pyrite, chalcopyrite and muscovite with strong D2 foliation. Pyrite grains are pulled apart perpendicular to S2 and chalcopyrite fills the pull apart fractures. Minor D3A foliation in bottom left hand corner BG18-1055 65.9m

B In contrast to A, this sample affected by both D2 and D3A foliation. Elongate pyrite-chalcopyrite lenses formed by D2 foliation are folded by D3A deformation. BG18-1003 94.6m

C Massive sulfide ore showing strong deformation, sulfides are very fine grains, muscovite lenses within sulfides deformed to lenticular shapes and overprinted by quartz-chalcopyrite-calcite veining. L14-732 302.2m

D Photomicrograph of sample adjacent to C. shows muscovite lenses formed by the combination of two deformation events D2 and D3A creating lenticular shapes. Note very fine grained nature of pyrite in this sample. L14-732 303.3m

E & F Banded ore sample from Battle lens. Banding is sub-horizontal however deformation by D3A creates the impression of disharmonic folding perpendicular to D3B (E). When cut parallel to D3B (F) ore shows no folding. M16167 P2 sample No.1

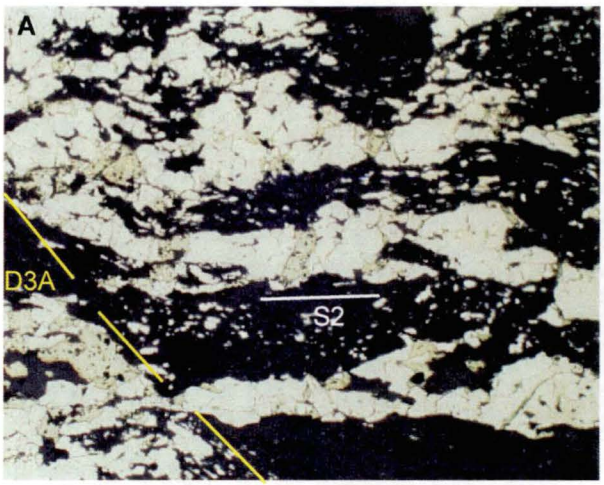

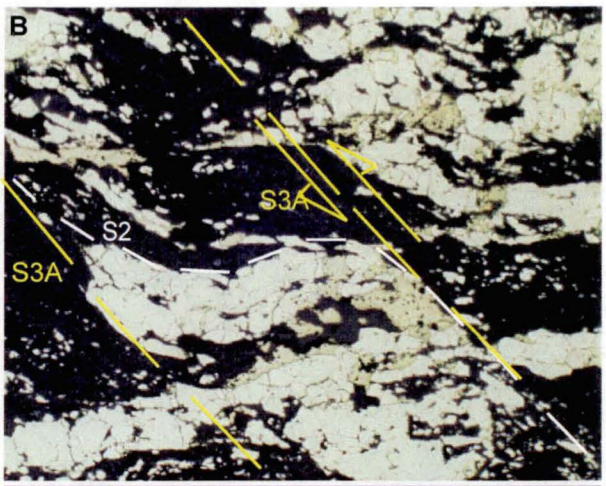

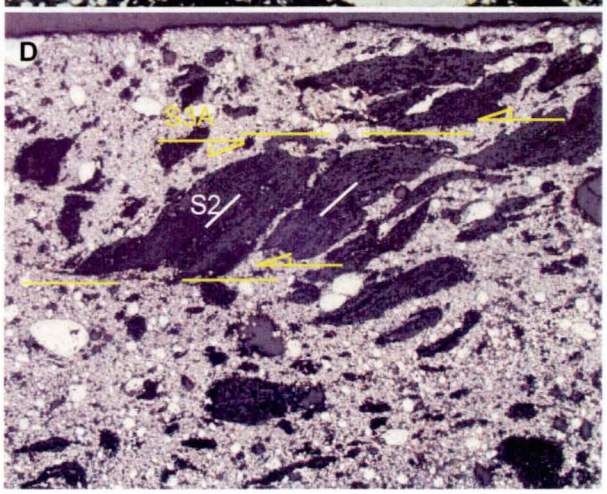

east-west face

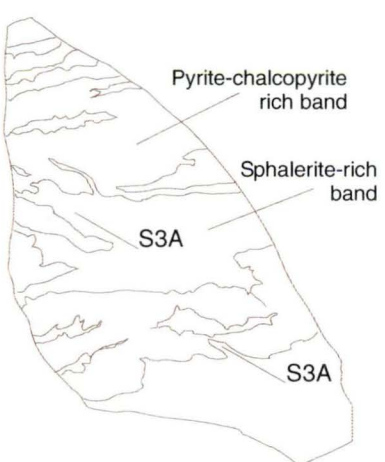

2cm

north-south face

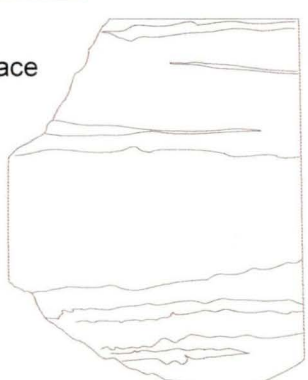

Ductile shear zones

Ductile shear zones are seen in all areas, cross cutting intensely foliated zones, forming 120-130° (075-085°) 45°N dipping structures (Fig. 79). These structures are defined by weak gouge coated margins 10-40cm wide with internal dragged cleavage showing top to south orientation (thrust style faults, Fig. 80A & B). They were commonly seen overprinting zones of D2 intense foliation, but not restricted to these zones. They also show a spatial association with quartz-carbonate veins.

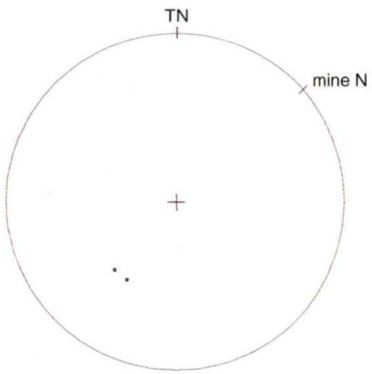

Figure 79. Lower hemisphere equal area projection of structural data from the Battle Zone, Ductile Shear. Poles to shearing plotted

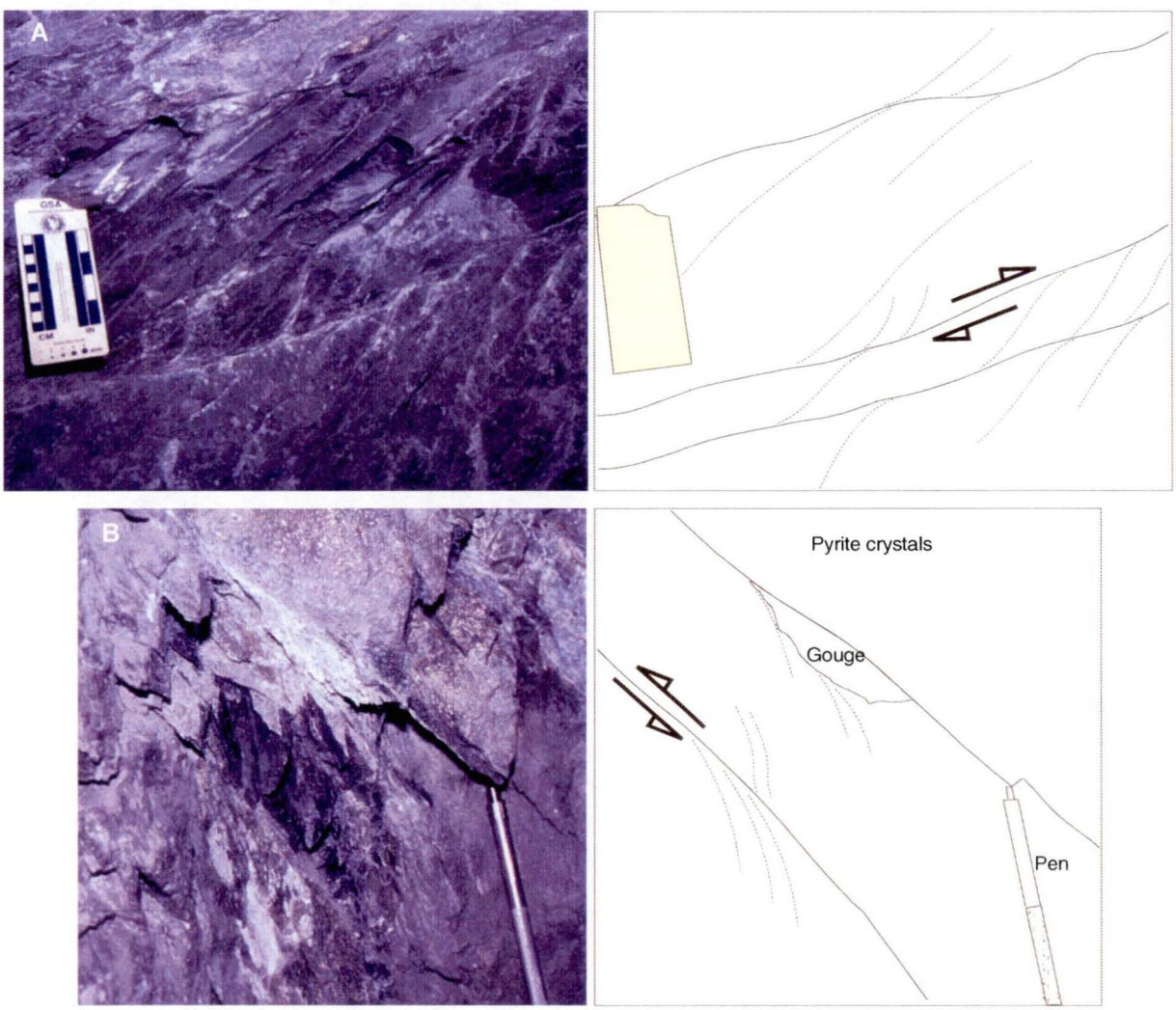

Figure 80. Ductile Shear Zone, showing reverse movement, over printing D2 foliation. A G154EX (Gopher footwall) looking east. B. H148EX Upper Zone (looking west)

South dipping thrusts faults

Thrust faults in the Battle Zone have a major effect on ore placement, transporting ore toward the north, and causing repetitions of ore blocks. Several types of thrust faults have been identified: flat lying thrust faults, high angle thrust faults and 080° striking moderately dipping thrust faults, Fig. 81. All these faults have a brittle ductile nature - gouge surrounded by a narrow zones of cleavage with accompanying quartz-carbonate veining. These faults cause significant disruption to the position of ore.

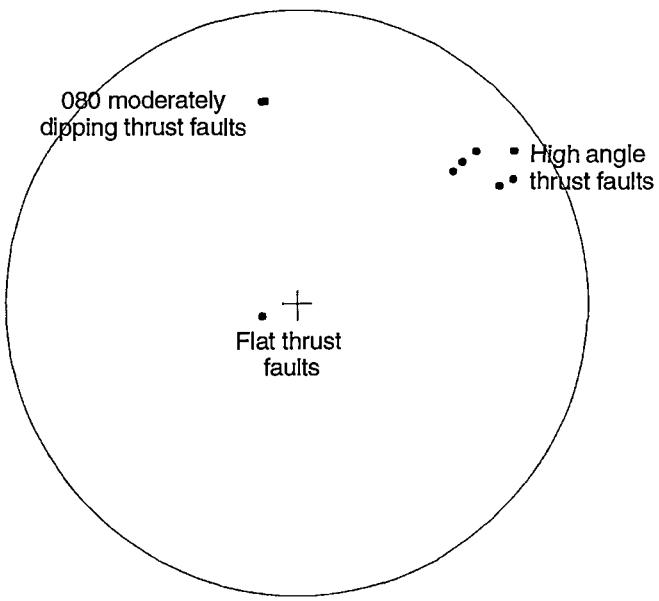

Figure 81. Lower Hemisphere equal area projection of structural data from the Battle Zone, South dipping thrusts.

The most common thrust faults seen in the Upper Zone are the flat lying thrust faults or flat faults. These are characterised by flat lying, weak to moderately gougy surfaces, minor foliation is developed when the host rocks are sericite altered. The flat faults anastomose from north to south dips, but generally dip less than 40°. The majority of these surface were not measured due to their anastomosing nature. However examples are shown in Figure 82 - 87. These structures commonly bound ore, particularly in the Upper Zones. The flat lying thrust faults are cut of by strong gougy structures (D5) Figure 82. In H169 Drift 2 Panel 8 mafic dykes in the footwall of the flat fault are bent parallel to the fault (Fig. 83). Flat faults also reactivate conjugate faults, forming gouge on the reactivated surfaces (Fig. 84). Flat faults curve into high angle reverse faults (see below).

High angle, reverse faults are south dipping structures defined by a strong foliation and anastomosing gougy faults. These structures correlate with the D3B structures of Berry (1996, & 1998), thus this terminology is continued here. The structures show an orientation of 140-150° (095-105°) 60-80°SW. These high angle structures are quite common in the Upper Zone (Fig. 85), and are also seen in the Battle lens.

Two structures both with the orientation 080° (035°) 60°SE (Plate 86 & 87) were observed during mapping in Battle Zone. Both structures show have reverse movement (thrusting). The first structure was seen in G158DD at the eastern end of the drift (Fig. 86), and shows quartz-filled tension veining associ-

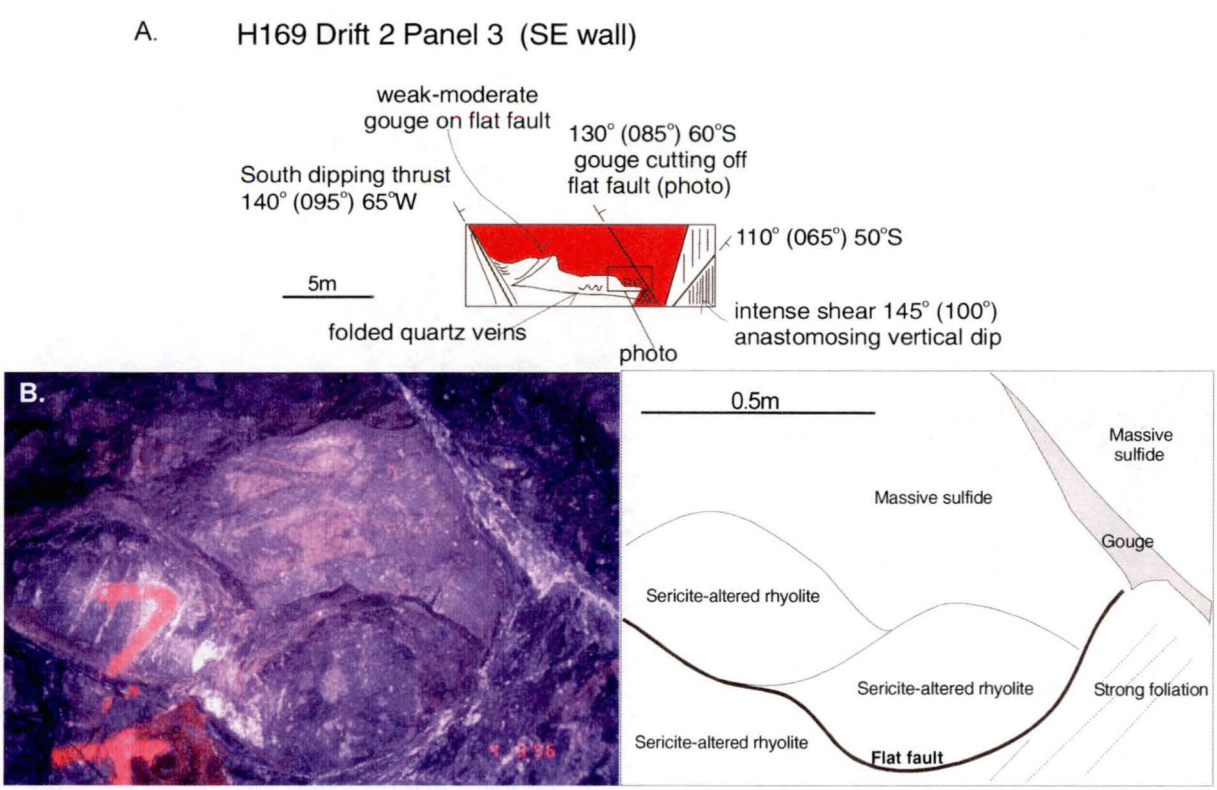

Figure 82 A.Wall map showing flat fault, cut of by a gougy structure (D5), D5 structure is defined by a narrow (10-20cm) zone of intense foliation and anastomosing gouge faults. The flat fault is also cut off at its western end by a gougy structure defined by upto 20cm of gouge with no foliation. Below flat fault sericite altered rhyolite is moderately to strongly foliated. The hangingwall to the flat fault is massive sphalerite-pyrite-bornite ore. H169 Drift 2 Panel 3.B. Photograph showing close up of flat fault and associated faulting, and termination by D5 gougy structure. Position of photo shown in A. H169 Drift 2 Panel 3.

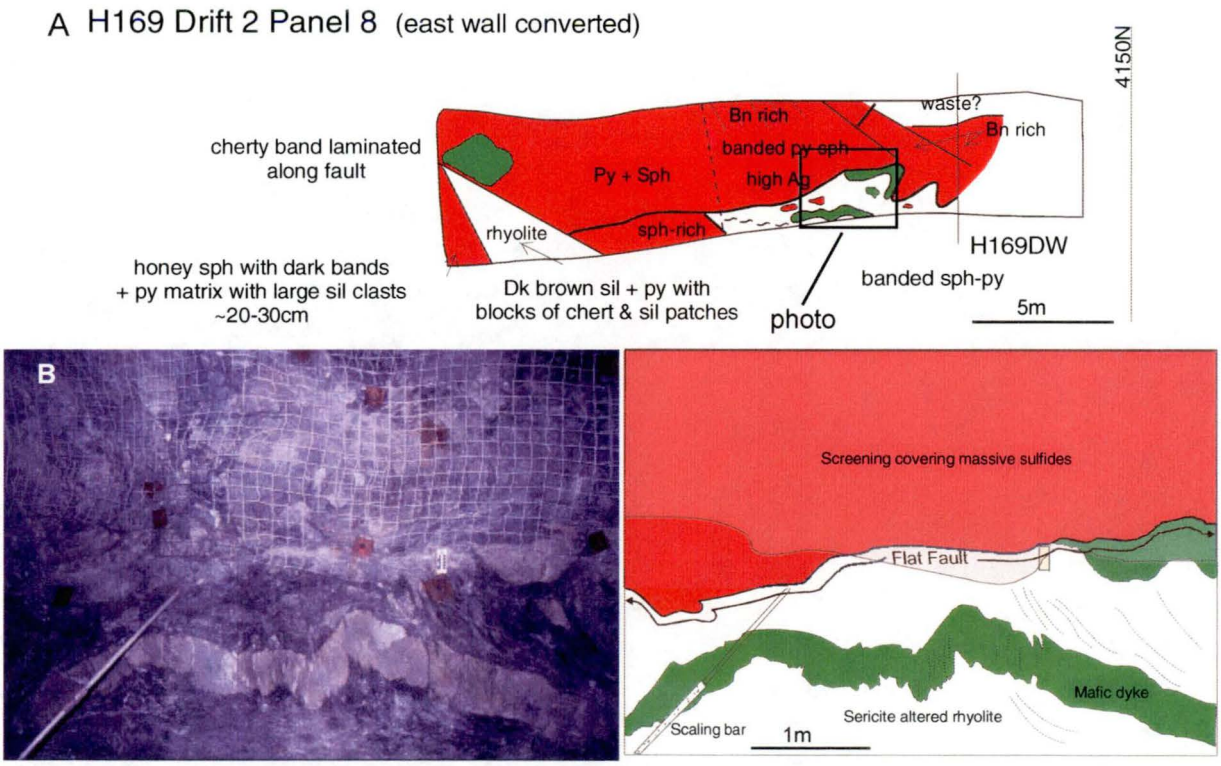

Figure 83 A. Upper Zone Drift showing strongly foliated sericite-altered rhyolite and mafic dyke, below a flat fault, mafic dyke along the flat fault bent / folded into the fault, massive sulfide ore above the fault. H169 Drift 2 Panel 3. B. Photograph showing close up view of fault and folded mafic dyke. H169 Drift 2 Panel 3.sph = sphalerite, py = pyrite, Bn = bornite, Ag = silver

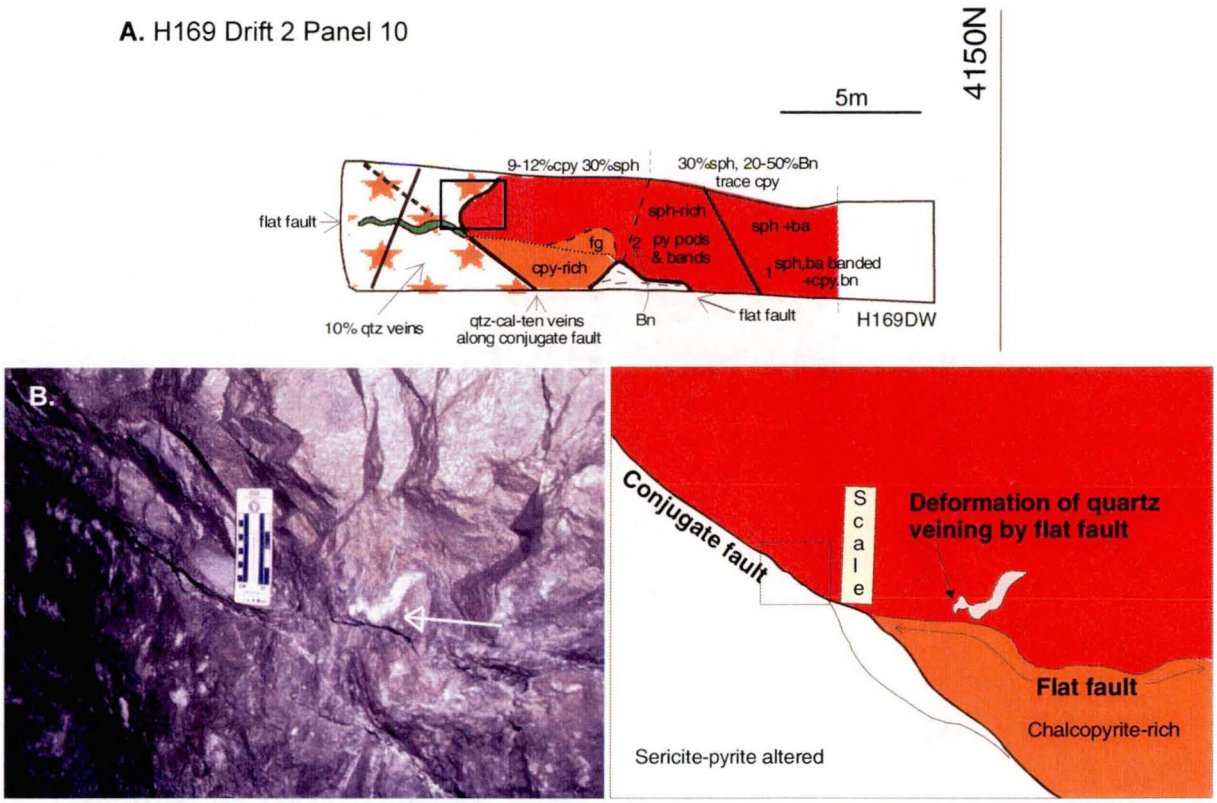

Figure 84 Wall map of H169 Drift 2 Panel 10 - Upper Zone lens (west wall) showing a flat fault running into and reactivating a conjugate (D3A) structure, note flat fault causing deformation of quartz veining associated with D3A structure. B. Photo of jucnction of two faults. H169 Drift 2 Panel 10. sph = sphalerite, cpy = chalcopyrite, zbn = bornite, ba = barite, py = pyrite, ten = tennantite, cal = calcite.

A H148EX - (west wall)

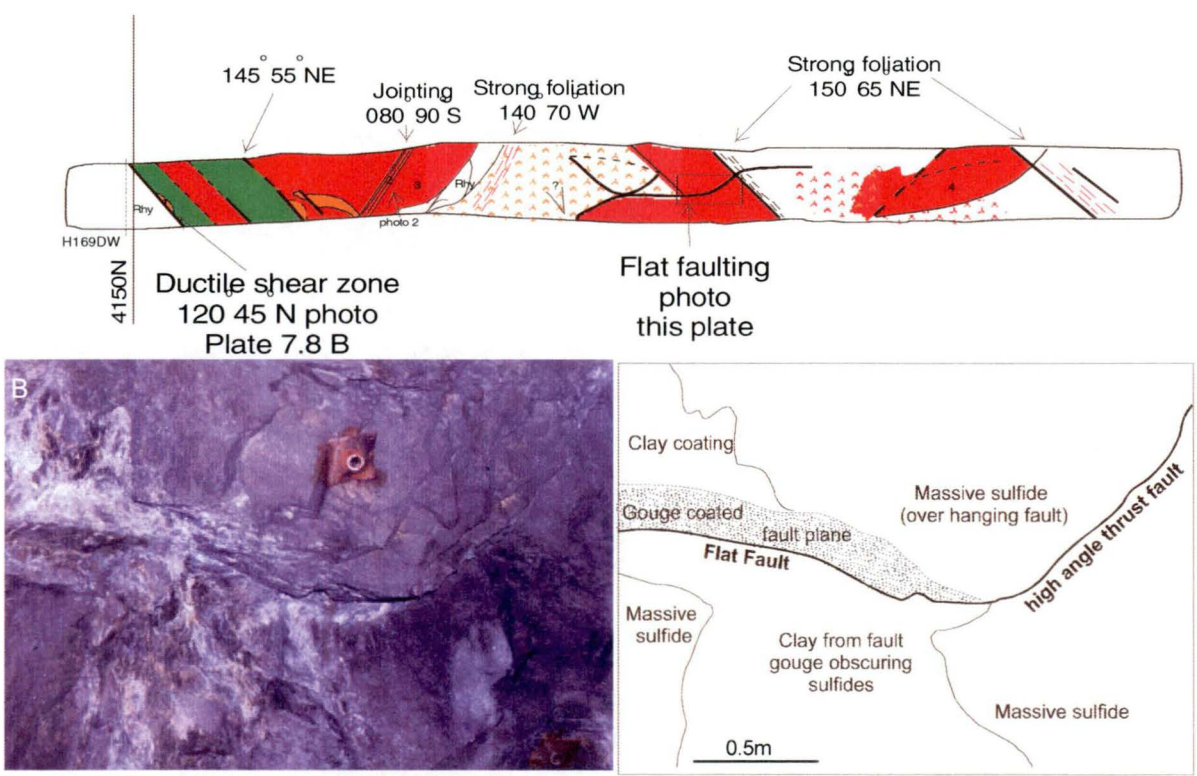

Figure 85. H148EX Upper Zone Drift, photos from centre of the drift showing a flat lying thrust fault transferring into a high angle south dipping thrust fault, gouge can be seen on the flat section of the fault, footwall and hanging wall to the fault both massive sulfide mineralsation.

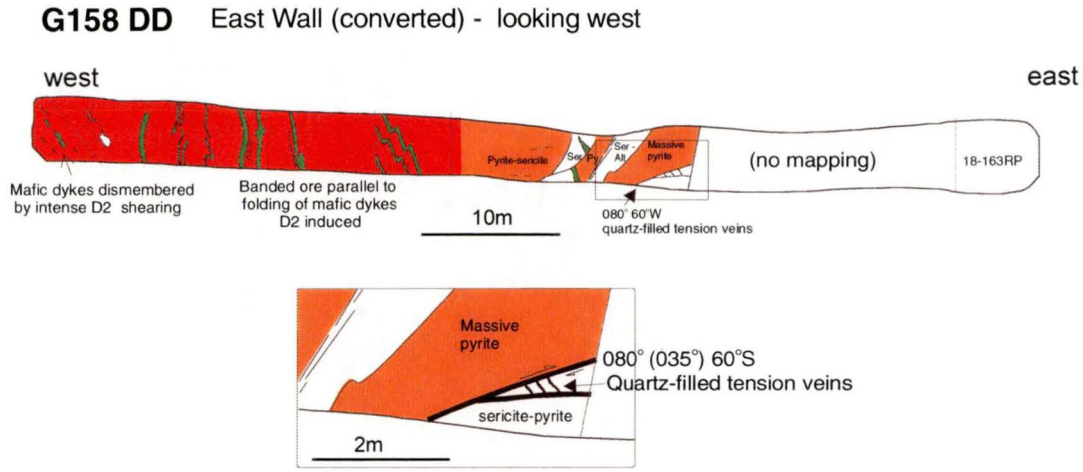

Figure 86. Eastern wall of G158DD converted to west wall orientation), at the eastern end of the drift, moderately dipping thrust fault has quartz-filled tension veins and shows reverse movement (enlarged).

A. T-174 Panel 2 - East wall (converted - looking west)

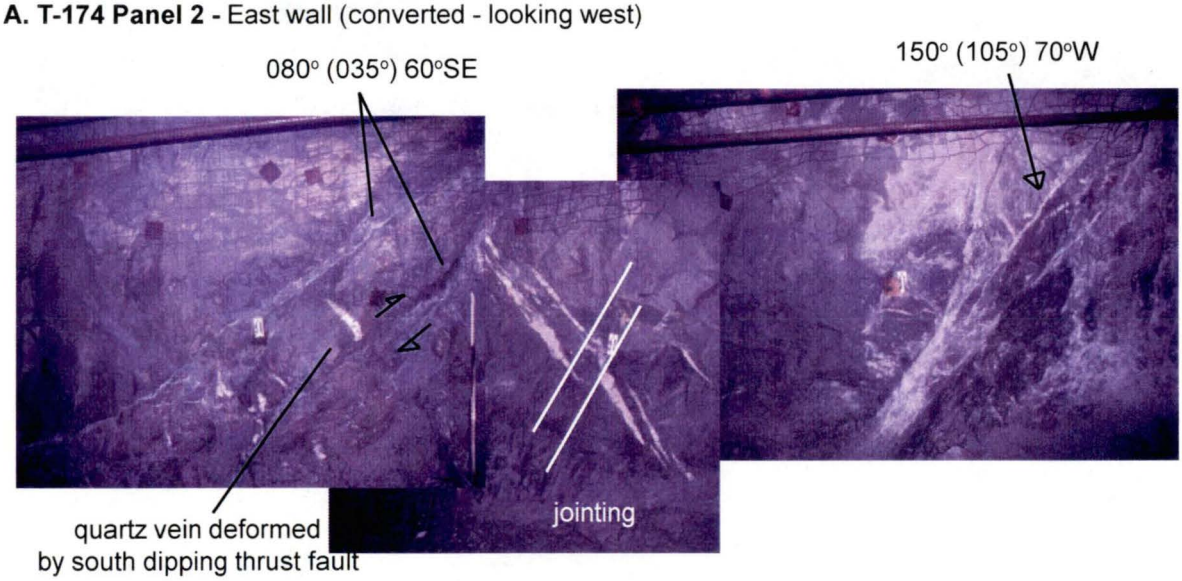

B.

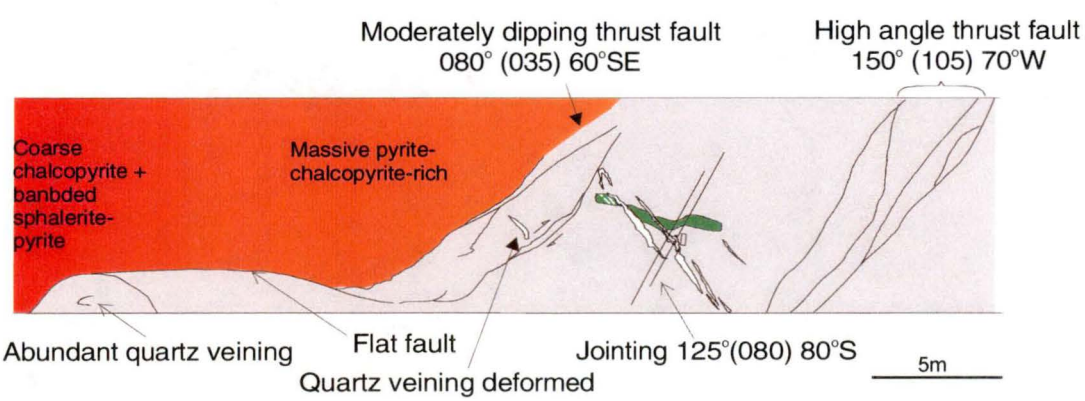

Figure 87. Photographs (A) and a sketch (B) show the interaction of flat faults with 080 moderately dipping thrust fault. Jointing associated with thrust fault off setting D3A conjugate structure shown by quartz-carbonate veining. High angle,south dipping strongly gougy structure (possibly D5) also shown. T174 Panel 2.

ated with the faulting. It's relationship to the D2 strong foliation zone and the gougy fault that cuts it off on the opposite wall (Fig. 71) is unknown. The second of these structures was seen in T174 panel 2 (Fig. 87), this structure post dates quartz veining and transfers movement from a flat dipping thrust fault.

Discrete faults

Also seen in the Battle Zone are a series of 100° to 110° (060-070°) steep dipping (65°N) faults (Fig. 88). The faults are characterised by their discrete, sharp natures and weak gouge coating and shuffle ore blocks in a mine east-west orientation (Fig. 89). Movement on these structures in not thought to be more than a few meters (possibly 10's meters), but its mine east-west orientation causes significant variations in ore position due to the dip of the Battle and Gopher lenses (see chapter 6). These faults truncate D2 intense foliation zones and are cut by conjugate faults (Fig. 88) .

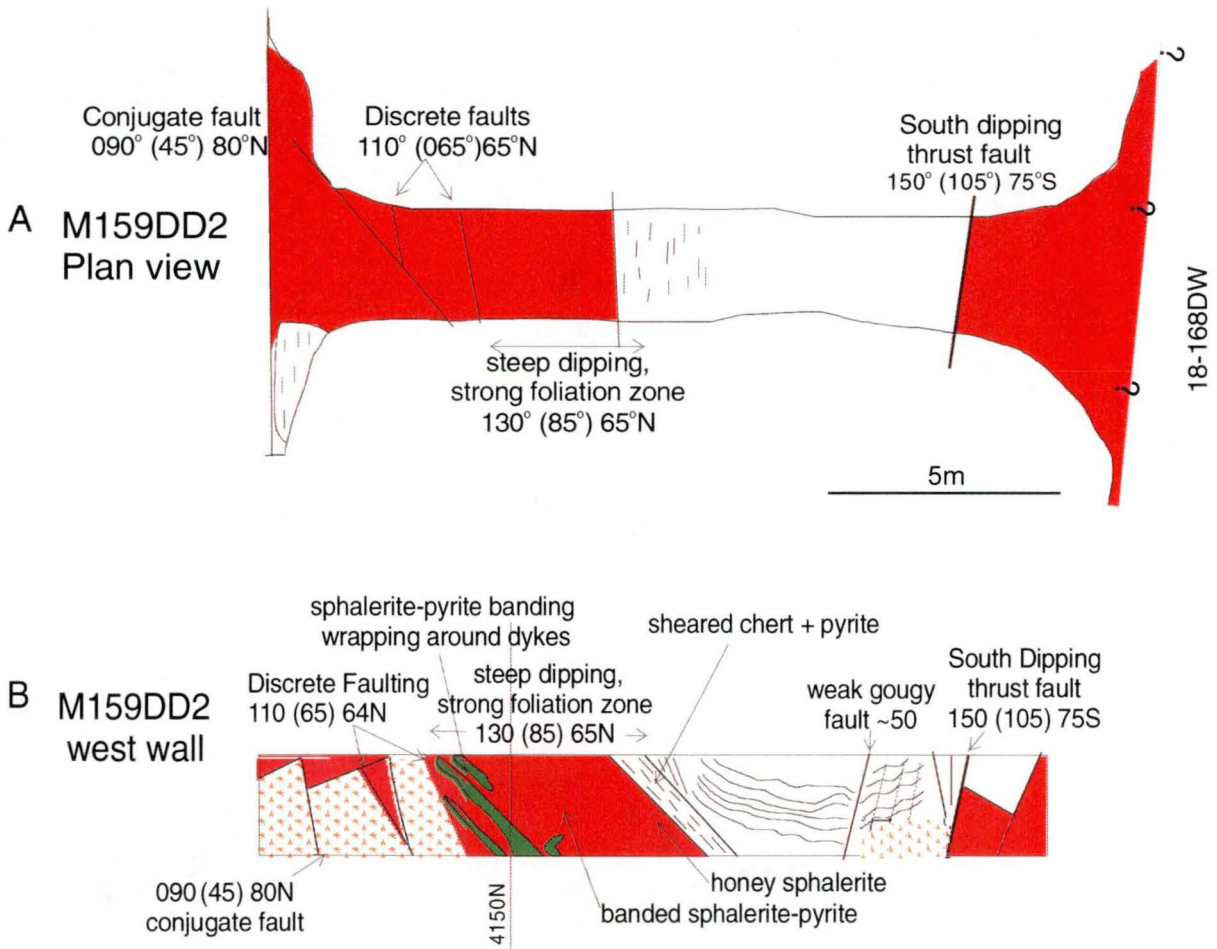

Figure 88. M159DD2 Showing discrete faults truncating a D2 intensely foliated zones which bounds the ore to the north. Discrete faults cut by a congujate fault to the south. Battle lens. A. Plan view M159DD2, B West wall section M159DD2. Also showing and a South dipping thrust fault at the northern end of the drift.

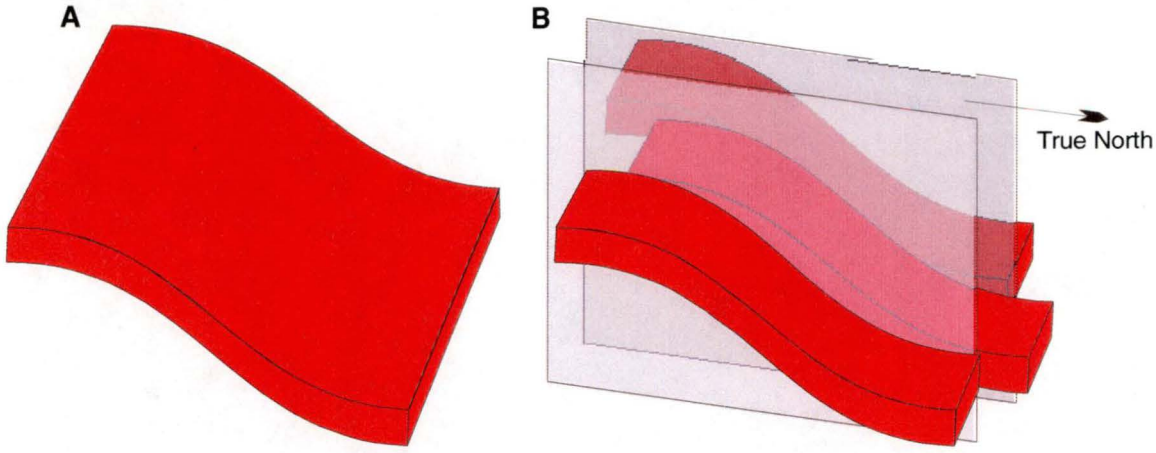

Figure 89. Schematic representation of the effect discrete faults have on ore, using sheet like morphology of the Battle lens as and example (dip emphasised). A pre-discrete faulting ore body, B. with discrete faults shuffling ore blocks in an north-south orientation.

D5 - Gouge & breccia zones

D5 structures occur as broad zones (4-5m wide) of anastomosing gougy planes and fault breccia to narrow zones of strong gouge (1-10cm wide) with strong foliation, they have minor quartz veining associated with faulting and brecciation. Their orientation range from 120°-155° (075-110°) 30-75°N for the broad anastomosing zones of gouge and breccia, to 110°-140° (065-096°) 35-40°E for the narrow zones of gouge and foliation (Fig. 90). The sense of movement on these structures is dominantly sinistral.

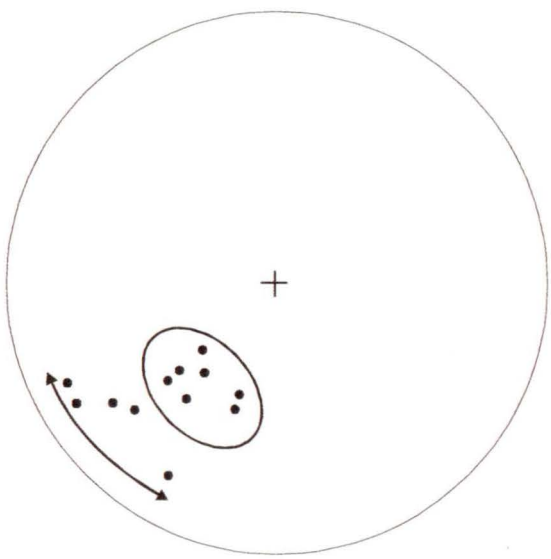

Figure 90. Lower hemisphere equal area projection of structural data from the Battle Zone showing D5 gouge and breccia zones (arrow), and discrete gouge zones (circled). Poles to planes plotted

D5 structures commonly overprint zones of D2 strong foliation. Examples in Figure 91 come from the northern margin of the Battle lens, D5 structures also seen underlying Gopher Zone and within the Gopher and Battle lenses. With in the lenses they form discrete gougy structures, which anastomose from south east to easterly orientations dipping moderately to the north. Brittle structures drag D2 cleavage into their orientation. They also reactivate D3B and to a lesser extent D3A structures or cross cut them. Where these structures cut massive sulfides and chert layers strong brecciation occurs (Fig. 92).

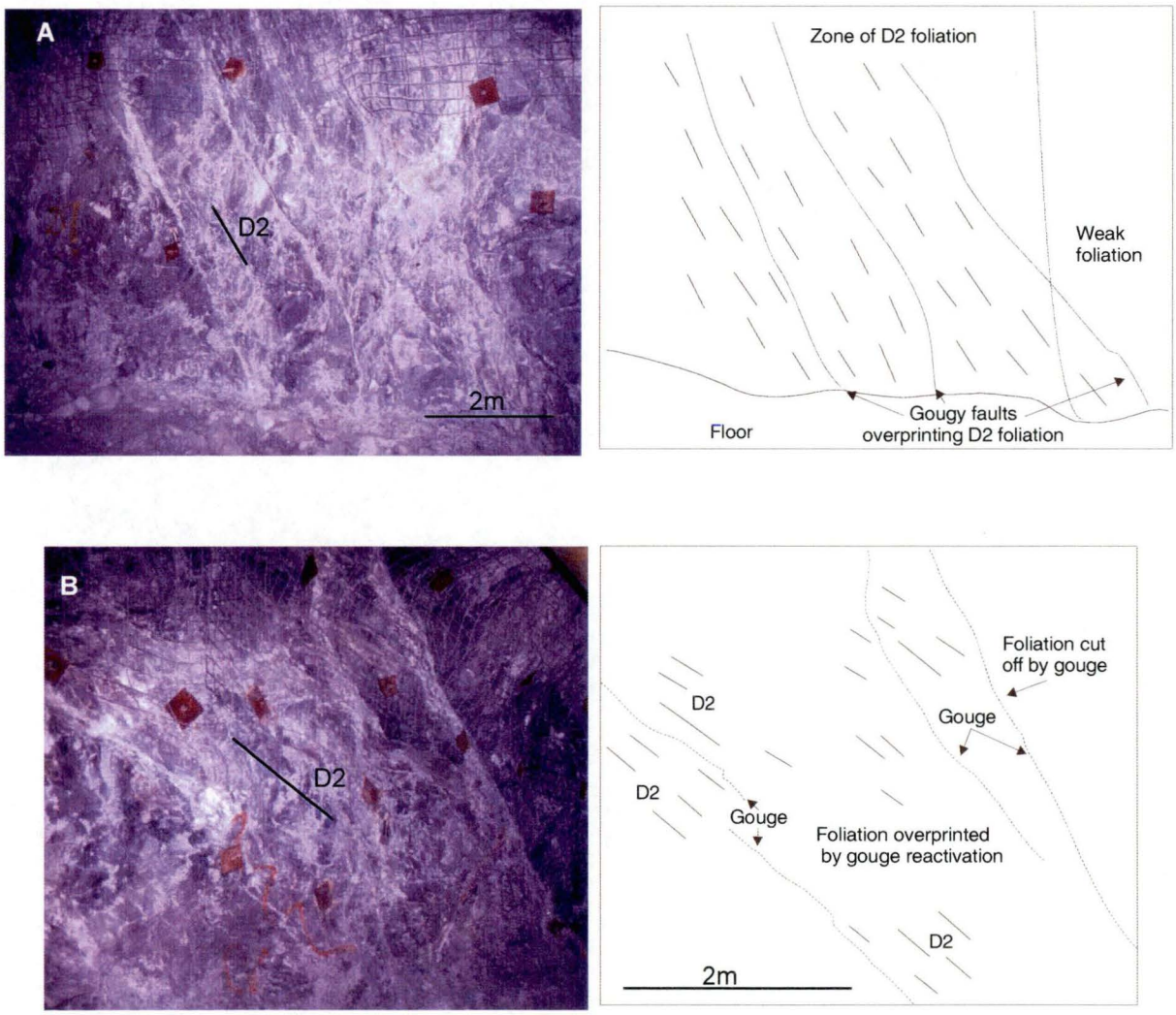

Figure 91. A. D5 Zone of abundant gougy planes, D2 foliation draged into D5 fault plane, zone 4m wide M172C1 (Shear Tail overcut). looking west. 120° (075°) 80°S.
B. D5 Zone of strong gougy and fault breccia on the northern edge of the Battle lens 140° (095°) 40°E. M161 P2 (Shear Tail). looking west Zone 2-4m wide.

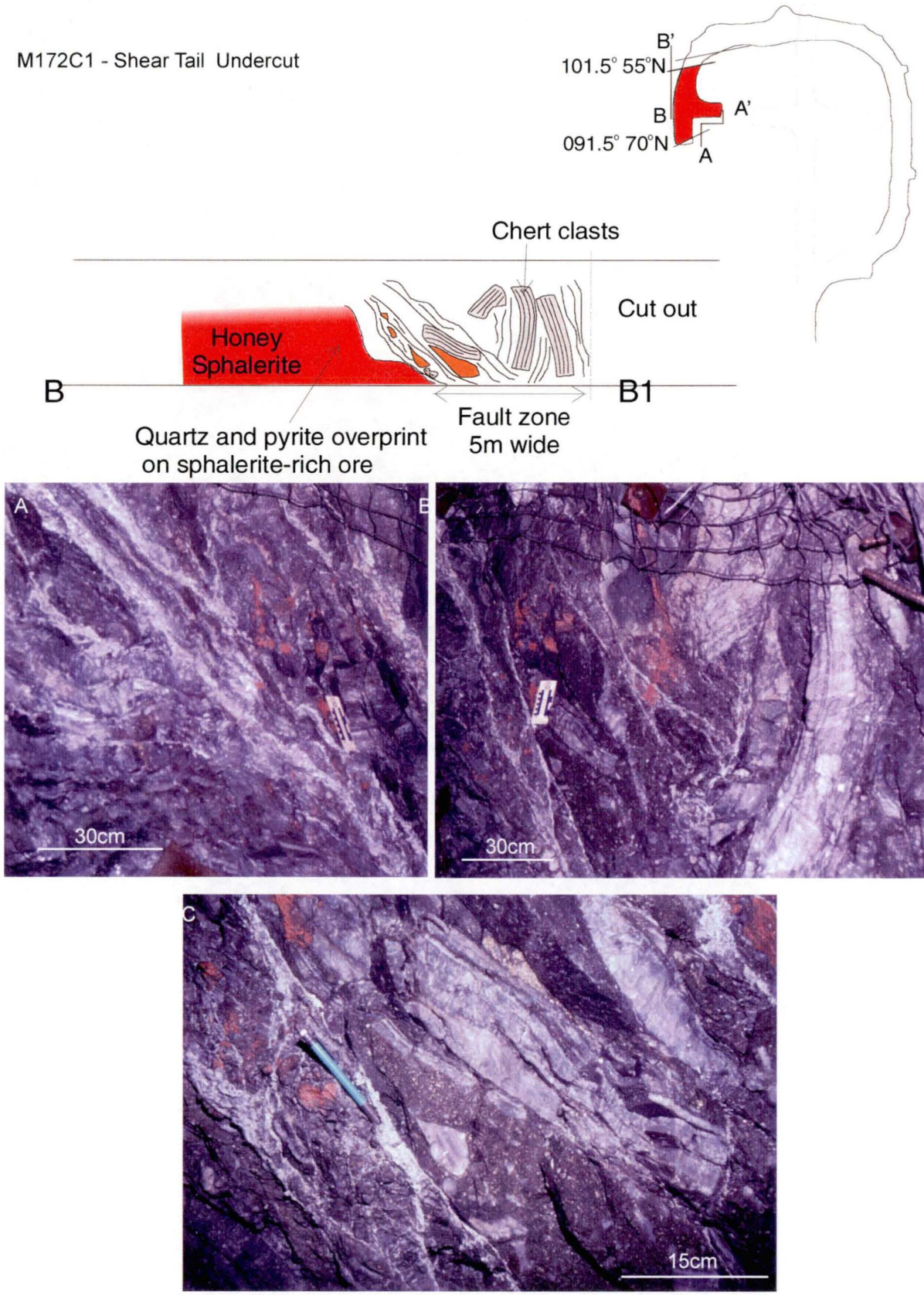

Figure 92. D5 Gouge and breccia zone. A. Strong anastomosing gougy fault planes. B. Chert and sulfide clasts in fault breccia, abundant gouge between the clasts. C. close up of area in B. showing sulfide-rich clast containing anglar chert clasts and pyrite-rich matrix from an earlier fault phase, forming clasts in D5 fault.

Unresolved gougy faults

A fair number of discrete gougy faults remain unresolved (Figure 93), most of these structures show gouge with little or no cleavage, some show down dip lineation. These faults may correlate with the fourth normal movement observed by Berry (2000) or may be D6 structures, crosscutting relations were not found to distinguish between these two events.

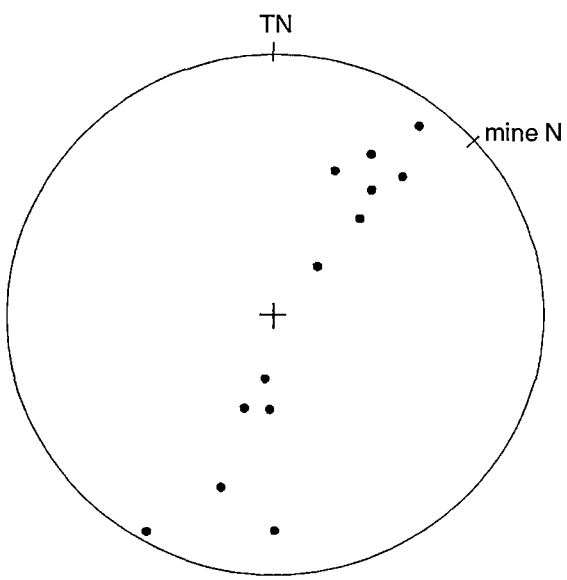

Figure 93. Lower hemisphere equal area projection of structural data from the Battle Zone showing unresolved gougy faults. Poles to planes plotted.

8.5 Discussion - Age of faulting and relation to other areas

The relative ages of faulting in the Battle Zone have been determined, where possible, via cross cutting relationships and are summarised in Figure 94. This section aims to compare the structures described in the Battle Zone with those seen by Berry (1995, 1996, 1998), Reid (1993) and other workers within the Myra Falls area, as well as the regional studies mentioned in section 8.2A to determine ages for the faulting.

The foliation recognised as the first structure in the Battle Zone fits well with the D2 of Berry (1998) and event 2 of Reid (1993). Juras (1987) observed that these structures were intruded by the Jurassic Island intrusions. Walker (1985) noted that all the Palaeozoic units of the Sicker Group were effected by D2 foliation. However, there is no evidence of this D2-foliation in the Buttle Lake limestone or the overlying Karmutsen Formation. Yole (1969), reported that the Buttle Lake limestone conformably overlies the Flower Ridge Formation in the Buttle Lake Uplift, however, the mapped distribution of the limestone around the Buttle Lake Uplift is also strong argument for an unconformity below the limestone in the Buttle Lake Uplift (Berry, 1998). Massey (1992) showed the Buttle Lake Group is unconformable on the Sicker Group volcanics in the Duncan area. Revised stratigraphy in Yorath et al. (1999) does little to alleviate this problem of conformability of the Buttle Lake Group on the Sicker Group. However the D2-foliation is interpreted as pre-Permian (Berry, 1998).

The D2 structures described here and in Berry (1995, 1996 and 1998) are anomalous. They lack any brittle features and have weak cleavage compared to the strain. Oriented thin sections of high strain zones on the Price hillside show stretching lineation with X/Z ratios between 2 and 5 (Berry, 1996). Berry (1995) interpreted these features as evidence limiting the timing of there structures to pre- to early syn-peak metamorphic in age. The lack of fault surfaces is interpreted as the result of annealing.

The conjugate faulting correlates well with the D3A structures of Berry (1998). Nixon et al. (1994) reported a Mid to Late Jurassic, east to northeast-directed compressional event, which caused regional tilting of Lower Jurassic and older strata in Northern Vancouver Island, Massey et al. (1992) also records a deformational event of this age resulting in regional scale warping of Vancouver Island. Alternatively these structures may be related to the Cretaceous event described by England and Calon (1991) and attributed to the accretion of Wrangellia on to the north American continent.

The ductile shear zones, are brittle-ductile in nature and have associated gouge and quartz-carbonate veining suggesting an association with the D3 events of Berry (1998). They may be thrust faulting associated with the Mid to Late Jurassic compressional event. Alternatively they may be correlated with the Late Cretaceous contractional event of Nixon et al. (1994) and England and Calon (1991).

The south dipping thrust faults (flat faults, high angle thrust faults and 080° moderately dipping thrust faults) are of an unknown age. They probably post date the conjugate faulting as they cause deformation of quartz-carbonate veining associated with the conjugate faults (Figure 84 & 87). Their relationship to the

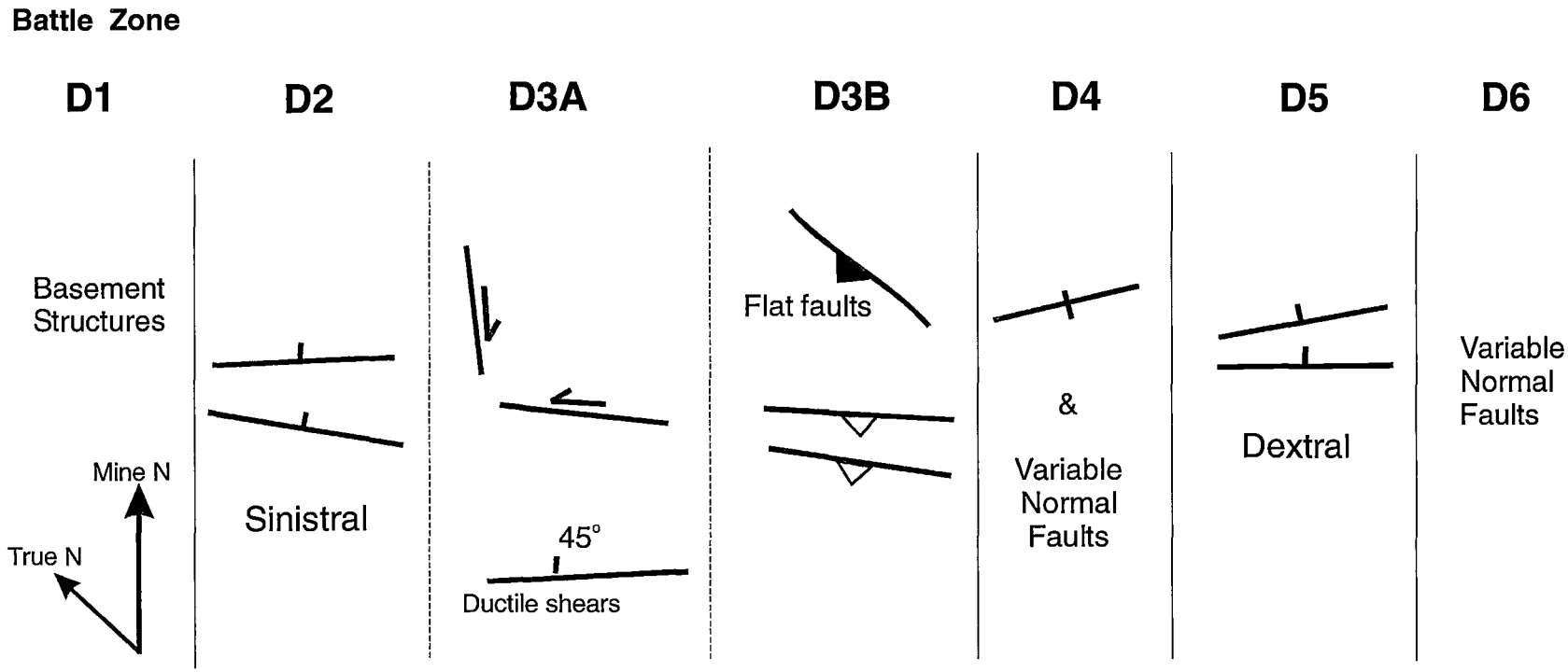

Figure 94. Summary of structural patterns in mine grid orientation for Battle Zone

Note : The orientations given above for D2 and D3 events are for the Battle Zone only, The anastomosing nature of the pre-Permian structures was also documented by Reid (1993), and causes structural measurements to vary up to 20 degrees from the NW (W) orientation given by Berry (1998)

ductile shears is unknown. They have a brittle ductile nature, moderate gouge and foliation, but it is uncertain how much of the gouge is related to late normal movement. They may correlate with the Late Cretaceous structures of Nixon et al. (1994) and England and Calon (1991).

The age of the discrete faults seen in M159DD2 (Fig. 88) is uncertain except that they appear to predate the conjugate faulting. However, their weak gougy nature and lack of cleavage is a problem. It is thought that they may be D4 (or D5) in age, with reactivation on the conjugate fault causing offset.

D5 Gouge & breccia zones fit with the northwest striking northeast dipping high angle thrust faults of the Cowichan fold and thrust system (CTS) described by England and Calon (1991). Massey et al. (1992) also described these structures noting they parallelled earlier axial foliation in Paleozioc rocks and dip 45° to 90° to the north-northeast. The age of these structures is mid Eocene (England and Calon, 1991 & Massey et al., 1992) and they are thought to result from the collision of the Pacific Rim and Cresent Terranes with North America.

D6 normal faulting required extension toward the northeast (Berry 1995) and may correlate with the formation of the Queen Charlotte basin (Miocene). Thus a Neogene age is tentatively assigned to these structures pending further evidence. England and Calon (1991) indicate the CTS was terminated by a large normal fault (the Outer Island Fault) in the Georgia Straight. This interpretation lens support to the existence of late normal faults in the Myra Falls area.

8.6 Discussions - Folding

The early D2-foliation and faulting produced a stretching lineation which parallels the regional folding (defined by Walker, 1983; 1985) and the cleavage is apparently axial plane to these folds. Berry (1996) also noted that the folds show a strong spatial association with intense NW striking shear zones with strong sub-horizontal stretching lineation on the Price hillside, with faults being most intense in the hinges of the folds. The sum of this evidence is very strongly pointing to a single event to explain the structures Berry (1996). This conclusion is supported by Reid's (1991) work which identified the open upright NW trending folds at the mine as early.

Regionally, a northwest trending gentle to open fold phase is associated with Mesozoic thrusting and considered responsible for the exposure of Sicker Group rocks in the three major structural uplifts on Vancouver Island (for example Massey et al., 1994). However, Berry (1996) was unable to find any of the features (e.g. down dip stretching lineation) expected if the northwest trending folds were associated with the Mesozoic northwesterly striking thrusts. Regional maps show no stratigraphic cut offs in the Buttle Lake uplift (Muller 1980) suggesting that any pre-Karmutsen Formation folding was very restricted or that folds pre-date the Permian Buttle Lake Formation (Berry, 1995). Massey (1994) showed that the Buttle Lake Formation sits unconformable on Sicker Group rocks in the Duncan area, and mentions folding

related to the penetrative fabrics correlated with the D2-foliation also in the Duncan area. However work by Yorath et al. (1999) is unconclusive as to the nature of this contact.

It is considered that the folding seen at the mine is related to the pre-Permian intense cleavage zones. The folding pre-dates the Permian Buttle Lake Formation and is limited to areas of intense D2 cleavage development. This interpretation fits the constrains implied by regional mapping. The effect of the regional Mesozoic northwesterly fold phase in the mine area is unknown. Further work outside the mine area is probably needed to answer this question and is outside the scope of this project. The drag folding related to the conjugate faulting (D3B thrusts of Berry), is not considered significant at a regional scale, but more important at the mine scale where strongly bedded silicified-horizons are encountered during mining.

8.7 Structural model for the Battle Mine

The aim of this section is to integrate geological data gained from face mapping and drill core logging in order to asses the structural style in the Battle Mine. In addition this study makes use of level plans produced by Myra Falls geologists between visits and the footwall topography generated by the DATAMINE™ model. The structures presented above here do not explain all variations in the Battle Zone however it is suggested that they help in the prediction of ore lens geometry in the future and aid in mine planning to reduce the ground control problems.

The Battle mine area is divided into 3 zones to aid in identification of structural styles (Fig. 95).

- The first zone covers the Battle lens. Within this lens ore banding is sub-horizontal, bedding in the cherts is sub-horizontal except where locally folded by D3A structures (Fig. 77 & 78) and mafic dykes are sub-vertical.
- The second structural zone is the Gopher lens, in this area, ore banding is commonly sub-vertical, mafic dykes show rotation and dismembering into the D2 cleavage and bedding orientation are highly variable often with quite steep dips.
- The third structural zone occurs from 1690mE to the 1800mE, this zone shows a similar structural style to the Battle lens with all types of faulting occurring. Bedding in the chert layers the ore banding are both sub-horizontal. However, the footwall topography in this area is distinctly different from the footwall topography underlying the Battle lens .

Zone 1 – Battle lens (west of 1690mE)

Footwall topography in this zone gives the impression of open folds with a 6° westerly plunge (Fig. 95). Berry (2000) interpreted these folds as major factors in defining the position of the ore lenses. However, drift mapping in combination with core logging shows the structural style off the Battle lens to be much more fault dominated (Fig. 96). The Battle lens shows the influence of all types of faulting (Fig. 97). D2/D5 structures are prominent in the Battle lens. These faults commonly have massive sulfides on the footwall side of the fault and cherts on the hangingwall side of the fault, giving the impression of normal movement. This offset is probably due to strike slip movement cutting the westerly dipping surface rather

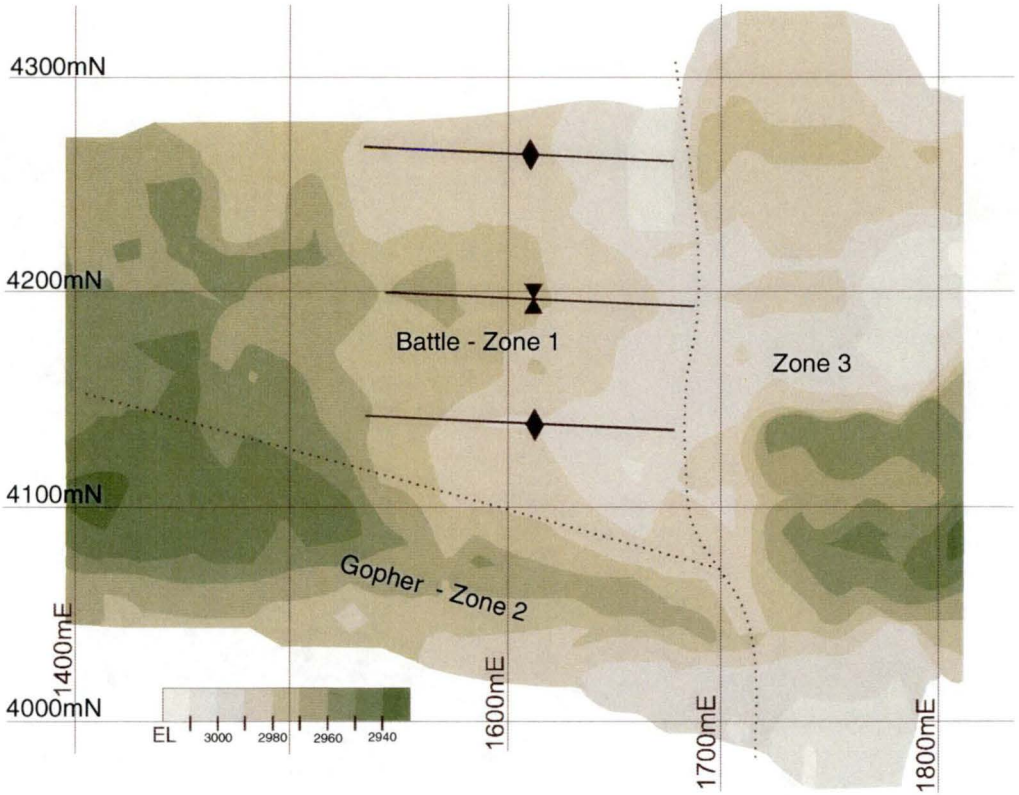

Figure 95. Contours of the top of the Price Formation showing distribution of the threee structural domains (dotted lines mark boundaries) and orientation of fold axes.

than true dip slip movement. D3A conjugate faults are visible through out the Battle lens seen deforming ore banding and causing folding of chert layers above the Battle lens. The influence of D3A structures also seen in footwall contour map (Fig. 97B). Discrete faults and unresolved gougy faults play a large part in influencing the position of the ore in the Battle lens (Fig. 96).

A D5 zones of anastomosing gouge and breccia are prominent along the northern margin of the Battle lens (Fig. 97A) this structure has been named the "shear tail fault" by mine geologists. A complex area of faulting occurs along the main Battle lens access drift (18-168DW) where several fault styles amalgamate creating bad ground conditions.

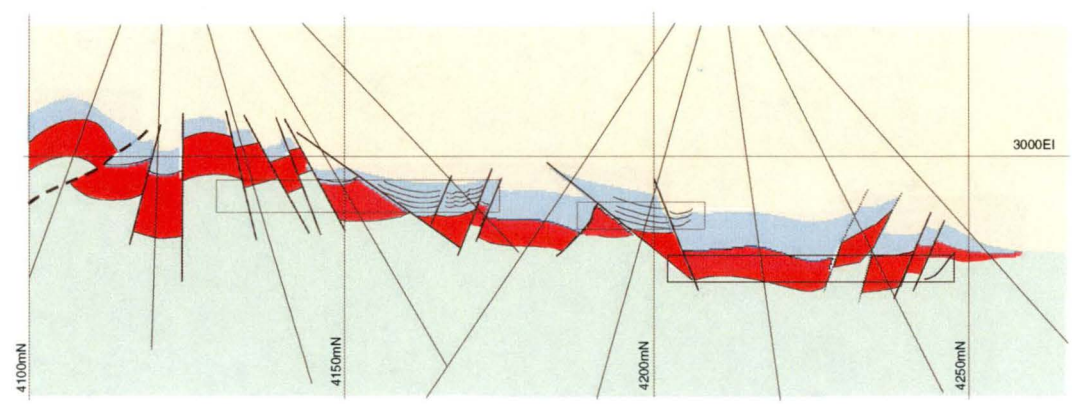

Figure 96. Structural interpretation for 1600mE Battle lens section from drift mapping and core logging.

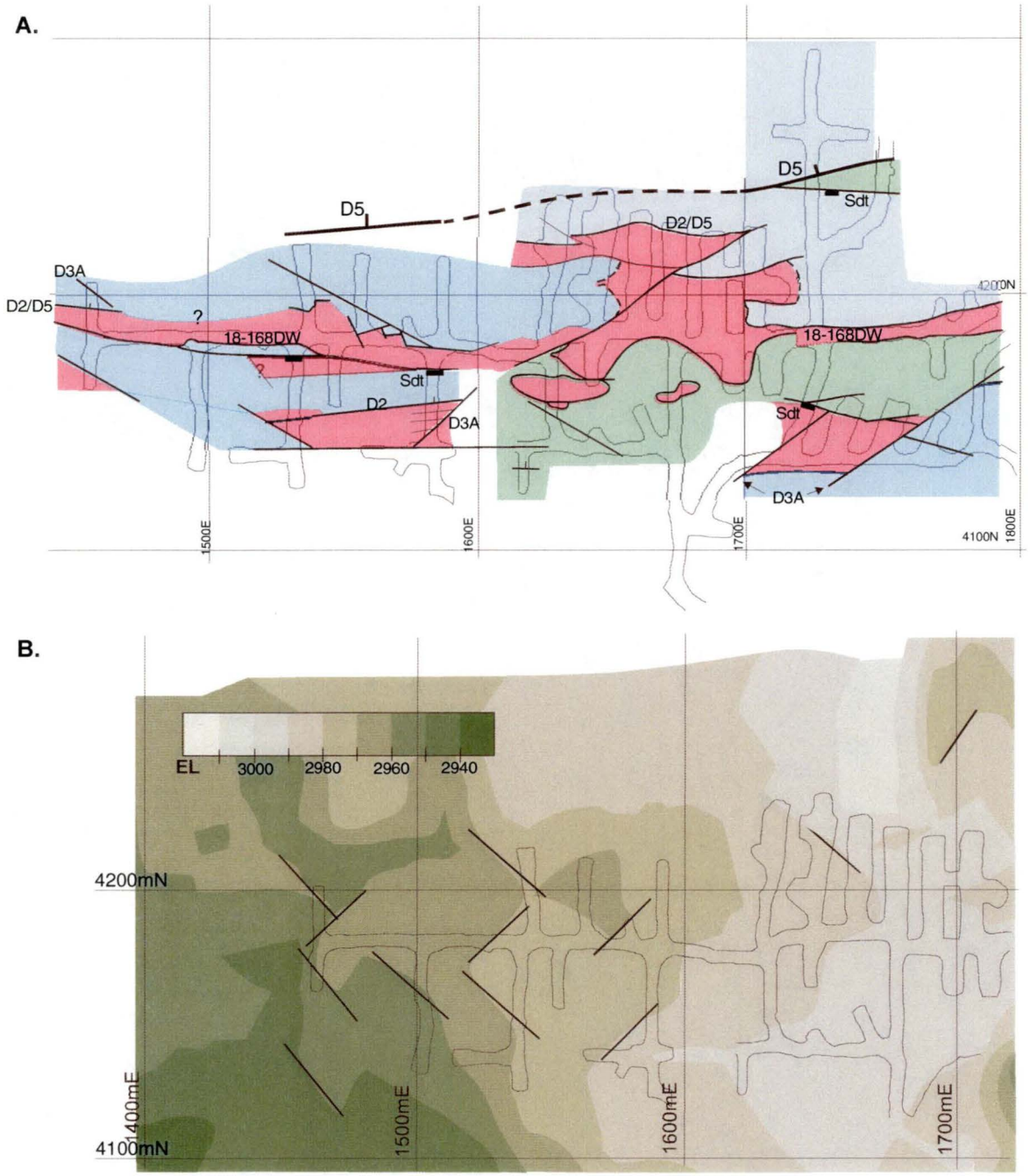

Figure 97. A. Simplified interpretation of the Battle lens structure, B Interpreted possible D3A faults from footwall contour.

Upper Zone lenses lie above the Battle lens and show a similar structural style with all types of faulting affecting the ore position. Tightly spaced drilling shows the Upper Zone lenses to be highly variable with faulted contacts between ore types (Fig. 98). Limited underground exposure shows complex fault patterns many of which cause considerable ground control problems (Fig. 99). South dipping thrust faults are prominent in Upper Zone drifts mapped and commonly form the footwall to the ore lenses exposed. West northwesterly (D2/D5) and D3A conjugate fault orientations are all common.

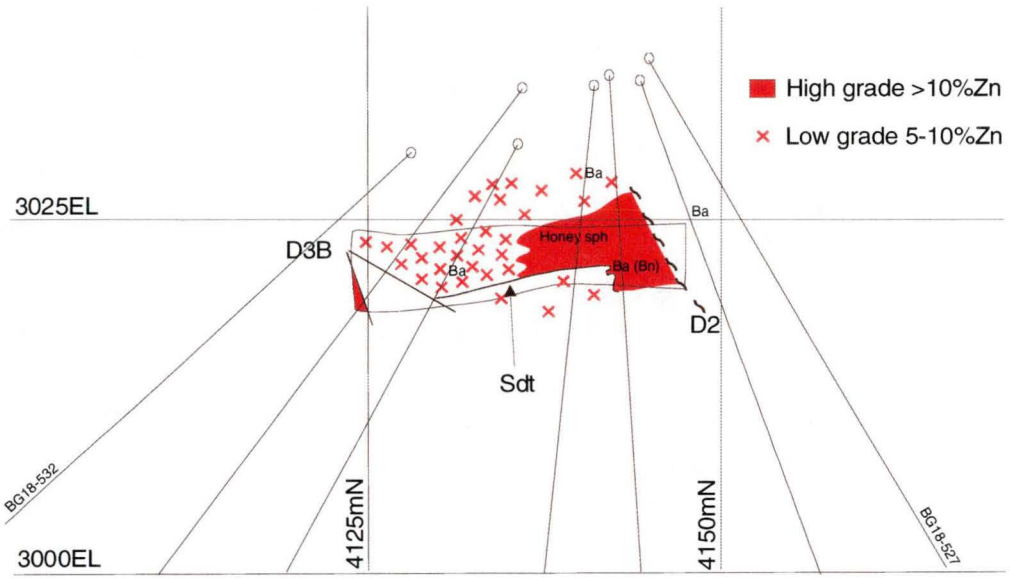

Figure 98. Tightly spaced drilling through Upper Zone lenses show rapid changes in ore types due to faulting. Flat faults and south dipping thrust faults are common in drifts mapped. (1570mE section, with wall map from H169 D2 Panel 8).

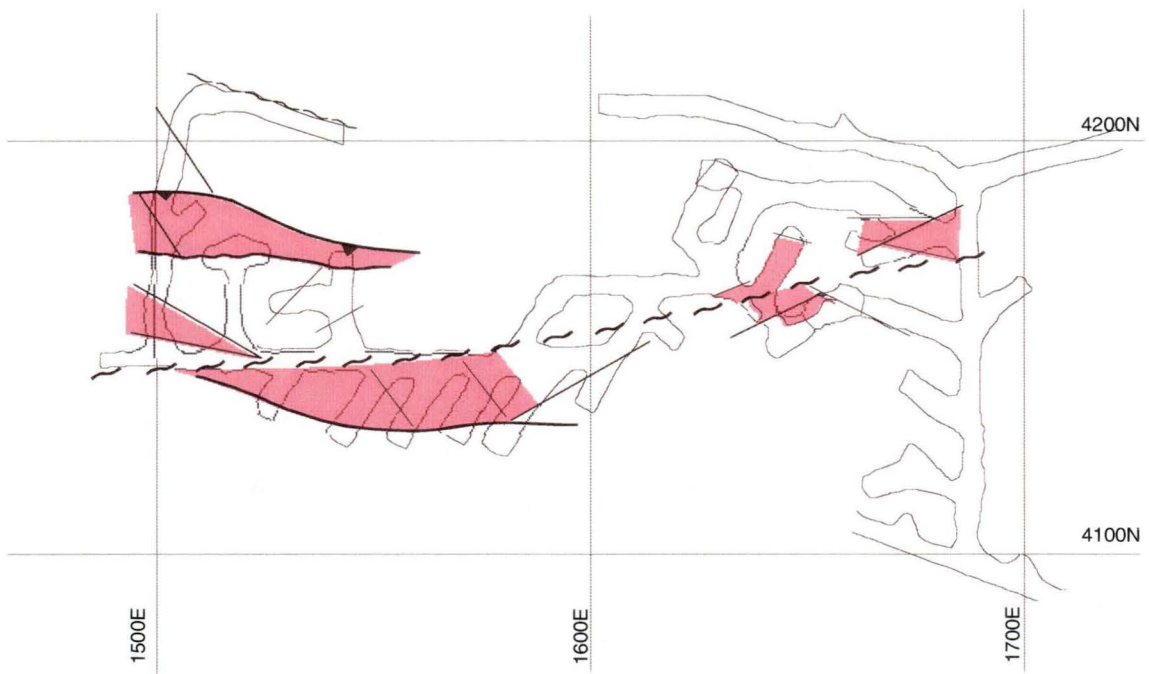

Figure 99. Interpreted geology for the Upper Zone drifts.

Zone 2 – Gopher lens

The Gopher lens is strongly affected by the D2/D5 structures. Ore banding is rotated into sub-vertical orientation parallel with S2 and mafic dykes are deformed and rotated into the S2 orientation (Fig. 71 & 73). Later ductile shears (D3) and D5 zones of breccia and anastomosing gougy faults variably overprint the D2 foliation zones (Fig. 73 & 75).

D5 faults have a major affect on the position of ore in the Gopher lens. Between zones of D5 deformation conjugate faulting affects the position of the ore in the Gopher lens (Fig. 100). The conjugate faults cut off the D2 intensely foliated zones and truncate banded ore and are cut off by later D5 gougy structures. However the movement on the D3A faults is not large (~10m), and the continuity of the ore is preserved along the strike of the Gopher lens. South dipping thrusts and discrete gougy faults are also seen in the Gopher lens (Fig.101)

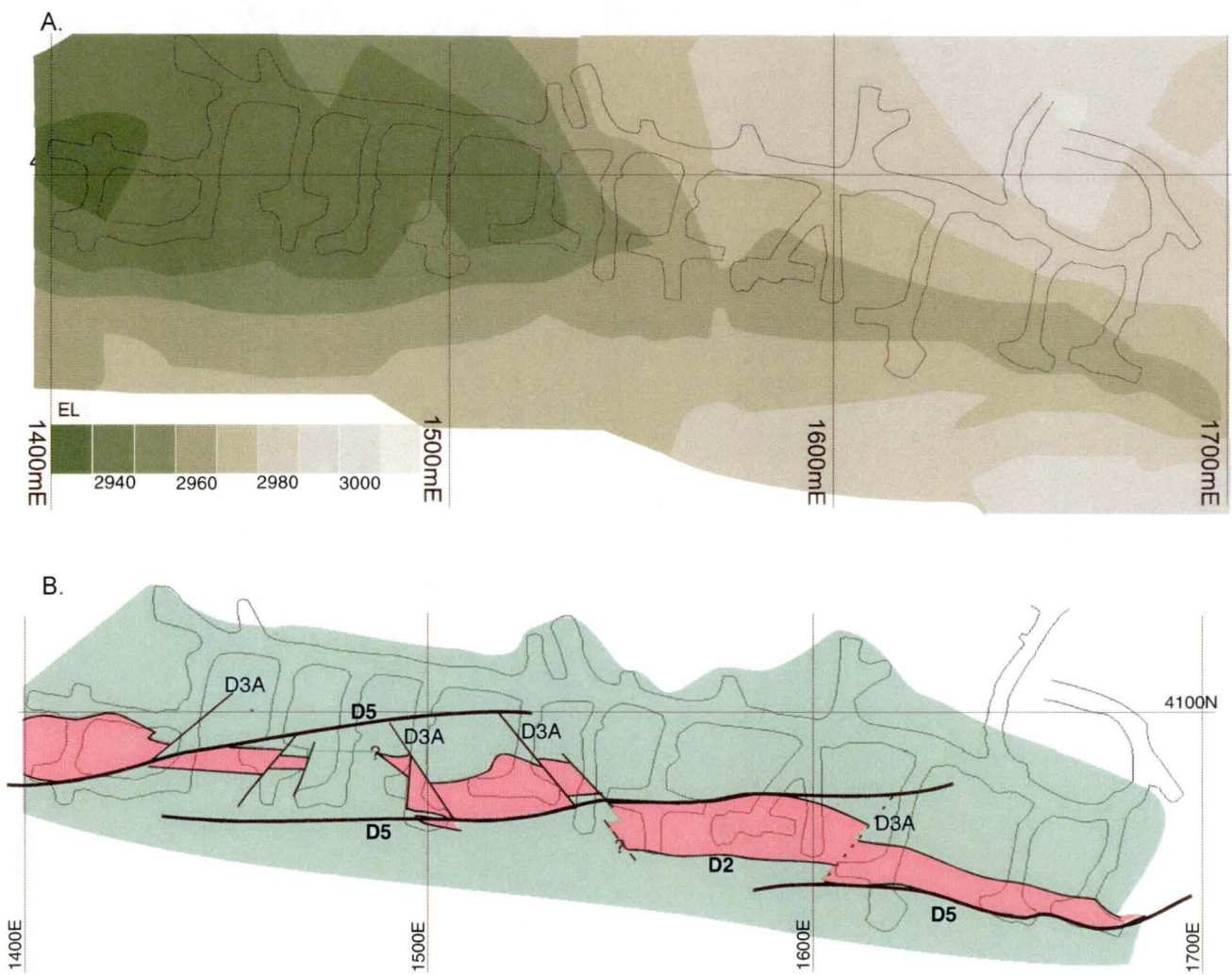

Figure 100. Footwall contour map showing position of Gopher extraction drifts. B Gopher Zone structure from mapping. Ore shown in red. The Gopher lens ore is controlled by D2/D5 structures, However D3A conjugate faults control the position of footwall thus influence ore intersections in extraction level drifts.

Bedding orientation in the cherts layers above the Gopher lens are highly variable often with quite steep dips (Fig. 102). The simple explanation for the steep dips and changes in ore thickness in the Gopher lens is the presence of folding. Folding most likely related to D2, with steep S2 cleavage axial planar. Faulting of folded sections causes juxtaposition of bedding at high angles as seen in G156DD (Fig. 103).

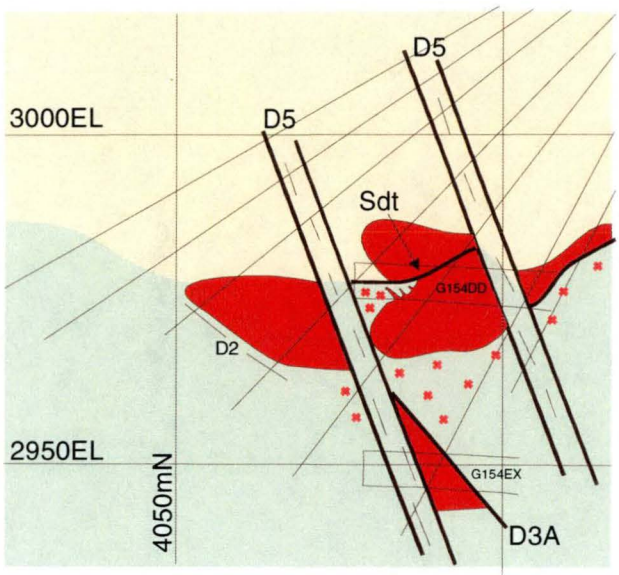

Figure 101. Cross section of the Gopher lens (1540mE) showing the influence of D3A, south dipping thrusts (Sdt) and D5 structure on the shape of the Gopher lens.

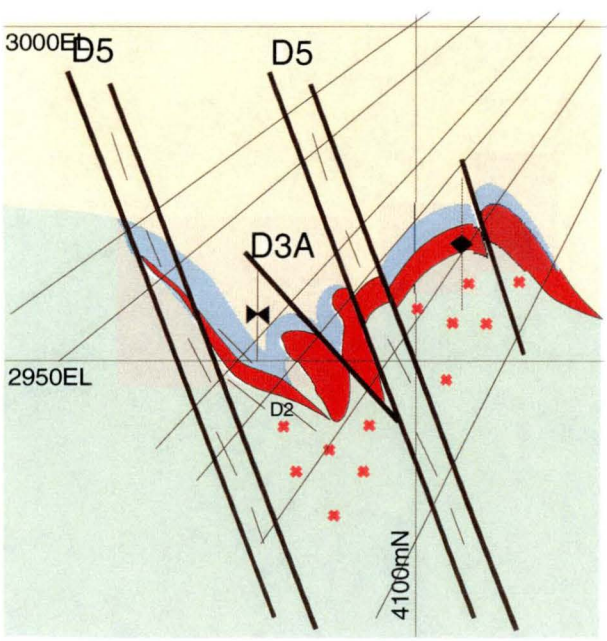

Figure 102. Cross section of the Gopher lens (1420mE) showing the influence of folding D3A, and D5 structure on the shape of the Gopher lens.

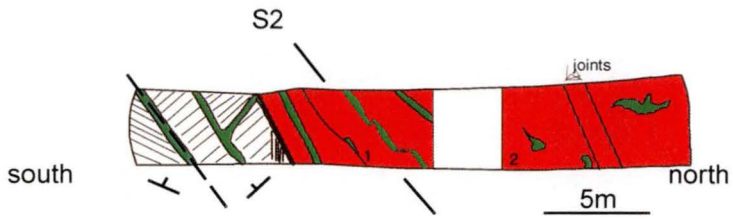

Figure 103. G154DD Mafic dykes are rotated into parallellism with D2, chert layers at the southern end of the drift show contrasting bedding orientations accross faults.

Zone 3

The third structural zone occurs from 1690mE to the 1800mE, this zone shows a similar structural style to the Battle lens with all types of faulting occurring (Fig. 96). Brecciation and gouge were particularly common in the drifts mapped. However, the footwall topography in this zone is distinctly different (Fig.104).

In the area between 1690mE and 1710mE a N-S ridge occurs. This ridge separates open folds with westward dip to the west from topographic highs and lows to the east. The topographic highs and lows are defined by an elevated area between 4150mE and 4220mE which drops off rapidly into a basin at 4140mE (Fig. 96 & 104). This basin hosts the South Trough lens. The South Trough basin margins may be explained by D2/D5 structures (Fig. 104). However, this basin does not extend through the N-S ridge as would be expected if it were caused by D2/D5 faulting. The N-S ridge structure and the South Trough basins does not fit with any of the known structures in the Battle Mine. It is highly likely that these highs and basins represent basement structures that existed prior to ore deposition.

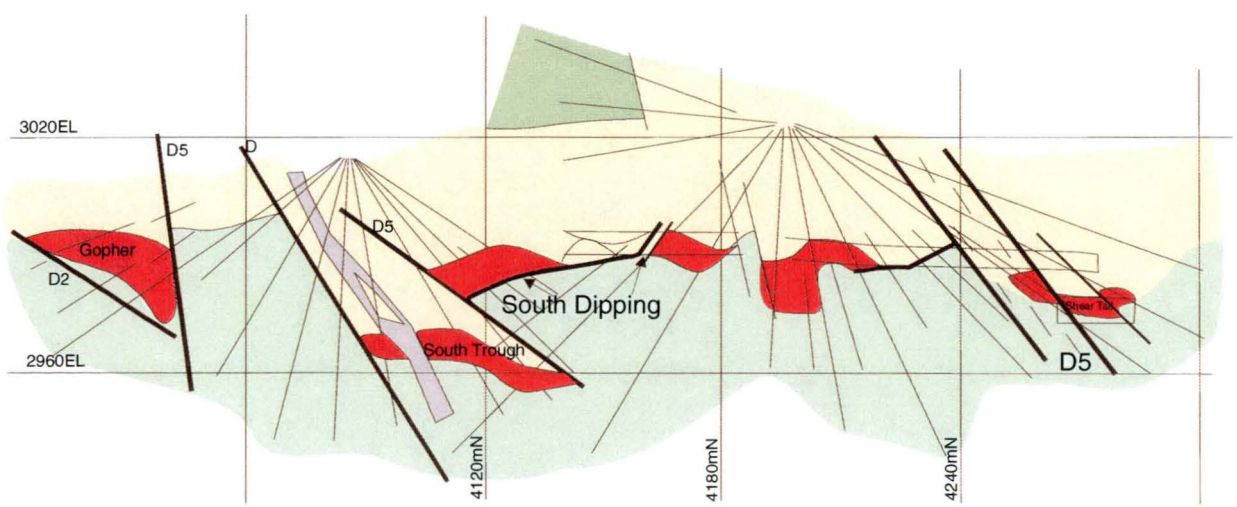

Figure 104. 1720mE section showing interpreted structure and basement topography.

Gap lens

No underground exposure to the Gap lens was available during fieldwork section of this study, thus interpretation of Gap lens structure conducted entirely form drill core. D3A style faults as well as latter gougy faults are common in the drill core surrounding the Gap lens, however none of these faults appear to be limiting the ore position (Berry 2000). In contrast the northern margin of the Gap lens is cut off by a strong gougy and breccia zone at least 5m wide (Fig. 105). D2 faulting may also be important along the margins of the Gap lens as indicated by strong foliation and elongation of pyrite grains in sericite-alteration surrounding the massive sulfides.

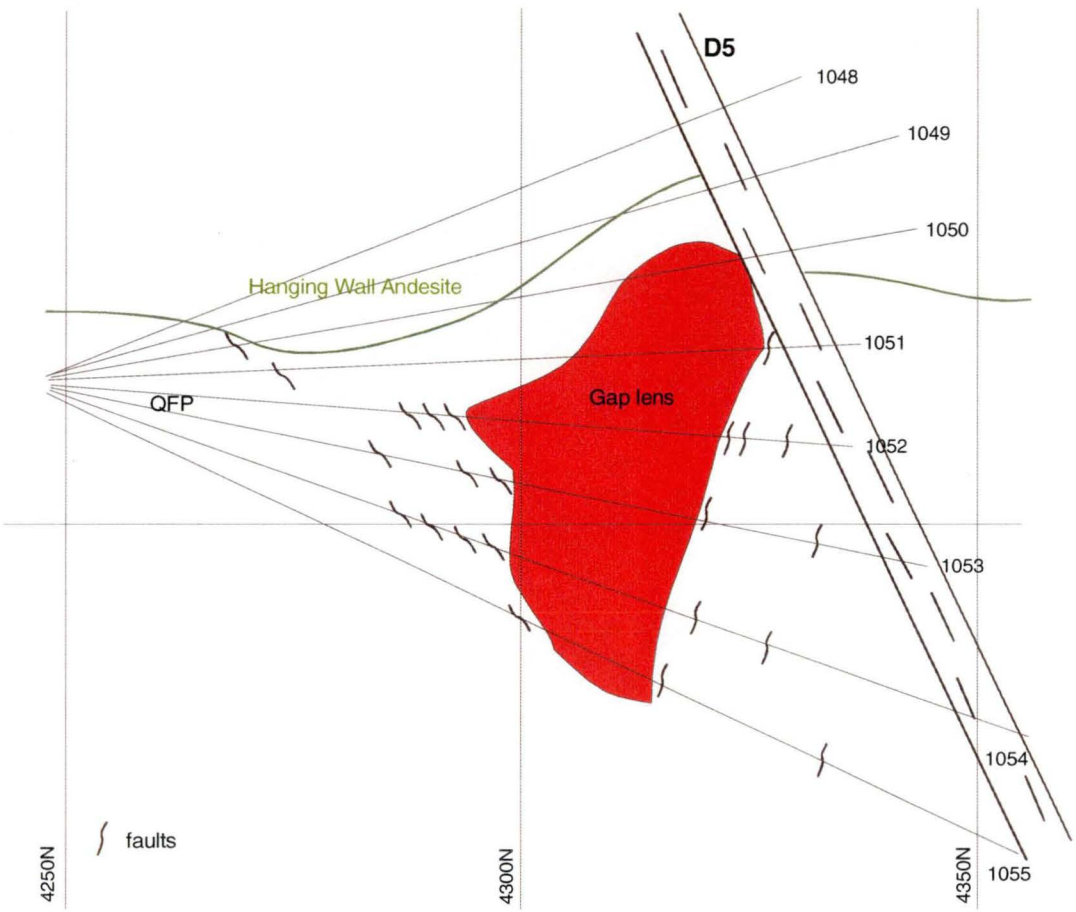

Figure 105. Schematic Gap lens section showing position of North Fault which cuts of the Gap lens to the north. Based on 1420mE section

8.8 Summary

The Battle Zone has evolved through a multi-stage structural history involving at least six generations of faulting and folding. Structures found in the Battle Zone are summarised in Table 32.

Devonian basement and growth structures are commonly obscured by alteration and overprinted by later deformation making them difficult to recognise in core and outcrop. In particular D2 structures mimic the criteria used to distinguishes basement and growth structures (i.e. stratigraphy can not be matched across D2 structures due to out of section movement). Careful note of cleavage is needed before deter-

Fault type	Age	Description	Orientation
D1	pre-Devonian to Devonian	N-S orientated ridge between 1690mE and 1710mE Basin that hosts the South Trough lens	
D2	pre-Permian	Pervasive foliation, varies from weak to intense, show sinistral movement.	Steep dipping: 130-155° 60°N to 80°S Moderately dipping· 110-150° 30-45°N
D3A	mid to late Jurassic	Conjugate faults: fault surfaces surrounded by an intense zone of cleavage, spatial association with quartz-carbonate veining	090-095° dip 70-80°N and 175-185° dipping 30-40°E
D3B	Late Cretaceous	Ductile shear zones: weak gouge coated faults with 10-40cm of internal dragged cleavage, top to the south movement South dipping thrust faults: gouge surrounded by a narrow zone of cleavage with accompanying quartz-carbonate veins	Ductile shear zones:120-130° 45°N South dipping thrusts. 140-150° 60-80°W
D4		weak gougy surfaces and no cleavage	100-110° 65°N
D5	Eocene	broad zones of gouge and breccia with abundant anastomosing gouge planes	Strike 110-155° 30-75°NE
D6	Tertiary	gougy surfaces and no cleavage	

Table 32 Summary of Structures found in Battle Mine, Myra Falls district, B.C, Canada.

mining the existence of basement and growth structures in the Battle Zone.

D2 foliation is pervasive and varies in intensity from weak to intense. These structures are anomalous, they lack brittle features and show a weak cleavage compared to the strain (Berry 1995) This fits with the pre metamorphic age (i.e. pre Jurassic) implied from the structural relationships.

D3 structures are brittle ductile in nature – gougy planes surrounded by narrow (<2m) of cleavage and show a spatial association with quartz-carbonate veining. These faults cause significant offsets to ore on mine scale but are probably less important on a regional scale.

D5 gouge and breccia zones broad zones are brittle structures that commonly form anomalous zones of deformation that can be traced for large distances across the mine property. These anomalous fault zones commonly show a variation of influences along their length depending on overprinting relations between D5 and earlier structures.

D4 and D6 faults are interpreted as gougy structures showing normal movement, these faults occur throughout the Battle zone and have an important effect on ore placement at a drift level. However the timing of these faults and their relationship to quartz-carbonate veining remains largely unresolved.

All types of faulting affect the Battle, South Trough and Upper Zone lenses. This creates complex fault pattern with ore blocks being shuffled making mining difficult. However most movements are not large <10m thus ore lenses hang together as coherent bodies on regional scale. In contrast the shape of the Gopher lens is dominated by D2/D5 structures with movement on D3 structures locally important within the ore lens.

Chapter 9

Metal Zonation

9.1 Introduction

General vertical and lateral metal zonation of VHMS deposits have been documented by Stanton (1965), Sangster (1972), Large (1977), Franklin et al. (1981), Eldridge et al (1983) and Ohmoto et al. (1983). These workers have shown that typical massive sulfide deposits exhibit a zonation in metal content from iron and iron-copper-rich bases, through to copper-zinc-lead-rich ore, then to lead-zinc-barium-rich sulfides at the top and distal regions. This zonation has been used to understand the mechanisms of sulfide deposition (eg Large, 1977; Knuckey et al , 1982) and in unravelling the structural history of deposits (eg Rosebery, Green et al., 1981; and Que River, Large et al., 1988)

The distribution of trace and major elements in the ores and wall rocks of VHMS have important implications for exploration, genetic modelling, and for the metallurgical treatment of the ore. Metal ratios such as the Zn number [100Zn/(Zn+Pb)] and Cu number [100Cu/(Cu+Zn)] have also been used to understand the genesis of VHMS deposits (Huston and Large, 1987). For example, the coincidence of the lowest Zn ratios, highest Cu ratios and most abundant pyrite within the footwall alteration zone at the Hellyer deposit has been interpreted to define the locations of high temperature feeder zones (Gemmell and Large, 1992).

The distribution of base metals, trace elements and metal ratios in the Battle Zone of the Myra Falls district are contoured on cross sections in order to determine: (1) how distribution of metals corresponds to the gross mineralogical zonation of the deposit; (2) to locate possible feeder zones; and (3) to help understand the structural complexity of ore zones. Three-dimensional modelling of the mine assay database and metal ratios has been conducted using DATAMINE™ software.

9.2 Methods

Drill holes are routinely sampled and analysed by Boliden-Westmin Ltd. for copper, lead, zinc and iron on sample interval of no more than 1.5 meters with individual intervals adjusted to lithological boundaries and changes in mineralogy. Barium is analysed where zinc content exceeds 3% or by request from company geologists. Gold and silver are analysed only by request. The pulps left over from these analyses (where possible) were collected for ICPMS analyses and barium, gold and silver analyses were

requested where absent. Where pulps were not available, holes were resampled taking into account previous analyses. Resultant composite samples were given exploration (EX-prefix) sample numbers and were crushed and pulverised in the Myra Falls lab prior to being sent to Chemex laboratories in Vancouver, British Columbia, Canada.

Multi-element analysis of 37 elements was carried out by Chemex labs, Vancouver, between the period February 1998 to April 1999. Silver, Al, As, Ba, Be, Bi, Cd, Ca, Cr, Co, Cu, Fe, Hg, K, Mg, Mn, Mo, Na, Ni, P, Pb, Sb, Sc, Sr, Tl, Ti, Te, U, V and Zn were analysed by the A30 ICP-AES multi element analysis (Table 2, Appendix 5). Tin, Te, Ge, and In were also analysed, methods are listed in Table 3, Appendix 5. Tl and Hg were re-analysed via the methods listed in Table 3, Appendix 5, to improve their detection limits.

The elements Al, Ba, Be, Ca, Cr, K, Mg, Na, Sb, Sc, Sr, Ti, Tl and Te were analyses via ICP-AES, however these elements are only partially leached by acid digestion. Titanium is a good example of this phenomenom, as the ICP-AES analysis failed to detect Ti with a 100ppm detection limit. However, rutile (TiO_2) crystals are clearly visible in the ore and host rocks to the Battle Zone lenses (chapter 4 and 7) and whole rock XRF analyses of the host rocks contain up to 0.89wt% TiO_2 in rhyolites and 1.23wt% TiO_2 in the altered andesites (Appendix 2). Since results of these analysis are not an accurate measure of their abundance in the samples, they were not considered during contouring.

9.3 Results

9.3.1 Introduction

In total 712 samples from 5 sections covering the South Trough, Battle, Gopher, Upper Zone and Gap lenses were analysed for major and trace elements. Results are shown in Tables 4-17 of Appendix 5. Silver, Cu, Pb, Zn, and Fe were re-analysed as part of the ICP-AES package (Appendix 5). Linear regression was performed on the data comparing mine assay to ICP-AES assay for each element, with the results plotted in Figures 106 & 107. Zinc (Fig. 106A) and Fe (Fig. 106B) show excellent correlation of 0.99, although Zn analyses show variations up to 9.5% between the two labs. These differences are rare enough to be insignificant. Iron shows a similar trend to Zn with difference up to 6% (where Fe < 30%). The Chemex upper limit of 30% for Fe is a major problem for ore grade samples with a variation from 29% to 41% Fe covered by > 30% in the Chemex analyses. Copper and Pb show less variation in the analyses < 1% for Cu and < 0.5% for Pb, however the trend lines on Figure 106C & D show correlations of 0 96 for both indicating a slight variation in analyses. The major reason for the variation may be the detection limits. Ag is the most worrying element with significant variation up to 1486ppm seen between mine and Chemex analyses and a correlation trend of 0.94 (Fig 107A). This variation in Ag analyses is minimal in the Battle, Gopher and South Trough lenses where Ag values are generally low (Fig 107B & C), however in the Gap and Upper Zone lenses Ag values are significantly higher and the discrepancies are more pronounced (Fig 107D & E). Mine Ag assays were obtained by fire assay while the Chemex results were obtained using a nitric acid-aqua-regia digestion and analyses by atomic absorption spectrometry. The difference in the two methods probably accounts for the variation in results (pers. com Chemex, 2000).

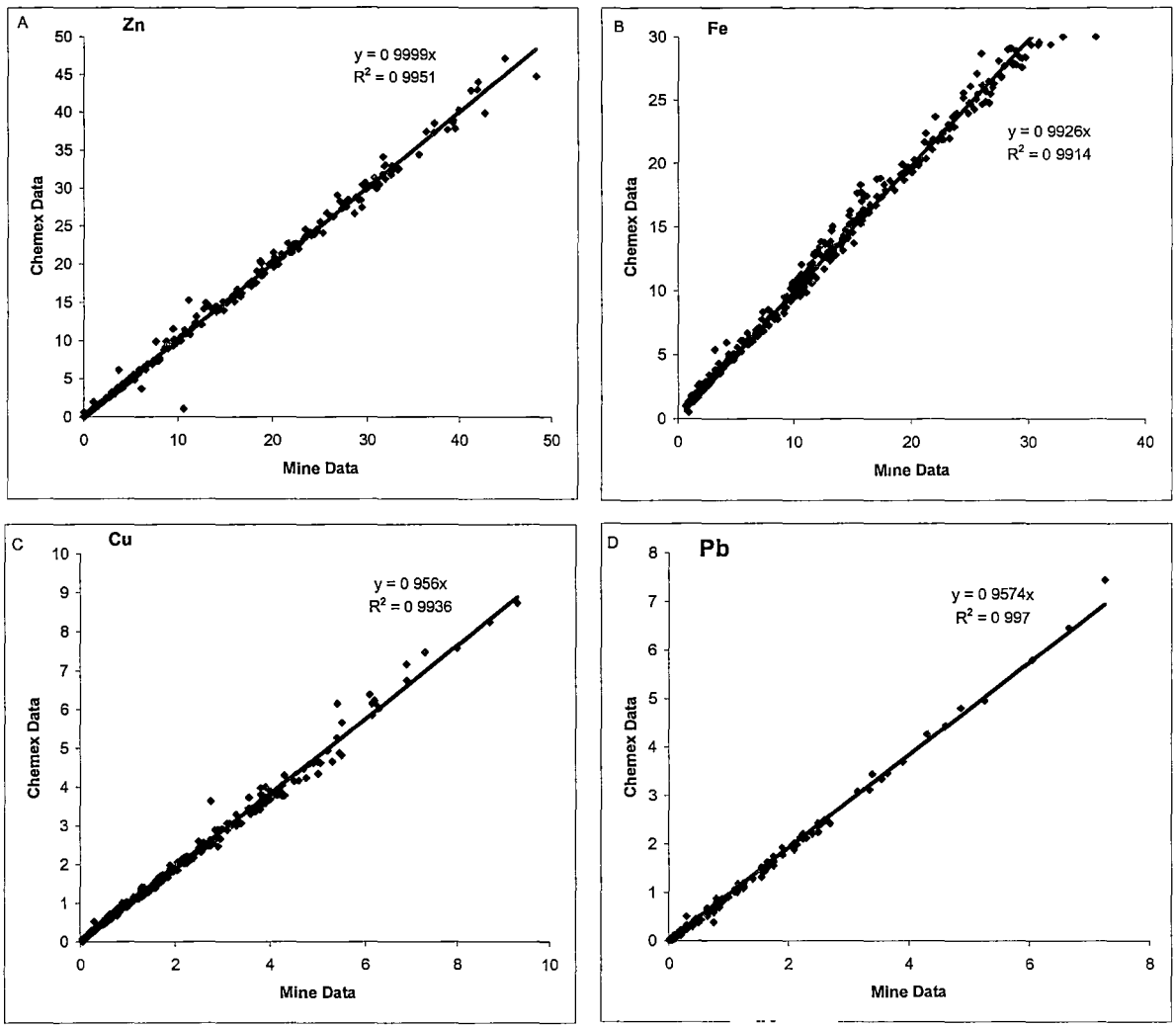

Figure 106 Linear regression plots for zinc (A), iron (B), copper (C) and lead (D) comparing mine assay data to analysis done by Chemex Ltd Vancouver (A30 ICP-AES package).

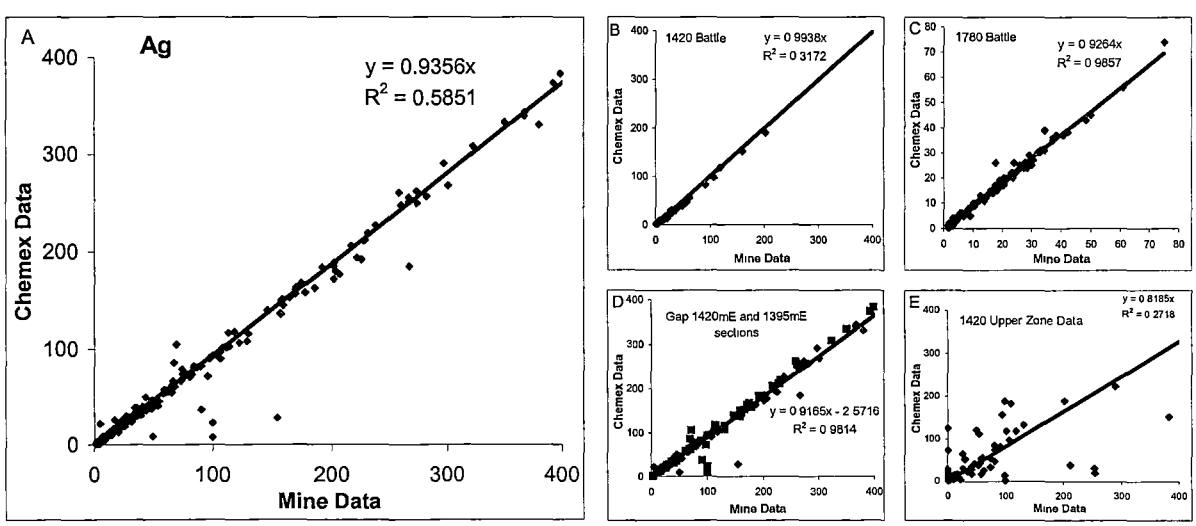

Figure 107 Linear regression plots for silver, comparing mine assay data to analysis done by Chemex Ltd. Vancouver (A30 ICP-AES package). (A) all data. (B) Battle data (1420mE section), (C) Battle data (1780mE section), (D) Gap data 1420mE and 1390mE sections, (E) Upper Zone data (1420mE section).

Minor and trace elements were analysed via the A30 ICP-AES multi element analysis at the Chemex laboratories in Vancouver. The range of values found for each element is listed in Table 33. Minor elements As, Cd, Mn and P show ranges of values of 1000's of ppm and constitute minor components of ore or host rock. Mo and Ni range by 100's of ppm, while Bi, Co, Ge, Te, Tl, U and V occur as trace elements. Mercury also occurs as a trace element but is measures in parts per billion (ppb) so its range is high. Tin was below detection (i.e. <0.01%) on all sections. Indium was measured only on sections 1540mE and 1780mE and was below detection (2 ppm) in all samples. Measurements of Bi and P suffer interference were Cu > 5 %, however, these elements were not considered important enough to correct the interference. Analyses of Hg from the A30 multi element package (10 ppm-detection limit) were discarded, as they show no correlation with the HNO_3/HCl – cold vapour results which gives a detection limit of 10ppb.

Element	Symbol	Mimimum =detection limit	Maximum
Zinc	Zn	<0.05	54%
Iron	Fe	<0.05	43.2%
Copper	Cu	<0.05	9.3%
Lead	Pb	<0.05	13%
Barium	Ba	<0.05	41.5%
Silver	Ag	<0.05	1367g/t
Gold	Au	<0.05	51g/t
Arsenic	As	10ppm	9860ppm
Bismuth	Bi	10ppm	100ppm
Cadmium	Cd	5ppm	>1000ppm
Cobalt	Co	5ppm	95ppm
Germanium	Ge	5ppm	15ppm
Mercury	Hg	10ppb	31100ppb
Manganese	Mn	10ppm	6410ppm
Molybdenum	Mo	5ppm	415ppm
Nickel	Ni	5ppm	460ppm
Phosphorus	P	100ppm	6400ppm
Selenium	Se	2ppm	120ppm
Uranium	U	20ppm	60ppm
Vanadium	V	20ppm	80ppm

Table 33. Range of values for each element found in the Battle Zone samples.

9.3.2 Sections

The distribution of metals has been contoured using Surfer 6.04™ software on each of the five sections analysed. Contour intervals were determined by inspecting the data and chosen to best represent the variations in elemental values within and between lenses. Contours are adjusted to include geological information (eg faulting, deposit boundaries) with the resultant plot redrawn and presented in Figures 108-8. Maximum metal values for each lens are summarised in Tables 34 – 9.7 according to section

1780mE

Four holes BG18-340 – 343 were logged and samples on 1780mE section for ICP-AES. The mine database for Zn, Cu, Pb, Ba, Fe Au and Ag was also utilised. Available data is summarised in Table 34 and plotted on Figure 108 along with sub-lens outlines from Datamine™. Zinc (Fig. 108A) is distributed toward the top of sub-lens outlines and is underlain by Cu and Fe (Fig. 108B & D). Iron forms a strong concentration on BG18-340 and 341 below and between the sub-lenses (Fig. 108D) and extends along a fault under the sub-lens on BG18-342 and 343. Pb values are elevated up to 10.9% in the hangingwall to the South Trough sub-lenses but are low (<1%) within the South Trough sub-lenses (Fig. 108C). Barium values are extremely low (<2%) in the South Trough sub-lenses and surrounding hangingwall (Fig. 108E). Silver (Fig 108G) follows the distribution of Zn being distributed toward the top of sub-lens outlines. Gold (Fig. 108F) shows an erratic distribution with generally low values (< 3g/t). Arsenic, Ni and Hg are concentrated at the base of the southern most sub-lens, at the top of the sub-lens on BG18-341 as well as in the upper most sub-lens on BG18-342. Cadmium has an association with the Zn distribution as well as following the As-Ni-Hg distribution (Fig. 108K). Molybdenum distribution broadly follows the outline of sub-lens with highs (100-200ppm) coincident with As highs. Manganese and P show highs underlying sub-lens on BG18-342 and 343 as well as at the top of this sub-lens (Fig. 108M & N). Selenium (Fig. 108O) shows highs at the centre of the southern sub-lens as well as a high at the top of the overlying sub-lenses. Selenium also forms a halo enclosing the sub-lenses and into the footwall. Bismuth (Fig. 108P) shows the most unusual distribution with highs on BG18-340 corresponding with high Fe and a high on BG18-

Element		Maximum value
Gold	Au	9 g/t
Silver	Ag	304 g/t
Copper	Cu	4.9 %
Lead	Pb	10.8 %
Zinc	Zn	49.6 %
Barium	Ba	1.9 %
Iron	Fe	43.2 %
Arsenic	As	160 ppm
Cadmium	Cd	830 ppm
Manganese	Mn	2260 ppm
Phosphorus	P	6400 ppm
Molybdenum	Mo	210 ppm
Nickel	Ni	175 ppm
Mercury	Hg	8860 ppb
Bismuth	Bi	30 ppm
Cobalt	Co	20 ppm
Germanium	Ge	D/L ppm
Uranium	U	B/D ppm
Vanadium	V	40 ppm

Table 34. Summary maximum assay values from 1780mE section, South Trough lens. D/L detection limit, B/D below detection.

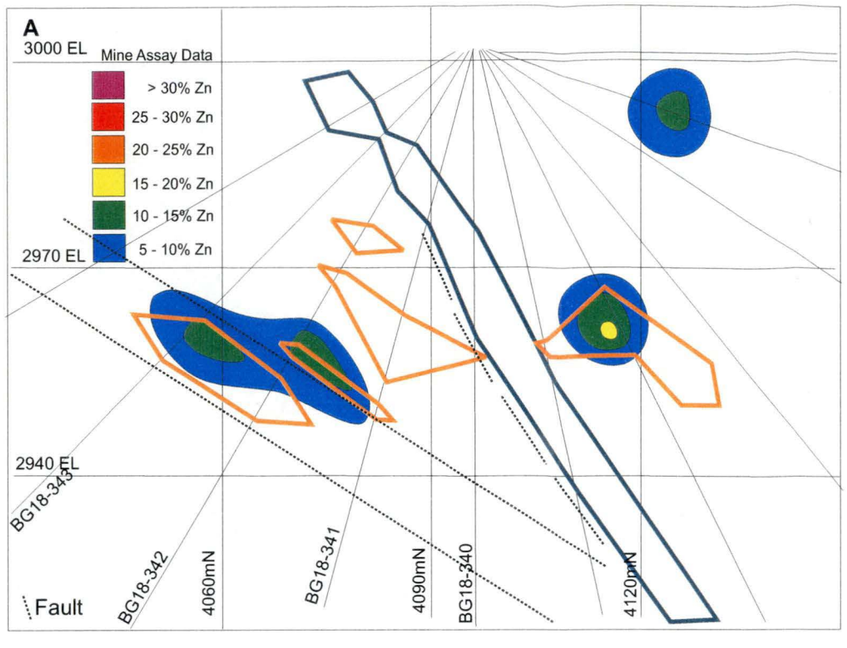

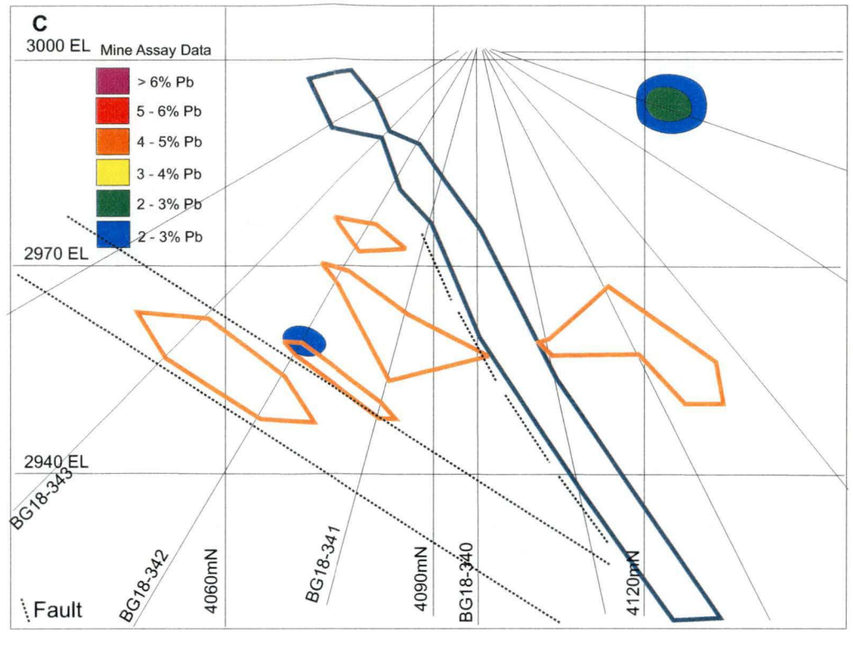

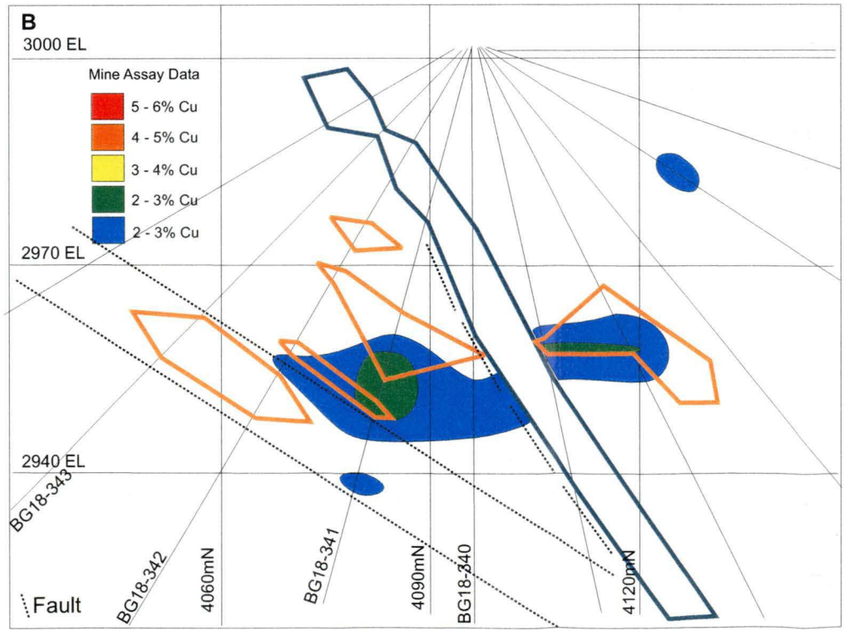

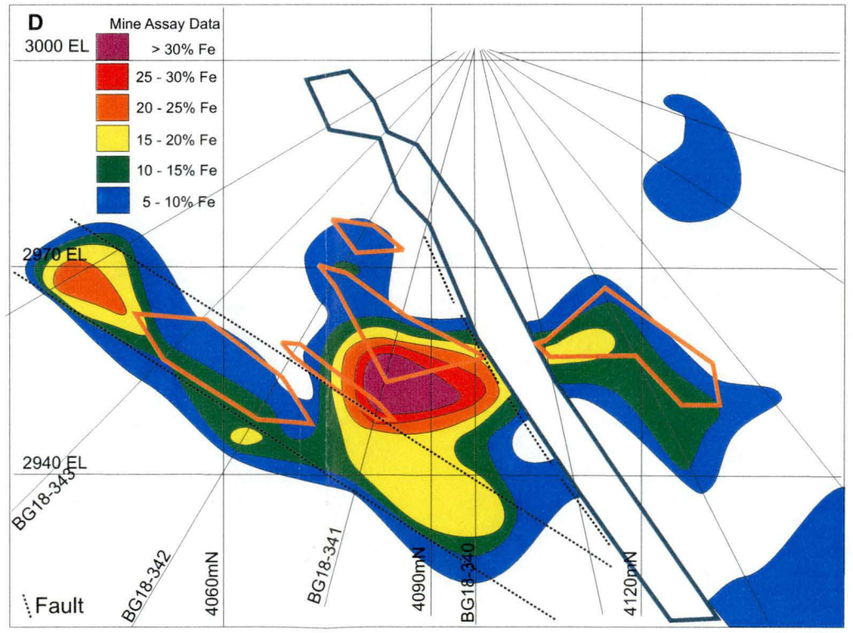

Figure 108 Contour plots for 1780mE section. (A) zinc, (B) copper, (C) lead (D) iron, from mine assay data base. Outlines in orange South Trough sub-lenses, green is a mafic dyke.

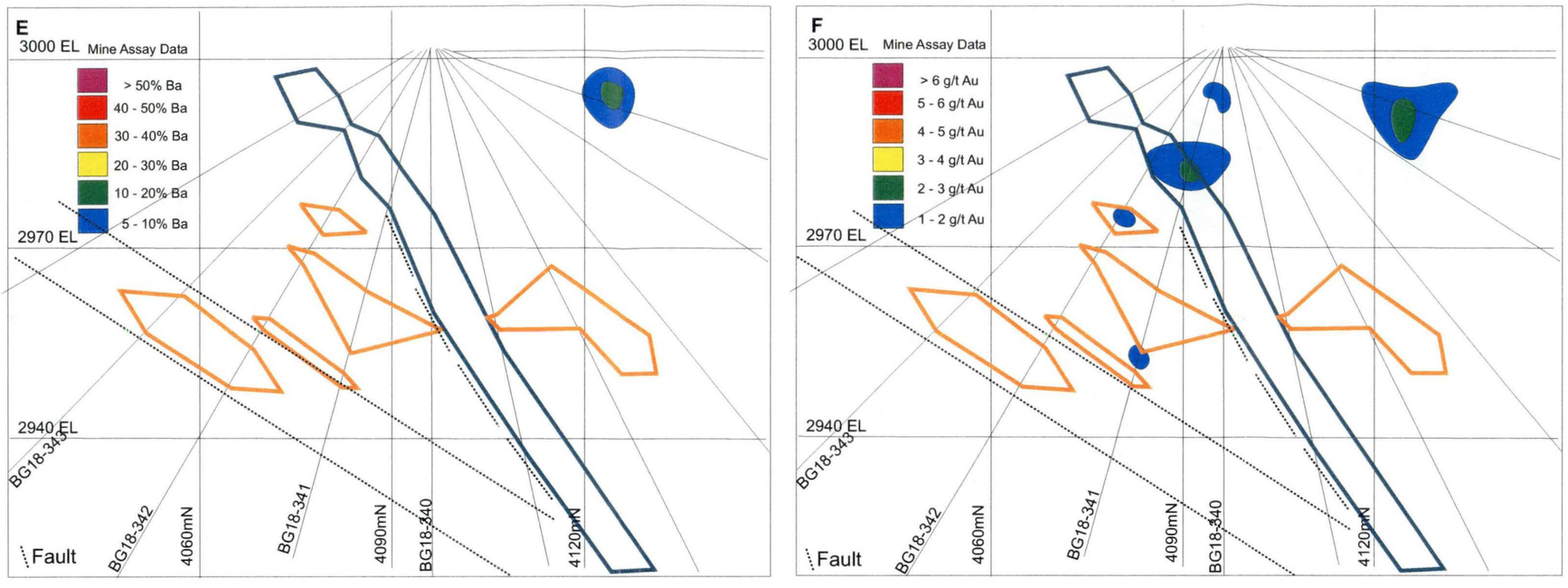

Figure 108continued. Contour plots for 1780mE (E) barium, (F) silver, (G) gold, (H) arsenic from mine assay data base(E - G) and ICP-AES analysis (H). Outline in orange - South Trough sub-lenses, green is a mafic dyke.

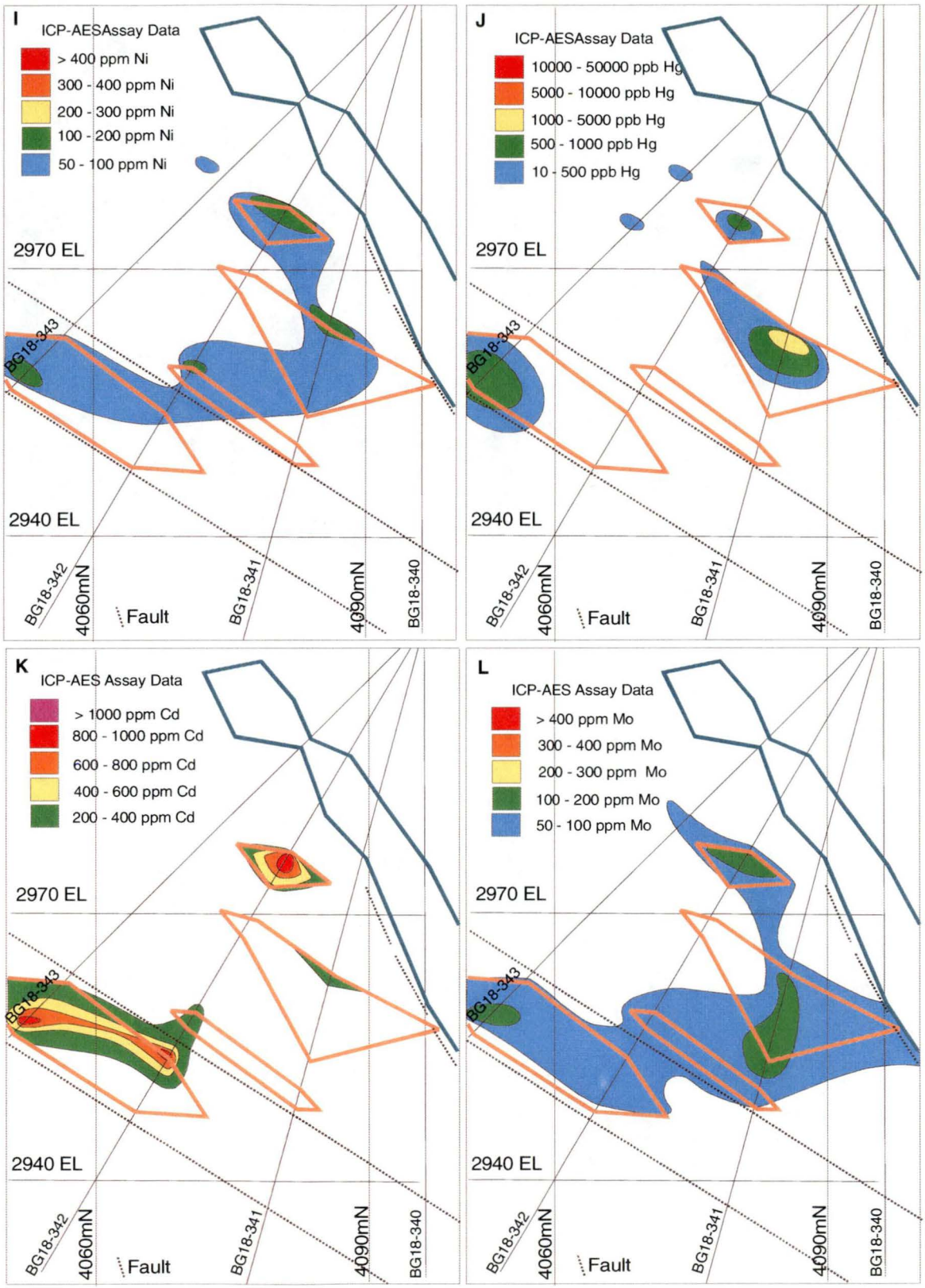

Figure 108continued. Contour plots for 1780mE (I) nickel (J) mercury, (K) cadmium, (L) molybdenum from ICP-AES analysis. Outlines in orange South Trough sub-lenses, green is a mafic dyke.

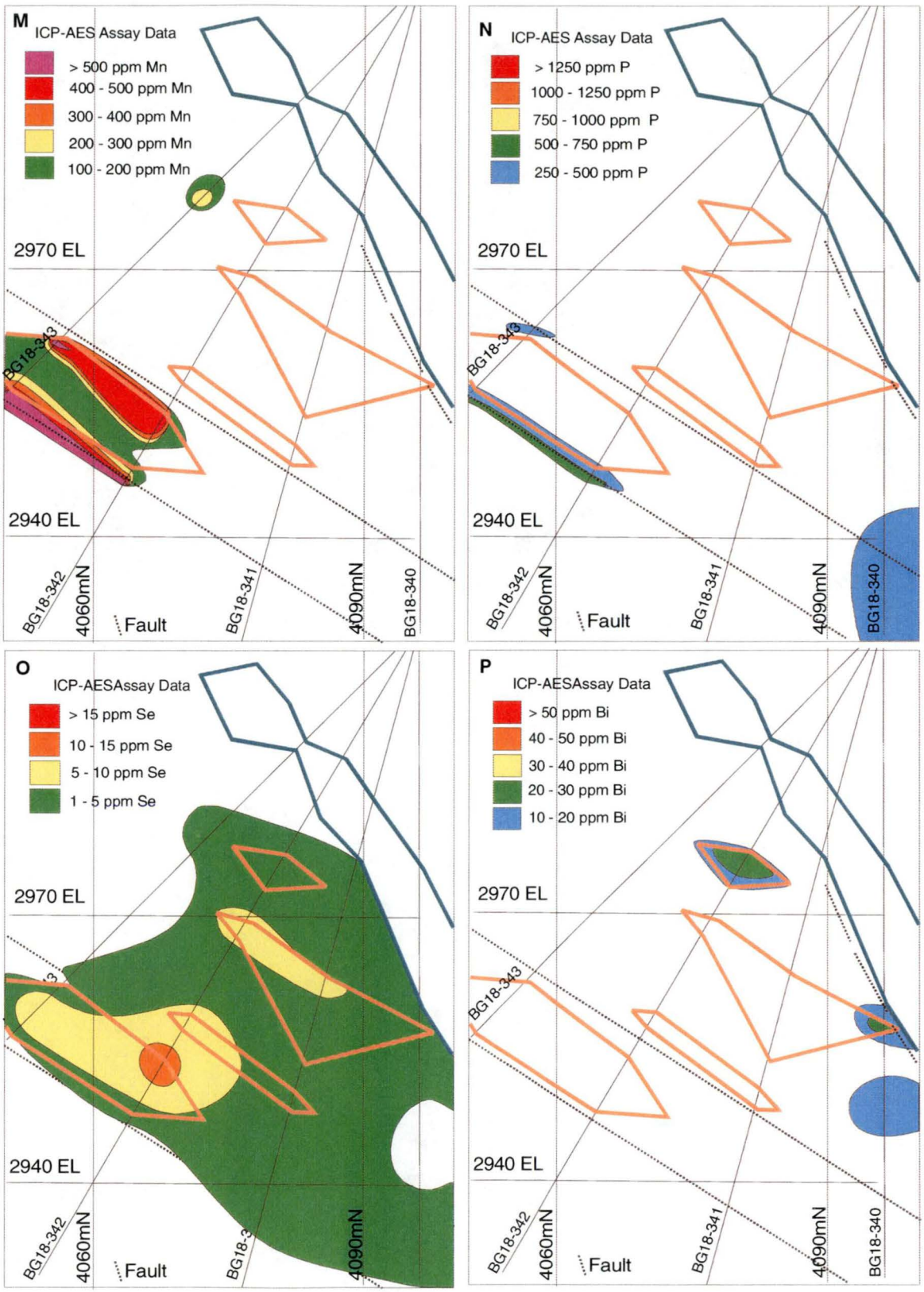

Figure 108continued. Contour plots for 1780mE (M) manganese, (N) phosporus, (O) selenium, (P) bismuth from ICP-AES analysis. Outlines in orange South Trough sub-lenses, green is a mafic dyke.

342 within the upper most sub-lens.

Metal ratios are plotted on Figure 108Q and R. The Zn number is high (>80) within all modelled sub-lenses and in the hangingwall surrounding the upper most sub-lens. In contrast the Cu number is low (<20) in the upper parts of the sub-lenses, and becomes elevated (60-80) toward the base of the sub-lenses with highs (>80) in the footwall.

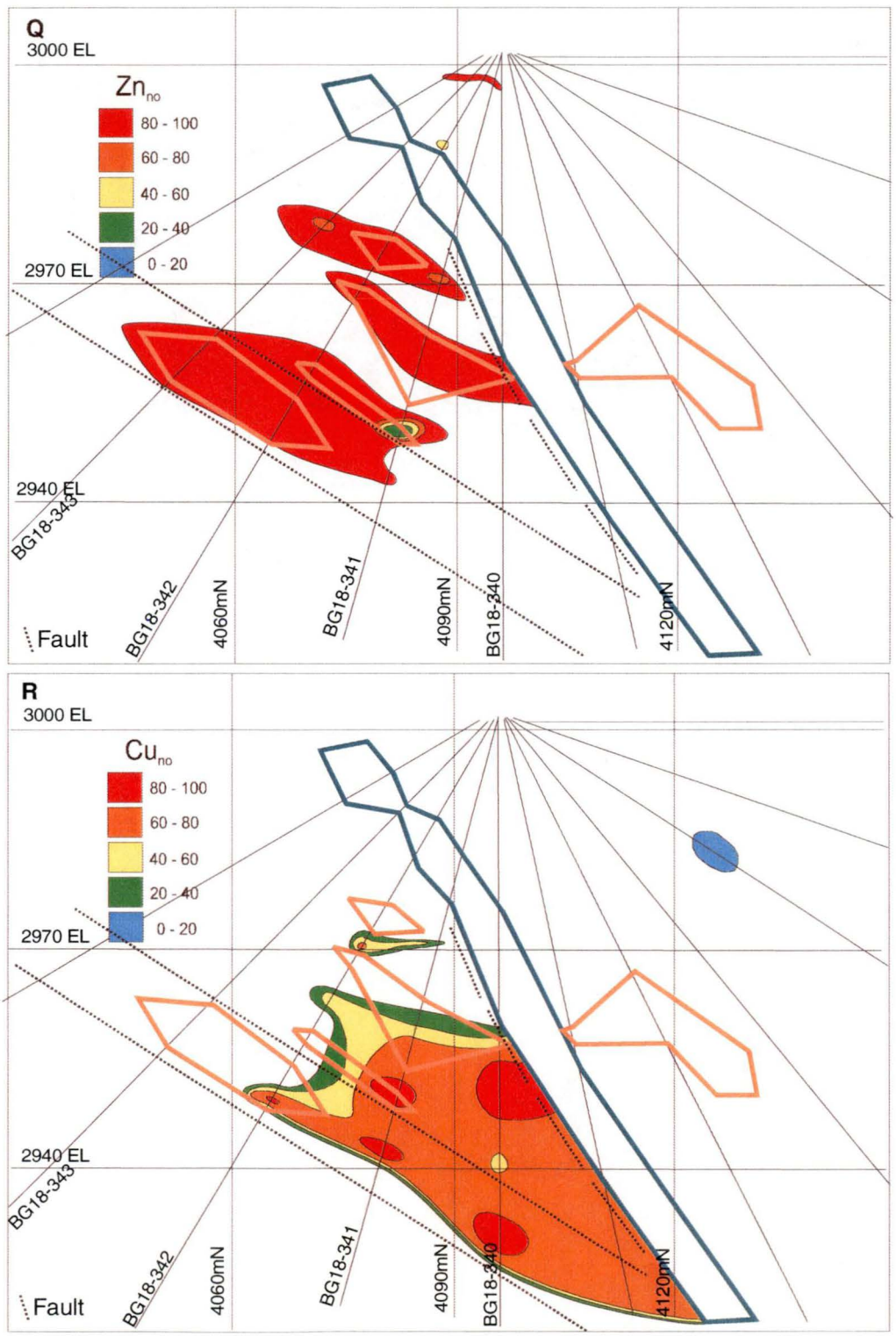

Figure 108continued. Contour plots for 1780mE section. (S) Zn number, (T) Cu number, from mine assay data base. Outlines in orange South Trough sub-lenses, green is a mafic dyke.

1750mE

1750mE section contains the South Trough lens and the base of Battle lens at its eastern most extent. South Trough sub-lenses are defined by drilling on two drill fans. Only one of these fans was available for logging and sampling thus trace element data is restricted. Major and trace element data along with lens outlines generated in DATAMINE™ are shown in Figure 109. Table 35 summarises the assay data for the 1750mE section. Zinc is enriched at the top of South Trough sub-lenses and depleted in the Battle lens footwall (Fig. 109A). Lead and Ba are depleted in the South Trough lens and Battle footwall (Fig. 109B & E). The distribution of Cu (Fig. 109C) underlies the Zn distribution on the northern side of the mafic dyke and is coincident with Zn to the south. Iron is strongly enriched in the South Trough lens occurring toward the base of and between sub-lenses (Fig. 109D). In the Battle lens footwall Fe is enriched directly below the mined ore and forms a halo extending into the Battle lens footwall. The distribution of Au (Fig. 109F) follows that of Cu in the South Trough lens and Battle lens footwall. The distribution of Ag (Fig. 109G), As (Fig. 109H) and Cd (Fig. 109I) overlies the Zn distribution, although Ag and As are also enriched in the hangingwall to the South Trough sub-lenses (Fig. 109G & H). Bismuth follows the distribution of Cu in South Trough, but underlies Fe at the base of the Battle lens (Fig. 109J). Nickel and Mo follow the distribution of Cu (Fig. 109K & L). The distribution of P and Mn (Fig. 109M & N) appear to be random on the 1750mE section with most enrichments occurring in host rocks away from massive sulfide lenses.

Element		Maximum value
Gold	Au	7 g/t
Silver	Ag	75 g/t
Copper	Cu	9.3 %
Lead	Pb	1.8 %
Zinc	Zn	43.4 %
Barium	Ba	7.6 %
Iron	Fe	40.8 %
Arsenic	As	2800 ppm
Cadmium	Cd	910 ppm
Manganese	Mn	3180 ppm
Phosphorus	P	1500 ppm
Molybdenum	Mo	340 ppm
Nickel	Ni	325 ppm
Mercury	Hg	N/A ppb
Bismuth	Bi	100 ppm
Cobalt	Co	35 ppm
Germanium	Ge	N/A ppm
Uranium	U	D/L ppm
Vanadium	V	80 ppm

Table 35. Summary maximum assay values from 1750mE section, South Trough lens.
N/A not analysed, D/L detection limit

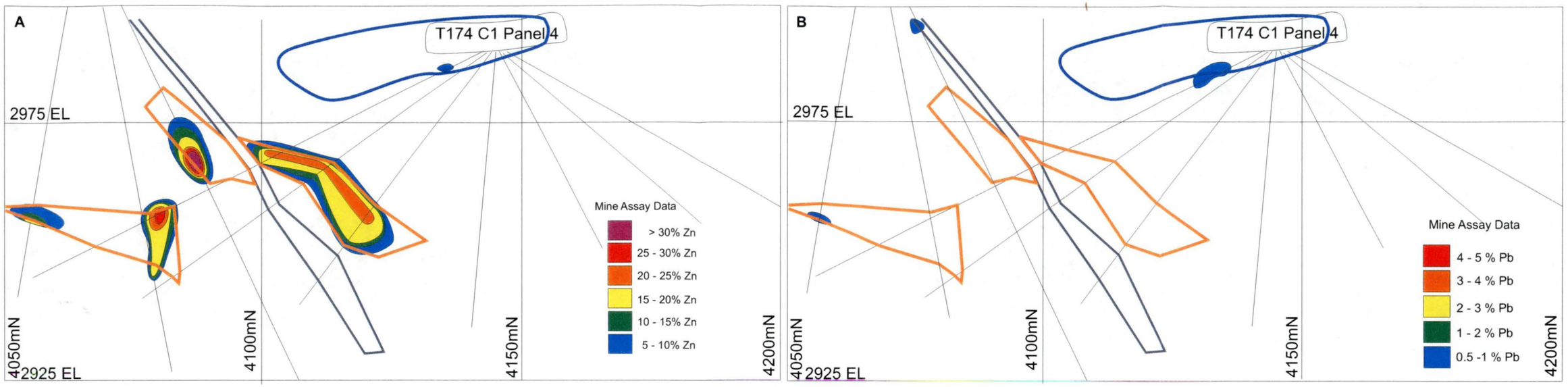

Figure 109 Contour plots for 1750mE section (A) zinc, (B) lead, (C) copper, (D) iron, from mine assay data base. Outlines in orange South Trough sub-lenses, green is a mafic dyke, blue is the Battle lens.

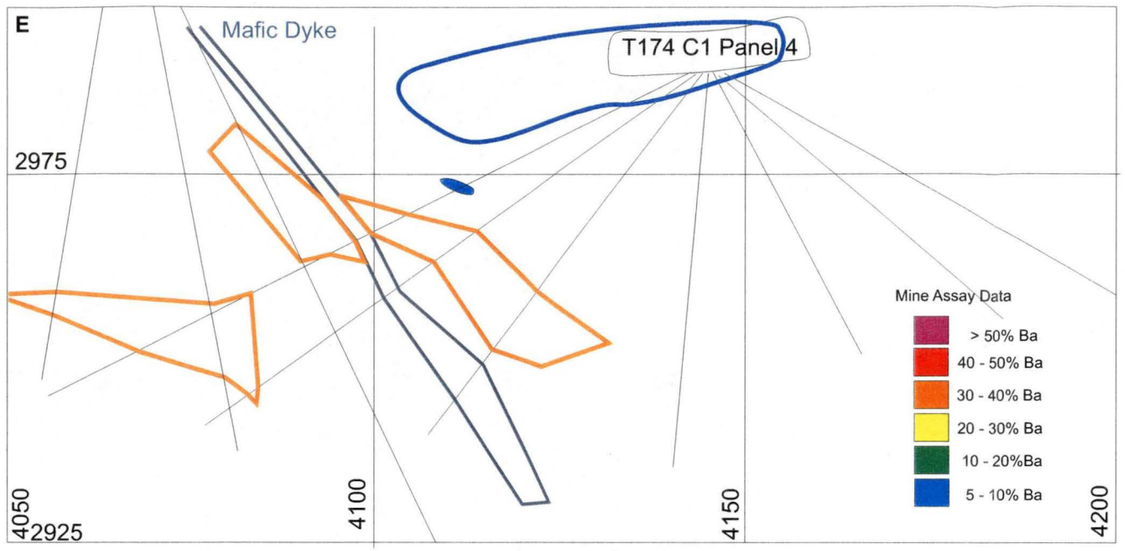

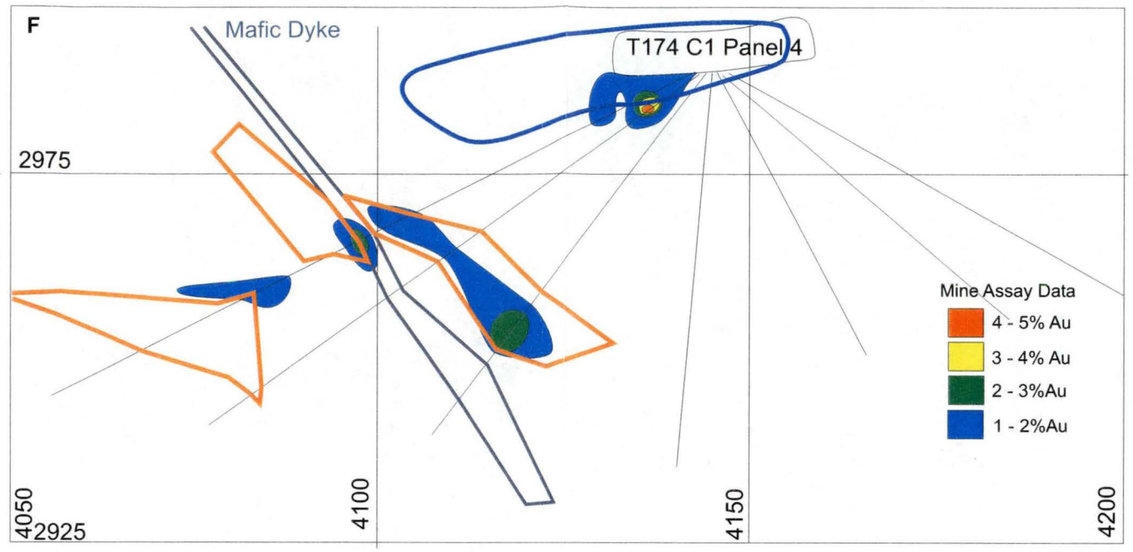

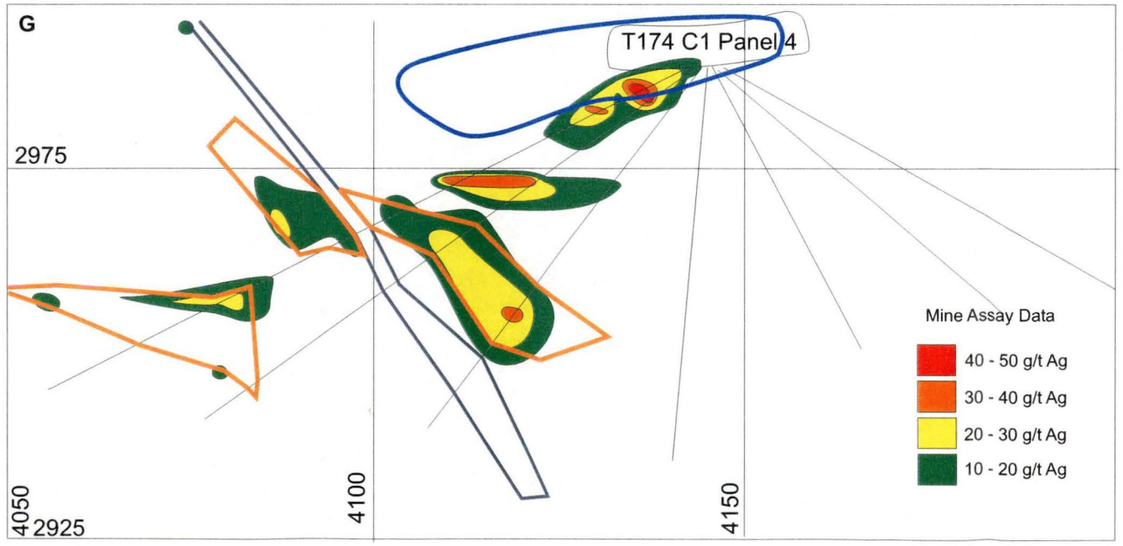

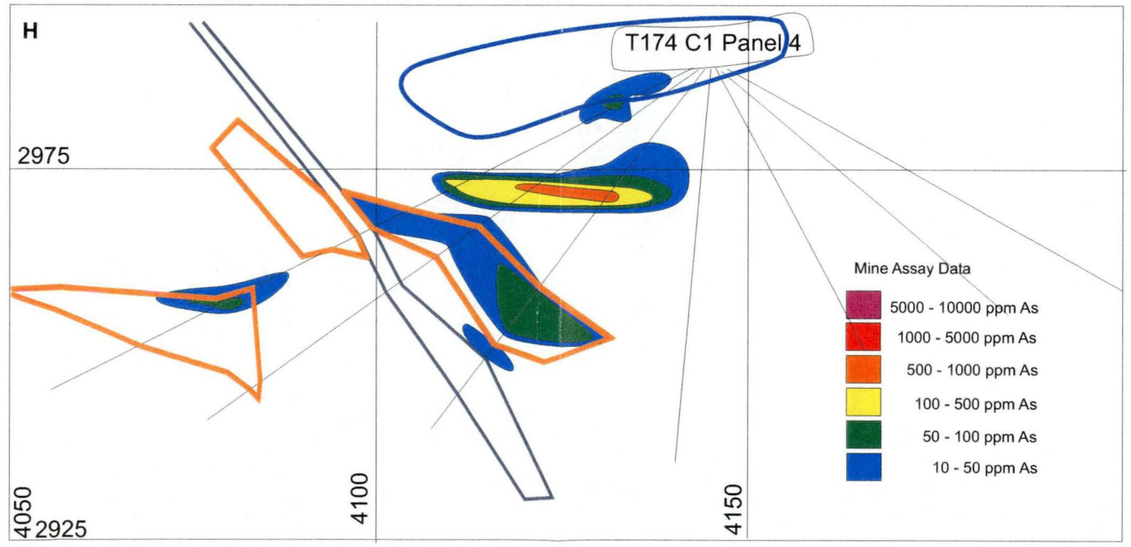

Figure 109continued. Contour plots for 1750mE section (E)barium, (F) gold, (G) silver (H) arsenic, from mine assay data base. Outlines in orange South Trough sub-lenses, green is a mafic dyke, blue is the Battle lens.

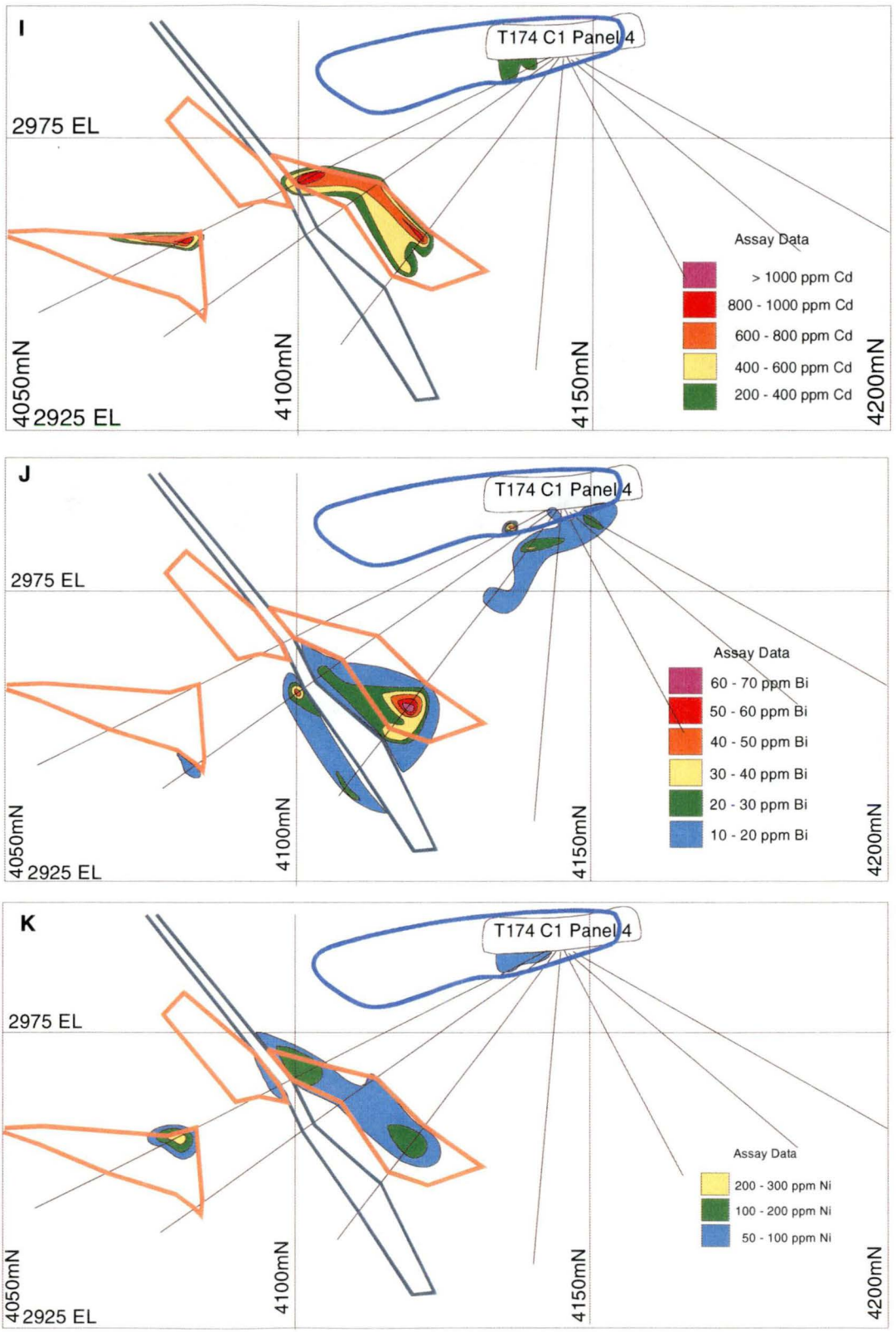

Figure 109continued. Contour plots for 1750mE section (I) cadmium, (J) bismuth, (K) nickel. Outlines in orange South Trough sub-lenses, green is a mafic dyke, blue is the Battle lens.

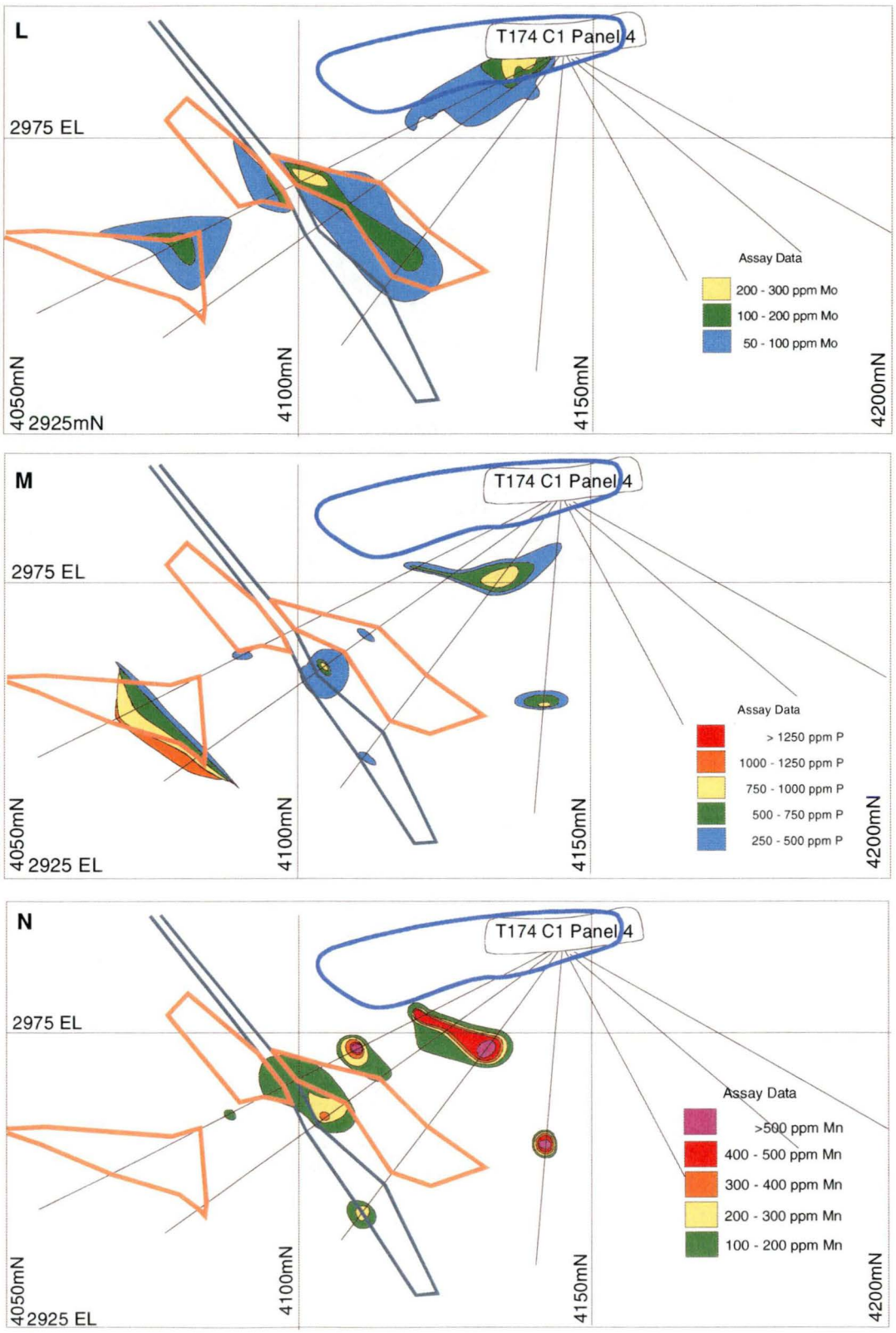

Figure 109continued. Contour plots for 1750mE section (L) molybdenum, (M) phosphorus, (N) manganese. Outlines in orange South Trough sub-lenses, green is a mafic dyke, blue is the Battle lens.

Metal ratios are plotted on Figure 9.4 O and P. The Zn number is high (>80) within all modelled sub-lenses. This high Zn number zone extends into the footwall and the base of the Battle lens overlying the South Trough. The Cu number forms a high below the modelled sub-lenses with lower values (40-60) extending into the base of all sub-lenses. The Cu number also forms a high underlying the Battle lens, while values at the base of the modelled Battle lens are sporadic.

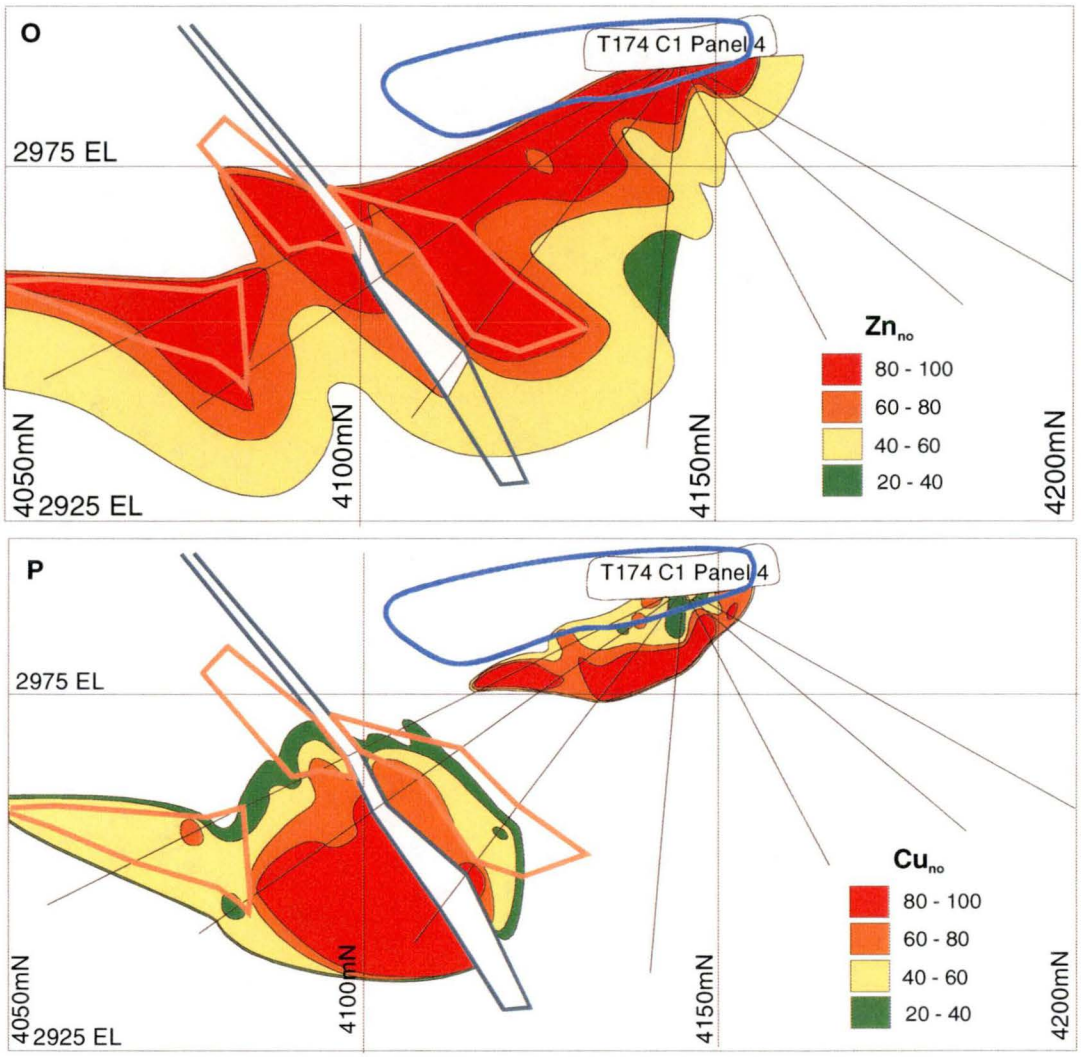

Figure 109continued. Contour plots for 1750mE section (O) Zn number, (P) Cu number, from the mine assay data base. Outlines in orange South Trough sub-lenses, green is a mafic dyke, blue is the Battle lens.

1540mE

The 1540mE section covers the Battle, Gopher and Upper Zone lenses. Major and trace element zonation is shown of Figure 110, and metal values within each lens summarised in Table 36.

Upper Zone lens: Zn forms a high (35%) toward the centre of the Upper Zone lens (Fig. 110A). Lead (Fig. 110B) and Cu (Fig. 110C) values are moderate (2-3%) and form zones coincident with the Zn distribution. Iron underlies the Zn-Cu-Pb zone with spot highs up to 35% and forms a footwall halo to the Upper Zone lens (Fig. 110D). Barium values in the Upper Zone lens are moderate with a zone of 10-20% Ba coincident with Zn-Cu and Pb distribution (Fig. 110E). Gold (Fig 110F) distribution is sporadic in the Upper

Element		Upper Zone lenses	Maximum value Battle lens	Gopher lens
Gold	Au	4 g/t	6 g/t	3 g/t
Silver	Ag	858 g/t	129 g/t	37 g/t
Copper	Cu	3.1 %	6.2 %	8.1 %
Lead	Pb	8.4 %	10.7 %	12.5 %
Zinc	Zn	34.9 %	53.9 %	49.0 %
Barium	Ba	33.4 %	33.6 %	10.4 %
Iron	Fe	34.6 %	34.9 %	40.9 %
Arsenic	As	5540 ppm	1560 ppm	1350 ppm
Cadmium	Cd	20 ppm	>1000 ppm	>1000 ppm
Manganese	Mn	830 ppm	3590 ppm	720 ppm
Phosphorus	P	2000 ppm	1500 ppm	1600 ppm
Molybdenum	Mo	90 ppm	260 ppm	390 ppm
Nickel	Ni	25 ppm	280 ppm	460 ppm
Mercury	Hg	1100 ppb	27000 ppb	7520 ppb
Bismuth	Bi	5 ppm	40 ppm	40 ppm
Cobalt	Co	1 ppm	25 ppm	95 ppm
Germanium	Ge	5 ppm	15 ppm	10 ppm
Selenium	Se	54 ppm	120 ppm	90 ppm
Uranium	U	60 ppm	60 ppm	10 ppm
Vanadium	V	10 ppm	20 ppm	80 ppm

Table 36 Summary maximum assay values from 1540mE section, UpperZone, Battle and Gopher lenses.

Zone lens. Ag, As and Hg (Fig. 110G-I) are all enriched (Table 36) in the Upper Zone lens. Their greatest enrichment corresponds to the Zn-Pb-Cu zone with lesser values extending into the Upper Zone footwall. Cadmium is not as enriched in the Upper Zones as in the underlying lenses (Table 36), however, its distribution follows that of Zn (Fig. 110J). Uranium has some of its highest values (up to 60ppm) in the Upper Zone lens on 1540mE and its distribution is also coincident with the Zn-Cu-Pb distribution in the Upper Zone lens (Fig. 110M). Vanadium was below detection in Upper Zone lens. The distribution of Mn (Fig. 110O), and P (Fig. 110P) show little relation to the distribution of other metals. Molybdenum, Ni, and Bi are all below detection in the Upper Zone lens. The Zn number (Fig. 110T) is extremely high (90-100) throughout the Upper Zone lens, while the Cu number (Fig. 110U) is low (<20).

Battle lens: In the Battle lens Zn is strongly enriched (up to 54%) in the central portion of the lens around 4150mN, and a halo of Zn >5% extends along the width of the Battle lens (Fig. 110A). Lead distribution is highest at the top of the Battle lens directly overlying the Zn high (Fig. 110B). However Pb values are generally low (2-3%) with spot highs up to 10.7%. Copper also forms a high of 4-5% coincident with the Zn high, and has a >2% halo extending the width of the Battle lens, underlying the Zn halo (Fig. 110C). Iron has its highest values either side of the Zn-Cu high with a >10% iron halo extending the width of the Battle lens coincident with the Cu halo (Fig. 110D). Barium values up to 34% occur at the top of the Battle lens. However when contoured these spot Ba highs are below the 5% cut off used in the contouring indicating overall Ba content of Battle lens is low (<5%). Gold distribution (Fig. 110F) is erratic in the

Battle lens with spot highs (2-4 g/t) occurring at the top of the lens and in the Cu-Fe rich basal portion of the lens. Silver forms a broad, but low halo of through out the Battle lens and immediate hanging wall (Fig. 110G). Arsenic (Fig. 110H) is concentrated up to 1560ppm at the top of the Battle lens overlying the distribution of zinc. Mercury also occurs concentrated at the top of the Battle lens overlying the central Zn-Cu high (Fig. 110I). Cadmium distribution in the Battle lens reflects the distribution of zinc with values >100ppm (upper detection limit for Cd; Fig. 110J). Uranium shows a very unusual distribution in the Battle lens on 1540mE section with highs up to 60 ppm seemingly unrelated to distribution of other elements (Fig. 110K). Vanadium contents are low (up to 20 ppm) in the Battle lens but below detection when modelled (Fig. 110L). Manganese is enriched in the sediments overlying the Battle lens (Fig. 110M). Phosphorus values are below detection when contoured in the battle lens although spot highs of up to 1500ppm do occur (Table 36). Molybdenum and Ni (Fig. 110O & P) occur in the central portion of the Battle lens coincident with the Cu distribution. Bismuth distribution is sporadic within the Battle lens with highs up to 40ppm (Fig. 110Q) Germanium is below detection when contoured, however spot values are consistent along the top of the Battle lens (Fig. 110R). The Zn number (Fig. 110S) is high (>90) throughout the Battle lens and closely follows the distribution of Zn. In contrast the Cu number (Fig. 110T) forms highs underlying the Zn number distribution. The Cu number highs correspond to the distribution of Fe in the Battle lens.

Gopher lens: Zinc highs of up to 49% occur toward the base of the Gopher lens just above the keel region (Fig. 110A). A halo of >5% Zn extends away from this high toward the southern portion of the modelled lens. Lead forms a high coincident with the Zn high (Fig. 110B). Copper underlies the Zn high in the keel region of the Gopher lens (Fig. 110C), with elevated Cu values (>2%) extending into the footwall. Iron occurs in the basal keel region of the Gopher lens with the highest values (up to 40.9%) occurring outside the modelled lens to the north (Fig. 110D). Barium contents in the Gopher lens are below detection when modelled. Gold occurs at the top of the Gopher lens overlying the Zn high (Fig. 110F) Silver forms a broad halo of (10-50 g/t Ag) toward the top and northern margin of the Gopher lens (Fig. 110G). Arsenic occurs at the top and southern margin of the Gopher lens with highest values (up to 1350ppm) occurring around the southern margin of the modelled lens (Fig. 110H). Mercury distribution, although sporadic, is concentrated around the southern margin of the Gopher lens suggesting an association with As (Fig. 110I). Cadmium shows a strong association with the Zn high, but does not reflect the Zn halo (Fig. 110J). Uranium is below detection in the Gopher lens (Table 36). A spot high of 80ppm V occurs toward the top of the Gopher lens (Fig. 110L). Manganese is highest at the top and southern portion of the Gopher lens similar to As (Fig. 110M). The distribution of P is erratic in the Gopher lens, showing little relation to other elements (Fig. 110N). Molybdenum and Ni (Fig. 110O & P) show a strong association with Zn and Cd in Gopher lens, while Bi is erratic and shows little relation to other elements in the Gopher lens (Fig. 110Q). The Zn number (Fig. 110S) forms an unusual pattern in the Gopher lens with elongate highs (>90) running parallel to the underlying flat fault, through the middle of the Gopher lens and at the top to overlying the lens. The Cu number (Fig. 110T) is moderate (40-60) at the base of the Gopher lens with the highest values occurring outside the modelled lens to the north, consistent with the distribution of Fe in the Gopher lens.

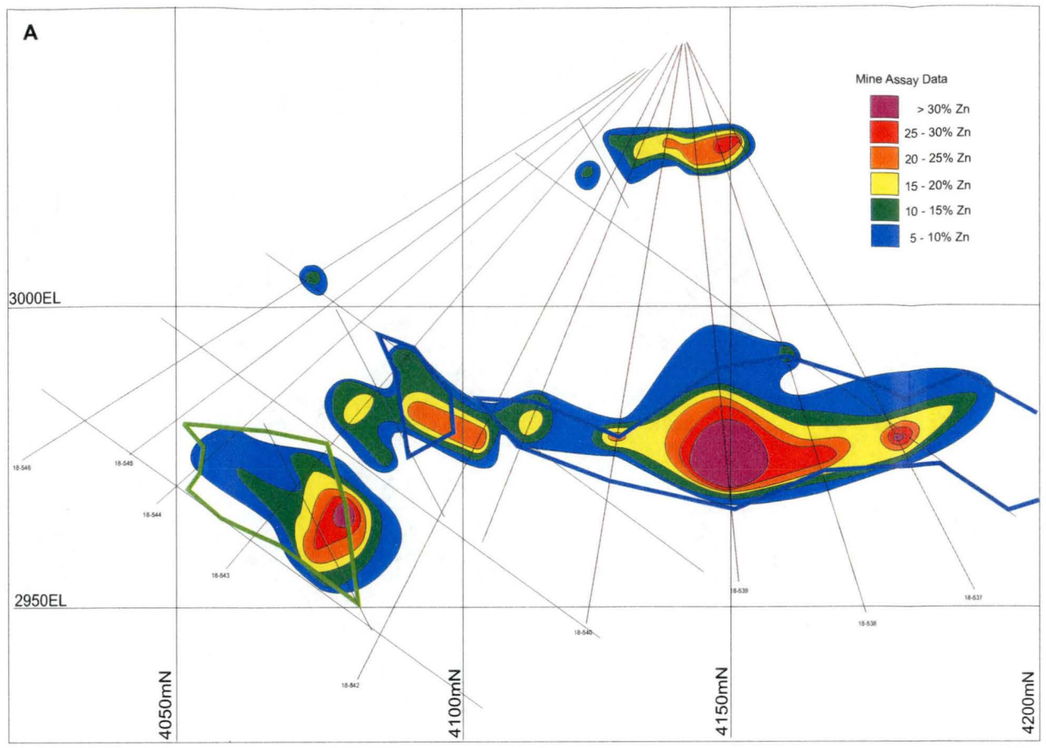

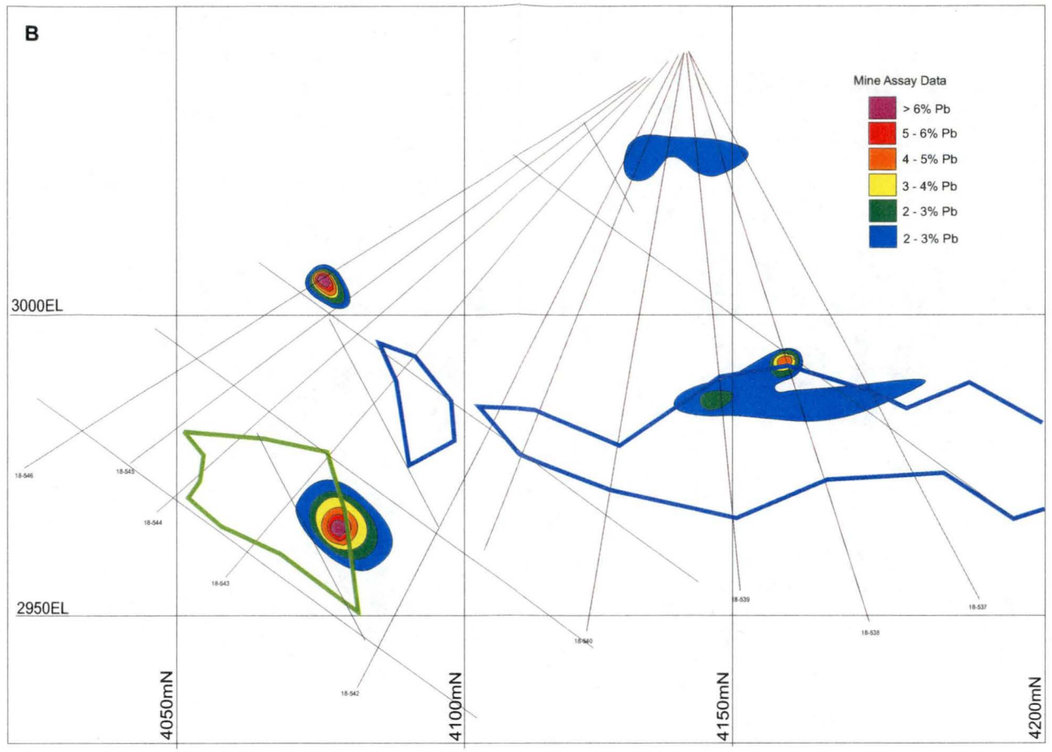

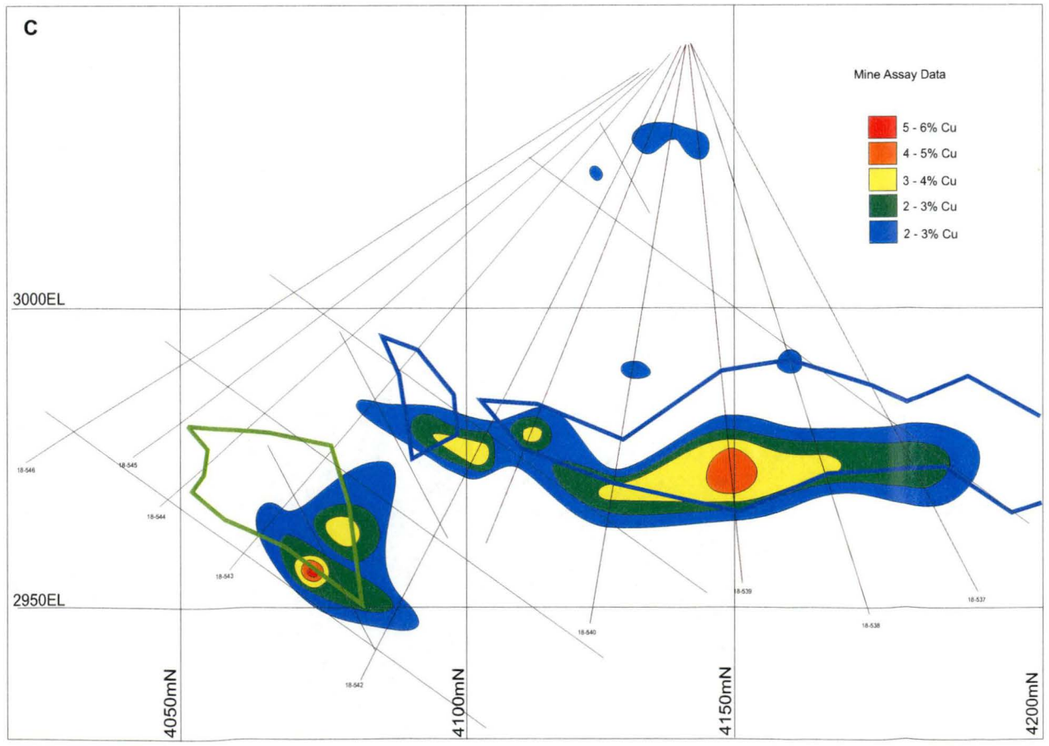

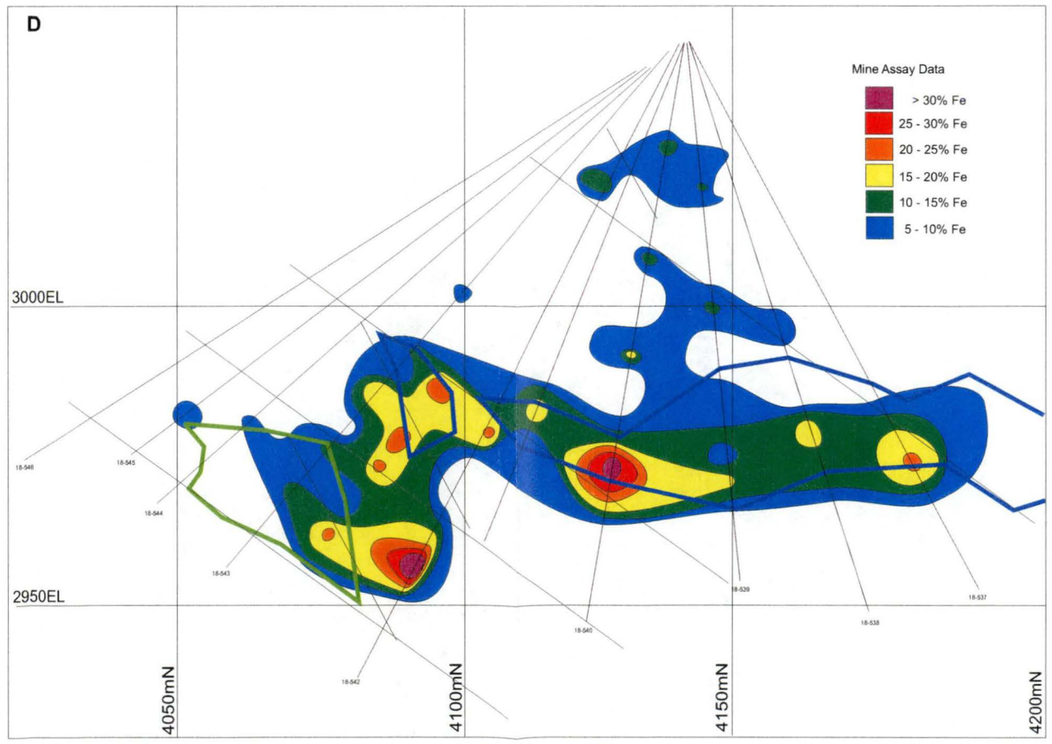

Figure 110 Contour plots for 1540mE section. (A) zinc, (B) lead, (C) copper, (D) iron, from mine assay data base. Outlines in green Gopher lens, blue- Battle lens, Upper Zone lens not modelled.

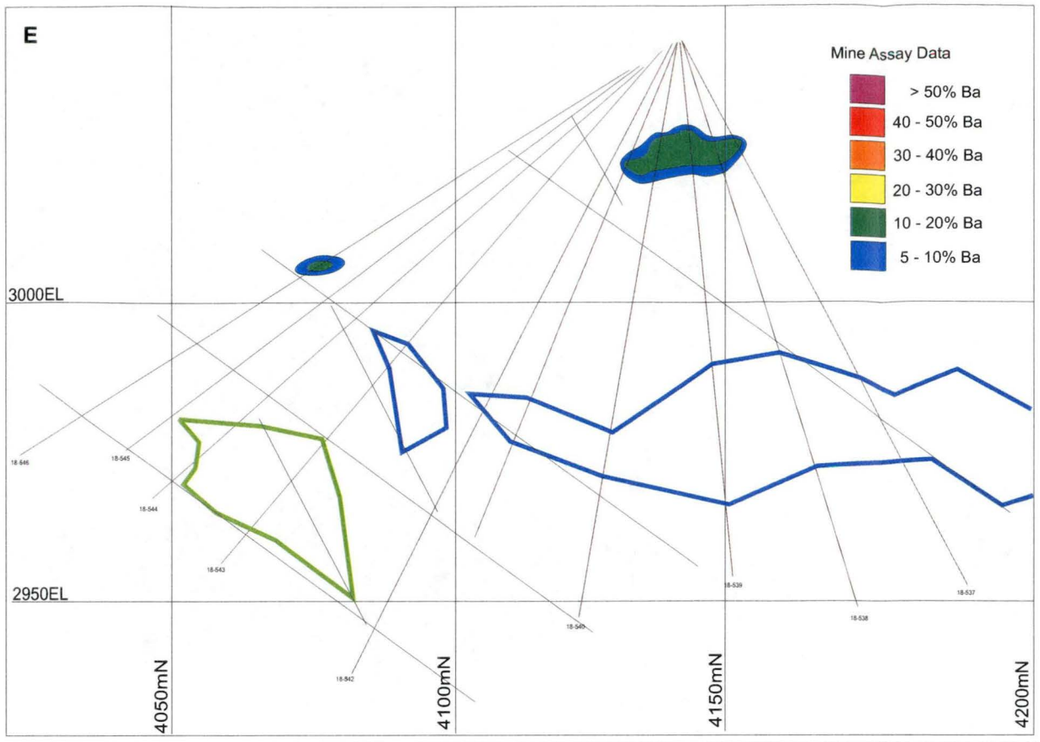

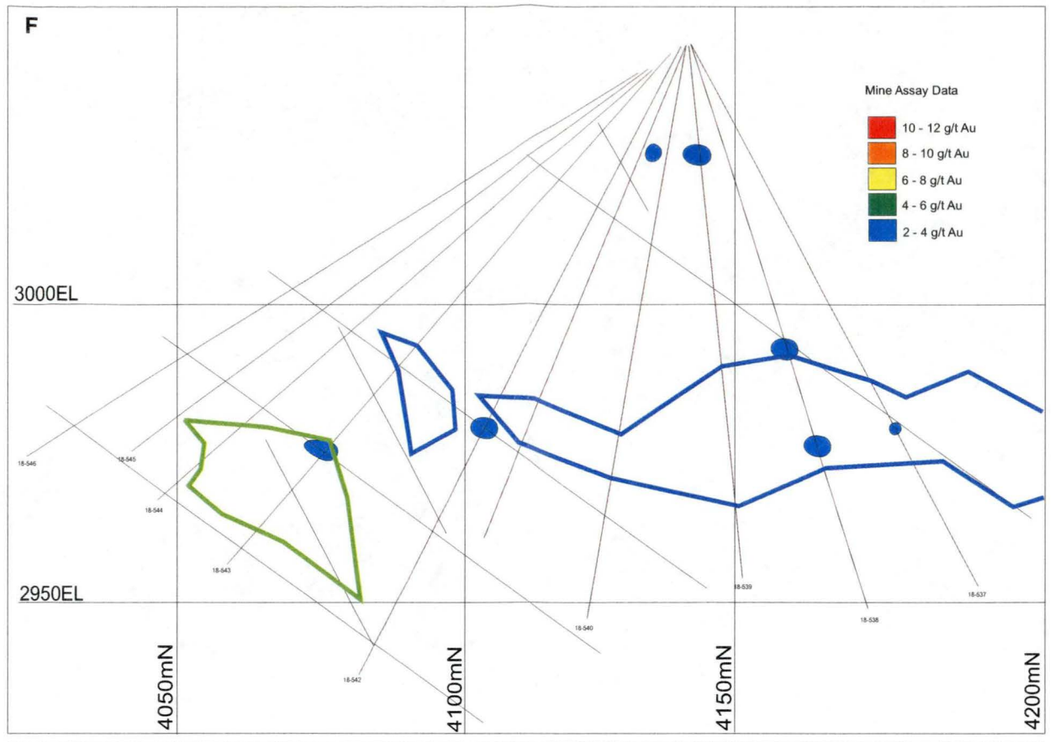

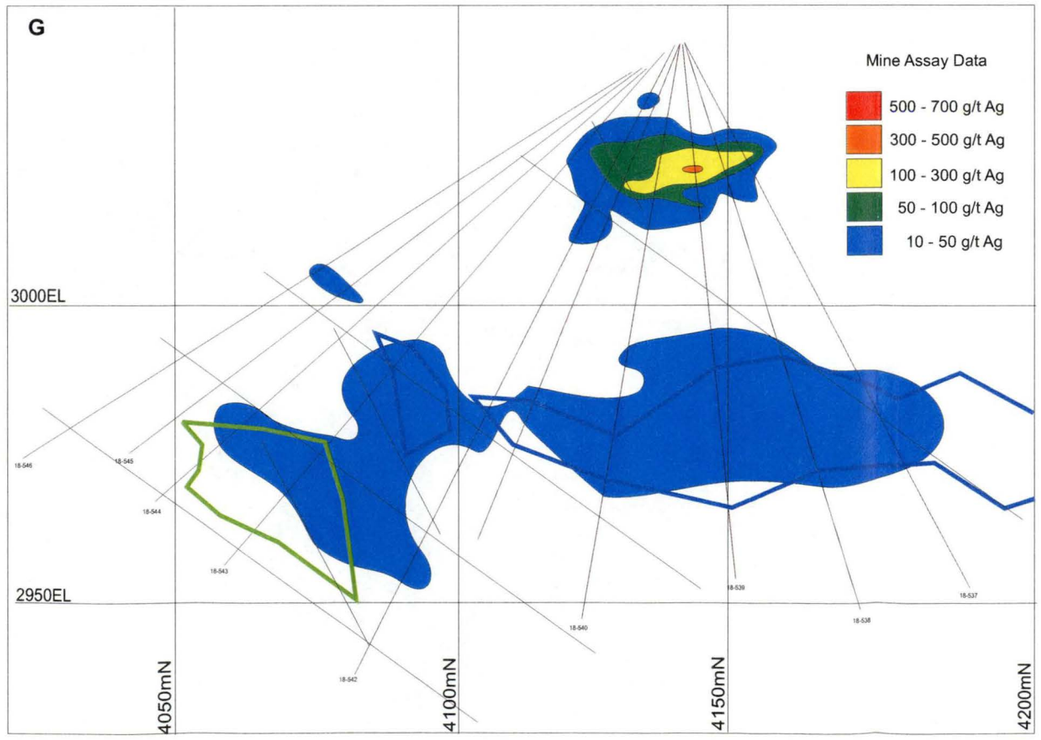

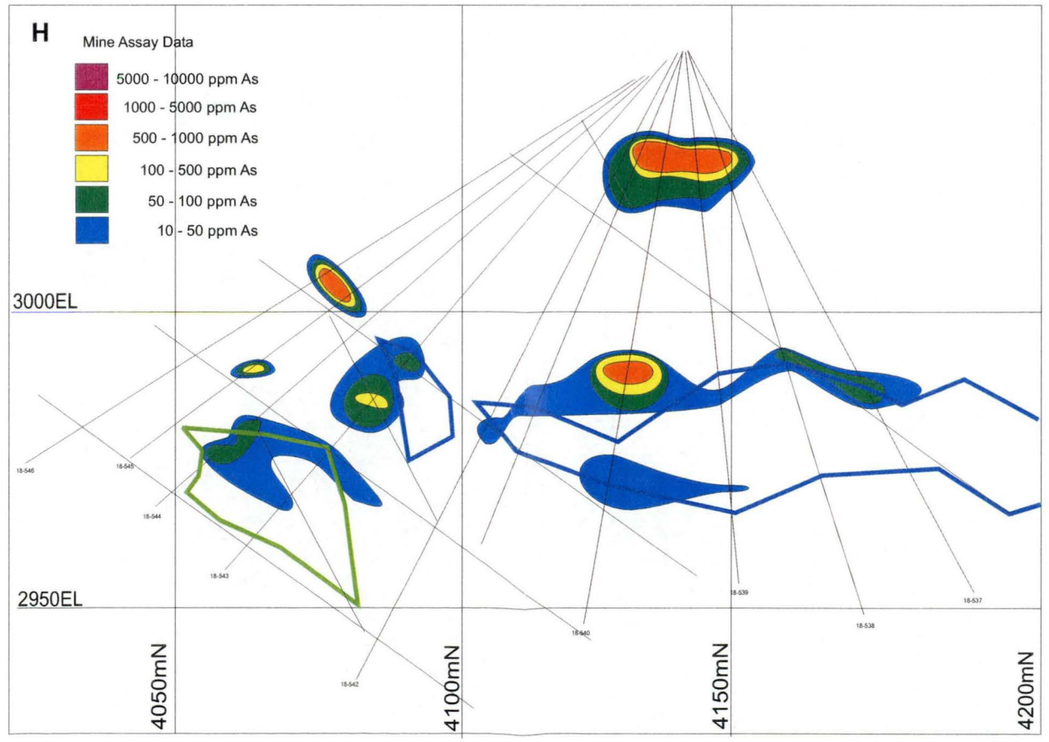

Figure 110 continued Contour plots for 1540mE section. (E) Barium, (F) gold, (G) silver, (H) arsenic, from mine assay data base Outlines in green Gopher lens, blue Battle lens, Upper Zone lens not modeled

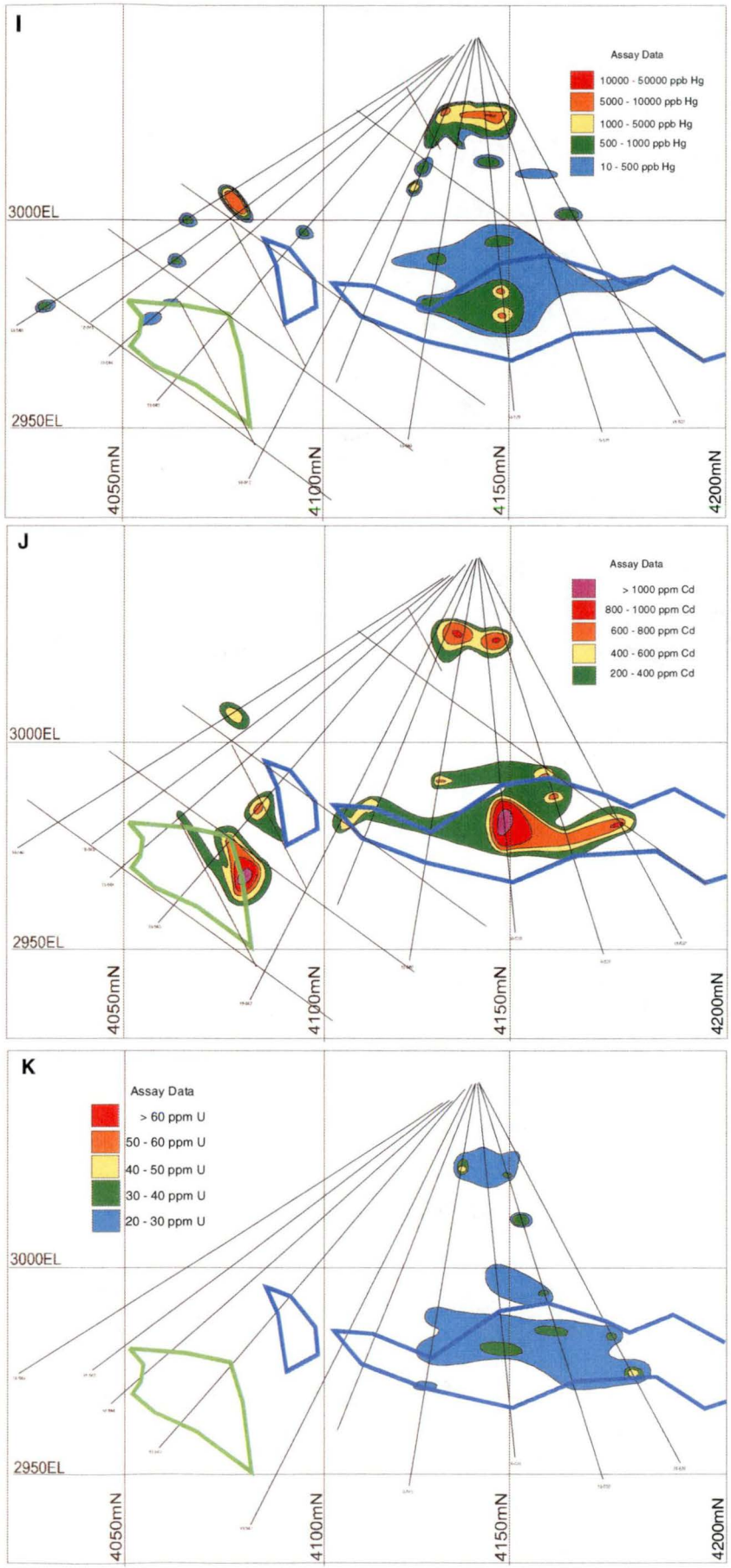

Figure 110continued. Contour plots for 1540mE section. (I) mercury, (J) cadmium, (K) uranium. Outlines in green Gopher lens, blue Battle lens, Upper Zone lens not modelled

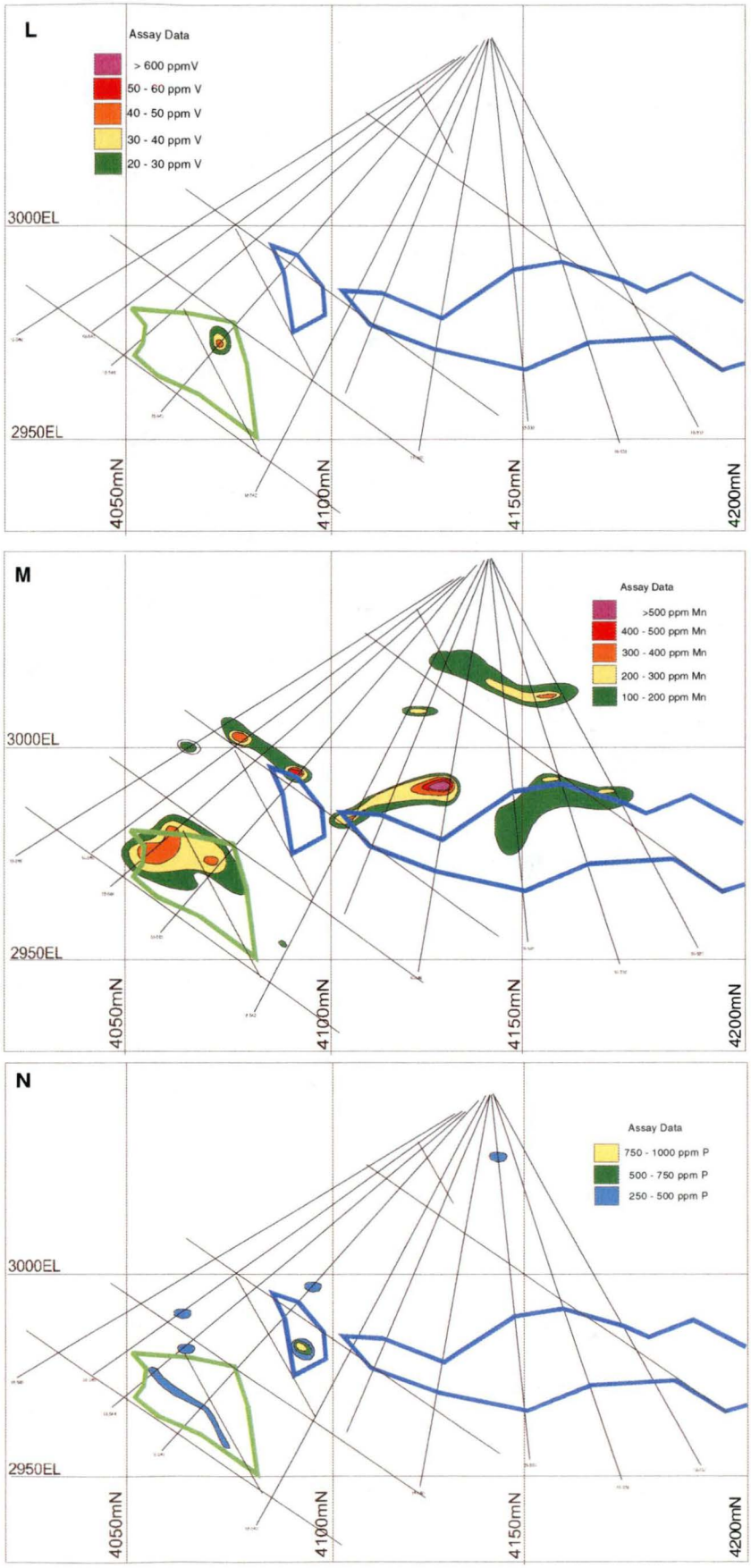

Figure 110 continued. Contour plots for 1540mE section. (L) vanadium, (M) manganese, (N) phosphorus. Outlines in green Gopher lens, blue Battle lens, Upper Zone lens not modelled.

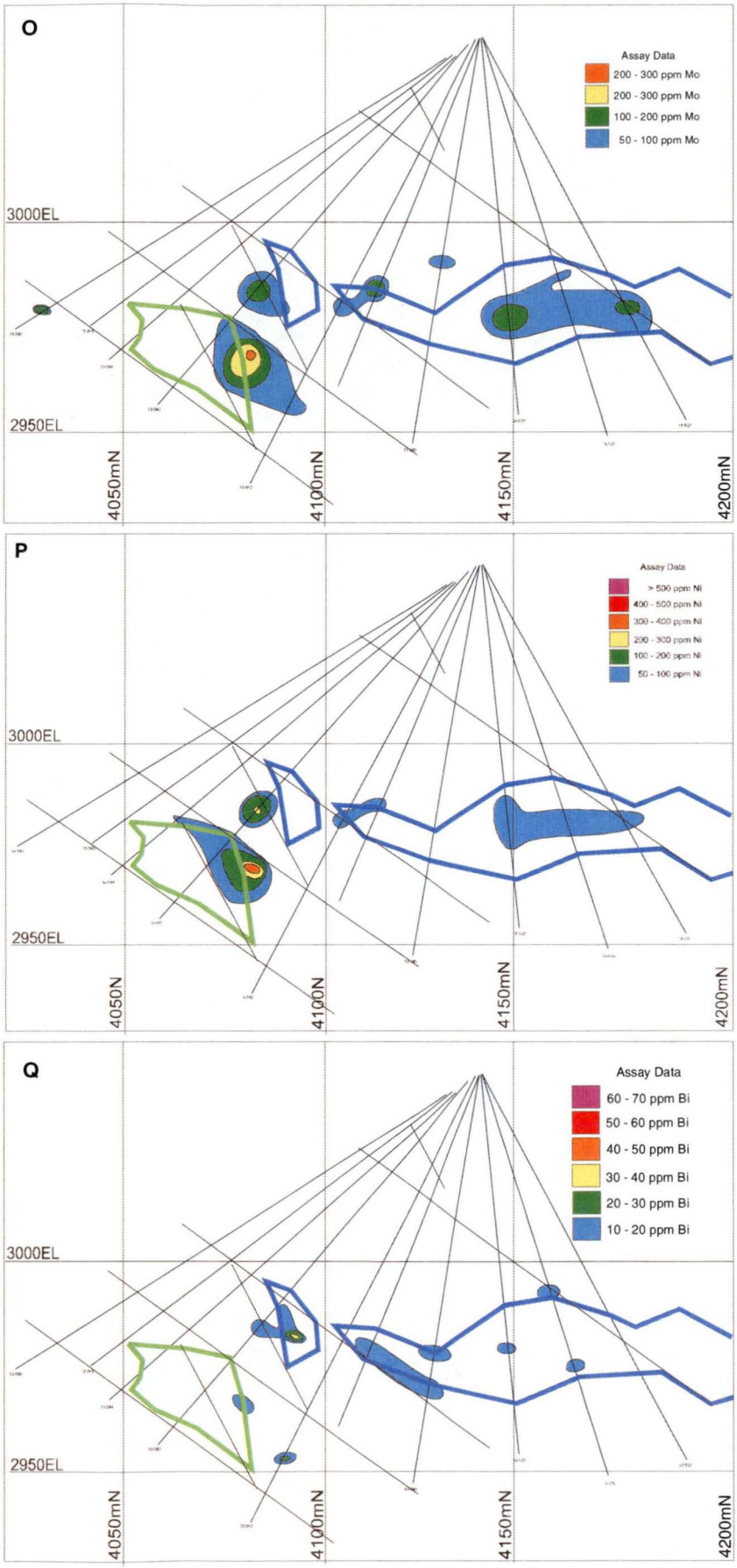

Figure 110continued. Contour plots for 1540mE section. (O) molybdenum, (P) nickel, (Q) bismuth. Outlines in green Gopher lens, blue Battle lens, Upper Zone lens not modelled.

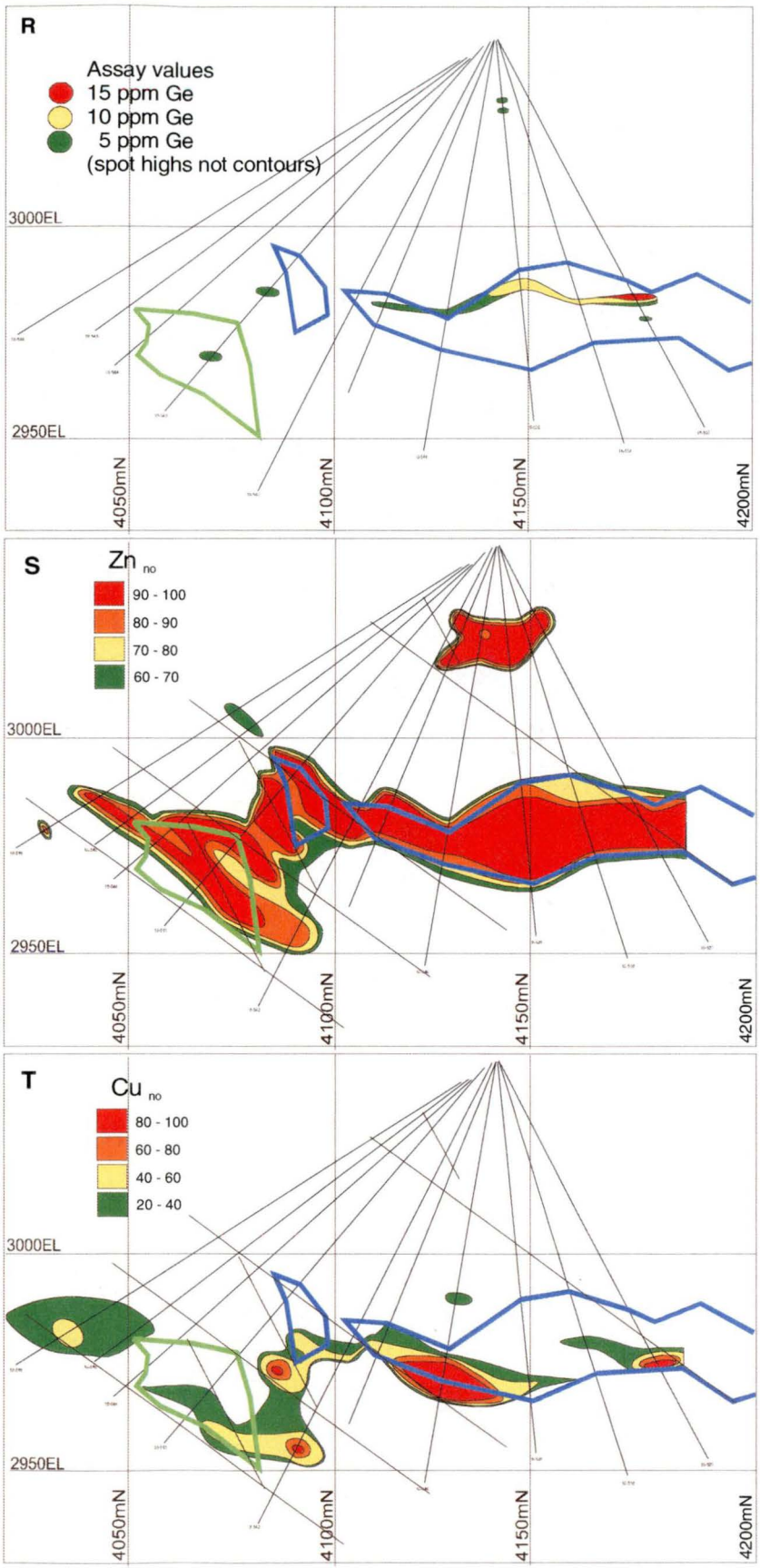

Figure 110continued. Contour plots for 1540mE section. (R) germanium, (S) Zn number, (T) Cu number . Outlines in green Gopher lens, blue Battle lens, Upper Zone lens not modelled.

1420 Section

1420 section covers the Battle, Gopher, Upper Zone and Gap lenses. Major and trace element data are shown on Figure 111 (Battle, Gopher and Upper Zone lenses), and Figure 112 (Gap lens) and summarised in Table 37 (Battle, Gopher and Upper Zone lenses) and Table 38 (Gap lens).

Element		Upper Zone lenses	Maximum value Battle lens	Gopher lens
Gold	Au	42 g/t	6 g/t	51 g/t
Silver	Ag	1367 g/t	160 g/t	117 g/t
Copper	Cu	4.2 %	9.0 %	4.6 %
Lead	Pb	13.0 %	6.7 %	7.5 %
Zinc	Zn	46.7 %	48 3 %	44.6 %
Barium	Ba	26.8 %	28.0 %	0.8 %
Iron	Fe	36.2 %	36.4 %	35.1 %
Arsenic	As	9860 ppm	4090 ppm	6700 ppm
Cadmium	Cd	>1000 ppm	>1000 ppm	>1000 ppm
Manganese	Mn	2910 ppm	6410 ppm	780 ppm
Phosphorus	P	300 ppm	500 ppm	3600 ppm
Molybdenum	Mo	70 ppm	415 ppm	245 ppm
Nickel	Ni	50 ppm	365 ppm	320 ppm
Mercury	Hg	27500 ppb	22800 ppb	7070 ppb
Bismuth	Bi	60 ppm	90 ppm	60 ppm
Cobalt	Co	35 ppm	20 ppm	25 ppm
Germanium	Ge	N/A	N/A	N/A
Selenium	Se	7.4 ppm	19.4 ppm	10.2 ppm
Uranium	U	B/D	B/D	B/D
Vanadium	V	10 ppm	80 ppm	10 ppm

Table 37. Summary maximum assay values from 1420mE section through the Upper Zone, Battle and Gopher lenses. N/A not analysed, B/D below detection.

Upper Zone lenses: shown on 1420mE section have moderate Zn (5-15%) defining the modelled lens outlines (Fig. 111A). Lead grades reach maximum values of 13% in the southern most Upper Zone lens. Copper grades are generally low and Fe occurs offset from the Zn highs (Fig. 111C & D). Barium and Au also show highs in the southern most lens but are low within the other Upper Zone lenses (Fig. 111E &F) Silver, As and Hg are notable enriched in the Upper Zone lenses (Table 37 and Fig. 111G-I). Arsenic and Hg (where measured) follow the distribution of zinc, however maximum Ag grades are offset from the Zn highs. Cadmium (Fig. 111J) shows maximum grades of >1000ppm and closely follows the distribution of Zn. All other elements (Mn, P, Mo, Ni, Bi, V and Co) show little in the way of consistent patterns in the Upper Zone lenses (Fig. 111K-Q). The Zn number (Fig. 111R) is high (>80) through out the Upper Zone lenses with extreme values (>90) occurring toward the top of one lens. In contrast the Cu number (Fig. 111S) is low (<40) throughout the Upper Zone lenses.

Battle lens: The Battle lens has high (up to 48%) Zn content at the centre of the lens in the region 4160-4180mN, with smaller highs to north and south (Fig. 111A). Lead is sporadically distributed in the Battle lens occurring mainly to the south and above the Zn highs (Fig. 111B). Copper also occurs predominantly toward the south in the Battle lens with highs >3% nestled between the Zn highs (Fig. 111C). In contrast Fe is concentrated in the northern portion of the Battle lens with maximum values (36%) occurring below and slightly off set toward the north of the central Zn maxima (Fig. 111D). Barium and Au (Fig. 111E & F) are low in the Battle lens and situated at the top of the lens Silver is low (Table 9.4) but evenly distributed at the top of the Battle lens (Fig. 111G). Maximum As values (up to 4090ppm) occur predominantly toward the southern margin of the Battle lens overlying Zn highs (Fig. 111H). Lower As values (10-50ppm) are more sporadic from the base to the top of the Battle lens. Mercury was only measured along the southern portion of the Battle lens where it forms a halo overlapping the distribution of Ag and As (Fig. 111I). Cadmium closely follows the distribution of Zn with a central Cd high (>100ppm) overlapping the central Zn high (Fig. 111J). Manganese, P, Ni and Bi are all elevated in the immediate hangingwall to the Battle lens, but not in the areas covered by Ag, Pb and As (Fig. 111K, L, N &). Molybdenum also follows the Zn-Cd distribution although shows much lower values (50-100ppm; Fig. 111M). Vanadium show spot highs (up to 80 ppm) overlying the Battle lens (Fig. 111P). Cobalt is erratically distributed along the footwall and hangingwall of the Battle lens (Fig. 111Q) The Zn number (Fig. 111R) is high (80-90) throughout the middle to upper portion of the Battle lens consistent with the distribution of Zn. High Cu number (60-100; Fig. 111S) underlie the high Zn number values and is coincident with the distribution of Fe.

Gopher lens: Contoured Zn values are moderate (5-20%) in the Gopher lens although the distribution of Zn appears patchy due to the orientation of drill holes (Fig. 111A). Contoured Pb values in the Gopher lens are below 2%, however spot highs up to 7.5% Pb are recorded. Copper values show an unusual distribution in the 1420 Gopher lens, the lower ore outline encloses a 2-3% Cu enrichment however Cu enrichment in the main portion of the Gopher lens occurs on the hangingwall side of the lens (Fig. 111C). Iron forms an extreme high underlying the Gopher lens with values consistently >30%. Iron values from 5-15% occur through out the Gopher lens (Fig. 111D). Barium is extremely low in the Gopher lens with a maximum value of only 0.8%. Gold is sporadic in distribution with highs up to 51 g/t (Table 37, Fig. 111F). Silver content is low (5-50 g/t) but evenly distributed through out the Gopher lens (Fig. 111G). Arsenic shows low values (10-50 ppm) evenly distributed through out the Gopher lens, with higher 50-100 ppm values occurring within the Datamine™ modelled outlines (Fig. 111H). The highest As value occurs at the top of the Gopher lens above the modelled ore outline. Mercury content of the Gopher lens is low and sporadically distributed (Fig. 111I). Cadmium distribution compares well with the distribution of Zn (Fig. 111J). The distribution of Mn, and P show little relation to modelled Gopher lens (Fig. 111K & L). The distribution of Mo, Ni and Bi show sporadic highs (ref table 37) within the Gopher lens (Fig. 111M to O). Vanadium is below detection in the Gopher lens (Table 37). Cobalt shows enrichment along the footwall of the Gopher lens (Fig. 111Q). The Zn number (Fig. 111R) is high toward the top of the Gopher lens, however in the Gopher lens the Zn number high (>80) shows a much wider distribution than the Zn number in the Battle lens. The Cu number distribution closely follows the distribution of Fe in the Gopher lens (Fig.

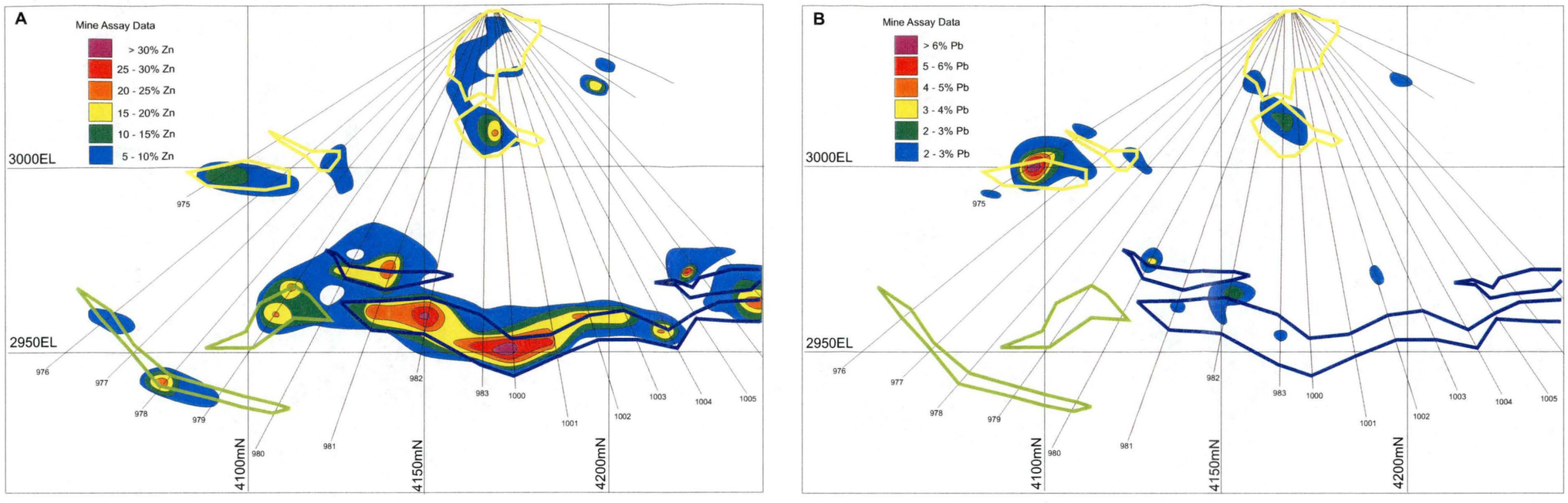

Figure 111. Contour plots for 1420mE section. (A) zinc, (B) lead, (C) copper, (D) iron, from mine assay data base. Outlines in green Gopher lens, blue Battle lens, yellow Upper Zone lenses

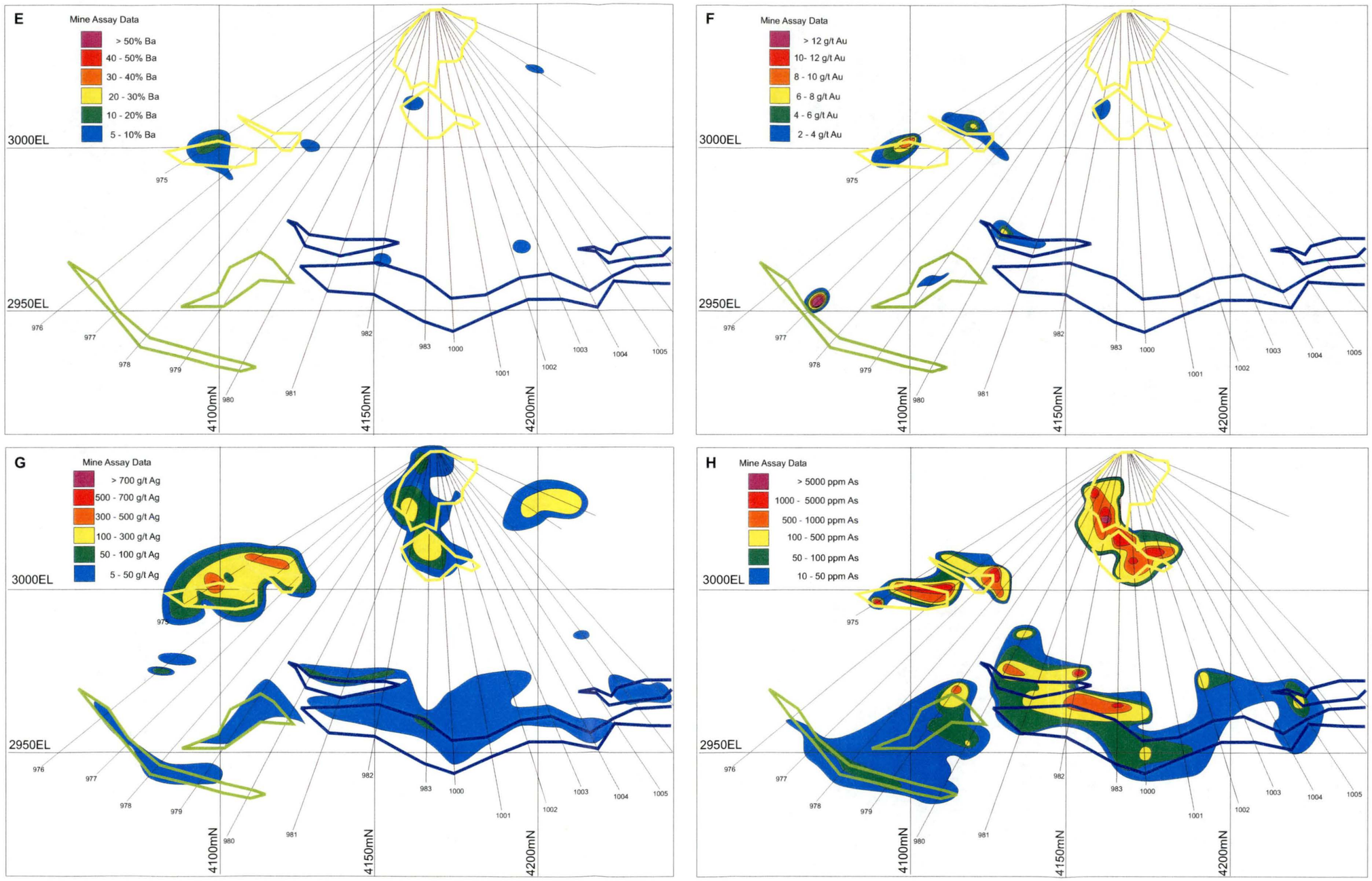

Figure 111continued Contour plots for 1420mE section. (E) barium, (F) gold, (G) silver, (H) arsenic, from mine assay data base. Outline in blue Battle lens, green Gopher lens, yellow Upper Zone lenses.

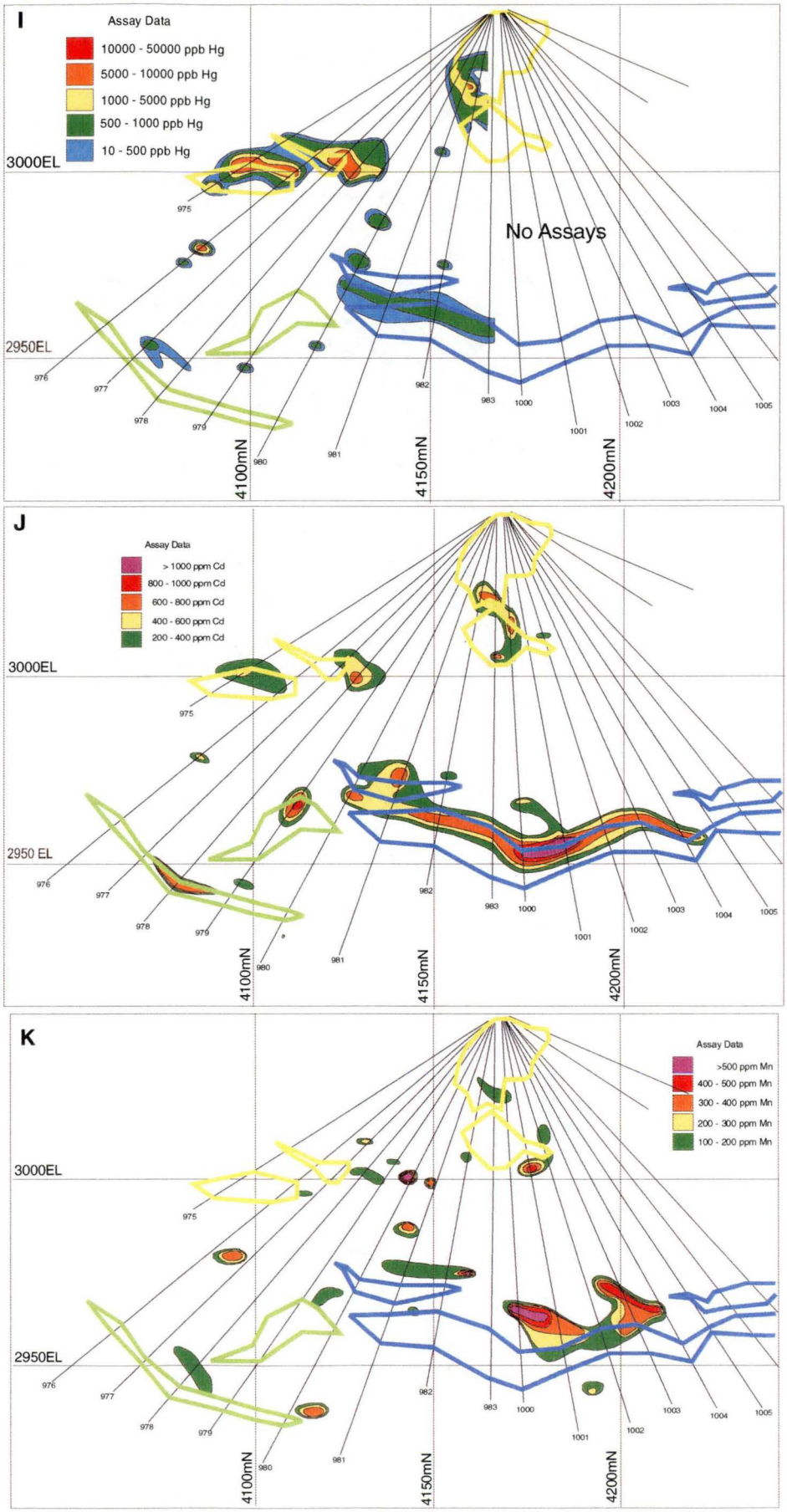

Figure 111continued Contour plots for 1420mE section. (I) mercury, (J) cadmium, (K) manganese. Outline in blue Battle lens, green Gopher lens, yellow Upper Zone lenses.

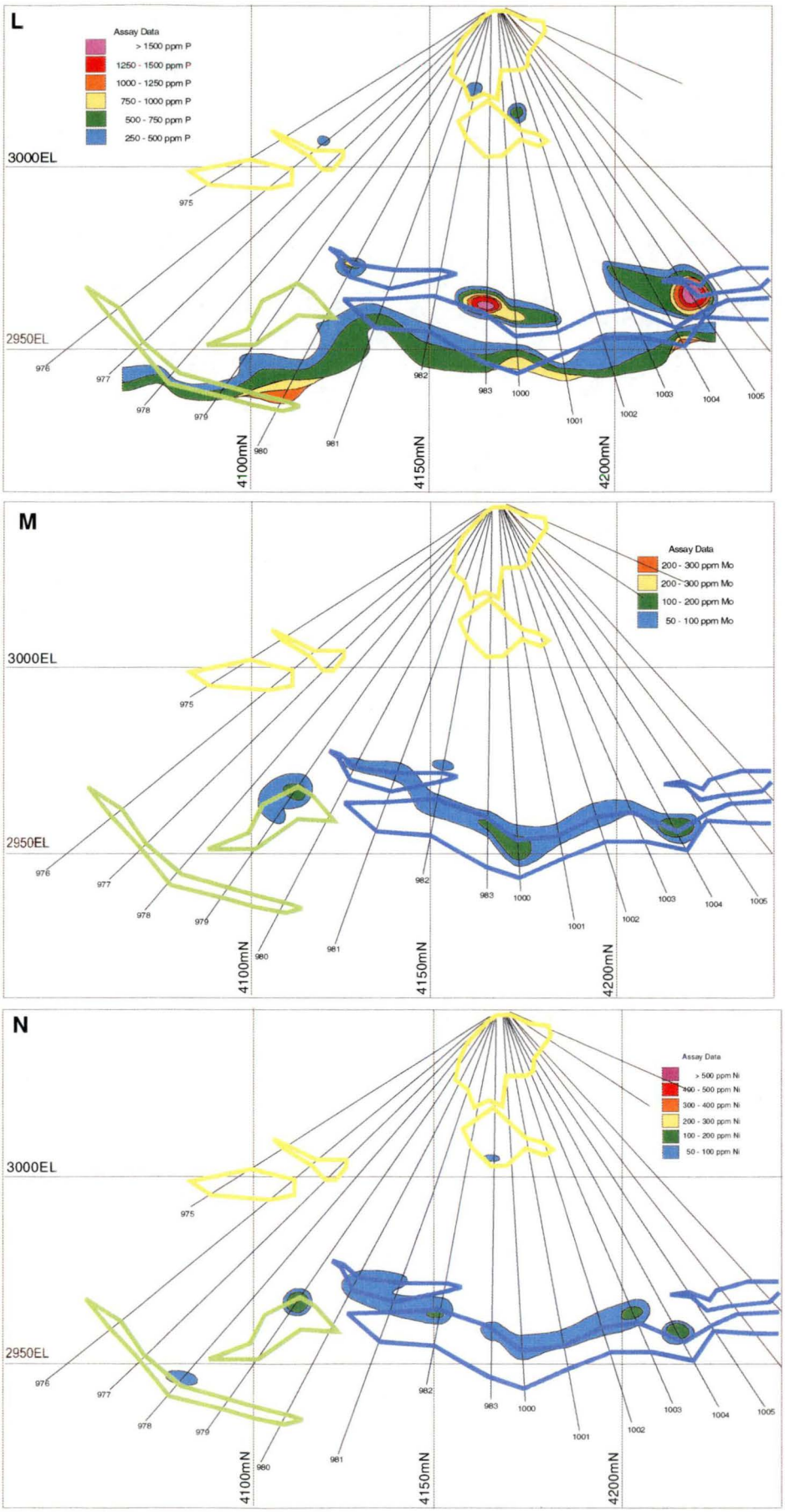

Figure 111continued Contour plots for 1420mE section. (L) phosphorus, (M) molybdenum, (N) nickel. Outline in blue Battle lens, green Gopher lens, yellow Upper Zone lenses.

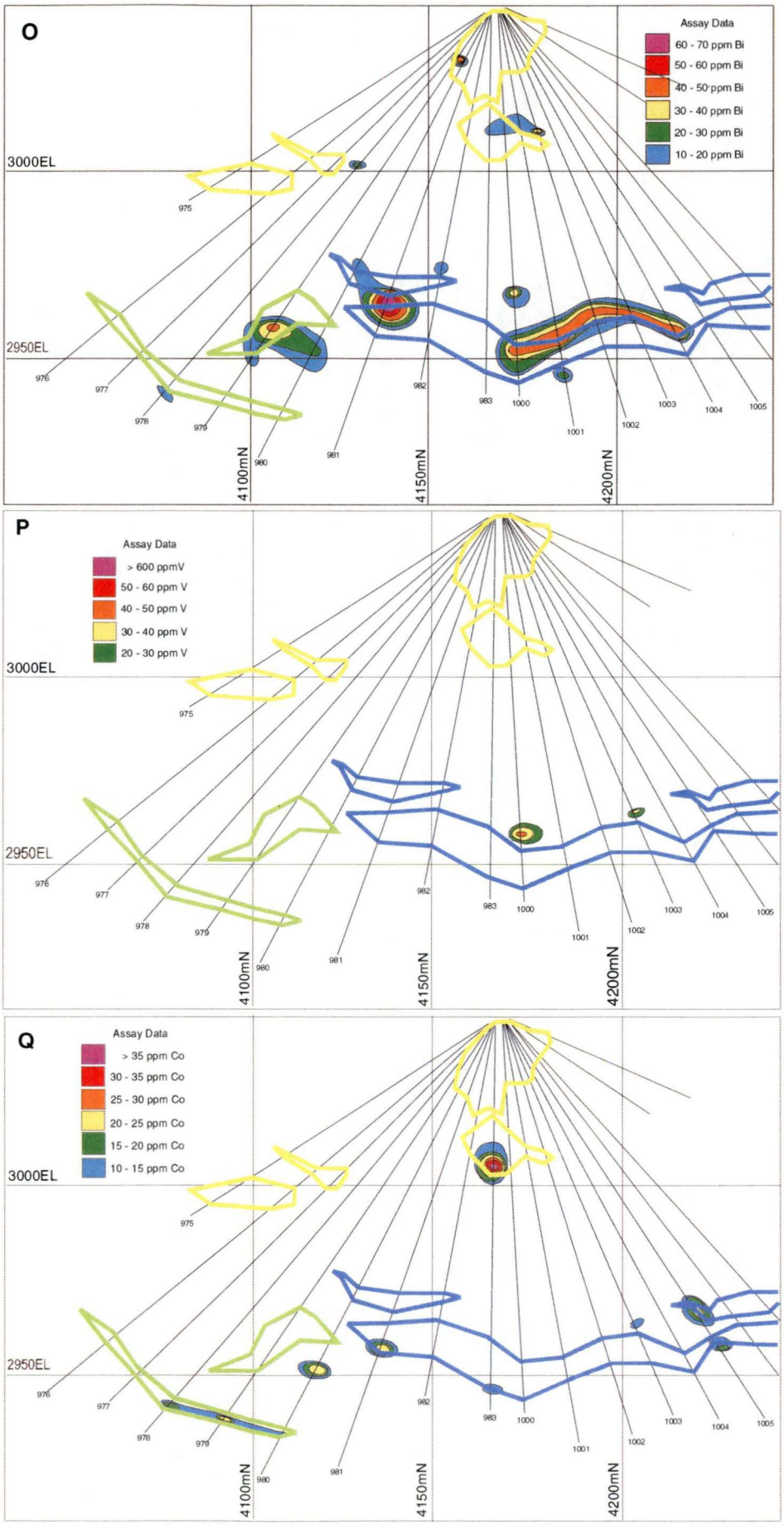

Figure 111continued Contour plots for 1420mE section. (O) bismuth, (P) vanadium, (Q) cobalt. Outline in blue Battle lens, green Gopher lens, yellow Upper Zone lenses.

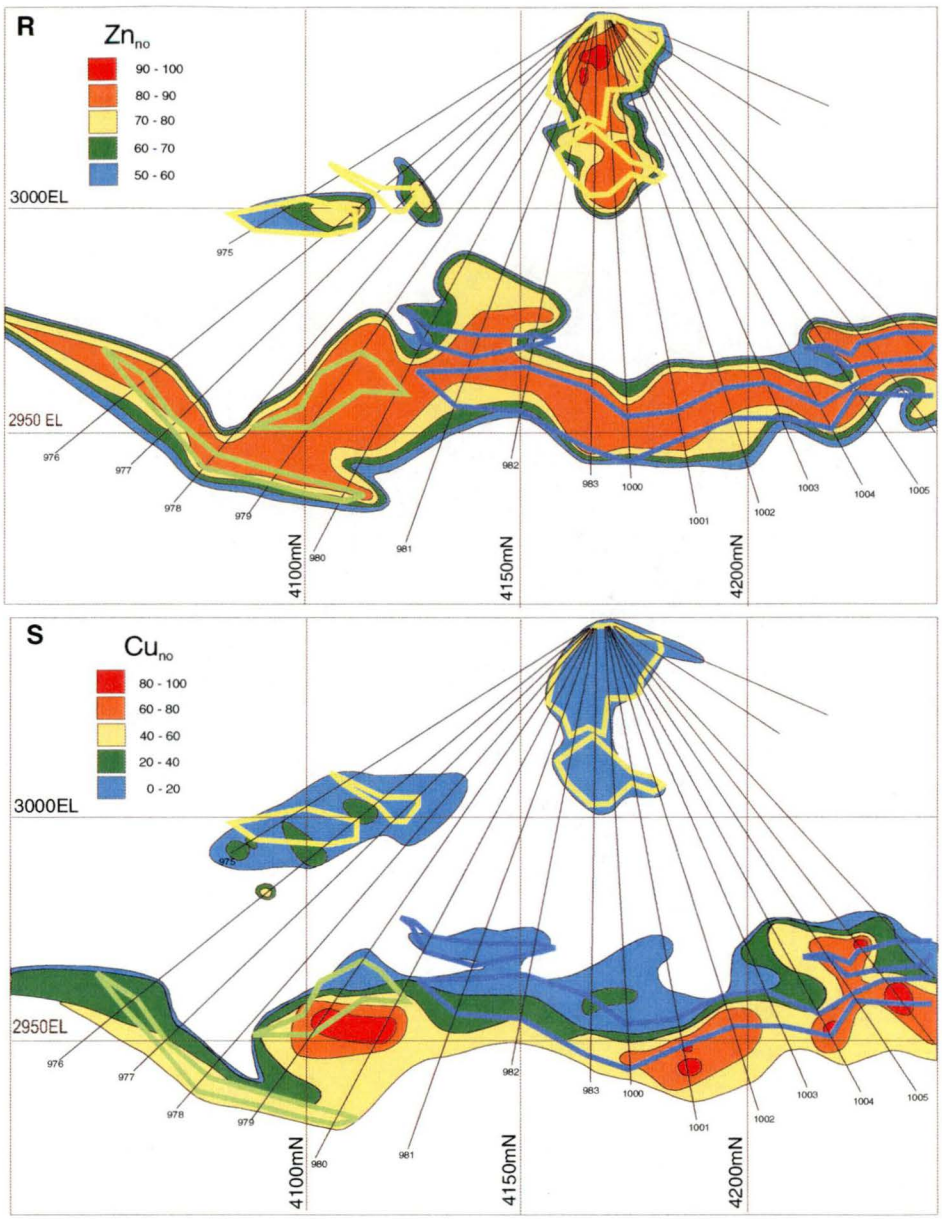

Figure111continued. Contour plots for 1420mE section. (R) Zn number, (S) Cu number. Outline in blue Battle lens, green Gopher lens, yellow Upper Zone lenses.

9.6S).

Gap lens: Zinc is high in the middle of the Gap lens with values up to 38.7% (Fig. 112A). Lead values are highest (up to 6%) at the top of the Gap lens and surrounding the Zn high (Fig. 112B). Copper show its highest values (7%) at the base of the Gap lens, with the distribution skewed slightly to the south (Fig.112C). A weaker spine of Cu extends up the northern side of the Gap lens giving Cu a bimodal distribution. Iron underlies the Cu high at the base and southern side of the Gap lens (Fig. 112D). Barium is strongly elevated (up to 41.5%) in the Gap lens, with the highest values occurring at the top of the Gap lens, moderately high values (20-30%) also occur in the middle of the Gap lens coincident with the elevated Zn (Fig. 112E). Gold distribution is sporadic in Gap lens although values are elevated (12 g/t) in comparison to underlying Battle and Gopher lenses (Fig. 112 F). Silver and Bi are also elevated in the Gap lens (Table 38) and show strongly bimodal distributions coincident with Cu (Fig. 112G & H). Cadmium distribution is also elevated (>100ppm) and shows a distribution similar to that of Zn (Fig. 112I). Arsenic is strongly elevated in Gap lens with values up to 5560ppm occurring at the top of the Gap lens, a smaller high also occurs in the middle of the Gap lens coincident with the Zn high (Fig. 112J). Vanadium is elevated (up to 80ppm) at the top of the Gap lens (Fig. 112K). Molybdenum forms a spine up the northern side of the Gap lens with values up to 285 ppm (Fig. 112L). Nickel, Mn and P show patterns unrelated to other elements in the Gap lens (Fig. 112M-O).

The Zn number is extremely high (>90) through out most of the Gap lens, except in at the very top of the lens, corresponding to the distribution of Pb where the ratio drops to 80-90 (Fig. 112P). In contrast the Cu number is low (<20) through out most of the Gap lens except at the base, where it forms highs (>60) off set toward the south consistent with the distribution of Cu (Fig. 112Q).

Element		Maximum value
Gold	Au	12 g/t
Silver	Ag	579 g/t
Copper	Cu	6.9 %
Lead	Pb	6.1 %
Zinc	Zn	38.7 %
Barium	Ba	41.5 %
Iron	Fe	40.2 %
Arsenic	As	5560 ppm
Cadmium	Cd	995 ppm
Manganese	Mn	5030 ppm
Phosphorus	P	800 ppm
Molybdenum	Mo	285 ppm
Nickel	Ni	175 ppm
Mercury	Hg	N/A
Bismuth	Bi	80 ppm
Cobalt	Co	20 ppm
Germanium	Ge	N/A
Uranium	U	B/D
Vanadium	V	80 ppm

Table 38 Summary maximum assay values from 1420mE section through the Gap lens. N/A not analysed, B/D below detection.

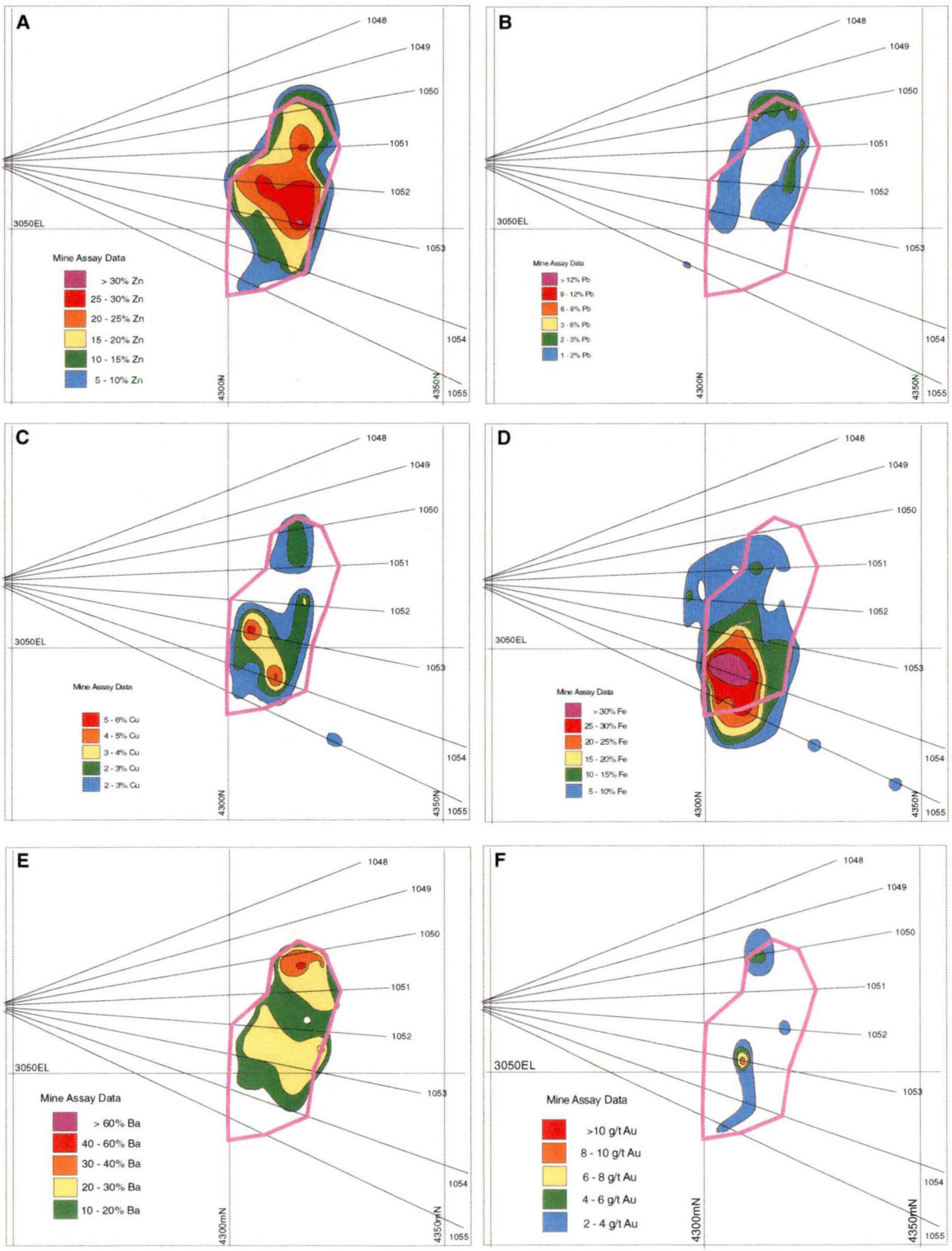

Figure 112. Contour plots for 1420mE Gap section. (A) zinc, (B) lead, (C) copper, (D) iron, (E) barium, (F) gold, from mine assay data base. Outlines in pink Gap lens

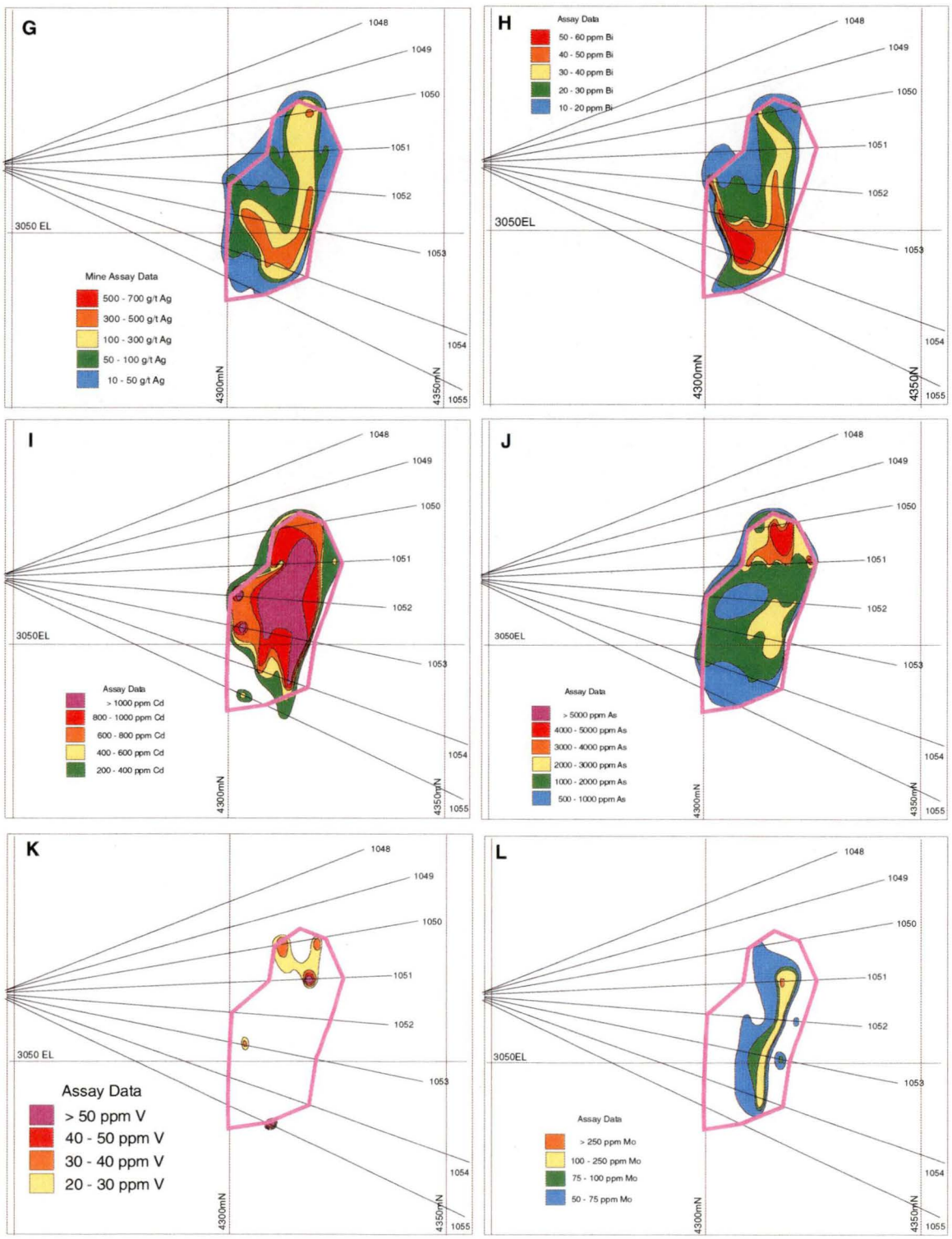

Figure 112continued. Contour plots for 1420mE Gap section. (G) silver, (H) bismuth, (I) cadmium, (J) arsenic, (K) vanadium, (L) molybdenum from mine assay data base. Outline in pink Gap lens.

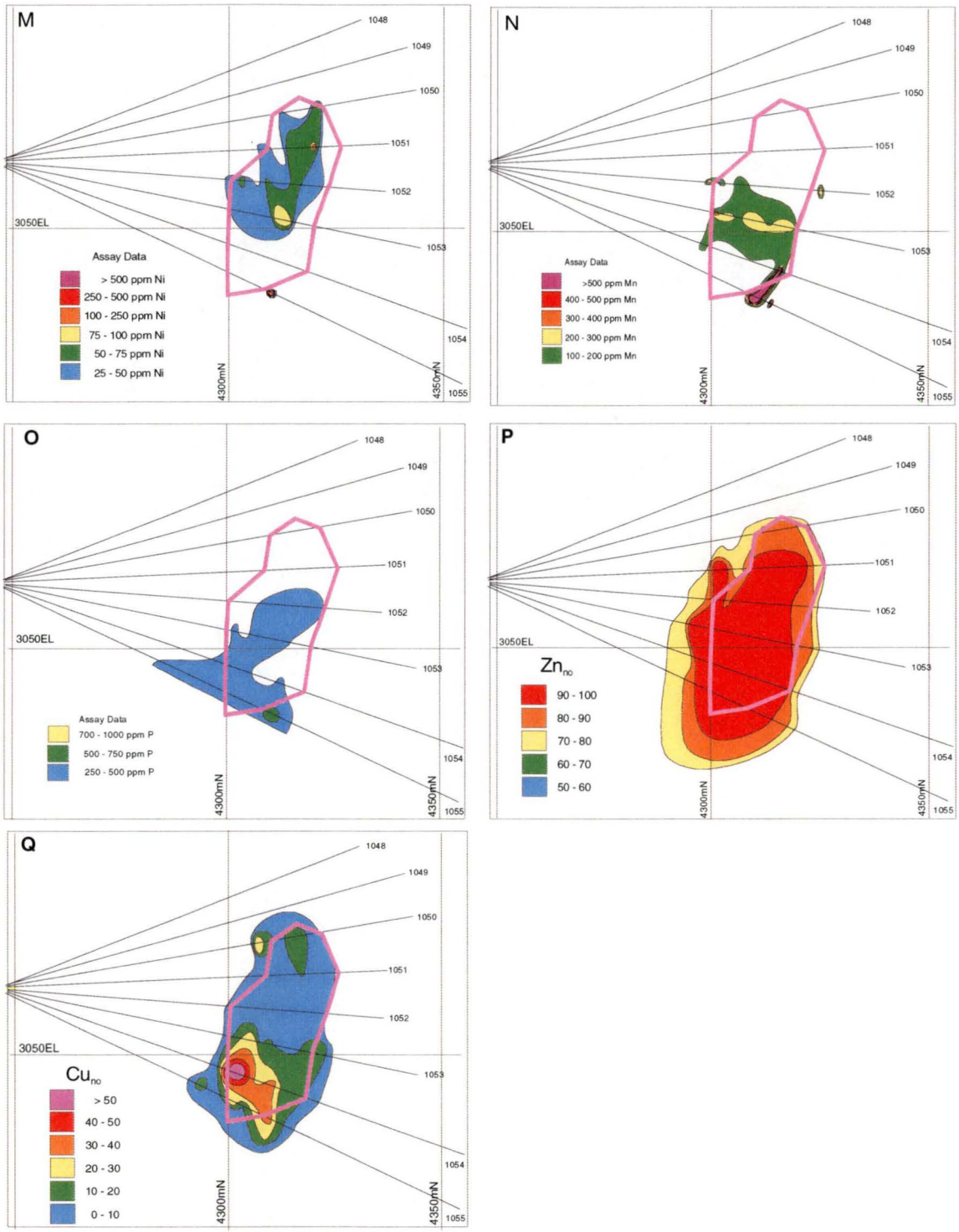

Figure 112continued. Contour plots for 1420mE Gap section. (M) nickel, (N) manganese, (O) phosphorus, (P) Zn number, (Q) Cu number from mine assay data base. Outlines in pink Gap lens

1390mE Section

The 1390mE section covers the Gap lens and contains only three drill intersections (compared to eight on 1420mE section). Maximum major and trace element values are summarised in Table 39 and contoured elemental values presented in Fig 113. Maximum Zn values (up to 39%) occur in the middle to top half of the Gap lens (Fig. 113A). Lead is concentrated at the top of the Gap lens with values up to 7.3 %, and a zone of elevated (2-3%) Pb extends down the northern side of the deposit (Fig. 113B). Copper shows a bimodal distribution with the highest values occurring at the base and southern side of the lens, and a secondary Cu high (2-3%) extending up the middle of the lens (Fig. 113C). Iron is concentrated at the base of the Gap lens with values up to 42% (Fig. 113C). Barium is strongly enriched in the Gap lens with values up to 40.8% and occurs at the top of the lens coincident with the Pb distribution (Fig. 113E). Gold distribution in the Gap lens is sporadic (Fig. 9.8F), however values up to 49g/t are recorded (Table 39). Silver has its highest values (399 g/t) in the centre of the Gap lens (Fig. 113G). A ridge of elevated Ag extends from this high toward the base of the lens. Cadmium is elevated (>1000ppm) in the middle to top of the Gap lens overlapping the distribution of Zn, and off set from the distribution of Pb and Ba (Fig. 113H). Arsenic has values up to 4580ppm and closely follows the distribution of Ba (Fig. 113I). Vanadium is concentrated at the top of the Gap lens with values up to 60ppm, however its distribution is narrow and occurs between the Zn and Cu zones (Fig. 113J). Molybdenum distribution shows a strong correlation with Ag (Fig. 9.8K). Bismuth is concentrated at the base of the Gap lens (Fig. 113L). Mn, Ni and P distributions show little relation to other elements in the Gap lens (Fig. 113M & N, P distribution not shown). The Zn number (Fig. 113O) is extremely high in the basal two thirds of the Gap lens, but slightly lower (80-90) in the top third. The Cu number is elevated (>20) at the base of the Gap lens (Fig. 113P).

Element		Maximum value
Gold	Au	49 g/t
Silver	Ag	399 g/t
Copper	Cu	6.3 %
Lead	Pb	7.3 %
Zinc	Zn	39.3 %
Barium	Ba	40.8 %
Iron	Fe	41.9 %
Arsenic	As	4580 ppm
Cadmium	Cd	>1000 ppm
Manganese	Mn	320 ppm
Phosphorus	P	400 ppm
Molybdenum	Mo	240 ppm
Nickel	Ni	70 ppm
Mercury	Hg	N/A
Bismuth	Bi	50 ppm
Cobalt	Co	D/L
Germanium	Ge	N/A
Uranium	U	B/D
Vanadium	V	60 ppm

Table 39 Summary maximum assay values from 1390mE section through the Gap lens. N/A not analysed, B/D below detection, D/L detection limit.

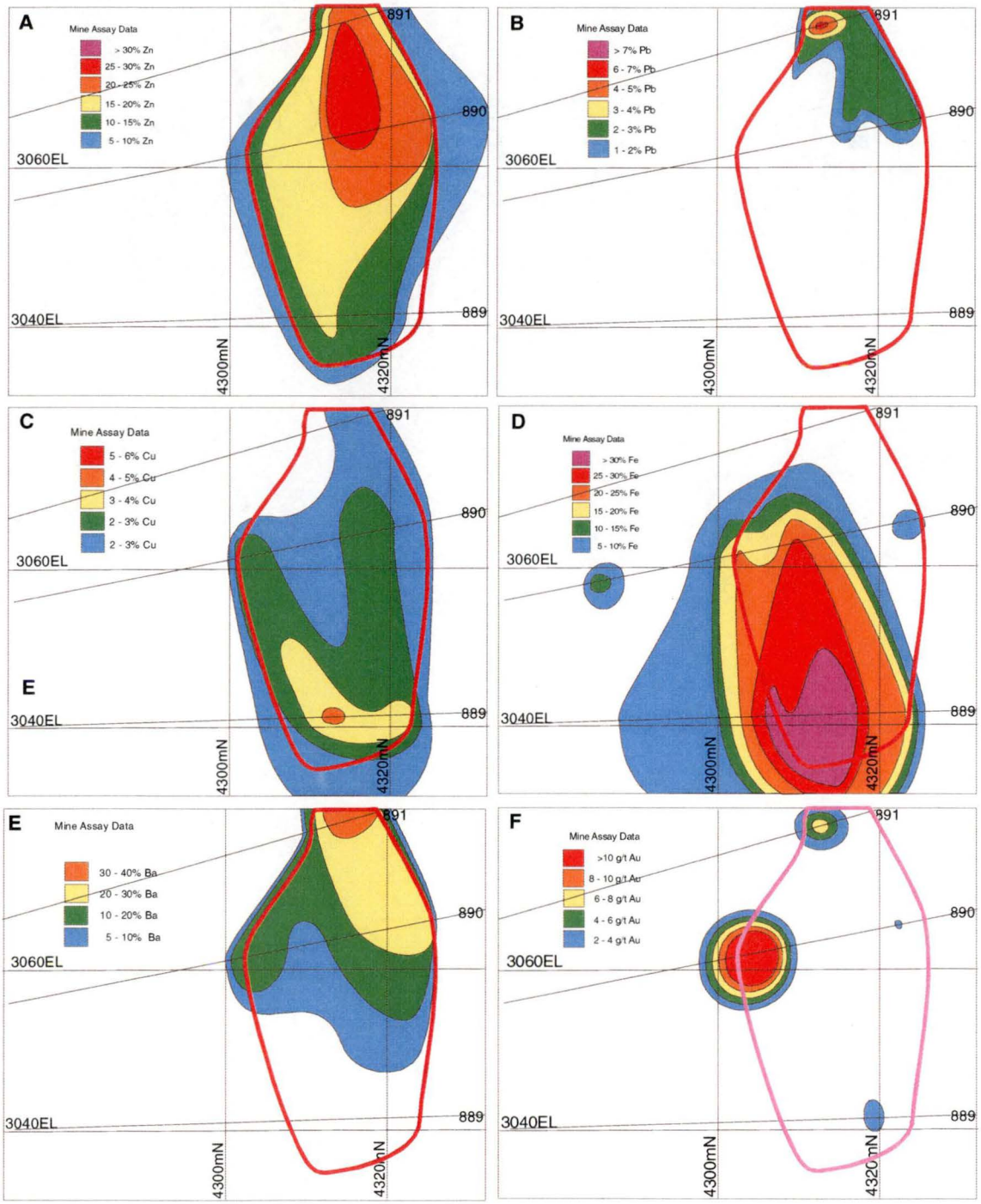

Figure 113. Contour plots for 1390mE Gap section. (A) zinc, (B) lead, (C) copper, (D) iron, (E) barium, (F) gold, from mine assay data base. Outlines in pink Gap lens.

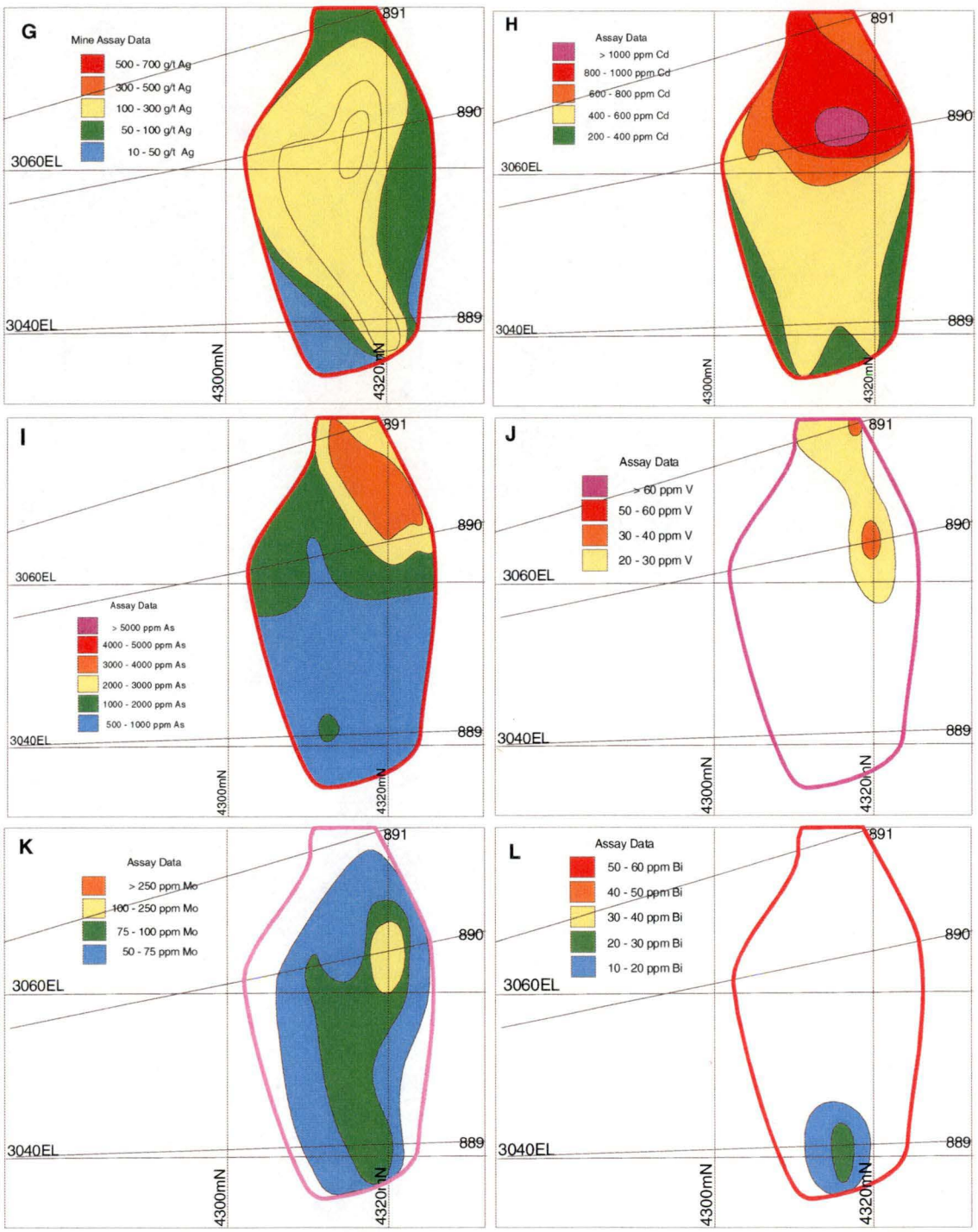

Figure 113continued. Contour plots for 1390mE Gap section. (G) silver, (H) cadmium, (I) arsenic, (J) vanadium, (K) molybdenum, (L) bismuth. Outlines in pink Gap lens

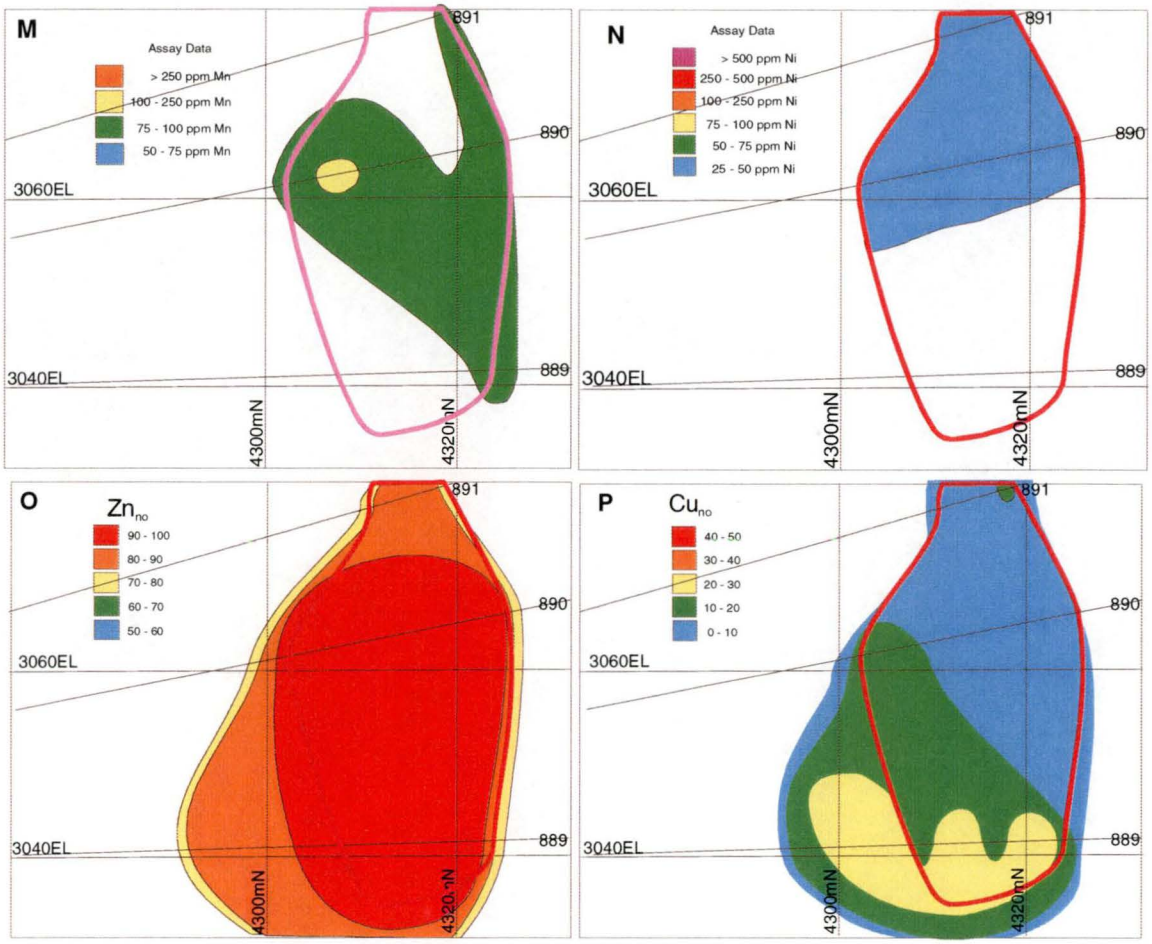

Figure 113continued. Contour plots for 1390mE Gap section. (M) manganese, (N) nickel, (O) Zn number (P) Cu number, from mine assay data base. Outlines in pink Gap lens.

9.3.3 Discussion – Elemental distribution between sections and ore lenses

The Battle Zone ore lenses occur at varying stratigraphic levels resulting in a zonation of metals from one ore lens to the next. The South Trough lens is within a depression twenty to thirty meters below the Battle and Gopher lenses and 10 to 50m to the south east (Chapter 6) while the Upper Zone lenses occur ten to thirty meters above the Battle lens and the Gap lens thirty to fifty meters above the Battle lens.

Zinc: Zn grades are high in all lenses, however the Gap lens shows significantly lower Zn grades (maximum of 39%) than the underlying lenses. In contrast the Battle, Gopher and South Trough lenses have maximum Zn grades in the range 48 - 53%.

Copper: Cu reaches a maximum of 9% in the South Trough lens but is also high in Battle and Gopher lens. The Upper Zone lenses have lower Cu values (< 5 %) while the Gap lens shows maximum Cu value of 7%. The distribution of Cu also varies between the lenses. In the South Trough, Battle, Gopher and Gap lens Cu occurs toward the base of the lenses. In contrast to the Upper Zone lenses where Cu is evenly distributed.

Lead: Lead shows a strong stratigraphic zonation with the lowest values occurring in the South Trough lens and highest values occurring in the Upper Zone and Gap lenses. Lead grades are generally low in the Battle, Gopher and South Trough lenses (<0.5%) with highs of 10.7%, 12.6% and 4.2% recorded in each lens respectively. In contrast the Upper Zone and Gap lenses are markedly enriched in Pb with values up to 5% common. Sporadic highs up to 13% in the Upper Zone lenses and 7% in the Gap lens also occur. Pb is distributed toward the top of the Battle and Gap lenses. In the Gap lens Pb forms a cap of 1-2% Pb draping over the lens (Fig. 112B & 113B). In the Battle lens the Pb distribution is more blanket-like mimicking the shape of the Battle lens (Fig. 110B). In both these lenses Pb grades drop off rapidly toward the base of the lenses. In contrast the Upper Zone lenses have an even distribution of Pb coincident with Zn and Cu highs (Fig. 110B). Lead distribution in the South Trough and Gopher lenses is patchy and does not show up well on contour diagrams due to low concentrations in these lenses.

Iron: Fe content of the Battle Zone lenses is fairly consistent between the lenses with maximum values between 40% and 43% in all lenses, except the Upper Zone lenses. The Upper Zone lenses show a lower maximum Fe value of 36%. The abundance of Fe in the lenses leads to a strong zonation with stratigraphic position with the highest Fe content occurring in the South Trough lens. Fe content of the lenses decrease in the Gopher and Battle lenses and is lowest in the Upper Zone lenses. The Gap lens, however, does not conform to this stratigraphic zonation of Fe with Fe content up to 42%.

Barium: Ba show a strong stratigraphic zonation with the lowest values occurring in the South Trough lens and highest values occurring in the Upper Zone and Gap lenses. The Gap lens has the highest Ba contents of up to 41.5%. Upper Zone, Battle and Gopher lens share similar Ba highs of 26-34% while the South Trough lens has the lowest Ba maximum of just 7.6%. However the Ba content of the Upper Zone lenses and the distribution of Ba in Upper Zone lenses is also considerably different to that seen in the Gopher and Battle lenses (Fig. 110E & 111E). In the Battle, Gopher and South Trough (Fig. 108E & 9.4E) lenses Ba highs appear randomly distributed with little coherence. In contrast Ba in the Upper Zone shows an even distribution throughout the lenses consistent with the distribution of Zn and Pb (Fig. 110E). In the Gap lens the highest Ba contents occur at the very top of the lens, with elevated values > 20% Ba dominating the top two thirds of the Gap lens consistent with the Zn distribution (Fig. 112E & 113E).

Silver: Ag contents of the lenses vary from < 100 g/t in South Trough lens to 300-500 g/t in the Gopher, Battle and Gap lenses to a high of 1366g/t in the Upper Zone lenses. Silver distribution also varies between the lenses. In the Battle and Gopher lenses Ag occurs throughout the lens with a range of 10 to 50 g/t, while slightly higher values (50 – 100 g/t) occur toward the top of the lenses. In the Upper Zone lens Ag is evenly distributed along with Zn-Cu-Pb and Ba. The Gap lens shows the most interesting distribution of Ag with a distinct zonation of Ag toward the centre of the lens.

Gold: Au values are generally low <10 g/t in the Battle, Gopher and South Trough lenses. In contrast Upper Zone and Gap lenses contain significantly higher Au grades of 40-50g/t. The distribution of Au also

varies between these lenses. Au highs in the lower lenses (South Trough, Gopher and Battle) occur dominantly toward the base of the lenses associated with Cu highs. However in the Gap and Upper Zone lens Au values are consistent through out the lenses with randomly distributed spot highs.

Arsenic is generally concentrated at the top of the ore lenses within the upper-most sphalerite-rich ores and in the adjacent hangingwall rhyolites. This relationship holds for the Battle, Gopher and Gap lenses, however in the Upper Zone lenses As is evenly distributed along with Zn-Cu-Pb-Ba and Ag.

Cadmium values are highest in the Battle and Gopher lenses where values >1000ppm are common. Gap and Upper Zone lenses also show Cd values up to >1000ppm however lower values are common in these lenses. In contrast, the South Trough lens has the lowest Cd content with maximum values reaching only 900ppm.

Manganese enrichment occurs mainly in the host rocks (hangingwall) in the Battle Zone with elevated values similar to host rock (Chapter 5). The only lens that contains significant Mn is the Gap lens where Mn occurs at the base of the Zn high overlapping the Cu high.

Phosphorus like Mn is also more concentrated in the host rocks that sulfide mineralisation. Phosphorus contents increase away from ore zones. The broad increase in P values into the footwall below the ore lenses beneath the Battle, Gopher and South Trough lenses is consiostent with P values for altered Price Formation andesites (Chapter 5).

Molybdenum elevated Mo (> 50 ppm) defines an area coincident with the overlap of the Zn and Cu highs in the Battle, Gopher and South Trough lenses (Fig. 108L, 109L, 110Q & 111L). In the Gap lens the lens with the highest values are in the central portion of the lens (Fig. 112L). Molydbenum is not enriched in the Upper Zones (Fig. 110Q & 111L).

Nickel: High Ni values are coincident with Zn in all lenses except the Upper Zone lenses. However Ni contents vary between the lenses. The Battle, Gopher and South Trough lenses, have higher Ni values (100-200ppm) than Gap and Upper Zone lenses (mostly between 25 and 70 ppm).

Mercury the distribution of Hg follows the same patterns as Pb, As, and Ba, being elevated at the top of the Battle, Gopher, South Trough and Gap lenses and evenly distributed in the Upper Zones. However Hg values vary considerably between the lenses. The South Trough and Gopher lenses have the lowest Hg grades (<500ppb). The Battle lens has higher Hg values with average Hg content between 500ppb and 1000ppb. The Upper Zone lenses show the highest Hg contents with values between 1000ppb and 10000ppb. Mercury was not measured in the Gap lens.

Bismuth. The distribution of Bi varies widely between lenses although it does show a common trend of concentration toward the base of lenses and into the footwall. In the South Trough lens Bi highs underly the sub-lenses, occurring in the Fe-rich core around the mafic dyke and underlying the Battle lens. In the Battle, Gopher and Upper Zone lenses Bi distribution is very sporadic with concentrations of Bi at the top of the massive sulfides as well as within the lenses and in the footwall. While the Gap lens shows Bi concentrations toward the base of the lens (Fig. 112H) mimicking the distribution of Cu and Ag.

Cobalt values in the Battle Zone are low with values from < 5ppm to 35ppm common. Only one drill hole BG18-546 showed Co values outside this range (55ppm and 95ppm) these elevated values occur in sheared ore associated with the flat fault below the Gopher lens.

Germanium was only measured on the 1540mE and 1780mE sections due to cost constraints. In the South Trough lens Ge remained below detection (< 5 ppm). However enrichments up to 15 ppm form a band along the top of the Battle lens and as sporadic 5 ppm highs in the Gopher and Upper Zone lenses.

Uranium generally low (< 20ppm) but reaches highs of 60ppm on 1540mE section (Fig. 110M).

Vanadium is primarily found in the Gap lens where it occurs concentrated at the top of the lens (Fig. 112K & 113J). Sporadic V enrichment is also seen at the top of the Gopher (Fig. 110N) and Battle (Fig. 111R) lenses.

9.4 3D – Zonation of metals in the Battle Zone

3D block model of the Battle Zone lenses was created with the assistance of Dr G. McArthur. The wire frames presented in chapter 6 were used to select assays from the Myra Falls database that fell within the lenses, selected assays were composited to 2m intervals. Silver grades were cut to 1500ppm in modelling to alleviate problems due to discrepancy between mine and Chemex assay. Lens orientation, strike, dip and plunge were used to optimise the block shape and search ellipse orientations used to create the block model. Mean grades (Table 9.8) for each lens were then calculated. The Zn number (Zn_{no} = 100Zn/(Zn+Pb)) and Cu number (Cu_{no} = 100Cu/(Cu + Zn)) were calculated for the whole zone.

Lens	Au g/t	Ag g/t	Cu %	Pb %	Zn %	Ba %	Fe %
Battle	1.24	22.5	2.35	0.45	16.8	0.56	14.1
Gopher	1.66	25.3	2.49	0.35	16.0	1.91	18.0
Gap	3.21	157.3	2.30	1.17	17.5	15.46	16.0
South Trough	1.08	19.9	2.23	0.26	15.0	0.25	18.0
Upper Zone	2.45	152.3	0.78	1.90	12.0	9.29	6.0
Total	***1.58***	***43.3***	***2.29***	***0.56***	***16.33***	***2.8***	***15.05***

Table 40. Summary of ore lens volume and grades for 3D Datamine block model. Note this data is not to be used as ore reserves figures.

3D block modelling of the Battle Mine assay database shows very similar trends to the sections discusses in section 9.3. However the model allows comparison of element trends between lenses which are used to highlight possible source areas for hydrothermal fluids. Results are presented in Figure 9.20 - 28 and as 3D model on CD (for viewing by the reader).The DATAMINE™ block model presents assay data as percentiles where each colour represents 12.5% of the total population, this leads to odd assay intervals especially in high regions but gives an even distribution of colours simplifying the block model.

Copper (Fig. 114) is depleted in the Upper Zone lenses (Table 40) and shows a strong zonation toward the base of all other lenses, with highest values occurring in the Gopher lens between 1600mE and 1700mE and toward the western end of the Battle lens, 1600mE to 1395mE.

In contrast Pb (Fig. 115) values are elevated (>0.66%) in the Upper Zone lenses and at the top of the Gap and Battle lenses. Interestingly the highest Pb values in the Gopher lens occur west of 1600mE, while Pb values in the 1600mE to 1700mE section of the Gopher lens are extremely low (<0.05%). Lead is also antipathetic with Cu in Battle lens.

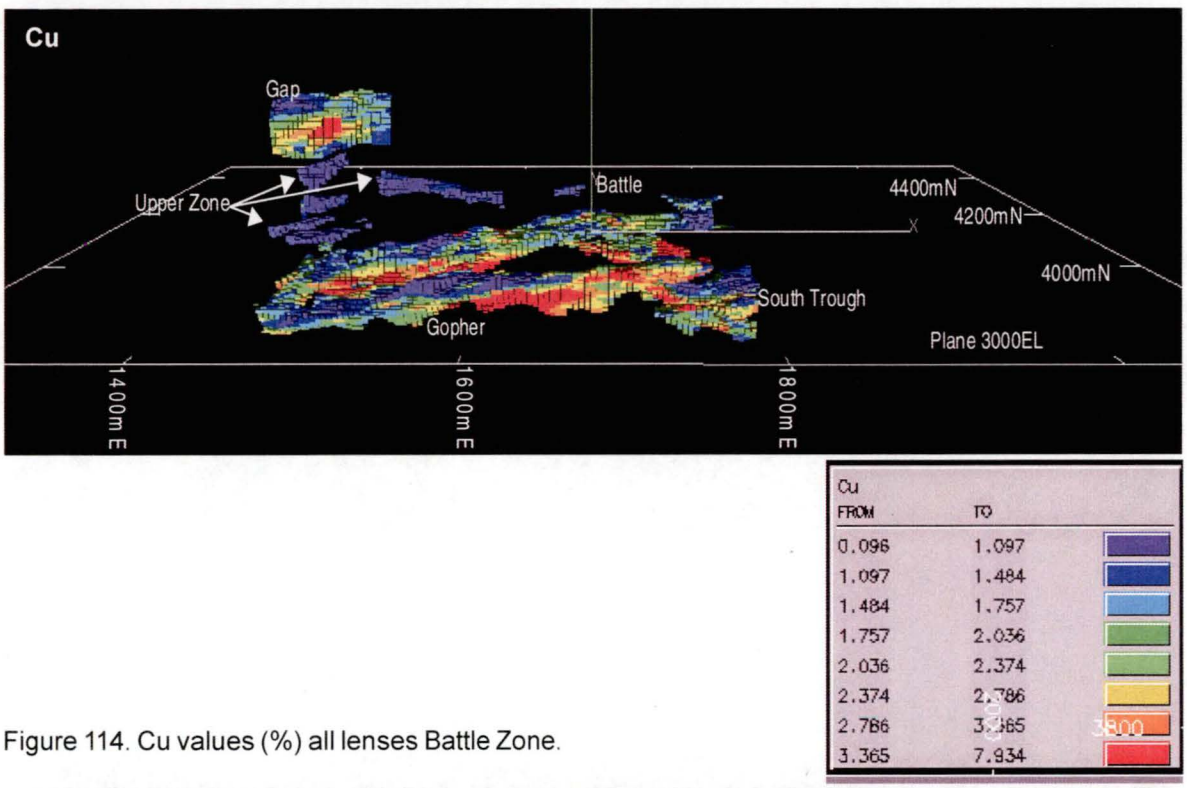

Figure 114. Cu values (%) all lenses Battle Zone.

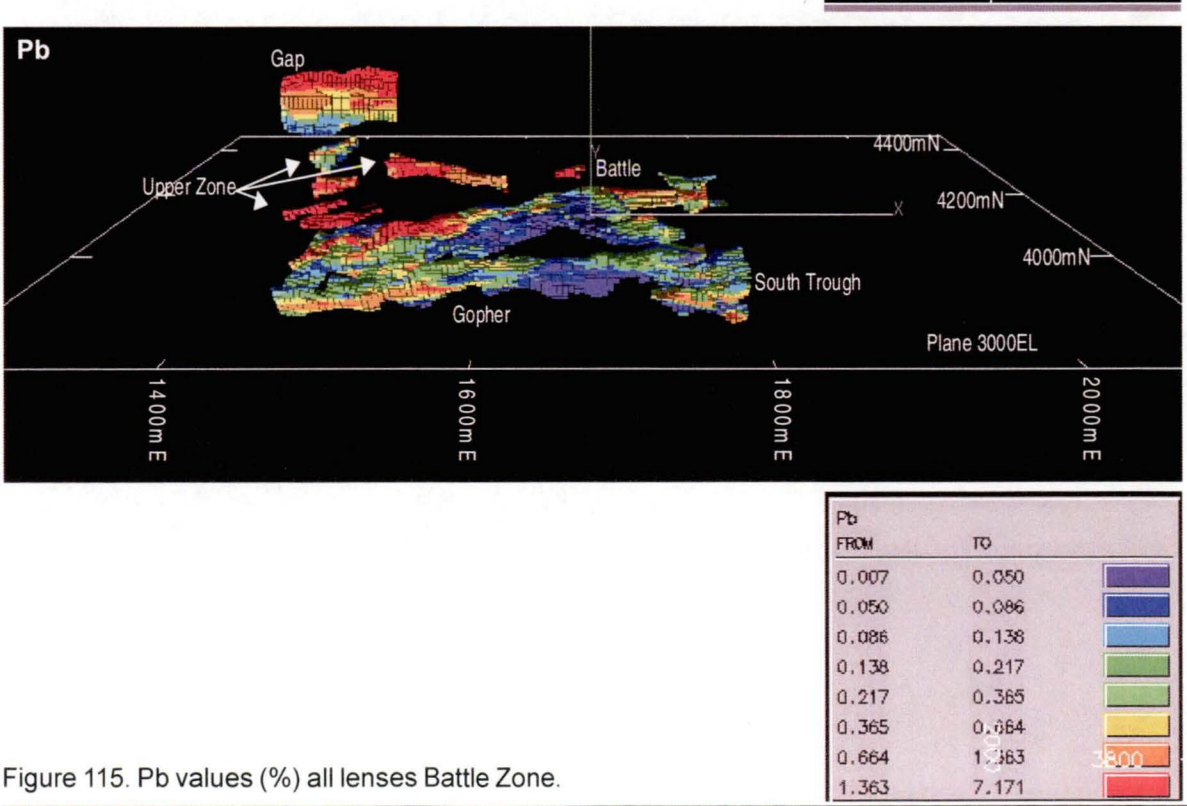

Figure 115. Pb values (%) all lenses Battle Zone.

Zn grades (Fig. 116) are lowest in the Upper Zone lenses. Zn grades are also low at the base of the South Trough and Gap lens, and in the Cu-rich core of Gopher lens between 1600mE and 1700mE but otherwise show a distribution overlapping with both Cu and Pb.

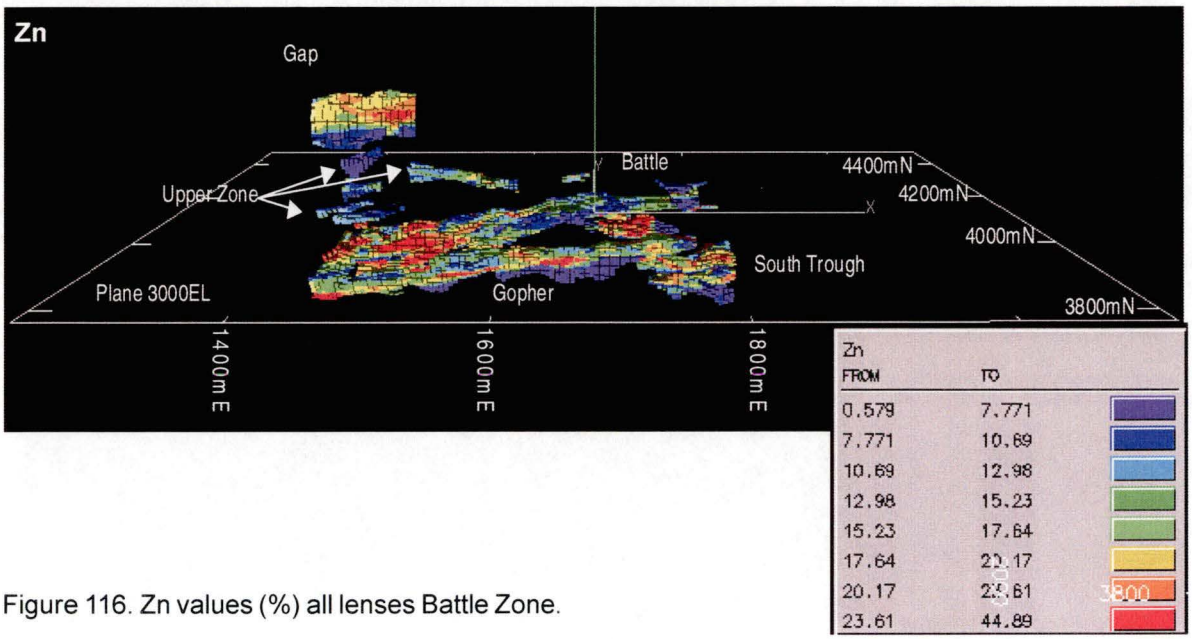

Figure 116. Zn values (%) all lenses Battle Zone.

In contrast Fe contents are highest in the South Trough and Gopher lenses. Figure 117 shows the base of the Gopher, Battle, South Trough and Gap lenses where Fe is strongly enriched, particularly along the keel of the Gopher lens. The Battle lens has lower iron values than the Gopher, South Trough

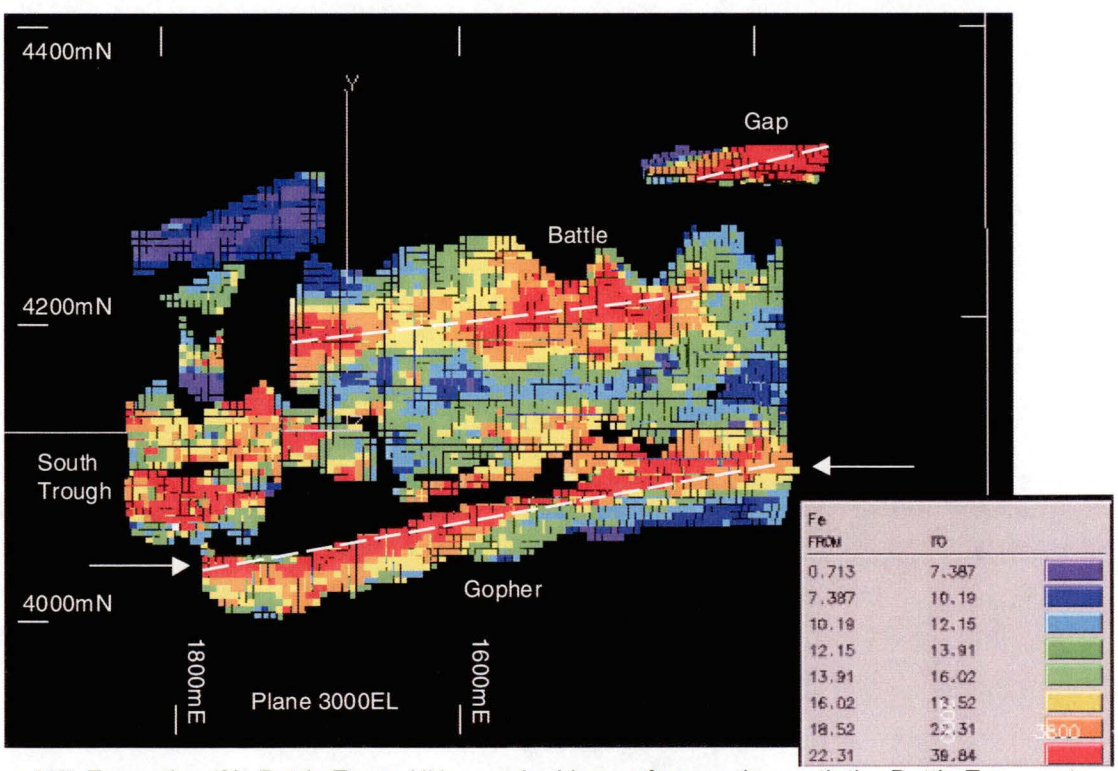

Figure 117. Fe grades (%) Battle Zone. All lenses looking up from underneath the Battle Zone, note east and west orientations are reversed and the Upper Zone lenses not visible. Arrows show strong pyrite enrichment along the keel of the Gopher lens. Dashed lines show position of interpreted feeder faults.

and Gap lenses with iron distributed away from elevated Zn and Pb toward the northern margin of the Battle lens. However, the >22% Fe enrichment overlaps the area of elevated Cu.

Barium (Fig. 118) is strongly elevated in the Gap and Upper Zone lenses with minor enrichment at the top of the Battle and Gopher lenses. The South Trough lens shows very low Ba values. Similarly Au (Fig. 119) and Ag (Fig. 1120) are also enriched in the Gap and Upper Zone lenses. Au shows more sporadic enrichment in the Battle and Gopher lenses, while Ag is lower but evenly distributed in the Battle and Gopher lenses.

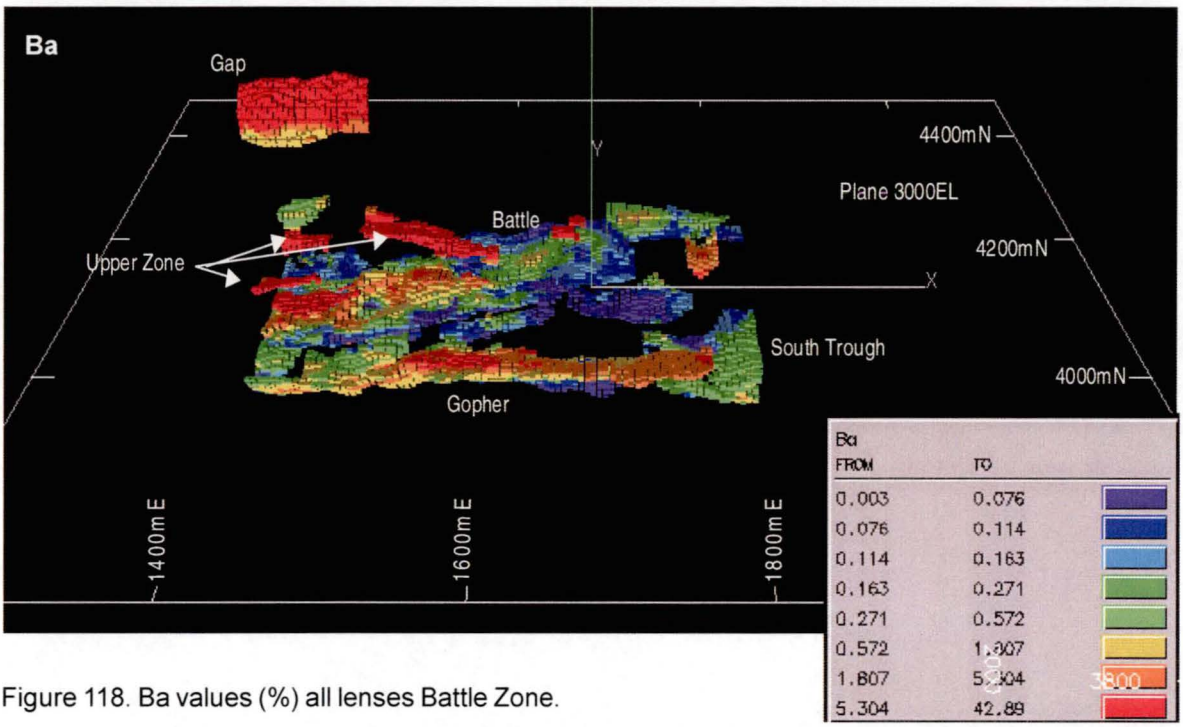

Figure 118. Ba values (%) all lenses Battle Zone.

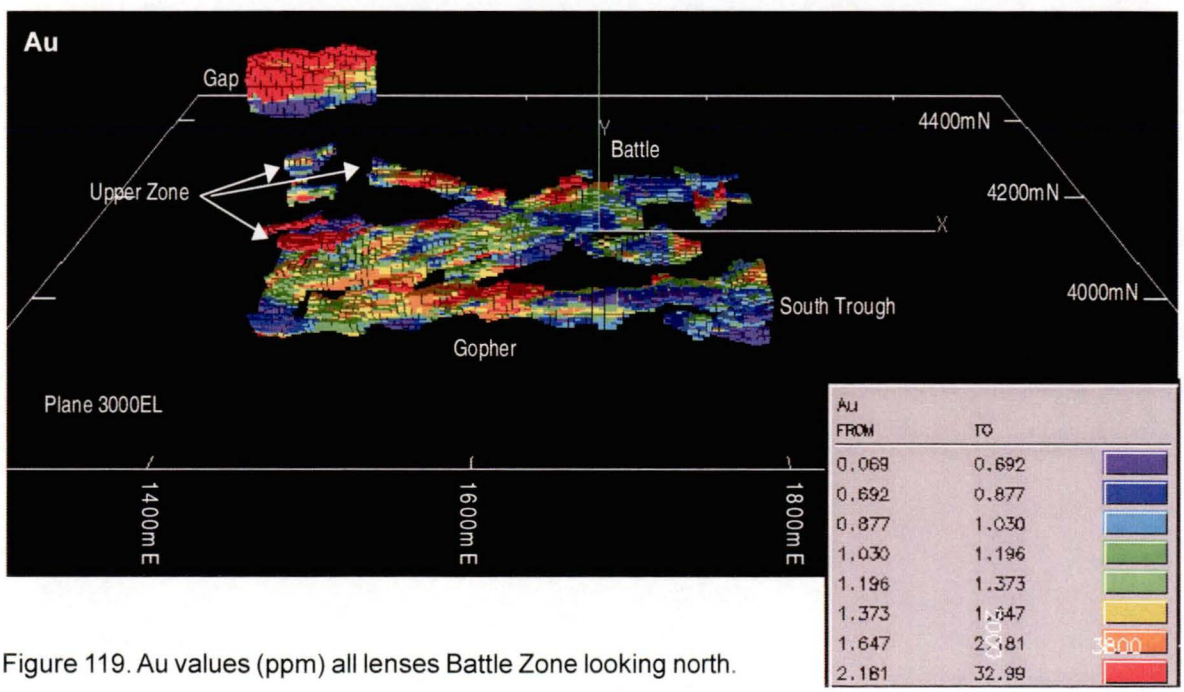

Figure 119. Au values (ppm) all lenses Battle Zone looking north.

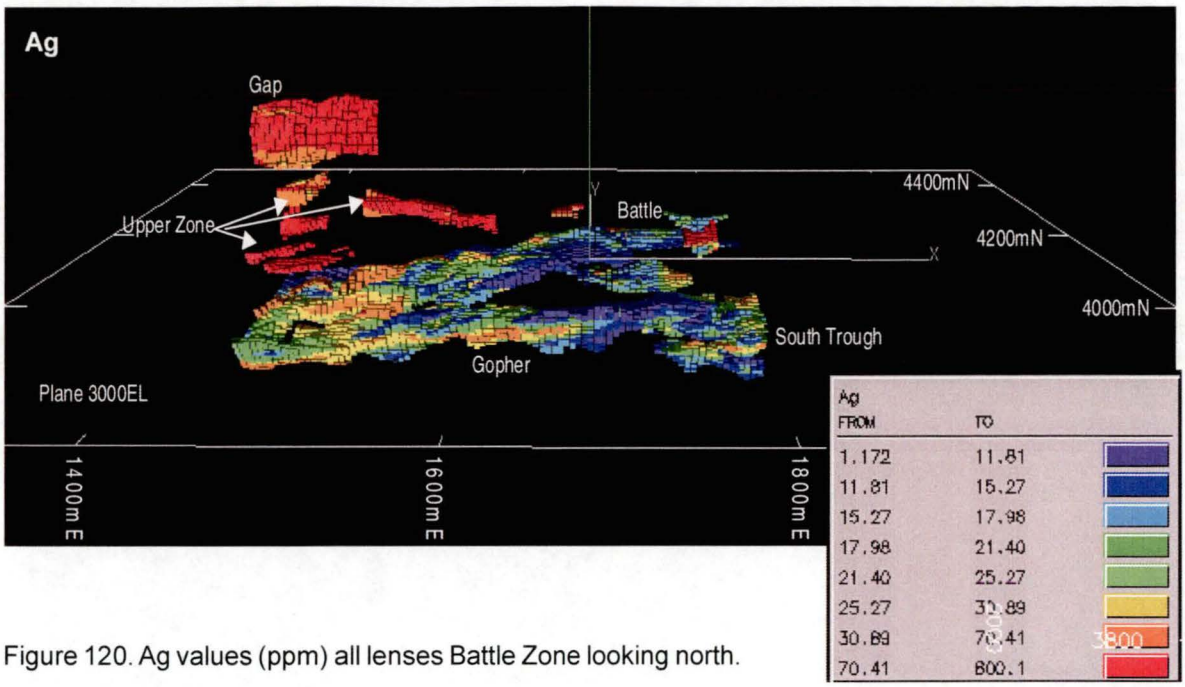

Figure 120. Ag values (ppm) all lenses Battle Zone looking north.

The highest Zn number (Fig. 121) occurs in the Gopher lens between 1625mE and 1700mE and in the Battle lens from 1550mE to 1750mE. The Zn number is lower in the Upper Zones and at the top of the Gap lens. Cu number (Fig. 122) shows a strong correlation with the distribution of Fe, with enrichment on the footwall side of all lenses except the Upper Zone lenses where the Cu number is uniformly low. This distribution suggesting feeder zones along the keel of the Gopher lens, particularly in the region 1600 to 1700mE, on the northern margin of the Battle lens and underlying the South Trough. Cu number values in at the base of the Gap lens are lower suggesting less intense (cooler) feeder zones to the Gap lens.

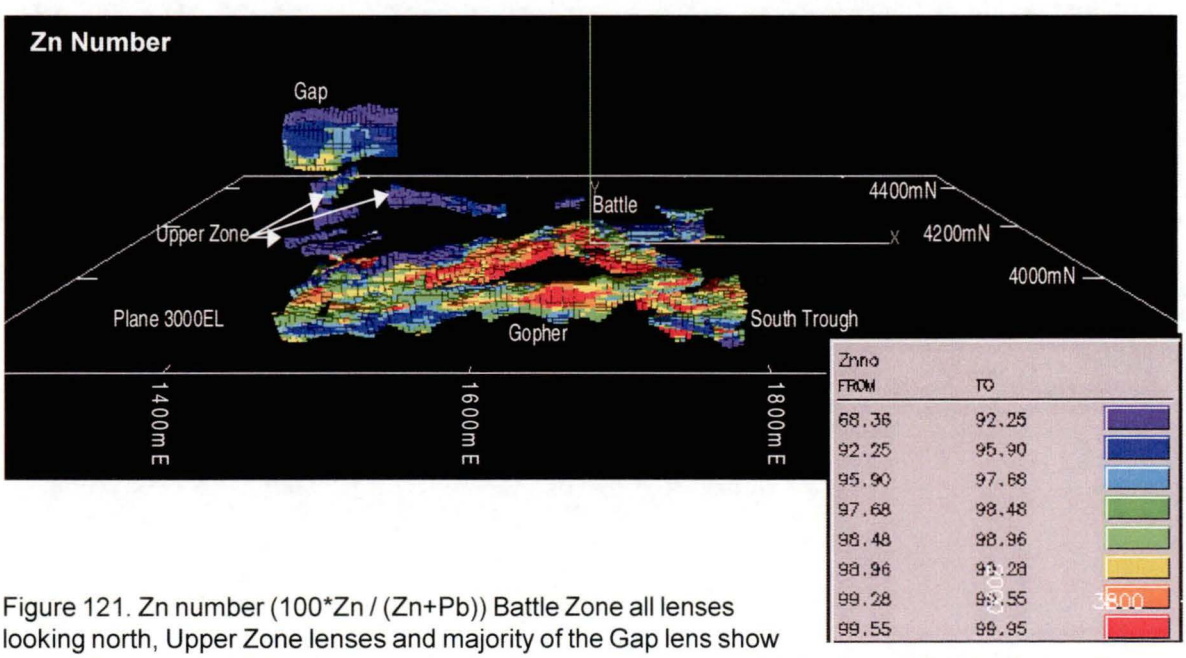

Figure 121. Zn number (100*Zn / (Zn+Pb)) Battle Zone all lenses looking north, Upper Zone lenses and majority of the Gap lens show lowest Zn number (68-97), while the highest Zn numbers occur in the Battle and Gopher lenses between 1550mE and 1750mE.

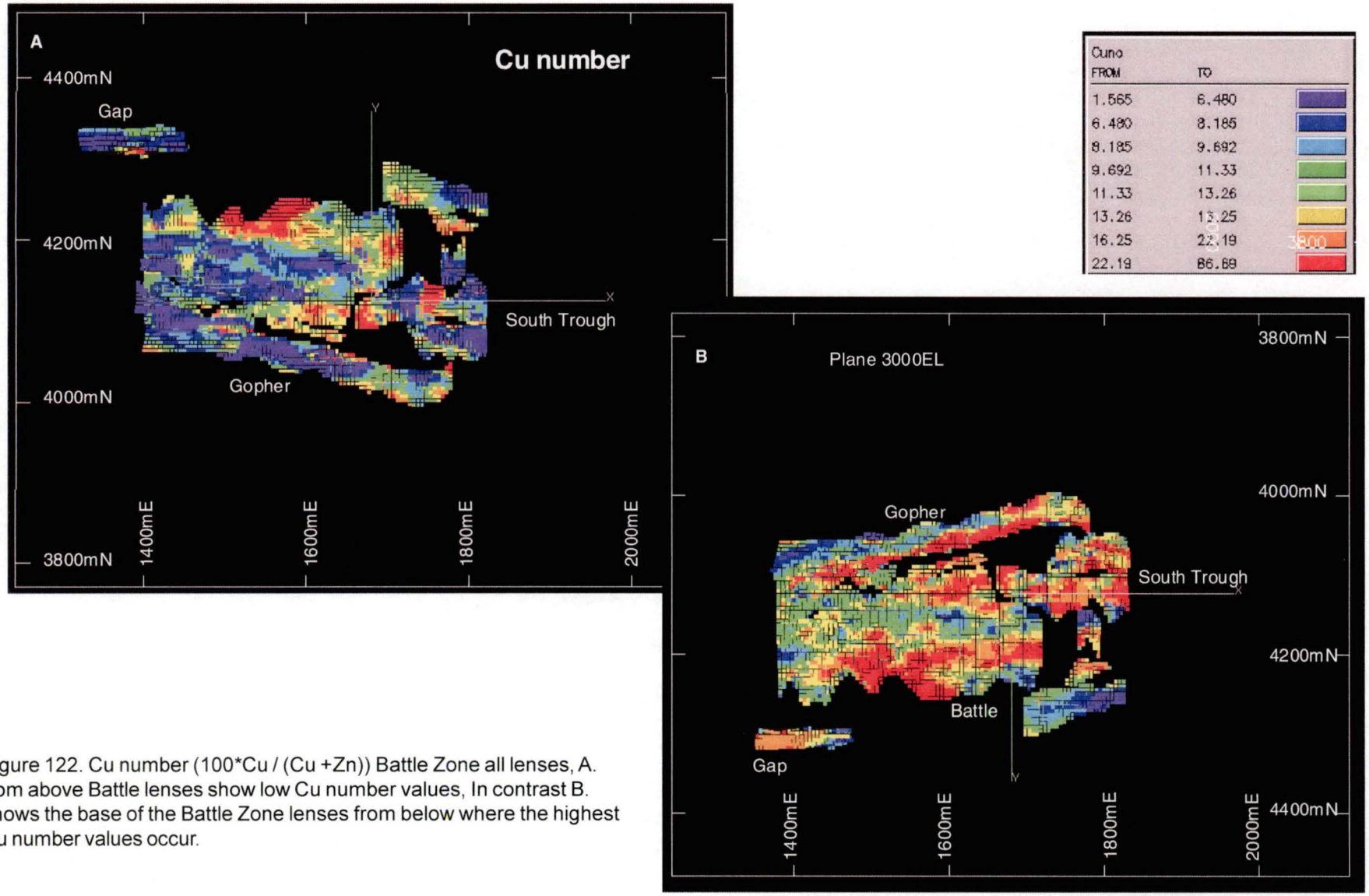

Figure 122. Cu number (100*Cu / (Cu +Zn)) Battle Zone all lenses, A. from above Battle lenses show low Cu number values, In contrast B. shows the base of the Battle Zone lenses from below where the highest Cu number values occur.

9.5 Elemental Zonation and relation to mineral zonation

This section describes the zonation of elements with in each lens then discusses the relationship of the observed elemental zonation with the observed mineralogical zonation detailed in Chapter 6.

9.4.1 Elemental Zonation

The Battle lens shows a strong vertical and lateral zonation of metals (Fig. 123). The centre of the Battle lens is dominated by high Zn. This high Zn zone is flanked by elevated Cu and Fe on the footwall side of the lens. Overlying this high Zn zone is an area of enriched Pb-As-Ag±Bi. Laterally away from this central region is a zone of As and Pb overlying the high Zn. A zone of high Cu underlies the Zn high and is underlain by a high Fe zone. Bismuth is sporadically distributed in the Cu and Zn rich zones.

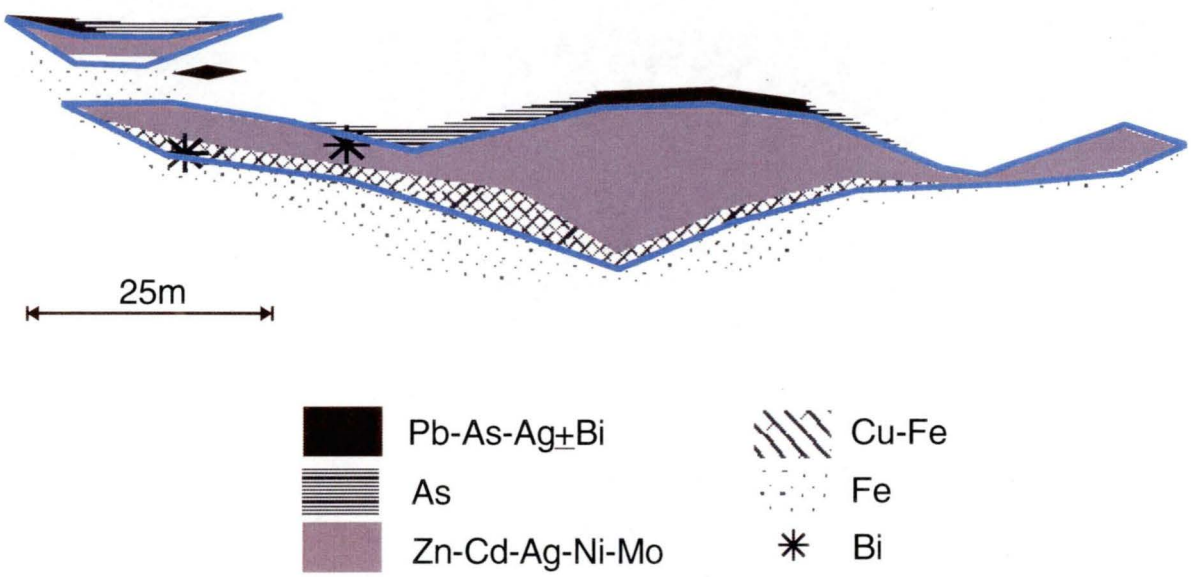

Figure 123. Schematic representation of a section through the Battle lens showing elemental zonation.

The Gopher lens (Fig. 124) has a more complex zonation, due to its strongly asymmetric shape (to the west) and intense deformation (to the east; Chapter 8). The top of the Gopher lens is variably enriched in Hg, As, Ag, and Zn. Underlying this zone is a zone of Zn and Ag. The centre of the lens is dominated by Zn-Cd and Ag. Lead, Mo, Ni, and Bi occur sporadically within the middle to upper part of the Gopher lens. The base of the Gopher lens is dominated by Cu and Fe,with Fe extending into the surrounding footwall.

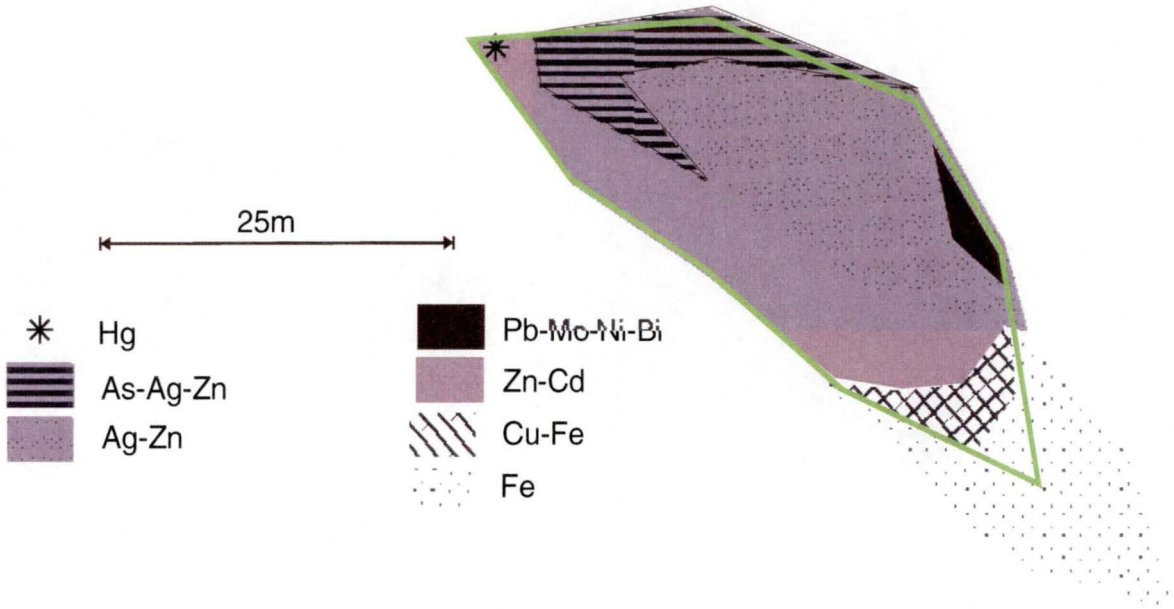

Figure 124. Schematic representation of the elemental zonation in Gopher lens.

The South Trough lens (Fig. 125) is dominated by an Fe enrichment at the base of the lens. The sub-lenses overlie this Fe zone and grade from Cu-Fe-rich at the base of each sub-lens through Zn-Cd-Ag-Ni -rich to a thin layer of Ag, As and Hg at the top of each sub-lens. Ag, As and Hg also occur in the hangingwall to the South Trough lens.

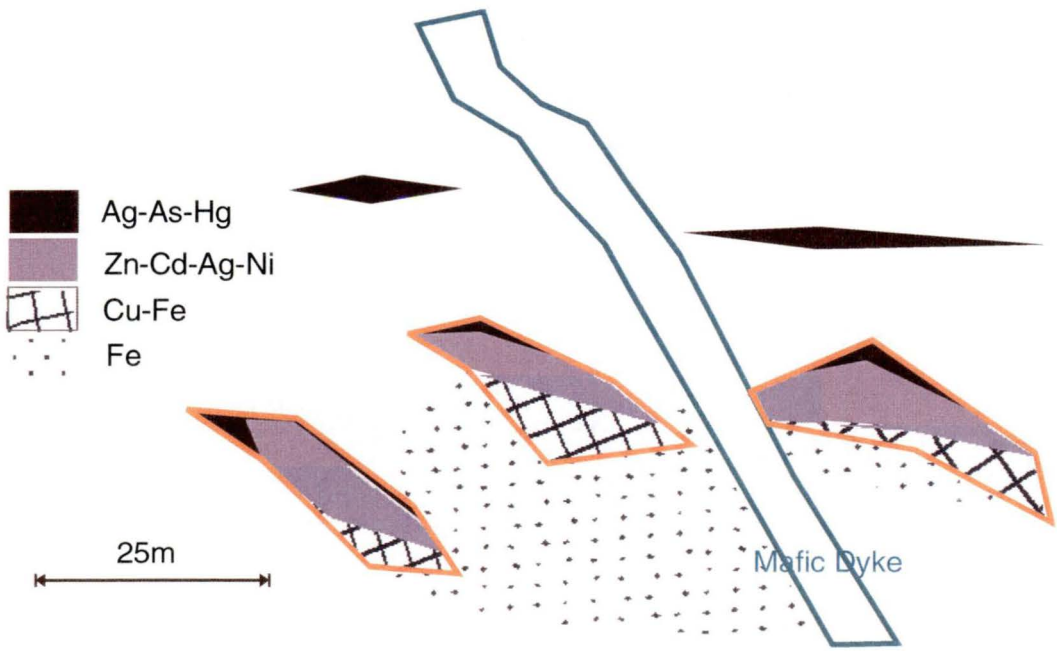

Figure 125. Schematic representation of the elemental zonation in South Trough lens.

The Upper Zone lenses show less zonation than the underlying lenses (Fig. 126). A Ag-As halo occurs in the surrounding rocks toward the hanging wall side of the Upper Zone lens. The lens itself is dominated by Zn, Cu, Cd, Ag, As, Ba and Hg which occur evenly distributed throughout the lens. Upper Zone lenses are is underlain by a zone of high Fe content.

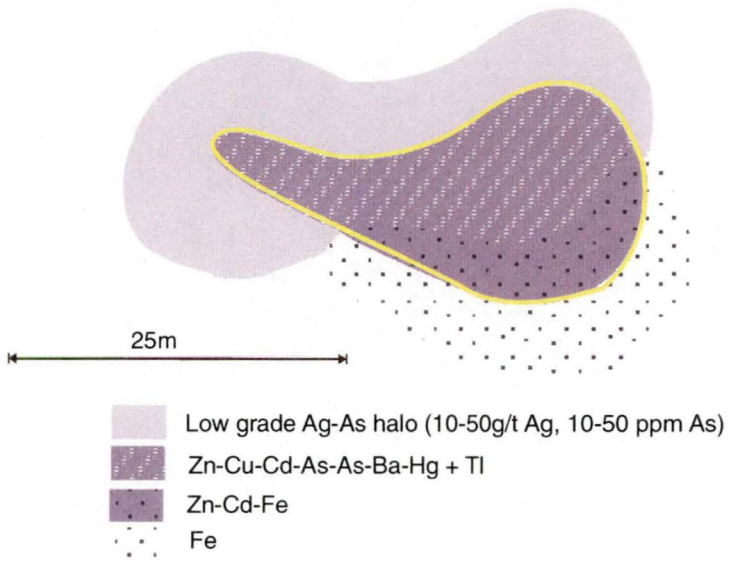

Figure 126. Schematic representation of the elemental zonation in the Upper Zone lenses.

The Gap lens shows a strong vertical zonation of elements (Fig. 127A). A zone of Ba, Pb and As occurs at the top of the Gap lens and grades downwards into a Ba-Zn-Cd zone. The gradation between these two zones is enriched in V. Further down lens the Ba content decreases and Zn and Cd dominate before Fe and then Cu begin to increase. Copper forms a high at the base of the Zn enrichment but decreases quickly leaving a zone of Fe enrichment at the base of the Gap lens. A zone of Ag-Cu and Mo occurs in the centre of the Gap lens (Fig. 127B).

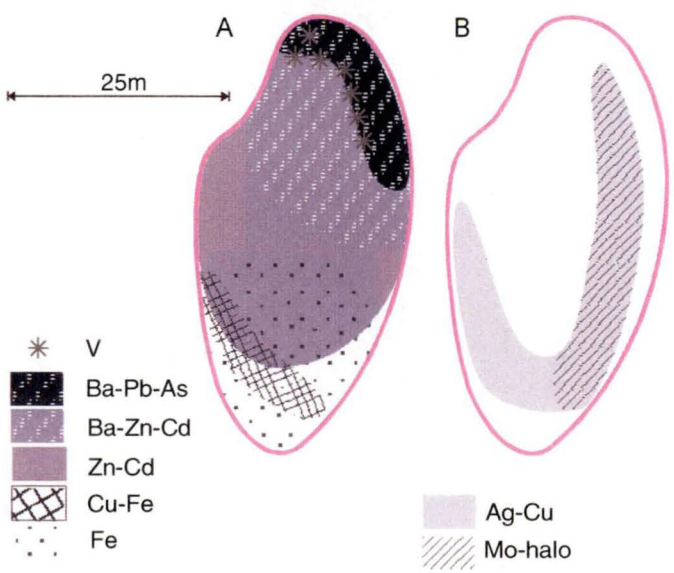

Figure 127. Schematic representation of the elemental zonation in the Gap lens.

9.4.2 Relationship to mineralogy

Mineralogical zonation of each ore lens in the Battle Zone is describeed in Chapter 6. Association of minerals with in each zone are describred in Chapter 7. This section combines the observations from chapter 6, 7 and elemental zonation to explain the association of elements with minerals.

Metal zonation shows a zone of Mn and P enrichment directly above the Battle and Gopher ore lens. This zone of enrichment corresponds to the base of the chert layer overlying these lenses. Whole rock analyses of chert show similar levels of Mn and P. Thus enrichment of Mn and P above the ore lenses represents the host rock composition and shows these elements are lower in the massive sulfides compared to the host rocks.

Phosphorus in the footwall (Price Formation) to the Battle, Gopher and South Trough lenses represents P in the host rocks. Least altered samples (sericite-chlorite-pyrite alteration type) below the Battle Zone also show enrichment in P (up to 6500ppm; Chapter 5).

Enrichment in Ag, Pb, Ba, As, Hg, Ge and V at the top of the ore lenses and in Upper Zone corresponds to a zone of galena-tennantite-barite-zinc sulfides. Elevation in Pb (galena), Ba (barite), As (tennantite) Ge and V (colusite) correspond directly to mineralogy. Scatter plots of Ag-Pb-As and Hg from the 1420 section (Fig. 128) show that Ag has a bimodal association with Pb possibly representing silver in galena and tennantite. However silver shows no association with Hg or As. Mercury shows no association with As or Pb. However Ba shows an association with Pb but not As suggesting an association of barite and galena in the sulfides independent of tennantite.

Underlying the Ag, Pb, Ba, As, Hg zone is the Zn-Cd zone. Cd shows a strong association with Zn in the scatter plots (Fig. 129A). Microprobe analyses of sphalerite from the Battle Zone contain 2000 to 4000ppm Cd (Table 21). Scatter plots of Cu-Zn and Pb-Zn from the Battle Zone show considerable scatter, however a trend appears in the low grade Cu (Fig. 129B) this probably represents the "chalcopyrite disease" in sphalerite. The Pb-Zn plot also shows a fair scatter an upper limit of Pb (Fig. 129C) suggesting a systematic saturation control of Pb in the hydrothermal fluid that deposited the Battle Zone lenses. Zinc shows little association with Ag (Fig. 129D).

Ni enrichment occurs at the base of the Zn-Cd zone and into the Cu-Fe zone. Scatter plots of Ni versus Zn, Cu and Fe are shown in Figure 130 A-C and indicate Ni has the strongest association with Cu. However, microprobe analyses of pyrites from the Battle lens show Ni content up to 1500ppm (Table 22) with a zonation in nickel content of pyrites from below detection at the top of the lens increasing toward the base. Cu and Fe show a strong association (Fig. 130D) thus the occurrence of Ni with Cu probably reflect zonation of Ni in pyrite, with Ni-rich pyrites being more abundant in the chalcopyrite-pyrite zone than the underlying massive pyrite to pyrite stringer zone. The enrichment of Ni in Zn-Cd zone shown on contour plots is due to the increase in pyrite content of ores toward the base of the Zn-Cd zone.

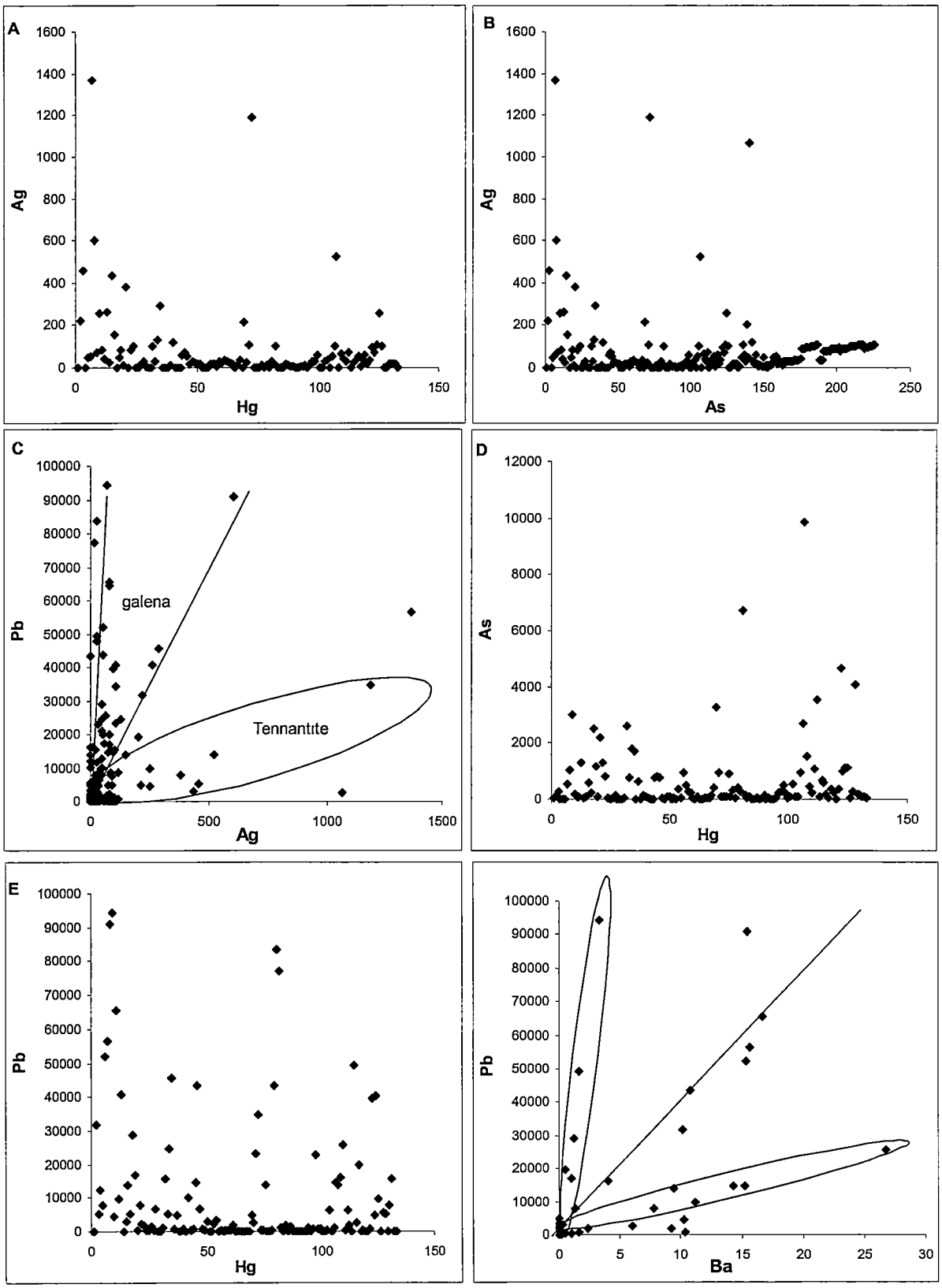

Figure 128. Scatter plots of (A) Ag-Hg, (B) Ag-As, (C) Pb-Ag, (D) As-Hg, (E) Pb-Hg, and (F) Pb-Ba. Showing the relationships between elements at the top of the Battle and Gopher lenses (1420mE section).

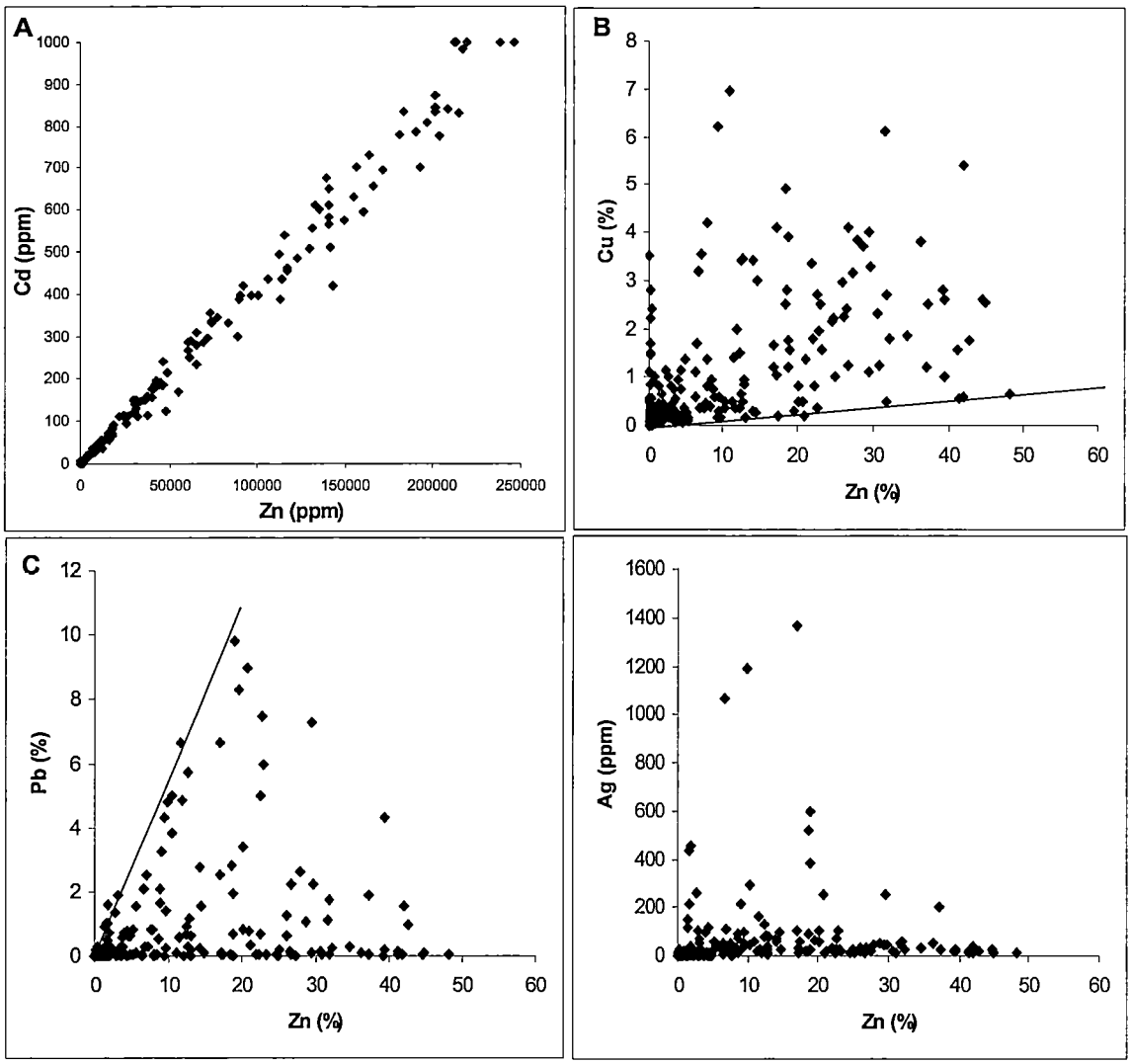

Figure 129. Scatter plots showing the relationships between elements in the Battle and Gopher lenses. (A) Zn-Cd, (B) Zn-Cu, (C) Zn-Pb (from 1420mE section).

Au shows a sporadic distribution through out the lenses, however in the South Trough, Battle and Gopher lenses Au enrichment is most commonly associated with the Fe-rich zone. Scatter plots of Au versus Fe and Ag (Fig. 122A and B) indicate a strong correlation between Ag and Au but little correlation between Au and Fe suggesting the Au probably occurs as electrum, as inclusions in pyrite-rich ore. The lack of correlation between Fe and Au suggests Au does not occur in solid solution in pyrite.

The minerals colusite and renierite (Chapter 7) are observed in the Upper Zone and Gap lenses (Fig. 112K and Fig. 113J) and account for the elevated Ge and V in these zones. However Ge and V are also elevated at the top of the Battle and Gopher lenses (Fig. 110N & T and 111R) suggesting that Ge and V were present in the hydrothermal fluid during deposition of the Battle and Gopher lenses.The lack of colusite in Battle and Gopher lenses suggests conditions were not favourable for deposition of colusite in the Battle and Gopher lenses.

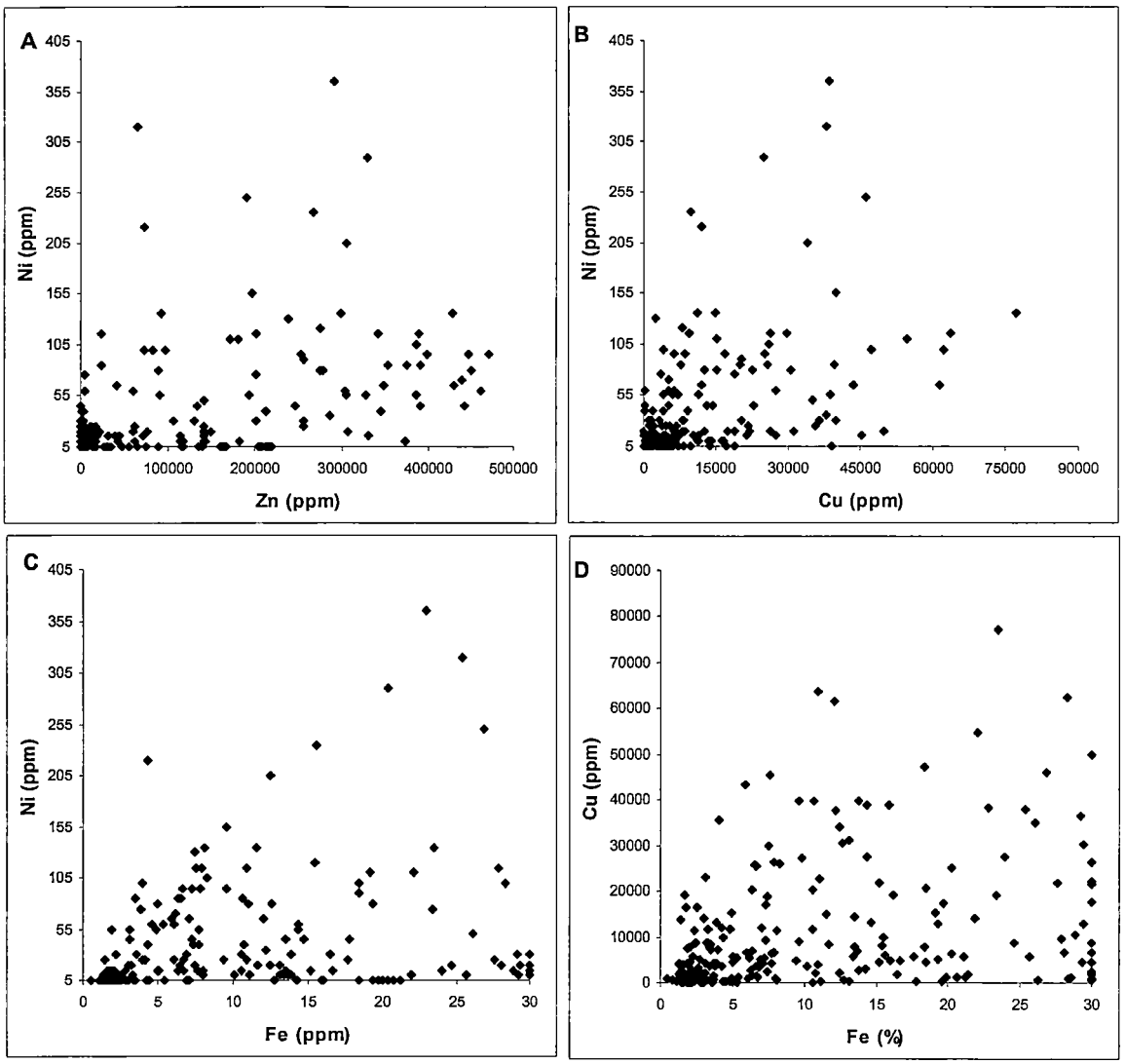

Figure 130. Scatter plots of Ni versus Zn, Cu and Fe and Cu versus Fe showing the relationships between elements in the Battle and Gopher lenses (from 1420mE section).

Bismuth shows a random distribution in the Battle and Gopher lenses, accessory altaite (BiTe; chapter 7) is the most likely cause of the erratic distribution of Bi in the Battle and Gopher lenses

Silver content is low (<50g/t) but relatively constant throughout the Battle, and Gopher lenses. Measured Ag content of minerals are up to 1.3wt% in tellurides, up to 7300ppm in tetrahedrite. Silver was not measured in galena or sphalerite and was below detection in chalcopyrite (0.1wt%). However, in the Battle and Gopher lenses Ag shows a strong correlation with Au (Fig. 131A) and a weak association with Pb (Fig. 128C) and little correlation with Zn (Fig. 131D). Thus it is suggested the low but consistent Ag concentrations throughout the Battle and Gopher lenses are due to Ag in galena and tennantite at the top of the lens and in electrum toward the base of the lenses.

Ag shows a much higher concentration in the Upper Zone and Gap lenses compared to the Battle, Gopher and South Trough lenses. Microprobe data from the Gap and Upper Zone lenses shows Ag contents in bornite (up to 7000ppm), chalcocite (up to 1.5wt%) and late chalcopyrite (1.6wt%) and as a major component of electrum and stromeyerite (CuAgS). Scatter plots of Ag against Cu, Au and Zn (Fig. 132 A-C) and Au-Cu (Fig. 132D) show a strong association of Ag with Cu and a weaker association with

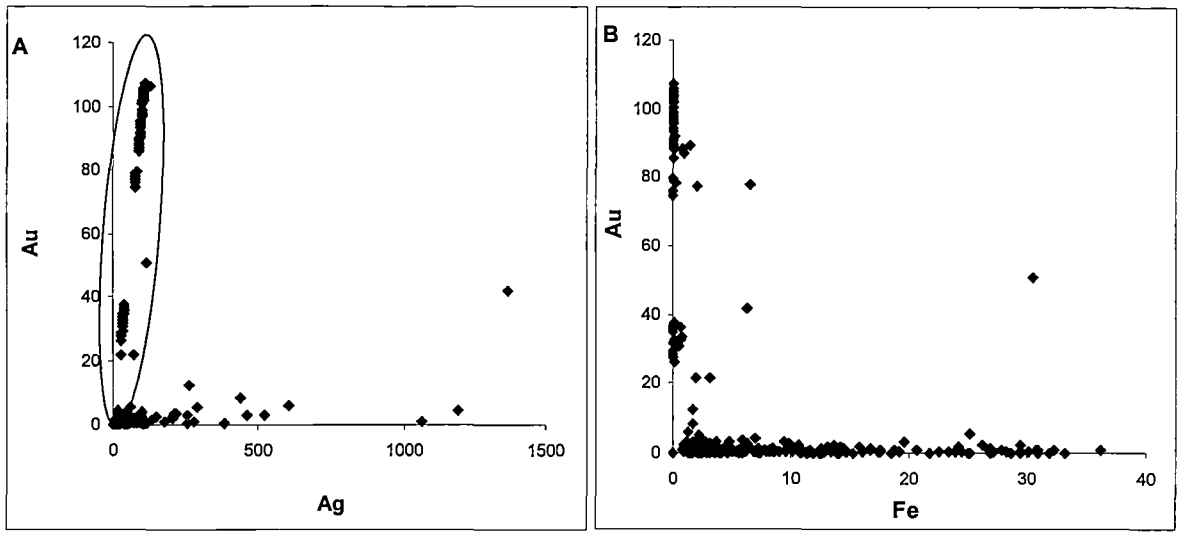

Figure 131. Scatter plots of Au versus Ag and Fe and showing the relationships between elements in the Battle and Gopher lenses (from 1420mE section).

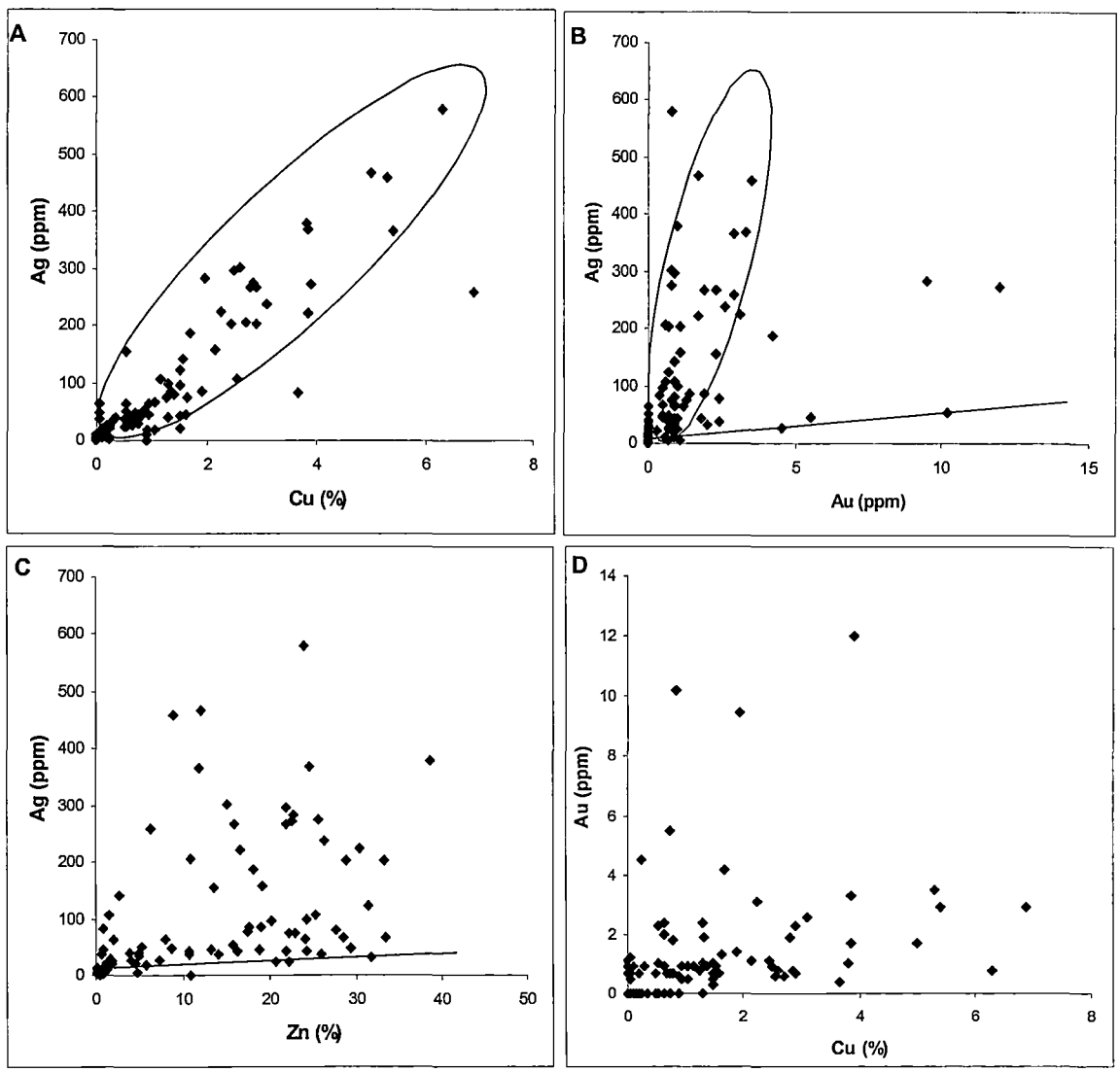

Figure 132. Scatter plots of Ag versus Cu, Au and Zn and Au versus Cu showing the relationships between elements in the Gap lens (from 1420mE section).

Zn and low Ag(<100ppm) values but little correlation between Ag and Au. Thus the distribution and enrichment of silver in the Gap and Upper Zone lenses is due to the bornite-anilite and stromeyerite-chalcopyrite-electrum assemblages.

Bismuth and Mo are associated with Cu-Ag-rich ore in the Gap lens (Fig 112L and 113K), however the presence of these elements is not easily explained by the observed mineralogy. Scatter plots (Fig. 133) show little association between Bi and Mo or with Ag and Cu.

Elemental associations and related mineralogy are summarised in Table 41.

Mineral Assemblage	Elemental Association
Siliceous Horizon	Mn-P-Zn-Cu-Fe-As-Pb
Sphalerite-galena-tennantite (barite-colusite)	Pb-Ag-As-Hg-Zn-(Ba-Ge-V)
Spahlerite-pyrite-chalcopyrite	Zn-Cd-Ag-Fe-Cu
Pyrite-Chalcopyrite	Fe-Cu-Ni-Mo
Pyrite	Fe-Au
Footwall Stringer Zone	Fe-P

Table 41. Summary of the mineral assemblages and corresponding elemental associations from Battle Zone lenses.

9.6 Comparison with other studies

Detailed major and trace element studies of VHMS deposits are not common in the literature. However their importance for understanding the genesis of massive sulfide deposits cannot be overstated. Four such metal zonation studies are described below and then compared with the results of this study. This comparison is particularly important for understanding the chemical conditions of ore formation at Myra Falls.

Hannington et al. (1999a and 1999b) published the results of a comprehensive study into the major and trace element distributions at Kidd Creek deposit, Canada. They recognised two main ore suites and a third more complex assemblage relating to bornite-rich ores. The two main ore suites consist of polymetallic ores (sphalerite-pyrite-pyrrhotite-galena-tetrahedrite-arsenopyrite and cassiterite) enriched in Zn, Ag, Pb, Cd, Sn, Sb, As, Hg, +Tl, + W, and a Cu, Co, Bi, Se, In, $\pm$ Ni suite associated with chalcopyrite-rich-ores. The bornite ores contain essentially the same suite as the chalcopyrite-rich ores (Cu, Co, Bi, Se, Ag, As, Ni) however Cu, Co, Bi and Se concentrations are five to ten times higher in the bornite ores at Kidd Creek. Hannington et al (1999a) also noted a halo of Hg in the hangingwall fragmentals at Kidd Creek and an enrichment in Tl associated with massive pyrite and pyrite stringer style mineralisation.

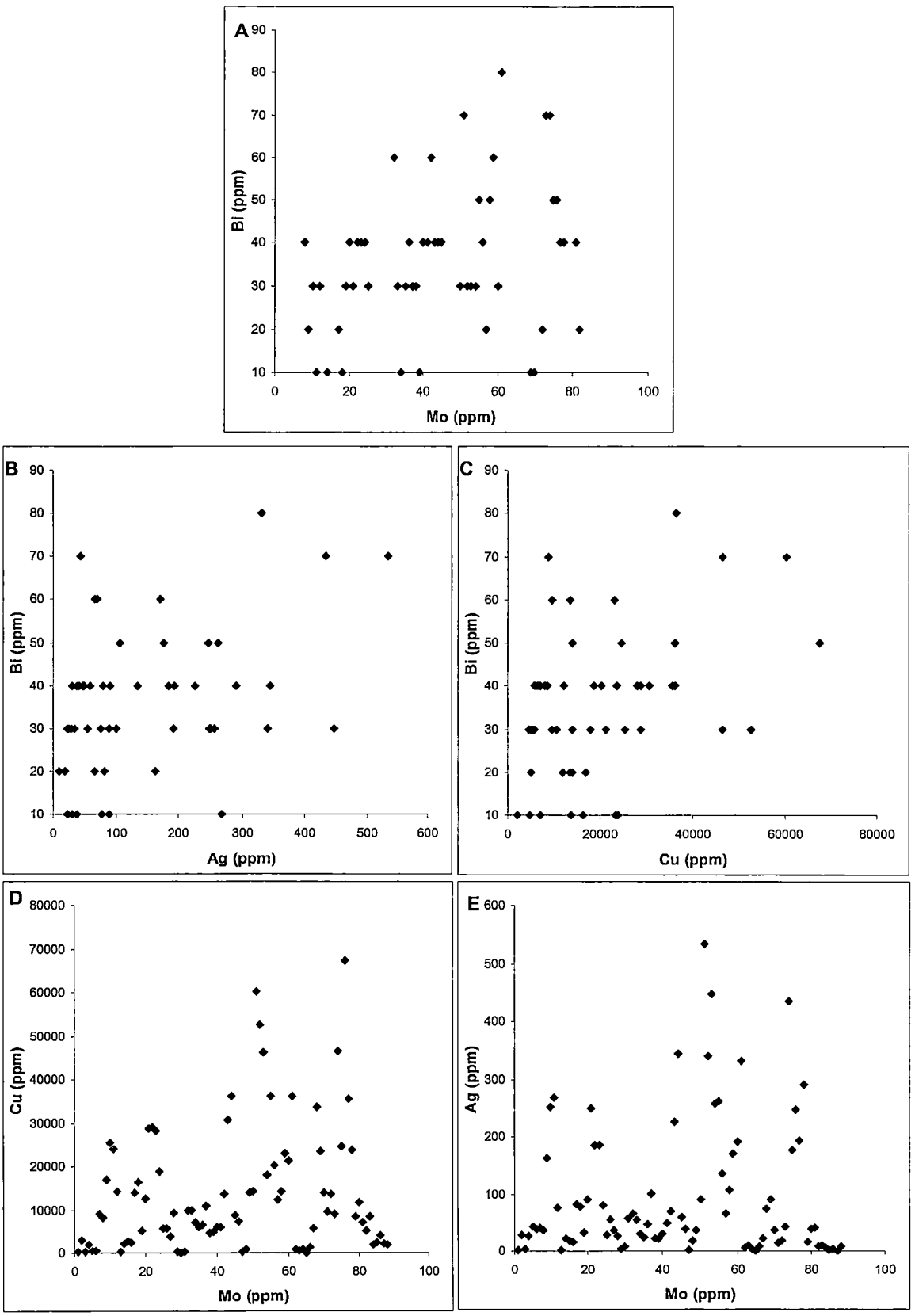

Figure 133. Scatter plots of Bi versus Mo, and Bi and Mo versus Ag and Cu showing the relationships between elements in the Gap lens (from 1420mE section).

McArthur (1996) provided a detailed study of the Hellyer VHMS deposit, Western Tasmania, Australia, and found a classical metal zonation pattern with Cu and Fe enrichment towards the footwall and Zn, Pb, Ag, Au, As and Ba gradually enriched toward the hangingwall. This work included an interpretation of scatter plots showing trend in Cu-Zn plot representing chalcopyrite-disease and a trend in the Pb-Zn plot indicating Pb saturation in the ore fluid.

Smith and Huston (1992) studied the distribution of trace elements in ores and wall rocks at the Rosebery deposit, Western Tasmania, Australia. Mineralisation at Rosebery occurs in two distinct blanket-like zones: a stratigraphically lower zinc-lead-copper massive sulfide and a higher massive barite. The lower horizon can be further divided into two types: a pyrite-chalcopyrite massive sulfide and a sphalerite-galena-pyrite massive sulfide. Chemically the massive barite is enriched in Ba-Ag and Sb when compared to the underlying massive sulfides. Two elemental suites were found in the massive sulfide ores: (1) Pb-Zn-Au-Ag-Cd and Sb association and (2) Cu-Bi-As-Fe association. The Pb-Zn association was found to be concentrated in the upper portions of the orebody and in the adjacent hangingwall rocks, while the Cu association occurred in the lower portions of the orebody and footwall rocks. These associations are observed up to 30m from the massive mineralisation (Smith and Huston, 1992). Outside this zone Zn and Pb are erratic and do not vary systematically. However Tl and Hg form a halo up to 2km from the zones of strong mineralisation (Smith and Huston, 1992).

Metal zonation of massive sulfide mineralisation in the Spanish section of the Iberian Pyrite Belt has also been studied by a number of authors (summarised in Leistel et al., 1998). Three ore types are distinguished within the massive sulfide bodies based on their mineralogical composition: polymetallic, pyritic and Cu-rich (Almodovar et al., 1998). The polymetallic type is characterised by sphalerite and galena with minor tetrahedrite, arsenopyrite, chalcopyrite and cassiterite. Cu-rich associations are characterised by chalcopyrite and Bi-minerals. A generalised zonation occurs from polymetallic ores at the top of massive sulfide lenses, down through Cu-rich ores and into stringer mineralisation where pyritic ores dominate. Chemical analysis indicates Ag, Au, Cd, Sn, Hg and Tl are more abundant in the polymetallic ores along with Zn, Pb and Sb, whereas Co and Bi are concentrated in Cu-pyrite and some pyritic ores (Almodovar et al., 1998). A more detailed study of the stringers style mineralisation was conducted by Marcoux et al. (1996) which found two paragenetic sequences within the stringer zone. The first is cobalt mineral assemblage which marks deep zones, while the second and more ubiquitous Bi-Cu-Pb-(Sb-Se) and Bi-Te-rich mineral assemblage which occurs in Cu-rich ore and at the top of the stringer system (Marcoux et al., 1996).

At Myra Falls the Battle Zone lenses show a similar elemental zonation to the Kidd Creek, Rosebery and Iberian Pyrite Belt deposits with polymetallic ores enriched in Zn-Ag-Pb-Au-Cd-Hg-Sb at the top of the massive sulfide lenses grading down to a Fe-Cu-Ni$\pm$Bi association at the base of the lenses. The major difference between Kidd Creek and the Iberian Pyrite Belt and the Battle Zone is the lack of Sn at Myra Falls. Massive barite ores at top of the Rosebery deposit show analogies with Upper Zone lenses and the top of the Gap lens with Ba-Ag-Sb association. Tl and Hg halos found at Kidd Creek and Rosebery also show similarities to the distribution of these elements in the Battle Zone. One of the most interesting observations is the presence of Bi in bornite rich ores at Kidd Creek. Bismuth occurs as Bi-Pb-Cu-Se-

sulfides which occur as small (<10um) disseminated grains in the bornite-rich ores (Hannington et al., 1999b). Bismuth-tellurides are known from the Battle lens however the observations at Kidd Creek may help to explain the distribution of Bi in the Gap lenses.

The bornite mineralogy in the Gap lens shows a different element zonation (Cu-Ag-Mo) to the bornite-zone at Kidd Creek suggesting the two are formed from different fluids. The stromeyerite-chalcopyrite-electrum assemblage has no analogy in any of the four deposits reviewed.

9.7 Conclusions

Battle Zone lenses (except the Upper Zone lenses) show typical VHMS metal zoning from Fe and Fe-Cu-rich base through Cu-Zn-rich sulfides to Pb-Zn-Ba-rich tops. Comparison of the Myra Falls lab with an outside commercial laboratory showed excellent results with correlation >0.96 for Cu, Pb, Zn and Fe. Only Ag showed variations which concerned the author. The variations are most likely the result of the difference in methods used by the two labs (fire assay – Boliden-Wesmin Ltd; nitric acid-aqua-regia digestion and atomic absorption spectrometry – Chemex) and are confined to the high Ag values found in the Upper Zone and Gap lenses.

The South Trough lens shows the highest Fe–grades and lowest Pb and Ba of all lenses studied in the Battle Zone. The South Trough lens shows a strong pyrite core defined by Fe and is zoned upward and toward the south, through a series of sub-lenses which grade from Cu-Fe-Ni±Au rich bases through Zn-Cd rich sulfides and weak Ag-Pb-As-Hg-rich tops. The hangingwall to the South Trough sub-lenses is enriched in Mo while the footwall shows Te and Se enrichment.

Battle and Gopher lenses lie just above the South Trough lens and have slightly lower Fe grades and higher Pb and Ba. Both lenses show a central Zn-Cd high underlain by Cu-Mo-Ni and then Fe±Au. The Zn-Cd high is directly overlain by Pb-Ba-As-Hg±Au enriched sulfides. Ag forms a low but even halo through the Battle and Gopher lenses and into the hangingwall. This zonation extends along the width of the Battle lens, but is disrupted in the Gopher lens by its asymmetric shape and strong faulting. The metal zonation in the Battle and Gopher lenses correlates well with mineralogical zonation of pyrite to chalcopyrite-pyrite rich sulfides in to sphalerite-rich ore and sphalerite-galena-tennantite+barite at the top of the lenses. 3D modelling of the Battle and Gopher lenses also shows a zonation of sulfides for high Fe-Zn in the 1600-1700nE portion of the lens, with Pb, and Ba increasing toward the west.

Upper Zone lens does not show the footwall to hangingwall zonation seen in underlying lenses, instead Zn-Pb-Cu-Ba-Au-Ag-As-Hg and Cd are evenly distributed through out the lenses which are underlain by Fe and have a halo of Ag and As extending into the hangingwall. Pb-Ba-Au-Ag-As and Hg are markedly enriched in the Upper Zones, while the Cd content of the Upper Zone lenses is slightly lower. The even distribution of metals through out the Upper Zone lenses is not compatible with the strong changes of ore types reported in chapter 6. The reason for this discrepancy is the tight drill spacing of Upper Zone intersection, which are averaged during the contouring process.

The Gap lens shows high Au-Ag-Ba-As-Pb values similar to the Upper Zone lenses, but also contains a strong mineralogical and metal zonation. The base of the Gap lens is Fe-rich due to pyrite and grades up through Cu-Fe-rich sulfides (pyrite-chalcopyrite) to Zn-Cd (sphalerite) and Pb-Ba-As-(Hg) enrichment at the top of the lens, a zone of V enrichment sits between the Zn-Cd and Pb-rich zones and corresponds to the presence of colusite in the lens. The Gap lens zonation is overprinted by a Cu-Ag-Bi-Mo rich spine, which runs up the centre of the lens and corresponds with the bornite-chalcocite assemblage. Gold and Ag values are elevated through out the Gap lens and correspond to late electrum-stromeyerite assemblage.

Chapter 10

Sulfur Isotopes

10.1 Introduction

Sulfur isotopes, when combined with detailed geological and geochemical studies, can provide information on (1) the source of sulfur in the ore forming fluid (2) the temperature of mineralisation, (3) the chemical conditions and mechanisms of ore deposition (Ohmoto and Rye, 1979). Examination of the spatial distribution of sulfur isotope values may also provide valuable information on the evolution of mineralising fluids (Ohmoto, 1986).

A sulfur isotope study was carried out to examine the sulfur isotopic compositions of sulfate and sulfide species of the Battle Zone. This is the first study of sulfur isotopes in the Battle Zone. Sulfur isotopes for lenses outside the Battle Zone have also been determined in conjunction with this study by Dr J.B. Gemmell. A previous study of sulfur and lead isotopes, in the Myra Falls district, was published by Seccombe et al., (1990), which focused on the HW, Lynx, Myra and Price lenses.

10.2 Methods

Sulfide and barite mineral separates were drilled from hand specimens and core with the aid of a small-diameter dentist drill. Minor contamination from fine grained intergrowths of other sulfides or gangue (muscovite, quartz, barite) was present in most samples. The sulfide samples were then combusted (950°C) with excess Cu_2O in vacuo to produce SO_2 by the method of Fritz et al. (1974). Sulfates were mixed with excess SiO_2 and Cu_2O and reacted at 1100°C in vacuo to produce SO_3. The SO_3 was then reduced to SO_2 by passing it over copper turnings at 600°C by the method of Robinson and Kusakabe (1975). SO_2 from the respective methods was then analysed on a VG SIRA series 10 micromass, dual inlet, stable isotope mass spectrometer, in the Central Science Laboratory at the University of Tasmania.

Fourteen samples of mixed sulfides were prepared as laser ablation sections, according to the method described by Huston et al., (1995) Pyrite in these samples were analysed using a laser ablation microprobe connected to a conventional VG Sira Series II mass Spectrometer, using the method detailed in Huston et al., (1995). The laser ablated an area 400-500μm in diameter, significantly larger than the 200-250μm diameter analyses standard for CSL- laser ablation samples (pers

com. K. Harris 2000). The reasons for this is thought to be the sphalerite rich matrix in most samples, the sphalerite ablating at a power lower than that needed to ablate pyrite.

Results are expressed in standard (δ) notation with the Canyon Diablo Troilite (CDT) used as a reference. Sample reproducibility for conventional sulfur isotope analyses is typically ± 0.05‰ with an analytical uncertainty less than ± 0.02‰. For the laser ablation sulfur isotopes analytical precision is estimated at 0.4-0.5‰ (Huston et al., 1995).

10.3 Results

Sulfur-isotope data for sulfides (conventional and laser ablation techniques) and sulfates from the Battle Zone are given in Appendix 5 and are plotted in Figure 134. The sulfur data forms a very tight cluster with a range of -1.11‰ to 4.06‰ and a mean of 1.76‰, with two exceptions -3.22‰ and -7.85‰. Sulfate data forms a spread with values ranging from 18.44‰ to 28.68‰ with a mean of 22.08‰.

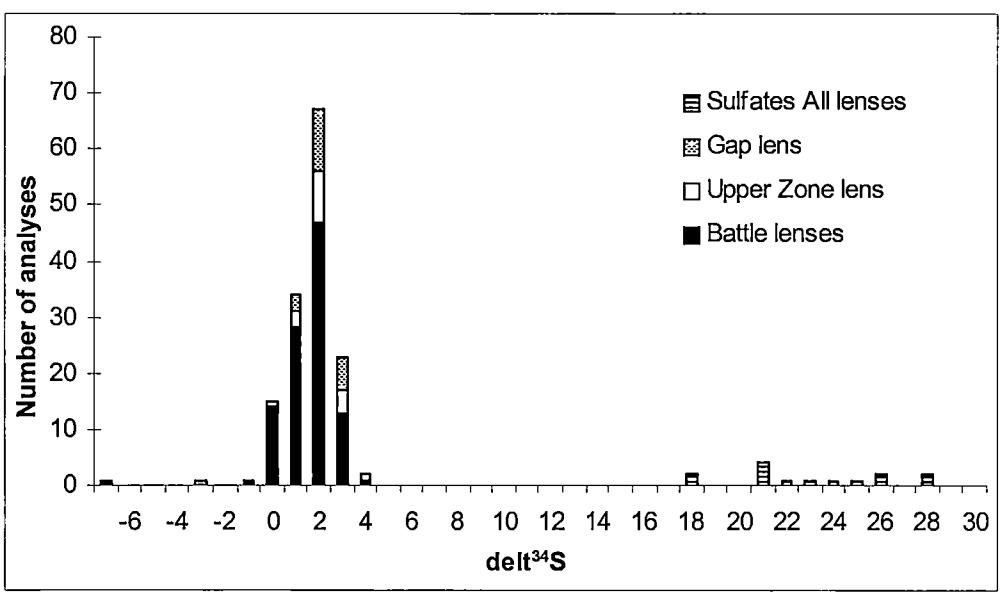

Figure 134. Sulfide and sulfate analyses from Battle Zone, total conventional and laser ablation data

Figure 135 displays sulfur isotope data by lens and mineral (pyrite, sphalerite, chalcopyrite). The Battle lenses (includes Battle, Gopher and South Trough lenses, Fig. 135A) shows a range of pyrite values from -1.11‰ to 4.06‰ with an average of 2.09‰. Stringer mineralisation (Fig. 135B) shows a similar range with a slight shift to lower values and one anomalous value of -7.85‰ and an average of 1.65‰. Chalcopyrites in the Battle lens show a very restricted range of values between $\delta^{34}S$ 2.01‰ and 2.44‰ in both the stringer and massive sulfides. Sphalerites show a larger range of values (1.84 - 2.90‰) but cluster around the same value as the pyrite and chalcopyrite. Pyrite from the hangingwall (chert and HW Rhyolite mass flows, Fig. 135C) show values between 1 00‰ and 2.93‰, with an average of 1.97‰, slightly lower than that for the underlying massive sulfides.

Upper Zone and Gap lenses (Fig. 136A & B) have a higher average $\delta^{34}S$ value for pyrite than the Battle lenses. The Upper Zone lens pyrites average $\delta^{34}S$ of 2.56‰, while the Gap pyrites show the

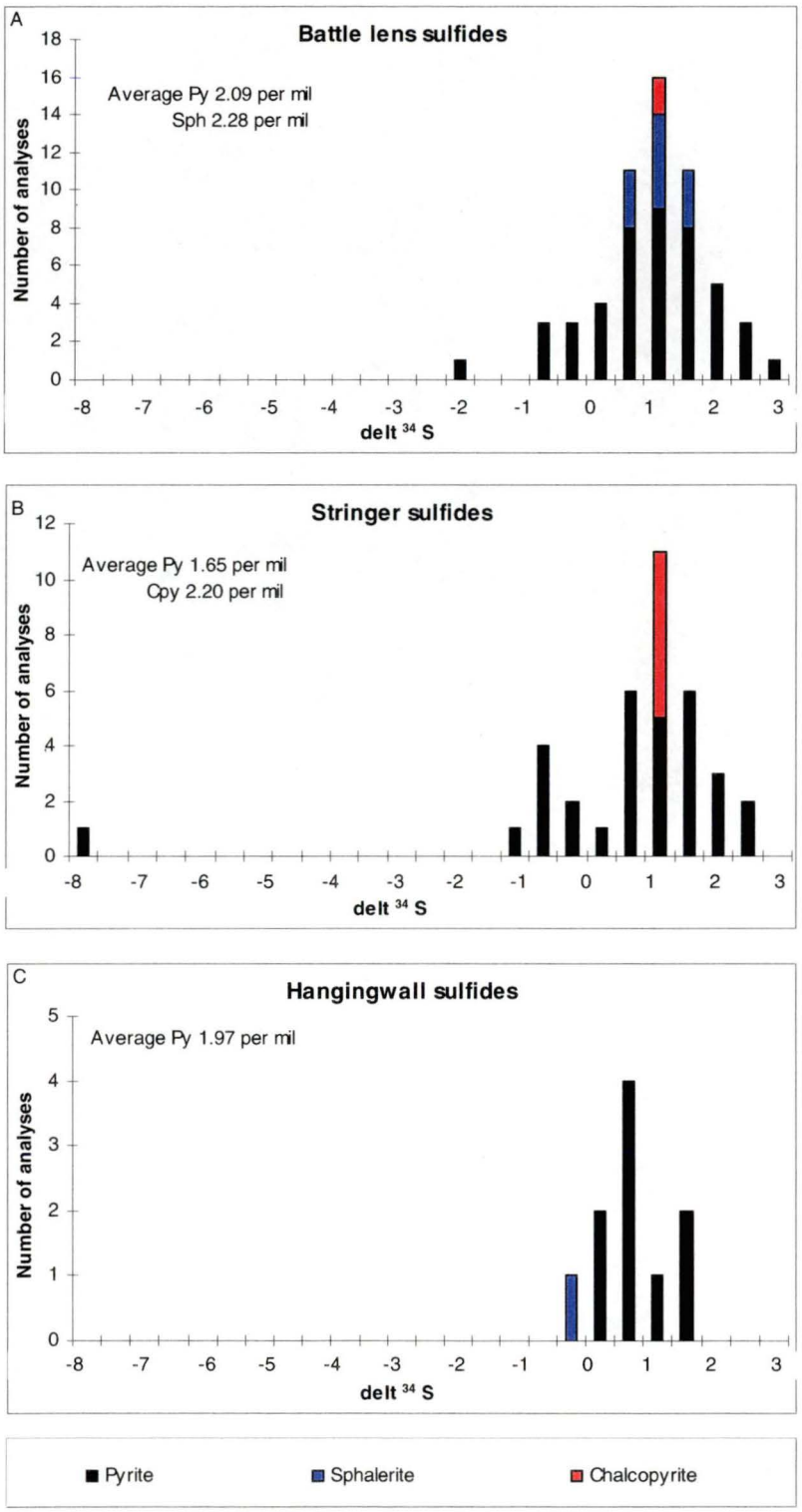

Figure 135. Sulfur isotopes for pyrite, sphalerite and chalcopyrite, A. Battle lens samples, B. Battle lens stringer zone (footwall) samples. C .Hangingwall to Battle lens samples.

Py = pyrite, Sph = sphalerite, Cpy = chalcopyrite

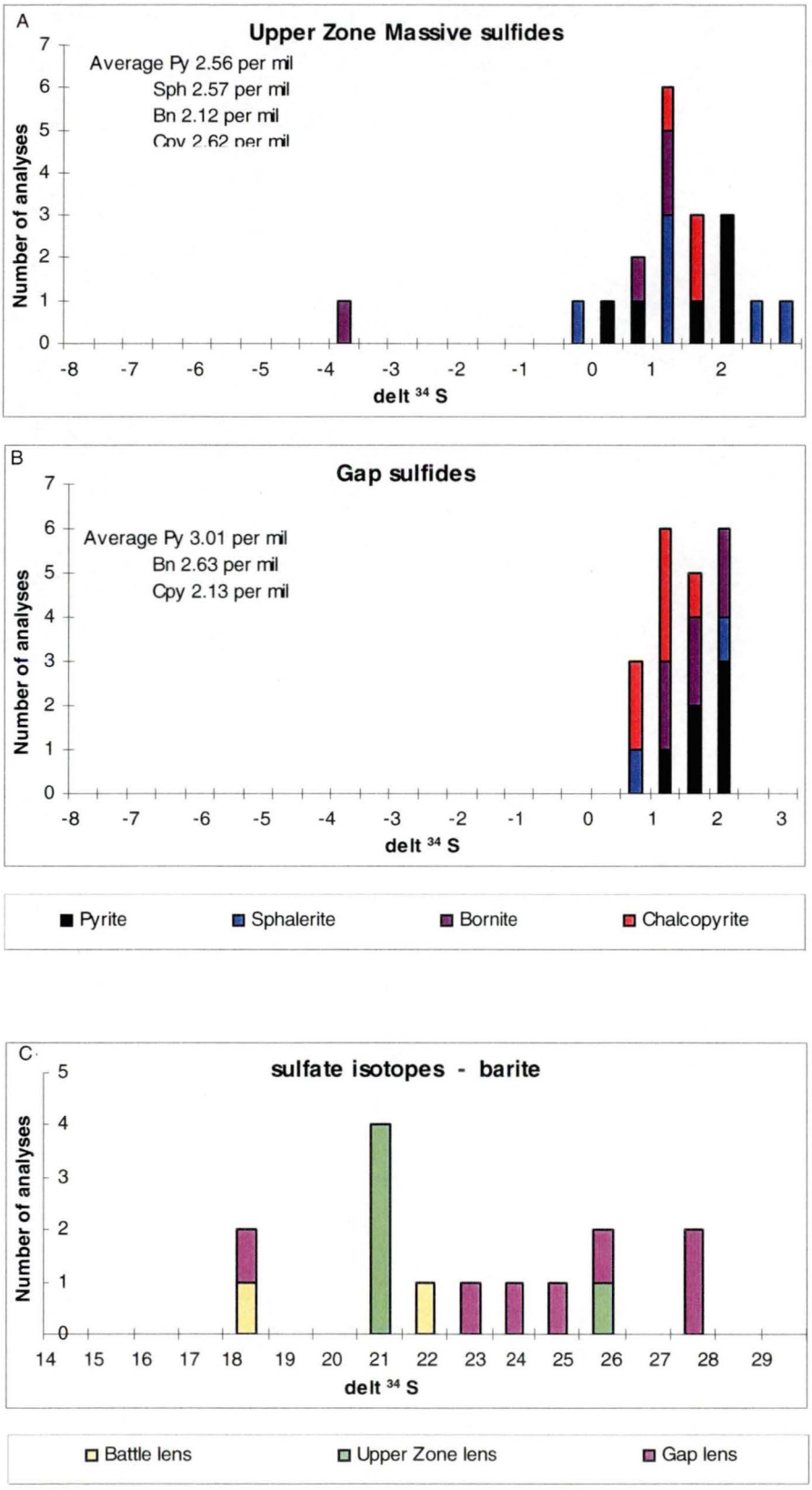

Figure 136. Sulfur and sulfate isotopes: A. Upper Zone lens B. Gap lens, C. sulfate isotopes all lenses.

Py = pyrite, Sph = sphalerite, Cpy = chalcopyrite, Bn = Bornite

highest $\delta^{34}S$ average of 3.01‰. $\delta^{34}S$ values for sphalerite in the Upper Zone lens show the broadest range of all lenses from 0.83‰ to 3.71‰. One bornite sample analysis from the Upper Zone lens has an anomalous $\delta^{34}S$ value of -3.22‰ this sample shows significant stromeyerite alteration of the bornite. Bornite-chalcopyrite mineral pairs were also determined for the Upper Zone and Gap lenses (Table 1, Appendix 5). The Gap lens has $\delta^{34}S$ values for bornite ranges from 2.00‰ to 3.26‰. These values are consistently higher than the $\delta^{34}S$ for chalcopyrite (1.70‰ to 2.55‰). In contrast the Upper Zone chalcopyrites are consistently higher than their corresponding bornites, with one exception.

Sulfates, in the form of barite, from the Gap and Upper Zone lenses and the top of the Battle lens give $\delta^{34}S$ values of 18.44‰ to 28.68‰ (Fig. 136C). In general, the Gap lens has the highest $\delta^{34}S$ values of 23.41‰ to 28.15‰ with one notable exception of 18.95‰ (Fig. 137). In contrast Upper Zone barites have $\delta^{34}S$ of 21.55‰ to 26.04‰, while two barites analysed from the Battle lens show the lowest $\delta^{34}S$ values of 18.44‰ and 22.35‰.

Laser ablation

Laser ablation sulfur isotope results are listed in Table 5, Appendix 5. $\delta^{34}S$ values vary from -0.25‰ to 4.06‰, with average $\delta^{34}S$ values for each sample between 0.66‰ and 2.62‰, very similar to that found by conventional techniques. Variation of $\delta^{34}S$ within each sample was between 0.5 per mil and 2.36 per mil. Detailed zonation of pyrites from the Battle Zone was not possible due to the size of actual laser ablation pits. Actual laser ablation pits are cone shaped, 400-500μm wide at the top to 100-200μm at the base of the sulfide chip (Fig. 138). The average grain size of pyrites in the Battle Zone lenses is 100μm to 700μm for the coarse euhedra (Fig. 139A & B), with features like cores and overgrowths being 100μm to 300μm in diameter (Fig. 139A).

Four pyrite samples were analysed by both conventional and laser ablation techniques (Table 5, Appendix 5). The pyrite porphyroblasts analysed have small but significant variations in their laser ablation sulfur isotopes (Fig. 140A) with averages close to that found via conventional methods. In contrast, recrystallised and annealed pyrites analysed have a wider variation in laser ablation results (Fig. 140B & C) and their averages do not conform well to the conventionally determined $\delta^{34}S$ values.

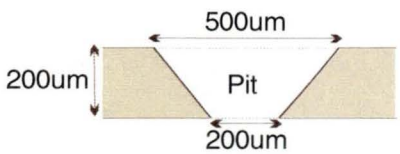

Figure 138. Diagram of laser ablation pit through a chip sample showing characteristic cone shape and approximate dimensions.

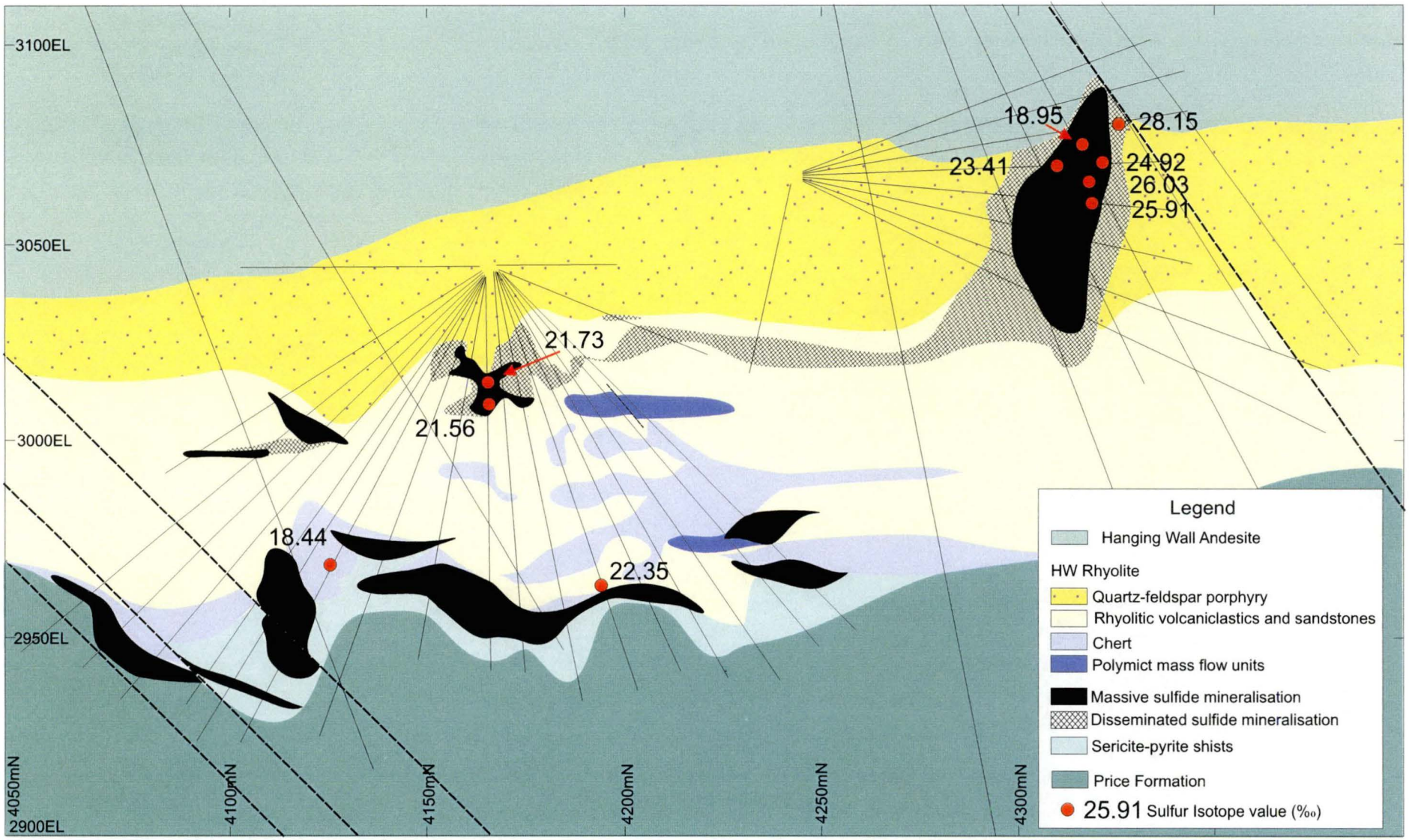

Figure 137 Sulfur isotope values (per mill) for sulfates in Battle Zone 1420mE section.

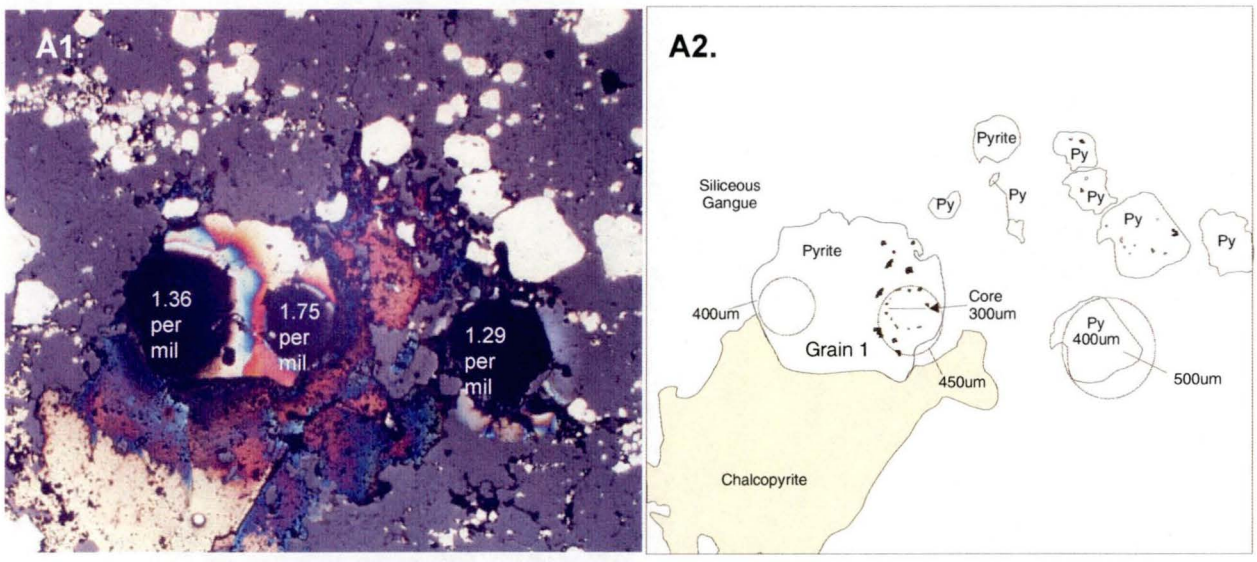

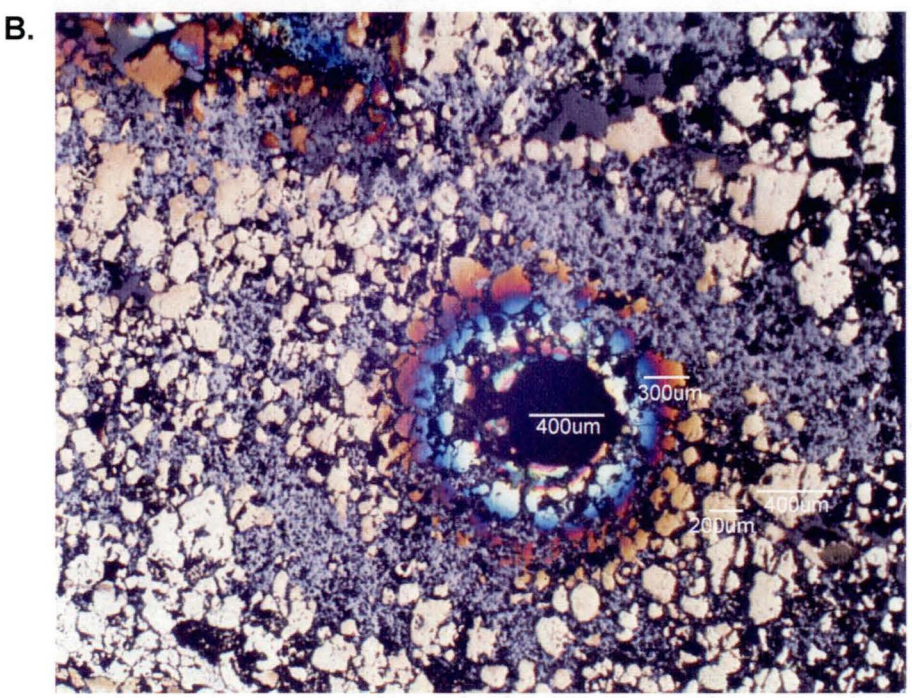

Figure 139. Laser ablation pits in recrystalised pyrite grains, with minor chalcopyrite in siliceous gangue. A1. Grain 1 - 1800um wide, with a 300um core. A2 400 to 500um laser pits are too large to determine the del^{34}S value of pyrite without contamination. BG18-482 34.8m. B. 400um laser ablation pit overlaps edge of even largest pyrite crystals in this banded ore sample causing contamination from the matrix sphalerite. The size of various pyrites surrounding pit are shown, BG18-484 74.0m.

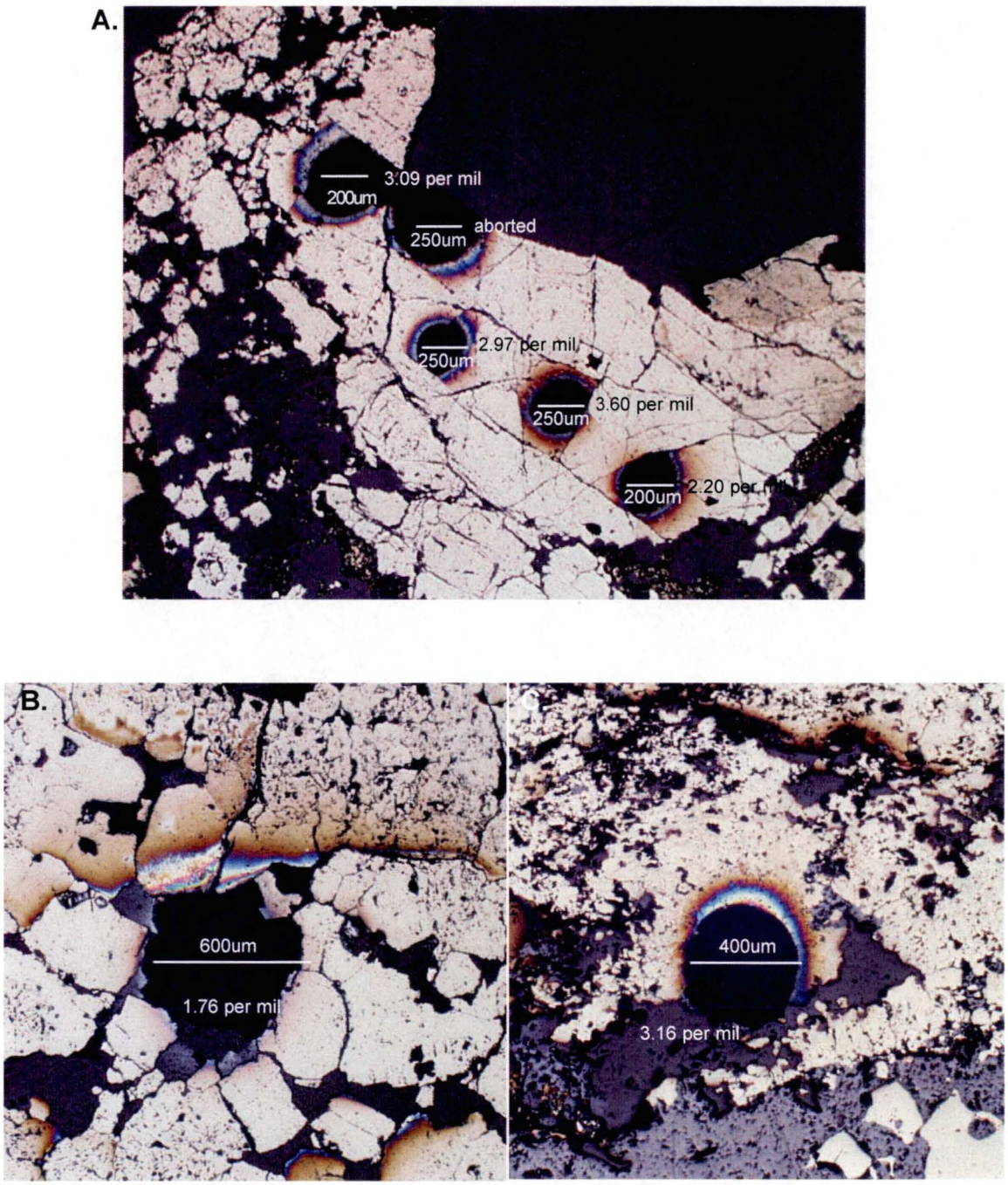

Figure 140A. Laser ablation pits in a pyrite porphyroblast, note the average of the laser ablation samples is 2.50 per mil, close to the 2.62 per mil determied for this sample by conventional sulfur isotopes. BG18-798-49.1m. B and C Laser ablation pits from two different pyrite types, B. recrystallised pyrite, C, fine grained annealed pyrite. The laser ablation average for this sample is 1.95 per mil, conventional delta^{34}S value 2.79 per mil. BG18-778 124.9m

10.4 Discussion

Source of Sulfur

It is generally considered that the two main sources of sulfur in seafloor volcanic-hosted massive sulfide systems are the reduction of seawater sulfate and magmatic sulfur. (Ripley and Ohmoto, 1977; Ohmoto and Rye, 1979). Magmatic sulfur may enter the hydrothermal fluid either as direct magmatic emanations, or as sulfur leached from the host rocks (magmatic origin) during circulation of the hydrothermal fluid (Ohmoto and Rye, 1979; Solomon et al., 1988). This sulfur will have $\delta^{34}S$ values of 0 $\pm$ 5‰ and may either form sulfides with $\delta^{34}S$ values in the range -5‰ to 5‰, or combine with other sources of sulfur to alter the overall $\delta^{34}S$ ratio.

Sangster (1968) first observed a correlation between $\delta^{34}S$ of syngenetic sulfide deposits and $\delta^{34}S$ of coeval seawater sulfate. Sangster (1968) demonstrated that, on average $\delta^{34}S$ of seawater sulfate is 17.5 $\pm$ 2.5‰ greater than that of the sulfide minerals in VHMS deposits. This is confirmed by Huston (1999) in a review of stable isotope characteristics of VHMS deposits. However, Huston (1999) found a greater variability in the data, which he attributed to imprecise age determinations in some districts. The ~17‰ shift between ambient seawater sulfate and the $\delta^{34}S$ of sulfide minerals in VHMS deposits is attributed to the reduction of seawater sulfate. Seawater sulfate may be reduced organically via bacterial reduction or by inorganic processes.

Bacterial reduction of seawater sulfate has largely been ruled out in VHMS systems. Biogenic fractionation of sulfur isotopes is considered to large to account for observed differences in $\delta^{34}S$ between coeval seawater sulfate and VHMS sulfide minerals (Ohmoto and Rye, 1979). Additionally, the host rocks in VHMS environments are generally too poor in organic carbon content, and the temperatures of deposition, and hence the hydrothermal fluid, are too high (200-350°C) to allow bacterial reduction (Ohmoto and Rye, 1979). However bacterial reduction may produce sedimentary sulfides near the seafloor, which may subsequently be leached by the hydrothermal fluids (Ohmoto and Rye, 1979).

Ohmoto et al (1983) and Solomon et al (1988) suggested that reduction could occur inorganically by the oxidation of ferrous iron or reduced carbon in the host volcanics. The fractionation of sulfur isotopes arises from the fact that chemical reaction rates are mass dependent and that one isotopic species reacts more rapidly than another. In general, the molecules containing the lighter isotope will have the faster reaction rate. Consequently, the initial products tends to be enriched in the lighter isotope. If the reduction is complete i.e. all seawater sulfate were reduced, the resulting aqueous sulfide (and sulfide minerals) would have $\delta^{34}S$ approximately equal to coeval seawater sulfate. At 250°C the equilibrium value of $\Delta(_{SO4^{=}\text{-}H2S})$ is approximately 25‰, although many deposits show smaller Δ values (eg Kuroko ores have a Δ of ~20‰; Ohmoto and Rye, 1979). Thus in VHMS systems where reduction of seawater sulfate is incomplete the resulting sulfides will have $\delta^{34}S$ values between 18‰ and 25‰ below ambient seawater sulfate and the $\delta^{34}S$ value of the ambient seawater

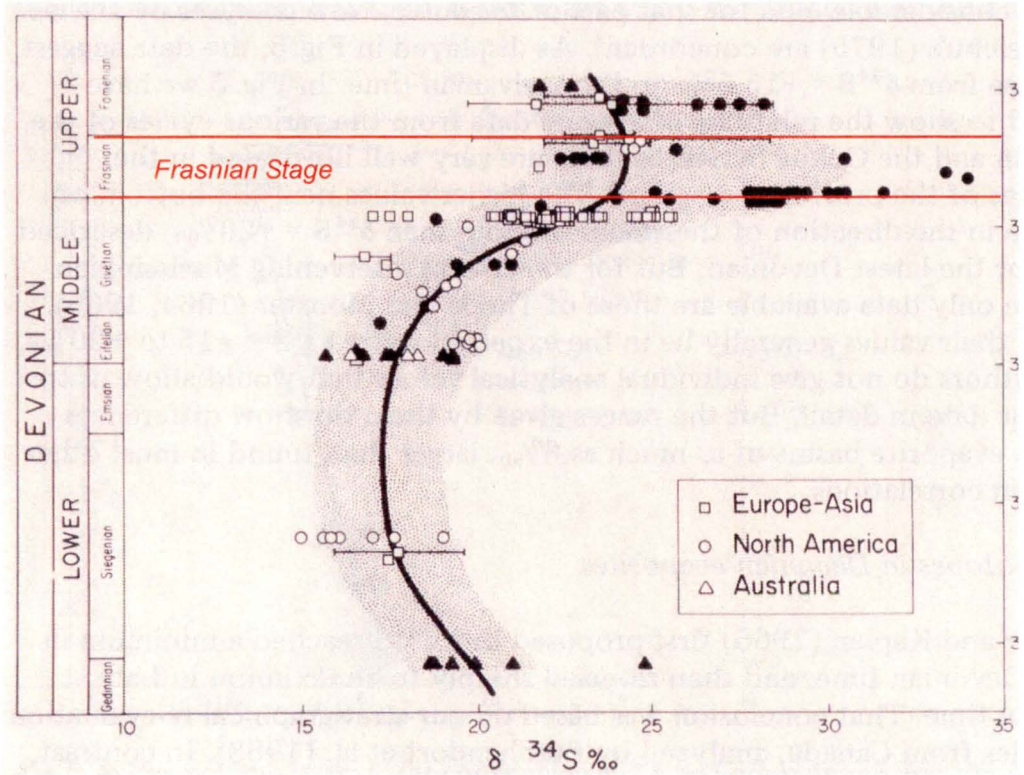

Figure 141. Seawater sulfate curve for the Devonian time from Claypool et al. (1980)

sulfate, depending on the extent of reduction and temperature of hydrothermal fluid (Ohmoto and Rye, 1979).

Sulfides

The sulfur data from the Battle Zone forms a tight cluster indicating a very homogenous source. The ambient seawater at the time of formation is assumed to have been from +23‰ to as high as +28‰ (Claypool et al., 1980; Goodfellow and Jonasson, 1984; Fig. 141). At 250-400°C, the 18‰ to 25‰ shift suggested by Ohmoto and Rye (1979) would give $\delta^{34}S$ values between -2‰ and 10‰. Battle Zone $\delta^{34}S$ measured were between -1.11‰ and 4.06‰. These data suggest that reduction of seawater sulfate in the hydrothermal system caused a shift around 25‰, or that there is an additional source of sulfur (possibly magmatic) in the system. Alternatively $\delta^{34}S$ values of between -1.11‰ and 4.06‰ found the Battle Zone could be generated by the direct input of magmatic sulfur. Unfortunately due to the overlap of these two processes in Frasnian time, it is difficult to distinguish between a reduced seawater ± leached magmatic sulfur and a direct magmatic source.

$\delta^{34}S$ of bornites from the Upper Zone and Gap lenses show similar values to the pyrite, sphalerite and chalcopyrite suggesting a similar homogeneous source. The possibility of a magmatic source with the same isotopic signature cannot be ruled out due to the overlap in values. The significance of the $\delta^{34}S_{bornite} > \delta^{34}S_{chalcopyrite}$ in the Gap lens and the reversal of this trend in the Upper Zone lenses has not been established.

Isotopically light values -3.11‰ and -7.85‰ found in the Battle Zone, may be due to a variety of processes. The bornite sample (-3.11‰) shows significant stromeyerite alteration, textural evidence from other samples suggests the stromeyerite is a late, metamorphic remobilisation of Cu-Ag and

Au. Alternatively, light sulfur isotopes in the footwall volcanics may be due to contribution of biogenetically reduced sulfate from intercalated sediments. G158DD5 the sample that gave the $\delta^{34}S$ of -7.35‰ shows no evidence of supergene alteration.

Sulfates

Barites may obtain sulfur from two sources (1) sulfate in the hydrothermal fluid, or (2) seawater sulfate. Sulfate in the hydrothermal fluid is likely to be in isotopic equilibrium with coexisting sulfides (Solomon et al., 1988). When sulfate reduction is complete the hydrothermal fluid will produce sulfate minerals with $\delta^{34}S$ values equivalent to coeval seawater. However, if sulfate reduction does not go to completion $\delta^{34}S$ values higher than those of coeval seawater will be produced (Gemmell and Large, 1993). Sulfates derived directly from seawater would retain their isotopic composition (1-2‰ fractionation factor, pers.com. Gemmell, 2000) and show $\delta^{34}S$ values similar to the ambient seawater. Barites from the Battle Zone give $\delta^{34}S$ values from 18.44‰ to 28.68‰. These values are consistent with a direct seawater derivation, from the ambient seawater of +23‰ to +28‰.

10.5 Effect of Stratigraphic position

Stratigraphic position influences the average $\delta^{34}S$ of sulfides and sulfates in the Battle Zone. The mean $\delta^{34}S$ value of pyrite starts at 2.09‰ in the Battle, Gopher and South Trough lenses, increases to 2.56‰ in the Upper Zone lenses and reaches a maximum of 3.01‰ in the Gap lens (Fig. 142). This increase in the mean $\delta^{34}S$ of pyrite with stratigraphic position may be caused by (1) increase in the $\delta^{34}S$ value of seawater feeding into the hydrothermal system through the Frasnian stage, or (2) by an increase in the amount of unreduced seawater mixing with the hydrothermal fluids. It is likely that mixing occurred within the highly permeable rhyolitic mass flows which form the footwall to the Upper Zone and Gap lenses.

The Battle, Gopher and South Trough lenses, formed under at least a thin cover of sediment as is evident by the replacive nature of the upper contact (see chapter 6). This cover may have restricted seawater interaction in the Battle lenses. The Upper Zone lenses ponded below quartz porphyritic rhyolite flows. The highly permeable rhyolitic mass flows deposits below the Upper Zones lenses would allow considerable interaction between the hydrothermal fluid and seawater. The Gap lens is overlain by unaltered Hanging Wall Andesite indicating it was probably open to the paleo seafloor allowing free interaction of hydrothermal fluid and seawater above the deposit as well as mixing of the hydrothermal fluid with seawater within the permeable volcanics below the Gap lens. The effect of additional seawater sulfur on the forming sulfide minerals would be an increase in their $\delta^{34}S$ ratios. Thus Battle Zone sulfides with minimal seawater interaction would have the lowest mean $\delta^{34}S$, while Gap sulfides with the greatest seawater interaction could show the highest mean $\delta^{34}S$ values.

The Battle lens shows an decrease in $\delta^{34}S$ values at the top of the stringer zone (Fig. 143). This decrease is not seen in all holes, due to incomplete sampling or faulting. $\delta^{34}S$ values within the

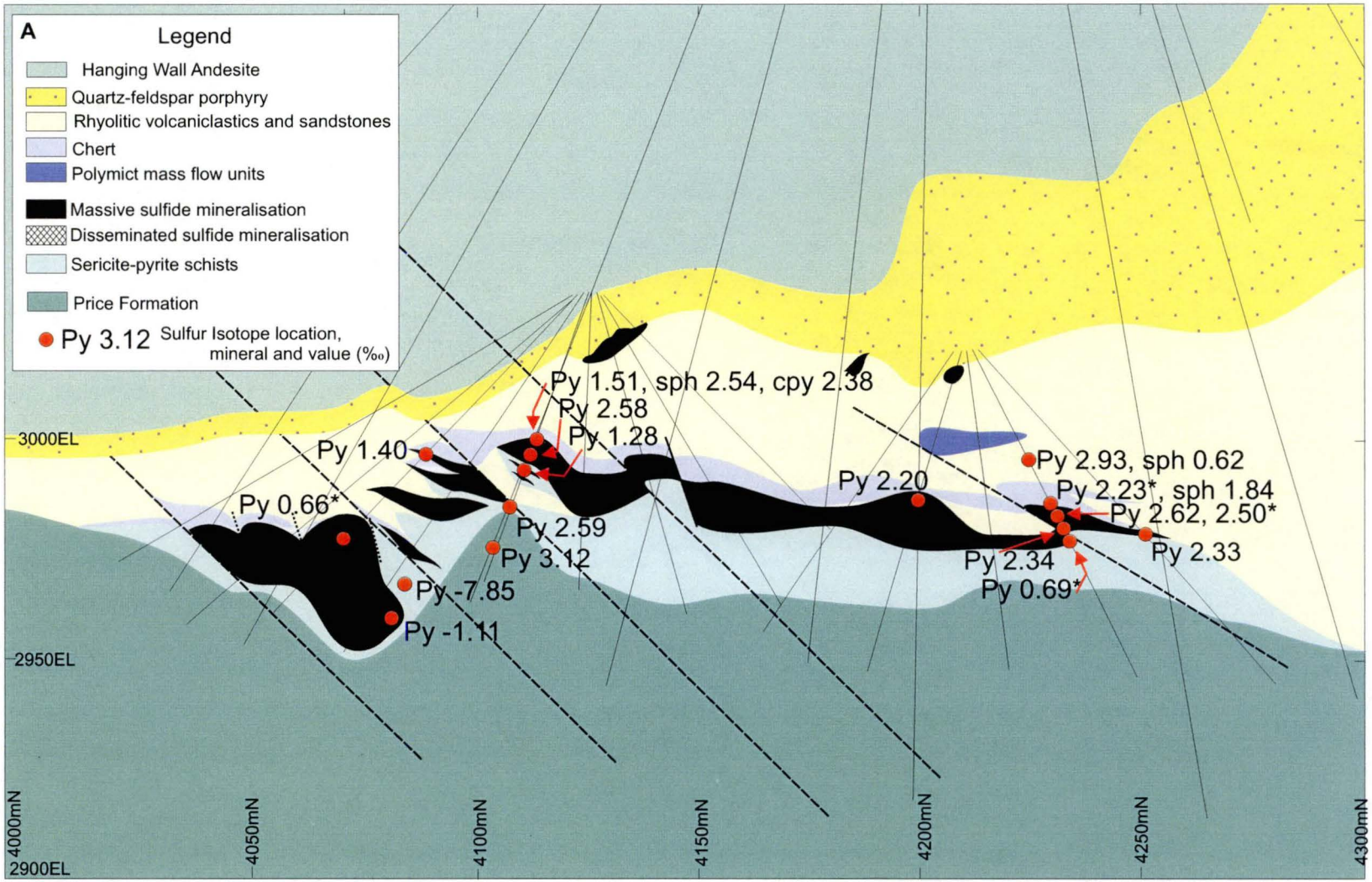

Figure 142A. Spatial distribution of sulfur isotopes on the 1600mE section, mineral analysed shown.

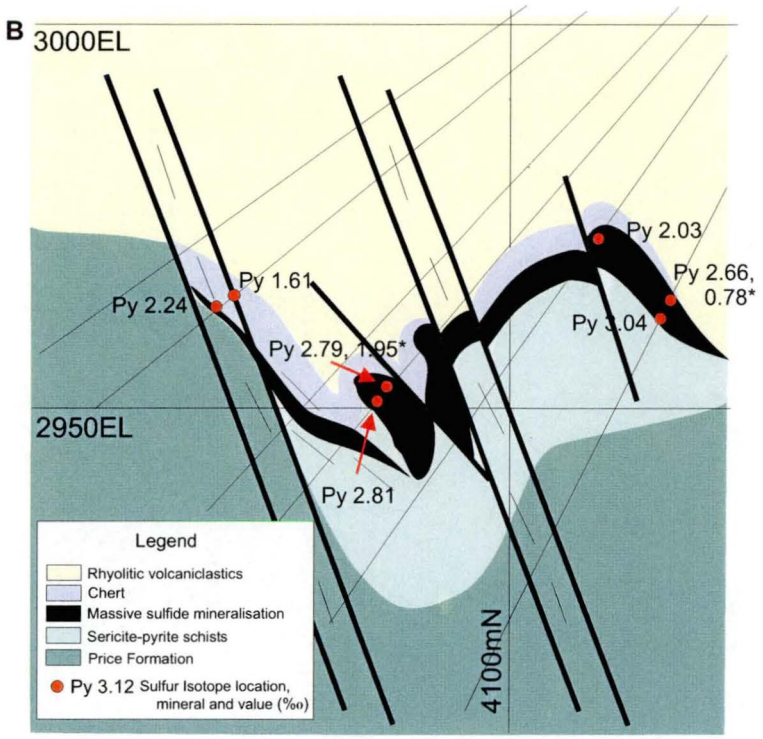

Figure 142continued B. Spacial distribution of sulfur isotopes from 1450mE section (Gopher lens)

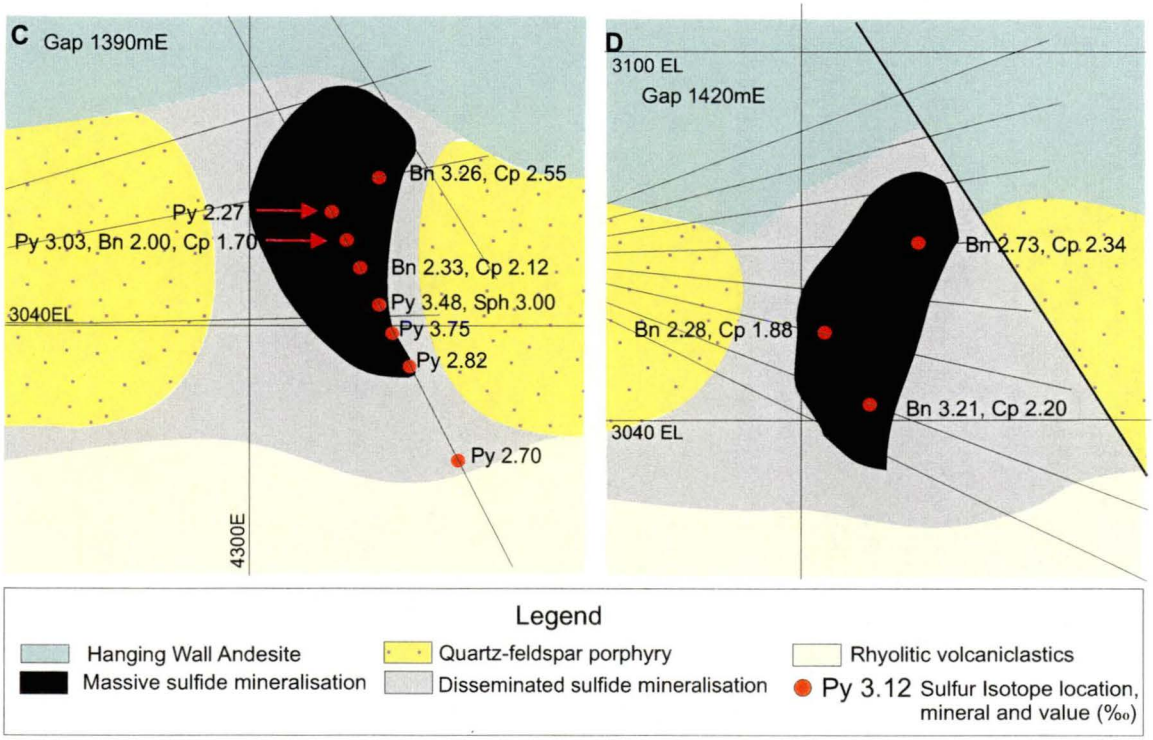

Figure 142continued - Sulfur isotope distribution for Gap lens - C. 1390mE and D. 1420mE sections minerals analyses shown

Figure 143. Down hole distribution of sulfur isotopes (‰) from selected holes. Dotted line represents the average $\delta^{34}S$ value for pyrite in each hole. All ore intersections through Battle lens (except intersection at top BG18-537 which represents an Upper Zone lens intersection.

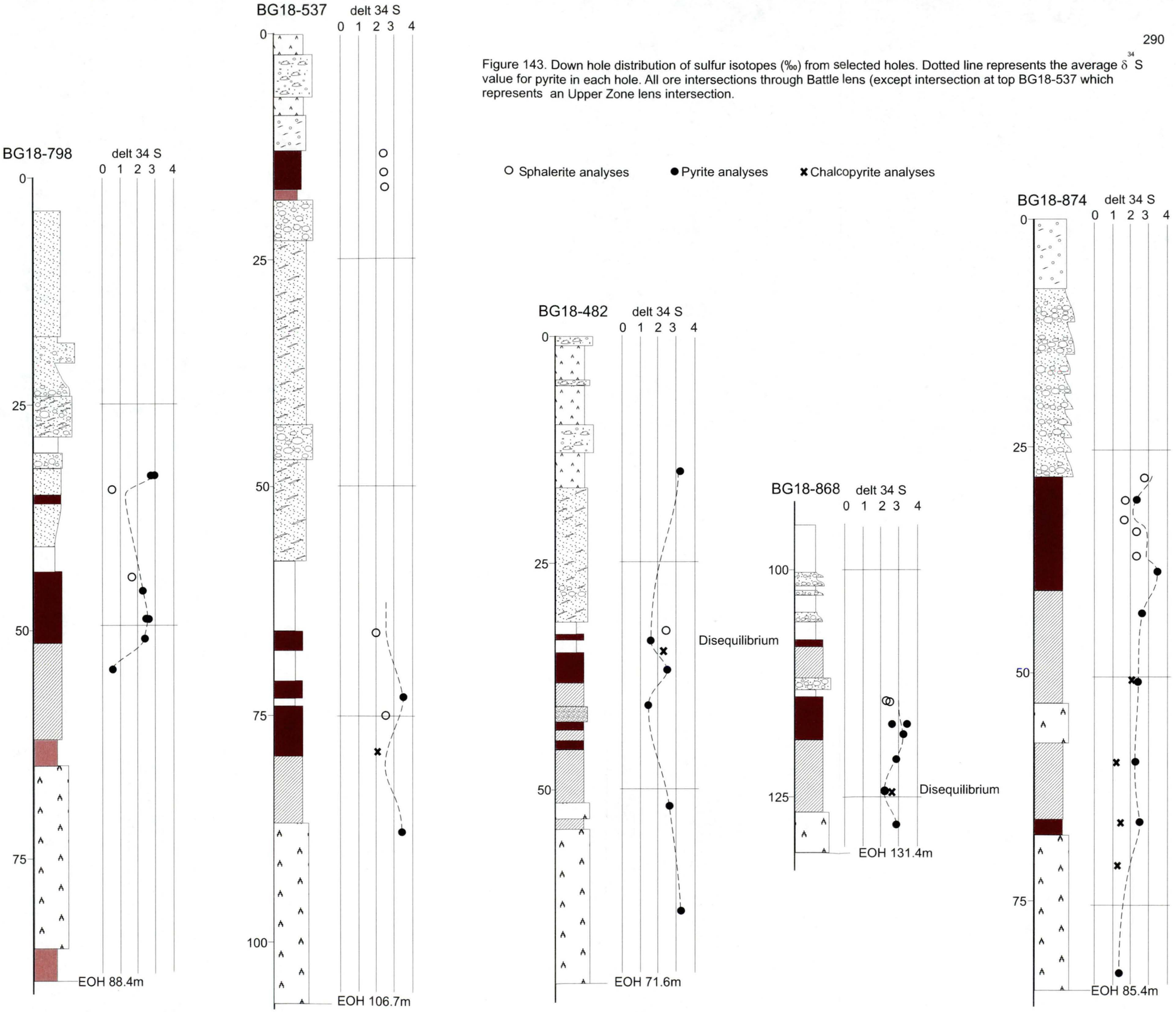

massive sulfide are quite erratic and show no systematic variation as seen in other VHMS deposits (Green et al., 1981; Huston et al., 1995). The area of decreased $\delta^{34}S$ directly below the massive sulfides may reflect focusing of the hydrothermal system that lead to the formation of the Battle lenses. The presence of this intense zone of fluid flow may explain the absence of a defined stringer "pipe" as seen at Hellyer (Gemmell and Large, 1993).

The Battle Zone barites are derived largely form seawater sulfate (as discussed above) and show a zonation with respect to stratigraphic position. This zonation may reflect (1) a change in the availability of seawater to interact with the forming sulfates, or (2) an increase in the $\delta^{34}S$ of seawater with time.

Increases in the $\delta^{34}S$ of seawater during the deposition of the Battle Zone sulfides may have been caused by localised events i.e. stratification of the water column or a restriction of the ore forming basin (Goodfellow and Jonasson, 1984). Or due to the increases in the $\delta^{34}S$ of seawater during the Frasnian stage (Claypool et al., 1982; Goodfellow and Jonasson, 1984). A stratified water column or restricted basin would be expected to produce anoxic conditions (Goodfellow and Jonasson, 1984). Argillite layers found on the margin of the Battle Zone may represent anoxic condition (pers. com. Jones, 2000). However, Goodfellow and Jonasson, (1984) also predicted that sulfates formed in a stratified water column or restricted basin would have $\delta^{34}S$ values significantly higher than the ambient seawater which is not seen in the Battle Zone. Thus a change in the availability of seawater is a more likely cause for the shift in $\delta^{34}S$ of barite in the Battle Zone.

10.6 Geothermometry

The difference between the $\delta^{34}S$ values of sulfide-sulfide and sulfide-sulfate pairs can be used to estimate temperatures of sulfide formation (Ohmoto and Rye, 1979). The successful application of sulfur isotope thermometry depends on the mineral phases forming in equilibrium, and no isotopic exchange occurring between the mineral phases or between mineral phases and a fluid after the formation of the minerals (Ohmoto and Rye, 1979). Pyrite-chalcopyrite pairs often give abnormal sulfur isotopic temperatures due to the fact that pyrite precipitates over a much longer period of the paragenesis than chalcopyrite (or other sulfides), thus allowing less chance for the minerals to precipitate under identical conditions (Ohmoto and Rye, 1979). The mineral phases, upon which the sulfur isotopes are determined, must also be pure.

Re-equilibration of sulfur isotopes among co-existing sulfides, has been suggested to take place during metamorphism (Lusk and Crocket, 1969). However, Ohmoto and Rye (1979) examined isotopic data from many metamorphosed deposits and suggested that the isotopic reequilibration usually was not complete at metamorphic conditions below upper amphibolite facies unless there was a change in mineralogy. The degree of isotopic reequilibration between coexisting mineral phases is dependant on the composition of the metamorphic fluid as well as the temperature and pressure of metamorphism (Ohmoto and Rye, 1979). However, metamorphism causes recrystallisation of the sulfides producing textural equilibrium (Chapter 7) that disguises original paragenetic relationships

making the determination of minerals in isotopic equilibrium difficult (Huston, 1997).

The expected order of $\delta^{34}S$ fractionation under equilibrium conditions between co-precipitating sulfide phases is:

$$\delta^{34}S_{pynte} > \delta^{34}S_{sphalente} > \delta^{34}S_{chalcopynte} > \delta^{34}S_{galena} \quad \text{(Bachinski, 1969)}$$

Comparison of the $\delta^{34}S$ values of co-existing sulfides for the Battle Zone shows that there is evidence of isotopic disequilibrium. Sulfur isotopic thermometers from Ohmoto and Rye (1979) were used to estimate the temperature of formation for co-existing sulfides, equations, sulfide mineral pair used are listed in Appendix 3. Only mineral pairs showing the expected fractionation order were used.

Results

Temperatures estimated vary from 89°C to 537°C, this broad range, overlaps the estimated temperatures for VHMS sulfide precipitation and greenschist facies metamorphism. However the variability of the data and lack of samples (6), evidence of disequilibrium, and likelyhood that mineral separates were not pure, make these temperature estimates unreliable. Thus they will not be used to constrain temperature of formation of the Battle Zone sulfides. This is not unusual for sulfur isotopes in VHMS deposits (Ohmoto, 1986), as sulfide pairs in hydrothermal ore deposits often give abnormal sulfur isotopic temperatures due to the fact that pyrite tends to precipitate over a much

Sample		Pyrite	Sphalerite	Chalcopyrite	
BG18-798	33.5m	2.93	0.62		89°C ± 26°C
L14-757	215.9m	3.03	1.89		242°C ± 37°C
L14-757	229.5m	3.48	3.00		521°C ± 58°C
BG18-874	30.5m	2.24	1.78		537°C ± 59°C
BG18-874	65.8m	3.69		2.19	274°C ± 33°C
BG18-874	59.9m	3.15		2.19	411°C ± 40.6°C
BG18-868	125.m	2.19	disequilibrium	2.28	not calculated

Table 42. Sulfide mineral pairs and estimated temperatures for the Battle Zone.See Appendix 3 for method of calculation.

longer period of the paragenesis than chalcopyrite or sphalerite, thus allowing less chance for the minerals to precipitate under identical conditions (Ohmoto and Rye, 1979).

10.7 Comparison with other studies

10.7.1 In the Myra Falls district

A previous study of sulfur isotopes in the Myra Falls district was conducted by Seccombe et al., (1990) while $\delta^{34}S$ isotopes for sulfides and sulfates for lenses outside the Battle Zone have also been determined in conjunction with this study by Dr J.B. Gemmell.

Data from Seccombe et al., (1990) and Gemmell are presented in Figure 144. Sulfur isotope values for the Lynx lenses (Fig. 144A) show a remarkably similar distribution to that seen in the Battle lens (Fig. 135 A). The two low $\delta^{34}S$ values (-2.8 and -6.7‰) come from galena samples found

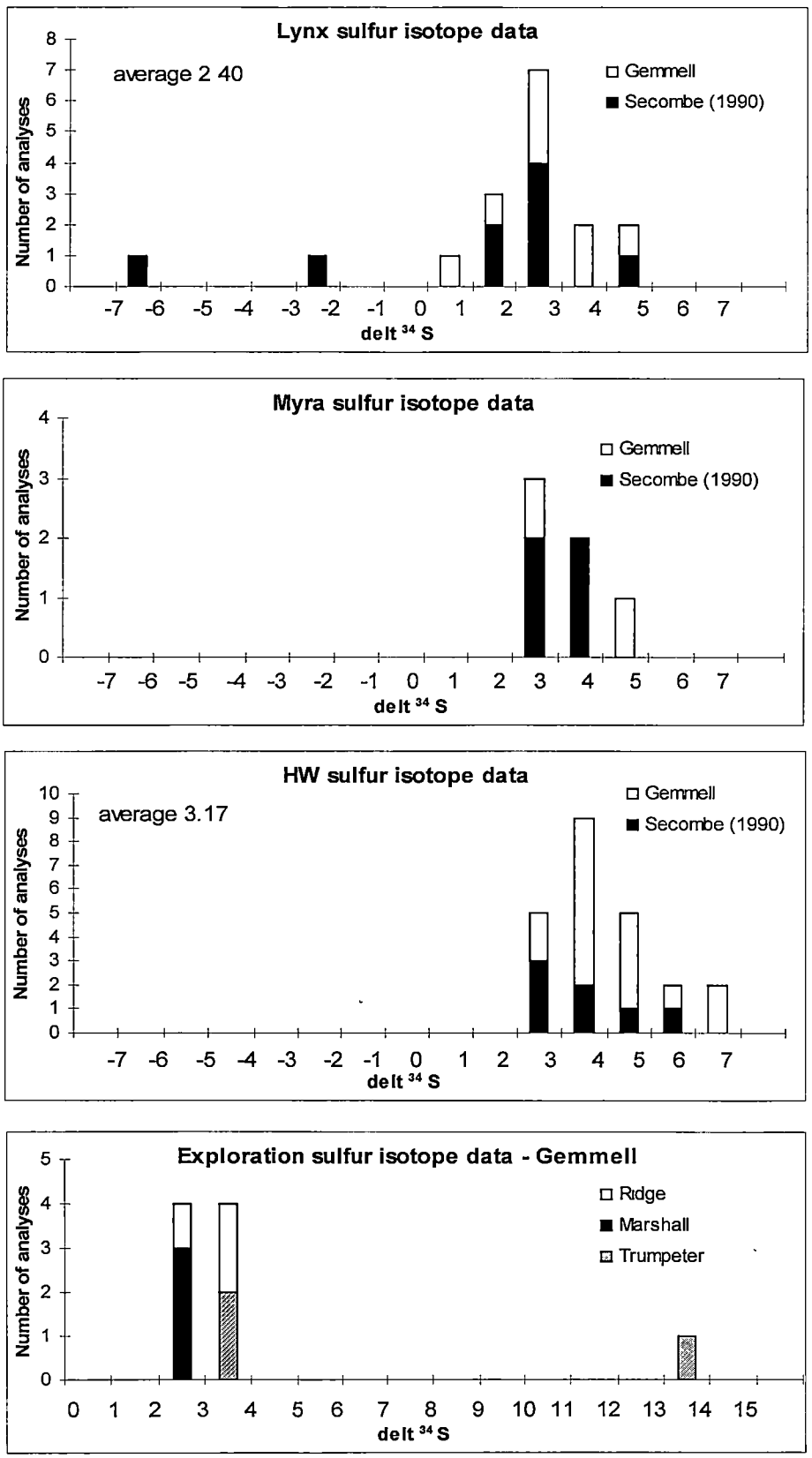

Figure 144. Sulfur isotope data for lenses outside the Battle Zone, from Secombe (1990) and Gemmell (unpublished in conjunction with this study). See appendix 3 for data.

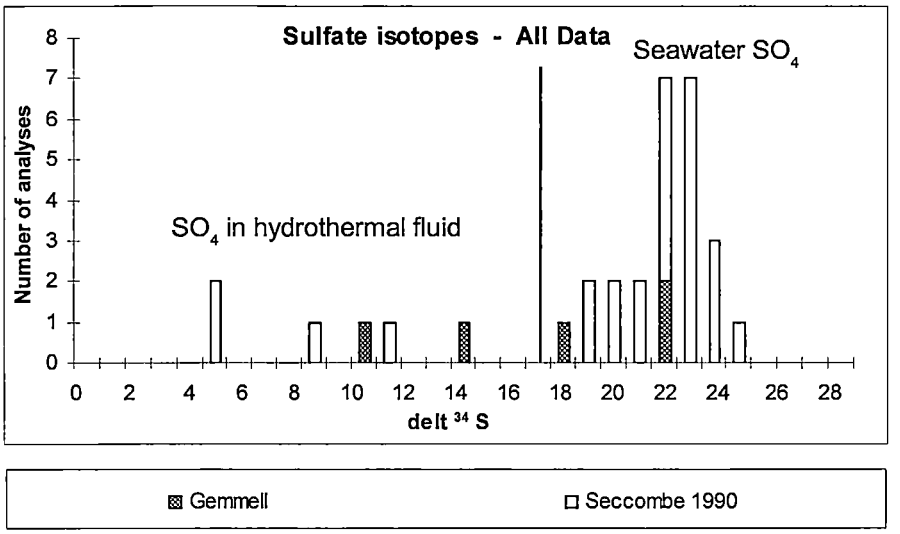

Figue 145. Sulfate isotope data for barites outside the Battle Zone, data from Seccombe (1990) and Gemmell (unpublished, in conjunction with this study). See appendix 3 for data.

in veins within altered andesites. Data from the Myra and HW lenses have higher ranges (2.5-4.91‰ for Myra and 2.7 - 6.77 ‰ for HW) and higher $\delta^{34}S$ averages (3.50‰ for Myra and 3.17 ‰ for HW), than the Battle lenses. Figure 144 D gives the $\delta^{34}S$ data for nine samples from three exploration lenses, however there is insufficient data to make conclusions about these lenses from current results.

Sulfate analyses from barites outside the Battle Zone are shown in Figure 145. Sulfates form two populations, with the majority of the data clustered tightly in the range 19.9 to 26.2‰ (mean 23.45 ‰) similar to the Battle Zone data. A second population occurs scattered between 5.1 and 15.0‰ indicating a depletion in the $\delta^{34}S$ of sulfate for these samples. Seccombe et al. (1990) noted that the samples giving light $\delta^{34}S$ appear to have a fragmental or transported texture. Barite in these samples occurred as rounded to oblate nodules which range in size from a few millimetres to 2 centimetres. Angular to rounded wallrock clasts of the same size range also occur in the samples. Both the barite nodules and the wallrock clasts are incorporated in a sulfide matrix which appears graded in some specimens. The Gemmell data also shows barites with low $\delta^{34}S_{SO_4}$ values (11.3 and 15.0‰) both these samples came from the HW mine, although neither sample has the fragmental nature described by Seccombe (1990).

These studies confirm the observation found in the Battle Zone that the sulfur source was homogeneous and non-varying along the 6km strike length of the known Myra Falls lenses. Although a slight shift (increase) in the $\delta^{34}S$ toward the east occurs (seen in the HW and Myra lenses). Sulfates in the range 19.9 to 26.2‰ are attributed to a direct seawater origin. The origin of the light $\delta^{34}S_{SO_4}$ is more complex and may represent a source of SO_4 carried in the hydrothermal fluid. The similarity of $\delta^{34}S$ for all lenses within the Myra Falls district regardless of stratigraphic position suggests that the was not a significant change in the $\delta^{34}S$ of seawater during the formation of massive sulfide

mineralisation through out the Myra Falls district.

10.7.2 Other Devonian VHMS Deposits

$\delta^{34}S$ results for Devonian VHMS Deposits, complied by Huston et al., (1999) are shown in Table 43. All the Devonian deposits show tight clusters of data in the range -3 to 12‰, with highly negative values (eg Big Mike -6.4‰) associated with primitive framboidal textures indicating a source other than the hydrothermal fluid (most likely biogenic reduction in sediments). Deposits such as Big Mike, California (Rye et al., 1984) and the West Shasta District of California (Casey and Taylor, 1982) show a similar ambiguity in their results, as that seen in the Battle Zone, due to low (< 5‰) $\delta^{34}S$ ratios. Casey and Taylor (1982) used oxygen and hydrogen isotopes to suggest a seawater derived source for the hydrothermal fluid but could not rule out a contribution of magmatic sulfur to the hydrothermal fluid. Deposits with higher $\delta^{34}S$ (5 - 10‰), e.g. the Trident and Delta districts in Alaska (Lange, 1993) are interpreted as having derived their sulfur from seawater via inorganic reduction.

Deposit	Age	Minimum d34S ‰	Average d34S ‰	Maximum d34S ‰	Number of sulfide analyses	Source of sulfur isotope data
Big Mike, California	L.Dev / Miss	-6.4	1	5.5	52	Rye et al. (1984)
Trident Glacier district, Alaska	Dev	6.2	7.6	10.4	36	Lange et al. (1993)
Delta District, Alaska	Dev	0.3	5.8	10.3	78	Lange et al. (1993)
Hodgkinson Province,	Dev	-10	1.8	11.8	178	Gregory and Robinson (1984)
Woolomin, New South Wales	Dev	-8.5	0.6	6.3	27	Herbert and Smith (1978)
Mount Morgan, Queensland	Dev	-0.5	2.1	3.6	27	Eadington et al. (1974); Golding et al. (1993)
Pyriton, Alabama	E. Dev		3.2		1	LeHuray (1984)
West Shasta, California	Dev	1.6	4	5.3	87	Casey and Taylor (1982); South and Taylor (1985)

Table 43. Sulfur isotope results for other Devonian VHMS deposits, compiled by Huston et al., (1997).

10.8 Conclusions

The sulfur isotopes from this study, and those of Seccombe et al., (1990) and Gemmell, indicate a very homogeneous source for the sulfur in the Myra Falls VHMS deposits. For the sulfide minerals the source may be either (1) a reduced seawater sulfate $\pm$ magmatic input leached from footwall volcanic during circulation of the hydrothermal system, or (2) a direct magmatic input. These two sources are difficult to differentiate as inorganic reduction of Devonian seawater sulfate at the inter-

preted formation temperatures and magmatic sulfur give the same $\delta^{34}S$ values for sulfides. However, alteration assemblages reflect seawater derived hydrothermal fluid, without acid alteration expected from a strong magmatic influence. Thus a reduced seawater sulfate is the preferred source for sulfur in sulfides in the Battle Zone. Sulfate minerals provide a clearer source for the sulfate, that derived directly from the ambient seawater.

Variations in mean $\delta^{34}S$ of pyrite and sulfate isotopes with stratigraphic position, are considered to be the result of variations in the availability of ambient seawater to mix with the hydrothermal fluids. In the Battle lenses this mixing is limited, however mixing increases within the permeable HW rhyolitic sediments as observed in the sulfide and sulfate $\delta^{34}S$ values in the Upper Zones and Gap lenses. The possibility of anoxic conditions, or a rise in the $\delta^{34}S$ of ambient seawater, during the formation of the Battle Zone lenses is ruled out by the lack of evidence for anoxia conditions and the similarity of $\delta^{34}S$ from the Lynx and Myra lenses which are interpreted to lie stratigraphically above the Battle Zone lenses.

Chapter 11

Genetic Model

This chapter brings together evidence from all previous chapters to create a genetic model for the formation of the Battle Zone massive sulfide lenses. It also reviews the changes due to metamorphism that have created the post-depositional mineral assemblages observed today.

11.1 Pre-mineralisation environment and Phase 1 mineralisation

Prior to the formation of the Battle, Gopher and South Trough massive sulfide deposits, andesitic volcanism ceased leaving a subaqueous environment with a substrate consisting of basaltic andesite flows, flow breccias and volcaniclastic deposits. Topographic reconstructions indicate there was a depression to the south and ridge to the east (Fig. 146 & 147). A series of north-west to north north-westerly trending, steeply dipping, syn-volcanic faults are interpreted. A thin veneer (<10m) of mud began to accumulate on the andesites.

Hydrothermal fluids then began to rise up the syn-volcanic faults altering the andesites to Mg-rich chlorite and muscovite-quartz-pyrite assemblages. Fluid flow was focussed in the pre-existing north-west to north north-westerly trending faults, however diffusion of the fluids through the upper 30m of the andesite created a stratabound alteration zone below the seafloor. Where the hydrothermal fluids reached the seafloor they cooled, deposited sulfides on the seafloor and silicified the accumulating mud (Fig. 148). Sulfide precipitation continued with the sulfide lenses forming outward and upward into the silicified sediments (Fig. 149A & B). Coarse rhyolitic and polymict mass flows were also deposited. Relics of these early mass flows are observed overprinted by sulfides at the edges of the massive sulfide lenses (Fig. 149C & D). The Battle, Gopher and South Trough massive sulfide lenses developed at this time.

The distribution of sulfide minerals and the metal zonation present in the Battle Zone deposits can be explained in a model where the growth of the lenses occurs by upward replacement of sulfide assemblages stable at higher fluid temperatures, leading to zone refining (Large, 1992). This model has been developed through the study of numerous VHMS deposits worldwide (Eldridge et al, 1983; Large, 1992). A summary of the model from Eldridge et al. (1983) is presented here. Initial hydrothermal fluids mixed with seawater and deposited fine grained sphalerite, galena, pyrite, tennantite, barite and minor chalcopyrite. The formation of these fine grained sulfides insulated rising hydrothermal fluids allowing higher temperature fluids to rise into the sulfide mound. As temperatures increased coarser grained sphalerite, pyrite, and chalcopyrite were deposited. Further temperature increases allowed hotter Cu-rich hydrothermal solutions into the ore lens resulting in the replacement of coarser sphalerite by chalcopyrite. Introduction of hotter, copper undersaturated fluids into the ore lenses resulted in the

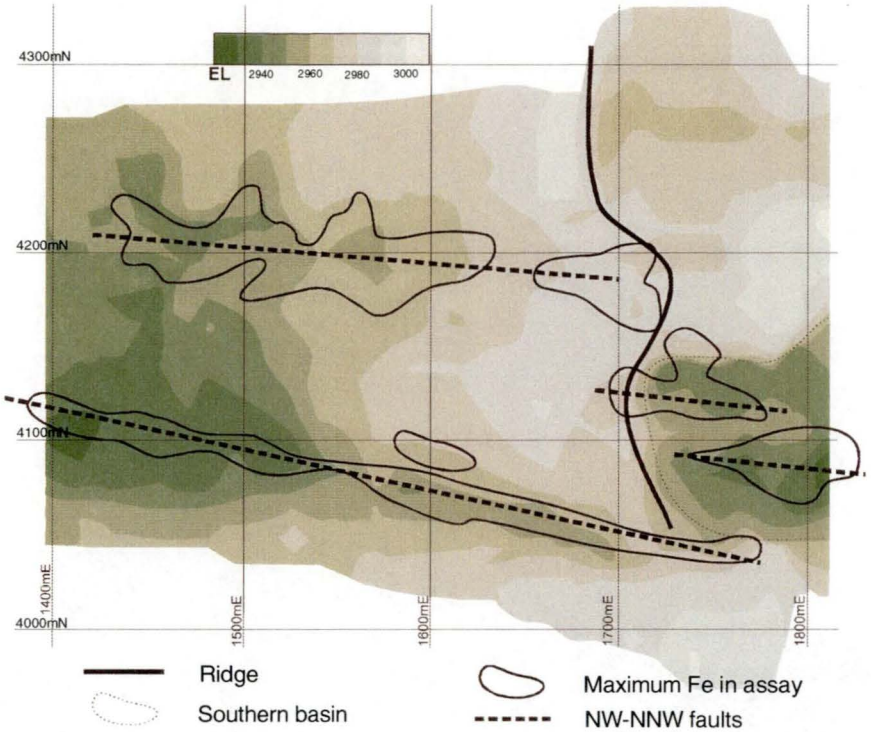

Figure 146. Footwall contours showing interpreted pre phase 1 deformation, outlines of maximum Fe from 3m composite assay data at the top of the Price Formation (see Fig. 117). Interpreted NW-NNW phase1 controlling faults, the southern basin and the N-S ridge to the east are highlited by the contours.

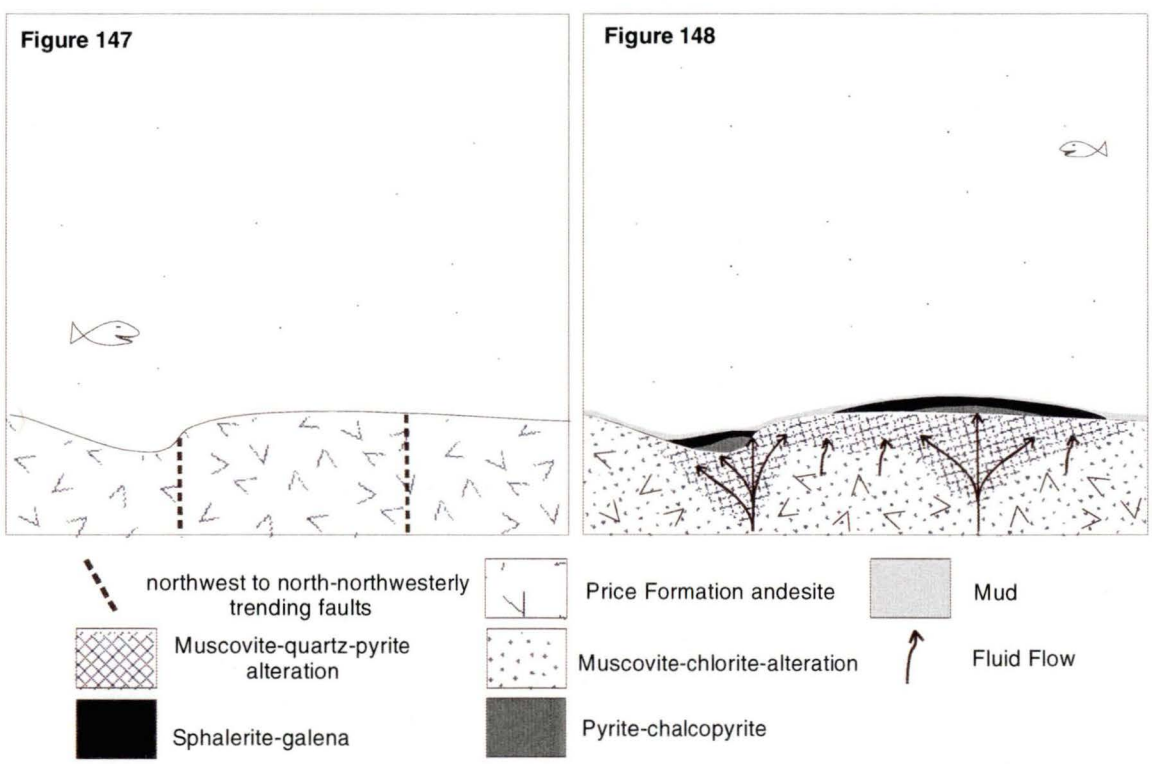

Figure 147. Pre-phase 1 environment consisting of andesitic lavas and volcaniclastics,northwest to north-northwesterly trending faults were present and a fine rain of mud was settling onto the seafloor.

Figure 148. Deposition of Phase 1 sulfides. Hydrothermal fluid was focused up towards the seafloor along northwest to north-northwesterly trending faults. Percolation of fluids through the footwall volcanics below the seafloor created a stratabound muscovite-quartz-pyrite alteration zone directly below the massive sulfide lenses. The sulfide lenses formed on the seafloor.

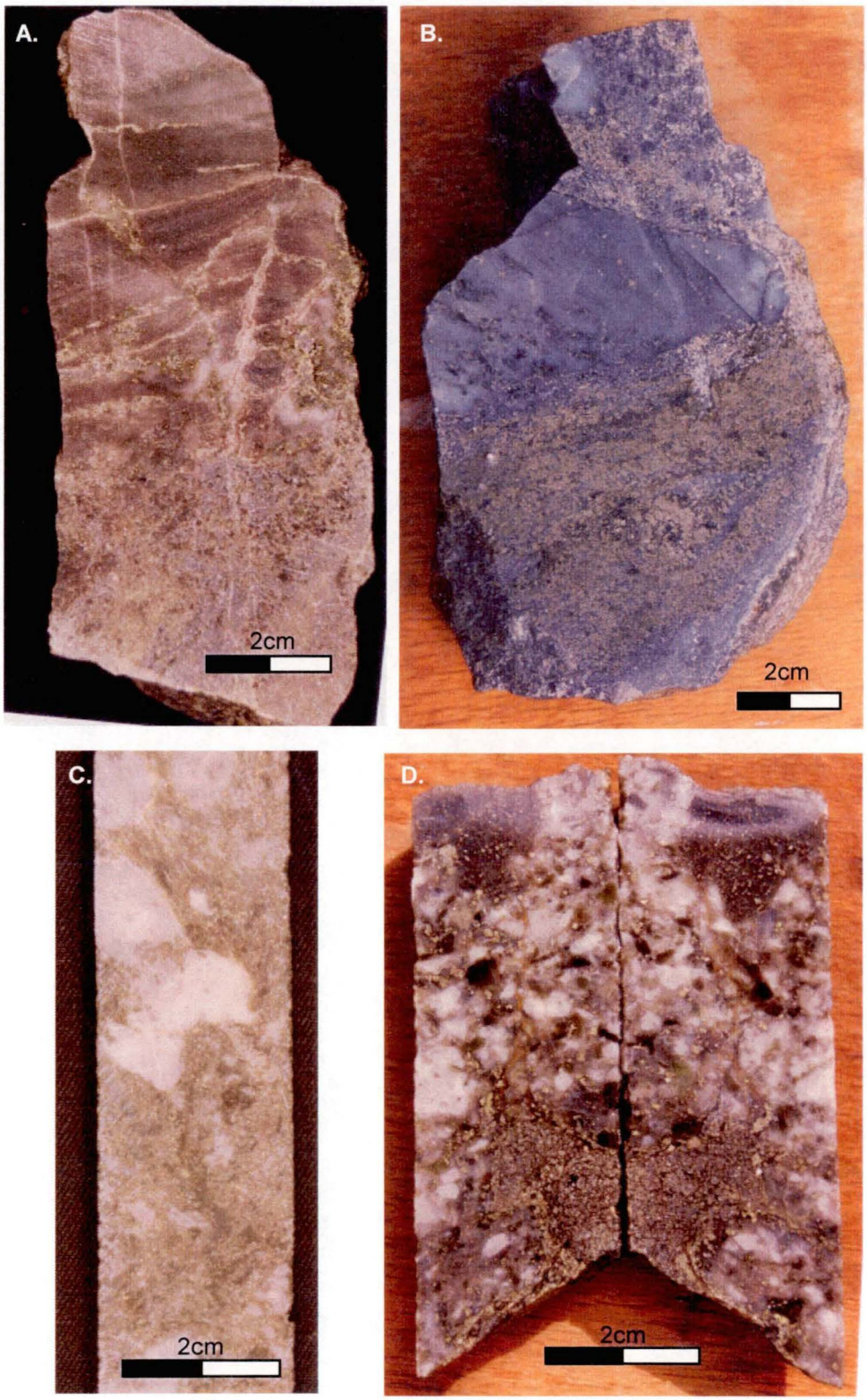

Figure 149. Textures supporting phase 1 genetic model. A. Sphalerite-galena rich ore replacing Facies 2 siltstone at the top of the Battle Lens (T174 South Wall). B. Sphalerite-pyrite ore with clasts of strongly silicified Facies 2 siltstone (G149DD No.1). C. Semi-massive sphalerite-pyrite in strongly sericite alteration with clasts of facies 1 sandstone (BG18-778-131.7-131.8m). D. Sericite altered Facies 3 polymict mass flow with sphalerite-pyrite mineralisation (BG18-868 116.1m).

dissolution of chalcopyrite and formation of pyrite ores. All of these stages of mineralisation may have taken place nearly contemporaneously but at different sites within the accumulating sulfide deposit (Eldridge et al., 1983).

The zone refining scenerio explains the observed mineralogical and metal zoning in the Battle Zone lenses. The base of the lenses consist of pyrite with a Fe-Au association and pass upwards through pyrite-chalcopyrite with a Fe-Cu-Ni-Mo association, sphalerite-pyrite-chalcopyrite with a Zn-Cd-Ag-Fe-Cu association and sphalerite-galena-tennantite-barite-colusite with a Pb-Ag-As-Hg-Zn-Ba-Ge association toward the top of the lenses. The same hydrothermal fluids interact with the thin veneer of sediment that accumulates on top of the Gopher and Battle massive sulfide lenses and enriches them in Si-Mn-Pb-Zn-Cu-Fe-As.

11.2 Phase 1 fluids

Characterisation of hydrothermal fluids within the massive sulfide lenses was not an aim of this study, however much information can be obtained about the hydrothermal fluid from the mineral assemblage deposited and previous research. Barrett and Sherlock (1996) and Hannington and Scott (1989) have measured fluid inclusions in quartz and sphalerite from the HW deposit. These data are used with caution due to deformed state of the ore lenses. However, in combination with studies from modern VHMS deposits and less deformed ancient examples (eg Kuroko, Sato, 1972; Pisutha-Arnond and Omoto, 1983; Hellyer, Zaw et al 1996) inferences can be made on the fluid chemistry responsible for the Battle Zone deposits.

Mineralogy of VHMS deposits is controlled by the pH, salinity, oxidation state and temperature of the hydrothermal fluid. Barrett and Sherlock (1996) measured temperatures of 146° to 247° (average 184°) in sphalerite from the HW deposit. These temperatures are consistent with low temperature fluids responsible for deposition of sphalerite, galena, pyrite, tennantite, barite and minor chalcopyrite from the Kuroko deposits (Pisutha-Arnond and Omoto, 1983) as modelled by Eldridge et al. (1983) The 146° to 247°C hydrothermal fluids are likely responsible for the deposition of the sulfide assemblage at the top of the Battle Zone deposits. Higher temperature (250-350°C) fluids are considered responsible for the deposition of chalcopyrite and pyrite at the base of the sulfide deposits in the Battle Zone.

Barrett and Sherlock (1996) measured salinity in fluid inclusions in the HW deposits and found salinities ranging from 3.2 to 8.1 wt% $NaCl_{eqv}$. Theses values are consistent with values obtained by Hannington and Scott (1989) for the HW deposit. These salinities are also consistent with salinities measured for the Kuroko deposits (Pisutha-Arnond and Ohmoto, 1983) and the Kidd Creek ores (Schandal and Bleeker, 1999) as well as being in the range of measured salinities from actively forming massive sulfides on the sea floor (Peter and Scott, 1988). Therefore, the fluid that formed the Battle, Gopher and South Trough lenses is interpreted to have had a salinity of 3 - 8 wt% $NaCl_{eqv}$.

The pH of the hydrothermal fluid is inferred from the alteration mineralogy, muscovite is dominant and there is no carbonate, kaolinite and K-feldspar. Calcite and dolomite observed in alteration assemblage are interpreted to have been introduced during metamorphism or formed due to mixing of

hydrothermal fluids with seawater (see below). Based on the alteration assemblage the phase 1 hydrothermal fluid is inferred to have been weakly acidic pH (4 – 5).

Sulfide mineralogy at Myra Falls gives an indication of the oxidation state during precipitation. In oxidised fluids (high fo_2) magnetite forms along with pyrite and hematite. While in reduced systems (low fo_2) pyrrhotite is common (Large, 1977). The Battle Zone lenses contain pyrite, but no magnetite or pyrrhotite is observed within the ore lenses, thus the ore forming fluids probably were neither highly reduced nor highly oxidised (Fig. 150).

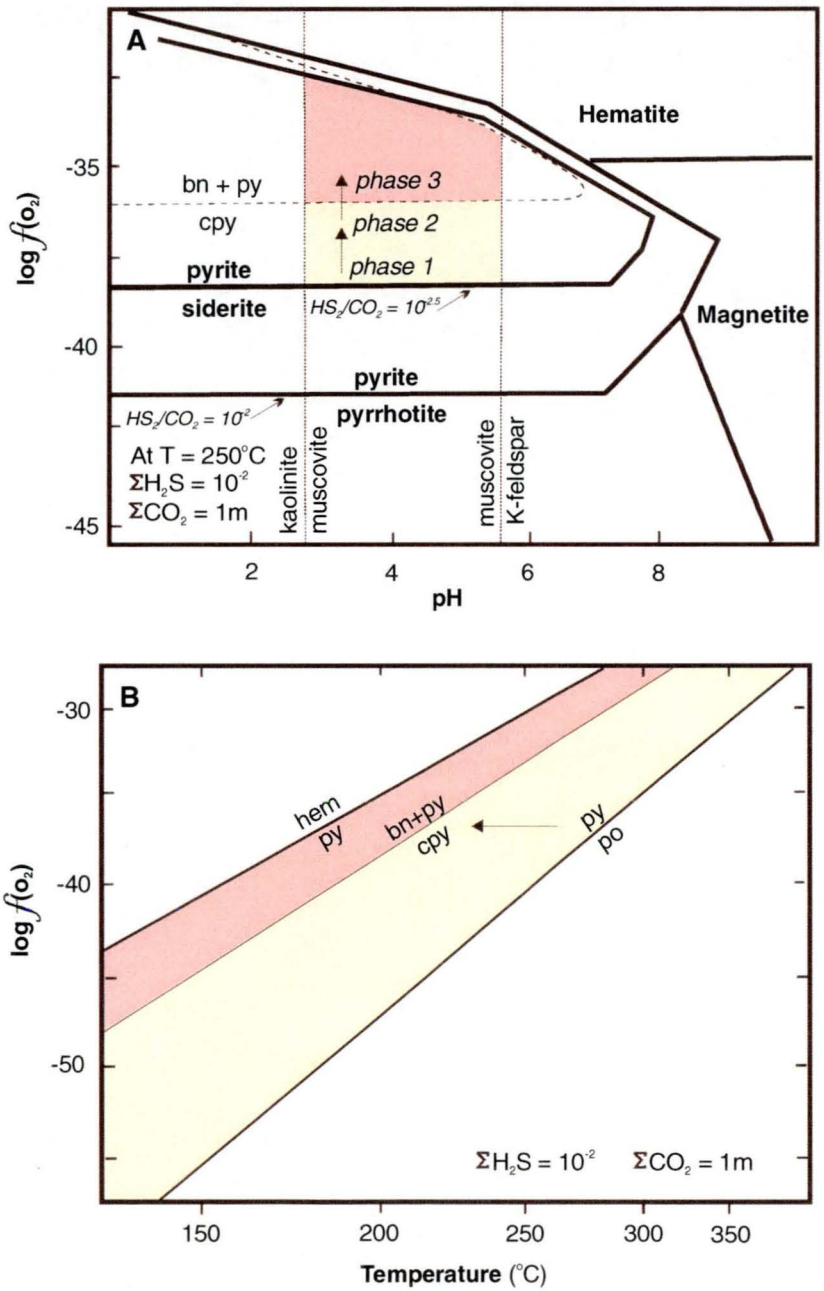

Figure 150. Stability fields for selected minerals in the Battle Zone massive sulfide lenses A. Log $f(o_2)$ - ph diagram at 250°C showing the stability fields of Fe oxides and sulfides, K-feldspar, muscovite and kaolinite. Yellow field for phase 1 and 2 Battle Zone hydrothermal fluids, pink field for phase 3 bornite precipitating fluid. B. Temperature - log $f(o_2)$ conditions for mineral deposition in the Battle Zone lenses. Decrease in temperature causes precipitation of sulfides (arrow). After Hannington et al. (1999a).

The source of the hydrothermal fluid can also so be inferred from alteration mineralogy and $\delta^{34}S$. Footwall alteration is rich in Mg-chlorite (Mg# = 0.82 – 0.93) suggesting a seawater source for the Mg. No mineralogical evidence to support addition of magmatic fluids has been found. Sulfur isotopes ($\delta^{34}S$ –1.11‰ to 4.06‰) from Battle, Gopher and South Trough lenses suggests sulfate reduction at temperatures of 150-350°C from Devonian (Frasnian) seawater of ($\delta^{34}S$ 23‰ - 28‰). Barite $\delta^{34}S$ from the Battle lens, along with data from the HW Mine, indicate sulfur in barite was derived from a mixture of seawater sulfate and reduced sulfur derived from the hydrothermal fluid (Table 44). The range of sulfur isotopes ($\delta^{34}S$ –1.11‰ to 4.06‰) also supports a reduced hydrothermal fluid (Cooke pers. com., 2000) as sulfides precipitated under oxidising conditions have negative sulfur isotope compositions (Ohmoto et al., 1983; Cooke & Simmons, in press).

11.3 Phase 2 mineralisation and volcanic setting

The rapid emplacement of rhyolitic mass flows followed deposition of the Battle, Gopher and South Trough lenses. The emplacement of a rhyolite lava dome (QFP) followed deposition of the volcaniclastics (Fig. 151). The emplacement of rhyolitic volcanics did not appear to stop the hydrothermal upflow. Hydrothermal fluids percolated up through the newly deposited porous and permeable volcaniclastics until they encountered the massive QFP. The QFP formed a barrier to the rising hydrothermal fluids resulting in the deposition of the Upper Zone and Gap lenses (Fig. 152).

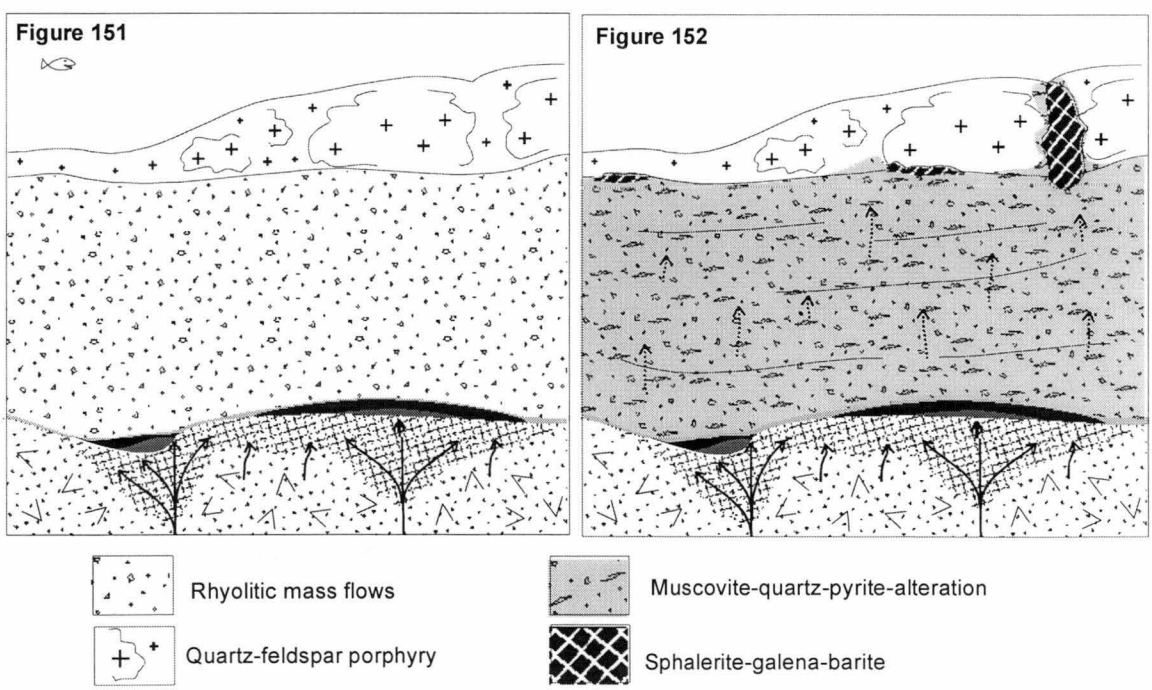

Figure 151. Rapid deposition of rhyolitic volcaniclastics was followed by the emplacement of rhyolite lavas and associated clastics of the QFP.
Figure 152. Deposition of phase 2 sulfides. Hydrothermal fluid percolated up through the porous and permeable, seawater saturated, rhyolitic volcaniclastics forming quartz-muscovite alteration. The hydrothermal fluid deposits sphalerite-galena-tennantite-barite-rich massive sulfide lenses below and within the QFP.

Gap and Upper Zone mineralisation formed as replacive bodies below the seafloor (Fig. 153A & B). The fluids that created the Gap and Upper Zone lenses are interpreted to be very similar to those described for Phase 1 (Table 44). However, during their percolation through the porous and permeable volcaniclastic the fluids were modified via mixing with seawater. This resulted in cooler, slightly more oxidised (but still pyrite stable) fluids. As a result Pb, As and Ag are precipitated due to the cooler nature of the fluids. Barium also more abundant in the Upper Zone and Gap lenses due to the increase in oxidisation state caused by the mixing with seawater (Fig. 150). The presence of barite also confirms that seawater was available at the site of deposition. $\delta^{34}S$ isotopes of barite in the Upper Zone and Gap lenses are between 21‰ and 28‰ reflecting seawater sulfate.

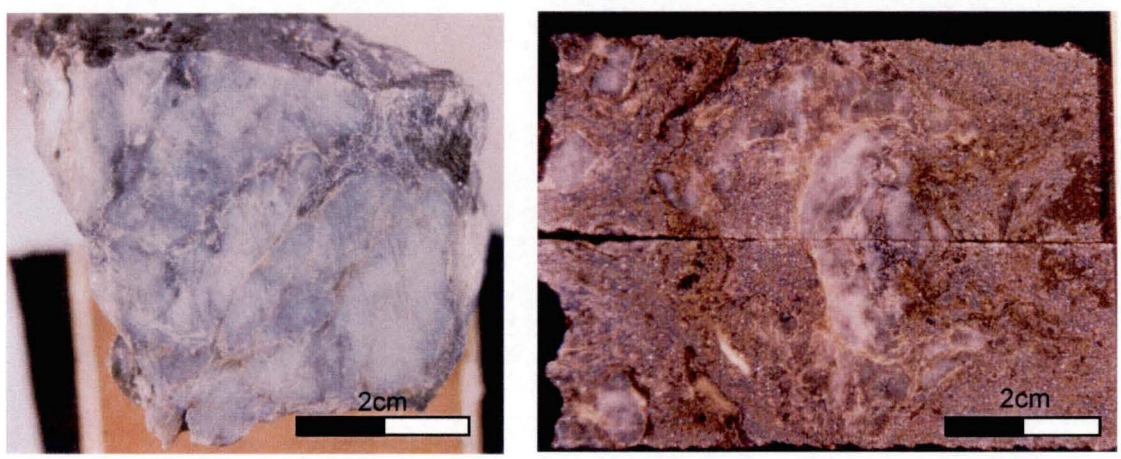

Figure 153. Textures supporting phase 2 genetic model. A. Veinlets of sphalerite, tennantite, galena and muscovite cutting weakly altered Facies 4 QFP (H169 P8 No.6). B. Sphalerite-pyrite-galena replacing Facies 4 QFP, remnant clasts show relic QFP textures (BG18-976 102.5m).

Conditions	Phase 1	Phase 2
Temperature	150°C-250°C sphalerite-galena 250°C-350°C pyrite-chalcopyrite	150°C-250°C
Salinity	3 – 8 wt% $_{eqv}$	3 – 8 wt% $_{eqv}$
fO_2	-32 to -38	Increasing
pH	4 - 5	4 – 5
$\delta^{34}S$ – Sulfides	-1.11 to 4.06‰	-3.22 to 3.71‰
- Sulfates	18.44 to 22.35‰	21.55 to 28.68‰
Hydrothermal Fluid	Reduced seawater	Reduced seawater + normal seawater
Depositional environment	seafloor	sub-seafloor

Table 44. Summary of the hydrothermal fluid composition for phase 1 and 2 fluids, Battle Zone, Myra Falls.

The mineral colusite occurs in addition to the mineralogy seen in Phase 1. The presence of the mineral colusite reflects the presence of Ge in the hydrothermal fluid. Germanium has also been reported from the Kuroko deposits (Kase et al., 1994), where it is interpreted as being derived from the leaching from rhyolitic volcanics. The formation of colusite is favoured under high fo_2 conditions (Kase et al., 1994). Thus the presence of colusite in Upper Zone and Gap lens is interpreted as the result of the increase in fo_2 stabilising colusite. Leaching of rhyolitic volcaniclastics by the hydrothermal fluid during its ascent may have also contributed to Ge content of the hydrothermal fluid.

Alteration of rhyolitic volcaniclastics to a quartz-muscovite assemblage is consistent with the hydrothermal fluid that formed the alteration below the Phase 1 sulfides. The neutralisation of acidic hydrothermal fluids, and/or the interaction of CO_2 from hydrothermal fluid with Ca-Mg-Mn bearing seawater are the most likely causes for the deposition of dolomite. Carbonate has an inverse solubility, thus temperature decrease will not cause deposition of carbonates (Ellis, 1963). The distribution of dolomite on the periphery of the hydrothermal system may be the result of the mixing of seawater that may increase the pH enough to cause deposition of dolomite.

The CO_2 content of hydrothermal fluids at Myra Falls is unknown. Barrett and Sherlock (1996) noted CO_2-rich fluid inclusions within the HW deposit, but no measurement of the CO_2 content was given. The absence of siderite within the ore lenses indicates CO_2 content of the fluid inclusion was not high and/or fo_2 of the fluid was too high to stabilise siderite (Hannington et al., 1999a).

Phase 3

Upper Zone and Gap massive sulfide lenses also contain bornite, anilite and renierite, all of which are rich in Ag and Ba. Mineralogical evidence suggests bornite resulted from the replacement of chalcopyrite and consideration of textures and chemistry suggest a zone refining process rather than a closed system re-equilibration during metamorphism (Chapter 7). Figure 150 indicates the change in mineralogy from chalcopyrite to bornite is due to higher fo_2 and lower temperatures within the hydrothermal fluid. The presence of Ba in the bornite indicates the fluid that formed bornite was probably oxidised supporting higher fo_2 conditions.

Alternatively the reaction of chalcopyrite to bornite may be due to oxidised seawater infiltration the Gap and Upper Zone lenses while they were close to the seafloor (prior to burial). However the distribution of bornite-anilite (as a spine through the middle of the Gap lens) is inconsistent with supergene alteration, which would be concentrated at the top and periphery of the lens.

11.4 Post hydrothermal system

Once the hydrothermal system had ceased, andesitic volcanism resumed depositing the basaltic andesite to andesite lavas and related breccias of the Hanging Wall Andesite (Fig. 152). Volcaniclastics at the base of the Hanging Wall Andesite incorporate clasts of altered rhyolitic volcaniclastics, QFP and sulfides, from the underlying HW Rhyolite but are not hydrothermally altered themselves.

Subsequent metamorphism and deformation of the ores, coarsened and annealed many of the sulfide textures. However, pyrite textures record a variety of stages in the formation of the Battle Zone

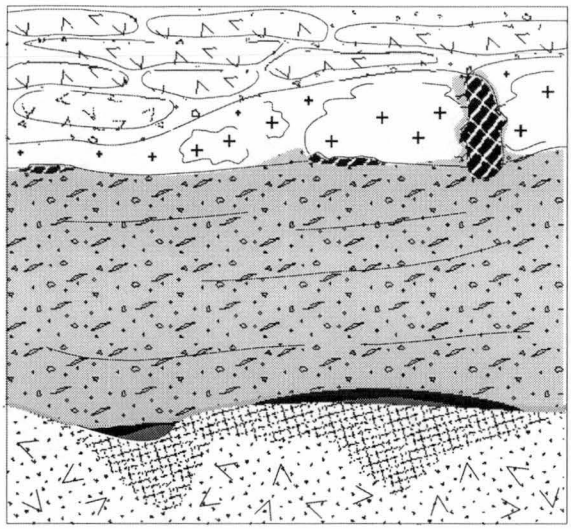

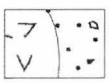 Lavas and associated clastics of the Hanging Wall Andesite

Figure 154. Post hydrothermal system but pre-metamorphism and deformation, the massive sulfide lenses and alteration are overlain by the emplacement of the Hanging Wall andesite.

lenses. The pyrite textures allow comparison of the Battle Zone lenses with undeformed VHMS deposits leading to an interpretation of the paragenetic sequence. Mineral chemistry is also useful in interpreting the paragenetic sequence especially where bornite occurs in the ore.

Metamorphism is interpreted to be responsible for the formation of the late stromeyerite-chalcopyrite-electrum association (Chapter 7). Metamorphism is known to have significant effect on the distribution of trace elements in VHMS Systems (Larocque and Hodgson, 1995). It is suggested that Cu and Ag released from the bornite-anilite assemblage during metamorphism and remobilisation of Au from pre-existing mineralogy could cause the precipitation of stromeyerite, chalcopyrite and electrum during retrograde metamorphism. Alternatively this mineralogy may also from a supergene alteration under oxidised and acidic conditions at temperatures as low as 25°C. However, if this were the case more supergene copper phases (covellite, digenite, chalcocite) would be expected in association with the veins, this was not observed.

Calcite veining seen throughout the Battle Zone and with in the Hanging Wall Andesite is interpreted to have been introduced during metamorphism. Calcite veins shows clear cross cutting relations to all alteration types. Calcite intergrown with chalcopyrite is consistent with a metamorphic origin, as chalcopyrite is highly mobile under greenschist facies metamorphic conditions.

11.5 Comparison with previous studies

This study is the first to provide a comprehensive model of ore formation at Myra Falls including characterisation of hydrothermal fluid. Previous studies (Walker, 1985; Juras, 1987) concentrated on the stratigraphy of the Myra Falls district and no attempt at comparing Myra Falls deposits with the other VHMS deposits was made. Work by Robinson (1992, 1993 & 1996) and Sherlock and Barrett (1994), Barrett and Sherlock (1995 & 1996) recognised the deposits as VHMS related. Robinson (1992) proposed the zone refining model of Eldridge et al., (1983) as a model for the formation of the Battle

Zone ores and recognised the Battle lens as being deposited in a period of quiescence between the end of andesitic volcanism and the onset of rhyolitic volcanism. Robinson (1992) also suggested the Battle Zone ores were controlled by deposition into fault bounded basins. Barrett and Sherlock (1996) recognised similar features in the HW deposit. However no attempt at characterising the hydrothermal fluid was made in either study.

Study of the volcanic facies by Allen (1993) led to the interpretation that the Battle lens mineralisation was partly replacing the Price Formation and partly formed at the seafloor. Allen (1993) noted "abundant relic pumiceous mass flow textures within the Gap mineralisation" and was the first to propose that the Upper Zone and Gap lenses were replacing the rhyolitic volcanics. Allen (1993) also recognised the Hanging Wall Andesite as post-dating the hydrothermal system.

In comparison with other VHMS deposits worldwide, the Battle lens shows similarities in mineralogy, metal zonation, and deformation textures. The Battle, Gopher and South Trough lenses show many similarities with exhalative to shallow sub-seafloor VHMS deposits (Large, 1992). The Upper Zone and Gap lens formed sub-seafloor and the Gap lens has some features similar to other pipe-shaped replacement deposits (eg Highway-Reward deposits; Australia Doyle, 1997).

Upper Zone and Gap lenses differ significantly from most VHMS deposits in having abundant bornite Hannington et al. (1999) provided a review of bornite in VHMS deposits. Bornite has been found in many VHMS deposits however in most cases it forms only an accessory phase. Only a few deposits: Kidd Creek (Hannington et al., 1999b), Bousquet mine, Val d'Or, Quebec (Tourigny et al., 1993) and Mt Lyell, Australia (Walshe and Solomon, 1981; Huston and Kamprad, in press) have significant bornite reported. In all cases metamorphism has significantly modified bornite textures and bornite ores are mineralogically complex containing a wide range of trace minerals.

At Kidd Creek Hannington et al., (1999b) concluded that the bornite zone was a late stage replacement body developed as part of the high-temperature, hydrothermal paragenesis of the south ore body. Conditions during the emplacement of the bornite ores were similar to those for the main chalcopyrite stringer zone with the reaction driven by a large influx of Cu. Formation of bornite ores in the Bousquet mine was considered to be similar to the formation of bornite ores at Kidd Creek (Hannington et al., 1999b).

The formation of bornite ores at Mt Lyell was first suggested to be due to the leaching of pre-existing chalcopyrite-rich ores (Walshe and Solomon, 1981). Later models suggested that the bornite ores were due to secondary enrichment of Cu. This enrichment event was considered to be significantly younger than the massive sulfide mineralisation (Solomon et al., 1987). The latest interpretation suggests bornite mineralisation in the Mt Lyell field is due to two-stages of one mineralising event with the bornite assemblage related to high sulfidation rather than VHMS-related alteration assemblages (Huston and Kamprad, in press).

The bornite in the Battle Zone lenses at Myra Falls differs from other bornite-rich VHMS deposits, as temperature of formation is low (200-250°C). However, the reaction is most likely driven by an influx of Cu similar to the formation of the bornite ores at Kidd Creek.

Chapter 12

Conclusions

12.1 Conclusions

- The Myra Falls VHMS district is located on Vancouver Island, British Columbia Canada, and is operated by Boliden-Westmin Ltd.

- Pre-mining reserves for the whole district consist of 40 million tonnes @ 2.1g/t Au, 47 5g/t Ag, 1.8% Cu, 0.5% Pb, 6.5% Zn, and 21.2% Fe. The Battle Zone contains a pre-mining reserve of 7 million tonnes @ 1.4g/t Au, 53.2g/t Ag, 1.8% Cu, 0.7% Pb, 12.5% Zn, and 13.5% Fe.

- The Myra Falls VHMS deposits lie within the Devonian Sicker Group a sequence of volcano-sedimentary rocks interpreted to have formed in an island-arc environment.

- In the Myra Falls district, the Sicker Group is divided into four formations: Price Formation, Myra Formation, Thelwood Formation and the Flower Ridge Formation. The Battle Zone lies at the base of the Myra Formation with footwall alteration extending into the Price Formation.

- The Price Formation is a >300m thick sequence of massive to pillowed basaltic andesite lavas and associated volcaniclastic rocks, and is divided into three facies: feldspar-phyric andesitic lava facies; pyroxene + feldspar porphyritic lava facies and a volcaniclastic facies.

- The Myra Formation is a 310-440m thick pile of intercalated volcanic and sedimentary facies. Volcanic facies originate from at least four distinct source areas and are interpreted to be deposited within a basin defined by the trend of the ore zones.

- In the Battle Zone the footwall consists of altered Price Formation andesite, while the ore lenses are hosted by rhyolite facies of the Myra Formation. Andesite facies from the Myra Formation overly rhyolite facies.

- The rhyolite facies of the Myra Formation in the Battle Zone are further divided into four facies on volcanic textures and clast types:

- Facies 1 volcaniclastic breccias and sandstones: consist of rhyolitic volcaniclastic deposits containing quartz crystals, rhyolite lithic clasts and pseudo-fiamme in a rhyolitic sandstone matrix. The unit is volcanic in origin, however textures indicate reworking of the constituents and redeposition by mass flow.
- Facies 2 Siltstone consists of very fine grained, laminated to thinly bedded (<1 to 10cm) siltstone. In the Battle Zone the siltstones are intensely silicified. Chemically the siltstones are unrelated to other facies in the Battle Zone, however they are interbedded with and show gradational contacts with Facies 1 volcaniclastic breccias and sandstones.
- Facies 3 polymict-graded beds consist of a sand matrix with varying proportions of quartz crystals and lithic clasts. Lithic clasts include, quartz-feldspar-porphyritic rhyolite, facies 1 sandstone, facies 2 siltstone, mudstone, andesite clasts and rare sericite altered clasts. Facies 3 units are interbedded with Facies 1 and 2 units on the northern margin of the Battle Zone. This polymict facies is unrelated to other facies in Battle Zone.
- Facies 4 quartz-feldspar porphyritic rhyolite (QFP) consists of massive to clastic evenly quartz-feldspar-phyric rhyolite. The QFP overlies the Facies 1 rhyolite and is chemically identical, suggesting these two facies are related. The QFP is thickest to the northeast and thins, becoming more clastic toward the south.

- Regional alteration in the Myra Falls district is lithology non-destructive and strongly controlled by rock composition (andesite versus rhyolite).
  - Price Formation andesite is altered to chlorite-epidote-calcite-albite assemblages. Weak sericite alteration is also noted in the regional samples forming a pseudo-clastic texture.
  - Rhyolite Facies of the Myra Formation (HW Rhyolite) have undergone weak sericite-quartz-albite alteration.
  - Andesite facies (Hanging Wall andesite) overlying the HW Rhyolite have undergone chlorite-epidote-calcite-albite alteration similar to the Price Formation. However, at the base of the unit, andesitic breccias contain a varying proportion of rhyolite and have local quartz and sericite alteration.

- Hydrothermal alteration associated with the Battle Zone ore lenses is divided into footwall alteration, which affects the Price Formation, and hangingwall alteration, which affects the HW Rhyolite. Hydrothermal alteration is texturally destructive and unrelated to the primary rock composition.
  - Footwall Alteration
    - Intense sericite-pyrite $\pm$ quartz alteration – This alteration type directly underlies the

Battle, Gopher and South Trough ore lenses and extends approximately 30m into the footwall. It consists of muscovite-quartz and pyrite in varying proportions. This alteration type is produced by large relative mass gains in K, Rb and Ba and lesser gains of Si, P, Sc and Nd and losses of Ca, Na, Mg, Mn Sr, Ni and Cr. These changes reflect the destruction of feldspar and the formation of quartz-muscovite dominated mineralogy. Copper, Pb and Fe are also gained reflecting the presence of pyrite-chalcopyrite and galena in the alteration.

- Intense Mg-chlorite alteration occurs within the intense sericite-pyrite alteration zone and consists of Mg-chlorite, quartz-muscovite and pyrite. Intense Mg-chlorite alteration shows relative gains of Ba, K, R, Mg and Mn and losses of Ca, Na, Sr, Ni and Si reflecting the change in bulk composition of the rock from intermediate-chlorite – epidote – carbonate to Mg-chlorite dominated.
- Approximately 30m below the base of the massive sulfides a less intense zone of sericite-chlorite–pyrite alteration becomes dominant. This alteration shows relative gains of Ba, K, Rb, and P and losses of Ca. Na, Sr, Ni and Cr reflecting the loss of epidote-calcite and most of the chlorite and replacement of theses minerals by muscovite.

- Hangingwall alteration in the Battle Zone consists of three styles which overlap.
  - Sericite alteration is most intense close to ore lenses in Facies 1 volcaniclastics, weakening away from ore lenses and in massive the Facies 4 QFP. Sericite alteration is texturally destructive obscuring most volcanic features in the Battle Zone Sericite alteration causes a relative mass gain of Cu, Ba, Zn, Pb, Ni, As and K and relative losses of S, Can P, Sr, Na, V, Mg, Si, Mn and Fe.
  - Silicification shows relative gains in Si, K, Cu, Ba, Zn, Ni, Cr, Pb and As and relative losses in S, Ca, Mg, and P. Silicification may preserve volcanic textures but generally post dates the sericite alteration. A combination of silicification and sericite alteration creates pseudo-fiamme texture.
  - Dolomite alteration occurs on the margin of the hydrothermal alteration system and overprints, and is overprinted, by sericite and quartz alteration. Dolomite alteration is texturally destructive forming massive blebs of dolomite up to 2cm in diameter. Relative mass gains of Cu, Ba, Zn, Ni, Mn, Mn, Ca, Pb and As along with relative losses of S, V, Na, P, Sr, Si and Cr characterise dolomite alteration.

- Ore lenses with in the Battle Zone lie at two stratigraphic levels. The Battle, Gopher and South Trough lenses lie at the base of the HW Rhyolite with footwall alteration extending into the Price Formation. Upper Zone and Gap lenses lie at the top of the Facies 1 volcaniclastics on the contact with (Upper Zone), and into (Gap), the Facies 4 QFP.

- Morphologically the Battle Zone lenses vary considerably. The Battle lens has a sheet like

morphology dipping gently to the west. The South Trough lens forms a series of stacked sheet like sub-lenses within a larger zone of disseminated sulfides. The Gopher lens has a strongly, asymmetric, wedge-shaped cross section and is elongated in a northwest-south-easterly direction, dipping gently to the west along with the Battle lens. The Gap lens has a pipe shaped cross section and is elongate along a northeast-southwest trend similar to the Gopher lens.

- All lenses except the Upper Zone lenses show a strong mineralogical zonation form semi-massive to massive barite-galena-tennantite-sphalerite at the top of the lens through massive sphalerite, to massive sphalerite-pyrite-chalcopyrite, massive pyrite-chalcopyrite to massive pyrite at the base of the lenses. However, these mineral assemblages are recrystallised destroying primary textures.

- The Upper Zone and Gap lenses have two additional sulfide assemblages overprinting the sphalerite-pyrite-chalcopyrite-tennantite-galena mineralogy. A bornite-renierite-anilite assemblage replaces chalcopyrite and shows recrystallisation textures typical of metamorphism. A third assemblage consisting of stromeyerite-electrum and fine-grained chalcopyrite cross cuts both the sphalerite-pyrite-chalcopyrite-tennantite-galena and the bornite-renierite-anilite assemblages. This stromeyerite-electrum-chalcopyrite assemblage shows delicate textures unlikely to be preserved during metamorphism.

- Battle Zone lenses have a strong vertical and lateral elemental zonation from a zone of Pb and Zn enriched in Ba, As, Ag and Hg at the top of the lenses passing downwards to a Zn-zone enriched in Cd, and Ag. Then to a Cu-Fe-zone enriched in Ni and Bi and a finally to a Fe-zone at the base of the lenses. Bi enrichment occurs sporadically throughout the Cu-Fe, Zn and Zn-Pb zones. The Upper Zone lenses are dominated by Zn, Cu and Ba and enriched in Ag, As and Hg with a halo of Ag and As enrichment extending into hangingwall and a zone of high Fe content below the lenses. The Gap lens shows similar distribution of elements to the Battle, Gopher and South Trough lenses. However, a Ba-zone occurs above the Gap massive sulfides and the upper most zone is a Zn-Pb-Ba zone enriched in As, Ag, Hg, Ge and V. In addition this elemental zonation is cut by a Ag-Cu-Mo enrichment up the centre of the lens. Zonation of metals in Battle Zone lenses corresponds well with observed mineralogy.

- Distribution of Fe enrichment and high Cu number [100(Cu/Cu+Zn)] suggests the presence of NW-NNW trending feeder faults underlying all the Battle Zone lenses.

- Sulfur isotope data for sulfides from the Battle Zone form a tight cluster indicating a very homogeneous source interpreted as reduced seawater sulfate. Sulfur isotopes of sulfates from Battle Zone indicate a direct seawater source.

- The Battle, Gopher and South Trough lenses were deposited in the Devonian, on top of the Price Formation on the seafloor with minimal (<10m) of sediment cover until swamped by a massive influx of rhyolitic mass flows. The hydrothermal fluid associated with the deposition of these lenses is interpreted to have had temperatures between 250-350°C, weak acidity (ph = 4-5) and a salinity in the range of 3-8wt%. Sulfur isotope data indicate a reduced seawater sulfate source for the sulfides and a direct seawater source for the sulfates The swamping of the depositional environment with volcaniclastics did not stop the hydrothermal system. Hydrothermal fluids continued to percolate up through the rhyolitic volcaniclastics until they encountered the QFP. The QFP provided a barrier to the ascending fluids which resulted in the subseafloor deposition of sulfide mineralisation as represented by the Upper Zone and Gap lenses. During percolation of the hydrothermal fluid up through the rhyolitic volcanicaniclastics the fluid cooled and became slightly more oxidised. Toward the end of the hydrothermal system the fO_2 of the hydrothermal fluid increased and the temperature decreased resulting in the formation of bornite from previously formed chalcopyrite After the hydrothermal system ceased the hangingwall volcaniclastics and associated massive sulfide lenses were covered by the Hanging Wall andesite. The entire sequence was then metamorphosed and deformed. Metamorphism caused the recrystallisation and annealing of all sulfide minerals except pyrite. Metamorphism also resulted in remobilisation of Cu, Ag and Au within the Upper Zone and Gap lenses, with these elements deposited in crosscutting veins during the waning stages of metamorphism.

12.2 Recommendations for future research

Work during this study highlighted the need for further research in the Myra Falls District. The following projects are proposed for further research at Myra Falls.

- Review of existing data (mainly work of Juras 1987) highlights the need for a reassessment of volcanic facies on the Myra Falls property. A project to study the distribution of volcanic facies and the variation of volcanic facies across the property and the influence of the volcanic facies on ore distribution is recommended. This project would also need to characterize the change in volcanic textures due to alteration of the host rocks, for example the formation of pseudo-fiamme.

- Are the HW Rhyolite and Lynx-Myra-Price horizons really two separate stratigraphic horizons and therefore represent two distinct mineralizing events? Studies of modern seafloor hyrdothermal systems shown significant topography on the seafloor which combined with the interfingering of volcanic debris for numerous sources has the potential to create syn-

chronous ore bodies with significant vertical separation. Facies mapping may provide important clues to the relationship of the Lynx-Myra-Price and HW Horizons.

- Documentation of the HW Dacite in the Thelwood Valley requires reassessment, sampling of holes for "least altered rocks" during this project showed that the HW Dacite had been logged as andesite. Careful observation of feldspar phenocryst populations and ground mass textures is required to differentiate the HW Dacite from Price Formation andesite, as both rocks are dark green in color. Whole rock lithogeochemistry may also help in distinguishing dacite from andesite.

- The significance of QFP bodies to mineralisation has been shown in other VHMS districts (Boliden, Allen et al., 1997; Rosebery, Allen 1994). However, although Upper Zone mineralisation occurs in proximity to QFP bodies at Myra Falls the relationship of the QFP bodies to zones of mineralisation is not fully known. Further study is required as the shape and distribution of these lenses is not fully understood and targeting of this style of mineralisation poor.

- The influence of burial and cap rocks on the formation of sub-seafloor massive sulfide lenses at Myra Falls also requires further study. Numerous cap rocks exist, eg Cherts overlying the Battle lens, QFP above the Upper Zone lenses, and ultramafics flows above the Lynx and Myra lenses. The role of cherts in the formation of massive sulfide mineralisation is currently being investigated (Jones) however a wider study is recommended to understand role of cap rocks in ore formation and their relationship to sub-seafloor mineral deposition.

- More work is required on the Price Formation. The Price Formation forms the footwall to the HW and Battle deposits, thus it may be expected that its nature (coherent versus clastic) and its topography may have influenced the evolving hydrothermal systems. There also exists some doubt as to the origin of the "regional chlorite-epidote-carbonate" alteration defined in this study. Is it a purely metamorphic assemblage or was the andesite altered by seawater prior to metamorphism? Regional mapping of the alteration to test if it is localized near mineralisation or zoned on a large scale is required to solve this problem.

- This study also highlighted the lack of knowledge about the footwall hydrothermal alteration system Directly underlying the Battle Zone lenses is a zone of intense sericite-quartz alteration, which contains areas of intense Mg-chlorite alteration and grades downward into strong chlorite-sericite-pyrite alteration. Pervasive, moderately chlorite-sericite +/- quartz altered Price Formation andesite has also been noted on 24 level (pers. comm., Gemmell, 2001). Within this zone of pervasive alteration were several more intensely altered zones

(chlorite-quartz) with quartz-pyrite stringer veins (pers comm., Gemmell, 2001). The significance of these zones and the extent of the alteration system is unknown. Potential exists for more altered and veined zones below 24 level. A research project, combining the exposure on the 24 level and deep drilling, to characterize the alteration mineralogy and geochemical characteristics of the footwall plumbing system to the Myra Falls lenses through the Price Formation may help in targeting new areas for the discovery of additional resources along the Price Formation contact.

- Present indications show a change in composition of chlorites (based on PIMA analyses) in the Price Formation from the regional alteration to more intense hydrothermal alteration associated with massive sulfide mineralisation. In the Battle Zone the composition of sericite (muscovilte/illite) also shows a weak spacial association with the Battle lens ore, this require further investigation using samples from a wider area. It is recommended that the work from this study be combined with the findings of A. Chong and S. Jones and extended to further investigate the changes in composition which may help define differing alteration styles useful in targeting ore zones of economic values.

References

Adachi M., Yamamoto K., and Sugisaki R. 1986 Hydrothermal chert and associated siliceous rocks from the northern Pacific: their geological significance as indicators of ocean ridge activity. *Sedimentary Geology,* v **47**, p.125-148.

Allen R.L. 1993. Volcanic facies analysis of massive sulfide deposits in British Columbia: Preliminary results from field work August-September. Report to MDRU, University of British Columbia

Allen R.L. 1994. Synvolcanic, subseafloor replacement model for Rosebery and other massive sulfide ores. *Contentious Issues in Tasmanian Geology,* GSA-Tasmanian division, Hobart 3-4 November.

Allen R.L., Weihed P., Svenson S 1997. Facies Analysis of a 1.9Ga, Continental Margin, Back-Arc, Felsic Caldera Province with Diverse Zn-Pb-Ag-(Cu-Au) Sulfide and Fe Oxide Deposits, Bergslagen Region, Sweden. *Economic Geology,* v.**91**, p 979-i 008.

Allen R.L., Weihed P., Svenson S., 1997. Setting of Zn-Cu-Au-Ag Massive Sulfide Deposits in the Evolution and Facies Architecture of a 1.9Ga Marine Volcanic Arc, Skellefte District, Sweden. *Economic Geology,* v.**91**, p 1022-1053

Allen R.L , Blake M., Large R.R. 1998. Carbonate alteration at the Rosebery mine: The relationships between alteration texture, paragenesis, chemistry of carbonate minerals, and distance to ore, in *Studies of VHMS-related alteration geochemistry and mineralogical vectors to ore* CODESIAMIRA / ARC Project P439.

Almodovar 3.R , Saez R., Pons J M., Maestre A , Toscano M., Pascual E. 1998. Geology and genesis of the Azalcolar massive sulfide deposits, Iberian Pyrite Belt, Spain. *Mineralium Deposita,* v.**33**, p.111-136.

Alt J.C. 1995. Subseafloor Processes in Mid-Ocean Ridge Hydrothermal Systems, in IUGG-Geophysical Monograph 91 Seafloor Hydrothermal Systems. Physical, Chemical, Biological and Geological Interactions, *American Geophysical Union.* p.85-114.

Andrew A. and Godwin C.I. 1989. Lead- and strontium-isotope geochemistry of Paleozoic Sicker Group and Jurassic Bonanza Group volcanic rocks and Island Intrusions, Vancouver Island, British Columbia. *Canadian Journal of Earth Sciences,* v.**26**, p.894-907.

Atkinson B.K 1975. Experimental deformation of polycrystalline pyrite. effects of temperature, confining pressure, strain rate, and porosity. *Economic Geology,* v **70**, p.473-487.

Barrett T.J and MacLean W.H. 1991. Chemical, mass, and oxygen isotope changes during extreme hydrothermal alteration of Archaean rhyolite, Noranda, Quebec. *Economic Geology,* v.**86**, p.406-414.

Barrett T.J., Sherlock R.L., Juras S.J., Wilson G.A., Allen R. 1994. Geological Investigation of the HW Deposit, Buttle Lake camp, Central Vancouver Island., *in* Selected mineral deposits of British Columbia, Canada. 1994, Society of Economic Geologists. p.37-44.

Barrett T.J. and MacLean W.H. 1994. Mass Changes in Hydrothermal Alteration Zones associated with VMS Deposits of the Noranda Area *Exploration and Mining Geology,* v.**3**, p.131-160

Barrett T.J. and MacLean W.H 1994 Chemostratigraphy and Hydrothermal Alteration for VHMS Deposits in Greenstones and Younger Volcanic Rocks, in *Alteration and Alteration Processes associated with Ore-forming Systems,* Lentz D R , Editor Geological Association of Canada, Short Coarse Notes. p.433-467.

Barrett T.J. and Sherlock R L 1996. Volcanic Stratigraphy, Lithogeochemistry, and Seafloor Setting of the HW Massive Sulfide Deposit, Myra Falls, Vancouver Island, British Columbia. *Exploration and Mining Geology,* v.**5**, p 421-458.

Barrie CT. and Hannington M.D. 1997. Volcanic-Associated Massive Sulfide Deposits: Processes and Examples in Modern and Ancient Settings. *GAC-MDD-SEG Short Course Manual,* Ottawa May 17-18.

Barton P.B. 1978. Some ore textures involving sphalerite from the Furutobe Mine, Akita Prefecture, Japan. *Mining Geology,* v.**28**, p.293-300.

Barton P.B. and Bethke J.P M. 1987. Chalcopyrite disease in sphalerite: Pathology and epidemiology American Mineralogist, v.**72**, p 451-467.

Bastin, E.S., Graton L.C., Lindgren w., Newhouse L4 H., Schwartz G.M , Short M N 1931. Criteria of age relations of minerals, with special reference to polished sections of ores. Economic Geology, v.**26**, p 561-610.

Bergstol, S. and Vokes F.M. 1974. Stromeyerite and Mckinstryite from the Godejord Polymetallic Suiphide Deposit, Central Norwegian Cajedonides. *Mineralium Deposita,* v.**9**, p 325-337.

Berry, R. 1995. Report on activities June 1995: Structure of the Westmin Mine at Myra Falls. *Internal company report*

Berry, R. 1996 Report on activities August 1996: Structure of the Myra Falls Operation. *Internal company report*

Berry, R. 1998 Structural Geology of the Myra Falls Operation. Centre for Ore Deposit Research, University of Tasmania *Internal company report*

Berry, R 2000 Structural geology of the Myra Falls Operation. Centre for ore deposit research, University of Tasmania. *Internal company report*

Binns, R.A and S.D. Scott S.D. 1993. Actively forming polymetallic sulfide deposits associated with felsic volcanic rocks in the eastern Manus Back-Arc Basin, Papua New Guinea. *Economic Geology,* v.**88**, p.2226-2236.

Binns RA., Parr J.M., Scott S.D., Gemmell J.B., Herzig P.M 1995. PACMANUS: An active seafloor hydrothermal field on siliceous volcanic rocks in the eastern Manus Basin, Papua New Guinea. PACRIM 1995 Conference Abstracts volume, 1995· p.49-54.

Bodon S B. and Valenta R.K. 1995. Primary and tectonic features of the Currawong Zn-Cu-Pb-(Au) Massive Sulfide Deposit, Benambra, Victoria. Implications for ore genesis. *Economic Geology,* v **90**, p.1694-i 721.

Bradely A. 1997. The Geology and Genesis of the chlorite-carbonate alteration in the footwall of the Hellyer volcanic-hosted massive sulfide deposit. Unpublished Honours thesis, University of Tasmania. p.101.

Brandon M.T., Orchard, M.J., Parrish R.R., Sutherland Brown A., Yorath C.J., 1956. Fossil ages and isotopic dates from the Paleozoic Sicker Group and associated intrusive rocks, Vancouver Island, British Columbia. *Current Research,* Part A, Geological Survey of Canada, Paper 86-lA, p.683-696

Cann J.R. 1970. Rb, Sr, Y, Zr and Nb in some ocean floor basaltic rocks. *Earth and Planetary Science Letters,* v.**10**, p 7-il.

Casey W.H and Taylor B.E. 1982. Oxygen, Hydrogen, and Sulfur Isotope Geochemistry of a Portion of the West Shasta Cu-Zn District, California. *Economic Geology,* v.**77**, p.38-49.

Chryssoulis S.L. 1989. Determination of invisible gold in flotation products and four ore types from the HW mine, British Columbia. Westmin Resources Ltd Internal company report.

Clarke, B.R. and Kelly W.C. 1973. Sulfide deformation studies I. Experimental deformation of pyrrhotite and sphalerite to 2000 bars and 500^{0}C. *Economic Geology,* v.**68**, p 332-352

Claypool, G.E., Holser W.T., Kaplan I.R., Sakai H., Zak 1.1950. The age curves of sulfur and oxygen isotopes in marine sulfate and their mutual interpretation. *Chemical Geology,* v.**28**. p.199-260.

Cooke D R. and Simmons S F. in prep. Characteristics and Genesis of Epithermal Gold Deposits. *Ecomomic Geology,* Special Issue: reviews in Economic Geology v.**13**.

Cox S.F., Etheridge MA , Hobbs B E. 1981. The experimental ductile deformation of polycrystalline and single crystal pyrite *Economic Geology,* v.**76**, p.2105-2117

Craig J.R. and Vokes F.M. 1992. Ore mineralogy of the Appalachian-Caledonian stratabound sulfide deposits. *Ore Geology reviews,* v.**7**, p.77-i 23.

Craig J R and Vokes F.M 1993. The Metamorophism of pyrite and pyritic ores: an overview. *Mineralogical Magazine,* v **57**, p.3-18.

Craig, J R. and Vaughan D.J. 1994. *Ore microscopy and ore petrography.* John Wiley and Sons New York. 434p.

Creswell, S.D. 1997. A study of the Upper Zone Mineralisation of the H-Zone of Westmin Resources Ltd , Myra Falls Operation, Vancouver Island, British Columbia, Canada., Unpublished M.Sc. Thesis, University of Exeter. Exeter. 112p.

Dawson, KM., Panteleyev A., Sutherland Brown A., Woodsworth G.J. 1991. Regional Metallogeny Chapter 19, in *Geology of the Cordilleran Orogen in Canada,* H. Gabrielse and C.J. Yorath, Editors, Geological Survey of Canada. p.707-768

Denniss A.M , Colman T.B., Cooper D.C., Hatton WA., Shaw M.H. 1999 The combined use of PIMA and Vulcan technology for mineral deposit evaluation at Parys Mountain mine, Anglesey, U.K. in *International Conference on Applied Geological Remote Sensing* Vancouver B.C March 1-3 1999.

Dimroth E. and Lichtblau A P., 1979. Metamorphic evolution of Archean hyaloclastites, Noranda area, Quebec, Canada. Part 1:Comparison of Archean and Cenozoic sea-floor metamorphism. *Canadian Journal of Earth Sciences,* v **16**, p.1315-1338.

Dishaw G. 1998. Price Orebody. Honours thesis. Unpublished

Doyle M.G. 1997. A Cambro-Ordovician submarine volcanic succession hosting massive sulfide mineralisation: Mount Windsor Subprovince, Queensland. Ph.D. thesis, University of Tasmania.

Ducworth, R.C 1991 The geology and depositional environment of the Early Proterozoic massive sulfide-bearing sequence, Renstrom, Northen Sweden. PhD thesis, University of Wales, College of Cardiff.

Eldridge, C S., Barton P.B., Ohmoto H. 1983. Mineral textures and their bearing on formation of the Kuroko orebodies. *Economic Geology,* **Monograph 5**, p.241-281.

Eldridge C.S., Bourcier W.L., Ohmoto H., Barnes H.L. 1988. Hydrothermal Inoculation and Incubation of the Chalcopyrite Disease in Sphalerite *Economic Geology,* v.**83**, p.978-989

Eldridge, C.S., Williams N , Walshe J.L., 1993. Sulfur Isotope Variability in Sediment-Hosted Massive sulfide Deposits as Determined Using the Ion Microprobe SHRIMP: II A Study of the H.Y.C. Deposit at McArthur River, Northen Territory, Australia. *Economic Geology,* v.**88**, p.1-26.

Ellis A.J. 1963. The solubility of calcite in sodium chlorite solutions at high temperature. *American Journal of Science,* v.**261**, p.259-267.

England T.D.J. and Calon T.J. 1991. The Cowichan fold and thrust system, Vancouver Island, southwestern British Columbia. *Geological Society of America Bulletin,* v.**103**, p.336-362.

England B.M. and Ostwald J. 1993. Framboid-derived structures in some Tasman fold belt base-metal sulfide deposits, New South Wales, Australia *Ore Geology Reviews,* v.**7**, p.381-412.

England, T.D.J., Currie L.D., Massey N.W.D., Roden-Tice M.K., Miller D.S. 1997. Apatite fission-track dating of the Cowichan fold and thrust system, southern Vancouver Island, British Columbia. *Canadian Journal of Earth Sciences,* v.**34**, p.635-645.

Finlow-Bates T. and Stumpfl E.F. 1981. The Behavior of so-called Immobile Elements in Hydrothermally Altered rocks Associated with Volcanic Submarine-Exhalative Ore Deposits. *Mineralium Deposita,* v.**16**, p.319-328.

Floyd, P.A. and Winchester J.A. 1975. Magma Type and Tectonic Setting discrimination Using Immobile Elements. *Earth and Planetary Science Letters,* v **27**, p 211-218.

Floyd, P.A. and Winchester J.A. 1978. Identification and Discrimination of Altered and Metamorphosed Volcanic Rocks using Immobile Elements. *Chemical Geology,* v.**21**, p.291-306

Fouquet, Y., Stackelberg U., Charlou J L., Erzinger J., Herzig P.M. Muhe R., Wiedicke M. 1993 Metallogenesis in Back-Arc Environments· The Lau Basin Example. *Economic Geology,* v.**88**, p 2154-2181.

Fouquet, Y., Wafik A., Cambon P., Mevel C., Meyer G., Gente P., 1993. Tectonic Setting and Mineralogical and Geochemical Zonation in the Snake Pit Sulfide Deposit (Mid-Atlantic Ridge at 23°N) *Economic Geology,* v.**88**, p.2018-2036.

Franklin, J.M., Lydon J.W , Sangster D,F. 1981. Volcanic-Associated Massive Sulfide Deposits. *Economic Geology,* **75th Anniversary Volume**, p.485-627.

Fritz P., Drimmie R.J., Nowocki V.K., Preparation of sulfur dioxide for mass spectrometer analyses by combustion of sulfides with copper oxide. *Analytical Chemistry,* v.**46**, p.164-166.

Fyles J.T. 1955. Geology of the Cowichan Lake Area, Vancouver Island, British Columbia. *B.C. Ministry of Energy, Mines and Petroleum Resources, Bulletin,* v.**37**, 79p.

Gabrielse H., Monger J.W.H., Wheeler J.O., Yorath C.J. 1991. Tectonic Framework - Part A. Morphogeological Belts, Tectonic Assemblages and Terranes, *in* Geology of the Cordilleran Orogen in Canada, H. Gabrielse and C.J. Yerath, Editors Geological Survey of Canada. p.15-28.

Gabrielse H. and Yorath C.J., eds. 1992. Geology of the Cordilleran Orogen in Canada Geological Survey of Canada. Geology of Canada. v 4.

Galley A.G., Watkinson D.H., Jonasson I.R., Riverin G. 1995. The Sub-seafloor Formation of Volcanic-Hosted Massive Sulfide:Evidence from the Ansil Deposit, Rouyn-Noranda, Canada. *Economic Geology,* v.go, p.2006-2017.

Gaspar 0. and Pinto A. 1991. The ore textures of the Neves-Corvo volcanogenic massive sulfides and their implications for ore benefaction. *Mineralogical Magazine,* v.**55**, p.417-422.

Geffery W.G. 1965. Lynx, Paramount, Price (Western Mines Ltd.). Minister of Mines and Petroleum Resources, Province of British Columbia, *Annual Report*, No.99, p.157-166.

Gemmell, J.B. and Large R.R 1992. Stringer system and Alteration Zones underlying the Hellyer Volcanic-Hosted Massive Sulfide Deposit, Tasmania, Australia. *Economic Geology,* v.**87**, p.620-649

Gifkins, C.C. and Allen R.L. in press. Textural and chemical characteristics of diagenetic and hydrothermal alteration in glassy volcanic rocks: examples from the Mount Read Volcanics, Tasmania. *Economic Geology* Special Issue: Alteration and its exploration significance associated with the spectrum of volcanic hosted massive sulfide deposits.

Giggenbach W.F. 1997. Chapter 15 The Origin and Evolution of Fluids in Magmatic-Hydrothermal Systems. *in* Geochemistry of hydrothermal ore deposits H.L. Barnes, Ed. John Wiley & Sons. p 750-758.

Gilligan L B and Marshall B. 1987. Textural evidence for remobilization in metamorphic environments. *Ore Geology reviews,* v.**2**, p 205-229.

Godwin C.I., Robinson M., Juras S.J. 1996. Galena Lead Isotopes, Buttle Lake Mining Camp, Vancouver Island, British Columbia, Canada *Economic Geology,* v **91**, p.549-562.

Goodfellow W.D and Jonasson I R. 1984. Ocean stagnation and ventilation defined by $\delta^{34}S$ secular trends in pyrite and barite, Selwyn Basin, Yukon. *Geology,* v.**12**, p1583-586

Goodfellow W.D., Grapes K., Cameron B., Franklin J.M., 1993 Hydrothermal alteration associated with massive sulfide deposits, Middle Valley, Northern Juan de Fuca Ridge. *The Canadian Mineralogist,* v.**31**, p 1025-1060

Gordey S P., Geldsetzer H.H.J., Morrow D.W., Bamber EW , Henderson C.M., Richards B.C., McGugan A., Gibson D W 1991.

Grant J A 1986. The Isocon Diagrarn - A simple solution to Gresens' Equation for Metasomatic Alteration. *Economic Geology,* v.**81**, p.1976-1 982.

Green G.R., Solomon M., Walshe J.L. 1981. The Formation of the Volcanic-Hosted Massive Sulfide Ore Deposit at Rosebery, Tasmania. *Economic Geology,* v.**76**, p.304-338

Greenwood H.J., Woodsworth G.J. Read P.B., Ghent E.D., Evenchick C.A. 1991 Metamorphism Chapter 16, *in* Geology of the Cordilleran Orogen in Canada, H. Gabrielse and C.J. Yorath, Editors. 1991, Geological Survey of Canada. p 533-570

Gresens R.L. 1967. Composition-Volume relationships of metasomatism. *Chemical Geology,* v **2**, p.47-65.

Gunning H.G. 1931. Buttle Lake Map Area, Vancouver Island, B.C. Geological Survey of Canada, *summary report,* Part A, p56A-78A.

Hannington M.D and Scott S.D. 1989. Sulfidation Equilibria as Guides to Gold Mineralisation in Volcanogenic Massive Sulfides Evidence from Sulfide Mineralogy and the Composition of Sphalerite. *Economic Geology,* v.**84**, p.1978-1995

Hannington, M.D., Jonasson I R. Herzig P.M. Petersen S. 1995. Physical and Chemical Processes of Seafloor Mineralisation at Mid-Ocean Ridges. *Geophysical Monograph 91,* Seafloor Hydrothermal Systems; Physical, Chemical, Biological and Geological Interactions: p.115-157

Hannington, M.D , W. Bleeker W., I. Kjarsgaard 1.1 999a. Sulfide Mineralogy, geochemistry, and Ore Genesis of the Kidd Creek Deposit: Part 1. North, Central, and South Orebodies. *Economic Geology* **Monograph 10**, p.163-224.

Hannington, M D., Bleeker W., I. Kjarsgaard I. 1999b. Sulfide Mineralogy, Geochemistry, and Ore Genesis of the Kidd Creek Deposit· Part II. The Bornite Zone *Economic Geology,* **Monograph 10**, p.225-266.

Herrmann W. and A. Hill A in press. The origin of chlorite-tremolite-carbonate rocks associated with the Thalanga VHMS deposit North Queensland, Australia. *Economic Geology* Special Issue: Alteration and its exploration significance associated with the spectrum of volcanic hosted massive sulfide deposits

Herrmann W. 1998. Use of immobile elements and chemostratigraphy to determine precursor volcanics. Centre for Ore Deposit Research, University of Tasmania, Internal publication.

Herrmann W., Blake M., Doyle M., Huston D., Kamprad J. 1998. Application of PIMA and FTIR spectrometry to VHMS alteration studies, Centre for Ore Deposit Research, University of Tasmania and AGSO, Canberra.

Herrmann W , Blake M., Doyle M., Huston D., Kamprad J. Merry N., Pontual S. in press. PIMA infrared spectral analysis of the hydrothermal alteration zones associated with base metal sulfide deposits at Rosebery and Western Tharsis, Tasmania, and Highway-Reward, Queensland. *Economic Geology,* Special Issue· Alteration and its exploration significance associated with the spectrum of volcanic hosted massive sulfide deposits.

Hill, A.P. and Orth K. 1994. Textures and Origin of carbonate associated with some Australian VHMS Deposits. *Contentious Issues in Tasmanian Geology,* GSA-Tasmanian division, Hobart 3-4 November.

Hunns S.R., *Zaw K., Large R. R. Dean JA., Ryan C G., McPhie J 1994* Preliminary geochemical results constraining the formation of the Mount Chalmers volcanic-hosted massive sulfide deposits *New Developments in Geology Metallogeny Northern Tasman Orogenic Zone,* 1994 (Townsville 21-22 February 1994).

Huston D L. 1997. Stable isotope systematics and VMS deposits. *in* Volcanic-Associated Massive Sulfide Deposits. process and examples in modern and ancient settings. A volume to accompany a GAC-MDD-SEG co-sponsored short coarse Ottawa, May 17-18.

Huston D.L. 1988. Aspects of the geology of massive sulfide deposits from the Balcooma district, northern Queensland a Rosebery, Tasmania: Implications for ore genesis, PhD thesis, University of Tasmania.

Huston D.L. 1993. The effect of alteration and metamorphism on wall rocks to the Balcooma and Dry River South volcanic-hosted massive sulfide deposits, Queensland, Australia. *Journal of Geochemical exploration,* v.**48**, p.277-307.

Huston D.L. and Large R.R. 1987. Genetic and exploration significance of the zinc ratio (100Zn / (Zn + Pb)) in massive sulfide systems. Economic Geology, v.**82**, p.1521-1539.

Huston D.L. Sie S.H., Suter G F., Cooke D R., Both RA. 1995. Trace Elements in Sulfide Minerals from Eastern Australian Volcanic-Hosted Massive Sulfide Deposits: Part I. Proton Microprobe Analyses of Pyrite, Chalcopyrite, and Sphalerite and Part II Selenium Levels in Pyrite: Comparison with $\delta^{34}S$ Values and Implications for the Source of Sulfur in Volcanogenic Hydrothermal Systems. *Economic Geology,* v.**90**, p 1167-1196.

Huston D.L., Kuronen U., Stolz J. 1995. Waterloo and Agincourt prospects, northern Queensland· contrasting styles mineralisation within the same volcanogenic hydrothermal system. *Australian Journal of Earth Sciences,* v.**42**, p.203-221

Huston D L., Power M., Gemmell J B., Large R.R. 1995. Design, calibration and geological application of the first operation Australian laser ablation sulfur isotope microprobe. *Australian Journal of Earth Sciences,* v **42**, p.549-555

Huston D L., Jablonski W., Sie S.H. 1996. The distribution and mineral hosts of Silver in Eastern Australian Volcanogen Massive Sulfide Deposits. *The Canadian Mineralogist,* v.**34**, p.529-546.

Huston D. 1999. Chapter 7 - Stable Isotopes and their significance for understanding the genesis of volcanic-hosted massive sulfide deposits: A review, *in* Volcanic-associated massive sulfide deposits processes and examples in modern and ancient settings CT. Barrie and M.D. Hannington, Editors. Society of Economic Geologists. p.157-179.

Huston D L. Kamprad J., Brauhart C. 1999. Definition of high-temperature alteration zones with PIMA. An example from the Panorama VHMS district, central Pilbara Craton. *Australian Geological Survey Organisation Research Newsletter* v.**30**, p.10-12.

Huston D L. and Kamprad J. 2000. The Western Tharsis deposit: A high sulfidation Cu-Au deposit in the Mt Lyell field, possible Ordovician age. Australian Geological Survey Organisation Research Newsletter, v.**32**, p.1-6.

Huston D.L. and Kamprad J. in press. Zonation of alteration fades at western Tharsis: implications for the genesis of Cu-Au deposits in the Mt Lyell field, western Tasmania Economic Geology, Special Issue: Alteration and its exploration significance associated with the spectrum of volcanic hosted massive sulfide deposits.

Hutchison M.N and Scott S.D. 1981. Sphalerite geobarometry in the Cu-Fe-Zn-S system. *Economic Geology,* v.**76**, p.143-153.

W C. Shanks III W.C., BohlkeJ.K , Seal II R.R., 1995. Stable Isotope in Mid-Ocean Ridge Hydrothermal Systems: Interactions between Fluids, Minerals and Organisms., in Seafloor Hydrothermal Systems, Humphris, Editor. American Geophysical Union. p.194.

Irving E. and Yole R W. 1987. Tectonic rotations and translation in Western Canada. New evidence from Jurassic rocks of Vancouver Island. *Geophysical Journal of the Royal Astronomical Society,* v.**91**, p 1025-1048.

Irving E. and Wynne P.J. 1990. Paleomagnetic Evidence bearing on the evolution of the Canadian Cordillera. *Philosophical Transactions of the Royal Society of London,* v **A331**, p.487-509.

Isachsen C. 1984. *Geology, geochemistry and geochronology of the west coast Crystalline Complex and related rock Vancouver Island, British Columbia* Thesis, University of British Columbia. 144p.

Ishihara S. 1974. Geology of Kuroko deposits. *Mining Geologists Japan,* **Special Issue No 6**, p.435

Ishikawa Y., Sawaguchi T., Iwaya S., Horiuchi M. 1976. Delineation of prospecting targets for Kuroko deposits based on modes of volcanism of underlying dacite and alteration halos. *Mining Geology,* v.**26**, p.105-117.

James J.A. 1986. The Isocon Diagram - A simple solution to Gresens' equation for Metasomatic Alteration *Economic Geology* v.**81**, p.1976-1982.

James J.R. and Vokes F.M. 1993. The Metamorphism of pyrite and pyritic ores: an overview. *Mineralogical Magazine,* v.**57**, p.3-18

Jeflery W.G. 1965 Lynx, Paramount, Price (Western Mines Ltd.). British Columbia Department of Mines and Petroleum Resources, Annual Report, p.157-i 66.

Jeffery W.G. 1970 Buttle Lake. British Columbia Department of Mines and Petroleum Resources, Annual Report.

Jolley W.T. 1978. Metamorphic history of the Abitibi belt. *Geological Survey of Canada, Paper,* **78-10**, p.63-78.

Jones D.L., Silberling N.J., Hillhouse J 1977. Wrangellia - A displaced terrane in northwestern North America. *Canadin Journal of Earth Science,* v.**14**, p.2565-2577.

Juras S.J 1987. *Geology of the Polymetallic Volcanogenic Buttle Lake Camp, with Emphasis on the Price Hillside, Central Vancouver island, British Columbia* Unpublished PhD thesis The University of British Columbia, 179p.

Juras S.J. and Pearson C.A. 1990a. The Buttle Lake Camp, Central Vancouver Island, B.C., *in* Geology and regional setting of major mineral deposits in southern British Columbia, 8th IAGOD Symposium Field Trip Guidebook *Geological Survey of Canada Open File 2167.* p.145-161.

Juras S.J. and Pearson CA 1990b. Mineral Deposits of the Southern Canadian Cordillera. Guidebook for Fieldtrip B2 Geological Association of Canada - Mineral Association of Canada Joint Meeting, p.1-21.

Kase K., Yamamoto M., Mitsuno C. 1994. Germanium-bearing Colusite from the Yanahara Mine, Japan, and its significance to ore genesis. *Resource Geology,* v.**44**, p.33-38.

Kelly W.C. and Clark B R. 1975 Sulfide deformation studies III Experimental deformation of chalcopyrite at 2000 bars and 500 degrees Celsius. *Economic Geology,* v **70**, p 431-453.

Knuckey M.J., Comba C.D.A., Riverin G. 1982. Structure, Metal Zoning and Alteration at the Millenbach deposit, Noranda, Quebec, *in* Precambrian Sulfide Deposits, Hutchinson R.W., Spence C.D., Franklin J.M., Editors Geological Association of Canada. p.255-295.

Lange I M., Nokleberg W.J., Newkirk S.R., Aleinikoff J.N., Church S.E., Krouse H.R., 1993 Devonian Volcanogenic Massive Sulfide deposits and Occurrences, Southern Yukon-Tanana Terrane, Eastern Alaska Range, Alaska *Economic Geology,* v.**88**, p.344-376.

Large R.R. 1977. Chemical evolution and zonation of massive sulfide deposits in volcanic terrains. *Economic Geology,* v.**72**, p.549-572.

Large R R., McGoldrich P.J., Berry R.F., Young C.H. 1988. A Tightly Folded, Gold-Rich, Massive sulfide Deposit. Que River Mine, Tasmania. *Economic Geology,* v **83**, p.681-692.

Large R.R. 1992. Australian Volcanic-Hosted Massive Sulfide Deposits: Features, Styles, and Genetic Models. *Economic Geology,* v.**87**, p.4711510.

Large R.R., Gemmell J.B., Paulick H. in press. The alteration box plot: A simple approach to understanding the relationship between alteration mineralogy and lithogeochemistry associated with VHMS deposits. *Economic Geology* Special Issue: Alteration and its exploration significance with the spectrum of volcanic hosted massive sulfide deposits

Larocque A C L., Hodgson C.J., Lafleur P.J 1993. Gold Distribution in the Morbrun Volcanic-Associated Massive Sulfide Deposit, Noranda, Quebec: A preliminary evaluation of the role of metamorphic remobilisation. *Economic Geology,* v.**88**, p.1443-1459.

Larocque A.C.L. and Hodgson C.J. 1995. Effects of Greenschist-facies metamorphism and related deformation on the Mobrun massive sulfide deposit, Quebec, Canada. *Mineralium Deposita,* v.**30**, p 439-448.

Leistel J.M., Marcoux E., Thieblemont D , Quesada C., Sanchez A., Almodovar G.R., Pascual E , Saez R. 1998 The Volcanic-hosted massive sulfide deposits of the Iberian Pyrite Belt. *Mineralium Deposita,* v.**33**, p.2-30.

Leitch C.H.B. and Lentz D.R 1994. The Gresens Approach to Mass Balance Constraints of Alteration Systems. Methods, Pitfalls, Examples, in Alteration and Alteration Processes associated with Ore-forming Systems. *Geological Association of Canada, Short Coarse Notes,* Lentz D R. (Ed). p 161-192.

Lianxing G. and McClay K.R. 1992. Pyrite deformation in stratiform lead-zinc deposits of the Canadian Cordillera. *Mineralium Deposita,* v.**27**, p.169-181.

Lusk J. and Crocket J.H. 1969. Sulfur isotope fractionation in co-existing sulfides from the Heath Steele B-i orebody, New Brunswick, Canada. *Economic Geology*, v.**64**, p.147-155.

MacLean W.H and Kranidjotis P.1987. Immobile Elements as Monitors of Mass Transfer in Hydrothermal Alteration: Phelps Dodge Massive Sulfide Deposit, Matagami, Quebec. *Economic Geology,* v.**82**, p.951-962.

MacLean W.H. 1990. Mass Change Calculations in altered rock series. *Mineralium Deposita,* v.**25**, p.44-49

MacLean W.H. and Barrett T.J. 1993 Lithogeochemical techniques using immobile element. *Journal of Geochemical Exploration,* v.**48**, p.109-i 33.

Maitre R.W.L. 1984. A proposal by the IUGS Subcommission on the Systematics of Igneous Rocks for a chemical classification of volcanic rocks based on the total alkali silica (TAS) diagram. *Australian Journal of Earth Sciences,* v.**31**, p.243-255

Marcoux E., Moelo Y., Leistel J.M. 1996 Bismuth and cobalt minerals as indicators of stringer zones to massive sulfide deposits, Iberian Pyrite Belt. *Mineralium Deposita,* v.**31**, p.1-26.

Markham N L and Lawrence L.J. 1965. Mawsonite, a new copper-iron-tin sulfide from Mt Lyell, Tasmania and Tingha, New South Wales. The American Mineralogist, v.**50**, p.900-908.

Markham N.L. 1968. Some genetic aspects of the Mt Lyell mineralisation *Mineralium Deposita,* v.**3**, p.199-221.

Marquis P., Hubert C., Brown A.C., Rigg D M. 1990. Overprinting of early, redistributed Fe and Pb-Zn mineralisation by late stage Au-Ag-Cu deposition at the Dumagami mine, Bousquet district, Abitibi, Quebec. *Canadian Journal of Earth Sciences,* v.**27**, p.1651-1671.

Marshall B. and Gilligan L.B. 1987. An introduction to remobilisation· information from ore-body geometry and experimental considerations. *Ore Geology Reviews,* v.**2**, p.87-131.

Massey N.W.D. 1992-4. Geology and Mineral Resources of the Duncan Sheet, Vancouver Island 92B/13. Mineral resources division - Geological Survey Canada.

Mathias G K., Simmons S.F., Fleming J. 1995. High sulfidation alteration at the Island Copper Porphyry Copper deposit Vancouver Island, Canada. *in* PACRIM 1995 abstract volume. Auckland, New Zealand: Australian Institute of Mining and Metallurgy.

McArthur G.J. 1996. Textural evolution of the Hellyer massive sulfide deposit Unpublished PhD thesis University of Tasmania.

McClay K.R. and Ellis P.G. 1983. Deformation and recrystallisation of Pyrite. *Mineralogical Magazine,* v.**47**, p 527-538.

McClay K.R. and P.G. Ellis P.G. 1984. Deformation of Pyrite. *Economic Geology* v.**79**, p.400-403

McClay K R 1991 Deformation of stratiform Zn-Pb-(barite) deposits in the northern Canadian Cordillera. *Ore Geology Reviews,* v.**6**, p.435-462.

McKinley S.D , C.A. Pearson CA, Juras S.J. 1997. Paleotopography and ore zonation of the Battle Zn-Cu-Au-Ag VMS Deposit, Vancouver Island, British Columbia. *in* 50th Anniversary GAC/MAC Annual Meeting. Ottawa.

McMillan W.J. and Panteleyev A. 1996. Porphyry deposits of the Canadian cordillera. *Geoscience Canada,* v.**23**, p.125-133

McPhie J., Doyle M., Allen R. 1993. Volcanic textures: A guide to the interpretation of textures in volcanic rocks Hobart· Tasmanian Government Printing Office. 198p

Mookherjee A. 1976. Ores and metamorphism: temporal and genetic relationships, in Handbook of strata-bound and stratiform ore deposits. Wolf K.H., (ed). Elsevier: Amsterdam. p.203-260

Morimoto N., Koto K., Shimazaki Y 1969. Anilite, Cu_7S_4, a new mineral. *The American Mineralogist,* v.**54**, p.1256-i 268.

Morimoto N. and Koto K. 1970. Phase relations of the Cu-S system at low temperatures stability of anillite. *The American Mineralogist,* v.**55**, p.106-1 17.

Muller J.E., Northcote K.E , Carlisle D. 1974. Geology and Mineral Deposits of the Alert Bay - Cape Scott Map-Area, Vancouver Island, British Columbia. *Geological Survey of Canada, Paper,* 74-8.

Muller J.E. 1977. Evolution of the Pacific Margin, Vancouver Island, and adjacent regions. *Canadian Journal of Earth Science,* v.**14**, p 2062-2085.

Muller J.E. 1980 The Paleozoic Sicker Group of Vancouver Island, British Columbia. *Geological Survey of Canada Paper,* v.**70-30**.

Ney C.S., Cathro R.J. Panteleyev A., Rotherham D.C 1976. Supergene Copper Mineralisation CIM Special Volume, *Porphyry Deposits of the Canadian Cordlilera* v.**15**, p.72-78.

Nixon G.T., Hammack J.L., Koyanagi V.M., Payie G.J. Panteleyev A., Massey N.W.D., Hamilton J.V. 1994 Preliminary geology of the Quatsino - Port McNeil Map areas, Northern Vancouver Island (92L/12,11), British Columbian Geological Survey Branch.

Ohmoto H. 1972. Systematics of sulfur and carbon isotopes in hydrothermal ore deposits. *Economic Geology,* v.**67**, p.551-578

Ohmoto H and Rye R.O. 1979. Isotopes of sulfur and carbon, *in* Geochemistry of hydrothermal ore deposits, Barnes H.L (ed), p.509-567.

Ohmoto H. and Skinner B.J. 1983. The Kuroko and related volcanogenic massive sulfide deposits. *Economic Geology,* **Monograph 5**, 604p.

Ohmoto H. 1986. Stable isotope geochemistry of ore deposits, *in* Stable isotopes in High Temperature Geological Processes, Taylor J.W and O'Neil (eds), Mineralogical Society of America, p.491-560.

Orlandi P., Merlino S , Duchi G., Vezzalini G. 1981. Colusite. A new occurrence and crystal chemistry. *Canadian Mineralogist,* v.**19**, p.423-427.

Orth K and Hill A.P. 1994. Textures and origins of carbonate associated with the Rosebery VHMS deposit *Contentious Issues in Tasmanian Geology,* GSA Tasmanian Division, Hobart 3-4 November p105.

Padgham WA. 1981. Western Mines - Myra, Lynx and Price Deposits. *CIM Bulletin,* v.74, p.106-108.

Pascual E. Toscano M., Almodovar G.R., Saez R. 1997. Zirconium mobility in footwall hydrothermal haloes in the Ibenan Pyrite Belt· geochemical and textural evidences. SEG Neves Corvo Field Conference - Abstract Volume, May 11-14.

Pearce T.H. 1968. A contribution to the theory of variation diagrams *Contributions to Mineralogy and Petrology,* v.**19**, p.142-157.

Pearce J.A. and Cann J.R. 1973. Tectonic setting of basic volcanic rocks determined using trace element analysis. *Earth and Planetary Science Letters,* v.**19**, p.290-300.

Pearson CA. 1993. Mining Zinc-Rich Massive Sulfide Deposits on Vancouver Island, British Columbia *in* International Symposium - World Zinc 93. Hobart, Australia.

Pearson C.A. 1997. Minesite Exploration - The Lifeblood of Myra Falls Operations in *CIM Conference v 97* Vancouver, British Columbia, Canada.

Pearson C.A., Juras S.J., and McKinley S.D.1 997. Paleotopography and Ore Zonation of the HW and Battle Zn-Cu-Au-Ag VMS Deposits, Myra Falls Camp, Vancouver Island, British Columbia, Canada. *in SEG Field Conference.* 1997 Neves Corvo - Lisbon, Portugal.

Peter J.M. and Scott S.D. 1988. Mineralogy, composition, and fluid-inclusion microthermometry of seafloor hydrothermal deposits in the southern trough of Guaymas basin, Gulf of California. *Canadian Mineralogist,* v **26,** p 567-587.

Pisutha-Arnond V. and Ohmoto H. 1983 Thermal History, and Chemical and Isotopic Compositions of the Ore-Forming Fluids Responsible for the Kuroko Massive Sulfide Deposits in the Hokuroku District of Japan. *Economic Geology* **Monograph 5**, p.523-558

Pontual S., Merry N., Gamson P.1997. G-Mex Vol 1, Spectral Interpretation Field Manual. Ausspec International Pty. Ltd.

Poulton T.P. , Chapter 8, Part A. Ancestral North America Upper Devonian to Middle Jurassic Assemblages, *in* Geology of the Cordilleran Orogen in Canada, H. Gabrielse and C.J. Yorath, Editors. 1991, Geological Survey of Canada p.219-327.

Ramdohr P.1979. The ore minerals and their intergrowths. Vol.2. Pergamon Press

Ramsay J.G. 1979 Shear zone geometry: a review. *Journal of Structural Geology,* **v1**, p 83-99.

Reid R.R. 1993. Westmin Structure 18 and 20 Level Data. Westmin Resources Ltd internal company report.

Robinson B.W. and Kusakabe M. 1975. Qantitive preparation of SO_2 for $^{34}S/^{32}S$ analyses from sulfides by combustion with cupreous oxide. *Analytical Chemistry,* v.**47**, p.1179-1181.

Robinson M. 1992. Geology, Mineralisation and alteration of the Battle Zone, Buttle Lake Camp, Central Vancouver Island Southwestern British Columbia. M.Sc. thesis, The University of British Columbia.

Robinson M., Godwin C.I., Juras S.J. 1994. Major Lithologies of the Battle Zone, Buttle Lake Camp, Central Vancouver Island *in Selected mineral deposits of British Columbia, Canada* Society of Economic Geologists. p 45-58.

Robinson M , Godwin C.I., Stanley C.R. 1996. Geology, Lithogeochemistry, and Alteration of the Battle Volcanogenic Massive Sulfide Zone, Buttle Lake Mining Camp, Vancouver Island, British Columbia. *Economic Geology,* v **91**, p.527-548.

Rollinson H. 1993. Using Geochemical Data: evaluation, presentation, interpretation. Addison Wesley Longman Limited, Essex, England. 352p.

Rona P.A. and Scott S.D. 1993. A special Issue on Sea-Floor Hydrothermal Mineralisation New Perspectives *Economic Geology,* v.**68**, p.1935-1957.

Rubin J.N., Henry C.D., Price J.G. 1993. The mobility of zirconium and other "immobile" elements during hydrothrmal alteration *Chemical Geology,* v. **110**, p.29-47.

Rye R.O. Roberts R.J., Snyder W.S., Lahusen G.L., Motica J.E. 1984. Textural and stable Isotope Studies of the Big Mike Cupriferous Volcanogenic Massive Sulfide Deposit, Pershing county, Nevada. *Economic Geology,* v.**79**, p.124-140.

Sato T. 1972. Behaviours of ore-forming solutions in seawater *Mining Geology,* v **22**, p.31-42.

Schandl E.S. and Bleeker W. 1999 Hydrothermal and metamorphic fluids of the Kidd Creek Volcanogenic Massive Sulfide Deposit: Preliminary evidence from fluid inclusions. *Economic Geology,* **Monograph 10**, p.379-388

Scott S.D. 1983. Chemical behaviour of sphalerite and arsenopyrite in hydrothermal and metamorphic environments. *Mineralogical Magazine,* v **47**, p.427-435.

Seccombe P.K Godwin C.I., Krouse H.R., Juras S.J 1990. Sulfur and lead isotopic studies of the Buttle Lake Massive Sulfide deposit, Vancouver Island, B.C., Canada: Sources of ore constituents in a submarine exhalative environment. *in Pacific Rim 90 congress* Gold Coast, Queensland, Australia: The Australian institute of Mining a Metallurgy.

Seraphim R.H. 1980. Western Mines - Myra, Lynx and Price Deposits. *CIM Bulletin:* December, p.71-90.

Shikazono N , Hoshio M., Utada M., Nakata M., Ueda A. 1998. Hydrothermal carbonates in altered wall rocks at the Uwamuki Kuroko deopsit, Japan. *Mineralium Deposita,* v.**33**, p.346-358.

Sillitoe R.H., Hannington M.D., Thompson J.F.H. 1996. High Sulfidation Deposits in the Volcanogenic Massive Sulfide Environment. *Economic Geology,* v.**91**, p.204-212.

Sinclair B.J. and Gemmell J.B. 1998. The Gap an unusual bornite-rich VHMS ore body, Myra Falls District, B.C. Canada *in 14th Australian Geological Convention.* Townsville: Geological society of Australia.

Sinclair B.J., Gemmell J.B Berry R., Juras S.J. 1997. Geology of the Battle Zone, Myra Falls VHMS Deposit Vancouver Island *in* 50th Anniversary GAC/MAC Annual Meeting. Ottawa.

Smith R.N. and Huston D.L. 1992 Distribution and Association of Selected Trace Elements at the Rosebery Deposit, Tasmania *Economic Geology,* v.**87**, p.706-719.

Solomon M., Vokes F M., Waishe J.L. 1987. Chemical remobilisation of volcanic-hosted sulfide deposits at Rosebery and Lyell, Tasmania. *Ore Geology Reviews,* v.2, p.173-190.

Solomon M., Eastoe C.J., Waishe J L., Green G.R. 1988. Mineral Deposits and Sulfur Isotope Abundances in the Mount Read Volcanics between Que River and Mount Darwin, Tasmania. *Economic Geology,* v.**83**, p.1307-1328.

Spry P.G., Marshall B , Vokes F M. 2000 Metamorphosed and metamorphogenic ore deposits *Reviews in Economic Geology,* v **11**, p.310

Stanely C.R. and Madeisky H.E. 1994. Lithogeochemical exploration for hydrothermal ore deposits using Pearce Element Ratio Analysis, *in* Alteration and Alteration Processes associated with Ore-forming Systems, Lentz, D.R. (ed). Geologic Association of Canada, Short Coarse notes. p.193-211.

Stanton R.L. 1964. Mineral Interfaces in Statiform Ores. Institute of mining and Metallurgy.

Stanton R.L. 1972 Ore Petrology. McGraw-Hill.

Steven S. 1974 Polymetallic sulfide Deposits, in Stable Isotope Geochemistry of Low Temperature Fluids. Kyser, T.K. (ed) Mineralogical Association of Canada.

Sutherland-Brown A. and Yorath C.J., *Lithoprobe Profile across southern Vancouver Island· Geology and Tectonics. Trip* 8 Field Trip Guide Book.

Sutherland-Brown A and Yorath C.J. 1999 Structural geology of the Alberni Region, in *Lithoprobe, Southern Vancouver Island British Columbia: Geology,* C.J. Yorath, A.Sutherland-Brown, and N.W.D Massey, (eds), Geological Survey of Canada. p.89-96.

Thompson F.H., Sillitoe R.H., Hannington M.D 1996. Magmatic contributions to sea floor deposits· Exploration implications of a high sulfidation VMS environment. *in* New Mineral Deposit Models of the Cordillera - 1996 Cordilleran Roundup Short Coarse, Vancouver, B.C.

Thorpe R I., Pringle G.J , Plant A.G. 1976 Occurrence of selenide and sulfide minerals in bornite ore of the Kidd Creek massive sulfide deposits, Timmins, Ontario. Geological Survey of Canada Paper 761A, p.311-317.

Tourigny G. Brown A.C , Hubert C., Crepeau R. 1989. Synvolcanic and Syntectonic Gold Mineralisation at the Bousquet Mine, Abitibi Greenstone Belt, Quebec. *Economic Geology,* v.**84**, p.1875-1690.

Tourigny G., Doucet D., Bourget A. 1993 Geology of the Bousquet 2 Mine: An example of a deformed, gold-bearing polymetallic sulfide deposit. *Economic Goology,* v.**88**, p.1578-1597.

Vokes F.M. 1969. A review of the metamorphism of sulfide deposits. *Earth Science Reviews,* v.5, p.99-143.

Vokes F M. and Craig J.R. 1993. Post-recrystallisation mobilisation phenomena in metamorphosed stratabound sulfide ores. *Mineralogical Magazine,* v.**57**, p.19-28.

Walker R.R. 1980 Western Mines - Myra, Lynx and Price deposits: A discussion. *Canadian Institute of mining and metallurgy Bulletin,* v.**73**, p.86-88.

Walker R.R. 1983. Westmin Resources Massive Sulfide deposits, in G.A.C. - M.A.C. - C.G.U. Field trip guidebook, Trip 9, May 13-16. P.W.J. Fleming, Editor. p.5-19.

Walker R.R. 1985. Westmin Resources Massive Sulfide Deposits, Vancouver island , *in* Geological Society of America, Cordilleran Section Meeting, May 1985, Vancouver, B.C., Field Trip Guidebook. p.1-13.

Walshe J.L. and Solomon M. 1981. An Investigation into the Environment of Formation of the Volcanic Hosted Mt. Lyell Copper Deposit Using Geology, Mineralogy, Stable Isotopes, and a Six-Component Chlorite Solid Solution Model. *Economic Geology,* v.**76**, p.246-284.

Wiggins L.B. and Craig J.R. 1980. Reconnaissance of the Cu-Fe-Zn-S system· sphalerite phase relationships. *Economic Geology,* v.**75**, p.742-751.

Winchester J.A and Floyd P.A. 1976. Geochemical magma type discrimination: Application to altered and metamorphosed basic igneous rocks. *Earth and Planetary Science Letters,* v.**28**, p.459-469.

Yole R.W. 1963. An Early Permian Fauna from Vancouver Island, British Columbia. *Canadian Petroleum Geologists Bulletin* v.**11**, p.138-149.

Yole R.W. 1965. A faunal and stratigraphic study of Upper Paleozoic rocks of Vancouver Island, British Columbia. Unpublished Ph.D. thesis, The University of British Columbia. 254p.

Yole R.W. 1969. Upper Paleozoic stratigraphy of Vancouver Island, British Columbia. *The Geological Association of Canada Proceedings,* v **20**, p.30-40

Yorath C.J. 1991. Upper Jurassic to Paleogene Assemblages: Chapter 9, in Geology of the Cordilleran Orogen *in* Canada, H. Gabrielse and C.J. Yorath, (eds). Geological Survey of Canada. p.329-371.

Yorath C.J and Nasmith H.W 1995. The Geology of Southern Vancouver Island - A Field Guide. Orca Book Publishers.

Yorath C.J., Southerland-Brown A., Massey N.W D. 1999. Lithoprobe, Southern Vancouver Island, British Columbia. *Geology* Geological Survey of Canada Bulletin, v.**498.**